Strongly interacting color-singlet exchange and photon exchange in high-energy proton-proton collisions

©2021

Cristian Xavier Baldenegro Barrera

Submitted to the graduate degree program in Department of Physics and Astronomy and the Graduate Faculty of the University of Kansas in partial fulfillment of the requirements for the degree of Doctor of Physics.

Committee members

Dr. Christophe Royon, Chairperson

Dr. Daniel Tapia Takaki

Dr. Michael Murray

Dr. Kyoungchul Kong

Dr. Jorge L. Soberón

Date defended: August 13, 2021

The Dissertation Committee for Cristian Xavier Baldenegro Barrera certifies that this is the approved version of the following dissertation :

Strongly interacting color-singlet exchange and photon exchange in high-energy proton-proton collisions

Dr. Christophe Royon, Chairperson

Date approved: August 13, 2021

Abstract

The CERN Large Hadron Collider (LHC) offers a unique opportunity to test the Standard Model (SM) of particle physics, the quantum field theory of elementary interactions, at the shortest distances probed in a laboratory. In this context, we want to identify and understand some of the emergent properties of the strong interaction, described by quantum chromodynamics (QCD). At the same time, we strive to find signatures of physics beyond the SM, in the hope that we can thereby develop an improved theory of fundamental interactions. In this vein, the work presented in this thesis is two-fold. First, we present the measurement of events where the two highest transverse momentum (p_T) jets are separated by a pseudorapidity interval devoid of particle activity, known as "jet-gap-jet" events, in proton-proton (pp) collisions at $\sqrt{s} = 13$ TeV with the CMS experiment. The signature is expected from hard color-singlet exchange, which corresponds to t-channel two-gluon exchange in perturbative QCD (pQCD), known as perturbative pomeron exchange. The fraction of events produced via color-singlet exchange, f_{CSE}, is measured as a function of dijet kinematic variables of interest. We obtain the most precise experimental value of f_{CSE} in an unexplored region of phase-space. The results are compared with previous measurements and with predictions from pQCD. In addition, we present the first study of jet-gap-jet events produced in association with an intact proton detected in the Roman pot (RP) detectors of the TOTEM experiment (effectively a "p-gap-jet-gap-jet" topology) in a joint CMS-TOTEM analysis. The fraction f_{CSE} is larger in this subsample of events. Furthermore, an analysis of diffractive dijet events at $\sqrt{s} = 13$ TeV, where at least one of the protons exchanges a pomeron, is presented. The study can help better elucidate the diffractive structure function of the proton in a larger kinematic domain in the fraction of the beam momentum carried by the pomeron and the four-momentum

transfer squared at the proton vertex. Also, the first investigation of double-pomeron exchange dijet events with two intact protons is presented ("p-gap-jet-jet-gap-p"). The second aspect of this thesis has to do with the phenomenology of new physics manifestations in photon-photon interactions. We consider central exclusive production reactions, $pp \to pXp$, where X is a hard-scale system produced by two-photon fusion and the forward protons are detected in RPs. We focus on projections for massive axion-like particles (ALPs) coupled to the electromagnetic field, which induces anomalous contributions to the scattering of light-by-light ($\gamma\gamma \to \gamma\gamma$). We make projections for the ALP–photon coupling for ALPs masses at the TeV scale. We also present a phenomenology analysis of anomalous $\gamma\gamma \to \gamma Z$ scattering using the proton tagging technique. Our projections for the anomalous coupling strength associated to dimension-eight $\gamma\gamma\gamma Z$ operators surpass the existing and projected constraints from the measurement of the branching fraction of $Z \to \gamma\gamma\gamma$ by about three orders of magnitude. Finally, a phenomenology study that targets the analysis of the SM and anomalous $\gamma\gamma \to WW$ scattering in the hadronic and semi-leptonic channels is presented. Updated projections on the coupling strengths for anomalous dimension-six $\gamma\gamma WW$ operators are presented.

This thesis is dedicated to my parents, and to the memory of my auntie Kina, my uncle Conrado, and my uncle Héctor.

Acknowledgements

I want to thank my advisor, Christophe Royon, for receiving me and welcoming me to his research group at the University of Kansas as his Ph.D. student in 2016. When I was in my last year of undergrad, I was looking into working on jet-related measurements and on particle physics phenomenology studies for my graduate degree. Christophe not only gave me the opportunity to work on these topics, he also encouraged me to conduct my research in a highly independent manner very early on, which fitted my style pretty well. He also provided me with the opportunity to embark in many other tasks related to academic life, such as directly being involved in conference organization, grant applications, and student mentorship. Christophe always encouraged me to present my work in numerous workshops and conferences, and motivated me to sharpen my training at various schools of high-energy physics. I feel very privileged that I had all these opportunities and experiences throughout my Ph.D., giving me a solid foundation for the rest of my career, and I will always be grateful to my supervisor for this.

I want to thank Daniel Takaki and Michael Murray for their advice and support on my professional career over my years as a Ph.D. student at KU. Thanks!

I would like to thank the members of my thesis committee for their feedback and for their careful reading of this document.

I am very grateful to all the colleagues and friends of the research group at KU, past and present: Hussein Al-Ghoul, Timothy Raben, Laurent Forthomme, Nicola Minafra, Georgios Krintiras, Guillaume Biagi, Federico Deganutti, William Doumerg, Florian Gautier, Gauthier Legras, Tommaso Isidori, Maxime Massa, Cole Lindsey, Zachary Warner, and Justin Williams. I also want to acknowledge the rest of the KU nuclear group for their support: Prof. Takaki, Prof. Murray, Prof. Sanders, Juan Marquez, Cole LeMahieu,

Matthew Nickel, and Quan Cheng.

I am also thankful to my CMS-TOTEM forward physics and small-x QCD colleagues. Thank you, Ksenia Shchelina, for helping me get my analysis framework up and running at the beginning of my Ph.D. I also want to thank Robert Ciesielski, whose contagious enthusiasm for diffraction and small-x physics kept me excited during the evolution of my analysis and the various internal reports within CMS and TOTEM. I am grateful to the SMP and SMP-HAD conveners who provided feedback and guidance during the review of the analysis, as well as the CMS-TOTEM analysis review committee members Ferenc Siklér, Máté Csanád, Mike Albrow, Stephen Sanders, Kenneth Oesterberg, Vincenzo Berardi, and Mario Deile for their efforts and help. I am thankful to Jan Kaspar and Georgios Krintiras for giving me the opportunity of contributing to the service tasks of the CMS collaboration with the PPS and LUM POG activities during my Ph.D. I wish to thank the engineers and technicians that operate the CERN LHC, as well as all the CMS and TOTEM colleagues who participated in the data taking and the following calibration of the data. Without calibrated, high-quality data, it would not have been possible to undertake my research.

I also want to thank my collaborators Sylvain Fichet, Gero von Gerdsdorff, Laurent Schoeffel, Samira Hassani, Michael Klasen, Jens Salomon, Pablo González, Mats Kampshoff, Michael Pitt, and Andrea Bellora for all the useful discussions and collaboration during my Ph.D. years.

I want to thank also the professors who mentored me in numerous ways at Universidad de Sonora during my undergraduate studies: Profs. María Elena Tejeda Yeomans, Carlos Calcáneo Roldán, Laura Lorenia Yeomans Reyna, and Antonio Jáuregui Díaz. I will be lucky if eventually I am at least 1% the scientists, mentors, and teachers you all were to me.

I want to thank Kristin Renells, Joel Sauerwein, Kayla Wegley, without whom the Department of Physics & Astronomy would surely crumble apart in flames! I want to

thank also Hume Feldman and Gregory Rudnick for their service to our department as Head and Director of Graduate Studies, respectively.

I want to thank the U.S. Department of Energy, the state of Kansas, the American Physical Society, and the taxpayers of the state of Kansas and of the U.S. for funding my research activities, conference attendance, and the various trips to CERN. Without this support, I would not have been able to carry out my research and complete my postgraduate studies. I also want to thank the taxpayers of Sonora and Mexico, whose contribution helped finance Universidad de Sonora's costs of operation, my Summer internships, and conference attendance while I was an undergraduate student. Thank you.

I am grateful to my parents, Arturo and Norma, who have unconditionally supported my career decisions and my studies enthusiastically with all the love in the world that they could possible give — which is impossible to quantify —. When I was around sixteen years-old in high school, and I expressed my interest in investing my professional life in a scientific career, my parents told me "*Well, we will support you, of course. But just so you know, you may have to do a Ph.D. in Physics eventually if you want to do Physics for a living. Are you sure you will be ready for that?*" To that, I answered "*Yeah, sure! Whatever that means. That is a problem for future Cristian.*" You see, I was just so excited to study Physics and do Physics for a living. So, here I stand paying the consequences of sixteen year-old Cristian's decision! I also would like thank my siblings Arturo, Daniel, Herman, as well as the newest member of our family, Shuang Ye (Caroline), wife of Daniel, for being there to cheer me up and for checking on me. I want to thank also my aunts, uncles, cousins, and grandmother for their support and for keeping up with my well-being during my Ph.D.

I am also deeply in debt and forever grateful to my friend, Cristina, who I tortured almost every evening during my Ph.D. with impromptu phone call conversations, particularly during the beginning of my Ph.D. studies. Thank you for our friendship, and thank you for always being there for me. I also want to thank my friend Luis Alberto ("Wisho")

for his friendship and for always being available to talk with and to bounce ideas about academic life, pop culture, and life in general.

I want to thank Tommaso for his friendship and companionship as a colleague, roommate, and friend. Thank you for inviting me to be a bit more outgoing, for teaching me that hiking is walking over anything other than concrete (!), and for reminding me to relax every now and then. I want to thank my long-time friend and roommate Pavel for his support throughout my higher-education years, as well as for introducing me to the world of physics together with Wisho when we were in high school. I want to thank all my friends who made my stay in Lawrence fun and pleasurable: Tommaso, Pavel, Hanna, Michell, Svetla, Calvin, Bryce, Zach, Alyssa, Cole, Justin, Sasha, Galya, Nick, Marcela, Tim, Hussein, James, and in general the graduate student peers I interacted and hung out with throughout these years in Lawrence.

Finally, I would like to offer my appreciation to all the places and centers that helped me relax during graduate school. Thanks to all the Lawrence and Kansas City area parks and hiking trails, their Final and First Friday's art gallery exhibitions, all the coffee shops and their baristas who warmly welcomed me (S&S, J&S, Sid and Nancy's, Signs of Life). I want to especially thank the baristas at Sunflower Outdoors & Bike Shop — my effective co-workers at the end of my Ph.D. — who cheered me up during the writing portion of my thesis and who prepared close to 10^6 cups of cortados, macchiati, beers, and americanos. I want to thank also the Lawrence Arts Center and Hobart Jackson Jr.'s open model drawing groups for welcoming me and giving me the space to express myself artistically via open model drawing.

Contents

Chapter 1

Preface

The Standard Model (SM) of elementary particles encompasses our current picture of the world at small distances. These elementary particles are excitations of quantum fields that permeate all space in the Universe. In this picture, the electron is an excitation of the electron field. The interaction between elementary particles is mediated by force-carrying particles exchanged between them. For instance, an electron interacts with another electron by exchanging a photon, the particle of light. These interactions can be treated mathematically in the framework of quantum field theory, which allows us to make predictions that can be contrasted to measurements in the laboratory.

Three of the four fundamental forces of Nature are described within the SM: electromagnetism, the weak force —responsible for nuclear decays & nuclear fusion, for example—, and the strong nuclear force —the force that binds protons and nucleons together—. The fourth fundamental force of Nature, gravity, is described by the theory of general relativity, where gravity is a deformation of spacetime in presence of energy and flow of momentum at a given point in spacetime, and is yet to be included in a quantum theory of elementary interactions. To this date, we know of twelve spin-$\frac{1}{2}$ fermions (quarks and leptons), twelve spin-1 gauge bosons that act as carriers of the fundamental forces (the photon for the electromagnetic force, the Z, W^+ and W^- bosons for the weak force, and eight gluons for the strong nuclear force), and one spin-0 boson that appears as a consequence of a spontaneous symmetry breaking mechanism (Higgs boson), which results in endowing particles with mass.

The SM has been thoroughly tested over the last decades in experimental high energy

physics. There are, however, several aspects of the SM that we are still trying to understand and test in the experiment. In one hand, we are trying to understand the non-trivial emergent properties expected from the SM, particularly in the sector of strong interactions. On the other hand, we are trying to find corners of the parameter and phase space where potential deviations from the SM expectations could be observed in the data, and provide us with a clear lead on possible extensions of the SM. One way of further understanding the SM is by judiciously studying short-distance physics interactions in high-energy proton-proton collisions at the CERN Large Hadron Collider (LHC). In this thesis, we consider two main fronts of research: the first one is the experimental investigation of emergent properties of strong interactions that are expected from the basic building blocks of quantum chromodynamics (QCD), the theory of the strong interaction, with the Compact Muon Solenoid (CMS) and TOTal Elastic and diffractive cross section Measurement (TOTEM) experiments. The second one is related to phenomenology efforts to extend our current theory of elementary interactions in pure gauge boson interactions in photon-photon physics and analyzing possible ways that new physics may yield different signatures in the measurement of a family of vector boson fusion scattering processes.

For the first aspect of this thesis, we focus on the strong interaction sector. In some of the high-energy proton-proton collisions at the LHC, the quarks and gluons from the colliding protons may interact to produce energetic quarks and gluons that carry a substantial amount of momentum transverse to the beam. These quarks and gluons manifest experimentally as energetic jets –collimated sprays of hadrons–. One can use perturbation theory to calculate the partonic cross section as a power series on the strong coupling α_s, which is then convolved with the nonperturbative, process-independent parton distribution functions of the proton. Such calculations are further supplemented with parton showering and hadronization effects, as well as underlying event activity to model the additional low momentum transfers that may take place in the collision. This technique works remarkably well for the phase-space region probed by most analyses carried out

by the experiments at the LHC. This is excellent, since it means we can reliably use perturbation theory to obtain high precision predictions and look for deviations of the SM for a large region of phase space.

Nevertheless, there are good theoretical reasons to expect that the standard fixed-order perturbative QCD (pQCD) corrections shall break down at some point, even in the presence of a hard energy scale. One such interesting kinematic region identified by the community is the *high-energy limit* of particle scattering, i.e., the limit where the center-of-mass energy of the colliding partons is much larger than any other momentum scale. In the context of QCD, Feynman diagrams with t-channel gluon exchange and multiple s-channel gluon emissions contribute significantly to the cross section in the high-energy limit. This is translated to large logarithms of the center-of-mass energy squared s that multiply the strong coupling $\alpha_s \ll 1$, in a way such that it compensates for the smallness of the strong coupling with terms of the form $\alpha_s^n \ln^n(s/s_0) \lesssim 1$ for $n = 1, 2, 3, \ldots$, where $s_0 \ll s$ is another characteristic momentum scale of the problem. In other words, one cannot rely on fixed-order pQCD techniques to calculate the cross section, since restricting the calculation at a given order in α_s ignores other diagrams that are of equal size with multiple parton emissions. Diagrams with multiple s-channel gluons strongly ordered in rapidity carrying similar amounts of momenta yield the leading contributions in this limit. In this case, one needs to sum up all these multi-gluon diagrams systematically in a procedure known as "resummation." This resummation is carried out via the Balitsky–Fadin–Kuraev–Lipatov (BFKL) evolution equations of pQCD, a renormalization group equation related to the evolution of scattering amplitudes as a function of the collision energy. Similar renormalization group equations are obtained in other contexts in QCD, for instance the equation describing the running of α_s with the momentum scale, which gives rise to the property of asymptotic freedom in QCD.

Upon solving the BFKL evolution equation for the cross section in the high-energy limit, one obtains that the cross section for parton-parton scattering scales with a power

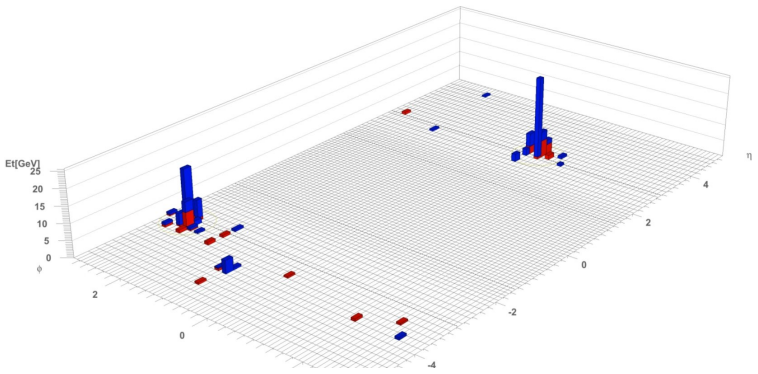

Figure 1.1: Event display of a jet-gap-jet candidate recorded by the CMS detector in pp collisions at 13 TeV (Event:248391105, Run:259431). The blue and red towers represent the hadronic and electromagnetic energy deposits in the detector, respectively. Each tower as a transverse energy larger than $E_{\mathrm{T}} > 1$ GeV in this event display. The jets have $p_T > 40$ GeV and $|\eta_{\mathrm{jet1,2}}| > 1.4$. The interval in pseudorapidity between the jets has no charged-particle tracks with $p_{\mathrm{T}} > 200$ MeV.

of the center-of-mass energy. This is the most famous prediction of the BFKL evolution equation of pQCD. The behavior of QCD in the high-energy limit is one of the key predictions of pQCD, and yet it remains elusive experimentally. It is generally believed that, at the current LHC energies, we might be sensitive to pre-asymptotic effects by considering certain kinematic configurations that would favor significantly the onset of BFKL dynamics. However, such effects are hard to isolate cleanly in the data, since other higher-order corrections, such as those treated within the Dokshitzer–Gribov–Lipatov–Altarelli–Parisi (DGLAP) evolution, are hardly suppressed.

In this context, the author of this thesis conducted a detailed measurement of events where the two highest-p_T jets are separated by a pseudorapidity interval void of charged-particle tracks in proton-proton collisions at $\sqrt{s} = 13$ TeV with the CMS and TOTEM Collaborations. A CMS event display for a candidate event is shown in Fig. 1.1. Such an event topology is referred to as "jet-gap-jet" or Mueller–Tang jets, and it is expected from a hard color-singlet exchange. While one gluon is always a color-octet charge, it follows from the SU(3) gauge symmetry of QCD that two or more gluons can form systems whose net color charge is singlet, octet, or higher multiplets. The hard color-singlet exchange between partons corresponds to t-channel two-gluon exchange in a color-singlet configu-

ration. When the two jets are largely separated in pseudorapidity, this hard color-singlet exchange is expected to be described by perturbative pomeron exchange. The perturbative pomeron exchange consists of two reggeized gluon ladder exchange. Upon a careful subtraction of the color-exchange dijet background —which dominates the inclusive dijet cross section—, the fraction of dijet events produced via color-singlet exchange was extracted as a function of several dijet kinematic variables of interest and was compared to predictions based on pQCD calculations in the BFKL framework. In addition, the case where at least one of the colliding protons remains intact and is detected with the Roman pots of TOTEM was considered. This is the first time this topology with two pseudorapidity gaps has been measured. The SMP-19-006 analysis, a paper signed by authors of both CMS and TOTEM Collaborations, has been published in Phys. Rev. D. (1). The author of this thesis was the analysis contact person and main contributor to the analysis. He was responsible for the derivation of the physics results, preparation of the analysis documentation, the paper draft, and of attending the feedback received by members of both experimental collaborations throughout the joint CMS-TOTEM internal review. The results of this analysis are covered in this thesis in Chapters 6 and 7, and are the main topic of this thesis.

Parallel to this measurement, the author contributed to the measurement of the diffractive production of dijets using the proton tagging technique ($pp \to pJJX$) at $\sqrt{s} = 13$ TeV with the CMS and TOTEM Collaborations. These dijets can be produced by color-singlet exchange off the proton. In the language of QCD, this would correspond to t-channel two-gluon exchange in a color-singlet configuration (pomeron exchange). Such a process can help us better elucidate the internal structure of the proton; more specifically its gluonic component and the spatial correlation between such gluons inside the proton. The phenomenon of hard diffraction is still not very well understood, and hence this study would help shed light on the properties of the color-singlet exchange off the proton. The progress on such analysis is reported in this thesis.

Another aspect of this thesis work has been on the phenomenological study of photon-induced interactions in high-energy proton-proton collisions using the proton tagging technique, i.e., reactions of the type $pp \to pXp$, where the central system X is produced by two-photon fusion $\gamma\gamma \to X$. Indeed, in these *ultraperipheral* collisions of protons — where the impact parameter is at least two times larger than the radius of the proton approximately—, the electromagnetic field generated by the colliding protons can be treated as a source of quasi-real photons. The energy spectrum and effective luminosity of these quasi-real photons is well-known theoretically from the electromagnetic form factors of the proton, which have been constrained in fixed target electron-proton elastic scattering measurements. Since photons are color-singlet particles, it is very likely that the proton remains intact after the quasi-real photon exchange. The process is also characterized by the presence of forward rapidity gaps between the central system X and the intact protons as a result of the null color-flow. This is in contrast to what is expected to occur in standard single-parton exchanges, where the net color-flow necessarily leads to the destruction of the colliding protons due to color confinement and the production of particles between the hard system and the protons' remnants.

Photon-induced interactions can be used to probe interactions that are otherwise very challenging to access in standard LHC analyses, particularly high-energy vector boson scattering with photon-fusion. For instance, one can probe in detail possible deviations from the SM expectations for the $\gamma\gamma \to \gamma\gamma, \gamma Z, ZZ, W^+W^-, t\bar{t} \ldots$ processes for masses at the TeV scale in an environment where the QCD-initiated backgrounds are highly suppressed. The work of the author on this direction has been mostly in collaboration with phenomenologists and with exchanges with members of the Precision Proton Spectrometer (PPS) group. The direct contribution of the author on these phenomenology studies has resulted in the publication of four few-authored articles in peer-reviewed journals(2; 3; 4; 5). Moreover, the work resulted in direct implementations of new physics processes in the Forward Physics Monte Carlo (`FPMC`) event generator, and has served as an input

for further experimental analyses by members of the ATLAS and CMS Collaborations. This work is described in detail in this thesis as well in Chapter 9.

1.1 Overview of this thesis

In Chapter 2, we introduce the basic elements of the SM of particle physics. Special attention is given to the QCD sector. In Chapter 3, we present the QCD collider phenomenology elements that we use to make predictions for high-energy proton-proton collisions at the LHC. In Chapter 4, we present the basics of the high-energy limit of QCD, the experimental probes of this regime. The topic of hard diffraction is discussed in Chapter 4 as well. In Chapter 5, we introduce the CERN LHC, and the CMS and TOTEM experiments. The measurement of jet-gap-jet events at $\sqrt{s} = 13$ TeV is split in two chapters: in Chapter 6, we present the measurement of jet-gap-jet events in inclusive dijet production ("CMS-only" measurement), whereas the measurement of jet-gap-jet events with an intact proton is covered in Chapter 7 ("CMS-TOTEM" measurement). In Chapter 8, we describe the progress and prospects on the measurement of diffractive dijet production at $\sqrt{s} = 13$ TeV with CMS and TOTEM. In Chapter 9, we give an overview of the phenomenology studies that the author of this thesis contributed to. A summary and prospects of the thesis work is laid down in Chapter 10. An Appendix with support material is presented at the end of this thesis.

Chapter 2

The Standard Model

In this Chapter, we summarize the basic theoretical foundations used to construct the Standard Model (SM), the quantum field theory of elementary interactions. Since this thesis targets both an understanding of the emergent properties of strong interactions, and a set of probes of physics beyond the SM, we discuss in detail how the structure of the interactions between the SM particles arise. In Section 2.1, we describe the particle content of the SM. In Section 2.2, we give an overview of the field theory basics. Gauge invariance as a dynamical principle is presented in Section 2.3. The discussion of the SM construction is broken down in two pieces: the electroweak interactions in Section 2.5 and the strong interactions sector in Section 2.6. Since the major part of this thesis is dedicated to the study of QCD, more detailed information on this sector will be covered. The physics we target in this thesis is related to that of the CERN Large Hadron Collider (LHC) with the CMS and TOTEM experiments. The phenomenology of hadron-hadron collisions is described in Chapter 4, and the LHC and detectors are described in Chapter 5.

2.1 The building blocks

In this Section, we introduce the elementary particle content of the SM. Particles are elementary in the sense that, to the extent that we have probed short distances in the experiment (down to distances of about 10^{-20} meters), they seem to not have internal substructure. The goal of this Section is to paint a broad picture for the uninitiated person. The mathematical treatment of the SM interactions and construction is covered in the

following Sections of this Chapter.

All elementary particles carry a quantum mechanical property known as "spin." The spin can be viewed as an intrinsic angular momentum. Particles can be classified as fermions or bosons depending on whether their spin is presented in odd or even multiples of 1/2, respectively. Identical fermions with the same quantum numbers obey the Pauli exclusion principle, which means that they cannot occupy the same quantum states at the same position and time. Bosons are not subject to the Pauli exclusion principle. The matter content of the SM is formed of spin-1/2 fermions. The matter content can be split in two sets according to their interactions: quarks and leptons. The spin-1 bosons of the SM are the mediators of the interactions. There is only one spin-0 boson in the SM, which appears as a result of a special mechanism that confers the SM particles with mass. We discuss these sets of SM particles in the following Subsections.

2.1.1 Quarks

Quarks are spin-1/2 particles that are sensitive to the strong, weak, and electromagnetic interactions. There are six types of quark (*flavors*): up, down, charm, strange, top, and bottom. The up, charm, and top quark have electric charge 2/3 and the down, strange, and bottom have -1/3. Quarks can be organized in three generations. The first generation is the up and down, the second is strange and charm, and the third one is top and bottom quarks. Ordered like this, the generations contain the pairs of quarks from the least to most massive quarks.

Quarks are not observed in isolation due to the property of color confinement; we find them as elements of "baryons" and "mesons", which are particles composed of an odd and even number of valence quarks, respectively (at least three valence quarks for baryons). Baryons and mesons are part of a larger group of composite particles known as "hadrons." For example, the proton is a baryon composed of two up- and one down-type valence quarks (uud). Most hadrons decay to lighter, more stable particles. The proton is

the only stable hadron (or at least the one with the longest lifetime of at least 10^{34} years). The neutron has a mean lifetime of about 10 minutes if it is not bound in a nucleus.

2.1.2 Leptons

Leptons are elementary particles of spin-1/2 that are not directly sensitive to the strong interactions. Like quarks, there are six types of leptons (flavors). Three leptons of electric charge -1 (electron, muon, and tau lepton) and three leptons of electric charge 0 (electron-neutrino, muon-neutrino, tau-neutrino). Leptons can also be organized in three generations. The electron is the lightest charged lepton, and the only stable lepton that we have discovered. A neutrino of a given flavor *oscillates* to another flavor as they propagate, since the neutrino mass eigenstates are not the same as the flavor eigenstates. Apart from this peculiarity, neutrinos do not decay to lighter particles.

2.1.3 Bosons

In the SM, there are twelve spin-1 bosons related to the three fundamental interactions. These correspond to eight gluons that mediate the strong interaction, the W^+, W^-, and Z bosons that mediate the weak interaction, and the photon (γ) that mediates the electromagnetic interaction. The aforementioned particles are known as *gauge* bosons, since they can be introduced in the theory to satisfy a set of gauge symmetries, as it will be discussed later in this Chapter.

There is only one spin-0 boson in the SM: the Higgs boson. The Higgs boson interacts with quarks and charged leptons, with weak gauge bosons, and with itself. In some minimal extensions of the SM, it may have a feeble coupling with neutrinos, too. The strength of the interaction of the Higgs field with fermions is directly related to their mass. The Higgs field is a consequence of a spontaneous symmetry being broken, which is necessary for the construction and mathematical consistency of the SM, as explained in

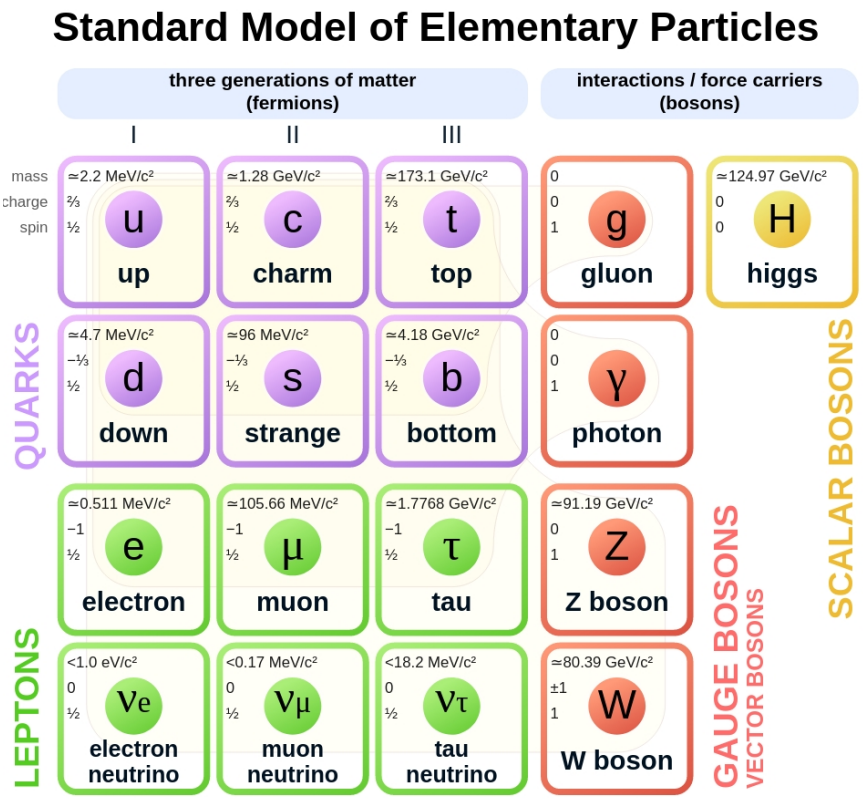

Figure 2.1: Elementary particles of the Standard Model in groups of quarks, leptons, gauge bosons, and scalar bosons. For a given square, the numbers represent (from upper to lower numbers): the mass of the particle, its electric charge, and its spin. Figure extracted from Ref.(6).

Section 2.5.

The list of elementary particles can be seen in Fig. 2.1, together with their masses, electric charge, and spin. We note that each of the particles have their corresponding *anti*-particle counterpart. Anti-particles have the same mass and spin as their particle counterpart, but with all other quantum numbers oppositely signed. For example, the anti-particle of the electron (negative electric charge), is the positron (positive electric charge), which has the same mass and spin as the electron. Some of the SM particles are their own antiparticle, like the photon.

Throughout the thesis, we use natural units $\hbar = c = 1$, where $\hbar$ and c are the reduced Planck constant and the speed-of-light in vacuum, respectively. The unit of energy that will be handled in this thesis is the electronvolt (eV), which is equivalent to 1.60218×10^{-19} joules. In mass, 1 eV is 1.782662×10^{-36} kg. To give a sense of scale, the proton has a mass of 938.3 MeV, whereas the electron has a mass of 0.511 MeV. The typical energies of chemistry reactions are of the order of a few eV, whereas those of nuclear physics are on the order of a few MeV. The energy scales we handle in particle physics colliders span a few GeV and up to 10^3 GeV. When we talk about electric charge, we will express them in units of the electric charge of the positron.

In the next Sections, we will sketch the mathematical formulation of the SM.

2.2 Basics of quantum field theory

2.2.1 Lagrangian formulation and principle of stationary action

We can formulate a physical theory in terms of a Lagrangian density function, $\mathscr{L}$. The Lagrangian density is a function that depends on a field Φ or derivatives of the field Φ with respect to position and time, $\partial_\mu \Phi \equiv \frac{\partial \Phi}{\partial x^\mu}$. This is in analogy with the Lagrangian function of classical mechanics of a particle or system of particles and their respective generalized coordinates and momenta. For a given $\mathscr{L}$, we can define the action $\mathscr{S}$. The

action $\mathscr{S}$ is a functional of the fields and their derivatives defined as the integral of $\mathscr{L}$ over spacetime,

$$\mathscr{S} = \int d^4x \mathscr{L}(\Phi, \partial_\mu \Phi) \tag{2.1}$$

one then needs to find the set of fields that leave the action stationary, i.e., its first-order variational derivative is zero, $\delta\mathscr{S} = 0$. This is known as the principle of stationary action of classical field theories, which is analogous to the principle of stationary action of classical mechanics. One finds that the fields are such that they satisfy the Euler–Lagrange equations,

$$\partial_\mu \frac{\partial \mathscr{L}}{\partial(\partial_\mu \Phi)} - \frac{\partial \mathscr{L}}{\partial \Phi} = 0 \tag{2.2}$$

then, for a given set of boundary conditions for Φ and/or $\partial_\mu \Phi$, on can solve the resulting partial differential equation for Φ. The Euler–Lagrange equation is also known as the equation of motion of the field. The principle of stationary action alone does not tell you what the specific structure of the Lagrangian density must be. Typically, the Lagrangian density can be written as the difference of a kinetic term and an interaction term, analogous to the Lagrangian function of classical mechanics. Indeed, such a structure is used when formulating the Lagrangian density of the SM, as will be shown later in this chapter.

Any symmetries of the Lagrangian density are also symmetries of the action, which allows for straightforward theory-building strategies. To construct a Lagrangian, one may set a number of desired symmetries and properties of the physical theory being constructed. For instance, a sensible requirement for the Lagrangian density is that it must be relativistic, i.e., the physical laws must not depend on a given frame of reference and the speed-of-light in vacuum must be the same in all frames of reference. One can go a further step and add internal symmetries on top of the aforementioned spacetime sym-

metries, such as invariance under gauge transformations –a special phase transformation of the fields– or discrete symmetries. A principle of internal symmetry like this dictates which interaction couplings are allowed in the Lagrangian density in a systematic fashion. Unitarity and causality may be invoked to bound the order of the derivatives of the fields (up to second order for bosonic fields and first order for fermionic fields). Additional hypotheses may be set by the person (people) developing the physical theory.

2.2.2 Quantization of a field

The Lagrangian formalism and the principle of stationary action are the foundation of classical field theories. Such foundations can be used to construct their quantum version: quantum field theories. Quantum field theories arise from the combination of the symmetries of spacetime of special relativity and the principles of quantum mechanics, namely the uncertainty principle. There are numerous ways of quantizing a classical field theory. The modern way of quantizing a field theory is via the Feynman path integral formalism.

In the Feynman path integral formalism, one calculates a generating functional $\mathscr{Z}$ in terms of a field path integral. For example, for a scalar field $\Phi = \Phi(x)$, it is given by (assuming natural units $\hbar = c = 1$)

$$\mathscr{Z}[J] = \int \mathscr{D}\Phi e^{i(\mathscr{S}[\Phi(x)]+J(x)\Phi(x))} \tag{2.3}$$

where $\mathscr{S}$ is the action for a given field configuration $\Phi(x)$ and $J(x)$ is a source field. The path integral is carried out over the possible time evolutions of the field over all space, hence the use of the symbol $\mathscr{D}\Phi$ to distinguish the path integral operation from a standard calculus integral operation. The field evolution that satisfies the Euler–Lagrange equations is included in the path integral calculation, but so are any other field configurations around the aforementioned classical field solutions, which are all permissible in quantum mechanics. This last point is key in the quantization of the field with this

prescription.

Given a generating functional $\mathscr{Z}$, one can then calculate the transition amplitudes of probability by means of variational derivatives (also called functional derivatives) of the generating functional with respect to the source $J(x)$. Indeed, the vacuum expectation value of the time-ordered operator products, also called the n-point correlation function, can be calculated from the generating functional as follows

$$\langle 0|\Phi(x_1)\Phi(x_2)\dots\Phi(x_{n-1})\Phi(x_n)|0\rangle = \frac{\delta}{i\delta J(x_1)}\frac{\delta}{i\delta J(x_2)}\cdots\frac{\delta}{i\delta J(x_{n-1})}\frac{\delta}{i\delta J(x_n)}\ln(\mathscr{Z}[J])\Big|_{J=0} \quad (2.4)$$

the particular structure of Eqn. 2.4 is characteristic of scalar fields, but a similar mathematical structure holds for spin-1/2 or spin-1 fields (with proper care of Fermi–Dirac statistics for the former). The *propagator* of a field is obtained from the two-point correlation function

$$\langle 0|\Phi(x_1)\Phi(x_2)|0\rangle = \frac{\delta}{i\delta J(x_1)}\frac{\delta}{i\delta J(x_2)}\ln(\mathscr{Z}[J])\Big|_{J=0} \quad (2.5)$$

such a two-point correlation function can be interpreted as the amplitude of probability for a field to evolve from a given configuration at x_1 to another configuration at x_2. These two-point correlation functions can be used to build so-called *Feynman rules*. The Feynman rules tells us how, starting from a Lagrangian density, one can identify a particle propagator and the interaction vertices starting from the Lagrangian density in order to calculate observables of interest in a way that conforms with quantum field theory. The Feynman rules can be derived in configuration space, but more frequently we refer to the Feynman rules in momentum space. Using these Feynman rules, one can calculate transition amplitudes of probability starting from Feynman diagrams. These amplitudes of probability are matrix elements that are then treated within S-matrix theory. This means that they can be used to calculate differential and integrated cross sections, branching

fractions, decay lifetimes, and other observables that are experimentally measurable. Of particular importance is the fact that one can use perturbation theory techniques to calculate these observables, i.e., these physical quantities can be expressed as a power series in the interaction coupling, as long as the coupling is weak enough.

2.3 Principle of gauge invariance

The SM is built on the principle of gauge invariance. A gauge transformation is such that it rotates the phase of the particle field by a finite amount. Such a phase rotation of the field can be global, which means that the same phase rotation is applied to all points of space, or local, meaning that the phase rotation depends on the position and time. Gauge invariance of a field theory means that the Lagrangian density is invariant under a given gauge transformation. The requirement of local gauge invariance as an internal symmetry of a physical theory requires the introduction of additional fields to the Lagrangian density, known as gauge fields. In addition, the principle of gauge invariance dictates the way that the gauge field and matter fields interact with each other and restrict other couplings that one might be tempted to write in by hand. The most famous example of a gauge field is the electromagnetic field or photon field, denoted by the symbol A_μ, as illustrated in Section 2.3.1.

Gauge theories can be abelian or non-abelian, which means that the generators of the symmetry group commute or do not commute, respectively. Non-abelian gauge theories, specifically Yang–Mills theories(7), are very interesting from a theoretical point of view, due to the rich structure of the interactions that arises from such a symmetry. Another reason there is a huge investment in gauge theories is that they are *renormalizable*, as demonstrated by Gerard 't Hooft and Martinus J. G. Veltman (8; 9). Renormalizability means that we just need a finite number of counterterms in the Lagrangian density in order to systematically remove the singularities that appear upon considering self-energy diagram calculations, where the momentum of the virtual particle(s) is allowed to go to

infinity. This is contrast to non-renormalizable theories, where the number of counterterms needed depend on the order of the calculation in perturbation theory. Thus, the fact that one needs a finite number of counterterms means that renormalizable theories have strong predictive power. The renormalization of the gauge coupling strength of quantum chromodynamics is discussed in Subsection 2.6.1.

The property of gauge invariance in a physical theory was first noticed in classical electrodynamics, described by Maxwell field equations. Indeed, starting from Maxwell's equations for the classical electric $\vec{E}$ and magnetic $\vec{B}$ fields, it was noted that they can be written in terms of an electric scalar potential function, ϕ, and a vector potential, $\vec{A}$, which are also functions of position and time. The fields ϕ and $\vec{A}$ are such that

$$\vec{E} = -\nabla\phi - \frac{\partial}{\partial t}\vec{A} \tag{2.6}$$

$$\vec{B} = \nabla \times \vec{A} \tag{2.7}$$

where $\nabla\phi$ represents the gradient of the field ϕ, $\frac{\partial}{\partial t}$ the partial derivative operator with respect to time, and $\nabla \times \vec{A}$ represents the curl of the field. Note that one can replace $\phi \to \phi - \frac{\partial}{\partial t}\chi$ and $\vec{A} \to \vec{A} + \nabla\chi$, where χ is an arbitrary scalar field that depends on position and time, and still obtain the same electric and magnetic fields upon performing this transformation. Such a symmetry transformation is known as a gauge transformation, and the fact that the electric and magnetic fields remain invariant reflects an intrinsic redundancy in the degrees of freedom used to describe the electromagnetic field. In classical electrodynamics, this is a property of the already existing theory. The idea then is to go one step further and reverse the argument: we want to investigate the properties of theories with an underlying gauge symmetry, and test whether such theories are able to describe Nature.

2.3.1 Example of a gauge theory: quantum electrodynamics

To illustrate the principle of gauge invariance, we discuss briefly how quantum electrodynamics (QED) -–the quantum theory of electromagnetic interactions— can be built based on such local gauge symmetry. We start first with the Lagrangian density of a free spin-1/2 field with mass m. This could be an electron field, for example. Such a Lagrangian density is given by

$$\mathscr{L} = \bar{\psi}(i\gamma^{\mu}\partial_{\mu} - m)\psi \tag{2.8}$$

where γ^{μ} are the Dirac matrices that satisfy a Clifford algebra, ψ is a fermionic spinor field that depends on position and time, and $\bar{\psi} = \psi^{\dagger}\gamma^{0}$ is its adjoint field. The corresponding Euler–Lagrange equation of this Lagrangian density is the Dirac equation for a freely propagating fermion.

Now, starting from the free Lagrangian density, we can test what would happen if we apply local gauge transformations that depend on the position x. To construct QED, the corresponding gauge symmetry is the unitary group $\mathrm{U(1)_{em}}$. The transformation is such that

$$\psi(x) \to \psi'(x) = U(x)\psi(x) = \exp\left[i\theta(x)\right]\psi(x) \tag{2.9}$$

where $\theta(x)$ is the position-dependent phase shift. The mass term $m\bar{\psi}\psi$ is invariant under such a symmetry transformation. However, the purely kinetic term is not. Indeed, the term with a field derivative transforms under $\mathrm{U(1)_{em}}$ as follows

$$\bar{\psi}\partial_{\mu}\psi \to \bar{\psi}\partial_{\mu}\psi + \bar{\psi}[i\partial_{\mu}\theta]\psi \tag{2.10}$$

there is no way of writing the right-hand side of Eqn. (2.10) in terms of ψ' to show that the term is manifestly invariant under local gauge transformations. In order to satisfy

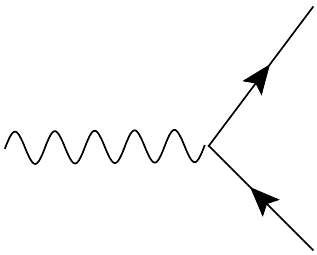

Figure 2.2: Tree-level coupling in quantum electrodynamics. The wiggly line represents the photon propagator, and the arrows represent a given fermion propagator (e.g., the electron field) coupled to the photon field.

gauge invariance, we have to add another term to the Lagrangian density that transforms in a way that cancels this problematic extra term from the derivative of the fields. This is done by replacing the standard derivative ∂_μ with the so-called *covariant derivative* D_μ. The latter, by definition, transforms covariantly under the gauge transformation. Mathematically, this means that the covariant derivative is such that

$$D_\mu \psi \to (D_\mu \psi)' = U(x) D_\mu \psi(x) \tag{2.11}$$

this way, by replacing the standard derivative with the covariant derivative, the term $\bar{\psi} D_\mu \psi$ will be invariant under $\mathrm{U(1)_{em}}$ transformations. The covariant derivative is given by

$$D_\mu = \partial_\mu - ieA_\mu \tag{2.12}$$

where A_μ is the associated gauge field that is added to the Lagrangian density and e is the gauge coupling. With this definition of the covariant derivative, the Lagrangian is given by

$$\mathscr{L} = \psi[i\gamma^\mu(\partial_\mu - ieA_\mu) - m]\psi \tag{2.13}$$

we see here that the gauge field A_μ couples directly to the fermion field with a gauge coupling strength e. Thus, given its strong resemblance with the scalar and vector po-

tential of classical electrodynamics, and the fact that such a field couples to the spin-1/2 fermions of the theory, we can associate the gauge field A_μ with the photon field and e with the electric charge of the fermion. The only missing piece to complete the Lagrangian is the kinetic term of the gauge field. Adding such a kinetic term, we have the Lagrangian of QED given by

$$\mathscr{L}_{\text{QED}} = \psi[i\gamma^\mu(\partial_\mu - ieA_\mu) - m]\psi - \frac{1}{4}F_{\mu\nu}F^{\mu\nu} \tag{2.14}$$

where the last term on the right-hand side of the Eqn. (2.14) is the kinetic term of the gauge field defined via the electromagnetic field tensor $F_{\mu\nu} \equiv \partial_\mu A_\nu - \partial_\nu A_\mu$. Such a kinetic term is on its own gauge invariant. The photon field is massless as a consequence of gauge invariance, since a mass term for the gauge field of the form $m^2 A_\mu A^\mu$ would violate gauge invariance.

The Lagrangian density of electromagnetic interactions is built starting from the requirement of local gauge invariance under the U(1)_{em} group on a free fermion theory. Such a symmetry necessitates the introduction of a massless vector gauge field, which we identify with the photon field. The coupling between the gauge field and the fermion field is fully determined by the invariance of the theory under U(1)_{em} transformations. Note that to properly quantize the theory one needs to follow a recipe similar to that discussed in the previous section. The resulting quantum theory of electromagnetic interactions (QED) was developed by Richard Feynman, Julian Schwinger, and Sin-Itiro Tomonaga(10; 11; 12; 13). For their work, they were awarded the Nobel Prize in Physics in 1965. Based on the comparison of the electron anomalous magnetic dipole moment — induced purely by quantum mechanical effects— and the Rydberg constant from atom recoil measurements, which can be used to extract the fine-structure constant $\alpha_{\text{em}} \equiv e^2/4\pi \approx 1/137$, the agreement between QED predictions and the measurements is within ten parts in a billion (10^{-8}). This makes QED one of the most accurate physical theories constructed thus far. Based on the success of QED, one might ponder if other gauge theories might

be able to describe other fundamental interactions in Nature. This sets the scene for the construction of the SM.

2.4 The Standard Model construction

The SM of particle physics, developed in the 1970s, is a renormalizable quantum field theory that describes Nature at subnuclear distances. The mathematical formulation of the SM is based on the local gauge invariance of its Lagrangian density under the gauge groups $\mathrm{SU(3)} \times \mathrm{SU(2)}_L \times \mathrm{U(1)}_Y$ to model the strong, the weak, and the electromagnetic interactions in a quantum theory. The SU(3) and $\mathrm{SU(2)}_L$ are non-abelian gauge symmetries associated to the Special Unitary SU(N) transformations (hence "SU") of $n \times n$ unitary matrices of determinant 1. The $\mathrm{SU(2)}_L \times \mathrm{U(1)}_Y$ symmetries are spontaneously broken to $\mathrm{U(1)}_{\mathrm{em}}$ due to the acquisition of a non-zero vacuum expectation value of a scalar field, as explained in Section 2.5.1.

The way the SM is structured allows for a "factorized" discussion of its internal gauge structure. Profitting from this, we divide the following discussion of the SM in two parts: the electroweak theory in Section 2.5 and the strong interactions in Section 2.6. Remarks on physics beyond the SM are drawn at the end of the Chapter 2.7. More emphasis is given to the theory of strong interactions, since this is the main topic of the measurement presented in this thesis. The discussion of electroweak symmetry breaking has the purpose of showing how the various couplings between the weak gauge bosons and the photon emerge. We explore how deviations from these fundamental assumptions of the SM can be explored in Chapter 9.

2.5 Electroweak theory

By the 1960s, there was a plethora of experimental measurements on nuclear β-decay for numerous isotopes, for which the four-fermion interaction theory by Enrico Fermi was

conventionally used (14). The phenomenon of nuclear β decay is such that a proton is transmuted into a neutron with the associated emission of a positron (the anti-particle of the electron), and a neutrino. The reaction ${}^{14}_{6}C \rightarrow {}^{14}_{7} N + e^{-} + \bar{\nu}_e$ is an example of nuclear β decay. In particular, there was recent experimental evidence for parity violations in weak interactions in the series of experiments led by Chien-Shiung Wu (15). Parity invariance means that a physical law must be the same in our world and in a "mirror" world where the sign of the spatial coordinates is flipped, i.e., the physical law must be invariant under a transformation of coordinates like this $(x, y, z) \rightarrow (-x, -y, -z)$. An example of a parity-invariant theory is electromagnetism. The observation of parity violations in weak interactions meant that, unlike the electromagnetic interaction, the weak interaction acts differently on left- and right-handed particles. In addition, there was evidence for the decay of the muon into an electron and neutrinos, for which it was demonstrated that the Fermi interaction could also be used to describe it rather well. It was suspected that weak interactions may be mediated by a spin-1 boson, similar to the photon in electromagnetic interactions. However, unlike the photon, the mass of such spin-1 boson has to be large enough to make the weak interaction of short-range and effectively explain the Fermi interaction theory at nuclear energies that had worked successfully.

Building upon the success of QED, attempts for a gauge theory of the weak interactions were developed. In this context, Sheldon Glashow(16), Abdus Salam(17), and Steven Weinberg (18) independently proposed a gauge theory that unified the weak and electromagnetic interactions in a single framework: electroweak theory. A key prediction of electroweak theory was the existence of an additional type of *neutral* weak interaction mediated by a new gauge boson, called the Z boson, with a mass larger than that of the charged weak interactions, the W boson. Glashow, Salam, and Weinberg were awarded the 1979 Nobel Prize in Physics for their contributions to the unification of the weak and electromagnetic interactions. The W and Z bosons were later discovered in the 1983 at the CERN Super Proton Synchrotron by the UA1 and UA2 Collaborations(19; 20; 21; 22),

where the W and Z bosons were found to have masses of 80 and 91 GeV, respectively. For this discovery, the leaders of the experiments Carlo Rubbia and Simon van de Meer were awarded the Nobel Prize in Physics in 1984.

The electroweak sector of the SM contains all fermions (quarks and leptons), a massless photon for electromagnetic interactions, and three *massive* vector bosons: the Z boson that mediate neutral weak currents, and the W^+ and W^- bosons, which mediate flavor changing charged currents. A common particle physics textbook exercise on gauge invariance shows that one must have massless gauge bosons in the Lagrangian density as a result of the underlying local gauge symmetry. This is the case for photons in QED, for example. Because of this, it was difficult to conceive of the weak gauge bosons as pertaining to a gauge theory in a consistent way. However, one can have massive gauge bosons as a result of a Lagrangian density with its gauge symmetry broken spontaneously with a special mechanism, known as the Higgs mechanism, which will be described in Section 2.5.1. When spontaneous symmetry breaking was introduced to particle physics, it was possible to put the pieces together to develop electroweak theory.

The SM of electroweak interactions is based on the gauge group $\mathrm{SU}(2)_L \times \mathrm{U}(1)_Y$, where $\mathrm{SU}(2)_L$ represents a non-abelian gauge piece and $\mathrm{U}(1)_Y$ represents an abelian piece associated with hypercharge. The L symbol emphasizes that only particles with left-handed chirality transform under $\mathrm{SU}(2)_L$ gauge transformations. A massless particle is said to be (left)right-handed if the direction of its spin is (anti)parallel to the direction of motion. As mentioned before, the experimental evidence demonstrates that parity is maximally violated in weak interactions. Thus, by construction, we distinguish the way particles interact by means of their chirality. Note that the $\mathrm{U}(1)_Y$ piece here is related to the weak hypercharge, Y, which is not the same $\mathrm{U}(1)_{\mathrm{em}}$ gauge group of electromagnetic interactions, although the two of them are related as it will be shown later.

The corresponding gauge fields are W_μ^i, $i = 1,2,3$ fields and one B_μ for the $\mathrm{SU}(2)_L$ and $\mathrm{U}(1)_Y$ gauge groups, respectively. To conform with gauge invariance, the W_μ^i and B_μ

fields are all massless. The corresponding gauge couplings are denoted by g and g' for $SU(2)_L$ and $U(1)_Y$, respectively. The left-handed fermion fields of the i^{th} fermion family transform as doublets under $SU(2)_L$. On the other hand, right-handed fermion fields are $SU(2)_L$ singlets. Both left- and right-handed fermion fields transform under $U(1)_Y$, i.e., both of them couple to the B_μ field.

Thus, the doublet spinor field can be represented as:

$$\Psi_L = \frac{1-\gamma^5}{2}\begin{pmatrix} \psi \\ \psi' \end{pmatrix} \equiv \begin{pmatrix} \psi_L \\ \psi'_L \end{pmatrix} \tag{2.15}$$

and the two singlet fields as

$$\Psi_R \equiv \frac{1+\gamma^5}{2}\psi, \qquad\qquad \Psi'_R \equiv \frac{1+\gamma^5}{2}\psi' \tag{2.16}$$

the fields ψ and ψ' represent the fermion fields of a given family of the SM. For instance, ψ and ψ' may represent the electron-neutrino and the electron fields or the up and down quarks, respectively.

The Lagrangian density that accounts for electroweak symmetry with just the fermion and gauge fields is

$$\mathscr{L} = i\bar{\Psi}_L \not{D}\Psi_L + i\bar{\psi}_R \not{D}\psi_R + i\bar{\psi}_R{}' \not{D}\psi'_R - \frac{1}{4}W_a^{\mu\nu}W^a_{\mu\nu} - \frac{1}{4}B^{\mu\nu}B_{\mu\nu} \tag{2.17}$$

where $\not{D} \equiv \gamma^\mu D_\mu$. The covariant derivative is defined as

$$D_\mu = \partial_\mu - igW^i_\mu T_i - ig'\frac{Y}{2}B_\mu \tag{2.18}$$

where $T_i \equiv \frac{1}{2}\sigma_i$ are the generators of the $SU(2)_L$ symmetry, with σ_i being the Pauli matrices ($i = 1,2,3$) associated to the SU(2) symmetry. The Pauli matrices obey a Lie algebra,

$$[\sigma_a, \sigma_b] = i\varepsilon_{abc}\sigma_c \tag{2.19}$$

where ε_{abc} is the Levi-Civita antisymmetric tensor.

The gauge couplings are denoted by g and g', which are associated to the $\mathrm{SU}(2)_L$ and $\mathrm{U}(1)_Y$ groups, respectively. The right-handed fields are singlet under $\mathrm{SU}(2)_L$, which means they are only sensitive to the gauge field of $\mathrm{U}(1)_Y$; one can thus set $g = 0$ in Eqn. (2.18) for the covariant derivative acting on right-handed fields.

The field strength tensors are defined as

$$B_{\mu\nu} = \partial_\mu B_\nu - \partial_\nu B_\mu \tag{2.20}$$

$$W^a_{\mu\nu} = \partial_\mu W^a_\nu - \partial_\nu W^a_\mu + g\varepsilon^{abc} W^b_\mu W^c_\nu \tag{2.21}$$

upon expanding the Lagrangian density, we can identify an interaction term that couples fermion fields of different flavors in a given generation (for example, the electron and the electron-neutrino fields, or the up- and down-quark fields). Such charged-current interaction can be written in a compact form as follows:

$$\mathscr{L}_{\mathrm{CC}} = \frac{g}{\sqrt{2}}(W^+_\mu \bar{\psi}_L \gamma^\mu \psi'_L + W^-_\mu \bar{\psi}'_L \gamma^\mu \psi_L) \tag{2.22}$$

where we express the W^1_μ, W^2_μ fields in a different basis,

$$W^\pm_\mu = \frac{1}{\sqrt{2}}(W^1_\mu \mp i W^2_\mu) \tag{2.23}$$

the coupling term shown in Eqn. (2.22) allows us to identify the $W^\pm$ fields as the mediators of the weak interaction.

In addition, we can identify an interaction term that couples fermion fields of the same flavor. This neutral-current term is written as follows,

$$\begin{aligned}\mathscr{L}_{\text{NC}} = \; & \tfrac{g}{\sqrt{2}} W_\mu^3 T^3 \left[\bar{\psi}_L \gamma^\mu \psi_L - \bar{\psi}'_L \gamma^\mu \psi'_L\right] \\ & + \tfrac{g'}{\sqrt{2}} B_\mu \left[Y(\bar{\psi}_L \gamma^\mu \psi_L + \bar{\psi}'_L \gamma^\mu \psi'_L) + Y \bar{\psi}_R \gamma^\mu \psi_R + Y \bar{\psi}'_R \gamma^\mu \psi'_R\right]\end{aligned} \tag{2.24}$$

part of this term has a strong resemblance with the interaction coupling for electromagnetic interactions. However, the electromagnetic interaction does not have a preference for left-handed or right-handed fermion fields. Indeed, one could think of a mechanism that somehow leaves us with the electromagnetic interaction term that we know from QED and an additional interaction term; a *neutral weak current* term. Thus, we define another basis of fields where we have the photon field A_μ and a new field Z_μ as a linear combination of the original B_μ and W_μ^3 gauge fields as follows:

$$\begin{pmatrix} \gamma \\ Z \end{pmatrix} = \begin{pmatrix} \cos\theta_W & \sin\theta_W \\ -\sin\theta_W & \cos\theta_W \end{pmatrix} \begin{pmatrix} B \\ W_3 \end{pmatrix} \tag{2.25}$$

where the θ_W parameter is known as the weak mixing angle or Weinberg angle after Steven Weinberg. Upon substituting the expressions for A_μ and Z_μ in the Lagrangian density, we obtain a QED-like coupling of the A_μ field and fermion fields. The coupling strength associated to the $A_\mu \bar{\psi}_{R,L} \gamma^\mu \psi_{R,L}$ and $A_\mu \bar{\psi}'_{R,L} \gamma^\mu \psi'_{R,L}$ terms is

$$g \sin\theta_W T_3 + g' \cos\theta_W \frac{Y}{2}$$

Inspired by the Gell-Mann–Nishijima formula ($Q = T^3 + \frac{1}{2}Y$) of flavor physics, we can identify the gauge coupling of QED as

$$e \equiv g \sin\theta_W = g' \cos\theta_W \tag{2.26}$$

this last point is very important: we are establishing a direct relation between the gauge couplings of the $\text{SU}(2)_L$ and $\text{U}(1)_Y$ gauge groups, which in principle are separate gauge couplings. In other words, in addition to performing a "rotation" of the B_μ and W_μ^3

fields into the A_μ and Z_μ fields, which is just a redefinition of the vector fields basis, we also connect the otherwise-disjoint gauge couplings with one another. For pedagogical reasons and simplicity in this thesis, we referred to the Gell-Mann–Nishijima formula used in flavor physics to make the connection between the gauge couplings of the $\mathrm{SU}(2)_L$ and $\mathrm{U}(1)_Y$ gauge groups, but it can be demonstrated that such a relation arises naturally with the proper mechanism to break electroweak symmetry.

What we have discussed thus far is responsible for most of the internal structure of the weak and electromagnetic interactions as we know them. The kinetic terms of the W_μ^i fields show a rich structure of self-interacting gauge bosons, which are mainly a consequence of the underlying non-abelian gauge symmetry of $\mathrm{SU}(2)_L$. After electroweak symmetry breaking (EWSB), we have triple (ZWW, γWW) and quartic ($WWWW$, $\gamma\gamma WW$, γZWW, $ZZWW$) couplings. The corresponding Feynman diagrams for these interaction terms, as well as the couplings with fermion fields, are shown in Fig. 2.3. However, the principle of gauge invariance forces us to use only massless vector gauge bosons. The nuclear β decay, which occurs at subnuclear distances, suggests that the particle that mediates the weak interaction must be very massive. Therefore, the gauge invariance requirement alone cannot explain the phenomenology of nuclear β decay.

There is an additional problem with the present formulation as it is laid out now in this thesis; we cannot write mass terms of the fermions for a theory with a $\mathrm{SU}(2)_L$ gauge symmetry by hand. The reason is that the mass terms for fermion fields are non-chiral. Since the gauge group $\mathrm{SU}(2)_L$ distinguishes left-handed from right-handed fermion fields, such non-chiral mass terms must be absent in the Lagrangian.

Perhaps one may use the principle of gauge invariance as a guide to write down the interaction terms in the Lagrangian density, and then insert the mass terms by hand, even if the latter breaks gauge invariance. Even if one continues with this undesired theoretical property, one obtains an even more worrisome problem: for the scattering of longitudinally polarized vector bosons —which is possible for massive vector bosons—,

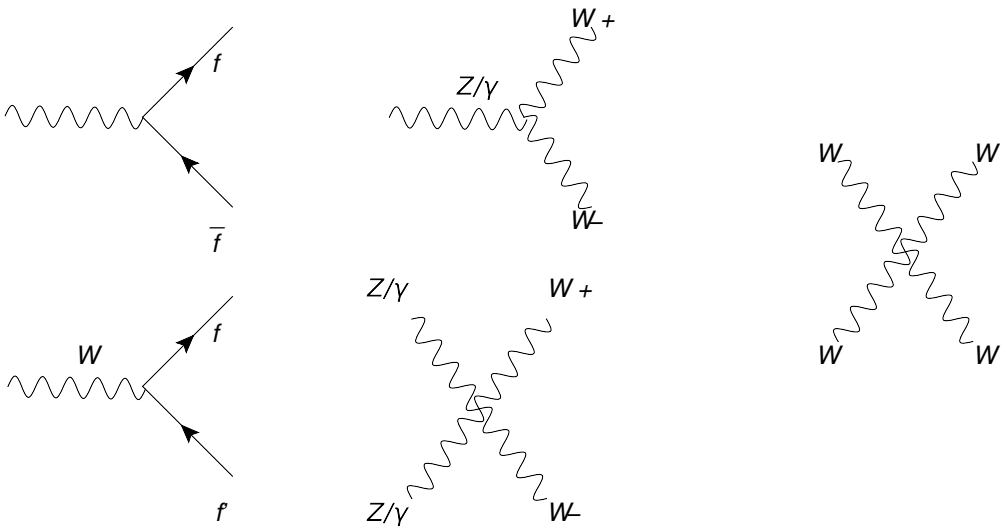

Figure 2.3: Interactions between gauge weak bosons (Z and $W^{\pm}$ bosons), the photon (γ), and fermions (f) after EWSB.

the scattering amplitude violates unitarity at high energies (close to 1 TeV). Thus, there are several issues at hand with a simple formulation of EWSB done "by hand." Either we give up gauge invariance, which is one way of generating the couplings of vector bosons with fermions, or we find a way of generating the mass of the gauge bosons and fermions while retaining some of the features of a gauge invariant theory.

2.5.1 The Higgs mechanism

A special mechanism was proposed independently by physicists Robert Brout and François Englert (23), Peter Higgs (24), and by the group of Gerald Guralnik, Carl Hagen, and Tom Kibble (25) as a solution to generate the masses of the gauge vector bosons. The mechanism is based on the concept of "spontaneous symmetry breaking." This is a phenomenon where a ground state configuration of a physical system does not respect the symmetry of the physical system itself. We will call this the "Higgs mechanism" hereafter, since this is a familiar shorthand term used in the literature.

In the Higgs mechanism, the spontaneous symmetry breaking is realized through the introduction of a complex scalar doublet of fields

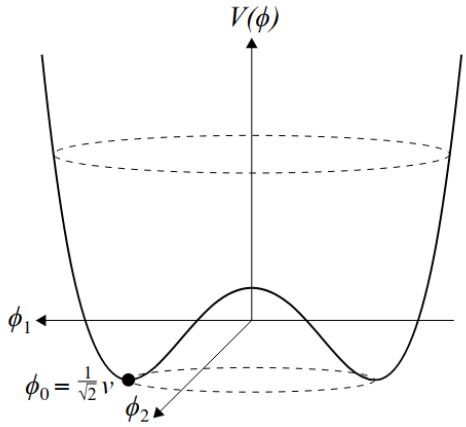

Figure 2.4: Graphical representation of the Higgs potential (the "Mexican sombrero" potential) described in text.

$$\Phi = \begin{pmatrix} \phi_+ \\ \phi_0 \end{pmatrix} \tag{2.27}$$

this SU(2) doublet complex field has quantum numbers $Y = 1$ and a $T_3 = -1/2$. Hence, it interacts with the gauge fields W_μ^i and B_μ through its covariant derivative in the electroweak sector.

The Higgs Lagrangian density is written as,

$$\mathscr{L}_{\text{Higgs}} = (D_\mu \Phi)^\dagger (D^\mu \Phi) - V(\Phi) \tag{2.28}$$

where the Higgs potential is defined as

$$V(\Phi) = -\mu^2 \Phi^\dagger \Phi + \lambda (\Phi^\dagger \Phi)^2 \tag{2.29}$$

where μ^2, $\lambda > 0$ are free parameters of the theory. The shape of the Higgs potential $V(\phi)$ in Eqn. (2.29), graphically represented in Fig. 2.4 is a fundamental assumption of the SM, which is a parametrically simple way of inducing the spontaneous breaking of electroweak symmetry. With these conditions, the field Φ develops a non-zero vacuum expectation value (VEV) given by $v/\sqrt{2} = \mu/\lambda$. The Higgs doublets satisfy the condition,

$$|\Phi|^2 = \frac{\mu^2}{2\lambda} \equiv \frac{v^2}{2} \tag{2.30}$$

this condition corresponds to the minima of the $V(\Phi)$ potential. The minima are connected via gauge transformations that change the phase of the field Φ, but not its modulus.

The symmetry is spontaneously broken to a ground state that is parallel to the ϕ^0 component of the doublet that is invariant under the $\mathrm{U(1)_{em}}$ gauge symmetry group. In this picture, there are no direct couplings of the electromagnetic field with the Higgs field as a result of this symmetry breaking process. One can expand the field Φ around this particular minimum,

$$\Phi = \frac{1}{\sqrt{2}} \exp\left[\frac{i\sigma_i \theta^i(x)}{v}\right] \begin{pmatrix} 0 \\ \\ v + H(x) \end{pmatrix} \tag{2.31}$$

this corresponds to the presence of a scalar real massive field $H = H(x)$ and three massless fields denoted by the symbol $\theta^i(x)$, with $i = 1, 2, 3$, known as Goldstone bosons. The latter are expected as consequence of the Goldstone theorem (26), which states that the spontaneous breaking of a continuous symmetry generates as many massless bosons as there are broken generators of the symmetry. However, such massless bosons are not observed in Nature. One way of dealing with this issue is by effectively removing these unobserved states with an $\mathrm{SU(2)}_L$ gauge transformation, such that

$$\Phi \to \Phi' = \frac{1}{\sqrt{2}} \begin{pmatrix} 0 \\ \\ v + H(x) \end{pmatrix} \tag{2.32}$$

this choice is known as the unitary gauge. Upon doing this transformation only the real scalar field $H(x)$ remains, whose excitation is the SM Higgs boson. Going back to the Lagrangian of the Higgs sector, with the Higgs field expressed in the unitary gauge, we

have that

$$\begin{aligned}\mathscr{L}_{\text{Higgs}} = \; & \tfrac{1}{2}\partial^{\mu}H\partial_{\mu}H - \tfrac{1}{2}(2\lambda v^2)H^2 \\ & + \left[\left(\tfrac{gv}{2}\right)^2 W^{+\mu}W_{-\mu} + \tfrac{1}{2}\tfrac{(g^2+g'^2)v^2}{4}Z^{\mu}Z_{\mu}\right]\left(1+\tfrac{H}{v}\right)^2 \\ & + \lambda v H^3 + \tfrac{\lambda}{4}H^4 - \tfrac{\lambda}{4}v^4\end{aligned} \tag{2.33}$$

the first line of Eqn. (2.33) represents the kinetic term of a real scalar field with a mass $m_H = \sqrt{2\lambda v^2}$. The second line represents the mass terms of the weak gauge bosons, which appear from explicitly expanding the covariant derivative in the unitary gauge. The gauge bosons have obtained a mass

$$m_W^2 = \frac{g^2v^2}{4}, \qquad\qquad m_Z^2 = \frac{(g^2+g'^2)v^2}{4} \tag{2.34}$$

we observe that the Goldstone bosons are "absorbed" as additional degrees of freedom of the $W^{\pm}$ and Z bosons. These additional degrees of freedom correspond to their longitudinal polarizations, confering them mass. There is also a nice relation between the Weinberg angle and the gauge couplings:

$$\cos\theta_W = \frac{g}{\sqrt{g^2+g'^2}} \qquad\qquad \sin\theta_W = \frac{g'}{\sqrt{g^2+g'^2}} \tag{2.35}$$

in the second line of Eqn.2.33, we see there are triple and quartic tree-level couplings between the weak gauge bosons and the Higgs field. Indeed, we have HWW and a HZZ interaction terms, and a $HHWW$ and a $HHZZ$ coupling. There is no tree-level coupling between the Higgs field and the photon field after EWSB. This is because, in the SM, the hypercharge and third-component of the isospin of the Higgs doublet is such that $Q = 0$.

In the third line of Eqn. 2.33, we see that there are triple and quartic couplings of the Higgs field with itself. These arise directly from the Higgs potential expressed in the broken phase. Indeed, the Higgs potential in the broken phase can be rewritten in terms of a triple and quartic coupling as

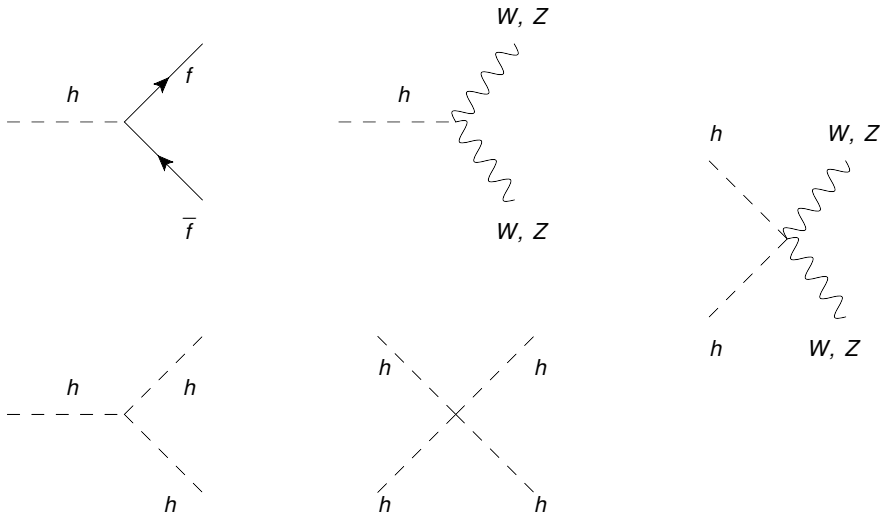

Figure 2.5: Couplings of the Higgs field to the fermion field, the weak gauge boson field, and to itself.

$$V(H) = \frac{1}{2}m_H^2 + \lambda v H^3 + \frac{1}{4}\lambda H^4 - \frac{\lambda}{4}v^4 \tag{2.36}$$

where $\lambda = \frac{m_H^2}{2v^2}$. The relation between the Higgs field self-couplings is a direct consequence of the Higgs potential ansatz.

In the end, there are two free parameters of the Higgs mechanism that need to be fit to the data. One such pair is the VEV v and the Higgs boson mass m_H, from which λ can be deduced. The VEV value $v \approx 246$ GeV sets the characteristic energy scale of EWSB and can be extracted from the Fermi constant G_F based on muon proper lifetime precision measurements. The Higgs boson was discovered in 2012 by the ATLAS and CMS Collaborations (27; 28) at the CERN LHC. Peter Higgs and François Englert were awarded the 2013 Nobel Prize in Physics for their work on the Higgs mechanism. The Higgs boson mass has been determined to be $m_H = 125.1$ GeV according to averaged values of the Particle Data Group (29), which are based on measurements by ATLAS and CMS. This fixes the self-coupling value to $\lambda \approx 0.13$.

The mass terms of the fermions are generated by means of a Yukawa interaction of the fermion fields with the Higgs field. For simplicity and pedagogical grounds, let us

assume that there is no flavor mixing in these Yukawa terms. Denoting the up and down-type fields as ψ and ψ', where the up- and down-type fields have isospin $T_3 = 1/2$ and $T_3 = -1/2$, respectively, we can write down the Yukawa Lagrangian density as

$$\mathscr{L}_{\text{Yukawa}} = -y'_f\big(\bar{\Psi}_L \Phi \psi'_R + \bar{\psi_R}' \Psi^\dagger \Psi_L\big) - y_f\big(\bar{\Psi}_L \tilde{\Phi} \psi_R + \bar{\psi}_R \tilde{\Phi}^\dagger \Psi_L\big) \tag{2.37}$$

where y_f and y'_f are the dimensionless Yukawa couplings. After EWSB, the Yukawa Lagrangian density results in the following expression

$$\mathscr{L}_{\text{Yukawa}} = -\sum_f m_f(\bar{\psi}_L \psi_R + \bar{\psi}_R \psi_L)\big(1 + \frac{H}{v}\big) \tag{2.38}$$

where the sum runs on both up and down-type fermions. We can identify the direct coupling of the Higgs field to the fermions after EWSB, as well as mass terms m_f that are given by

$$m_f = y_f \frac{v}{\sqrt{2}} \tag{2.39}$$

the fermion masses are thus explained in the SM as the interaction of the fermion fields with the Higgs field. The larger the coupling strength y_f is, the more massive fermions become after EWSB. Note that, in principle, one can have fermion flavor mixing through combinations of mass eigenstates of the fields in the Yukawa terms.

The corresponding Feynman diagrams for the Higgs couplings after EWSB are shown in Fig. 2.5. Without the Higgs boson, the SM predicts that there must be unitarity violations in scatterings of longitudinally-polarized vector bosons at the TeV scale and beyond. Higgs boson exchange in vector boson scattering regularizes the amplitude for longitudinally-polarized vector boson scattering, which prevents the theory from violating unitarity. The Higgs mechanism is a parametrically simple way of solving this problem. At the same time, the Higgs mechanism provides an explanation for the origin of the spontaneous breaking of electroweak symmetry, and leaves us with massive

vector gauge bosons and fermions. The Higgs mechanism is such that the resulting theory remains renormalizable (9), which renders a theory with strong predictive power in perturbation theory.

2.5.2 Remarks on electroweak theory

Electroweak theory, and the spontaneous breaking of its respective gauge symmetry via the Higgs mechanism, successfully gives us a picture of the weak and electromagnetic interactions for the range of energies that we have probed thus far experimentally. Several features of the electroweak sector were tested at the Large Electron Positron (LEP) collider at CERN. Most of the electroweak gauge boson couplings have been observed already at the LHC, the most recent one being the quartic $\gamma\gamma WW$ coupling measured by the ATLAS Collaboration in 2020 (30), a coupling that was elusive for a long time. The Higgs boson, discovered in 2012 by the CMS and ATLAS Collaboration, was the last piece of the SM to be uncovered, and provided the last SM parameter to be fit to the data. The characterization of the Higgs boson (and fthereby of the Higgs field and its couplings to the rest of the fields of the SM) is intensely being investigated at the LHC. Of particular importance is the verification that the coupling of the Higgs field with the fermions of the SM is indeed related to the mass of such particles. To this date, the Yukawa couplings of the Higgs field to the top quark, bottom quark, tau lepton, and muon fields have been measured by the CMS and ATLAS experiments, which seem to be consistent with the SM expectations. The coupling of the Higgs field with the weak gauge fields seems to be consistent with SM expectations as well. For the upcoming years, it will be very important to further verify the coupling of the Higgs field with the SM fermions and with itself. Such measurements are expected to take place during the operation of the High Luminosity Large Hadron Collider (HL-LHC), for instance.

Following EWSB, we observe that there are no tree-level couplings between the neutrally charged electroweak gauge bosons of the form $\gamma\gamma\gamma\gamma$, $\gamma\gamma ZZ$, $\gamma\gamma\gamma Z$ or γZZ, for instance.

In the SM, these can only be induced when considering virtual particle production. This is why the scattering of light-by-light ($\gamma\gamma \to \gamma\gamma$) is highly suppressed in the SM ($\sigma \propto \alpha_{\text{em}}^4$). Tree-level-like couplings at LHC energies could be generated as well with the presence of very heavy particles that are charged under hypercharge and isospin. As it will be shown later in this thesis in Chapter 9, these can be constrained or discovered in central exclusive production processes $pp \to p(\gamma\gamma \to VV)p$, for V being a vector gauge boson.

2.6 Quantum chromodynamics

Quantum chromodynamics (QCD) is the quantum field theory of the strong interactions. It was developed starting in the 1950s with the discovery of several hadrons and their subsequent classification by George Zweig and Murray Gell-Mann (31; 32), and it culminated in the early 1970s with the discovery of the property of asymptotic freedom in non-abelian gauge theories by David Politzer (33), David Gross and Frank Wilczek (34), which will be discussed later in this Section. The proposal by Politzer, Gross, and Wilczek was supported strongly by Fritzsch, Gell-Mann, and Leutwyler (35), which is often regarded as the foundation of QCD in its modern presentation.

The matter component of QCD are quarks and antiquarks. Quarks are spin-1/2 particles that carry an electric charge of either 2/3 or -1/3. There are six flavors of quarks: up, down, charm, strange, top, and bottom, each of them with non-zero mass. The strong interaction does not distinguish different quark flavors, which leads to an approximate flavor symmetry in QCD that is only broken due to the mass differences between the various quark flavors. Then, we have eight massless spin-1 gauge bosons that mediate the strong interaction, the gluons. Gluons are massless bosons, which are not charged under weak isospin or electric charge. Quarks and gluons, collectively known as partons, are known as the fundamental degrees of freedom of QCD.

In QCD, the analog of the electric charge is the *color* charge (hence the *chromo* of chromodynamics). Color charges come in three different types: "red," "green," and "blue,"

together with their anti-color charge counterparts anti-red, anti-green, and anti-blue. The labelling of the charges with colors is arbitrary, and has no connection with the psychological everyday experience of colors other than in the metaphorical sense. Quarks carry one color charge, whereas gluons carry one color charge *and* one anticolor charge (e.g., red and antiblue). Particles that are charged under color are subject to the strong interaction. Color-neutral particles are not directly sensitive to the strong force.

QCD has a characteristic non-abelian SU(3) local gauge symmetry. Unlike the $SU(2)_L \times U(1)_Y$ symmetry, the SU(3) one is unbroken, and data thus far is consistent with it being an exact symmetry of Nature. The non-abelian nature of the SU(3) gauge group is what gives rise to all the emergent properties that make QCD unique, which derive mainly from the triple and quartic self-interaction couplings between gluons, the gauge bosons of QCD. The SU(3) gauge symmetry reproduces experimental measurements related to the structure of the proton and the production of hadrons, as will be explained in Section 2.6.2. For example, an alternative U(3) gauge symmetry would give rise to color-singlet gluons, which in principle lead to infinite range strong interactions that are not observed experimentally.

The Lagrangian density of QCD can be written down in its compact presentation,

$$\mathscr{L}_{\text{QCD}} = \sum_f \sum_{i,j} \bar{q}_i^f [i\gamma^\mu D_\mu - m_f] \delta_{ij} q_j^f - \frac{1}{4} G^a_{\mu\nu} G^{a,\mu\nu} \tag{2.40}$$

where q_i^f and $\bar{q}_i^f$ represent a quark field of flavor f that carries a color $i = 1,2,3$. The symbol δ_{ij} is the Kronecker delta. The gauge invariant gluon field strength tensor is represented by $G^a_{\mu\nu}$, and is defined as

$$G^a_{\mu\nu} = \partial_\mu A^a_\mu - \partial_\nu A^a_\mu + g_s f^{abc} A^b_\mu A^c_\nu \tag{2.41}$$

where g_s is the strong gauge coupling and A^a_ν represents the gluon field with index $a = 1, \ldots, 8$. This corresponds to eight gluon fields in QCD. The $G^a_{\mu\nu}$ strength tensor is

analogous to the electromagnetic field strength tensor $F_{\mu\nu} = \partial_\mu A_\mu - \partial_\nu A_\mu$, with the difference that $G^a_{\mu\nu}$ has an additional coupling term between the gluon fields that ensures SU(3) local gauge invariance. When the gluon strength tensors are contracted in $\mathscr{L}_{\text{QCD}}$, this gives rise to triple and quartic gluon couplings. The f^{abc} coefficients are known as the structure constants of SU(3). The latter are directly related to the Lie algebra of the theory. Indeed, the commutation relationship between the generators of the SU(3) symmetry denoted by t^a for a color index a, is given by

$$[t^a, t^b] = i f^{abc} t^c \tag{2.42}$$

like in the SU(2)_L case, the generators of the SU(3) group do not commute. This another way of saying that the theory is non-abelian. In Eqn. (2.40), the D_μ symbol represents the gauge covariant derivative of QCD, defined as

$$D_\mu = \partial_\mu - i g_s t^a A^a_\mu \tag{2.43}$$

where t^a are the eight generators of the SU(3) symmetry. Such generators can be represented by the Gell-Mann 3x3 matrices multiplied by a factor of $1/2$. The covariant derivative ensures that the Lagrangian density of QCD remains invariant under SU(3) local gauge transformations. Note also that, in writing down the covariant derivative, one introduces a fundamental coupling between quarks and gluons, which is analogous to the coupling between electrically charged fermions and the photon.

There is one more renormalizable term that we could add to the Lagrangian density of QCD without breaking gauge invariance,

$$\mathscr{L}_{\text{CP}} = \theta \varepsilon^{\mu\nu\alpha\beta} G^a_{\mu\nu} G^a_{\alpha\beta} \tag{2.44}$$

where θ is a free parameter and $\varepsilon^{\mu\nu\alpha\beta}$ is the rank-4 Levi-Civita symbol. This term violates CP symmetry in QCD interactions. Such an additional term can be written down

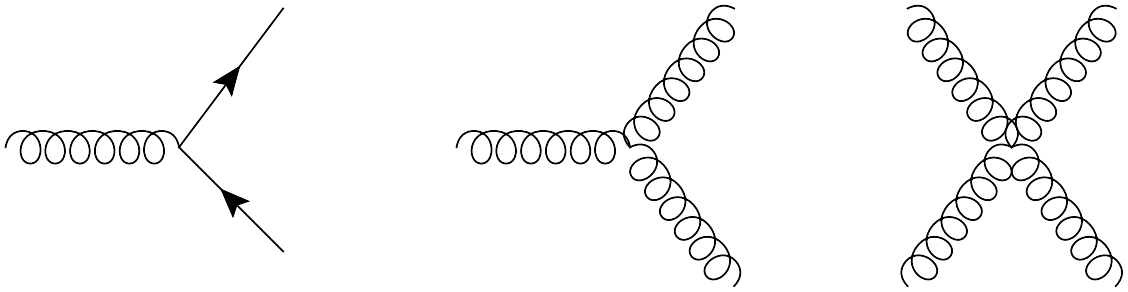

Figure 2.6: Tree-level couplings of quantum chromodynamics. From left to right: coupling of gluon to quarks, triple and quartic self-interaction coupling between gluons.

in terms of a total derivative, which means it will not contribute at any order of perturbation theory. However, non-zero values may have manifestations in non-perturbative QCD calculations. Precision measurements of the neutron electric dipole moment, which is very sensitive to non-zero θ values, show that the value of θ is consistent with 0 (36). The fact that $\theta \approx 0$ can be used as a motivation to postulate additional symmetries in the SM Lagrangian that would explain the smallness of θ. A popular example of this will be discussed in the Section of beyond the SM2.7.

There are three main characteristics in QCD that make it very special:

Color confinement: Quarks and gluons are confined within hadrons, which are color-neutral composite particles. For instance, the proton is composed of three valence quarks (two up quarks, one down quark) bound together by gluons and a sea of quark-antiquark pairs.

Color confinement has yet to be proven analytically from first-principles calculations based on the fundamental Lagrangian of QCD. We accept the property of color confinement as a phenomenological truth of strong interactions, which is well supported by experimental data in hadron production from the last several decades and from lattice QCD calculations. Such lattice QCD calculations consist of directly solving the equations of motion of QCD numerically with a given set of boundary conditions by slicing the continuous Euclidean spacetime into a grid of spacetime cells of finite size smaller than the typical hadronic dimensions. The smaller the cells, the closer the numerical calculation

is to the "true" QCD prediction (37). These calculations are computationally demanding and require the use of supercomputers for serious calculations. These calculations are able to reproduce the measured masses of hadrons within the uncertainties. Lattice QCD is the closest approach we have to understand the phenomenon of confinement and hadron formation from first principles.

Asymptotic freedom: The strength of interactions between quarks and gluons decreases at short distances (high energies). This property is a consequence of the anti-screening effects that emerge in the vacuum polarization diagrams of QCD, owing to the creation and annihilation of gluons by quantum fluctuations. Since this is related to the self-interaction of gluons, asymptotic freedom is ultimately a consequence of the underlying SU(3) non-abelian gauge symmetry of QCD. The property of asymptotic freedom in SU(3) gauge theories was discovered in 1973 by David Gross, Frank Wilczek (34), and independently David Politzer (33). For their theoretical findings, and once QCD was established as the quantum theory of strong interactions, they were awarded the 2004 Nobel Prize in Physics. The emergence of asymptotic freedom is related to the renormalization of the gauge coupling, and is discussed more in detailed in Section 2.6.1.

Chiral symmetry breaking: The spontaneous symmetry breaking of a global symmetry in the light-quark sector, known as chiral symmetry, results in the generation of mass for hadrons composed of light-quarks far larger than the masses of the individual valence quarks. Chiral symmetry breaking is most evident in the mass generation of neutrons and protons, accounting for approximately 99% of their mass that comes from the QCD binding energy. Hence, the bulk of the mass of "visible" matter comes from the binding energy keeping nucleons bound together, *not* from the Higgs mechanism.

Chiral symmmetry breaking as a mechanism for hadron mass generation has some resemblance with the Higgs mechanism in the electroweak sector. Chiral symmetry breaking explains why pseudoscalar mesons are exceptionally light; they can be associated to the (theoretically massless) Goldstone bosons from the associated spontaneous symmetry

breaking. Yoichiro Nambu, who described this phenomenon (38), was awarded the 2008 Nobel prize in Physics for the development of chiral perturbation theory and for identifying the role of spontaneous symmetry breaking in QCD. In this thesis, we only consider the effect chiral symmetry breaking in regards to the generation of mass for nucleons.

2.6.1 Renormalization of QCD coupling

In a quantum field theory, the mass and interaction couplings are not static quantities. Instead, they run with the characteristic momentum scale of the process. This is a direct consequence of the presence of virtual particles that pop in and pop out of existence due to quantum fluctuations of the vacuum. The higher the energy scale of the process, the more likely it is that one can "resolve" these quantum fluctuations. One can account for the presence of such virtual particles in a procedure known as "renormalization."

In quantum field theories, physical quantities can be expressed in a perturbation series in powers of a weak coupling parameter. In QCD, one can perform a power series expansion in the strong coupling $\alpha_s \equiv g_s^2/4\pi$. If the coupling strength is small $\alpha_s \ll 1$, the series may converge sufficiently quickly such that it allows for a reliable prediction of a physical quantity, even if only a limited number of perturbative orders are known/calculable.

Examples of physical quantities of interest are cross sections, decay rates, branching fractions, event shapes, among others. Consider $\mathscr{R}$ a dimensionless physical quantity that depends on α_s and on a characteristic energy scale Q, which is larger than any other energy dimensionful scale. This characteristic energy scale can be the Lorentz invariant momentum transfer, for example. The quantity $\mathscr{R}$ can be calculated as a perturbation series in α_s. When doing so, so-called "ultraviolet" divergences occur. They are called ultraviolet since they correspond to contributions with very high energy (short distances), analogous to the fact that ultraviolet light has shorter wavelength than visible light. These ultraviolet divergences appear in Feynman diagrams with virtual corrections, where the four-momenta of the virtual particles is unbound, and is therefore allowed to go to infin-

ity under the phase-space integrals used to calculate scattering amplitudes. These divergences are systematically removed by the renormalization of a set of physical parameters in the Lagrangian density. Fixing these parameters at a given scale, and thus "absorbing" the ultraviolet divergences, introduces a second – although artificial – momentum scale μ_R known as the renormalization scale. As a consequence, $\mathscr{R}$ and α_s become functions of μ_R. Since $\mathscr{R}$ is a dimensionless quantity by construction, one can assume that it can only depend on ratios of Q^2/μ_R^2, and on the renormalized strong coupling $\alpha_s = \alpha_s(\mu_R^2)$.

Because the choice of μ_R is arbitrary and ultimately μ_R is an nonphysical quantity, the value of the physical observable $\mathscr{R}$ cannot depend on μ_R. Thus,

$$\mu_R^2 \frac{d}{d\mu_R^2}\mathscr{R} = \Big(\mu_R^2 \frac{\partial}{\partial \mu_R^2} + \mu_R^2 \frac{\partial \alpha_s}{\partial \mu_R^2}\frac{\partial}{\partial \alpha_s}\Big)\mathscr{R} \equiv 0, \tag{2.45}$$

Eqn. (2.45), known as renormalization group equation, implies that any explicit dependence of $\mathscr{R}$ on μ_R must be cancelled by a counteracting dependence of α_s on a scale μ_R to all orders in the perturbative expansion. One typically identifies the renormalization energy scale with the physical energy scale of the process, $\mu_R = Q$, although there are other procedures that can be used to optimize the μ_R scale, for instance with the Brodsky-Lepage-Mackenzie optimization prescription (39). In this case, α_s transforms into the *running coupling* α_s, and the energy dependence of $\mathscr{R}$ enters only through the energy dependence of $\alpha_s = \alpha_s(\mu_R^2)$. It is said that the strong coupling "runs" with the renormalization scale.

The dependence of $\alpha_s(\mu_R^2)$ on μ_R is given by the β-function, defined as

$$\beta(\alpha_s) \equiv \mu_R \frac{\partial \alpha_s}{\partial \mu_R} \tag{2.46}$$

the β-function can be calculated in perturbative QCD (pQCD) as a power series in α_s,

$$\beta(\alpha_s) = -\beta_0 \alpha_s^2 - \beta_1 \alpha_s^3 - \beta_2 \alpha_s^4 + \ldots \tag{2.47}$$

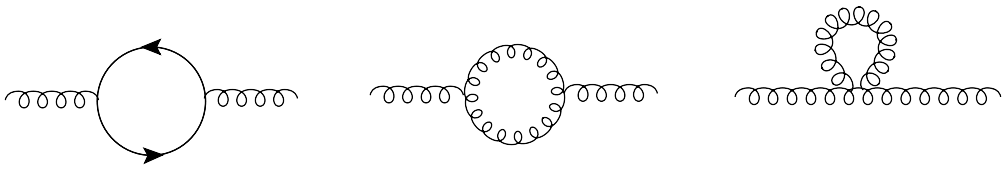

Figure 2.7: Self-energy diagrams that modify the gluon propagator. The momenta of the virtual particles is allowed to go to infinity, which renders ultraviolet divergences in the perturbative calculation. This requires the introduction of a renormalized coupling that runs with a renormalization energy scale, as described in the text.

in QCD, the β_i coefficients only depend on the number of active quark flavors, n_f. The calculation of the β-function coefficients is related to the self-energy corrections to the gluon propagator shown in Fig. 2.7. Note that the first diagram, which includes the splitting of the gluon into virtual quark-antiquark pairs, is directly analogous to the one present in quantum electrodynamics, which is related to "screening" effects. The other two are self-energy diagrams involving only gluons, and leads to anti-screening effects.

The β function is known up to α_s^6, which corresponds to the contribution of up to 150,0000 five-loop Feynman diagrams(40). For pedagogical reasons, we can focus on the one-loop β function. Indeed, already the one-loop β function gives insight into the dependence of the strong coupling with the renormalization scale. The one-loop β function reads

$$\beta = -\beta_0 = \frac{2n_f - 33}{12\pi} \tag{2.48}$$

turning back to the renormalization group equation, we have

$$\mu_R \frac{\partial \alpha_s}{\partial \mu_R} = -\beta_0 \tag{2.49}$$

solving for $\alpha_s = \alpha_s(\mu_R)$, we have the following solution

$$\alpha_s(\mu_R) = \frac{12\pi}{(33 - 2n_f)\ln(\mu_R^2/\Lambda_{\rm QCD}^2)} \tag{2.50}$$

where $\Lambda_{\rm QCD}$ is the integration constant and n_f is the number of quark flavors. The

value of $\Lambda_{\rm QCD}$ is not predicted in pQCD, but global fits to α_s indicate that $\Lambda_{\rm QCD} \approx 200$ MeV. The parameter $\Lambda_{\rm QCD}$ is regarded as the energy scale where the theory becomes strongly coupled. Considering $n_f = 5$ (to account for up, down, strange, charm, and bottom quarks), we see here that the strong coupling decreases logarithmically with the renormalization scale. If we lived in a world where the number of quark flavors is $n_f > 16$, we would obtain a coupling that increases logarithmically with energy. Measurements that rely on a large variety of probes support the expected asymptotic freedom effect, as shown in Fig. 2.8. This is the property of asymptotic freedom of QCD, a result that gave David Gross, Frank Wilczek, and David Politzer the Nobel Prize in Physics in 2004.

The strong coupling increases rapidly as the renormalization scale approaches Λ_{QCD}. When $Q \approx \Lambda_{QCD}$, we are in a regime where the theory becomes strongly coupled; the natural degrees of freedom stop being quarks and gluons, and one instead obtains a simpler description based on a hadronic picture. This delimits the perturbativity of the theory significantly. In the regime where the theory becomes strongly coupled and perturbativity is lost, one can use other methods. For example, those based on the duality of theories in the Anti-de-Sitter space with conformal field theories (AdS-CFT correspondence), which was conjectured by Juan Maldacena more than twenty years ago (41), or the lattice QCD calculations mentioned in the context of color confinement proposed by Kenneth Wilson in the 1970s (37).

Usually, for a given measurement one quotes the value of α_s evaluated at the mass of the Z boson, so for $\mu_R = m_Z = 91.1876$ GeV. The world-average value quoted in the 2020 Review of the Particle Data Group is (29),

$$\alpha_s(\mu_R = m_Z) = 0.1179 \pm 0.0010 \tag{2.51}$$

at face value, this seems to be very small. However, when we compare it with its analogue of electromagnetic interactions, $\alpha_{em} \equiv e^2/4\pi \approx 1/137 = 0.00729927$, we see we are dealing mostly with a (not) so small coupling strength in the case of QCD. The fact

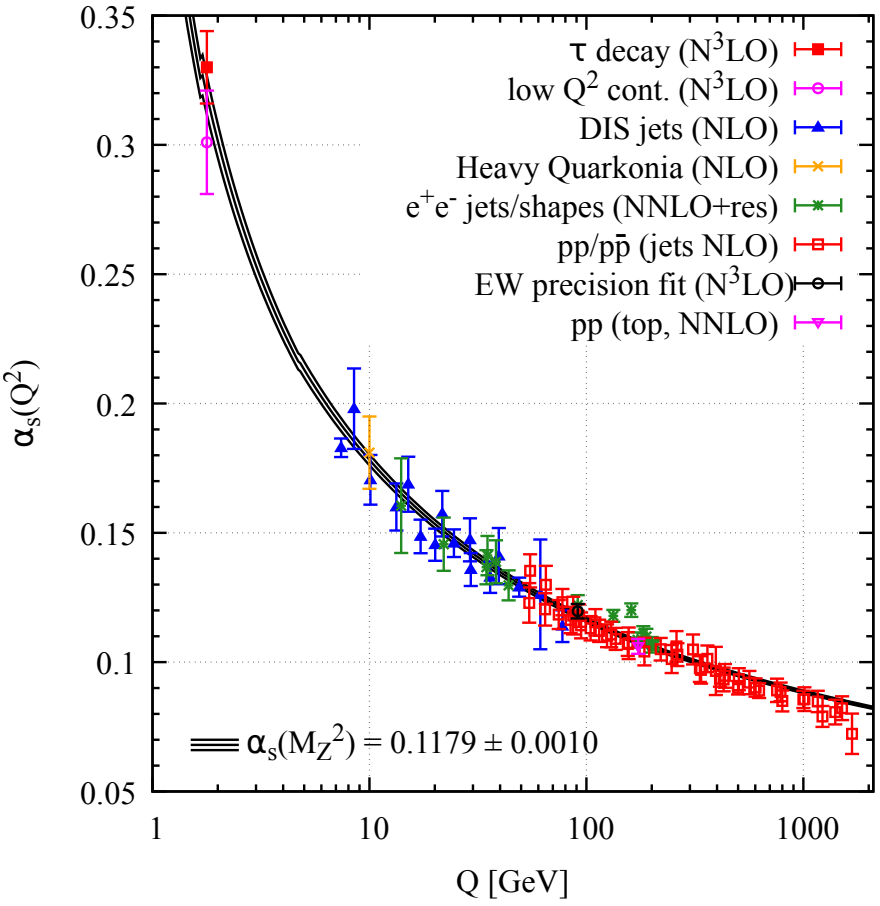

Figure 2.8: Summary of extractions of α_s as a function of the energy scale Q. The respective degree of QCD perturbation theory used in the extraction of α_s is indicated in brackets. The calculations are presented at next-to-leading order (NLO), next-to-NLO (NNLO), NNLO matched to a resummed calculation (NNLO+res), next-to-NNLO (N^{3}LO). The values at lower Q require higher precision due to the stronger coupling value. Figure extracted from Ref.(29).

that $\alpha_s \gg \alpha_{em}$ means that, in practice, one needs higher order corrections to capture the dominant corrections for QCD processes than for electromagnetic or weak processes. The coupling α_s decreases slowly (logarithmically) with the hard energy scale of the process, meaning that for typical hard processes at the Tevatron and at the LHC, one can think of a strong coupling $\alpha_s \approx 0.1$ for $Q \approx 100 - 1000$ GeV as a rule of thumb.

The verification of the running of the strong coupling validates several aspects of the theoretical foundations of QCD. It is a confirmation of the quantum field theory formalism and the renormalization procedure, as well as the conjectured internal gauge symmetry of strong interactions. In addition to the gauge coupling, other quantities in the Lagrangian density of QCD, such as the fields and masses of the quarks, are renormalized following a similar procedure, which is outside of the scope of this thesis.

2.6.2 Experimental evidence in support of QCD

Since the main topic of this thesis is on measurements that probes the behavior of QCD interactions, we give here an overview of the main pieces of experimental evidence that support the current formulation of strong interactions in a quantum field theory. Such overview also helps us lay down several concepts and phenomena that are important to contextualize QCD in modern collider physics, such as the notion of parton distribution functions and their associated renormalization group equations (the Dokshitzer–Gribov–Lipatov–Altarelli–Parisi evolution equations of pQCD) as well as the concept of "jets" as an experimental signature of quarks and gluons.

Given that quarks and gluons cannot be directly observed in an experiment, it took a long time for the experimental community to establish the validity of QCD in a number of experiments in electron-positron (e^-e^+), electron-proton, and proton-(anti)proton collisions. Several tests over the last decades of the 20th century helped establish the modern picture that we have now of strong interactions. There is a long list of experimental results that have validated the formalism of QCD, and that supports our current picture of

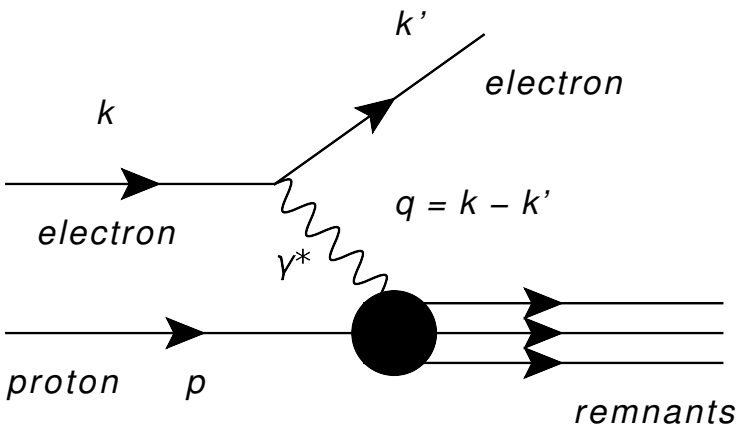

Figure 2.9: Deep-inelastic scattering in electron-proton collisions. The photon is able to probe the proton at distances smaller than the proton radius.

the microscopic world in terms of quarks and gluons. In the following subsections, we summarize some of the most important ones. We finalize this Section with remarks on QCD.

2.6.2.1 Bjorken scaling

The first piece of evidence that quarks are real constituent elements of hadrons –such as the proton or neutron– was obtained in *deep-inelastic scattering* (DIS) electron-proton experiments. The logic is the following: if one can probe the proton "deep" enough with a virtual photon emitted from the incoming electron –i.e., if the wavelength of the virtual photon is much shorter than the radius of the proton –, then one should be able to resolve whatever internal structure there is inside of the proton — if there is one. The virtual photon emitted off the electron will interact elastically with such point-like subnucleonic particles. In that case, if these particles are truly point-like, then at some point it does not matter how hard we are hitting the proton with the electromagnetic probe; we should see the same internal structure at shorter and shorter distances. In other words, the DIS cross section should be independent of the four-momentum transfer, Q, when $Q^2 \gg m_p^2 \approx 1$ GeV^2. This scaling behavior is known as Bjorken scaling named after physicist James Bjorken who worked on this problem together with Emmanuel Paschos (42) based on the

ideas of the parton model of Richard Feynman (43). A schematic diagram of DIS is shown in Fig. 2.9.

For the discussion of DIS, it is convenient to introduce the set of frequently used Lorentz invariant quantities that are typically used to describe this process. In deep-inelastic electron-proton scattering, more likely than not we will have interactions of the type $e(k)p(p) \rightarrow e(k')X$, where X denotes any physically allowed hadronic final state. The symbols k, p, k' represent the four-momenta of the incoming electron, the proton, and the outgoing electron, respectively. The following set of Lorentz invariant variables is introduced to describe the kinematics of the process:

$$s = (k+p)^2 \tag{2.52}$$

$$Q^2 = -q^2 = -(k-k')^2 \tag{2.53}$$

$$y = \frac{qp}{kp} = \frac{E_{\text{lab}} - E'_{\text{lab}}}{E_{\text{lab}}} \tag{2.54}$$

$$x = \frac{Q^2}{2pq} \tag{2.55}$$

$$W^2 = (q+p)^2 \tag{2.56}$$

where E_{lab} and E'_{lab} are the energies of the initial- and final-state electron in the laboratory frame, s is the square energy in the center-of-mass frame, Q^2 is the four-momentum transfer squared, which can be used as a proxy of the resolution that is used to probe inside the proton. The variable y measures the relative loss of energy of the electron. The fraction x is known as the Bjorken scaling variable. As stressed later in this Chapter, assuming that the proton is made out of point-like particles, the variable x may be interpreted as the fraction of the proton momentum carried by the interacting point-like particle inside the proton. The variable W is the invariant mass of the hadronic system X. One can use two of the aforementioned kinematic variables to describe the DIS process. Traditionally, Q^2 and x are the variables used to describe DIS, which we will do as well in

this thesis.

For DIS, it can be shown that the most general Lorentz-invariant expression for the double-differential cross section for $ep \to eX$ inelastic scattering mediated by the exchange of a virtual photon is given by

$$\frac{d^2\sigma}{dxdQ^2} = \frac{4\pi\alpha_{\text{em}}^2}{Q^4}\Big[\big(1-y-\frac{m_p^2 y}{Q^2}\big)\frac{F_2(x,Q^2)}{x} + y^2 F_1(x,Q^2)\Big] \tag{2.57}$$

where m_p denotes the mass of the proton and $\alpha_{\text{em}} \approx 1/137$ is the fine structure constant of QED. The functions F_1 and F_2 are known as the *structure functions* of the proton, which can generally be functions of x and Q^2. The $F_1(x,Q^2)$ function can be identified as being purely magnetic in origin, and $F_2(x,Q^2)$ is related to the charged-particle content of the proton, as it will be discussed later.

For DIS, where $Q^2 \gg m_p^2$, the expression for the cross section can be reduced to

$$\frac{d^2\sigma}{dxdQ^2} = \frac{4\pi\alpha_{\text{em}}^2}{Q^4}\Big[(1-y)\frac{F_2(x,Q^2)}{x} + y^2 F_1(x,Q^2)\Big] \tag{2.58}$$

in a fixed-target ep experiment, the Lorentz invariant kinematic variables Q^2, x, and y, can be obtained event-by-event from the energy of the outgoing electron and its scattering angle. One can measure the double-differential cross section at values of x and Q^2, and disentangle the contributions to $F_1(x,Q^2)$ and $F_2(x,Q^2)$ according to the parametrization of Eqn. (2.58) by measuring y (at large y the $F_1(x,Q^2)$ structure function dominates, whereas for small y the $F_2(x,Q^2)$ structure function dominates).

The first studies of structure functions in inelastic electron-proton scattering were obtained at SLAC (45). Electrons of energies between 5 to 20 GeV were fired at a liquid hydrogen target. The scattering angle of the electron was measured using a large movable spectrometer. The energy of the scattered electron could be selected by using a magnetic field. The differential cross sections, measured over a range of incident electron energies, were used to determine the structure functions. The data confirmed Bjorken scaling be-

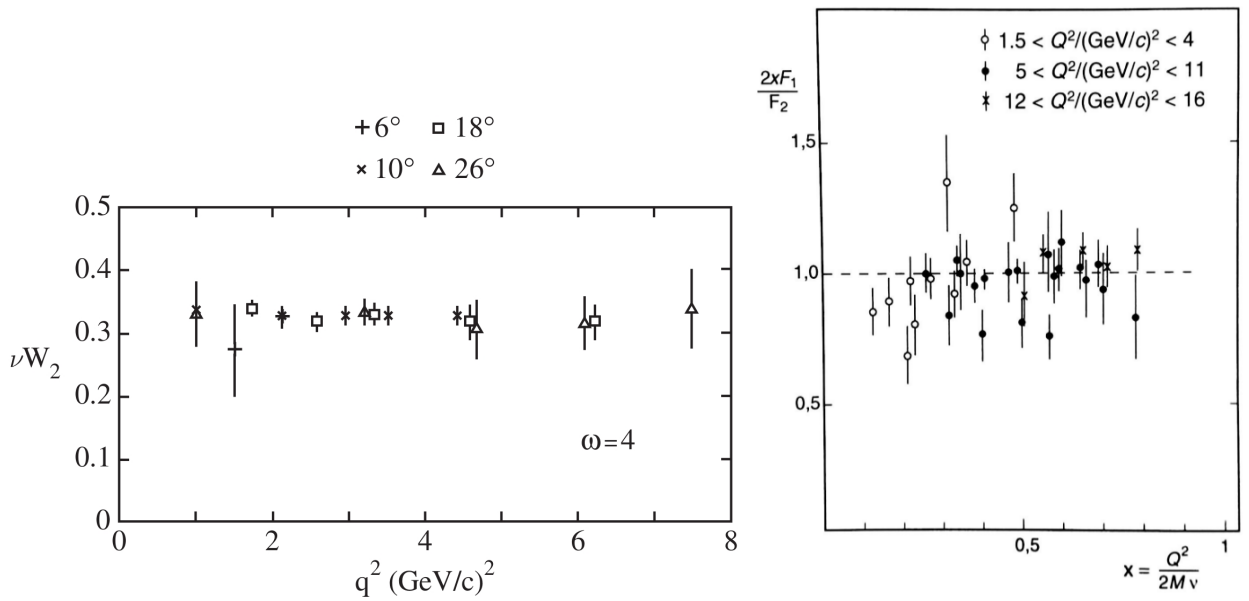

Figure 2.10: (Left) Evidence of Bjorken scaling in DIS data (44). The vertical axis is an alternative way of parametrizing the structure function (F_2 in the text). The horizontal axis represents various virtualities Q^2 of the electromagnetic probe. (Right) Measurement of Callan-Gross relation in DIS. The ratio $2xF_1/F_2$ as a function of Bjorken-x suggests that the point-like particles inside the proton are spin-1/2 particles.

havior, i.e., the fact that both $F_1(x,Q^2)$ and $F_2(x,Q^2)$ are nearly-independent functions of Q^2, i.e., $F_1(x,Q^2) \to F_1(x)$ and $F_2(x,Q^2) \to F_2(x)$.

To further understand the properties of these point-like particles inside of the proton, one can extract the Callan-Gross relation between the $F_1(x,Q^2)$ and $F_2(x,Q^2)$ structure functions(46). For spin-1/2 particles, the expected Callan–Gross relation is

$$\frac{1}{2x}F_2(x,Q^2) = F_1(x,Q^2) \tag{2.59}$$

whereas for spin-0 particles, the expected Callan–Gross relation is

$$\frac{1}{2x}F_2(x,Q^2) = 0 \tag{2.60}$$

as shown in the right panel of Fig. 2.10, the ratio of $2xF_1/F_2$ as a function of Q^2 indicates that the point-like particles inside the proton are of spin-1/2. The direct relationship

between the two structure functions suggests that the magnetic moment of the point-like particles is related to its electric charge, which is expected for a Dirac spin-1/2 particle. This is an important piece of the puzzle used to convince the scientific community of the physical reality of quarks inside the proton. Furthermore, the establishment of $F_2(x)/2x = F_1(x)$ allows for a discussion of the structure of the proton in terms of only one structure function. Traditionally, we use only $F_2(x)$, which we will do for the rest of this thesis.

Before quarks and gluons were generally accepted, Feynman proposed that the proton was made up of point-like constituents that he called "partons", since they are "part" of the proton(43). Since these partons are nowadays identified with quarks, this is referred to as the quark-parton model. In the quark-parton model, the basic interaction in DIS is that of an elastic scattering of the photon with a spin-1/2 quark within the proton. In the quark-parton model, the quark is an exactly free particle. This is a good approximation, but eventually one needs to account for interactions between quarks to describe the data in QCD.

In the quark-parton model, the Bjorken x variable can be identified as the fraction of the momentum of the proton carried by the struck quark (assuming that the mass of the proton is much smaller than the energy scale of the process). Therefore, the measurements of the x dependence of the structure functions could be related to the momentum distributions of the quarks within the proton through the structure function F_2.

The distributions of quarks inside the proton can be expressed in terms of so-called *parton distribution functions* (PDFs). In the quark-parton model, the distributions have a probabilistic interpretation. For instance, the up-quark PDF for the proton $u(x)$ is such that one can calculate the number of up-quarks within the proton with momentum fraction between x and $x+dx$ by calculating the product $u(x)dx$. One can similarly define a PDF for the down-quark, and in principle for all other "active" quarks. The PDFs are quantities that are extracted from the experiment (mostly from DIS data, but more generally from all experiments that can probe the internal structure of the proton in a clean way).

The parton model de facto predicts Bjorken scaling, since there are no interactions between quarks embedded in the model. Since in the quark-parton model the quarks are treated as spin-1/2 partons, the Callan–Gross relation is also automatically satisfied. The advantage of the parton model is that it can help elucidate further how the quarks might share their energy with the proton, which can be done from the F_2 measurement. The structure function $F_2(x)$ is related to the proton PDFs by

$$F_2(x) = x\sum_i Q_i^2 q_i(x) \tag{2.61}$$

in the static model of the proton (the one that can be used for flavor physics), the proton is only made up of two up quarks and one down quark. In the quark-parton model —and in fact, the way it was envision by Feynman—, there might be numerous point-like particles inside the proton, not only the "valence" quarks from the static model. Nowadays, we understand this comes from the fact that the proton is a dynamic system where the quarks are constantly exchanging virtual gluons, which can thereafter split into quark-antiquark pairs. In addition to up- and down-quarks, we can have the contribution of virtual strange quark and antiquark pairs, or even heavier, off-shell quarks (charm, bottom quark). For the moment, let us consider the lightest flavors of quarks. In the quark-parton model, we have that the structure function is given by

$$F_2(x) = x\left[\frac{4}{9}u(x) + \frac{1}{9}d(x) + \frac{4}{9}\bar{u}(x) + \frac{1}{9}\bar{d}(x)\right] \tag{2.62}$$

where $u(x)$, $d(x)$, $\bar{u}(x)$, and $\bar{d}(x)$ are the PDFs for up- and down-quarks and up- and down-antiquarks, respectively. The factors of $4/9$ and $1/9$ come from the electric charge of $2/3$ and $1/3$ of the up- and down-quarks. The quark distributions are extracted by fitting them to $F_2(x)$. One could define a set of PDFs to parametrize the neutron structure function, where there are two down quark and one up quark intrinsic distributions. By isospin arguments, one can relate the down (up) quark distribution of the neutron with

the up (down) quark distribution of the proton, as well as their sea of quark-antiquark distributions.

After fitting the up-quark and down-quark distributions, one can integrate them over x to obtain the total fraction of the momentum carried by the quarks in the proton:

$$f_u = \int_0^1 [xu(x) + x\bar{u}(x)]dx, \qquad f_d = \int_0^1 [xd(x) + x\bar{d}(x)]dx \tag{2.63}$$

where f_u represents the fraction of momentum carried by the up quark and antiquarks, and f_d the fraction of the proton momentum carried by the down quark and antiquarks. Assuming this was the total subnucleonic content of the proton, $f_u + f_d \approx 1$. However, experimentally it was found that

$$f_u \approx 0.36, \qquad f_d \approx 0.18 \tag{2.64}$$

the result confirms that the up-quark distribution is roughly twice as large as the down-quark distribution, consistent with the expectations from the static quark model. However, $f_u + f_d \approx 0.54$, i.e., there is nearly half of the proton momentum that is not accounted for by the quarks. Where is this momentum going? Nowadays, we understand that the remaining half of the proton's energy comes from gluons, as first suggested in Ref.(47). It is very interesting that, despite our lack of direct access to the gluon distribution in DIS, we can indirectly learn from it by analyzing the electrically charged quark content.

One can further analyze and constrain the PDFs by imposing so-called sum rules. For example, the up-quark PDF can be split into the contribution from the two valence quarks $u_V(x)$ and a contribution from the sea of up-quarks $u_S(x)$. Likewise, one can define a valence and sea component for the down quark. Then we have,

$$u(x) = u_V(x) + u_S(x), \qquad d(x) = d_V(x) + d_S(x) \tag{2.65}$$

for the antiquark PDFs, there are no valence quark component.

Since the proton consists of two valence up-quarks and one-valence down-quark, one can set of sum rules:

$$\int_0^1 u_V(x)dx = 2, \qquad \int_0^1 d_V(x)dx = 1 \tag{2.66}$$

for the sea of quark and antiquarks, it can be assumed that they should all be similar between each other. This is based on arguments that the strong force is flavor-blind, and that the light quarks mass can be neglected in DIS. Thus,

$$u_S(x) = \bar{u}_S(x) = d_S(x) = \bar{d}_S(x) \equiv S(x) \tag{2.67}$$

in the next section, now we see how QCD perturbative corrections give rise to violations from Bjorken scaling, and how this has been used to test pQCD to high precision.

2.6.2.2 Scaling violations in QCD

The observation of Bjorken scaling in DIS served as experimental evidence for the existence of point-like particles inside the proton, which we now identify with quarks and antiquarks. Bjorken scaling is expected for a theory with non-interacting particles, i.e., if quarks do not radiate gluons. This is the essence of the quark-parton model, and it works well for small $Q^2 \gg m_p^2$ at moderately large $x \approx 10^{-1}$ values. However, it should be expected that at high enough Q^2, such a scaling behavior should be broken. The reason is that, at larger Q^2, one should be able to "resolve" the quantum fluctuations that occur at shorter timescales and shorter distances. These quantum fluctuations are related to the radiation of gluons off the quarks $q \to qg$, and the splitting of these gluons into gluons $g \to gg$, and of gluons into quark-antiquark pairs $g \to q\bar{q}$. The interaction between quarks and gluons give rise to deviations from the simple quark-parton model, i.e., there should be Bjorken scaling violations in the structure function. In fact, as it will be shown later,

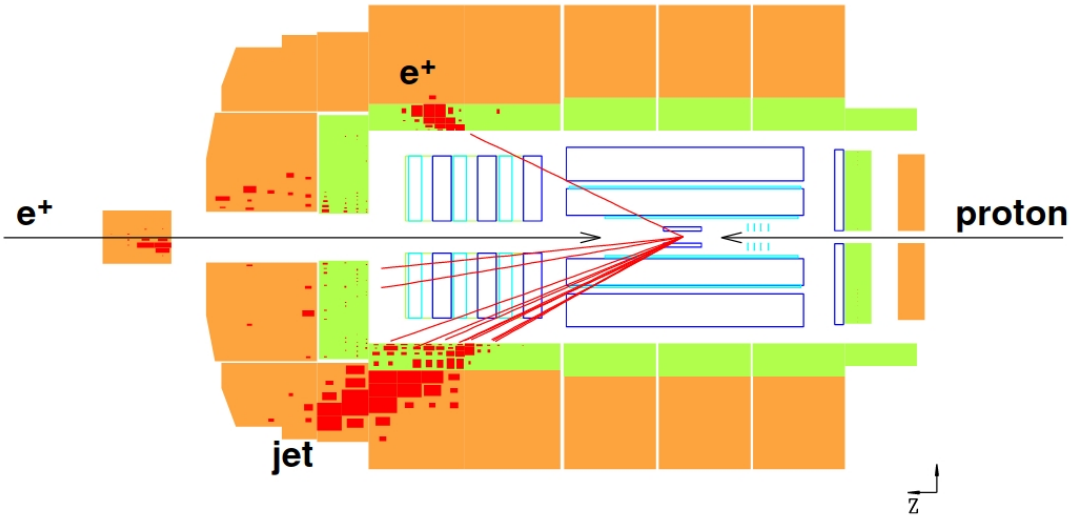

Figure 2.11: Deep-inelastic positron-proton scattering event display from the H1 experiment. The positron is scattered by the proton, which fragments in the forward region, and leads to the production of a hard jet.

the quark-parton model is now regarded as the "zeroth-order" prediction of QCD.

While early signs of scaling violations in the structure function were already known by the 1970s, initially it was rather hard to conclude if this were due to short-distance physics "lurking in" in the data or due to the missing nuclear corrections that may blur possible QCD signatures in the data. Fixed-target DIS experiments were not able to probe at high enough Q^2 values and low enough x to clearly see a systematic deviation from Bjorken scaling, and in fact it was believed that it would not be possible to observe these violations –which are logarithmic in Q^2– in the structure function.

The studies of DIS at very high Q^2 and at very low x were carried out at the HERA electron-proton collider ring that operated from 1991 to 2007 at the Deutsches Elektronen-Synchrotron (DESY) laboratory in Hamburg, Germany. Electrons (or positrons) with energy of 27.5 GeV were collided with 820 or 920 GeV protons. There were two large experiments at the HERA collider: the H1 and ZEUS experiments. Each experiment recorded over one million $e^{\pm}$p DIS collisions with $Q^2 > 200$ GeV^2. With a center-of-mass energy of about 300 GeV, the structure function of the proton was probed to values down to $x \approx 10^{-4}$ and Q^2 up to 10^4 GeV^2. An example of an event display from the H1 Collabora-

tion is shown in Fig. 2.11.

Deviations from Bjorken scaling were observed at low x, which are more pronounced at higher Q^2. An array of the measurements by the DIS experiments, which includes fixed-target and HERA results, is shown in Fig. 2.12. Such deviations from Bjorken scaling were more pronounced at higher Q^2. This implied that, at high Q^2, the proton is observed to have a larger fraction of small x quarks. These scaling violations are expected when one considers that the quarks inside the proton are not free particles; they interact with each other by the exchange of gluons. These gluons will further split into quark-antiquark pairs, which will further radiate gluons. The higher Q^2 is, the more we can resolve these parton splittings inside the proton. The more parton splittings are available, the more low x partons we have inside the proton. This trend is expected from QCD, and can be used to test QCD in detail. The advantage is also that the measurements of $F_2(x,Q^2)$ by the HERA experiments are so precise, that they can be used to set strong constraints and a challenging test of perturbation theory calculations. We describe briefly how these QCD corrections affect the general expression of the structure function $F_2(x)$ beyond the quark-parton model result of Eqn. 2.61. We will see that, by including the virtual and real emission of gluons, explicit dependence on Q appears, i.e., $F_2(x) \to F_2(x,Q^2)$ in QCD.

In terms of QCD perturbation theory, the quark-parton model formula of Eqn. (2.61) may be regarded as the zeroth-order term in the expansion of $F_2(x,Q^2)$ in α_s. For the α_s corrections to the quark-parton model expression, one has to calculate the photon-parton process diagrams shown in Fig. 2.13. The quark-parton model component corresponds to the QED vertex.

To evaluate this contribution, we need to sum over all the possible values of the new variables, y and k_t, that are introduced to describe the gluon. The result is

$$F_2(x,Q^2) = x\sum_i \int_x^1 \frac{dy}{y} f_i(y) Q_i^2 \left\{ \delta\left(1-\frac{x}{y}\right) + \frac{\alpha_s}{2\pi}\left(P\left(\frac{x}{y}\right) \ln\frac{Q^2}{\mu^2} + C\left(\frac{x}{y}\right)\right)\right\}, \qquad (2.68)$$

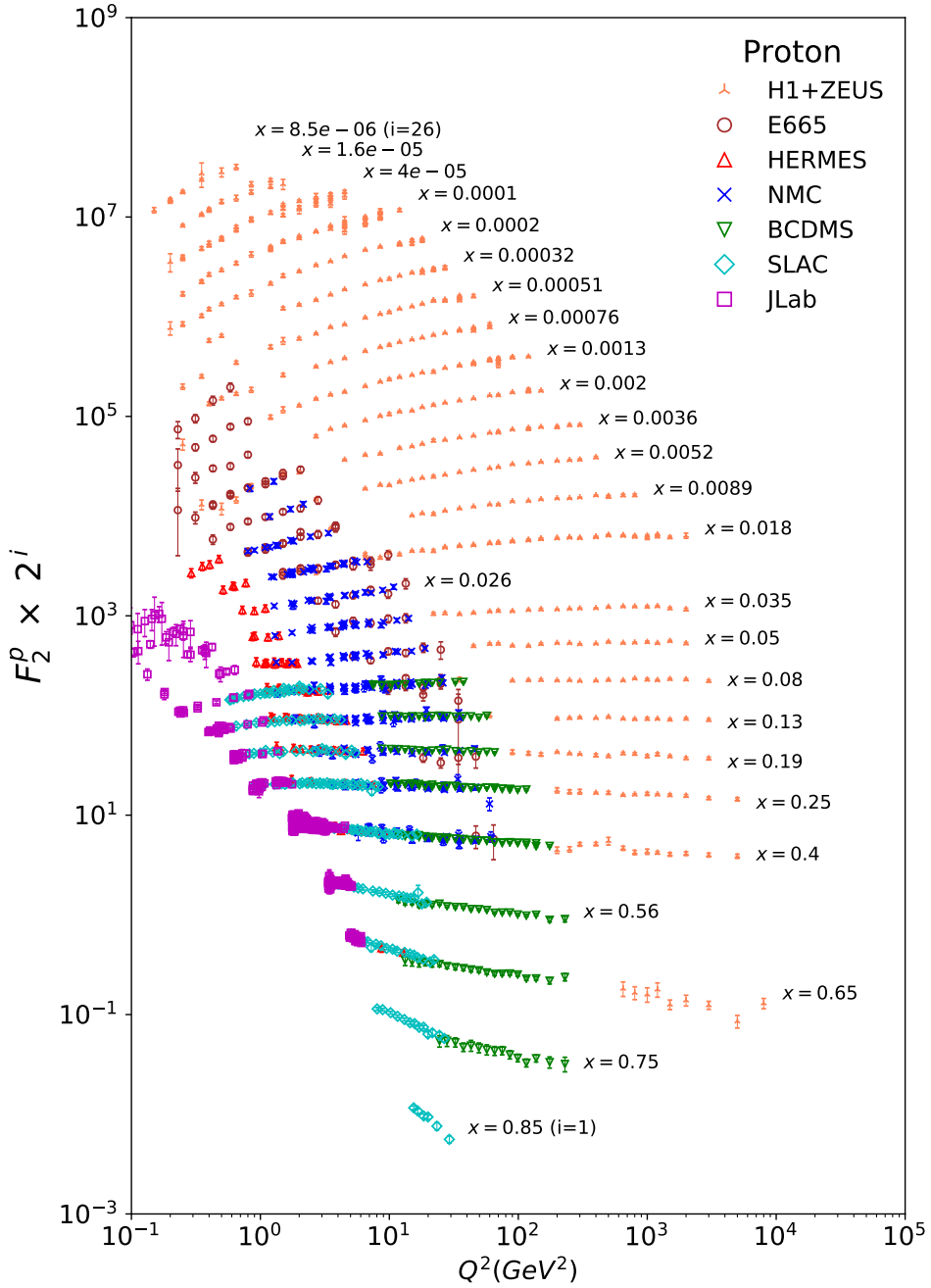

Figure 2.12: Proton structure function $F_2^p(x,Q^2)$ (vertical axis) as a function of Q^2 (horizontal axis) in bins of Bjorken-x. The families of points for a given value of x are artificially displaced by powers of 2^i, where $i = 0,1,2,\ldots$, for visibility purposes. Data from several fixed-target and electron-proton colliders are shown in this plot. The dependence of $F_2(x,Q^2)$ with Q^2 is evidence of Bjorken scaling violations in the data, which can be described in QCD. Figure extracted from Ref.(29).

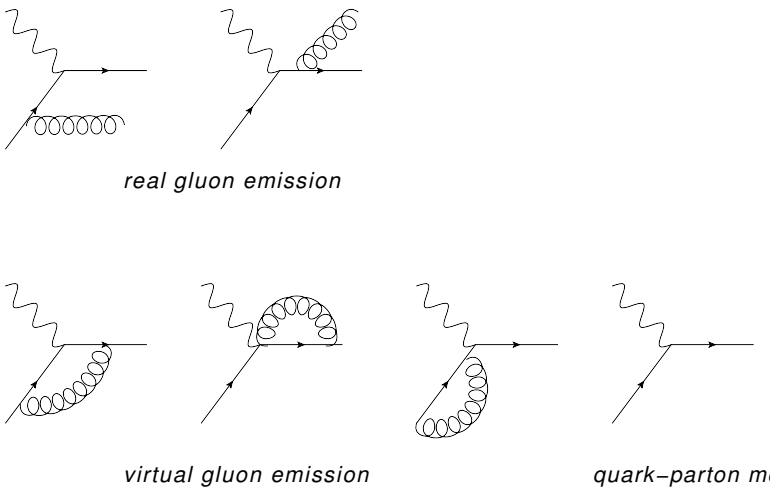

Figure 2.13: Leading order diagrams that contribute to the proton structure function. The diagram that yields the quark-parton model result is given by the lower right diagram, which is a pure QED diagram.

where P and C are known, calculable functions in perturbation theory. These are identified as the universal parton splitting functions (here, $P \equiv P_{qq}$ describes the $q \to qg$ splitting process, for example) and a process-dependent coefficient function C. The δ-function term in (2.68) is the zeroth-order quark-parton model contribution with $y = x$. The $\ln(Q^2/\mu^2)$ originates from the phase-space integration of the gluon bremsstrahlung $\int_{\mu^2}^{Q^2} \frac{dk_t^2}{k_t^2} = \ln\left(\frac{Q^2}{\mu^2}\right)$. The upper limit is set by the virtuality of the photon that scatters off a quark of transverse size $\approx 1/Q$. The lower bound is set on the grounds that the gluon could not resolve the individual color of the quark at $Q \ll \mu$.

Based on Eqn. (2.68), we can replace $f_i(x)$ by a well-behaved running parton density that runs with μ^2

$$f_i(x,\mu^2) \;=\; f_i(x) \;+\; \int_x^1 \frac{dy}{y} f_i(y)\, \frac{\alpha_s}{2\pi}\left(P\left(\frac{x}{y}\right)\ln\left(\frac{\mu^2}{\mu^2}\right) + C_1\right), \tag{2.69}$$

such that

$$F_2(x,Q^2) = x\sum_i \int_x^1 \frac{dy}{y} f_i(y,\mu^2) Q_i^2 \left[\delta\left(1-\frac{x}{y}\right) + \frac{\alpha_s}{2\pi}\left(P\left(\frac{x}{y}\right)\ln\frac{Q^2}{\mu^2} + C_2\right)\right], \tag{2.70}$$

where the division of the known function $C(x/y)$ into $C_1(x/y) + C_2(x/y)$ depends on the choice of factorization scheme.

The dependence of $f_i(x,\mu^2)$ on the scale μ can be treated in a similar way as it is done for the running of the strong coupling α_s. From Eqn. (2.69), we assert that the PDF must not depend on this arbitrary energy cut-off scale. With this requirement, the resulting renormalization group equation is,

$$\frac{\partial f_i(x,\mu^2)}{\partial \ln \mu^2} \;=\; \frac{\alpha_s}{2\pi} \int_x^1 \frac{dy}{y} f_i(y,\mu^2)\; P\left(\frac{x}{y}\right), \tag{2.71}$$

which describes the evolution of the parton density with μ^2. The resulting equation is known as the Dokshitzer–Gribov–Lipatov–Altarelli–Parisi (DGLAP) evolution equation of pQCD (48; 49; 50). The collinear and infrared sensitivity is "absorbed" in a way into a well-defined parton density function $f_i(x,\mu^2)$ that runs with the characteristic energy scale μ. We cannot use perturbation theory to calculate the absolute value of $f_i(x,\mu^2)$; the parton densities need to be extracted from the data. This is analogous to the situation of the strong coupling α_s discussed in Section 2.6.1, where its value at a given hard scale Q has to be extracted from the experiment, but its evolution with Q is dictated by a renormalization group equation of QCD. In the case of the parton densities, the corresponding renormalization group equation are the DGLAP evolution equations, which dictate their μ dependence. It can be shown that the DGLAP evolution equation effectively resums Feynman diagrams where the parton branchings are strongly ordered in transverse momentum.

The complete α_s correction to the $q \to qg$ splitting function is the interference of the diagrams shown in Fig 2.13. The resulting P_{qq} splitting function with this correction gives,

$$P_{qq} \;=\; \frac{4}{3}\,\frac{1+z^2}{(1-z)} \;+\; 2\delta(1-z). \tag{2.72}$$

In addition to the $\gamma q \to gq$ subprocesses, the $\gamma g \to qq$ processes need to be considered.

The $g \to q$ splitting function

$$P_{qg} \;=\; \frac{1}{2}(z^2 + (1-z)^2). \tag{2.73}$$

Then, the DGLAP evolution equation (Eqn. 2.71) for the quark density $q \equiv f_i$ becomes

$$\frac{\partial q(x,Q^2)}{\partial \ln Q^2} \;=\; \frac{\alpha_s}{2\pi}\,\left(P_{qq} \otimes q \;+\; P_{qg} \otimes g\right) \tag{2.74}$$

where g is the gluon density and $P_{qq} \equiv P$ is the $q \to qg$ splitting function of (2.72).

In general, P_{ab} describes the $b \to a$ parton splitting. The $\otimes$ symbol represents the convolution integral

$$P \otimes f \equiv \int_x^1 \frac{dy}{y} f_i(y)\; P\left(\frac{x}{y}\right). \tag{2.75}$$

Likewise, for the evolution of the gluon density we have

$$\frac{\partial g(x,Q^2)}{\partial \ln Q^2} \;=\; \frac{\alpha_s}{2\pi}\,\left(\sum_i P_{gq} \otimes (q_i + \bar{q}_i) \;+\; P_{gg} \otimes g\right), \tag{2.76}$$

where the sum is over the i quark flavors, and where the $q \to g$ and $g \to g$ splitting functions are given by

$$P_{gq} \;=\; P_{qq}(1-z) \;=\; \frac{4}{3}\,\frac{1+(1-z)^2}{z}, \tag{2.77}$$

$$P_{gg} \;=\; 6\left[\frac{1-z}{z} + \frac{z}{(1-z)_+} + z(1-z)\right] + \left(\frac{11}{2} - \frac{n_f}{3}\right)\delta(1-z). \tag{2.78}$$

In general, the splitting functions can be expressed as a power series in α_s

$$P_{ab}(\alpha_s, z) \;=\; P_{ab}^{\mathrm{LO}}(z) + \alpha_s P_{ab}^{\mathrm{NLO}}(z) + \alpha_s^2 P_{ab}^{\mathrm{NNLO}}(z) + \ldots \tag{2.79}$$

for the parton splitting functions at LO, next-to-leading (NLO) order, next-to-NLO (NNLO), and so forth.

If we are given the x dependence of the parton densities at some input scale Q_0^2, then we may solve the DGLAP evolution equations to determine the parton densities at a

higher Q^2. If one assumes that there is no intrinsic gluon distribution in the proton, the fit to HERA data fails to describe the data for all values of Q^2, as shown in Fig. 2.14. If one assumes there is a gluonic component at low Q^2, the branching of $g \to gg$ and $q \to qg$ embedded in DGLAP evolution correctly predicts the evolution of the structure function with Q^2 as a function of x. The presence of gluons generates generous amounts of quark-antiquark pairs at larger Q^2, which leads to a faster rise of $F_2(x, Q^2)$, especially at small-x. In conclusion: we need an intrinsic gluonic contribution to the proton in order to consistently describe the data for all Q^2 and x.

An example of the extracted parton distribution functions from HERA data is shown in Fig. 2.15. These can be interpreted as the energy profile of the proton in terms of its partonic constituents. The gluon distribution is much, much larger than the quark distributions, with the gluon distribution is mostly located at small-x. The valence quark distributions are located at higher x, consistent with our picture that the proton is (in the static quark model) a *uud* color-singlet state. The gluon densities increase from $Q_0^2 \to Q^2$ according to DGLAP evolution. This means that, the larger the resolution we use to probe the parton densities, the more partons created by quantum fluctuations we see inside the proton. In addition, the larger Q^2 is, the PDFs tend to be at smaller values of x. This is because, since we are resolving more parton splittings, they share, on average, a smaller amount of the fraction x.

The correct (global) parametrization of the DIS data has served as one of the most successful and stringent tests of pQCD. Nowadays, data that goes beyond the DIS process are included in these global fits. Indeed, in order to cover the kinematic regime to larger Q^2 values, one needs to use high-energy hadron-hadron collider data. The Tevatron and LHC experiments have given important input in this, complementing the kinematic reach of the DIS precision data. A diagram with the (approximate) coverage in x and Q^2 of the proton wavefunction at various collider setups is shown in Fig. 2.16. It is quite remarkable that one can have a unified description of data from different experiments with no sign

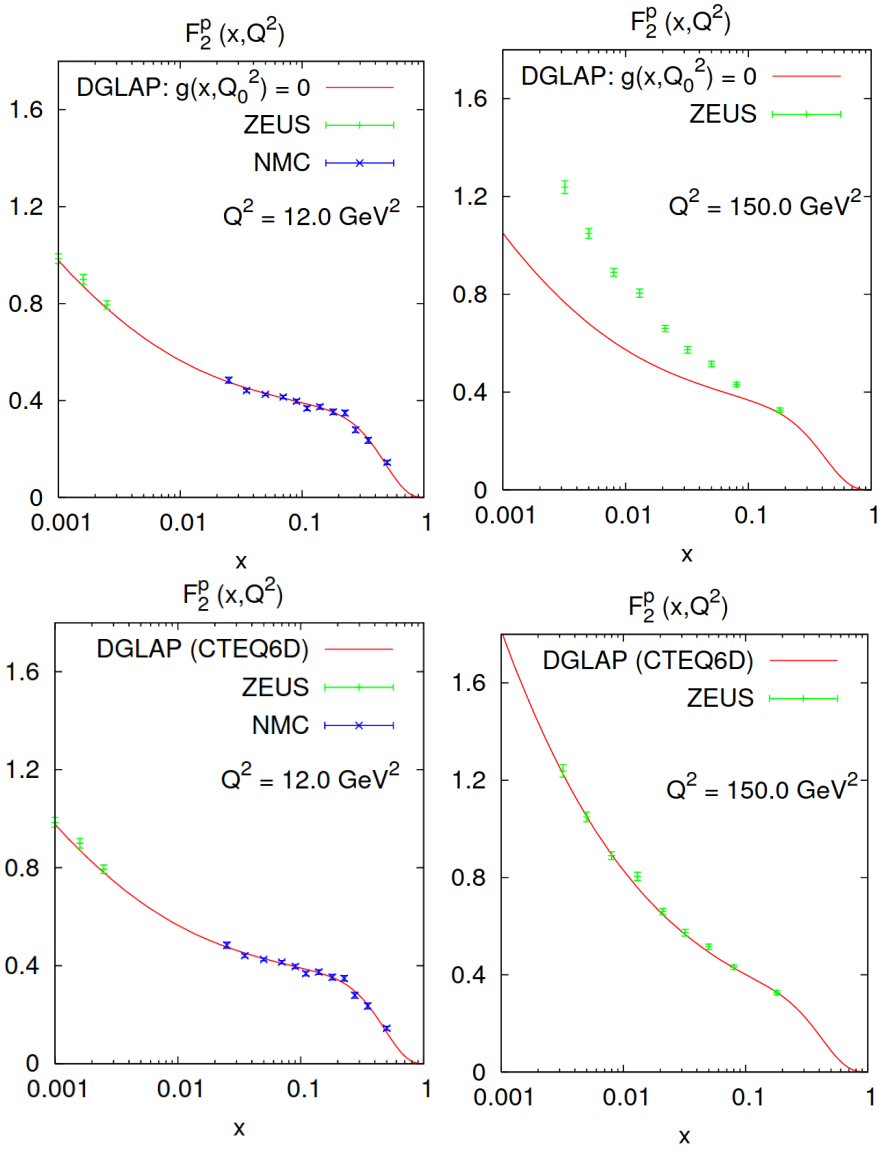

Figure 2.14: Upper panels: Fit to $F_2(x, Q^2)$ assuming there is no intrinsic gluon distribution correctly fits the data at low Q^2 over x. The prediction from DGLAP evolution from such a parametrization fails to predict the structure function at larger Q^2. Bottom two panels: A fit to $F_2(x, Q^2)$ assuming an intrinsic gluon distribution correctly fits the data at low Q^2 over x. Starting from such a parametrization, the prediction correctly describes the measured $F_2(x, Q^2)$ at higher Q^2. Conclusion: one needs intrinsic gluon PDFs to describe DIS data. The figures were prepared by the CTEQ Collaboration, and are extracted from Gavin Salam QCD lectures.

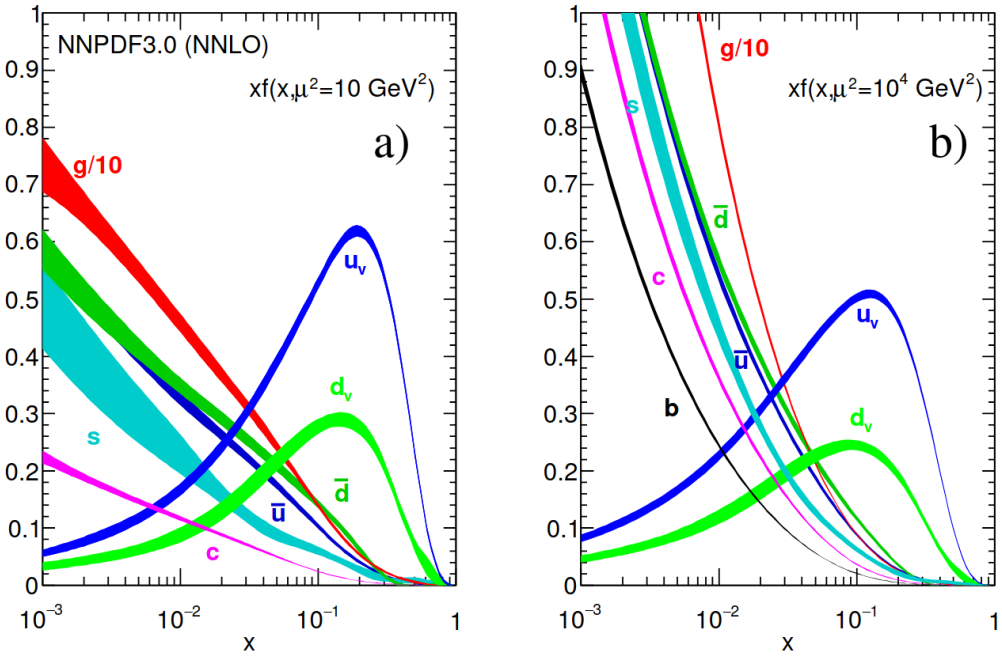

Figure 2.15: Parton distribution functions (PDFs) extracted from global fits to the data by the NNPDF Collaboration (51). On the left panel, we have the extracted PDFs at a low value of $\mu^2 = 10$ GeV^2. On the right panel, we have the predicted PDFs at a larger value of $\mu^2 = 10^4$ GeV^2 obtained with DGLAP evolution starting from the left panel. Note that the gluon distribution is scaled down by a factor of 10. Figure extracted from Ref.(29).

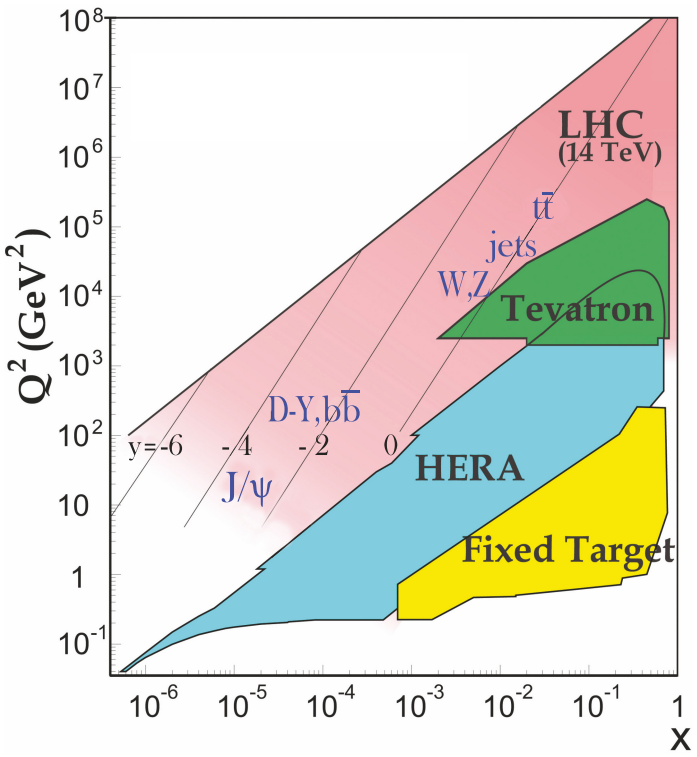

Figure 2.16: Phase-space region in the x versus Q^2 plane reached in several collider setups. Figure extracted from Ref.(29).

of serious tensions in the description. As it will be shown in Chapter4, one can identify other evolution equations in the regime of small-x, which are similar in spirit to DGLAP, but that capture different physics.

There are a number of theory-experiment collaborations in charge of extracting PDF sets using different techniques, such as CTEQ (52) or NNPDF (51). The universal PDFs are instrumental for the prediction of hadron-level cross sections at the CERN LHC, as discussed in Chapter 3.

The structure of the proton gave insight into QCD and helped settle several questions related to asymptotic freedom and the physical reality of quarks and gluons in the data. In the next Subsections, we cover other experimental aspects that were related to more "direct" manifestations of quarks and gluons, which helped establish the universality of the strong interactions. Such direct manifestations also serve as introductions to the concept of "jets", the collimated sprays of hadrons that are used as proxies for quarks and

gluons, which are used for the main data analyses carried out in Chapters 6, 7, and 8.

2.6.2.3 Evidence of gluons and their interactions

Another kind of prediction that combines the notion of parton splittings and color confinement was the expectation of collimated jets of particles in high-energy e^+e^-, electron-hadron or hadron-hadron collisions. One can imagine that, historically, it was hard to paint a unified picture where one could simultaneously have the same particles responsible for the internal structure of the proton manifest themselves directly in the experiment. A series of measurements looking for these signatures were carried out at e^+e^- colliders. These occurred in parallel to the initial measurements of Bjorken scaling at SLAC described in the previous subsection.

Such a striking "jet" signature was observed in e^+e^- collisions. Since quarks couple to the photon field, it was expected that the main production mechanism would be $e^+e^- \rightarrow \gamma^* \rightarrow q\bar{q}$. Indeed, in the 1970s, the emergence of a two-jet structure was observed when increasing the electron-positron collision energy to up to 7.4 GeV SPEAR at SLAC(54).

The radiation of energetic gluons off quarks is expected from QCD. The experimental signature would be that of a third jet sharing a substantial amount of the transverse momentum and emitted at a wide angle with respect to the other jets. At the end of the 1970s, three-jet events with these characteristics were observed by the TASSO experiment at the PETRA e^+e^- collider at the collision energy of 30 GeV(53). The MARK-J, PLUTO, JADE experiments confirmed such an observation (55; 56; 57). An event display of such a trijet topology is shown in Fig. 2.17. The angular distributions between the jets were studied in detail, and several hypotheses were tested related to the properties of the particle that gives rise to the third jet. The best fit was obtained assuming the presence of a third parton with no electric charge and spin-1, precisely the properties of the gauge boson of QCD. A more detailed investigation based on hadronic event shapes further established the existence of gluon-like radiation in the data. Other properties, such as the "string-

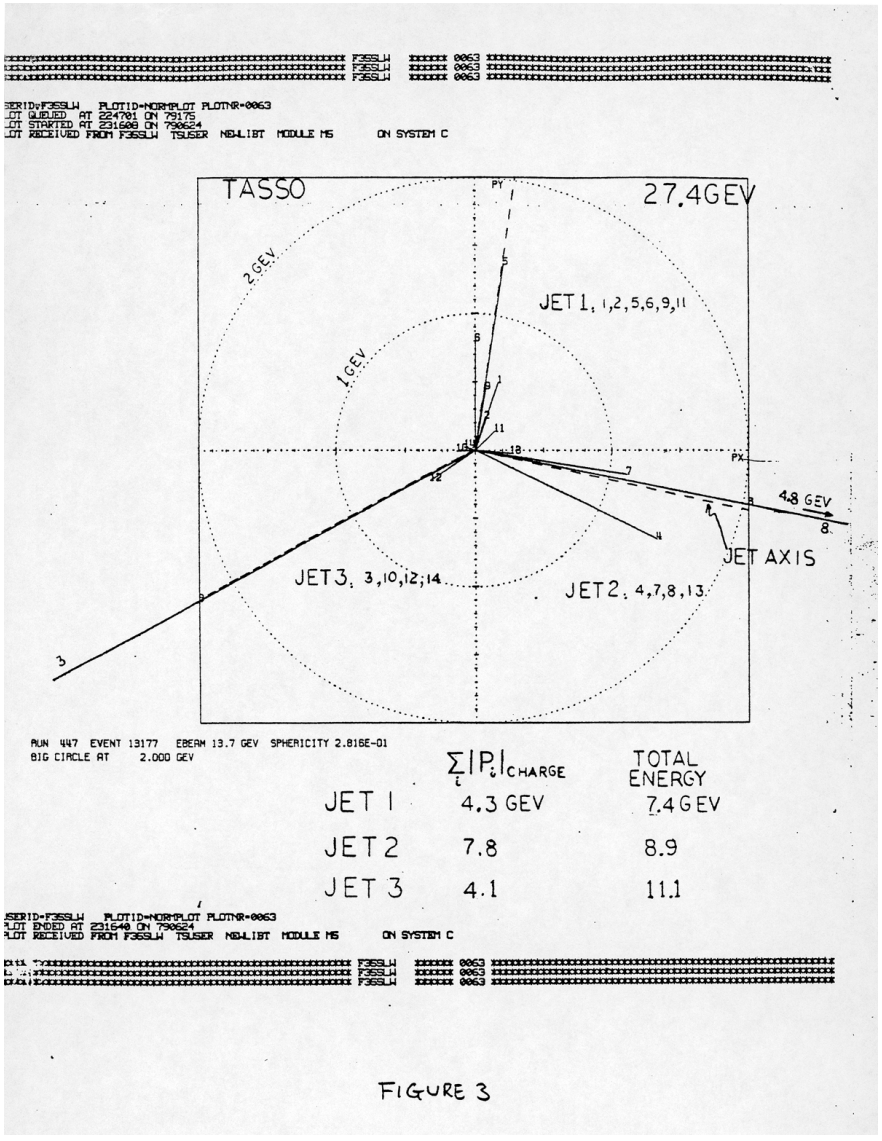

Figure 2.17: Event display of the first trijet event observed by the TASSO Collaboration (53). Events like this were used to establish the existence of gluons. This topology is consistent with $e^+e^- \to q\bar{q}g$ scattering.

like" effect in the production of hadrons between the quark-like jets and gluon-like jets were established as well, which confirmed that the gluon-like jet carries effectively nearly twice as many color charges than the quark-like jet.

So, even if one has compelling evidence for the quark-gluon interaction vertex, one can imagine it would be rather difficult to establish the existence of the self-interaction vertex of the gluons. The gluon self-coupling, as a direct consequence of gluons carrying color charge themselves, is essential for the prediction of asymptotic freedom and the Bjorken scaling violations in DIS. A direct method to isolate the effects of gluon self-couplings was done at the LEP collider at CERN, where kinematic distributions sensitive to the spin structure of the hadronic four-jet final state was used, created from $q\bar{q} \to q\bar{q}(g \to gg)$ splitting. Of particular importance is the Bengtonson–Zerwas angle, χ_{BZ}, defined as the angle between the two planes defined by the two highest- and the two lowest-energy jets. Such a variable is very sensitive to the difference of a gluon jet splitting into two gluons, which in QCD would dominate the source of four-jet final states, and a gluon splitting into a quark-antiquark pair, which should be the dominant mechanism in an abelian vector theory where gluons do not have a self-interaction coupling. The definition of the χ_{BZ} angle, and the result from the measurement, are shown in Fig. 2.18. Figure 2.18 shows that the non-abelian coupling largely favors the angular distributions observed in data.

In principle, other consequences that stem from this elementary interaction vertex and the other vertices of QCD should be observed in other observables. The so-called Casimir factors of SU(3) gauge symmetry are denoted by $C_A = 3$ and $C_F = 4/3$. At the LEP collider, it was possible to recast the four-jet angular correlation and hadronic event shape measurements into precise experimental extractions of C_A and C_F in an agnostic fashion. The data, with combined values of $C_A = 2.89 \pm 0.01(\text{stat}) \pm 0.21(\text{syst})$ and $C_F = 1.3 \pm 0.01(\text{stat}) \pm 0.09(\text{syst})$, which are in excellent agreement with the expected values of QCD. Such measurements rule out other possibilities for the internal symmetries for the theory of strong interaction, which yield different color factors.

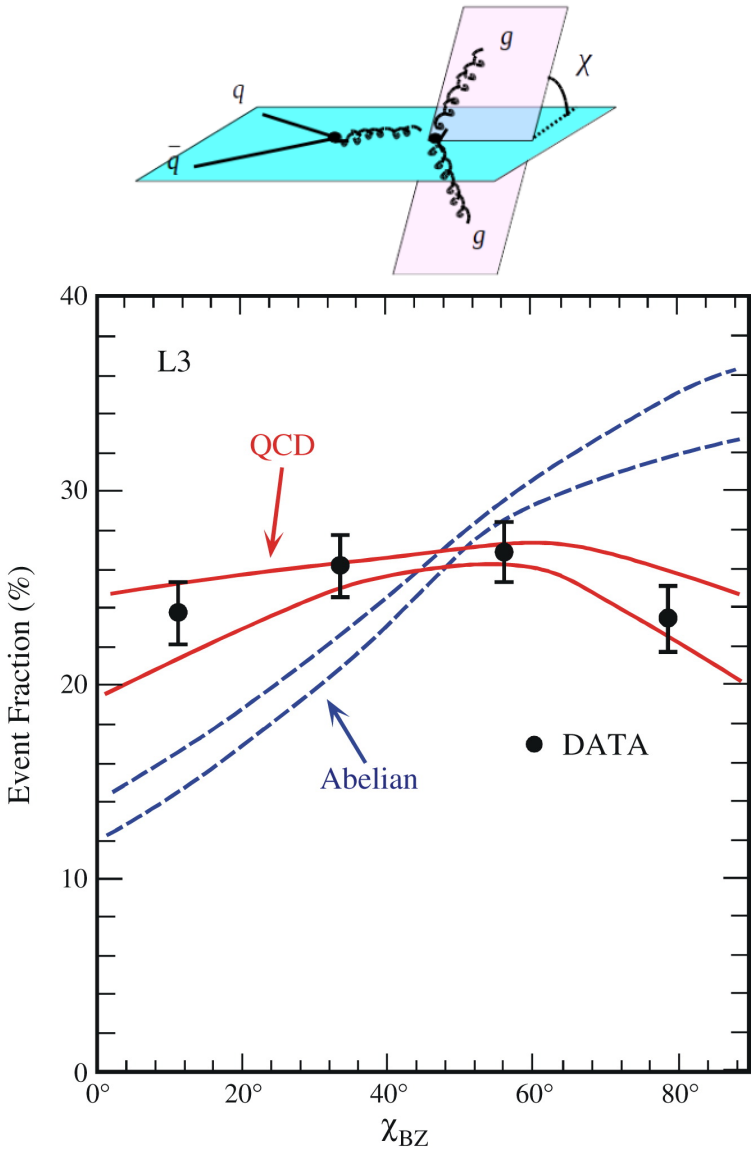

Figure 2.18: (Upper) Diagram of the two planes created by $e^+e^- \to q\bar{q}$ and by $g \to gg$. (Lower) Distribution of the azimuthal angle (the Bengtonson-Zerwas angle, χ_{BZ}) between two planes spanned by the two high- and the two low-energy jets of hadronic four-jet events measured at the LEP collider compared to the predictions of QCD (non-abelian vector gluon model) and of an abelian vector gluon model, where gluons carry no color charge (58). The data largely disfavors abelian-only couplings.

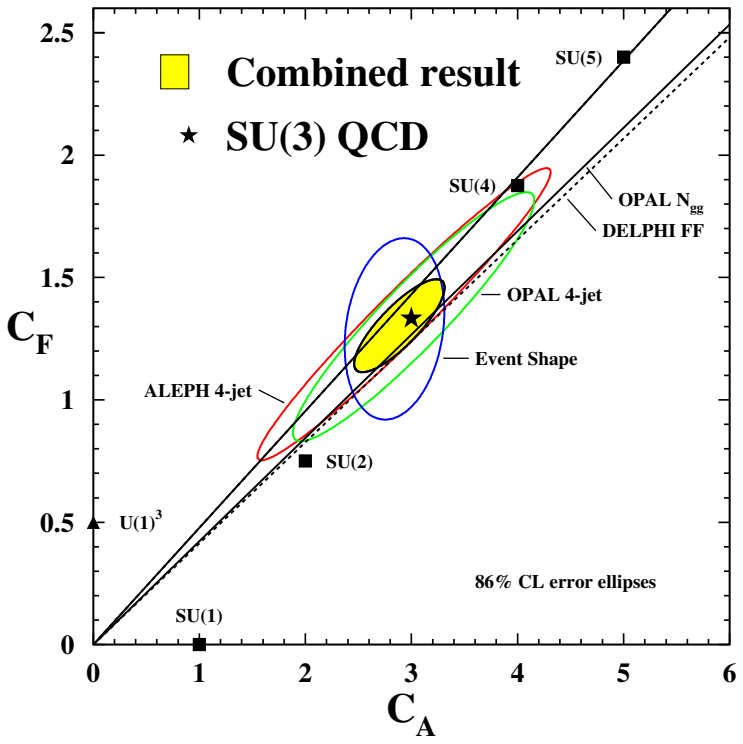

Figure 2.19: Measurements and combination of color factors C_A and C_F from measurements of four-jet angular correlations and hadronic event shapes in electron-positron collisions at LEP. The dark boxes represent the expected Casimir factors for other non-abelian gauge symmetries (SU(1), SU(2), SU(4), SU(5)), the expectation for an abelian U(1)×U(1)×U(1) symmetry is represented by the triangle symbol. The star symbol represents the expectation from QCD, which is consistent with the combination of the measurements at LEP. The figure is extracted from Ref. (59).

Together with the observation of Bjorken scaling and the logarithmic deviation from Bjorken scaling in the study of the structure of the proton, and in addition to the observation of a running coupling α_s with energy, this has convinced the community that QCD can be regarded as the quantum theory of strong interactions. What remains now for the field is to test whether intricate emergent properties manifest in the data.

2.6.3 Remarks on QCD and open problems

Nowadays, to the extent that we have tested interactions at subnucleonic distances, QCD is largely regarded as *the* quantum theory of strong interactions. Its only free parameters are the masses of the quarks and the gauge coupling. In principle, from there one should be able to explain all the phenomenology of strong interactions. This is easier said than done; while QCD has a wide range of applicability for short-distance physics via perturbation theory, there rarely are measurable observables where long-distance physics do not play a role. However, the community has been able to do high precision physics by combining the long-distance physics techniques and phenomenology with the short-distance first principles calculations from perturbative QCD.

At this point in time, there are several emergent properties of QCD that have yet to be observed and studied experimentally. For example, it is still not clear if bound states composed purely of gluons, known as *glueball* states, exist in Nature. The existence of glueballs is a major prediction of QCD, which has been further supported with lattice QCD calculations. Their characteristics, which include their spin, invariant mass, and branching fractions, have been known for a number of years now, but no measurement has shown clear evidence for their existence yet. The existence of such bound states with no valence quarks would be a major validation of the lattice QCD framework and of the SM.

Generally, we also target to understand how nucleons and hadrons can be formed starting from the fundamental degrees of freedom of QCD. For example, how does the

orbital angular momentum of the gluonic component of the proton give rise to its spin-1/2? How does the proton look like at high energies? Is there a point at which the proton or nucleus wave function looks like a "glass-like" object composed purely of gluons? In other words, does a "color-glass condensate" manifest in Nature?

In recent years, we have been able to produce a state of matter of *deconfined* quarks and gluons, known as the quark-gluon plasma, in ultrarelativistic nucleus-nucleus collisions. What are the different phase transitions that such a state of matter can have? What are its hydrodynamic properties? Is it possible to predict from the microscopic theory of interactions their macroscopic properties? To what extent can we produce quark-gluon plasma droplets in "small" systems?

Another set of phenomena to be understood in the sector of strong interactions is the phenomenon of diffraction. A diffractive interaction is one where we have a strongly interacting multi-parton exchange that carries the quantum numbers of the vacuum in high-energy hadronic collisions. Diffraction is intimately related to the phenomenon of t-channel multi-parton color-singlet exchange, for example t-channel two-gluon exchange in a color-singlet configuration. For instance, one can have a high-energy collision of protons where both protons remain intact after the interaction, and yet they are able to produce other particles that carry some amount of transverse energy. Such a reaction can be used to characterize the gluonic structure of the proton in impact parameter space, complementing the standard analyses of the proton structure. It is believed that the phenomenon of diffraction may have connections with the glueball states of QCD, but this has yet to be confirmed experimentally. The exchange of a CP-even strongly interacting color-singlet object is known as "pomeron." Recently, there has been evidence for a CP-odd strongly interacting color-singlet exchange, known as "odderon" (60). It would be interesting to see whether there is a connection with the recently observed pomeron and odderon exchanges with glueball states. Pomeron and odderon exchange are intimately related to the properties of the vacuum in QCD. While we have some understanding of

how these interactions come to be, we still do not have a unified picture of how exactly these phenomena can be described in terms of the fundamental QCD degrees of freedom.

In this thesis, we aim to address the question of the behavior of the interactions between quarks and gluons when the center-of-mass energy is much larger than any other momentum scale. In this limit, the emission of multiple real and virtual gluons should yield interesting properties of the scattering amplitudes. These give rise to interesting evolution properties of the scattering amplitudes as a function of the center-of-mass energy. This can be analyzed in events with a diffractive interaction in presence of a hard energy scale. These will be discussed more in detail in Chapter 4.

2.7 Beyond the SM extensions

Now that we have discussed the basic elements of the SM, it is worth discussing what are some of the different strategies and directions we have to expand it that are currently under investigation. Anything that is outside of the SM is known as beyond the SM (BSM) physics or new physics. In this thesis, we address how some of these potential scenarios could be observed in photon-photon interactions in Chapter 9.

The SM is our best description of interactions of elementary particles, and has no known mathematical inconsistencies in its formulation. However, it is well-known that the SM has shortcomings, some of which serve as guides for possible extensions of the SM of particle physics. The most notorious one is the absence of a description of gravitational interactions at short distances (spacetime in quantum field theories is flat). This is perhaps the strongest lead to develop the next theory, since we know —from the construction of quantum field theory and of classical general relativity—, that at some point aspects of both theory frameworks have to meet up. The expected energy scale at which this would occur is known as the Planck energy scale, $\Lambda_{\text{Planck}} = \mathcal{O}(10^{15})$ GeV, well beyond our current reach at the LHC. Thus, an extension of the SM has to include a description of *quantum* gravity. Examples of quantum gravity theories are string theory and loop

quantum gravity.

Another clear theoretical imperfection is the lack of an explanation for the existence of "dark matter" in the Universe in the SM. By dark matter, we mean matter whose interaction is mostly of gravitational nature and, if it has interactions with "normal" matter (the SM particles) or with themselves, this interaction must be *very* weak. Dark matter comprises about five times as much of the Universe as ordinary matter. Numerous cosmological and astrophysical observations support the hypothesis of dark matter existence. The strongest measurements to substantiate dark matter comes from fits to data that aim to describe the accelerated expansion of the Universe, the power spectrum of the cosmic microwave background, and large-scale structure formation (galaxy clusters and galaxy formation). None of the SM particles fit the bill when it comes to describing the presence of dark matter in our world. Isolated neutrons, while they are massive and electrically neutral, they have a mean lifetime of about 15 minutes if they are not bound in a nucleus. Also, while being electrically neutral, they can still interact with light by means of their electric and magnetic dipole moments. Neutrinos would be the perfect candidates to account for dark matter if they were heavier; hence they are considered to be a small component of the observed dark matter ("hot" dark matter). Thus, it is hypothesized that dark matter might be composed of particles that are not present in the SM, but that interact very weakly. These are known as "weakly interacting massive particles" (WIMPs). If these dark matter particles interact weakly with the SM particles, we may be able to probe them experimentally.

Several extensions of the SM aim to introduce new fields that are very weakly coupled to the SM particles that may be potentially observed directly in Earth-based experiments, be it collider experiments (indirect searches via "missing transverse energy" searches, which might be more model-dependent) or with dark matter detectors (direct searches, which are more model-independent), where dark matter particles present on Earth may seldomly recoil against nuclei in a background-controlled environment. One hypothetical

particle to explain dark matter is the “axion.” The QCD axion is a pseudoscalar field that emerges after the breakup of a symmetry known as the Peccei–Quinn symmetry (61), akin to the way the Higgs field emerges upon EWSB. The Peccei–Quinn symmetry breaking mechanism allows to explain the observed non-CP violating nature of strong interactions by means of a custodial symmetry that "protects" the θ coupling parameter of the CP-violating term in the Lagrangian of QCD from being different than zero. The θ parameter is promoted to a full fledged pseudoscalar field. Axions, if they exist, could be a form of cold dark matter. However, as of now, we have no candidate particle to explain the evidence. This remains one of the major open questions in physics.

The hypothesis of dark matter is somewhat challenged by alternative explanations that modify directly Einstein’s equations of general relativity at very large length scales. Such alternative explanation is generally known as modified gravity. This is still part of the ongoing scientific discussion, but the community seems to favor more a picture in terms of dark matter, since it is a parametrically simpler explanation.

Beyond the aforementioned shortcomings of the SM, theorists also consider extensions based on additional assumptions on the theory that go beyond the introduction of new fields or interactions by hand. For example, one could consider additional dimensions of space, which only become accessible at very short distances. The extension on its own is very interesting, since there is no reason that the Universe has to have three dimensions of space and one dimension of time (3+1 dimensions). It could well be that, at very short distances, additional spatial dimensions become important, which would change the way particles interact with each other. These are theoretically attractive, since they give a natural explanation as to why the force of gravity is so weak compared to the other fundamental forces. Large extra-dimensions tries to explain this problem by postulating that our universe, with its 3+1 dimensions exists on a membrane floating in 11-dimensional space (62; 63). It is then suggested that the other forces of nature (those of the SM) operate within this membrane and its four dimensions, while gravity can operate

across all 11 dimensions. This would explain why gravity is very weak compared to the other fundamental forces. The other seven dimensions, which we do not observe, previously have been assumed to be very small. Large extra-dimension theories assert that they might be very large, yielding measurable tests at current collider setups. Another class of models (such as Randall and Sundrum models (64)) uses one extra-dimension in a highly warped anti-de-Sitter space.

There are many signatures for large extra-dimension models, including the production of "mini" black holes in high-energy proton-proton collisions (65). These black holes evaporate almost instantly via Hawking radiation into numerous particles. So far, the existence of such black holes has been ruled out for some of these models. Extra-dimensions are also theoretically attractive, since current string theory models *need* the existence of additional dimensions of space for the theory to work.

Perhaps the most popular extension of the SM is the supersymmetric extension of the SM. By supersymmetry (SUSY), we mean an additional spacetime symmetry that makes a natural connection between fermions and bosons. In particular, each fermion (boson) is accompanied by a bosonic (fermionic) supersymmetric partner. Such a symmetry is not currently observed, implying that SUSY, if it exists, it is broken. Typically, we consider the minimal supersymmetric standard model (MSSM) extension, which realizes SUSY with the least number of new particles and interactions in consistency with phenomenology (66; 67).

The SUSY extension of the SM was initially introduced to explain a theoretically unaesthetic property of the SM, known as the hierarchy problem, in the early 1980s (66; 67). The hierarchy problem has to do with the radiative corrections to the mass of the Higgs boson. The Higgs boson, being a scalar particle, can in principle receive very large radiative corrections from the physics at very high energies. Since we know that eventually we have to account for quantum fluctuations of particles at very high energies —which is expected from a theory of quantum gravity—, we can estimate what the impact of these

virtual corrections should be at low energies. These corrections can be of the order of 10^{15} GeV on the mass of the Higgs boson via quantum corrections to its mass. This sounds alarming at face value. However, this does not jeopardize the predictability of the theory, since what we measure experimentally is the renormalized mass of the Higgs boson (i.e., the difference of the virtual corrections and the "bare" mass of the Higgs boson). In the assumption that these corrections are unnaturally cancelled in the SM, one can develop extensions of the SM to explain the smallness of the mass of the Higgs boson. When one introduces supersymmetric particles in the quantum corrections for the Higgs mass, one gets partial cancellations in the quantum corrections from the SM-only contributions, making the theory natural. As a side note, another example to solve the hierarchy problem is the aforementioned extra-dimension theories, which makes the onset of quantum gravity effects manifest at energies much lower than the Planck scale.

Additional reasons that SUSY is theoretically appealing is that one naturally obtains dark matter particle candidates, namely the neutralino, an electrically neutral fermion of the MSSM model. The neutralino is massive enough and weakly interacting enough that it could fit the current dark matter abundance and structure characteristics observed in cosmological scales, and also be searchable in collider-based experiments. No evidence for neutralino has been found at the electroweak scale (i.e., LHC energies). String theories that target to describe quantum gravity require the existence of supersymmetry for the theory to work. Finally, another reason SUSY is of interest is that it gives a unification of the SM interactions at energies higher than those of the LHC. Gauge coupling unification is not a mathematical or consistency requirement of any extension of the SM, but it is an interesting property that is obtained "for free."

As more LHC experiments analyses come out (based on Run-1 and Run-2 data), the more we suspect that SUSY particles, if they exist, must have masses much larger than those currently probed at the LHC. The heavier SUSY particles are, the larger the radiative corrections to the Higgs boson mass become, bringing back the original problem of fine-

tuning in the SM. The gauge coupling unification becomes harder to achieve for heavy SUSY particles. It is possible that we live in a world where SUSY manifests at energies much higher than the TeV scale. It is thus of upmost importance to continue the search for supersymmetric particles –or other exotic particles– at the LHC and other experiments.

To the date of writing this thesis, there is no collider-based measurement that gives a clear (beyond reasonable doubt) path towards the extension of the SM. Dedicated searches for some of these particles have been carried out in the last decade at the CERN LHC. A summary of the current constraints on new physics by the ATLAS experiment for a selected number of BSM extensions is shown in Fig. 2.20. We see here that, a lot of model-specific particles have been heavily constrained. If they exist, they must have invariant masses larger than a few TeV for the specific models considered in Fig. 2.20. For a detailed review of recent BSM searches in ATLAS and CMS and the various strategies deployed in the experiment, we refer to Ref. (68).

One of the primary goals of the LHC program is to look for possible ways that new physics might manifest in our data. This can be done in direct searches (where new particles are directly produced and decay into SM particles), or indirect searches (new particles that modify SM processes via virtual corrections). The advantage of model-dependent searches is that they allow us to constrain specific new physics scenarios with laser-focus precision. On the other hand, model-independent searches —where several families of models can be recast to the same measurement or cross section—, while very powerful in principle, they are not able to give us all the properties of possible new physics manifestations in case they were observed in data. A reasonable strategy for new physics searches combines both direct- and indirect searches for BSM signatures. In this thesis, we will summarize the results of a series of phenomenology papers by the author that aim to provide a venue where possible deviations from the SM expectations can be observed in a relatively clean environment. This aspect of the thesis has to do with the sector of pure gauge boson interactions in $\gamma\gamma \to V_1 V_2$ scattering, where $V_{1,2}$ is a SM electroweak

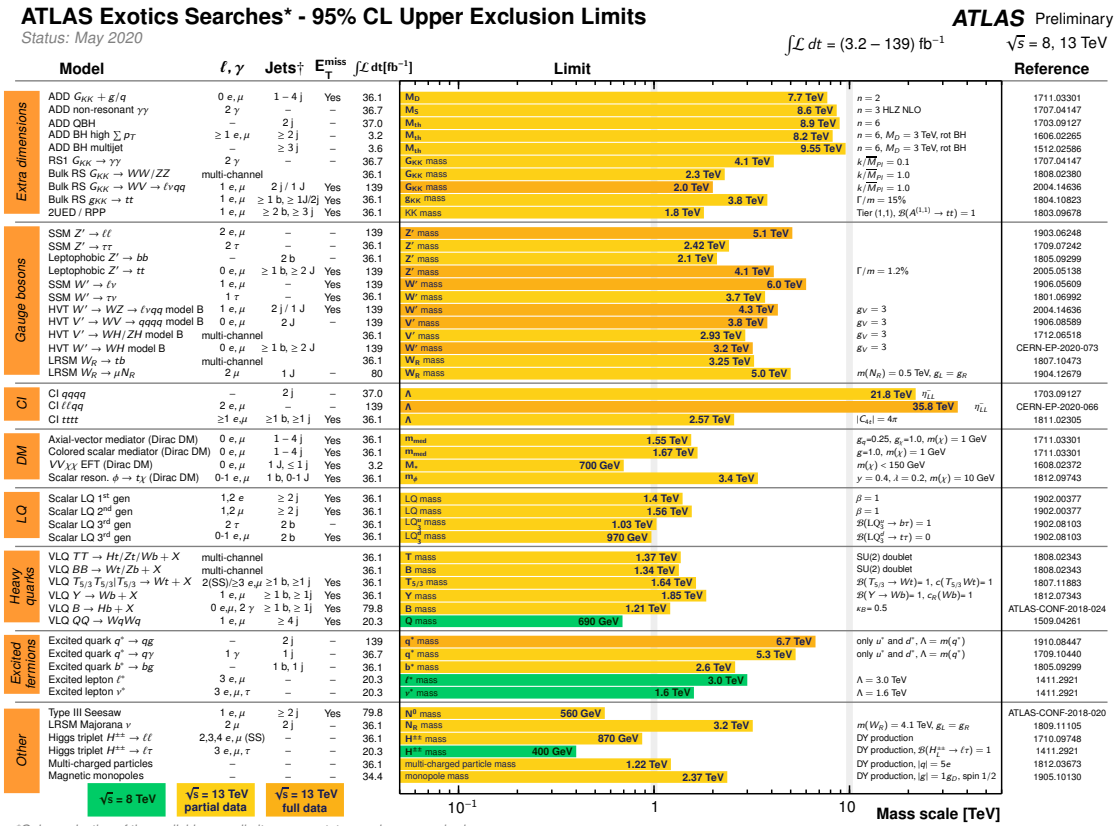

*Only a selection of the available mass limits on new states or phenomena is shown.
†Small-radius (large-radius) jets are denoted by the letter j (J).

Figure 2.20: Summary of searches for new physics by the ATLAS Collaboration. These are interpreted in terms of limits on the mass of new particles in models containing extra-dimensions, extra gauge bosons, new contact interactions (CI), dark matter (DM), lepto-quarks (LQ), heavy quarks, excited fermions or miscellaneous others. The yellow (green) bands indicate 13 TeV (8 TeV) data results. Figure extracted from Ref. (69).

gauge boson ($V_1V_2 = \gamma\gamma, Z\gamma, ZZ, WW$). New physics particles charged under the SU(2)$_L\times$ U(1)$_Y$ groups of the SM can induce anomalous contributions to such scattering amplitudes, most of which are suppressed at tree-level in the SM. Particles that are charged under hypercharge and/or isospin would contribute to such vector boson scattering processes. This can be achieved in high-energy $\gamma\gamma$ collisions at the LHC, as will be discussed in Chapter 9.

Note that in this discussion, we have not described much of how we deal with the description of neutrinos in the SM. Historically, neutrinos were assumed to be massless in the SM. Nevertheless, evidence of neutrino flavor oscillation demonstrates that neutrino flavor eigenstates mix with neutrino mass eigenstates. Such mixing can only occur for neutrinos with non-zero mass. The flavor eigenstates are related to the mass eigenstates via the Pontecorvo–Maki–Nakagawa–Sakata (PMNS) matrix.

Currently, there are two main proposals to introduce neutrino mass generation in the SM. The first proposal is based on generating the mass of the neutrino via the Dirac mechanism, i.e., via EWSB based on their corresponding Yukawa couplings to the Higgs doublet field. Such an approach would require the existence of an SU(2)$_L$ singlet particle, known as a "sterile neutrino", for it to work. The prospect for sterile neutrino particles is that, if they exist and are massive enough, they could be a component of dark matter. The second approach is the Majorana mechanism, which is allowed to work only if the neutrino field is exactly the same as the antineutrino field. The neutrino is the only SM fermion that could be its own antiparticle. Both approaches are extensions of the SM that leave the rest of the description of SM particles untouched. To this date, neither of the models are strongly favored over the other.

2.8 Chapter remarks

Chapter 3

QCD collider phenomenology

To investigate the interactions between elementary particles at very short distances, we collide leptons or hadrons at high-energies. The work of this thesis is mostly focused on the study of elementary particles interactions in high-energy proton-proton (pp) collisions. Thus, in this Chapter, we describe the conventional workflow used to make predictions that can be compared to the measurements carried out at the Large Hadron Collider (LHC), the present most energetic and largest proton accelerator. The LHC and the particle detectors thereby will be described in Chapter 5.

The prediction machinery for QCD collider phenomenology relies on a conjunction of the dynamics that occurs at short-distances described in fixed-order perturbation theory, where quarks and gluons are the appropriate degrees of freedom, as well as the phenomena that occurs at long-distances, where the language of hadrons —particles composed of quarks and gluons— is more natural. These predictions can be implemented in *Monte Carlo simulations* to calculate the relevant quantities of interest. Monte Carlo simulation is a general technique used to simulate stochastic processes and calculate integrals using random numbers. An advantage of Monte Carlo simulations is that it allows to generate samples from it that are (ideally) close to the real-world events. Collision events are generated from the theoretically-known scattering hard cross sections, and the events may be supplemented with other effects, such as the ones that will be described in this Chapter. A list of particles with their energies and momenta is obtained, which can be used for offline analysis, similar to what is done with real data. In high-energy physics, some of the general purpose Monte Carlo generators are the PYTHIA (71), HERWIG (72), and

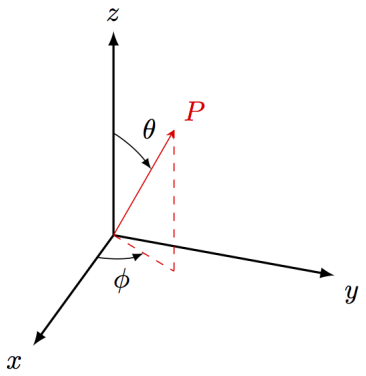

Figure 3.1: The coordinate system used throughout the thesis. The y axis points against the direction of gravity, the z axis is parallel to the beam line. The x axis is perpendicular to both y and z axes. The ϕ angle is defined between the x and y axes, measured from the x axis. The θ angle is the angle between the z and y axes, measured from the z axis.

SHERPA(73) generators. A few other specialized Monte Carlo generators would be mentioned throughout this thesis, but in essence they use the same numerical techniques for creating the list of events and calculate the cross sections by numerical integration.

3.1 Standard variables and coordinates in collider physics

It is instructive to consider the standard variables and coordinates used in high-energy hadron-hadron colliders. These coordinates will be used throughout the rest of the thesis. The y-axis points upwards, against the direction of gravity. The z-axis is parallel to the beam, with its positive direction defined along the counter-clockwise beam direction (when looking from the above). The x axis is perpendicular to both y and z axes. One can use spherical coordinates to describe the position of a particle or a detector component relative to the collision point. In this spherical coordinates system, we define the polar angle θ as the angle between the particle three-momentum relative to the z axis, such that $\theta = 0$ means that the particle is moving along the beam line, and $\theta = 90^\circ$ means that the particle's trajectory is upwards. The azimuthal angle ϕ is measured from the x-axis on the transverse plane (x–y plane). Such a coordinate system is shown in Fig. 3.1. Finally, a radial coordinate projected on the transverse plane, r, is defined as $r = \sqrt{x^2 + y^2}$.

The transverse momentum, p_T, is defined as:

$$p_T = \sqrt{p_x^2 + p_y^2} \tag{3.1}$$

where p_x and p_y represent the components of the three-momentum of the particle projected onto the x and y axes. This quantity is frequently used in collider physics, since most of the times it is a proxy scale used to define whether the scattering process is hard or soft. The p_T is also of interest since it is invariant under Lorentz boosts along the beamline, which helps add robustness to theory versus experiment comparisons.

In particle physics, we often use a variable known as rapidity y, defined as

$$y = \frac{1}{2} \ln \left(\frac{E + p_z}{E - p_z} \right) \tag{3.2}$$

where E and p_z are the energy and z component of the three-momentum of the particle. The rapidity is exactly 0 for particles fully contained in the transverse plane and it corresponds to infinity for particles lying on the beam axis. The rapidity is of interest, since a Lorentz boost along the beam axis corresponds to a shift in rapidities by an amount of y_{boost} to all particles irrespective of their E and p_z values in the original frame of reference. Hence, differences of rapidity are invariant under Lorentz boosts along the beam axis.

For massless particles, such as a photon, or on the limit where $p_T \gg m$, the rapidity is equal to the pseudorapidity η, defined as

$$\eta = \ln \left(\tan \frac{\theta}{2} \right) \tag{3.3}$$

where θ is the previously defined polar angle. In experimental particle physics, we sometimes prefer the use of η, since it is uniquely related to a given angle θ. This is useful since the calibration of the detector, the location of the detector components, and so forth, can be unambiguously referred to by means of the η and ϕ, irrespective of the

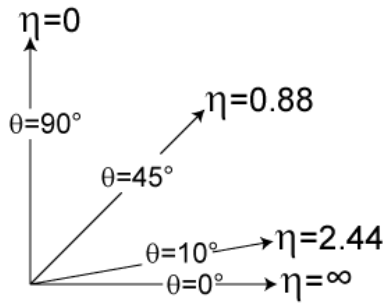

Figure 3.2: Pseudorapidity (η) values as a function of the angle θ made between the beam axis z and the three-momentum of a probe particle. The y axis points vertically, against the direction of gravity. An $\eta = 0$ corresponds to $\theta = 90°$, whereas an $\eta \to \infty$ corresponds to $\theta = 0°$.

three-momentum of a probe particle. However, one must be careful not to come to strong conclusions based on pseudorapidity-based observables, particularly in cases where the $p_T \approx m$. Notice how η is defined in terms of a logarithm of a tan function of θ. Such a dependence means that η evolves rather slow with θ in the central region, and then grows faster and faster at smaller θ values (forward region).

3.2 QCD factorization theorem

In high-energy pp collisions, most of the time we talk about the interaction of one parton from one of the colliding protons with another parton from the other proton. If the interaction between these two partons is "hard" enough (meaning, if there is a momentum scale that is much larger than Λ_{QCD}), we can use pQCD calculations to make predictions at short-distances. However, since we cannot observe the bare partons due to color confinement, we have to use observables defined at hadron-level.

The most important observable is the hadron-level *cross section*. The cross section is a physical quantity that quantifies the production rate. The cross section is independent of the intensity and focus of the particle beams, which allows for a better comparison with the numbers measured by other accelerators. The cross section is calculable via the *QCD factorization theorem* (74; 75), which tells us that we can separate the long- and short-

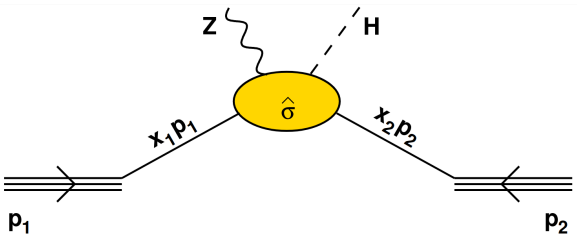

Figure 3.3: Schematic diagram of the QCD factorization theorem. Two partons from the proton-proton collision collide to produce a Z boson and Higgs boson. The partons carry energy fractions x_1 and x_2. Diagram extracted from Gavin Salam QCD lectures.

distance phenomena. The hadronic production cross section is calculated as a convolution of a parton-level cross section calculable with perturbative QCD (short-distance physics) techniques and the universal process-independent parton distribution functions (long-distance physics),

$$\sigma = \sum_{i,j} \int dx_1 f_i(x_1, \mu_F^2) \int dx_2 f_j(x_2, \mu_F^2) \times \hat{\sigma}(x_1, x_2, \mu_F^2, \mu_R^2) + \mathscr{O}(\Lambda_{\rm QCD}^2/Q^2) \tag{3.4}$$

where $f_{i/p}, f_{j/p}$ are the process-independent parton densities that are extracted from global fit analyses introduced in Chapter 2, $\hat{\sigma}(x_1, x_2, \mu_F^2, \mu_R^2)$ is the parton-level cross section calculable in perturbation theory, x_1 and x_2 are the fractions of the proton momentum carried by the struck partons. The sum over i, j is carried over all the gluon and quark flavors. The quantities μ_F and μ_R are the factorization and renormalization scales, respectively, and they are related to the infrared and ultraviolet divergences related to the renormalization of the parton densities and the renormalization of α_s. The QCD factorization theorem holds up to power corrections of the form $\mathscr{O}(\Lambda_{\rm QCD}^2/Q^2)$, which for very hard processes ($Q^2 \gg \Lambda_{\rm QCD}^2$) is negligible. A schematic diagram of the factorization theorem is shown in Fig.3.3.

The partonic cross section $\hat{\sigma}$, in presence of a hard energy scale $Q \gg \Lambda_{\rm QCD}$, can be calculated as a perturbative expansion in the interaction coupling (in powers of α_s for QCD interactions). This calculation can be done systematically order-by-order using the Feynman rules of the SM. An example of a few Feynman diagrams for $2 \to 2+n$ parton

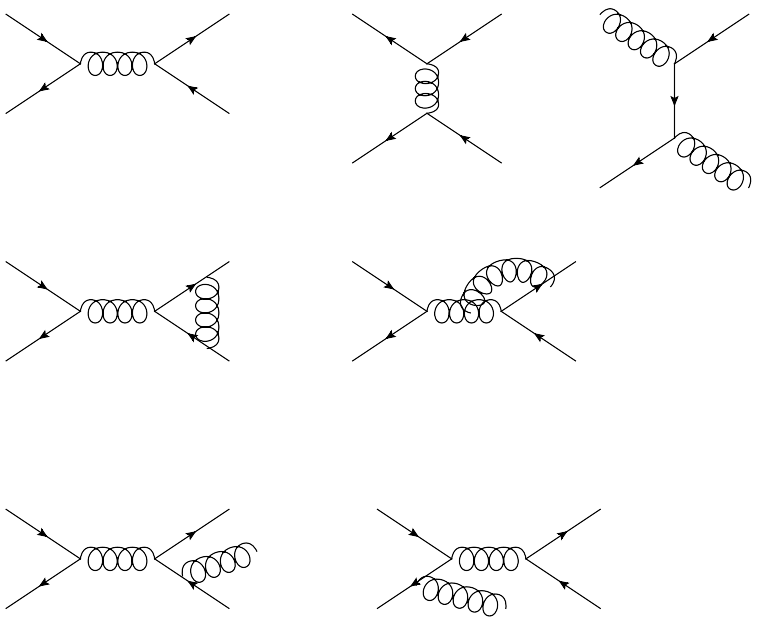

Figure 3.4: Subset of Feynman diagrams that contribute to the cross section for $q\bar{q}$ scattering at LO and NLO in α_s. The upper diagrams represent the tree-level contribution, the middle diagrams show two diagrams with virtual radiative corrections, and the lower three diagrams represent the real radiative corrections.

scattering at LO and NLO diagrams with real and virtual gluon emissions in QCD is shown in Fig. 3.4.

However, the story does not end there; we know that quarks and gluons are not observed in isolation. Indeed, an energetic quark or gluon would lead to a cascade of partons. Such a cascade can be, to a good extent, be treated theoretically using pQCD-inspired techniques. Eventually, when the partons that are created in the cascade are sufficiently soft (i.e., when their momenta is close to Λ_{QCD}), there is a transition of degrees of freedom that occurs by virtue of color confinement; the formation of color-singlet hadrons takes place. This is known as the hadronization process. It is very difficult to derive from first principles exactly how this transition of degrees of freedom takes place, so empirical models need to be used for this. In addition to the aforementioned effects, one needs to account for the so-called underlying event activity. This has to do with the fact that the proton has an extended structure of quarks and gluons; there will not only be a single hard parton-parton interaction at a given proton-proton collision, but several ex-

changes, mostly at low momentum transfers. These effects that are important ingredients in the prediction machinery of QCD are described in this Chapter.

3.3 Parton shower

The parton shower is the process of quarks and gluons radiating other quarks and gluons —mostly gluons— as they propagate in vacuum. The process is repeated iteratively in a fractal-like manner, provided that the transverse momenta is larger than the mass of the quarks ($Q \gg m_q$). The self-similarity is broken by the running of the coupling $\alpha_s = \alpha_s(Q)$ and ultimately by color confinement. Indeed, the cascade of soft partons then undergoes a transition of degrees of freedom from partons to hadrons, a process known as "hadronization," which is described in the next section.

The phenomenon of parton shower is strictly related to the phenomenon of jet formation —the collimated spray of particles observed experimentally—. To understand how parton showers come to be, it makes sense to begin with the question: why do quarks and gluons radiate so many gluons so rapidly? Is it possible to have a freely propagating quark transition into hadrons without the emission of gluons along the way? Based on perturbation theory arguments, one would think that an additional parton splitting would decrease the cross section by a factor of α_s, and therefore should be negligible at parton splitting. So, what is going on?

To understand this, let us consider a back-on-the envelope calculation for the emission of a soft, collinear gluon off a quark and examine how this correction affects the "bare" cross section σ_0. With a collinear gluon emission, we have that the cross section is modified as follows (using Feynman rules of QCD and leaving the phase-space integral to be performed),

$$d\sigma \approx \sigma_0 \frac{2\alpha_s C_F}{\pi} \frac{dE}{E} \frac{d\theta}{\theta} \tag{3.5}$$

this has a divergence when the quark propagator goes on-shell ($E \to 0, \theta \to 0$). From here, we can extract the factor multiplying the bare cross section. The factor multiplying σ_0 can be interpreted as the probability of emitting a gluon off the quark,

$$P_g \approx \frac{2\alpha_s C_F}{\pi} \int_{Q_0}^{Q} \frac{dE}{E} \int_{Q_0/E}^{1} \frac{d\theta}{\theta} \tag{3.6}$$

the integral is cut-off for transverse momenta $p_T \approx E\theta$. The scale Q_0 denotes some non-perturbative threshold. This threshold is applied on the grounds that perturbation theory does not apply for $p_T \ll \Lambda^2_{\mathrm{QCD}}$. With this cutoff, the result of the integral is (retaining the dominant terms)

$$P_g \approx \frac{\alpha_s C_F}{\pi} \ln^2 \frac{Q}{Q_0} + \mathcal{O}(\alpha_s \ln Q) \tag{3.7}$$

at first sight, it seems that the probability P_g is proportional to the strong coupling α_s, in accordance with perturbation theory expectations. However, we can work with the expression above a bit further. Assuming that the non-perturbative energy scale is given by $Q_0 = \Lambda_{\mathrm{QCD}}$ (the scale where the theory becomes strongy coupled), and recalling that the coupling runs as $\alpha_s(Q) = 1/(\beta_0 \ln(Q^2/\Lambda^2_{\mathrm{QCD}}))$ at LO, the expression for P_g can be rewritten as

$$P_g \approx \frac{\alpha_s C_F}{\pi} \ln^2 \frac{Q}{Q_0} \to \frac{C_F}{4\beta_0^2 \pi \alpha_s} \tag{3.8}$$

so we have a P_g that depends on $1/\alpha_s$, not α_s. Notice that in order to derive this, one has to introduce the running of α_s, which, uniquely in QCD, decreases with $1/\ln(Q)$. Putting in some numbers to get an idea of how large or small the probability for emitting a gluon is, we have that $P_g \approx 1$. In other words, with freely propagating quarks, we will eventually have at least one gluon emission. This is ultimately a consequence of the infrarred and collinear divergences of QCD and the running of α_s. One can imagine that this analysis is applicable iteratively; after the quark emits a gluon and continues

propagating, the outgoing quark and gluons will radiate other gluons, and this procedure could be repeated until the non-perturbative threshold is reached.

Now, the aforementioned back-on-the envelope calculation neglected the running of the coupling under the integral over E and θ for the soft- and collinear gluon emission. Proper calculations include the running of the coupling under the integral sign, although the general conclusion remains the same: quarks and gluons will inevitably radiate gluons as they propagate. Indeed, in modern Monte Carlo event generators, the parton shower is simulated via the calculation of the probability of no-splitting, defined as

$$P_a(t,t_0) = \Gamma_a(t) \exp\Big[- \int_{t_0}^{t} \Gamma_a(t') dt' \Big] \tag{3.9}$$

here, the factor $\exp\Big[- \int_{t_0}^{t} dt' \Gamma_a(t') \Big]$ is known as the "Sudakov form factor", and it quantifies the probability that a parton with flavor a at an initial time t_0 evolves to a time t without branching. The virtual splitting effects are accounted for via unitarity relations. The function $\Gamma_a(t')$ has in it the parton splitting functions introduced in the context of DGLAP evolution of PDFs in Chapter 2. The parton emissions in the parton shower are generated sequentially and the evolution is numerically calculated via Monte Carlo integration, which yield effectively the DGLAP radiation pattern at leading logarithmic accuracy. Due to color coherence effects, the emission of gluons must obey angular ordering. This means that the emission angles must decrease along the chain of emissions. In PYTHIA, the ordering is in transverse momenta, whereas in HERWIG it is in the angle of emission.

Thus far, we have been focusing mostly on so-called final-state parton showers. However, the interacting partons are allowed to radiate partons before and after the hard scattering in what are known as the initial and final state parton showers. For the initial-state parton shower, however, there is an additional difficulty: the final step of the shower must match the kinematical variables generated for the hard scattering process. The initial-state parton shower is therefore generated backwards, taking the parton densities evaluated at

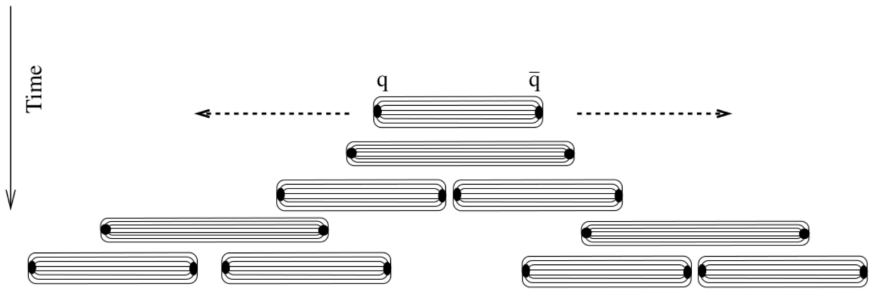

Figure 3.5: Schematic diagram of the string fragmentation model. One starts with a quark-antiquark pair, where each of the quarks carry enough energy to be split one from the other. As the color string between them keeps stretching, there is enough energy to produce another pair of quark-antiquarks from the vacuum. Figure extracted from Ref. (76).

a given Q^2 as boundary conditions.

3.4 Hadronization

Hadronization, sometimes called fragmentation, is the transition from the fundamental degrees of freedom of QCD to color-neutral composite particles in the final-state. Hadrons, or their decay daughters, can be directly measured experimentally. Hence, a proper description that connects the hadrons to the experimentally inaccessible quarks and gluons is essential. Such a transition of degrees of freedom is highly non-trivial, since it involves the strongly coupled regime of QCD interactions. Nevertheless, ever since the experimental establishment of QCD as the fundamental theory of strong interactions, several phenomenological and empirical attempts have been presented over the years. There are two major phenomenological descriptions of hadronization: the Lund string fragmentation model (77) and the cluster fragmentation model (78). The former is implemented in PYTHIA(71) and SHERPA generators, wheras the latter is implemented in the HERWIG(72) generators.

The Lund string model is based on the classical interaction potential V between partons, which can be described by a potential that depends linearly on their separation r (for $r \gg 1/\Lambda_{\mathrm{QCD}}$),

$$V(r) = \kappa r \tag{3.10}$$

where $\kappa \approx 1$ GeV/fm sets the natural scale for long-distance hadronic interactions. Thus, we can think of an interaction between two partons with an attractive potential as if they were connected by a "string" that stretches and stores energy with a linear dependence on their separation, akin to the harmonic oscillator interaction potential. Very frequently, we use the language of "color strings" and their "breaking" when discussing the fragmentation process. A schematic diagram showing the evolution with time of the string breaking leading to the creation of quark-antiquark pairs is shown in Fig. 3.5.

Strings are massless objects that extend from a triplet charge to an anti-triplet charge. When both color charges are separated, the energy stored in the string increases until a quark-antiquark pair can be created from the vacuum. This quark-antiquark pair is also connected with color strings to the previous pair, in a way such that two color-singlet particles are formed. The color string connecting newly formed color-singlet particles might have enough energy stored to further break and create another quark-antiquark pair by fluctuations in the vacuum. Thus, this process of breaking and creating strings is repeated until no further splits are kinematically allowed to occur. At that point, there are only color-neutral particles in the final state, with no parton left behind, finishing the fragmentation process.

The second model, known as the "cluster model" for hadronization is based on the property of confinement in QCD. Here, the partons produced in the shower are clustered into colorless groups (clusters) with a given invariant mass distribution. It is then possible to start the hadronization starting from these clusters, which can be seen as proto-hadrons. Such proto-hadrons decay into pairs of color-singlet hadrons.

Such phenomenological approaches have been validated and refined based on e^+e^- collision data, where the fragmentation process can be cleanly isolated. The string fragmentation model has most notably been validated with lattice QCD calculations, bag

model results, and Regge phenomenology

3.5 Jet clustering

A direct signature of the creation of an energetic quark or gluon is the collimated spray of particles known as a "jet." The jet is formed after the struck quark or gluon undergoes the parton showering and hadronization processes, as shown in Fig. 3.6. Such collections of hadrons or their decay daughter particles (such as photons, electrons, muons) have "memory" of the initial direction of the mother quark or gluon struck in the collision. Hence, the jet can be used as a proxy for the original quark or gluon. As mentioned in Chapter 2, the observation of jets in e^+e^- collisions were instrumental in the solidification of QCD as the theory of strong interactions. It turns out that in modern collider physics, they continue to be essential tools for better understanding the underlying dynamics of interest.

The systematic clustering of the collimated sprays of hadrons and their decays into jets is of extreme importance in the study of strong interactions at high-energy particle colliders. This is the case for the data analyses presented in Chapters 6, 7, and 8 of this thesis. QCD does not tell us what algorithm or strategy we should use to cluster all the particles created in the collision into well-defined jets; that is up to us (theorists and experimentalists) to come up with in our understanding of Nature.

For a given event, a jet algorithm must be such that all the particles with their respective four-momenta are mapped onto a set of jets with their respective four-momenta. Ideally, we would like the jet algorithm to give a faithful mapping of the "bare" struck partons to the detector-level signatures.

Over the last decades, several definitions of what a jet is have been introduced, all of which have been useful and have given us deeper insight into the parton emission patterns of QCD. As an experimentalist, one can come up with definitions of what a jet is and obtain results that are satisfactory at face value. However, not every definition of a

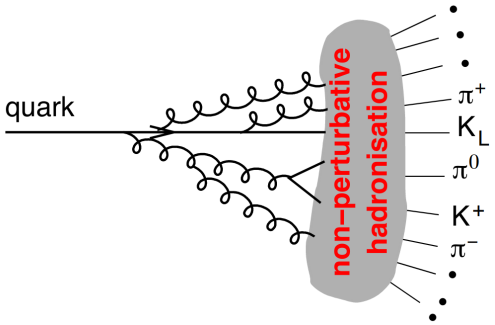

Figure 3.6: Transition of a struck quark to the collimated spray of stable particles known as a "jet." Figure extracted from Gavin Salam lecture notes on QCD.

jet is theoretically robust, in the sense that theoretical predictions may not necessarily be "mapped" to the experimental-level observables in a stable fashion. This can jeopardize the physical interpretation of a given measurement, and the potential impact that a given measurement can have for understanding Nature.

Indeed, stronger conclusions can be drawn if the jet clustering algorithm is infrared and collinear safe. Infrared safety means that a given observable or algorithm output is resilient to the addition of soft particles. Similarly, collinear safety means that one could replace a given particle in two collinear particles, and the results from the observable or algorithm should be resilient to the angular separation between the particles. As described in the context of parton showers in QCD, these divergences are related to the limit where the mass goes on-shell. It is generally preferable to have a jet clustering algorithm (or observables, for that matter) that "respects" the divergences of QCD. A special set of sequential clustering algorithms that respect these divergences has been identified in recent years. With the advent of the LHC era, there has been an "informal" agreement between both theory and experimental communities on an algorithm that is useful in both contexts: the anti-k_T algorithm. The anti-k_T algorithm, discussed in Subsection 3.5.3, is one particular instance of a family of *sequential clustering* algorithms, which are discussed next.

Sequential clustering algorithms consider both the transverse momentum and angular

separation of the particles when combining them. Two distance measures, d_{ij} and d_{iB}, are calculated for every particle. The d_{ij} quantity is defined between every particle pair, i and j, as

$$d_{ij} = \min(p_{T,i}^{2a}, p_{T,j}^{2a}) \frac{R_{ij}^2}{R^2} \tag{3.11}$$

where $R_{ij} = \sqrt{(\Delta y_{ij})^2 + (\Delta \phi_{ij})^2}$ is the separation in rapidity and azimuth between the pair of particles, and R is the jet distance parameter in the rapidity and azimuth plane. The distance parameter is chosen to be $R = 0.4$ or 0.5 for jet analyses at the CERN LHC experiments. The exponent a controls the relative power of the transverse momentum measure versus the geometric measure. The a parameter is the key parameter that distinguishes the various jet clustering algorithms between each other, as it will be discussed in the following paragraphs. The d_{iB} quantity is the momentum space distance between the beam-axes and the ith particle, and is defined as

$$d_{iB} = p_{T,i}^{2a} \tag{3.12}$$

once the distance measures d_{ij} and d_{iB} have been calculated for all particles, they are sorted in increasing order and the smallest value is picked. If d_{ij} is smaller than d_{iB}, then particles i and j are combined into one particle. In the combination E-scheme, the particles i and j would be replaced by a new particle whose four-momentum is the sum of the four-momenta of particles i and j. The new particle is added to the list of particles, replacing particles i and j. All affected d_{ij} and d_{iB} values are recalculated with this new particle. If the d_{iB} is smaller than d_{ij}, then the particle i is labeled as a jet and is removed from the list of particles. This process is repeated until either all particles are part of a jet (inclusive clustering) or until a predetermined number of jets has been found (exclusive clustering). It has been demonstrated that such a clustering algorithm is both collinear and infrared safe (79).

One can distinguish three different classes of sequential clustering algorithms defined by the chosen value value of $a = -1, 0, 1$. These are discussed in the following subsections.

3.5.1 k_T algorithm

The k_T algorithm is the case of the sequential recombination algorithm with $a = 1$. In this case, all d_{ij} pairs of particles that are separated by distances smaller than R will be sorted in increasing order of the pair's lowest p_T particle. This means that the k_T algorithm will begin by clustering soft particles first, and only brings hard particles together in the final steps of the algorithm sequence. This results in irregularly shaped jets, since soft particles are clustered together first and these can in principle populate all the rapidity and azimuth phase-space for a given collision.

3.5.2 Cambridge–Aachen algorithm

The Cambridge–Aachen algorithm (C/A) corresponds to the special case where $a = 0$. This removes any transverse momentum dependence on the clustering algorithm. Thus, the clustering is purely geometrical, and ultimately depends on how far or close the particles are in rapidity and azimuth in comparison to the characteristic distance parameter R. The clustering begins by clustering the particles that are the closest to each other in rapidity and azimuth, and clusters the particles that are the farthest apart for the last step.

3.5.3 anti-k_T algorithm

The anti-k_T algorithm is the case of the sequential recombination algorithm when $a = -1$. In this case, the d_{ij} pairs of particles that are separated by distances smaller than R will be sorted in increasing order of the pair's highest p_T particle. This means that the anti-k_T algorithm will cluster hard particles first, leaving the soft particles to be clustered at the

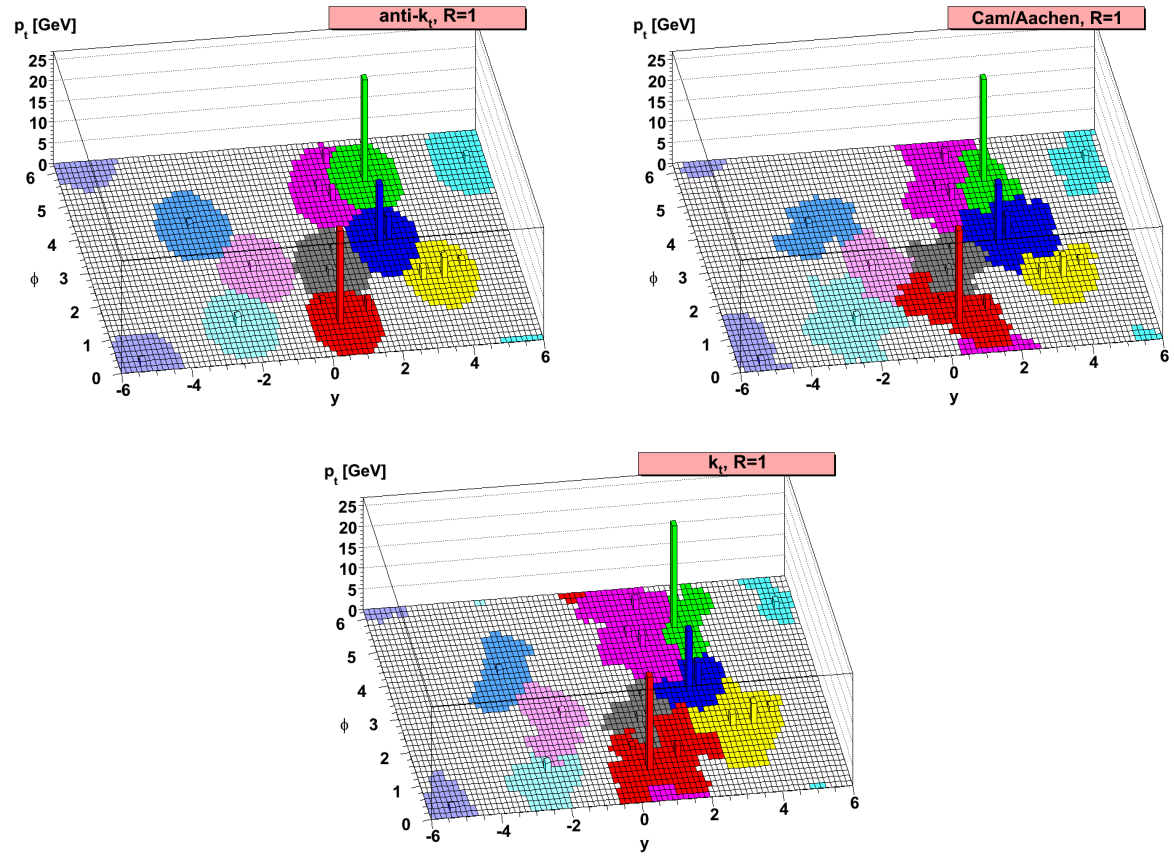

Figure 3.7: Results from different clustering algorithms for a given set of particles in ϕ–y–p_T space. Upper left panel is the result from the anti-k_T algorithm, upper right is the result from the Cambridge–Aachen algorithm, lower panel is the result of the k_T algorithm. The plots are extracted from Ref. (79).

last steps of the algorithm. The anti-k_T algorithm yields nearly circularly-shaped jets in the rapidity–azimuth plane. This feature is very useful for a reliable calibration of the jet energy, particularly for the controlled removal of pileup contributions and multiple partonic interactions, which tend to populate the rapidity-azimuth plane uniformly. The experiment and theory communities have informally agreed on using the anti-k_T algorithm as the standard algorithm for jet clustering at the CERN LHC. The k_T and C/A algorithms are used for studies that target the substructure of jets.

3.6 Multiple parton interactions

In addition to the primary parton-parton interaction, there can be one or more additional parton-parton interactions. These are known as "multiple parton interactions" (MPI). Indeed, since the proton is an extended object with numerous partons created by quantum fluctuations within it at a given timescale, this can easily occur in a given high-energy proton-proton collision. MPI are typically much softer than the primary parton-parton interaction.

The possibility that several parton pairs undergo simultaneous interactions is currently implemented in modern Monte Carlo event generators. Let us discuss how this is done in PYTHIA. Since MPI are elementary parton-parton interactions, it makes sense to first start with the pQCD prediction for $2 \to 2$ parton scattering. The first necessary ingredient is the regularization of the partonic QCD cross section, which is divergent for $p_T \to 0$. On the grounds of color confinement at low energies, this divergence can be regularized by taking into account that the colliding proton has a finite size in impact parameter space. This translates to a modification of the partonic cross section at low p_T to regularize this divergence as

$$\frac{d\sigma}{dp_T^2} \propto \frac{\alpha_s^2(p_T^2)}{p_T^4} \to \frac{\alpha_s^2(p_T^2+p_{T0}^2)}{(p_T^2+p_{T0}^2)^2} \tag{3.13}$$

the parameter p_{T0} is energy-dependent, since the partonic structure of the proton is a function of the collision energy itself. Such energy dependence is controlled by two addtional parameters, p_{T0}^{ref} and E_{pow}, which are fit to data. The energy dependence is parametrized as

$$p_{T0} = p_{T0}^{\mathrm{ref}}\Big(\frac{E}{E_{\mathrm{ref}}}\Big)^{E_{\mathrm{pow}}} \tag{3.14}$$

the reference energy is conventionally set to 1800 GeV (one of the collision energies at the Tevatron). This regularization strategy is currently implemented in the `PYTHIA` gen-

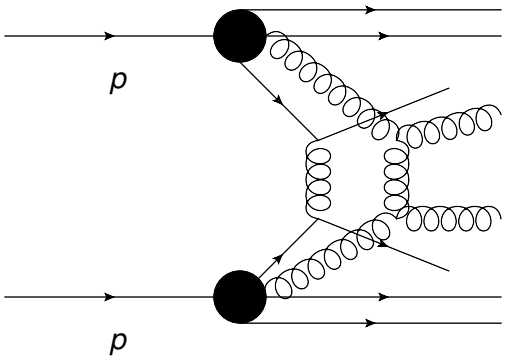

Figure 3.8: Schematic diagram of multiple-parton interactions in the same proton-proton collision. Two scattering processes, $qq \to qq$ and $gg \to gg$, occur in the same collision.

erator. The parameters of the MPI are fit to measurements of well-understood standard candle processes, such as Drell–Yan, at various center-of-mass energies.

The additional partons, since they are colored particles, they may rearrange the color field generated by the partons struck from the main interaction. Such color reconnection effects are included in the Monte Carlo event generators.

In addition to MPI, we also have the effects from the beam remnants. The beam remnants, initial-state radiation effects, and MPI, fall under the umbrella of the so-called *underlying event activity*. For what concerns this thesis, the most important component is the MPI contribution.

3.7 Jet measurements as a probe of QCD collider phenomenology

One of the benchmark measurements to test QCD at all scales comes from differential cross section measurements for inclusive (multi)-jet production in pp collisions at several center-of-mass energies at the CERN LHC. An example of such measurements is shown in Fig. 3.9, where the double-differential cross section for inclusive jet production at $\sqrt{s} = 13$ TeV by the CMS experiment is presented. For the typical region of phase-space that is probed in LHC analyses, there is excellent agreement with the fixed-order perturbative QCD calculations supplemented with parton showering, hadronization, and underlying event activity effects. The cross section measurement spans orders of magnitude as a func-

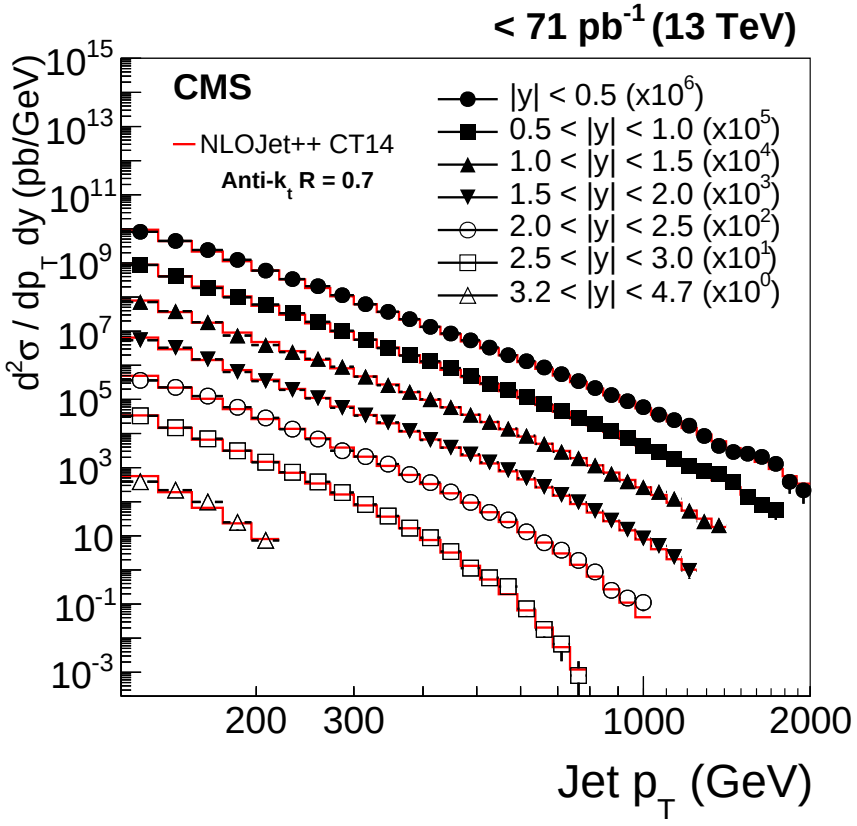

Figure 3.9: Double-differential jet cross section at $\sqrt{s} = 13$ TeV by the CMS experiment. The cross section is presented as a function of the jet p_{T} for various bins in jet rapidity y. The data (symbols) are compared to NLO theoretical predictions based on NLOJet++ calculations. The data for a given bin in $|y|$ is artificially displaced by powers of 10, as indicated in the label. Figure extracted from Ref. (80).

tion of p_{T} at a given bin in y. The theoretical prediction is able to describe simultaneously all aspects of these measurements. Similar to the inclusive jet cross section measurement, one can measure single-, double-, and even triple-differential cross sections for other hard probes, such as photon+jet, Z+jet, ..., which are well described by these calculations. This gives us good reasons to think that, to a large extent, the standard prediction machinery works well at the LHC.

3.8 Summary of the Chapter

In this Chapter, we covered the basic elements of QCD phenomenology for collider physics. These involve the use of calculable parton-level cross sections in pQCD, convolved with universal, process-independent parton densities, and supplemented with parton shower, hadronization, and underlying event activity effects. Monte Carlo event generators can be used to simulate events based on all these tools in order to draw comparisons with data.

These are the fundamental computational elements used in modern particle physics, and, for the most part, they work rather well for the typical phase-space region (in p_{T} and y) of interest at the LHC. In the next Chapter, we will see that certain aspects of this traditional approach need to be carefully taken care of in special corners of phase-space, particularly the region at large y and at low p_{T}.

Chapter 4

High-energy limit of QCD and hard diffraction

In this Chapter, we cover the basic elements of the high-energy limit of QCD interactions, also known as the small-x limit of QCD. We will see that, in this limit, we are led to account for the summation of an infinite number of Feynman diagrams with multiple gluon emissions, which leads to a renormalization group equation known as the Balitsky–Fadin–Kuraev–Lipatov evolution equation of pQCD. We describe the typical experimental probes of this prediction of QCD. Particular attention is given to the hard color-singlet exchange process, since this is the main analysis that is carried out in this thesis described in Chapters 6 and 7. Then, we describe the phenomenon of hard diffraction in the context of DIS and in hadron-hadron physics, and how we can probe it in interactions with intact protons and hard jets at the CERN LHC, which motivates the analysis carried out in Chapter 8.

4.1 High-energy limit of QCD

Perturbation theory calculations are usually based on fixed-order calculations in the strong coupling α_s. In the fixed-order approach, one considers the Feynman diagrams that contribute up to a given order in α_s. For an inclusive jet cross section calculation at NLO in α_s, for example, one can consider tree-level diagrams that contribute to the $2 \to 2$ parton scattering process, followed by higher-order virtual and real corrections Feynman diagrams ($2 \to 2$ and $2 \to 3$ parton scattering). The associated theoretical uncertainty, which comes from neglecting higher-order terms in the perturbative expansion, are usually es-

timated by varying the renormalization and factorization energy scales. These uncertainties usually decrease at higher-orders in α_s, as more diagrams are incorporated into the calculation and the dependence on the unphysical renormalization and factorization scales diminishes. The number of Feynman diagrams that need to be considered increases rapidly as one goes to higher orders in α_s, but in principle one can always go through such a calculation systematically, provided we are always in a kinematic region where perturbation theory is applicable. Fixed-order calculations are the bread-and-butter of collider physics phenomenology, and is widely successful in predicting several observables for various final-states, such as vector boson production in association with jets, top quark production, jet production, jet+photon production, and many others. The QCD fixed-order calculation for $2 \to 2+n$ parton scattering can be symbolically represented as (ignoring pre-factors)

$$\mathrm{d}\hat{\sigma} \simeq \alpha_s^2 + \alpha_s^3 + \alpha_s^4 + \ldots \tag{4.1}$$

while the fixed-order pQCD approach works rather well for the phase-space that is typically covered at the LHC (central rapidities and high transverse momenta), there can be regions of phase-space where the fixed-order pQCD calculation misses contributions that are as large as the (expected) leading contributions at LO, NLO, NNLO, ... in α_s. Such missing contributions are not properly captured by the variation of the renormalization and factorization scales, and a completely different procedure is thus needed in order to take them into account properly.

Such a situation occurs in cases where we have a strong hierarchy of energy scales. In that case, it may happen that a family of Feynman diagrams with multiple real and virtual radiative corrections are kinematically enhanced, in a way such that they compensate for the smallness of the coupling used in the perturbative expansion. In gauge field theories, these contributions usually exhibit a peculiar pattern of terms with powers of logarithms of ratios of energy scales multiplying powers of the gauge coupling strength.

In QCD, owing to the self-interaction of the gluon and a not-so-small strong coupling coefficient $\alpha_s \approx 0.1$, these radiation patterns are more important to take into account in the perturbative calculations.

Such a systematic pattern of logarithmically-enhanced terms allows for a systematic summation of these terms to all orders in α_s in a procedure known as "resummation." This resummation of logarithms of energy to all orders in α_s can usually be carried out by means of a renormalization group equation. A famous example is the renormalization group equation of α_s itself, which can be interpreted as the result of the resummation of an infinite number of vacuum polarization diagrams of QCD that modify the propagator of the gluon in QCD. Another well-known example is the renormalization group equations of the parton densities of the proton described in Chapter 2.

In the regime where $\hat{s} \gg -\hat{t} \gg \Lambda^2_{\rm QCD}$, known as the high-energy limit of QCD, where $\hat{s}$ is the partonic center-of-mass energy squared, $\hat{t}$ is the transferred four-momentum squared and $\Lambda_{\rm QCD} \approx 200$ MeV, large logarithms of $\hat{s}$ may accompany each power of α_s in the perturbative expansion of the parton-level cross section. These enhancements are such that they compensate for the smallness of α_s with logarithmic enhancements of the form $\alpha_s^n \ln^n(\hat{s}/|\hat{t}) \lesssim 1$ for $n = 1, 2, ...$ The high-energy limit of QCD is reached in kinematic configurations where the scattered partons are separated by a large rapidity interval, since $\Delta y = \ln(\hat{s}/|t|)$. Indeed, the production rates in the high-energy limit of QCD may be rearranged as (ignoring pre-factors),

$$\mathrm{d}\hat{\sigma} \simeq \alpha_s^2 \sum_{n=0}^{\infty} \alpha_s^n \ln^n\left(\frac{\hat{s}}{-\hat{t}}\right) + \alpha_s^3 \sum_{n=0}^{\infty} \alpha_s^n \ln^n\left(\frac{\hat{s}}{-\hat{t}}\right) + \alpha_s^4 \sum_{n=0}^{\infty} \alpha_s^n \ln^n\left(\frac{\hat{s}}{-\hat{t}}\right) + \ldots \tag{4.2}$$

as suggested by this expression, an all-orders resummation of $\alpha_s^n \ln^n(s)$ terms is required in the high-energy limit of QCD in order to obtain finite, stable cross sections that properly capture the dominant terms in the perturbative expansion. We can see how the simple fixed-order pQCD diagrams would not capture all the dominant terms of the perturbative expansion. The resummation to all orders in α_s is done via a renormalization

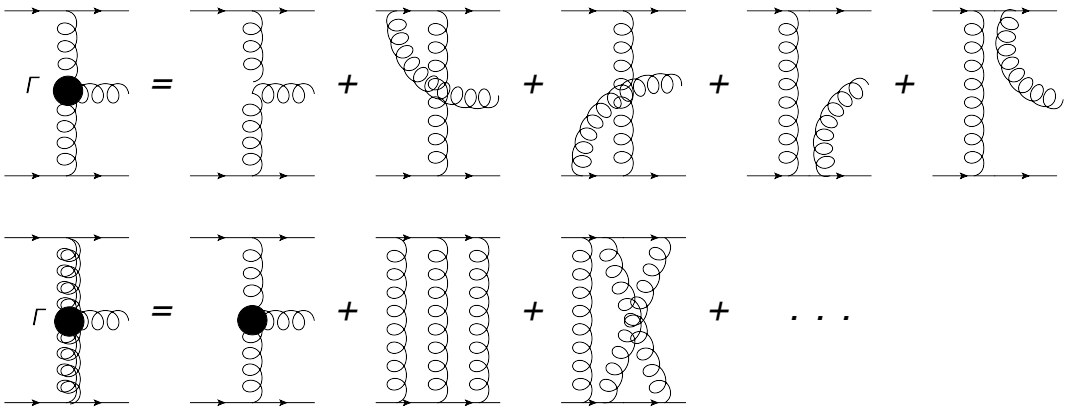

Figure 4.1: Upper diagrams: definition of the Lipatov effective vertex, Γ, which contains the dominant real emission diagrams in the leading-logarithm (LL) approximation. Lower diagrams: reggeization of the gluon obtained by summing up all the virtual gluon emission diagrams in the LL approximation. The double-gluon lines in the lower left diagram represents the *reggeized* t-channel gluons.

group equation known as the Balitsky–Fadin–Kuraev–Lipatov (BFKL) evolution equation (81; 82), named after Ian Balitsky, Victor Fadin, Eduard Kuraev, and Lev Lipatov, who first derived it in the late 1970s. Notice how the behavior of QCD interactions in this limit has been a problem investigated just a few years since the development of QCD in the early 1970s.

The relevant diagrams in the high-energy limit of QCD are those of t-channel gluon exchange with multiple s-channel gluon emissions. The t-channel gluons are in fact "reggeized" gluons, meaning that they have modified propagators that account for all the relevant virtual corrections in the high-energy limit of QCD. The dominant real gluon emission diagrams can be modelled with a gauge invariant, non-local effective vertex known as Lipatov vertex. Figure 4.1 shows how these reggeized t-channel gluons and Lipatov vertices are defined in terms of elementary QCD Feynman diagrams. Self-energy diagrams are subleading in the leading logarithm approximation.

The leading-logarithmic contributions are obtained in a kinematic configuration known as "multi-Regge kinematics," where the gluon splittings are strongly ordered in rapidity and with no ordering in transverse momentum. When we say "BFKL dynamics", this is part of the mental picture one can use as a rule of thumb. A schematic diagram with

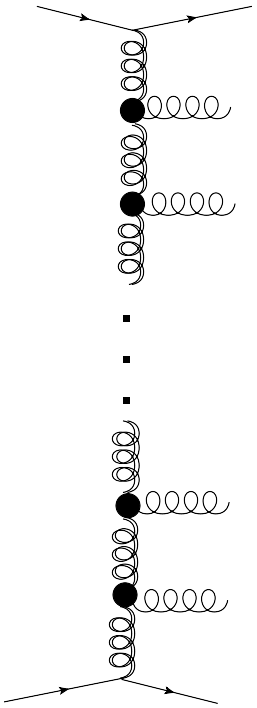

Figure 4.2: Gluon ladder diagram that contributes significantly in the high-energy limit of QCD. The t-channel gluons are "reggeized" gluons. The disks represent the Lipatov effective vertices.

such multi-gluon diagrams is shown in Fig. 4.2. These conditions may be represented mathematically as,

$$\begin{aligned} \mathbf{k_T}_1^2 \simeq \mathbf{k_T}_2^2 \simeq ... \simeq \mathbf{k_T}_n^2 \simeq \mathbf{k_T}_{n+1}^2 \simeq \mathbf{k_T}_{n+1}^2 \gg -\hat{\mathbf{t}}^2 \\ y_1 \gg y_2 \gg y_3 \gg ... \gg y_{n-1} \gg y_n \gg y_{n+1} \end{aligned} \tag{4.3}$$

where $k_{T,i}$ and y_i represent the transverse momentum and rapidity of the i-th gluon in the ladder.

The BFKL equation, in its representation as an integral equation in Mellin space, reads

$$\omega \mathscr{G}(\mathbf{k_T}^a, \mathbf{k_T}^b) = \delta^2(\mathbf{k_T}^a - \mathbf{k_T}^b) + \int d^2\ell \mathscr{K}(\mathbf{k_T}^a, \ell) \mathscr{G}(\ell, \mathbf{k_T}^b) \tag{4.4}$$

where the complex angular momentum ω is the Mellin conjugate variable to $\hat{s}$, $\mathscr{K}$ is

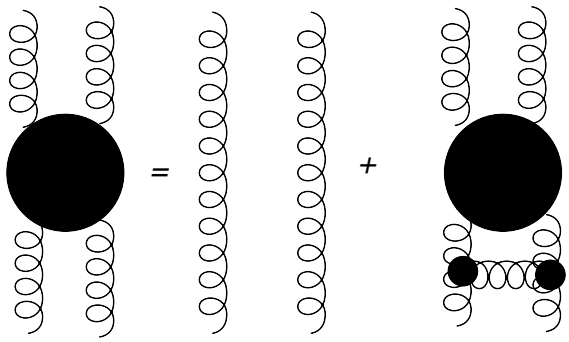

Figure 4.3: Graphical representation of the BFKL equation in its integral form. This is telling us that the BFKL gluon ladder is built iteratively. The large black disks represent the BFKL gluon Green function described in text. The smaller black disks represent the Lipatov vertices.

the BFKL kernel that contains the virtual and real radiative corrections, and $\mathscr{G}$ is the BFKL gluon Green function. Solving the BFKL equation amounts to solving this equation for the BFKL gluon Green function in Mellin space, applying the inverse Mellin transform to map the calculation to momentum space, followed by integrating over the transverse momenta of the "outermost" reggeized gluons. This is then used to calculate the scattering amplitude. The BFKL equation in its integral representation has a nice interpretation; it is telling us that you can build the gluon ladder Feynman diagram iteratively, as shown schematically in Fig.4.3. The summation of these iteratively-generated Feynman diagrams is the soul of BFKL evolution.

The BFKL evolution equation describes the evolution of the scattering amplitude with the collision energy. The resummation of large logarithms of s is known at leading logarithmic (LL) (81; 82) and next-to-LL (NLL) accuracy (83; 84), which corresponds to the resummation of $\alpha_s^n \ln^n(s)$ and $\alpha_s^{n+1} \ln^n(s)$ terms, respectively. The resummation in the LL approximation was presented by the BFKL authors in the late 70s. It was not until the late 90s that the resummation in the NLL approximation was carried out, nearly 20 years apart. The resummation at next-to-NLL (NNLL) accuracy is not known, although there are efforts into analytically performing this calculation (85).

A famous prediction of BFKL evolution is that the QCD high-energy cross section of

partonic scattering must scale with a power of $\sigma \propto \hat{s}^{2\lambda}$. The exponent is valued at $\lambda = \frac{\alpha_s N_C}{\pi} 4\ln(2)$ at the LL approximation. With $\alpha_s = 0.1$ and $N_C = 3$, we have a $\lambda^{\mathrm{LL}} \approx 0.26$, the cross section that increases moderately with $\hat{s}$. At NLL, the same power-law structure is expected, although now we have an α_s^2 correction to λ. Here, $\lambda^{\mathrm{NLL}} = \frac{\alpha_s N_c}{\pi} 4\ln(2)(1 - 6.2\alpha_s)$, which corresponds to $\lambda^{\mathrm{NLL}} \approx 0.1$, which is a large correction.

In contrast to the BFKL regime, one can distinguish another limit of QCD, where the dominant scale is the momentum transferred in the collision $Q \gg \Lambda^2_{\mathrm{QCD}}$. Terms of the form $\alpha_s^n \ln^n(Q^2/\Lambda^2_{\mathrm{QCD}})$ become large in the perturbative expansion, and need to be resummed systematically to all-orders in α_s. This resummation amounts to solving another renormalization group equation: the DGLAP evolution equation. This evolution equation of pQCD was introduced in the context of PDFs and of the proton structure in Chapter 2 of this thesis. The kinematic configuration that yields the leading terms for the DGLAP evolution is such that the multiple gluon emissions are strongly ordered in transverse momentum and weakly ordered in rapidity. As we will see later when reviewing the experimental probes of BFKL dynamics, separating DGLAP from BFKL evolution is perhaps the most difficult aspect of isolating BFKL dynamics in the experiment.

4.1.1 Connection to small-x evolution of proton structure

Owing to the universality of QCD interactions, Feynman diagrams with multiple gluon splittings emerge also in the study of the internal structure of the proton. In the context of DIS, the high-energy limit of QCD is equivalent to the $x \to 0$ limit at perturbatively large virtualities $Q^2 \gg \Lambda^2_{\mathrm{QCD}}$. For this reason, the high-energy limit of QCD is sometimes known colloquially as "small-x physics." Indeed, one finds that the parton cascade that is produced from the gluon splitting process $g \to gg$ produces an uncountable number of softer, softer, and softer gluons at small-x. The growth of the gluon densities inside the proton is expected to be governed by the same evolution equation of pQCD used for high-energy partonic scattering: the BFKL evolution equation. In this case, BFKL

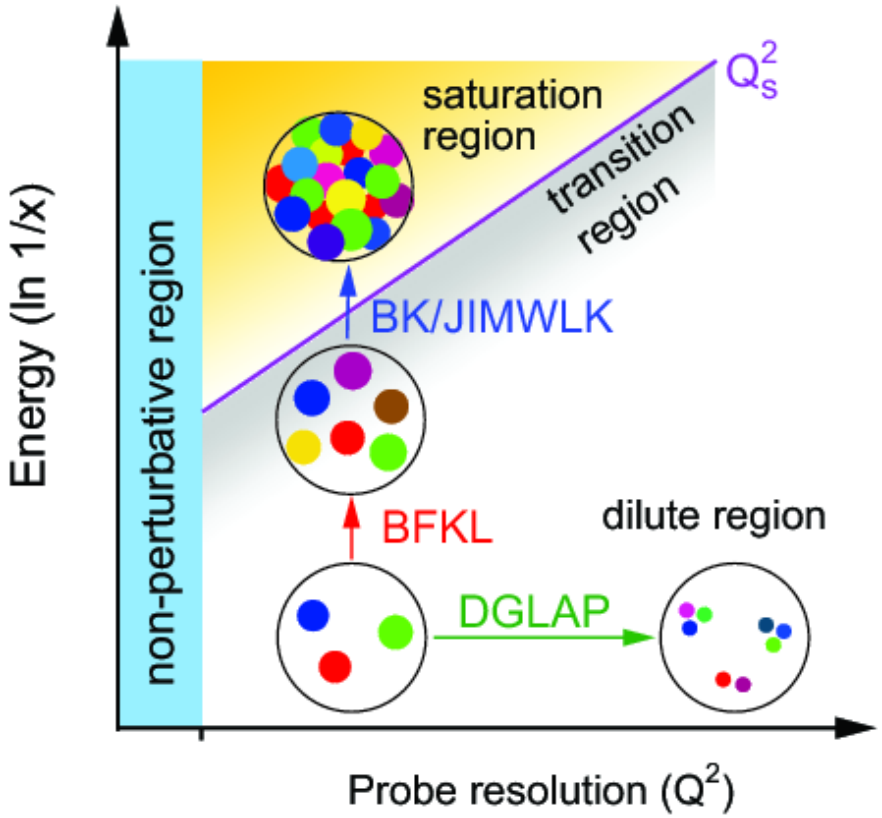

Figure 4.4: Evolution of the proton wave function in the x versus Q^2 plane, where x is the fraction of momentum carried by the struck parton and Q^2 the characteristic energy scale used to probe the proton (virtuality in the context of DIS). At fixed x, the pQCD evolution of the parton densities of the proton are described by the DGLAP evolution equations of pQCD. At fixed $Q^2 \gg \Lambda^2_{\mathrm{QCD}}$, the small-$x$ evolution is described by the BFKL evolution equation. Eventually, gluon recombination effects are expected to play a significant role. In this case, they are described by the JIMWLK/BK evolution equations. Figure extracted from Ref. (86).

evolution resums terms of the form $\alpha_s^n \ln^n(1/x)$ at all orders in α_s.

In the context of the proton structure function, the BFKL equation in its presentation as an integro-differential equation is given by

$$\frac{\partial \mathscr{G}(x,k_T^2)}{\partial \ln(1/x)} = \int dk_T'^2 \mathscr{K}(k_T^2, k_T'^2) \mathscr{G}(x, k_T'^2) \tag{4.5}$$

where $\mathscr{G}(x,k_T^2)$ is the unintegrated gluon density, and k_T is the transverse momentum of the gluons within the proton. One can think of these intrinsic k_T of the gluons as arising from the multiple gluon splittings in the small-x limit, which would give tiny "kicks" to the gluons inside the proton at each gluon splitting. The kernel $\mathscr{K}$ is the BFKL kernel introduced in the context of high-energy scattering. The function $\mathscr{G}(x,k_T^2)$ is called "unintegrated", since one may recover the conventional gluon PDF by integrating over k_T,

$$xg(x,Q^2) = \int^{Q^2} \frac{dk_T^2}{k_T^2} \mathscr{G}(x,k_T^2) \tag{4.6}$$

considering BFKL evolution alone, one would expect that gluon densities should grow with $x^{-\lambda}$ in the small-x limit, where $\lambda = \frac{\alpha_s N_c}{\pi} 4\ln(2)$ in the LL approximation. At first sight, it seems that eventually, in the $x \to 0$ limit, the gluon densities should grow indefinitely, leading to a violation of unitarity in the calculations of cross sections. Theoretically, we expect that the gluon splitting process $g \to gg$ described by BFKL evolution should be countered by the gluon recombination processes $gg \to g$, which would preserve unitarity. The regime where the gluon splitting and recombination processes balance each other is known as *parton saturation*. The characteristic energy scale at which these effects become important is known as the saturation energy scale, $Q_s = Q_s(x)$. In this regime, where the recombination effects become more important, the proper QCD evolution is given by the Jalilian-Marian–Iancu–McLerran–Weigert–Leonidov–Kovner (JIMWLK) (87; 88; 89; 90) or the Balitsky–Kovchegov (BK) (91; 92) evolution equations of QCD. The aforementioned

equations have BFKL dynamics embedded in them for the gluon splitting process at small-x, but they incorporate in addition the gluon recombination mechanism to counterbalance the rapid gluon splitting from BFKL. There is no outstanding evidence for parton saturation effects in the data, although some observables and measurements are consistent with these effects. In order to clearly identify the onset of such higher-order effects, which is one of the long-term goals of nuclear physics, it is reasonable to also have a clear understanding of the onset of the BFKL gluon splitting dynamics in a controlled environment. This, among other topics of nuclear physics, will be a subject of intense study at the future Electron Ion Collider (EIC) (86) at Brookhaven National Laboratory to be built in the U.S., which is expected to be built in the 2030s at the time of writing this thesis.

It is worth mentioning that, as mentioned in Chapter 2, the DGLAP evolution of the proton wavefunction works rather well for most of the kinematic plane in x and Q^2, at least in regards to the typical phase-space region covered by standard CERN LHC measurements. In DGLAP evolution, starting from a PDF at a fixed x value at a given Q_0^2, we can predict the proton wavefunction at a higher Q^2. Nevertheless, we are reaching observables where these effects start to become more and more important. For example, for the description of small p_{T} of weak gauge bosons and Higgs boson, where the effect from small-x physics is mostly responsible for the generation of the p_T of the boson. Nevertheless, it is expected that DGLAP evolution alone is not able to describe the whole kinematic plane. A schematic diagram with the expected domains of validity of the various evolution equations of QCD are shown in Fig. 4.4.

4.1.2 Remarks on BFKL evolution

The high-energy limit is a venue to further understand the quantum field theory formalism, which is the foundational framework of the SM. This is important for QCD in particular, but it is important for all quantum field theories in general. The reason we

usually focus on QCD for testing the high-energy limit of quantum field theories is that, in QCD, given the strength of α_s, and the fact that gluons have a self-coupling interaction at tree-level, the expected emergent properties of elementary interactions in the high-energy limit are expected to appear more easily within our current experimental reach than it is for the weak interactions or electromagnetic interactions.

Indeed, in electromagnetic interactions, since there is no photon self-coupling, the logarithmic contributions appear with the emission of a cascade of electron-positron pairs. This means that the logarithms that need to be resummed are of order $\alpha_{QED}^{2n}\log^n(s)$, i.e., they suppressed by an additional power of α_{QED}. Since $\alpha_{QED} \approx 1/137$, the resummation of these terms only becomes relevant at center-of-mass energies that are beyond the reach of the experiment. For weak interactions, where we do have tree-level couplings between the Z and W bosons, in principle it should be feasible to produce a cascade of gauge bosons produced in the s-channel, similar to the one we find in QCD. The difference here is that one needs to have sufficient energy to produce the Z and W bosons in the weak gauge boson ladder (analogous to the gluon ladder in QCD). The weak gauge coupling is so small that the onset of the high-energy limit of the theory occurs at much larger energies. This is not much of a problem if $s \to \infty$, since there will always be energy available to produce the weak gauge bosons in this limit. However, this would mean that probing the high-energy limit with W or Z boson emissions at the LHC or other foreseeable colliders is not feasible. Thus, the only quantum field theory we could use to realistically test particle scattering in the high-energy limit is QCD.

The challenge is to identify the set of experimental probes that can clearly show us evidence for these virtual and real gluon emissions reflected in the data. The challenge is analogous to that of seeing the Bjorken scaling violations in the structure function of the proton, or the running of the coupling constant. The complication arises from the fact that other higher-order corrections appear in most of the experimental probe, which "contaminate" the dynamics of interest.

4.2 Standard probes of BFKL evolution

In this Section, we give an overview of some of the standard probes of BFKL dynamics that have been tested against the experiment. This is by no means an exhaustive list of processes, and the intention here is to mostly paint a broad picture of the processes that have been considered. The main process addressed in Chapters 6 and 7 this thesis, namely the hard color-singlet exchange dijet process, is described in Sec. 4.2.5.

In order to probe BFKL dynamics experimentally, one needs a process with a hard energy scale to justify the use of perturbation theory. Moreover, the process needs to be such that other higher-order corrections are as suppressed as possible. The high-energy limit is related with very forward particle production, so the detector acceptance sets a challenge for some of these measurements as well. Ideally, we should be able to describe all these measurements in a cohesive picture.

4.2.1 Small-x evolution of structure function

A renewed interest in BFKL dynamics appeared upon the discovery of the fast rise of the structure function $F_2(x)$ extracted from DIS data. With the availability of more DIS data at small-x, it was possible to do a differential analysis of the structure function $F_2(x,Q^2)$ to analyze its dependence on x at a fixed Q^2 in the small-x regime. One can do fits to $F_2(x,Q^2)$ at small-x as a function of Q^2 with a simple functional form $F_2(x,Q^2)|^{x\ll 1} = A(Q^2)x^{-\lambda_{\text{eff}}}$. Such a functional form provides an adequate description of DIS data from HERA and fixed-target experiments.

Initially, it was thought that the power-law growth of parton densities at small-x might be indicative of an underlying $g \to gg$ splitting dynamics described by BFKL evolution. If so, then $\lambda_{\text{eff}}(Q^2) \approx \lambda_{\text{BFKL}} = \frac{\alpha_s N_c}{\pi} 4\ln(2) \approx 0.5$ for $\alpha_s = 0.2$ (for LL resummation in BFKL). However, when performing these fits, it is found that $\lambda_{\text{eff}} \neq \lambda_{\text{BFKL}}$ at small-x for a given Q^2. Not only that, but $\lambda_{\text{eff}} = \lambda_{\text{eff}}(Q^2)$ at small-x, as shown in Figure 4.5. Does this mean

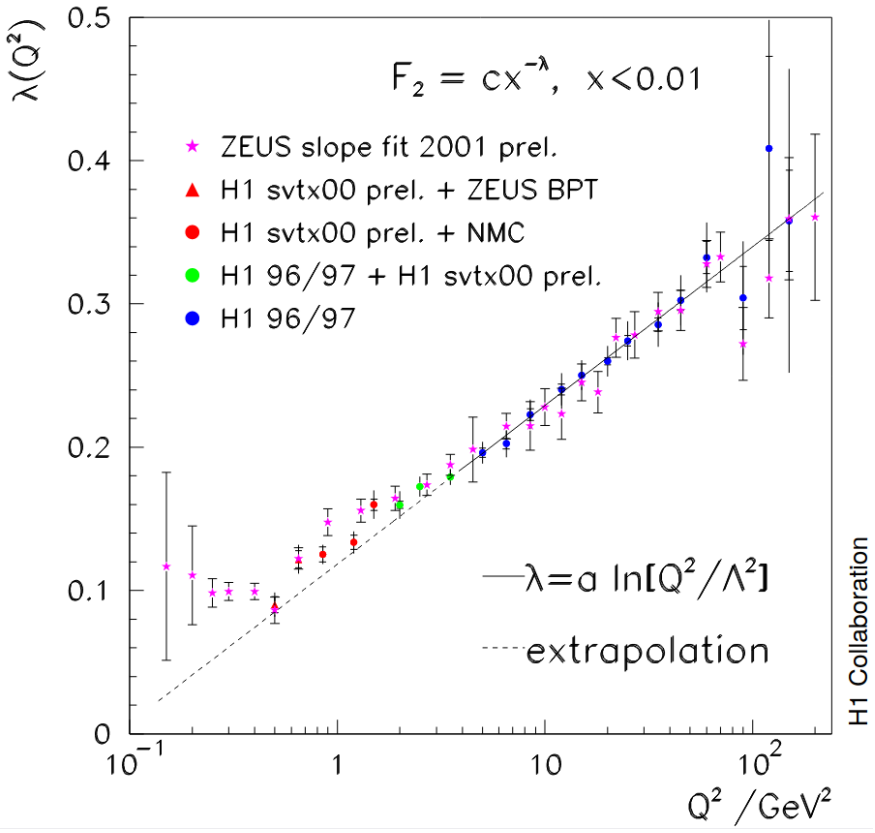

Figure 4.5: Effective slope λ of $F_2(x,Q^2)$ at low-x, for $F_2(x,Q^2) \propto x^{-\lambda(Q^2)}$, as a function of Q^2, extracted from HERA data. Figure extracted from Ref.(93).

that BFKL evolution is wrong? Not quite; the reason is that DGLAP evolution predicts also a power-law increase with small-x. What this suggests is that it is not possible to just use BFKL evolution to describe the parton densities at small-x; the observed trend of the structure function $F_2(x,Q^2)$ at small-x might be due to a combination of DGLAP and BFKL evolution effects, which is highly non-trivial to separate one from the other.

The effects of BFKL resummation might be better elucidated when *matched* with DGLAP evolution. By matching, we mean that no diagrams are "double-counted" in both pictures. This way, one can account for the resummation of large logs of Q^2 in DGLAP, while accounting also for the relevant small-x contributions that might be missed by DGLAP. This was done in a recent analysis (94) of the longitudinal structure function of the proton, $F_L(x,Q^2)$, which is also extracted from global fit analyses of DIS data. For this study,

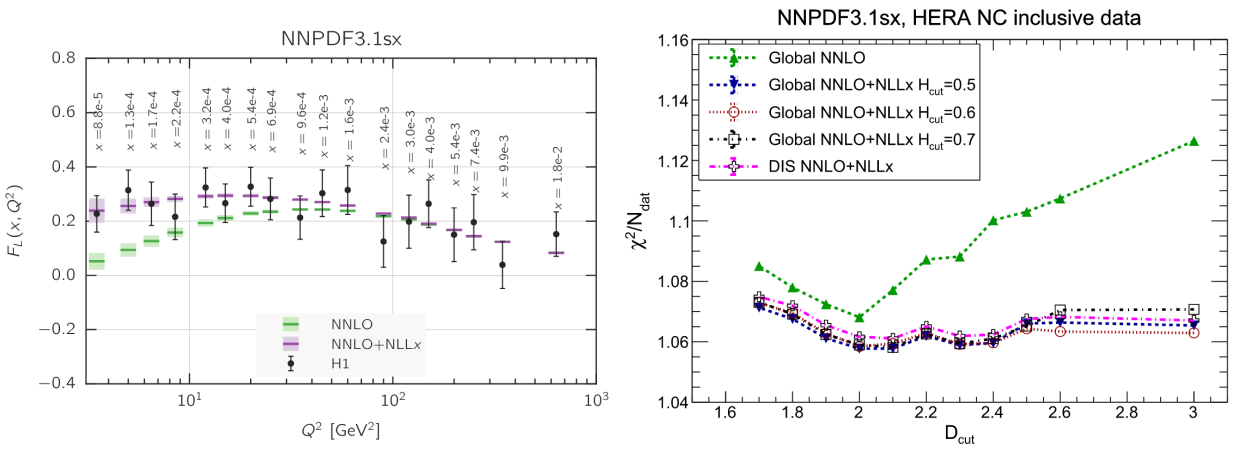

Figure 4.6: Result of global fit analysis using DGLAP evolution at NNLO in α_s in comparison to the case where no BFKL resummation of small-x terms is carried out (NNLO, green curves) and when the resummation of small-x terms is supplemented (NNLO+NLLx, purple curves). The black markers represent the data points. On the left-hand side, we find the result coming from the fits to $F_L(x,Q^2)$ structure function from H1 data, whereas on the right-hand side we find the χ^2/ndof of the global fit as a function of the variable D_{cut}. The larger D_{cut} is, the more small-x data is included. The plots are extracted from Ref.(94).

techniques of the NNPDF Collaboration were employed. A better description of $F_L(x,Q^2)$ is obtained with the calculation of NNLO DGLAP matched with NLLx resummation in BFKL. As shown in Fig. 4.6, the more small-x data is included in the global PDF fit, the more unstable the global fit with NNLO DGLAP evolution becomes (without BFKL resummation effects). The fit only becomes stable when NNLx resummation effects are included together with DGLAP evolution (NNLO+NNLx). Such results likely point to BFKL evolution in the proton structure. Details of this analysis are described in Ref.(94). An objection that might be raised in studying BFKL evolution directly with studies of the proton structure function that a lot of the small-x data is also at very low $Q^2 \approx 3$ GeV^2. Therefore, it is less clear if we are in a region where the perturbative evolution is valid or not. This is a topic of debate within the community.

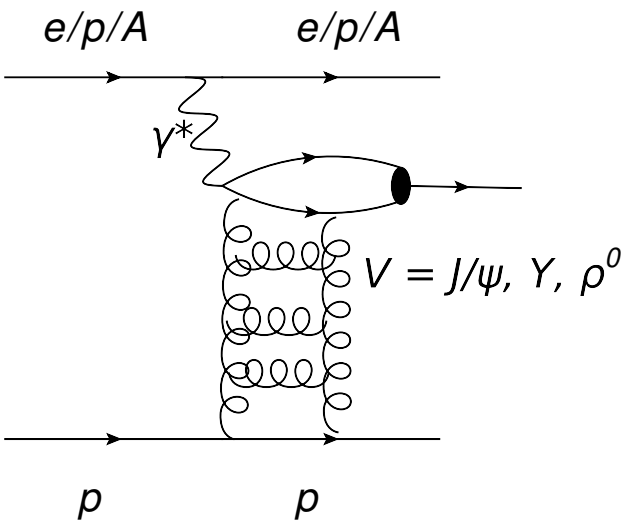

Figure 4.7: Exclusive vector meson production. A vector meson is produced by the interaction of $\gamma^* p \to V p$ via two-gluon exchange off the proton.

4.2.2 Exclusive vector meson production

Exclusive vector meson production, where the subprocess of interest is $\gamma^* p \to V p$, with $V = J/\psi, \Upsilon, \rho^0$, is expected to be very sensitive to the small-x gluon PDF. The process is shown in Fig. 4.7. A virtual photon emitted from an electrically charged particle (an electron, proton, or heavy-ion A) fluctuates into a quark-antiquark pair. This quark-antiquark pair is a color dipole that then interacts with the proton via t-channel two-gluon color-singlet exchange. The quark-antiquark pair forms a vector meson state, such as the J/ψ, Υ, or ρ^0 mesons, which can be analyzed by studying its decay in an experimentally clean decay channel (a pair of muons, for example). At LO in pQCD, the cross section is proportional to the square of the gluon densities $\sigma(\gamma^* p \to V p) \propto [xg(x, Q^2)]^2$, hence its sensitivity to small-x physics. The mass of the vector meson is large enough to justify the use of pQCD calculations.

These measurements were part of the HERA physics program (96; 97; 98; 99; 100; 101; 102; 103; 104), and have made a comeback at the CERN LHC with the advent of ultra-peripheral heavy-ion collisions, where the electromagnetic field created by a relativistic nucleus can be treated as a luminous source of quasi-real photons(105; 106; 107; 108; 109;

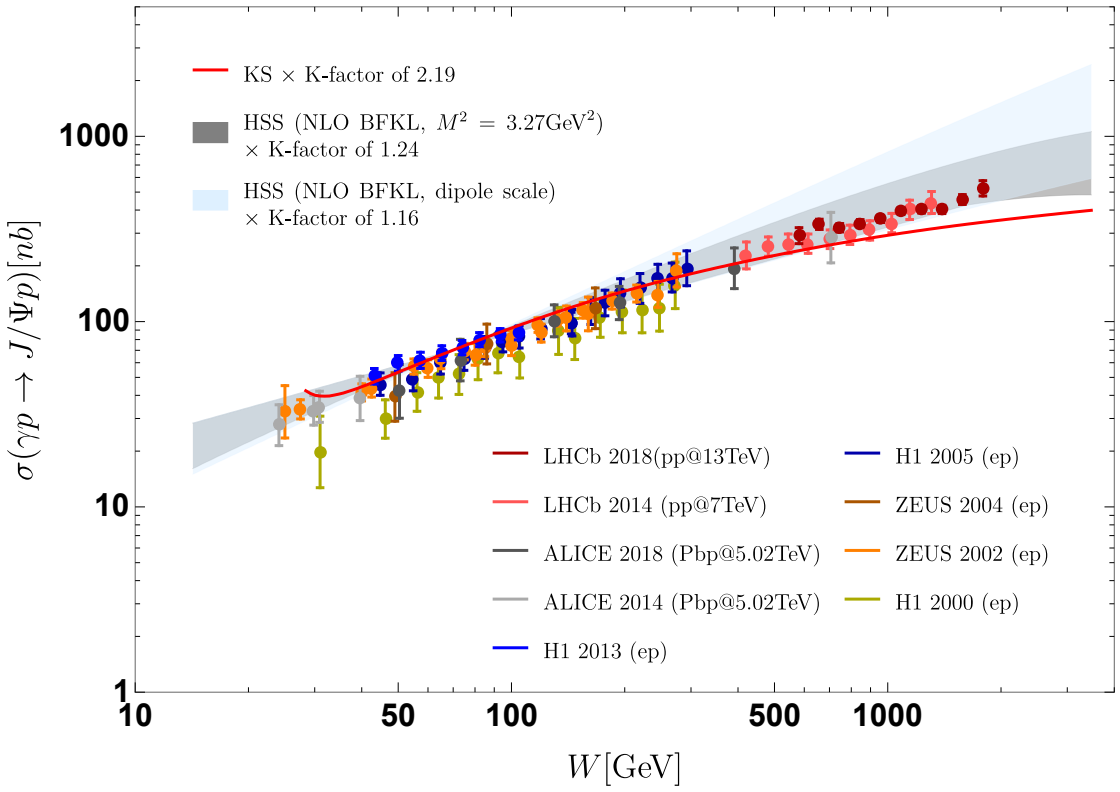

Figure 4.8: Photoproduction cross section $\sigma_{\gamma^* p \to J/\psi p}$, as a function of the photon-proton center-of-mass energy $W_{\gamma^* p}$. The data comes from different measurements by the H1, ZEUS, ALICE, and LHCb experiments. Predictions based on BFKL calculations are denoted by the shaded, grey curves. A prediction based on parton saturation is represented by the red line. The data points come from different collider setups (electron-proton, proton-proton, proton-lead) and experiments. Figure extracted from Ref. (95).

110; 111). The kinematic domain is extended to larger values of the center-of-mass energy of the $\gamma^* p$ system, denoted by $W_{\gamma p}$, which corresponds to lower values of x. Each of the LHC experiments covers different kinematic domains of the vector meson kinematics. The different species of vector mesons yield independent sets of probes of parton densities of the proton, as well as different effective sizes of the color dipoles that probe the proton. Calculations for exclusive vector meson production in the BFKL framework have been presented over the years. For recent examples of NLL BFKL calculations are presented in Refs. (112; 113; 95) An instance of the extracted measurements of J/ψ photoproduction cross section as a function of the mass of the photon-proton system compared with BFKL calculations at NLL accuracy is shown in Fig. 4.8. These calculations are consistent within the uncertainties with the data. Other approaches, based on parton saturation effects, are also consistent with the data. Further measurements at larger $W_{\gamma p}$ for different vector mesons will help draw a more coherent picture. These measurements will be very important to understand the gluon PDFs of nucleons and nuclei at small-x at the future EIC (86).

4.2.3 Forward jet

The onset of BFKL dynamics can be also be investigated in the production of very forward jets in electron-proton DIS. To probe the small-x regime of the proton structure function, the jets have to be produced in an opposite direction to the proton beam. The high p_T of the jets allows us to perform perturbative calculations. Such a measurement of very forward jets in DIS was carried out by H1 (115). A comparison of BFKL-based calculations at LL and NLL accuracy with the H1 measurement is presented in Fig. 4.9. For reference, predictions based on DGLAP evolution is shown in the same plot (114). As shown in Fig. 4.9, the BFKL-only approach is able to describe the double-differential cross section for smaller photon virtualities Q^2 and at lower jet p_T. The prediction based on NLO DGLAP calculations improve at larger photon virtualities Q^2 and larger jet p_T. Neither

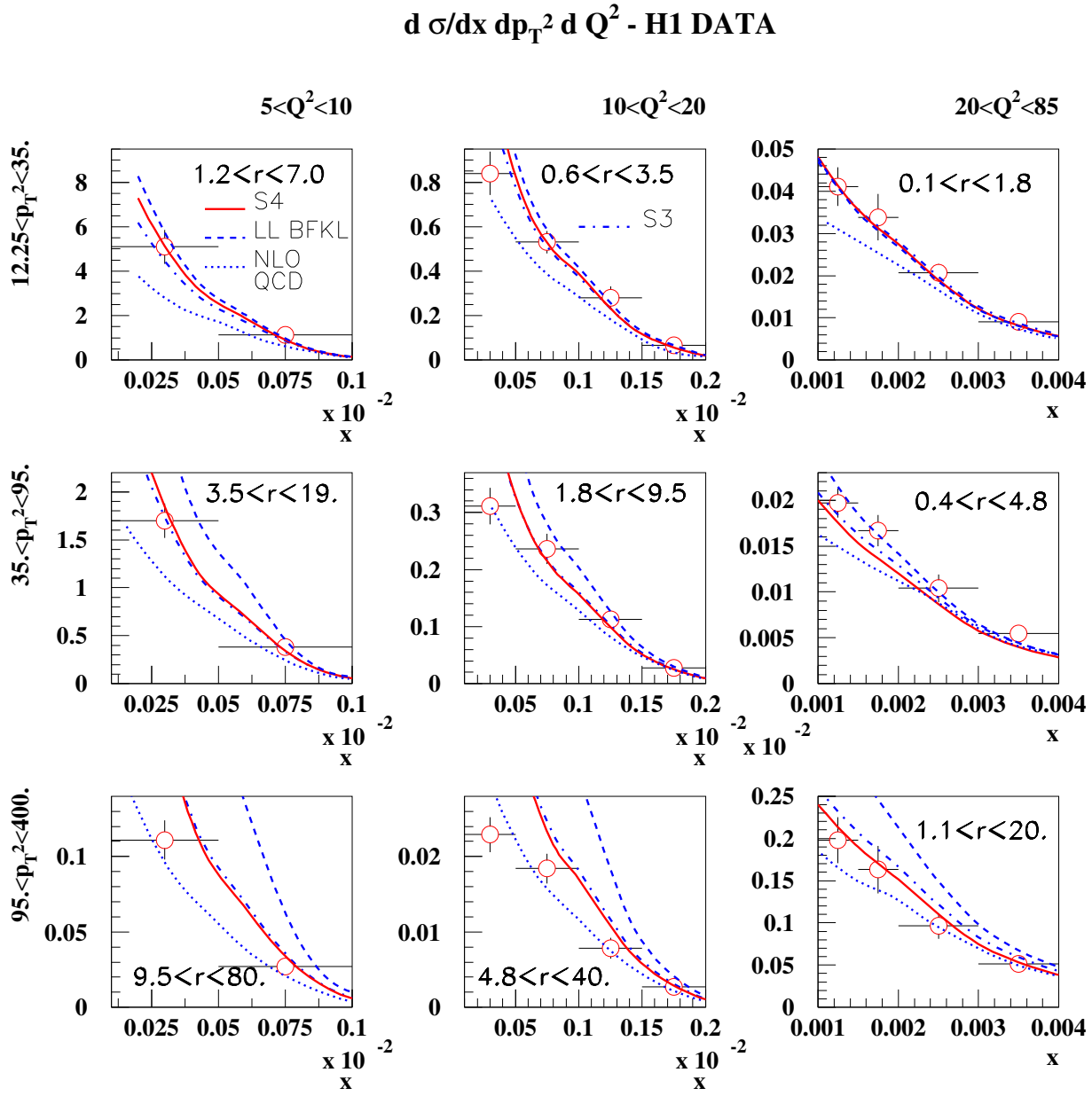

Figure 4.9: Very forward jet production in DIS. The dashed line represents the prediction from LL BFKL evolution. The *S*4 solid red line represents the prediction from NLL BFKL evolution with collinear resummation in the S4 scheme. The dotted line represents the expectation from DGLAP evolution at NLO. The open points are measurements from the H1 experiment. Figure extracted from Ref. (114).

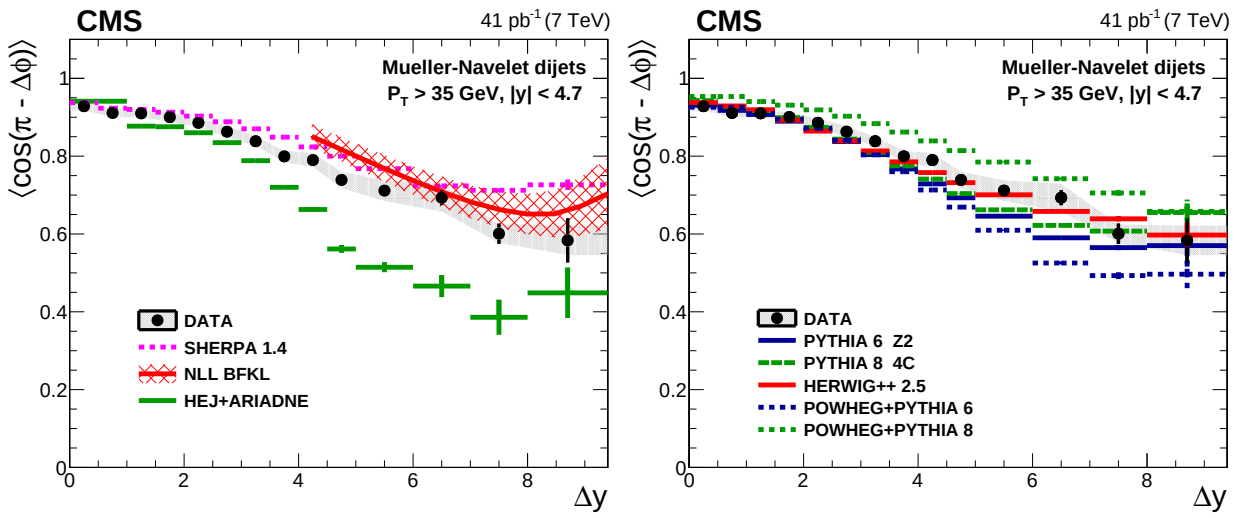

Figure 4.10: Average of cosine of the azimuthal angle difference between the outermost jets $\langle\cos(\pi-\Delta\phi)\rangle$ at $\sqrt{s}=7$ TeV presented as function of the rapidity difference between the two outermost jets by CMS. Predictions based on BFKL calculations at NLL accuracy are shown on the left panel (red curve with hashed band). DGLAP-based predictions are shown on the right panel. Figure extracted from Ref.(117).

approach on its own is able to describe all features of the data at the same time. Measurements like this will be crucial at the future EIC as well (86).

4.2.4 Mueller–Navelet jets

Events where the two outermost jets are separated by a large rapidity interval $\Delta y \equiv |y_{\text{jet1}} - y_{\text{jet2}}|$ are known as Mueller–Navelet jets (116). The process is inclusive, i.e., there is no requirement on other particle activity. At large Δy, decorrelations in the azimuthal angle between the two outermost jets $\Delta\phi_{\text{jj}}$ are expected to be present, caused by interjet radiation. These $\Delta\phi_{\text{jj}}$ decorrelations can be caused by parton emissions as described by DGLAP evolution, but they are not as strong as the ones described by parton splittings described by BFKL dynamics. This is because in BFKL dynamics the multiple parton emissions can have similar p_{T} as the two outermost jets, which can lead to significant decorrelations in $\Delta\phi_{\text{jj}}$ between the forward-backwardmost jets.

It has been expected that azimuthal angle decorrelations in Mueller–Navelet jets would

be a clean way of disentangling BFKL dynamics from DGLAP dynamics. The latest experimental investigation has been presented by the CMS experiment, with the measurement of average cosine moments of the azimuthal angle separation between the outermost two jets in pp collisions at $\sqrt{s} = 7$ TeV (117). The different Fourier coefficients, which are equal to the average cosines of the decorrelation angles, were measured as a function of Δy between the two jets, for example as in Fig. 4.10. Ratios of these Fourier coefficients as a function of Δy allowed for further tests of pQCD predictions. In this study, comparisons of the experimental results with LO and NLO Monte Carlo event generators where parton emissions are simulated following parton shower algorithms inspired in DGLAP evolution, were presented (PYTHIA6, PYTHIA8, HERWIG++, POWHEG+PYTHIA8, POWHEG +PYTHIA6). The DGLAP-based parton splittings are able to describe the $\Delta\phi$ correlations for a vast range in Δy, as illustrated in Fig. 4.10. The NLL BFKL calculations are able to describe the $\Delta\phi_{jj}$ decorrelations for large Δy. The ATLAS Collaboration presented a similar measurement as the one presented by CMS, except that they were looking for the two leading p_T jets (118).

Given these results by the CMS experiment, it is not possible to draw a strong conclusion on whether BFKL dynamics can be disentangled from other QCD effects in this kinematic regime with the observables based on the $\Delta\phi$ decorrelations. It is expected that similar studies at 13 TeV may help assess the differences better, since larger $\sqrt{s}$ favors pre-asymptotic effects of BFKL dynamics. Members of the theoretical community have come up with ideas to better isolate BFKL dynamics, which includes the use of asymmetric p_T cuts on the outermost jets in order to suppress possible instabilities in the predictions of fixed-order perturbation theory calculations. For example, for more asymmetric p_T dijet configurations, where the two forward jets have very different transverse momentum, it is expected that the collinear resummation approach (DGLAP-like) dominates the physical description of this process. The asymmetric cuts remove the sensitivity to other higher-order effects related to the resummation of so-called Sudakov logarithms. For

more symmetric p_{T} configurations, it is expected that the BFKL picture must work better. Parallel to these adjustements, it has been proposed to look into the radiation pattern between the Mueller–Navelet jets ("mini-jets")(119; 120). The BFKL-like radiation pattern should yield minijets with strong ordering in rapidity and with similar p_{T} between them. Perhaps an interesting measurement would be a combination of the $\Delta\phi$ and minijet observables. It has also been proposed to use tagged-hadrons, or to tag Higgs boson or Drell–Yan events in the forward region, instead of using the outermost jets (121; 122; 123). These probes can cover complementary sections of phase-space compared to the two jets case, and they can also remove angle decorrelation effects induced by parton shower and hadronization effects of the jets.

4.2.5 Hard color-singlet exchange in dijet production (Mueller–Tang jets)

This Subsection discusses the main process of interest targeted in Chapters 6 and 7 of this thesis: the hard color-singlet exchange process in dijet events. As seen in the previous Subsections, it is rather difficult to fully disentangle BFKL dynamical effects in the data, as there are always higher-order QCD effects that need to be taken into account. One way of looking for BFKL effects is in very "exclusive" processes. This may suppress these higher-order corrections, with the price of significantly reducing the cross section.

We can isolate the onset of BFKL dynamics in events where two jets are separated by a large rapidity gap –an interval in rapidity void of radiation– due to strongly interacting color-singlet exchange (124). In pQCD, the simplest color-singlet configuration requires at least two gluons exchanged in the t-channel, where the color charge of one of the gluons screens the color charge of the other. A single gluon t-channel exchange necessarily results in a net transfer of color charges, as shown in Fig. 4.11.

This process was first proposed and described by Mueller and Tang in the early 1990s (125) and after whom they are called "Mueller–Tang jets." The "jet-gap-jet" process has

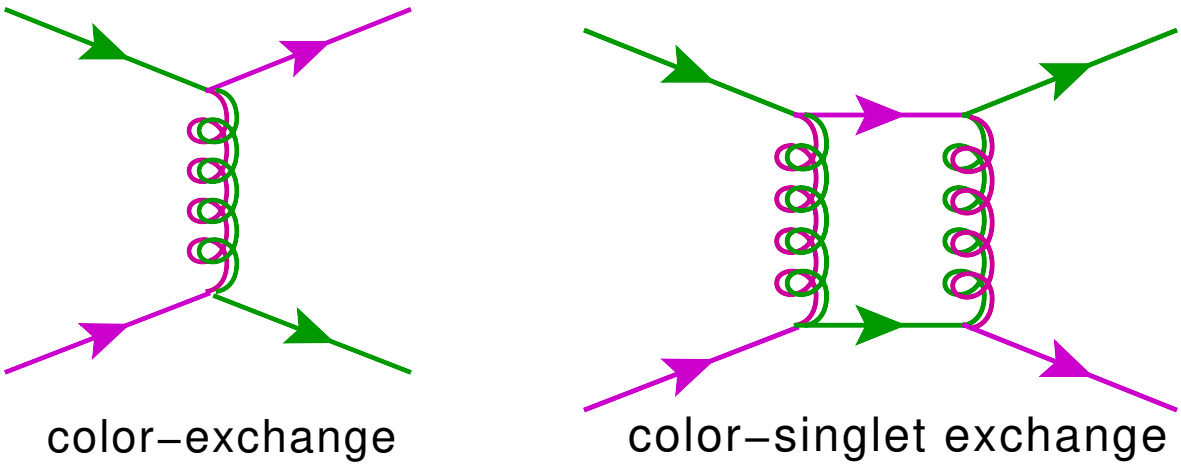

Figure 4.11: Schematic diagram of the color-flow for single-gluon t-channel exchange and two-gluon t-channel exchange. The two-gluon color-singlet exchange leaves the initial- and final-state quarks with the same colors. The single-gluon exchange "repaints" the quark color.

been further explored in phenomenology studies in Refs. (126; 127; 128; 129; 130; 131; 132). In the high-energy limit of QCD, the color-singlet exchange is described by the exchange of a reggeized two-gluon ladder exchange, known as BFKL pomeron or perturbative pomeron exchange. The schematic diagram of the process is shown in Fig. 4.12. The larger the pseudorapidity separation between the jets is, the closer we get to the expected onset of BFKL dynamics becomes since $\Delta\eta_{jj} \approx \ln(\hat{s}/|\hat{t}|)$ (in the limit where $m_j \ll p_T^{\text{jet}}$). In contrast, in most collisions that lead to dijet production, the net color charge exchange between partons results in final-state particle production over wide intervals of rapidity between the jets. An example of a color-exchange diagram is shown in Fig. 4.13 These are known as color-exchange dijet events, and they constitute the most common color-flow topology in dijet production. Dynamical effects predicted by the DGLAP evolution equations are largely suppressed in events with pseudorapidity gaps, since the predicted dijet production rate is strongly reduced by way of a Sudakov form factor (124; 133; 134; 135). This factor, which accounts for the probability of having no additional parton emissions between the hard partons, is not necessary for BFKL pomeron exchange (125).

The main observable of interest for the study of hard color-singlet exchange is the

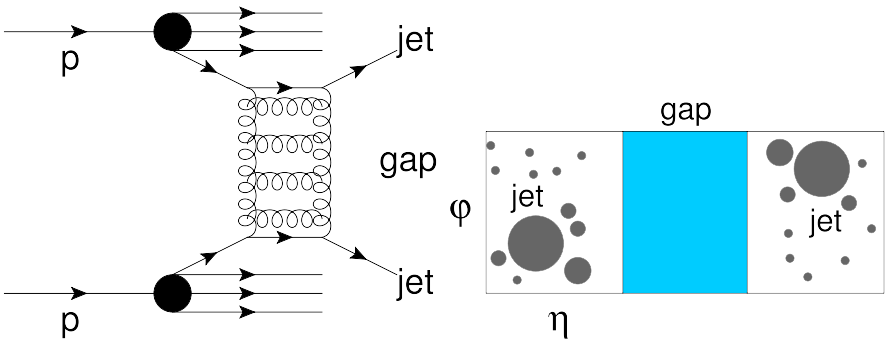

Figure 4.12: (Left) Schematic diagram of color-singlet exchange dijet event (jet-gap-jet). (Right) Particles produced in η–ϕ plane (the filled circles represent particles). The blue, shaded area is absent in particles (rapidity gap).

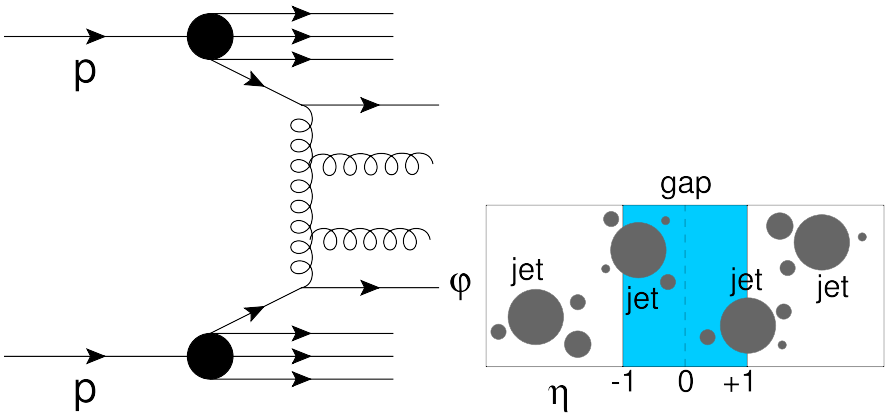

Figure 4.13: (Left) Schematic diagram of color-exchange dijet event. (Right) Particles produced in η–ϕ plane (the filled circles represent particles). The blue, shaded area represents an interval in η used to measure the particle multiplicity distribution.

fraction of dijet events produced by hard color-singlet exchange, f_{CSE}, also called gap fraction, which is defined by

$$f_{\text{CSE}} = \frac{N^{\text{CSE dijet}}}{N^{\text{all dijet}}} \tag{4.7}$$

where N are the number of dijet events produced by hard color-singlet exchange, and $N^{\text{all dijet}}$ is the number of all dijet events (dominated by color-exchange dijet production). The ratio has the advantage that correlated experimental and theoretical uncertainties cancel in the ratio, such as those that come from the calibration and reconstruction of the jets, or those coming from the parton densities of the proton or the dependence on the renormalization and factorization scales, for example. The fraction f_{CSE} can be extracted as a function of kinematic variables of interest, for example $\Delta\eta_{\text{jj}}$ between the jets.

Predictions on the f_{CSE} fraction that consider corrections at NLL accuracy in the BFKL framework and a sum over conformal spins have been computed in Refs. (128; 131; 129; 130; 136). These BFKL calculations for the hard color-singlet exchange process include partial corrections at NLO in α_s within the BFKL framework, namely those coming from the resummation of large logarithms of energy at NLL accuracy using LO impact factors. The impact factor tells us how the BFKL pomeron couples to the quark and gluon PDFs of the proton. These corrections have yet to be included in the BFKL theoretical calculations to complete the NLO phenomenology analysis of the jet-gap-jet process. Higher-order corrections to impact factors are known to have significant effects in the description of similar processes, such as Mueller–Navelet jets (137). Recently, major progress has been made in the calculation of NLO impact factors for the jet-gap-jet process (138; 139; 140). The convolution of these NLO impact factors and the NLL BFKL gluon Green function will yield the complete NLO calculation. At the time of writing this thesis, this is a topic of intense study by theorists, as discussed in Ref. (141).

Color-singlet exchange can occur in quark-quark ($qq \to qq$), quark-gluon ($qg \to qg$), and gluon-gluon ($gg \to gg$) scattering. The partonic cross section for $qq \to qq$ scattering in

terms of the scattering amplitude $\mathscr{A}(\Delta y, p_T^2)$ is given by

$$\frac{d\sigma^{qq\to qq}}{dp_T^2} = \frac{1}{16\pi}\left|\mathscr{A}^{qq}(\Delta y, p_T^2)\right|^2 \tag{4.8}$$

where $\mathscr{A}^{qq}(\Delta y, p_T^2)$ is the scattering amplitude calculable in pQCD. Δy and p_{T} are the rapidity difference between partons and the p_T of the struck parton. For t-channel two-gluon color-singlet exchange, the qg and gg and amplitudes are the same as the $qq \to qq$ ones, modulo global color factors:

$$|\mathscr{A}^{gg}(\Delta y, p_T^2)|^2 = \left(\frac{C_A}{C_F}\right)^2 |\mathscr{A}^{qg}(\Delta y, p_T^2)|^2 = \left(\frac{C_A}{C_F}\right)^4 |\mathscr{A}^{qq}(\Delta y, p_T^2)|^2 \tag{4.9}$$

where $C_F = 4/3$ and $C_A = 3$ are the Casimir factors of QCD. We see that $gg \to gg$ scattering is largely favored over $qg \to qg$ and $qq \to qq$ scattering by a factor of $9^2/4^2 \approx 5$ and $9^4/4^4 \approx 25$, respectively. This enhancement is observed already at parton-level, and is a consequence of the color structure of the two-gluon exchange. Even if the BFKL cross section has the same kinematic dependence regardless of the parton flavor, the color factors will play a significant role for the hadron-level observables that we extract experimentally. In particular, we should expect that there will be a strong competition of the behavior of the PDFs with the BFKL parton-level amplitudes when convolving them together to compute the hadron-level cross section, particularly the decrease of the gluon PDF at high-x.

The Mueller–Tang prescription is used to couple the BFKL gluon Green function to the (colored) quark and gluon densities of the proton (125). In the high-energy limit, the BFKL NLL amplitude can be expressed as an expansion in the basis of conformal eigenfunctions of the BFKL kernel, and reads

$$\mathscr{A}^{qq}(\Delta y, p_T^2) = \frac{16\pi\alpha_S^2(p_T^2)}{p_T^2} \sum_{p=-\infty}^{\infty} \int \frac{d\gamma}{2i\pi} \frac{[p^2-(\gamma-1/2)^2]\exp\left\{\bar{\alpha}(p_T^2)\chi_{\mathrm{eff}}[2p,\gamma,\bar{\alpha}(p_T^2)]\Delta y\right\}}{[(\gamma-1/2)^2-(p-1/2)^2][(\gamma-1/2)^2-(p+1/2)^2]} \tag{4.10}$$

where the complex integral is calculated along the imaginary axis from $1/2-i\infty$ to $1/2+i\infty$ and the sum is performed over even numbers p, where p is known as the "conformal spin." The strong coupling is included in the definition of $\bar{\alpha}(p_T^2) = \alpha_s(p_T^2)N_c/\pi$. The NLL BFKL effects are taken into account in the conformal eigenfunction with eigenvalue $\chi_{\text{eff}}(2p, \gamma, \bar{\alpha})$. This particular representation of the scattering amplitude was introduced in Ref. (130).

In addition to the short-distance physics mechanism for generating the rapidity gap between jets, there can be other soft-parton exchanges that could effectively destroy the gap between the jets that needs to be taken into account. The presence of soft rescattering effects between partons and the proton remnants modify the visible cross section of jet-gap-jet events. These soft interactions can induce the production of particles in the η interval that would otherwise be devoid of particles. This results in a reduction of the number of events identified as having a jet-gap-jet signature. This reduction is parametrized using a multiplicative factor known as the rapidity gap survival probability, $|\mathscr{S}|^2$. The survival probability is a process-dependent, non-perturbative quantity (124; 142; 143; 144; 145; 146) that is expected to have values of the order of $|\mathscr{S}|^2 = 1$–10% at LHC energies. This factor is often assumed to be largely independent of the dijet event kinematics (124), although some non-perturbative models, such as the soft color interactions (SCI) model (128; 131), suggest that this is not always the case. In particular, MPI can further reduce the survival probability in dijet events with a central gap, as discussed in Refs. (128; 131; 132).

4.2.6 Previous measurements of jet-gap-jet events

The jet-gap-jet process has been studied in electron-proton, proton-antiproton, and proton-proton collisions at the HERA, Tevatron, and LHC colliders. Generally speaking, to identify and characterize these jet-gap-jet events, one needs to have a clean sample of collision events with no "pileup" interactions, where the two jets are separated by an interval in η void of particle activity above the detector noise thresholds. This is an operational defini-

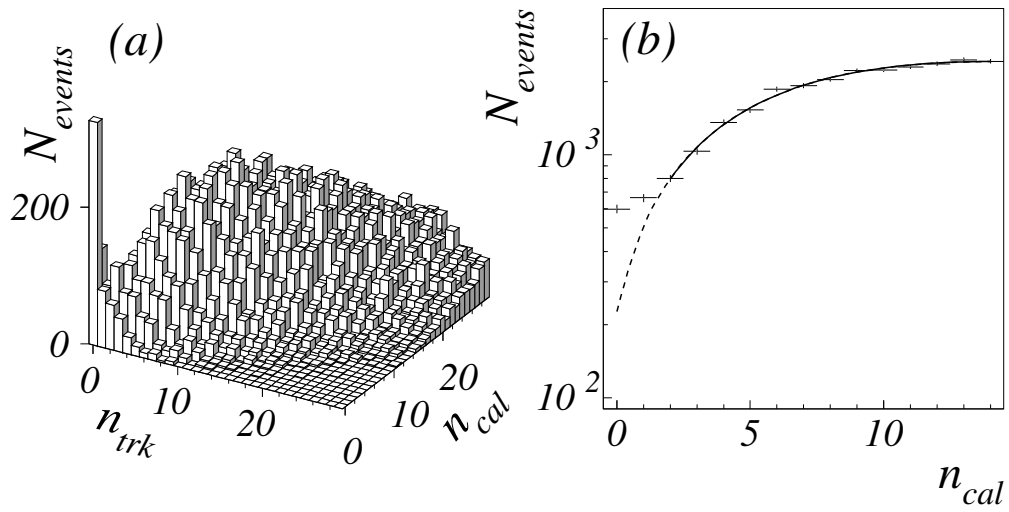

Figure 4.14: Left panel: number of calorimeter towers and charged-particle tracks with $E_T > 200$ MeV between the jets. Right panel: one-dimensional calorimeter tower multiplicity, with the color-exchange background estimated at $n_{cal} \approx 0$. Figure extracted from Ref. (147).

tion of the pseudorapidity gap that is directly implementable in an experimental context. Even after requiring this pseudorapidity gap, one needs to carefully model the color-exchange background. An example of the manifestation of color-singlet exchange events in the particle multiplicity distribution is shown in Fig. 4.14. The dashed line represents the expected contributions from color-exchange dijet events at low multiplicities. Assuming the modeling of the color-exchange background is done correctly, then the yields for color-singlet exchange can be extracted from the data.

An overview of previous measurements is laid down below:

- *H1 and ZEUS measurements:* The H1 and ZEUS experiments analyzed jet-gap-jet events in electron-proton DIS. The measurements used a "floating" gap approach (i.e., the rapidity gap depends on the η of the jets). They found gap fractions of about 7–10% for $140 < W_{\gamma p} < 280$ GeV using this technique (148; 149).

- *D0 measurements at* $\sqrt{s} = 0.63$ *and* 1.8 *TeV: (147)* D0 defined the rapidity gap between jets as the absence of calorimeter towers in $|\eta| < 1$ with transverse energies $E_T > 200$ MeV. The jets were clustered with the cone algorithm with a cone radius $R = 0.7$.

The pseudorapidity of each of the leading two jets was required to be $|\eta_{\text{jet1,2}}| > 1.9$ with $\eta_{\text{jet 1}}\eta_{\text{jet 2}} < 0$. The study at 1.8 TeV was divided in three subsamples: low-$E_{\text{T}} = 15 - 25$ GeV, medium-$E_{\text{T}} = 25 - 30$ GeV and high-$E_{\text{T}} > 30$ GeV.

- *CDF measurement at $\sqrt{s} = 0.63$ TeV (150)* CDF relied on the charged particle tracks in $|\eta| < 1$ with transverse energies $E_{\text{T}} > 300$ MeV. The jets were clustered with the cone algorithm with a cone radius $R = 0.7$. The pseudorapidity of the leading two jets was required to be $|\eta_{\text{jet1,2}}| > 1.8$ with $\eta_{\text{jet 1}}\eta_{\text{jet 2}} < 0$.

- *CDF measurement at $\sqrt{s} = 1.8$ TeV: (151)* Sample of events with two jets of $E_{\text{T}}^{jet} > 20$ GeV each, pseudorapidity in the range $1.8 < |\eta^{\text{jet1,2}}| < 3.5$ and $\eta_{\text{jet 1}}\eta_{\text{jet 2}} < 0$. The measurement relied on the N_{tracks} in the region $|\eta| < 1$ with energies $E_{\text{T}} > 300$ MeV.

- *CMS measurement at $\sqrt{s} = 7$ TeV (152) :* The measurement by CMS at 7 TeV was performed in three bins in $p_{\text{T, jet 2}} = 40 - 60$ GeV, $60 - 100$ GeV and $100 - 200$ GeV. The jets were clustered with the anti-k_{t} algorithm with a distance parameter of $R = 0.5$. The pseudorapidity of each of the leading two jets was of $|\eta_{\text{jet 1,2}}| > 1.5$ units with $\eta_{\text{jet 1}}\eta_{\text{jet 2}} < 0$. The measurement of f_{CSE} as a function of $\Delta\eta_{jj}$ was performed in three bins of $\Delta\eta_{\text{jj}} = 3$–$4$, 4–5, 5–7 units in pseudorapidity for each bin of $p_{\text{T, jet2}}$.

The aforementioned measurements have demonstrated that there is a non-negligible contribution of hard color-singlet exchange dijet events in the data, which represents about $0.5 - 1\%$ of the inclusive dijet cross section for the configuration of forward-backward jets. It is well-known that the t-channel exchange of electroweak gauge bosons between quarks is not able to explain the observed rates of jet-gap-jet events. The simple two-gluon color-singlet exchange of QCD, while it has a larger production cross section than the single-electroweak boson exchange between quarks, it is not able to explain the observed rates either. In principle, such a contribution should be describable in terms of pQCD calculations, given the presence of a hard energy scale by the p_{T} of the jets. The natural candidate is BFKL pomeron exchange, which, due to the additional contributions

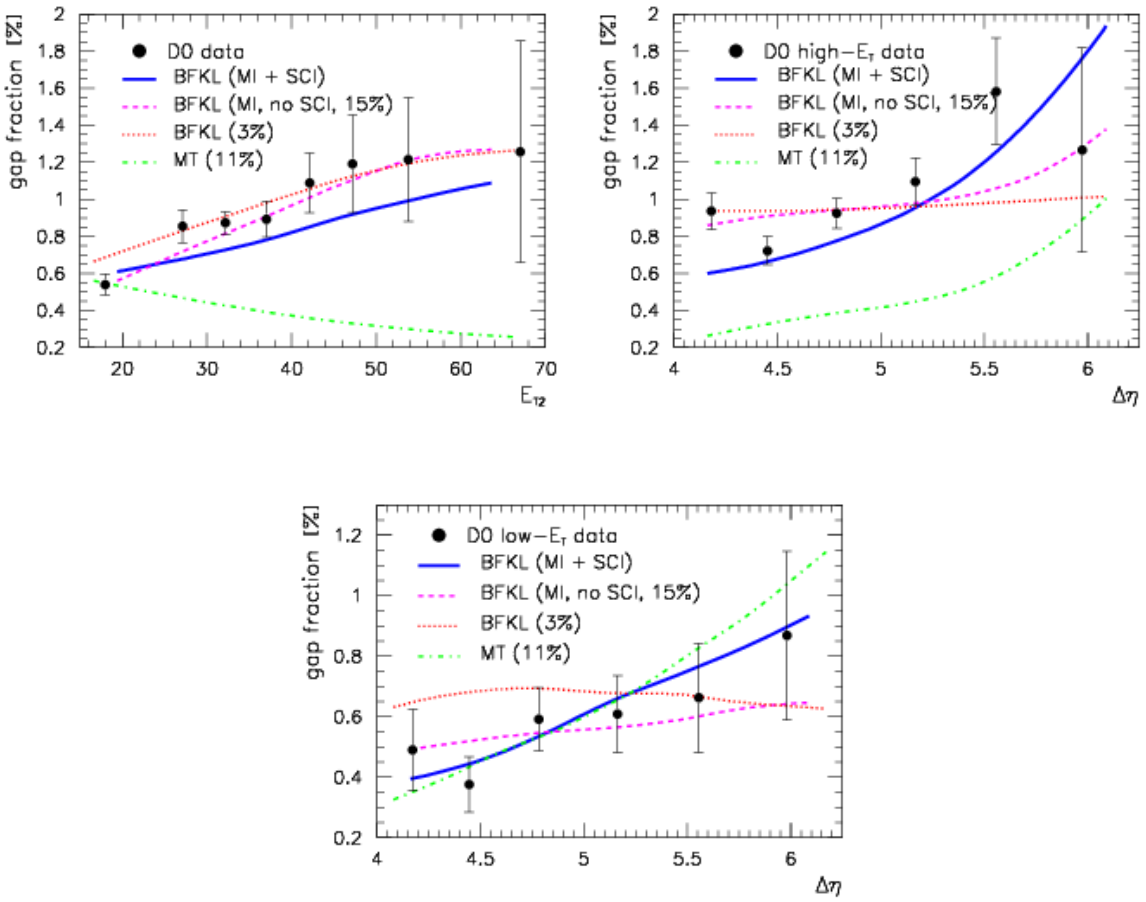

Figure 4.15: Gap fraction as a function of the pseudorapidity difference $\Delta\eta$ by the DØ experiment and compared to predictions by Enberg–Ingelman–Motyka based on BFKL calculations. The soft-color interaction model is used to dynamically simulate soft-rescattering effects, as well as multiparton interactions, and a uniform soft-survival probability factor of 3%. Figure extracted from Ref. (128).

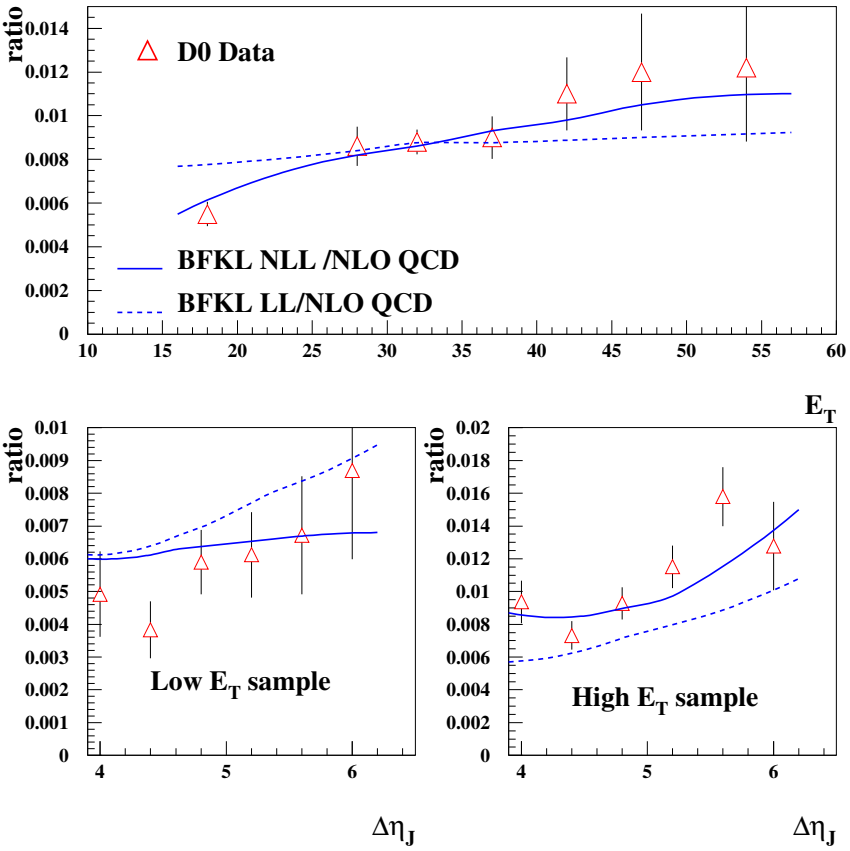

Figure 4.16: Predictions of Royon–Kepka–Marquet (RMK) based on BFKL calculations at LL (dotted) and NLL (solid) accuracy compared with published jet-gap-jet results from the D0 Collaboration. The figures are extracted from Ref. (130).

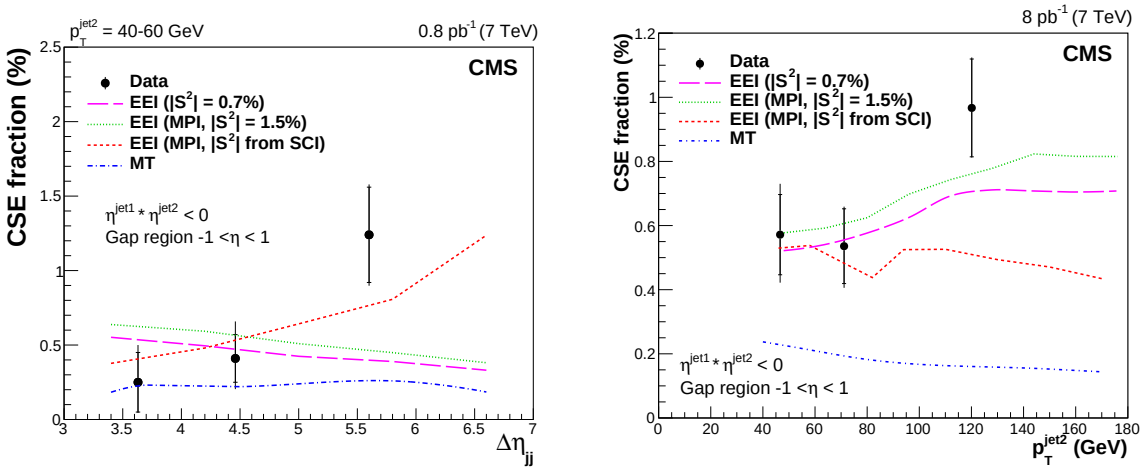

Figure 4.17: Measurement of the color-singlet exchange fraction f_{CSE} as a function of the $\Delta\eta_{jj}$ between the jets (left), and of the second-leading jet p_T (right) at $\sqrt{s} = 7$ TeV by the CMS Collaboration. Predictions of Ekstedt–Enberg–Ingelman (EEI) against the $\sqrt{s} = 7$ TeV data of CMS are plotted. The figures are extracted from Ref. (152).

from higher-order corrections in the gluon ladder diagram, yields a cross section that is more compatible with the observed jet-gap-jet rates. The observed rate is not inconsistent with the BFKL pomeron exchange expectations, but it is not clear if it is possible to describe the whole differentially process just with the pQCD calculation. Examples of previous attempts to describe the observed color-singlet exchange rate relative to the inclusive dijet production rate are shown in Figs. 4.15, 4.16 and 4.17.

Previous measurements are statistically limited, which unfortunately complicates the comparison of pQCD calculations for the hard color-singlet exchange against the data. Moreover, previous measurements only reach $\Delta\eta$ values of up to about 6.5 units. The onset of BFKL dynamics is expected to appear at larger $\Delta\eta_{jj}$ separations. With the CMS detector acceptance, the largest possible separation we can have between the jets is of 9.4 units. These forward-backward configurations are more easily accessible by increasing the collision energy of the protons. With these motivations in mind, in Chapter 6 of this thesis we address the measurement of jet-gap-jet events at $\sqrt{s} = 13$ TeV with the CMS experiment.

A particular caveat of the jet-gap-jet process is the possible kinematic-dependence of

the survival probability, which may hinder the interpretation of the hard color-singlet exchange process in terms of pQCD calculations. These soft rescattering effects can be suppressed in processes where one or both of the colliding protons remain intact after the interaction, such as in single- or central-diffractive dijet processes. Such hard diffractive processes will be described more in detail in the upcoming Section 4.3. Reactions with intact protons can be used to better separate events with a central gap between the jets, as discussed in Ref. (153). Jet-gap-jet events produced in double-pomeron exchange (effectively a three rapidity gap topology) should theoretically be absent of soft parton exchanges from the remnants of the collision. The gap fraction expected for this topology can in principle be large, as shown in Fig. 4.18. The price to pay is that the cross section is reduced due to the requirement of two intact protons in the final state and a rapidity gap between the jets. Hence, parallel to the study of jet-gap-jet events in inclusive dijet production described in Chapter 6, a study of jet-gap-jet events with at least one intact proton is also presented. This diffractive event topology has not been previously measured. Although no forward rapidity gap is required in the analysis, these events are referred to as "proton-gap-jet-gap-jet" throughout the thesis, where the forward rapidity gap signature is inferred from the detection of the intact proton. This part of the analysis uses a subset of CMS dijet events that, in addition, have intact protons detected with the forward proton spectrometers of the TOTEM experiment (154). The corresponding data analysis is presented in Chapter 7.

4.3 Hard diffraction

Typically, in standard proton-proton collisions, we think of single parton exchanges off each proton. These partons then interact to produce a physical system with a characteristic hard energy scale. For example, in Drell–Yan production, we consider (at LO in α_s) the $q\bar{q} \to Z/\gamma^* \to \ell^+\ell^-$ channel, where the quark is probed from one of the protons and the antiquark from the other proton. For a given hard process, the bulk of its cross section

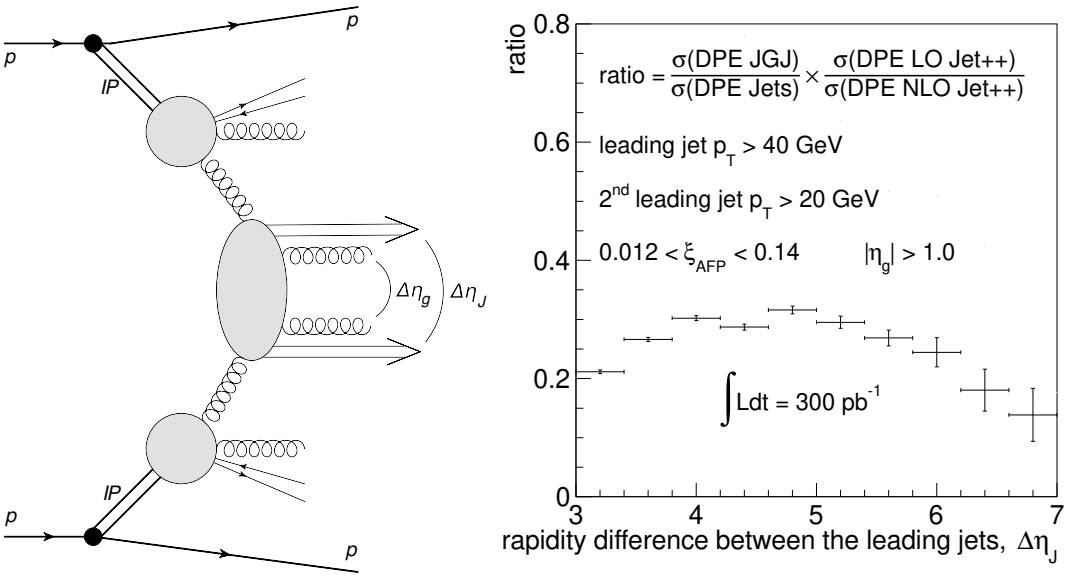

Figure 4.18: Expected fraction of jet-gap-jet events in double-pomeron exchange dijet events as a function of the separation in η between the jets. Figure extracted from Ref. (153).

comes from processes of the type $pp \to XY$, where X is a hard-scale system and Y is the associated hadrons, which include the destroyed protons.

However, this is not the only way of having a hard scattering process in a proton-proton or electron-proton collision. There can be cases where multiple partons (mostly gluons) are exchanged in a color-singlet configuration in the same collision. At LO in pQCD, this would correspond to t-channel two-gluon exchange in a color-singlet configuration. In fact, we have seen an example for this in the discussion of exclusive vector meson production in the previous Section. This can be generalized for numerous other processes, where the color-singlet exchange might have a more complicated composition. Interactions with strongly interacting color-singlet exchange off the proton with a hard-scale process are known as *hard diffractive* reactions. Due to the color-singlet exchange, a forward rapidity gap signature is observed in the detector. This is because, since there is no net color flow, there is no hadron production due to the breakup of a color-string connecting the colored systems. This is contrast to processes with single parton exchanges off the hadron, where the rapidity gap is exponentially suppressed with the gap width.

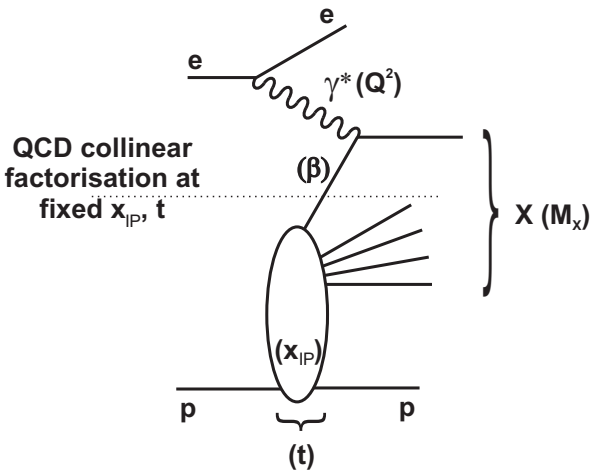

Figure 4.19: Schematic diagram of diffractive DIS in electron-proton collisions. A color-singlet exchange carrying a fraction of beam momentum $x_{\mathbb{P}}$. The amount of four-momentum transfer square at the proton vertex is $t = (p_f - p_i)^2$. The color-singlet object is probed by the virtual photon in a deep-inelastic reaction. Figure extracted from Ref. (155).

In the context of QCD, diffraction is synonymous with rapidity gaps and with strongly interacting color-singlet exchanges. The dominant exchange is hard pomeron exchange.

Hard diffraction is very interesting from the physics point of view, since it can be used to learn more about the structure of hadrons in a way that it complements the "standard" hard scattering processes (i.e., single-parton exchange off the hadron). Indeed, one can imagine that by "plucking" two colored partons in a color-singlet state at a given hard energy scale, we are probing how spatially correlated these particles are inside the colliding hadron. It can thus give us information on how "lumpy" or how "diffused" the profile of gluons is for a given hadron at a given collision energy and at a given virtuality. The future EIC has foreseen a comprehensive program of diffractive physics in electron-ion collisions (86).

In the 1980s, Gunnar Ingelman and Peter Schlein predicted that we might be able to observe hard scattering processes where the proton exchanges a color-singlet object with its own partonic structure (156). In this case, one could have the production of a hard scale system and an outgoing proton with a rapidity gap between the proton and the hard system. The production of hard dijets were observed thereafter at the Sp$\bar{\text{p}}$S by the

UA8 experiment (157). This was the first time a Roman pot was used to trigger a central collider experiment. A very clean signal for jets in diffractive dissociation was observed after the first year of data-taking. This striking signature consisted of the production of jets in association with forward intact protons in the final state. At the time, it did not receive much attention by the particle physics community. This changed however, when the phenomenon of hard diffraction was observed at HERA in electron-proton collisions in the early 1990s. It was observed that a significant fraction of DIS events (about 10% of the DIS events) yielded a forward rapidity gap in the direction of the incoming proton beam with an electron scattering with large momentum transfers $-q^2$ (large photon virtualities Q^2). In some cases, there would not be even remnants of the proton observed in the forward calorimeter, as it was almost always the case for "standard" DIS events. This came as a big surprise to experimentalists and theorists at the time, and it essentially started the field of hard diffraction in the 1990s. In such cases, the colliding proton remain completely intact. A diagram of diffractive DIS is shown in Fig. 4.19. The Roman pot detectors were used to measure such intact protons. Hence, diffractive DIS can be symbolically represented as $ep \to eXp$, in contrast to the standard DIS $ep \to eX$. It was observed that the dependence on Q^2 exhibited weak logarithmic evolution wiht Q^2 as those previously observed for the F_2 structure function of the proton. This also confirmed that the phenomenon did not have to do with higher-twist effects (i.e., non-perturbative). An event display of the H1 experiment of one of these striking electron-proton diffractive interactions is shown in Fig. 4.20.

Similar to the factorization theorem of QCD for single-parton exchanges in Chapter 3, it was demonstrated that a factorization theorem holds as well for hard diffraction (158). Such a factorization theorem was formally demonstrated for diffractive DIS, but not for diffractive hadron-hadron scattering. The QCD factorization theorem for hard diffractive requires the introduction of a *diffractive structure function* of the proton, which is extracted mostly from DIS data. The diffractive structure function can be used to fit a set of diffrac-

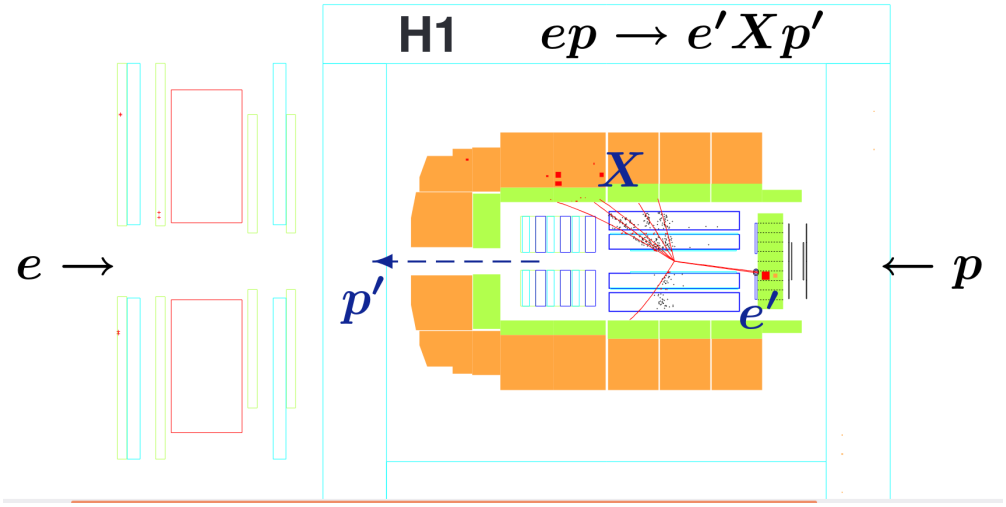

Figure 4.20: Event display of a diffractive DIS event recorded by the H1 experiment. There is no hadronic activity registered in the detector in a wide angular region in the direction of the outgoing proton, unlike standard DIS interactions.

tive PDFs with global fit analyses, analogous to the way we fit the conventional PDFs of the proton. The claim is then that we should be able to use these universal "diffractive PDFs" to predict the production rates for a number of processes. Hard diffraction requires the introduction of two additional kinematic variables to describe the color-singlet exchange off the proton. Typically, we use the fraction of momentum loss of the proton, denoted by the symbol ξ at the Tevatron and at the LHC and denoted with $x_{\mathbb{P}}$ at HERA, and the four-momentum transfer square at the proton vertex, $t = (p_f - p_i)^2$, where p_f and p_i are the final- and initial proton four-momenta. The values of t are typically close to the non-perturbative regime.

Let us analyze the phenomenon of hard diffraction in the context of DIS. One can express the diffractive DIS multi-differential cross section in analogy to the standard DIS cross section presented in Chapter 2, by introducing a diffractive structure function of the proton $F_2^D(x, Q^2, x_{\mathbb{P}}, t)$,

$$\frac{d\sigma}{dx dQ^2 dx_{\mathbb{P}} dt} = \frac{4\pi\alpha_{\text{em}}^2}{xQ^4}\left(1 - y + \frac{y^2}{2}\right)F_2^D(x, Q^2, x_{\mathbb{P}}, t) \tag{4.11}$$

the variables y, x, Q^2 are the standard DIS variables used in Chapter 2, and $\alpha_{\text{em}} =$

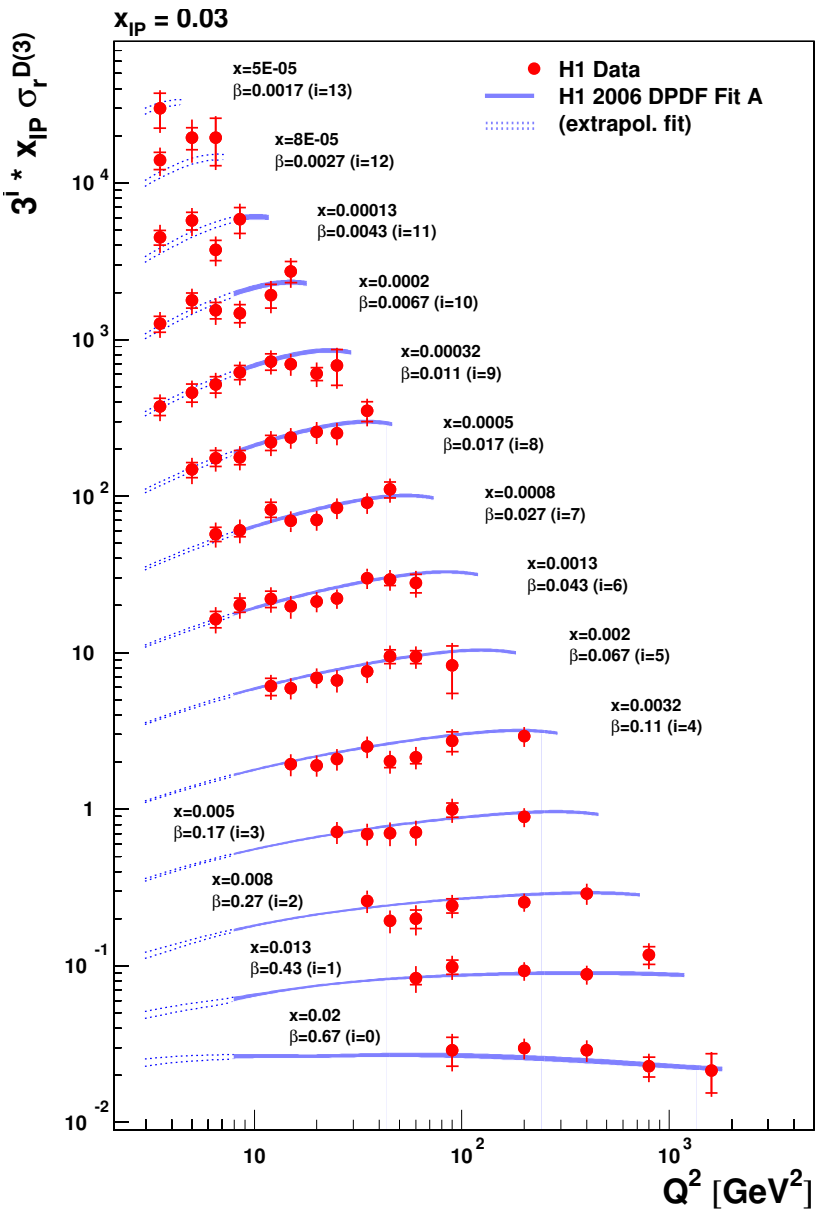

Figure 4.21: The β and Q^2 dependences of the diffractive reduced cross section σ_r multiplied by $x_{\mathbb{P}}$ at $x_{\mathbb{P}} = 0.03$ (shown in the vertical axis). The inner and outer error bars on the data points represent the statistical and total uncertainties, respectively. The data are compared with the reduced cross section at $E_p = 820$ GeV derived from the results of 'H1 2006 dPDF Fit A'. The different curves are artificially displaced by powers of 3^i, for $i = 4, 5, 6, \ldots, 13$. Figure extracted in Ref. (155).

$e^2/4\pi \approx 1/137$. One can go a step further, and assume that hard diffraction is a two-step process. In this picture, the pomeron is emitted off the proton with a given value of $x_{\mathbb{P}}$ and t, and then the parton densities of the pomeron are probed at a given value of $\beta = x/x_{\mathbb{P}}$ and Q^2 for the hard scattering process. This means that we can factorize F_2^D,

$$F_2^D(x, Q^2, x_{\mathbb{P}}, t) = f_{\mathbb{P}/p}(x_{\mathbb{P}}, t) F_2^{\mathbb{P}}(\beta, Q^2) \tag{4.12}$$

this is known as Regge factorization. The quantity $f_{\mathbb{P}/p}$ is known as the pomeron flux, $F_2^{\mathbb{P}}$ is the structure function of the pomeron, and $\beta = x/x_{\mathbb{P}}$ is the parton momentum fraction relative to the pomeron. The variable β plays the role of Bjorken-x, after adjusting for the "beam-energy" carried by the pomeron. This way, one can separate the component $F_2^{\mathbb{P}}$ of the structure function that is expected to obey DGLAP evolution. One can then perform a global fit of diffractive DIS data, analogous to the DIS analysis presented in Chapter 2. In Fig. 4.21, the results for the reduced cross section (which is related to $F_2^{\mathbb{P}}$) measured by the H1 experiment as a function of β, integrated over t and the mass of the diffractive system m_Y, at a fixed $x_{\mathbb{P}} = 0.03$ value are shown. The pomeron is seen as having its own partonic structure. In diffractive DIS, the pomeron is emitted from the proton, which may survive, and the DIS process probes the pomeron structure.

The pomeron flux can be parametrized with the guidance of Regge theory,

$$f_{\mathbb{P}/p}(\xi, t) = A_{\mathbb{P}} \frac{e^{Bt}}{\xi^{2\alpha_{\mathbb{P}}(t)-1}}, \tag{4.13}$$

where $\alpha_{\mathbb{P}}$ is known as the pomeron trajectory, B is the slope parameter, and $A_{\mathbb{P}}$ is a normalization parameter. In the assumption that the hard pomeron has a partonic structure that evolves with Q^2 with DGLAP evolution, one can use the same universal parton splitting functions of DGLAP in performing these global fits. A result of these global fits to diffractive DIS data is shown in Fig. 4.21. The resulting parton distribution functions are shown in Fig. 4.22. About 70% of the momentum of the pomeron is carried by the gluon

PDFs, whereas the gluon PDFs correspond to about 50% of the proton momentum. This is consistent with the pQCD picture of the pomeron being composed of mostly gluons.

Hints of possible factorization breaking in diffractive dijet production were observed by the H1 experiment (159; 160) by comparing the NLO QCD calculations with the data, which were off by a factor of about 0.6. The ZEUS experiment did not see quite the same suppression (161; 162). This tension between H1 and ZEUS remains an open problem in the field of diffraction, since factorization is expected to hold to a large extent in diffractive DIS (158). A possible explanation (for which there is still some contention) is that the virtual photon emitted off the electron might develop a hadronic structure large enough to act as an effective hadron-hadron diffractive scattering process.

Assuming that the QCD factorization theorem is valid for hard diffractive hadron-hadron interactions, and that the diffractive PDFs are indeed universal quantities, the hadron-level cross section for single-diffractive scattering can be written as

$$\frac{d\sigma}{d\xi dt} = \sum_{i,j} \int d\beta dx f_{\mathbb{P}/p}(\xi,t) f_{i/\mathbb{P}}(\beta,\mu_F) f_{j/p}(x,\mu_F) d\hat{\sigma}(x,\beta,\mu_R) + \mathcal{O}(\Lambda^2_{\mathrm{QCD}}/Q^2), \qquad (4.14)$$

where the sum is over all parton flavors. The variable x is the parton momentum fraction relative to the proton momentum for the proton that breaks up. The quantities μ_F and μ_R are the factorization and renormalization scales, respectively. The function $f_{j/p}(x,\mu_R)$ is the PDF of the proton that breaks up, such as those introduced in Chapter 2. The quantity $\hat{\sigma}(x,\beta,\mu_R)$ is the parton-level cross section calculable with pQCD techniques. The diffractive PDFs and pomeron flux factors are extracted from HERA data using the global fits mentioned a few paragraphs before, on the grounds that we suspect that they must be universal quantities. The expression for the hadron-level cross section is valid up to power corrections $\mathcal{O}(\Lambda^2_{\mathrm{QCD}}/Q^2)$.

Factorization breaking is expected to take place in diffractive hadron-hadron scatter-

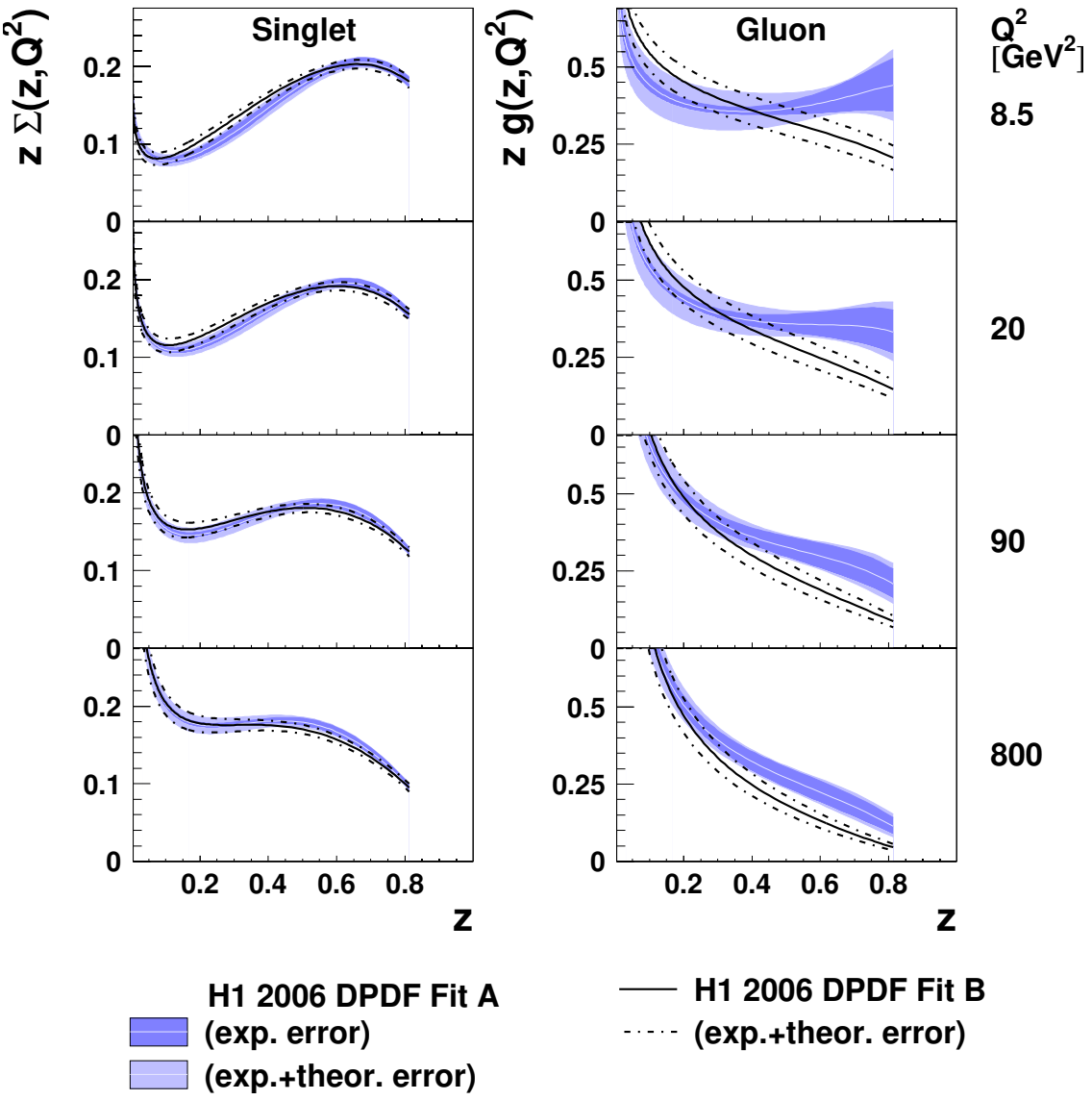

Figure 4.22: Extracted quark singlet ($z\Sigma(z,Q^2)$) and gluon ($zg(z,Q^2)$) PDFs ("of the pomeron") obtained from an NLO DGLAP fit to H1 diffractive DIS data. From the upper to lower panels, we have an increasing virtuality Q^2. Figure extracted from Ref. (155).

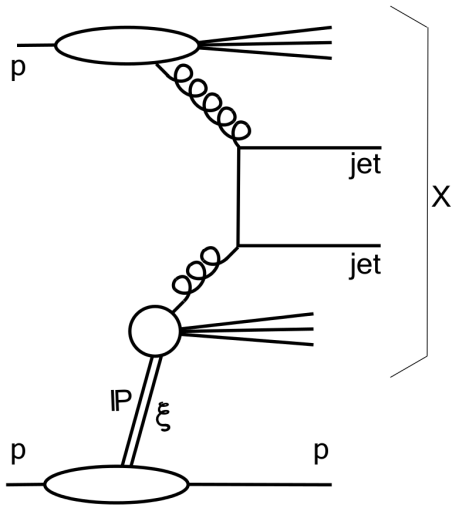

Figure 4.23: Hard diffractive dijet production with an intact proton. The hadronic system X consists of two hard jets and the proton and pomeron remnants in this diagram. The pomeron exchange carries a fraction ξ of the proton momentum, with a finite amount of four-momentum transfer t at the proton vertex.

ing, since the theoretical arguments used to derive the factorization theorem of diffractive DIS do not necessarily hold for diffractive hadron-hadron scattering(163). As it will be discussed more in detail later on, this was indeed observed by the CDF Collaboration. In diffractive hadron-hadron scattering, one needs to account for survival probability effects, which are related to the additional exchanges of low momentum transfer partons that may affect the likelihood that the rapidity gap or the proton remain intact. Similar survival probability effects were introduced before in the jet-gap-jet discussion in Section 4.2.5.

There are numerous questions on hard diffraction that remain to be explored. The HERA experiments gave us insight into some of the properties of hard diffraction, which continue to be investigated and understood years after the HERA physics program ended. At the future EIC, the phenomenon of diffraction will be investigated as well. We can obtain very valuable information about the gluonic structure of nucleons and nuclei in

diffractive interactions. In addition to the HERA experiments, we can analyze the phenomenon of hard diffraction in hadron-hadron collisions. Indeed, the Tevatron and the LHC experiments are equipped with detection technology to continue this path of study.

Some of the open problems and questions in hard diffraction to be investigated include:

- Is the color-singlet object from diffractive DIS the same as the color-singlet object in diffractive reactions at the Tevatron and at the LHC? If not, what are their differences? Is there a connection between them? Is the pomeron exchange in hard diffraction universal?

- Does the diffractive structure function of the proton obey DGLAP evolution? That is, to what extent can we treat the partonic structure of the pomeron the same way as that of the proton? Is it possible to have a picture based purely on quarks and gluons to explain hard diffraction?

- Is there a breakdown of Regge factorization at large ξ (large $x_{\mathbb{P}}$)? In other words, how well does the factorization of a pomeron flux and the diffractive PDFs hold up? There might be a point where $f_{\mathbb{P}/p}(x_{\mathbb{P}}, t)F_2^{\mathbb{P}}(\beta, Q^2) \to F_2^D(x, Q^2, x_{\mathbb{P}}, t)$.

- What is the behavior of the survival probability as a function of $\sqrt{s}$? Is it the same behavior as for other diffractive processes with a hard scale?

- What is the dependence of the t-slope parameter with other kinematic variables? For example, with the characteristic energy scale Q^2. This can give important input into the gluon distribution in configuration space.

Moving on from the HERA discussion, we now continue to contextualize hard diffraction at the Tevatron and at the LHC. In principle, the pomeron exchange in presence of a hard scale can be used to understand hard diffraction. The Tevatron experiments investigated the diffractive production of W and Z bosons, jets, and $b\bar{b}$. They found these

processes contribute to about 1% of the inclusive cross section, much smaller than the 10% rate observed at HERA. This is because of the aforementioned survival probability effects that reduce the "visible" cross section for hard diffractive processes. In the CDF experiment, the suppression factor was investigated in detail by comparing the rates of single diffractive and inclusive events at a center-of-mass energy of 1.8 TeV.

These probes give insight to different regions of x and Q^2 of the diffractive structure function and different information in terms of the quark flavor content of the pomeron. They also test the universality of the pomeron exchange. In this thesis, we focus mostly on diffractive dijet production $pp \to pJJX$. At the Tevatron, numerous studies of diffractive dijet production were conducted, both with the rapidity gap method and by tagging the intact antiprotons. The advantage of the rapidity gap method is that one has a direct signature of the diffractive process in the central detector. The disadvantage is that this method only gives access to very low ξ ($x_{\mathbb{P}}$), and we lose information on t since we do not detect the scattered proton. For exclusive vector meson production, t can be estimated by studying the p_T of the reconstructed vector meson.

The CDF Collaboration conducted a series of measurements that focused on the ratio $R(x,\xi,t)$ of single-diffractive and inclusive dijet cross sections, $\sigma_{jj}^{pX}(x,Q^2,\xi,t)$ and $\sigma_{jj}(x,Q^2)$. The interesting feature about this ratio of cross sections is that, at LO in α_s, it is proportional to the ratio of the corresponding structure functions, i.e:

$$R(x,Q^2,\xi,t) = \frac{\sigma_{jj}^{pX}(x,Q^2,\xi,t)}{\sigma_{jj}(x,Q^2)} \approx \frac{F_{jj}^{pX}(x,Q^2,\xi,t)}{F_{jj}(x,Q^2)}. \tag{4.15}$$

where F_{jj} and $F_{jj}^{pX}(x,Q^2,\xi,t)$ are the effective standard and diffractive structure functions probed with the dijet system, respectively. Such a ratio also leads to cancellations of correlated experimental and theoretical uncertainties for the numerator and denominator quantities. Note that, in the assumption that both the diffractive and standard PDFs obey DGLAP evolution, the ratio $R(x,Q^2,\xi,t) \to R(x,\xi,t)$. Such a ratio quantity will be used in Chapter 8 as well. The measured ratio $R(x,Q^2)$ can be used to reconstruct an effective

diffractive structure function $F_{jj}^{diff}(x, Q^2, \beta, t) = R(x, Q^2) \times F(x, Q^2)$, where $F(x, Q^2)$ is the structure function of the proton calculable with the quark and gluon densities.

The CDF Collaboration used such ratios $R(x, Q^2, \xi, t)$ to test the assumption of Regge factorization by analyzing the ratio R in bins of ξ and performing a detailed analysis of the slopes of the ratios R as a function of the reconstructed β (164). If the diffractive exchange is independent from the hard scattering process, then the exponential slope of the ratio R at small-x should be independent of the bin of ξ used to extract R. An instance of such an fit analysis is shown in Fig. 4.24. CDF found that, for the phase-space region probed, the diffractive dijet data was consistent with the Regge factorization hypothesis used for the HERA fits. More strikingly, they discovered the breakdown of factorization, as mentioned a few paragraphs before, shown in Fig. 4.26. This means that the QCD factorization theorem for hard diffraction cannot be directly used in hadron-hadron collisions without consideration of soft rescattering effects. The ratio R as a function of x and $Q \equiv (p_{T,jet1} + p_{T,jet2})/2$ can be used to test whether the diffractive structure function of the proton obeys DGLAP evolution or not. As shown in Fig. 4.25, the measurement reported by CDF is consistent within the experimental uncertainties with a diffractive structure function that obeys DGLAP evolution, just like the standard structure function of the proton (165). It could be that there are very weak deviations from such a behavior, in which case it could point to a description of hard diffraction that is not based on the concept of parton densities of a color-singlet exchange off the proton. More data, particularly at higher jet p_T, is necessary to understand if this is the case in Nature or not.

In addition, the CDF Collaboration conducted a series of measurements of the measured $-t$ distribution in hard diffractive processes. Such a distribution is highly sensitive to the impact parameter distribution of the gluons inside of the proton. In general, they can be used to test different models of hard diffraction that may yield a slope that is not exponential at high $-t$ values. One can test if the $-t$ distribution has an explicit dependence on kinematic variables of interest. For example, one can measure the exponential

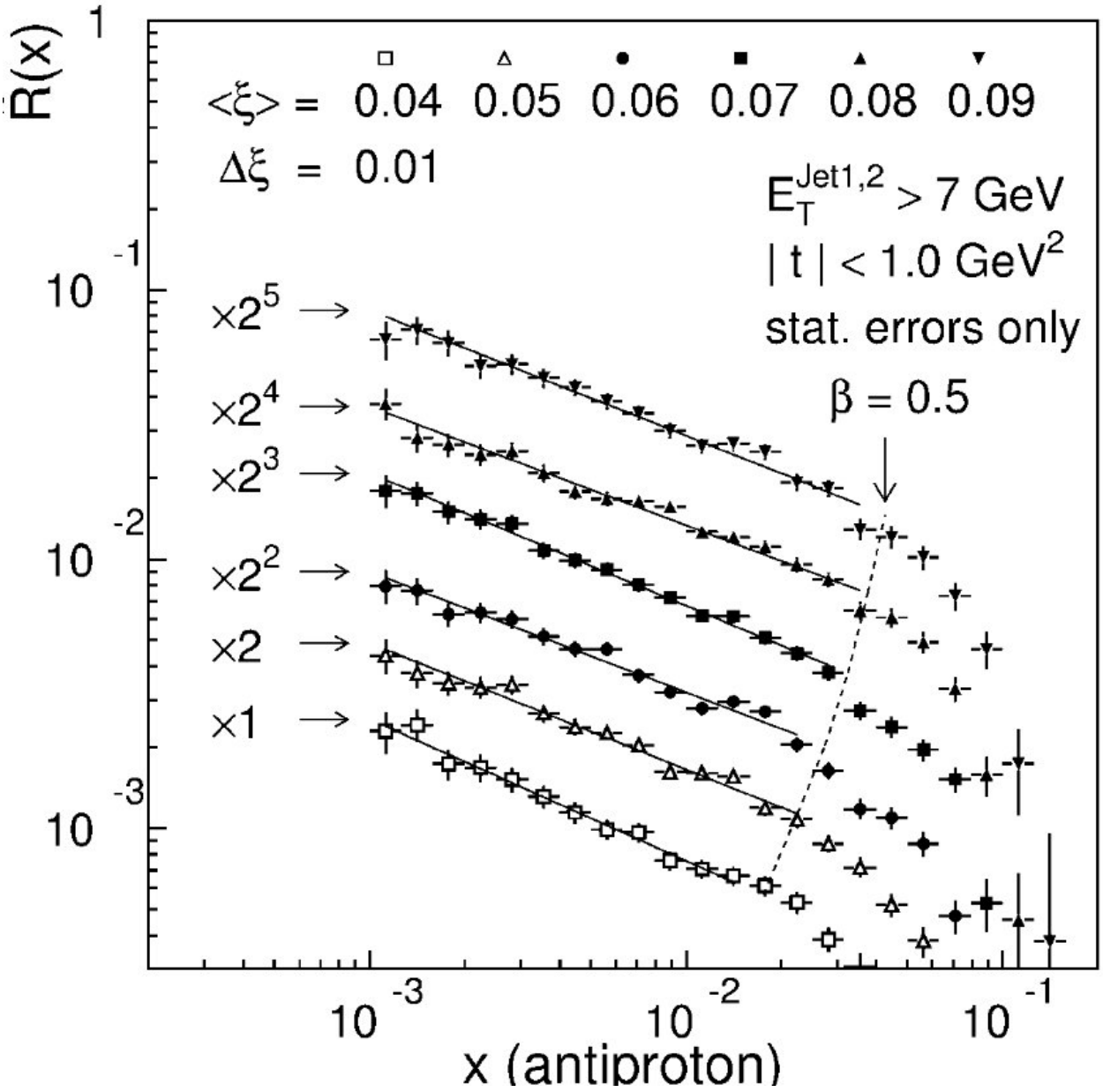

Figure 4.24: Ratio of single-diffractive to inclusive dijet production as a function of Bjorken-x of the parton sampled from the intact antiproton in bins of the fractional momentum loss of the antiproton ξ. The points are artifically displaced on the Y axis in multiples of powers of 2. Figure extracted from Ref. (164).

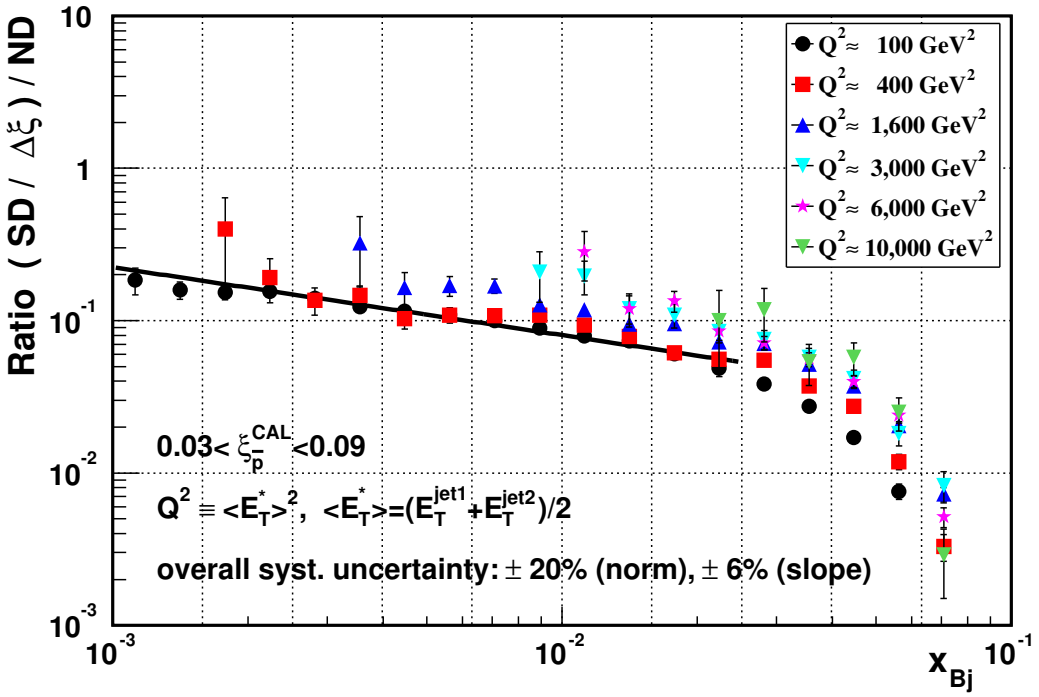

Figure 4.25: Test of DGLAP evolution of diffractive structure function in CDF data. The ratio of single-diffractive to inclusive dijet events is presented as a function on x_{Bj} estimated from the jets kinematics, in bins of the average jet transverse energy $Q \approx (E_{\mathrm{T,\,jet\,1}} + E_{\mathrm{T,\,jet\,2}})/2$. If the diffractive structure function did not follow DGLAP evolution, the points would not lie in a universal curve as they do for this plot in bins of Q^2. Figure extracted from Ref. (165).

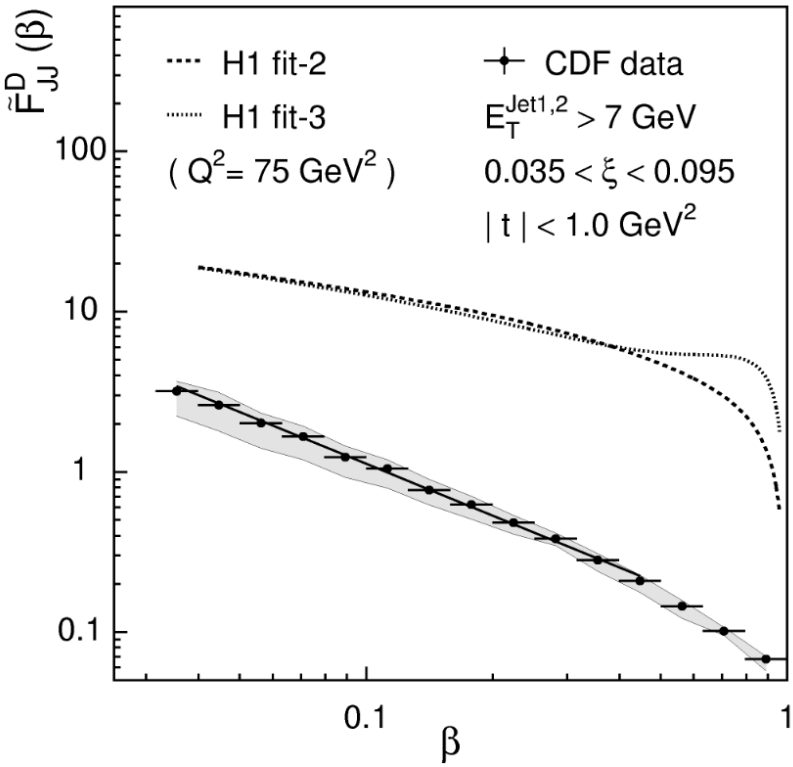

Figure 4.26: Factorization breaking in diffractive dijet production discovered by CDF. The vertical axis represents the effective diffractive structure function F_{jj}^{diff}. The horizontal axis represents the parton momentum fraction relative to the pomeron, β. The dotted lines are the expectation from the H1 parametrizations of the diffractive structure function. The predictions from the H1 fits overestimate the cross section by nearly an order of magnitude. Figure extracted in Ref. (164).

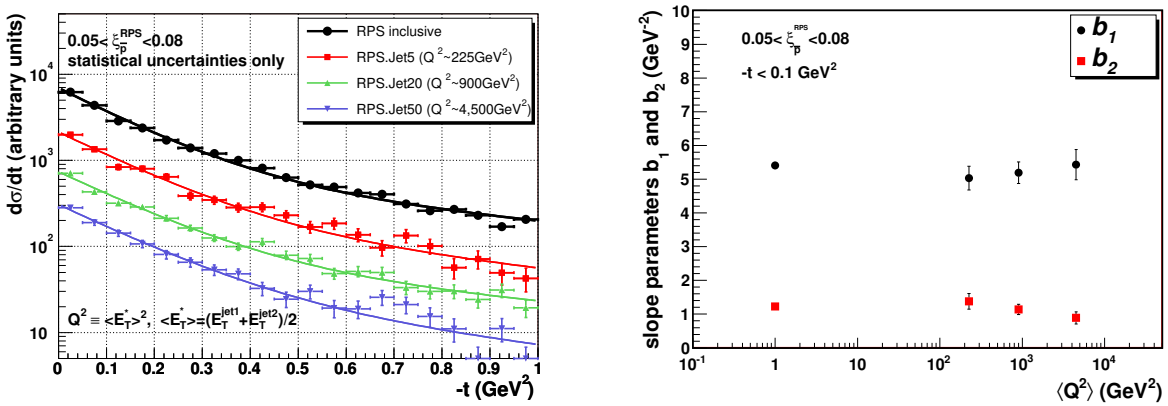

Figure 4.27: Left panel: measurement of the $-t$ distribution in bins of the mean jet p_T squared $\langle Q^2 \rangle$ by CDF. Right panel: Exponential slopes extracted from fits to the $-t$ distribution (sum of exponentials) as a function of $\langle Q^2 \rangle$. Figures extracted from Ref. (165).

slope of the $-t$ distribution in bins of the average p_{T} of the leading two jets. This was done for $\sqrt{s} = 1.96$ TeV by CDF. The results showed no dependence for the exponential slope as a function of the jet p_{T}, as shown in Fig. 4.27. Note also that so far we do not have evidence for a diffractive dip in the t distribution. A diffractive dip would give us valuable input into the black-dis-like behavior of the proton (or possible hotspots). Since the jets are typically very hard, it is likely we are in a regime where such dips do not manifest at low t. The diffractive production of vector mesons is more promising in this regard. Such a t-dip signature has been observed in high-energy pp elastic scattering.

Some calculations predict a logarithmic deviation from DGLAP evolution equation for the ratio of single-diffractive dijet events to non-diffractive dijet events. In the calculations by Kopeliovich et al. (166), where they do not use the parametrization of the diffractive structure function of the proton by the HERA experiments or the Regge factorization hypothesis, they expect a deviation that accentuates towards larger values of the jet p_{T}. This is shown in Fig. 4.28. Their calculations also predict a $\sqrt{s}$ dependence on the survival probability. Such calculations are performed in the color-dipole formalism of QCD.

In regards to diffractive dijet measurements at the LHC, the ATLAS and CMS experiments presented the first round of diffractive dijet production measurements at $\sqrt{s} = 7$

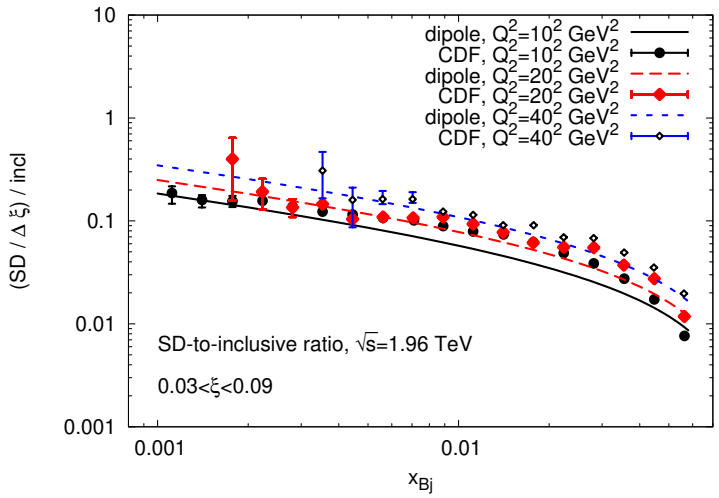

Figure 4.28: Predicted violations of DGLAP evolution of the diffractive structure function reflected on the ratio of single-diffractive to inclusive dijet production as a function of Bjorken-x, as expected from the color-dipole formalism (166), compared with CDF data. If the diffractive structure function obeyed the same DGLAP evolution as the proton structure function, then the curves would all lie in a universal curve. Figure extracted from Ref. (166).

TeV using the rapidity gap method (167; 168). Such measurements gave insight into the expected rates for hard diffractive reactions at a larger center-of-mass energy. They confirmed that there was further suppression of the survival probability as a function of $\sqrt{s}$ for single-diffractive production. Nevertheless, as mentioned before, the rapidity gap method has the disadvantage that it is mostly sensitive to very low ξ events, and in addition one loses information on t due to the lack of a detected proton. A result of the cross section measurement as a function of the reconstructed ξ value with the central detector calorimeters and charged particles is given in Figure 4.29.

A follow-up study by the CMS and TOTEM experiments for hard diffractive dijet production at $\sqrt{s} = 8$ TeV using the proton tagging technique improved over the capabilities achieved by the measurements based on the rapidity gap method presented by the ATLAS and CMS experiments at $\sqrt{s} = 7$ TeV. In this case, it was possible to measure the ratio R originally measured by the CDF Collaboration, as well as the absolute cross section as a function of ξ and t, which were accessible because of the detected protons. Several

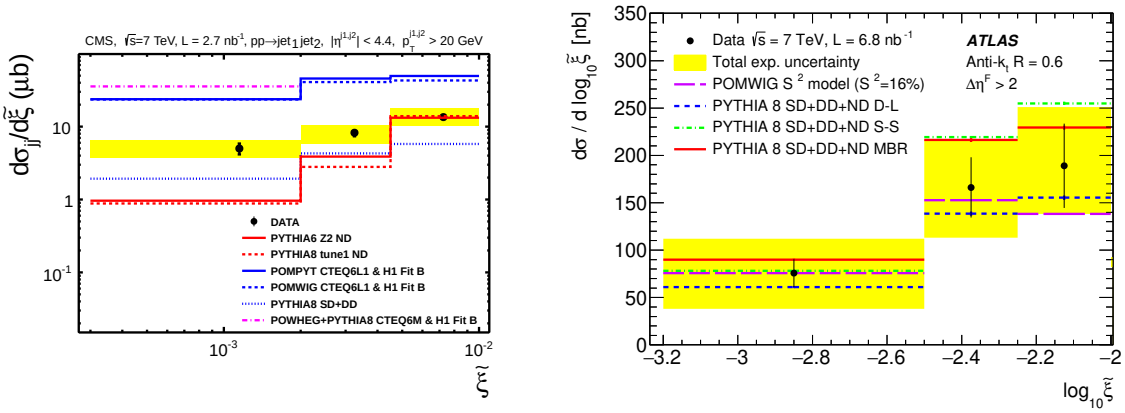

Figure 4.29: Differential cross section of diffractive dijet production as a function of the fractional momentum loss $\tilde{\xi}$ in 7 TeV pp collisions measured by the CMS (167) (left) and ATLAS (right) experiments (168). The diffractive dijet events are extracted with the rapidity gap method and a Monte Carlo based background subtraction.

comparisons to model-dependent treatments of the diffractive exchange were presented as well in this measurement by CMS and TOTEM. The amount of data collected for this study was insufficient for carrying out a differential measurement, so it was not possible to perform a measurement like the one by CDF in order to test several properties of hard diffraction. Hence, a new measurement at $\sqrt{s} = 13$ TeV with larger amounts of data calls for such a differential analysis. The ratio of single-diffractive to inclusive dijet events reported by the CMS-TOTEM analysis is presented in Fig. 4.30, together with the CDF measurement at lower $\sqrt{s}$.

As a final remark, in the context of heavy-ion collisions, there have been other studies for hard diffractive dijet production in lead-lead (PbPb) collisions. The CMS Collaboration presented such an investigation in Ref. (170). By analyzing the angular correlations between the jets, it is possible to learn more about the so-called Wigner gluon distribution of the proton. The Wigner gluon distribution gives more information than the standard collinear PDFs used at the CERN LHC. It would be interesting to learn more about hard diffractive reactions in heavy-ion collisions in the future, in preparation of the future EIC operation.

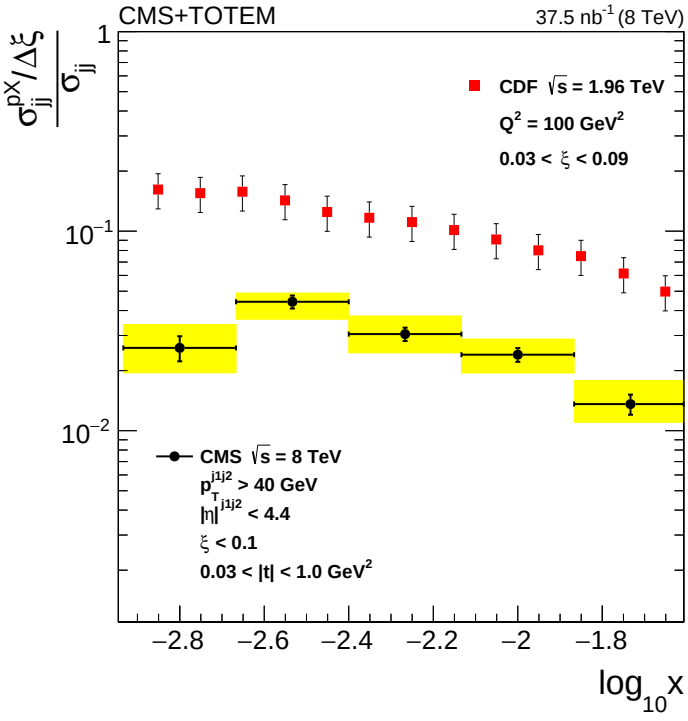

Figure 4.30: Ratio of diffractive dijet production as a function of Bjorken-x as measured by the CDF Collaboration at 1.96 TeV and by CMS-TOTEM at 8 TeV (169). The difference between the two measurements is indicative of a $\sqrt{s}$-dependent survival probability for hard diffractive processes with intact protons. Figure extracted from Ref. (169).

4.4 Chapter remarks

Clear signatures of the behavior of QCD interactions in the high-energy limit have not been observed yet experimentally. However, existing measurements are not inconsistent with the predictions based on BFKL calculations. While there are several probes for such a behavior, it is not clear that what we are seeing is just the effect from BFKL dynamics, or if it is a combination of several higher-order corrections in QCD. Measurements where the expected BFKL dynamics manifest clearly are necessary to test the framework of pQCD and of quantum field theories. In this thesis, we address the predictions of pQCD based on the BFKL framework in the measurement of hard color-singlet exchange in dijet events in proton-proton collisions at $\sqrt{s} = 13$ TeV with the CMS and TOTEM experiments, as described in Chapters 6 and 7. The physics case for such a process is discussed in Section 4.2.5.

On the other hand, the phenomenon of hard diffraction, where at least one of the proton remains intact due to pomeron exchange, has yet to be understood. Hard diffraction can potentially give us further information about the gluonic component of the proton structure, complementary to the "standard" inclusive measurements that are carried out by the LHC experiments. Measurements that rely on the proton tagging technique are particularly useful, since one can access the full kinematics of the diffractive exchange with a direct measurement of the forward scattered proton.

The phenomenon of diffraction is in general one of the long-standing mysteries of QCD. We have strong suggestions that diffraction ultimately has to do with the phenomenon of two- or multi-gluon dynamics and possibly is intimately related to confinement in QCD. It is likely that the proton interacts with color-singlet exchanges due to the presence of "lumps" or "hotspots" of gluons, which are ultimately formed from its internal degrees of freedom. This is a remarkable property of hadronic physics that requires a clear understanding from our community. The phenomenon of diffraction will be instrumental for the success of the future EIC in the U.S. Hence, any information we can learn

from hard diffraction at the CERN LHC has the potential of providing an interesting input in preparation for the EIC operations, together with the experience at HERA. In this thesis, we aim to understand, based on CMS-TOTEM 13 TeV data, how we could possibly progress in this direction. This is addressed in the measurement of Chapter 8.

Chapter 5

The Large Hadron Collider and the CMS and TOTEM experiments

The work of this thesis focuses on the physics program at the CERN Large Hadron Collider (LHC) (171), where protons collide against each other at a given interaction point to collision energies of up to $\sqrt{s} = 13$ TeV. The idea is to detect the debris of these high energy proton-proton collisions around a given interaction point (IP) at the LHC. For this thesis, the author mainly worked with the CMS and TOTEM experiments. Thus, particular attention is given to these experiments in this Chapter. After presenting this Chapter, we move to the description of the data analysis work carried out by the author in Chapters 6, 7, and 8, which is inspired in the physics motivation laid down in Chapter 4.

5.1 The Large Hadron Collider

The LHC is the largest and most energetic particle accelerator in the world. It has a circumference of 26.7 km and is located about 100 m underground between the French and Swiss border at the CERN laboratory (171). The LHC consists of two intersecting rings, where one of the proton beams circulate in a clockwise direction and the other proton beam in an anti-clockwise direction. The "beam" is comprised of "bunches of protons" that move at nearly the speed of light. Each one of these proton bunch contain about 10^{11} protons. The beams are guided around the accelerator ring by a strong magnetic field maintained by superconducting electromagnets. The electromagnets are built from coils

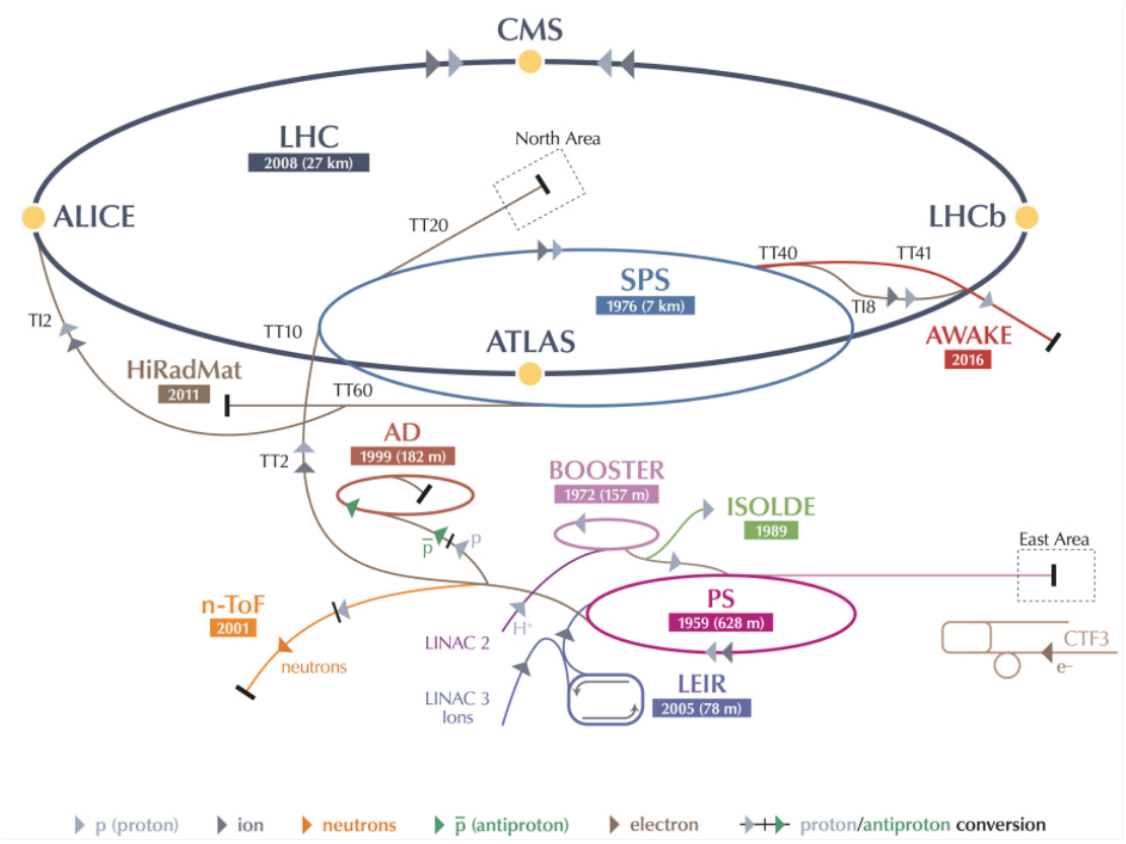

Figure 5.1: Diagram of the CERN accelerator complex. The larger ring represents the Large Hadron Collider. Figure extracted from Ref. (172).

of special electric cable that operates in a superconducting state, efficiently conducting electricity without loss of energy. Various magnets are used to direct the beams around the accelerator. These include 1232 dipole magnets 15 metres in length which bend the beams, and 392 quadrupole magnets, each 5–7 metres long, which focus the beams. Just prior to collision, another type of magnet is used to "squeeze" the particles closer together to increase the chances of collisions. The two proton beams meet each other at specific IPs, where one then installs complex particle detectors in order to reconstruct the collision debris. An overview of the particle detectors is given in Section 5.2. A schematic diagram of the CERN accelerator complex is shown in Fig. 5.1.

The design collision energy of the LHC is of 14 TeV for proton-proton collisions, with a design instantaneous luminosity of $\mathscr{L} = 10^{34}$ cm^2 s^{-1}. The number of events produced per unit time for a given process with cross section σ is given by the master formula

$$\frac{\mathrm{d}N}{\mathrm{d}t} = \sigma \mathscr{L} \tag{5.1}$$

where $\mathscr{L}$ is the machine instantaneous luminosity and σ is the hadron-level cross section of the process of interest. The machine luminosity is dependent on parameters related to the beam profile. In the case of circular accelerators, the luminosity can be expressed as

$$\mathscr{L} = \frac{k_b N_{b,1} N_{b,2} f_{\mathrm{rev}} \gamma}{4\pi \varepsilon_n \beta^*} F \tag{5.2}$$

where k_b is the number of bunches of protons collided, $N_{b,1}$ and $N_{b,2}$ are the number of particles per bunch in the two beams, f_{rev} is the revolution frequency, and γ is the Lorentz gamma factor. The normalized transverse beam emittance and the amplitude function at the IP are denoted by ε_n and β^*, which are both related to the width of the beams. The geometric luminosity reduction factor due to the crossing angle is denoted by F. The collision rate at the LHC is driven by the spacing between the bunches of protons in the

beam. At peak operating conditions, this bunch spacing can be as small as 25 ns.

The LHC primarily collides protons. During its proton-proton operation, the LHC collides several protons per bunch crossing at a given IP. This helps achieve the goal of obtaining a larger instantaneous luminosity, while paying the price of having larger amounts of interactions per bunch crossing ("pileup"). This works well for final-states where the physics objects are produced at high-transverse momentum and at high-masses, and for which the particle physics detector is able to reconstruct reliably. In special pp runs, however, the LHC collides protons at a rate where we have mostly single proton-proton interactions per bunch crossing. This is usually done for high precision measurements of certain parameters of the SM, such as the mass of the W boson, or the study of soft jet production or diffractive interactions in an environment clean of beam-background. For the studies presented in this thesis, we use one such special run at low pileup and with special optics settings for the operation of the detector system of the TOTEM experiment.

While the LHC primarily collides protons for its physics program, the LHC is also capable of colliding heavy-ion nuclei at relativistic energies. Indeed, typically at the end of a given year of data taking, the LHC collides heavy-ions (mostly lead (Pb) nuclei stripped from all their electrons) against heavy-ions, or heavy-ions with protons. The physics goals here are very different; here, one is interested in studying the emergent properties of strong interactions at high-densities and high-temperatures via the creation and evaporation of the so-called quark-gluon plasma.

5.2 LHC experiments

At the LHC ring, there are various experiments installed at around the IPs of the colliders with a diverse – yet somewhat overlapping in some cases – set of physics goals:

A Large Ion Collider Experiment (ALICE): The ALICE experiment main focus is the understanding of nuclear matter at high densities and high temperatures. Such conditions

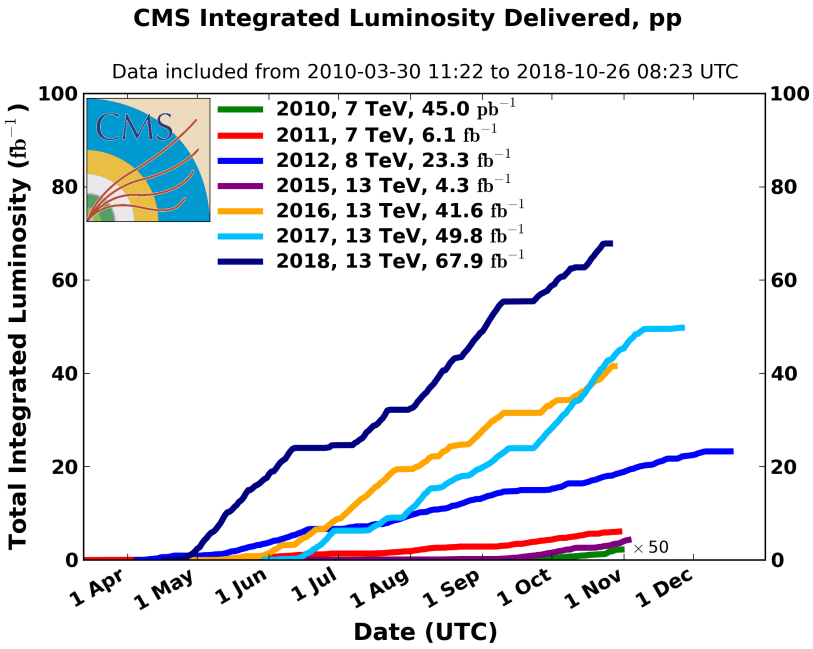

Figure 5.2: Integrated luminosity by the CMS experiment since 2010 through 2018 at various $\sqrt{s}$ for proton-proton collisions. The horizontal axis represents the month of data taking for a given year.

can easily be reached in ultrarelativistic collisions of heavy-ions, but can also be searched in high energy proton-ion and proton-proton collisions. Investigations of diffractive and photon-induced processes have also been possible with the ALICE detector. ALICE is made of 18 subdetectors that can be grouped in three main ensembles: the global event detectors that characterize the centrality of the collision (i.e., how much geometric overlap there is in a given nucleus-nucleus collision), the central barrel at mid-pseudorapidity optimized for the reconstruction of charged hadrons, electrons and photons, and the muon spectrometer to reconstruct muons at forward pseudorapidities.

A Toroidal LHC ApparatuS (ATLAS) (173) : ATLAS is the largest detector at the LHC. ATLAS is a multipurpose detector, meaning that in principle it is able to reconstruct the decay products of very heavy particles in numerous decay channels. The ATLAS instrumentation also allows it to participate in the heavy-ion program of the LHC, with capabilities that complement those of the ALICE experiment. The ATLAS detector has a large acceptance, covering nearly 4π radians in a solid angle w.r.t. the IP. ATLAS has the shape

of a cylinder that contains an inner tracker, an electromagnetic and hadronic calorimeter, a toroidal magnet, and a muon spectrometer.

Compact Muon Solenoid (CMS) (174): Like ATLAS, CMS is a multipurpose particle detector. CMS is able to carryout a similar physics program as ATLAS, while relying with different detector technologies and algorithms for the reconstruction of particles. Since the main focus of this thesis is on a measurement based on CMS data, the CMS detector will be described in detail in Section 5.3.

LHC beauty (LHCb) (175) : The LHCb experiment main target is the investigation of the properties of mesons containing bottom quarks (also known as beauty quarks). B mesons have a relatively long lifetime, and some of their decay channels can be used to fully reconstruct the B meson four-momenta with high precision. The reconstruction of the B meson can profit greatly from the boosts given given by the high-energy of the initial-state beam proton. B mesons that decay closer to the beam will generally have a larger displacement distance for the secondary vertex relative to the primary vertex. For this reason, the LHCb detector has been designed as a single-arm forward spectrometer with excellent tracking capabilities, covering very large pseudorapidities. The bulk of the program of LHCb is carried out in proton-proton collisions, but LHCb has also collected data in proton-lead and lead-lead collisions. In addition, the LHCb detector has been used to study the production of particles in the very forward region, which can be used to better understand the structure of the proton at small parton momentum fractions x. This is complimentary to the kinematic reach of the "central" detectors of the LHC.

LHC forward (LHCf) (176) : LHCf is equipped with two detectors located very far from the IP of the ATLAS detector. The main physics goal of LHCf is to carry out detailed studies of forward particle production at LHC energies which can then be used to interpret the measurements of ultra high-energy cosmic rays, where there is not much control on the collision energy of the cosmic ray with the atmosphere.

MOnopole and Exotics Detector at the LHC (MOEDAL) experiment (177): The primary

goal of MOEDAL is to directly search for the production of magnetic monopoles, dyons, or other highly ionizing (pseudo)stable massive particles. To detect these particles, the project uses nuclear track detectors (NTDs), which suffer characteristic damage due to highly ionizing particles.

TOTal cross-section, Elastic scattering and diffraction dissociation Measurement at the LHC (TOTEM) (154; 178) : TOTEM, which shares the same IP as CMS, is dedicated to the study of soft and hard diffraction. This includes: the measurement of the proton-proton total hadronic cross section, the elastic scattering cross section, and soft and hard diffractive cross sections. These phenomena require the detection of very forward intact protons, which can be detected with the forward proton spectrometer of the TOTEM experiment. The TOTEM experiment components will be described in detail in Section 5.4.

5.3 The CMS detector

The CMS detector, one of the two general purpose detectors at the CERN LHC, is organized in a set of subdetectors arranged concentrically in a cylindrical fashion around the beam axis. This "onion-like" structure is equipped with different layers of detector technologies that target to detect most of the collision debris in a nearly 4π solid angle. A superconducting solenoid magnet is used to bend the trajectories of charged particles. A schematic diagram showing the layered structure of the detector is shown in Fig. 5.3. The jet analyses presented in Chapters 6, 7, and 8 effectively rely on all the CMS detector components within its full acceptance. We thus give an overview of the important characteristics of the various subcomponents of the CMS detector in this Section.

5.3.1 Superconducting solenoid

Something extremely important for the reconstruction and identification of particles is the presence of a strong magnetic field within the volume of the detector. The stronger

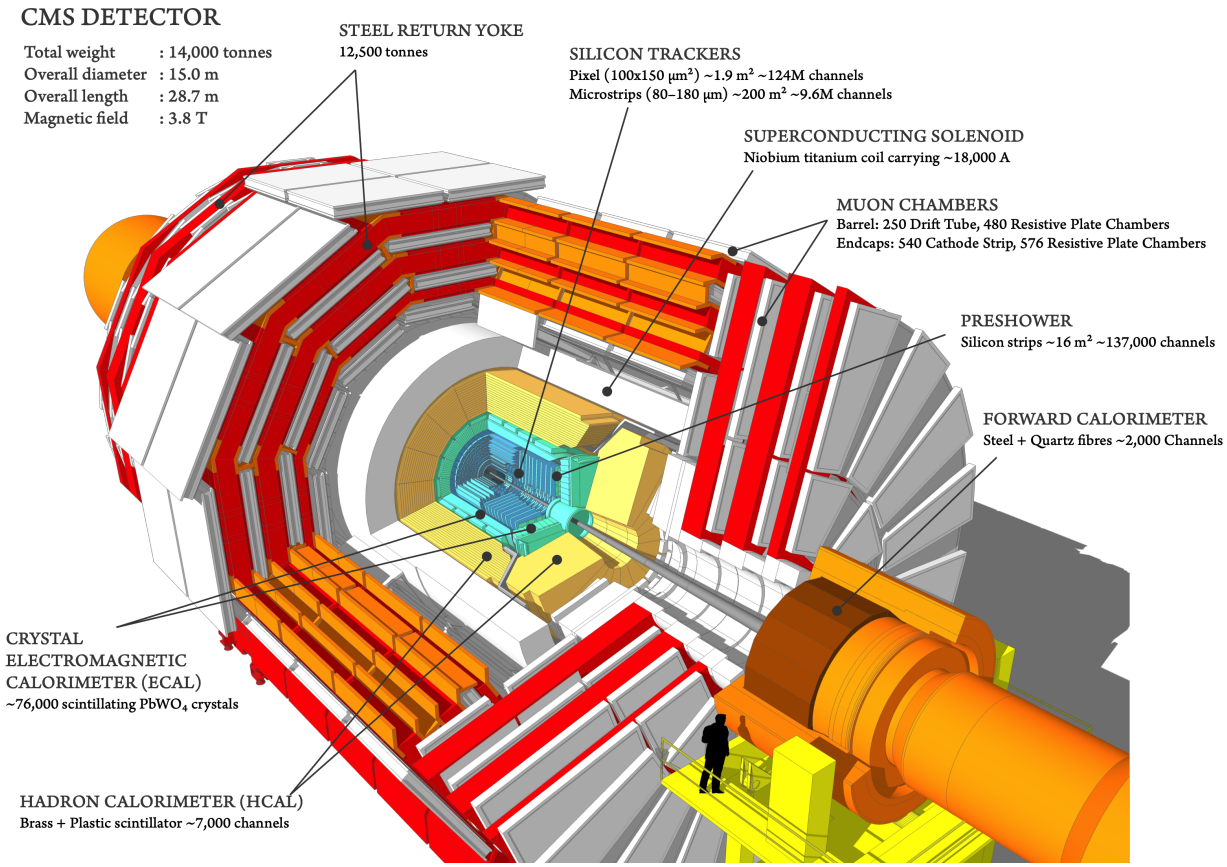

Figure 5.3: Schematic diagram of the CMS detector and its subcomponents. A person is placed to give a sense of scale. Figure extracted from Ref. (179).

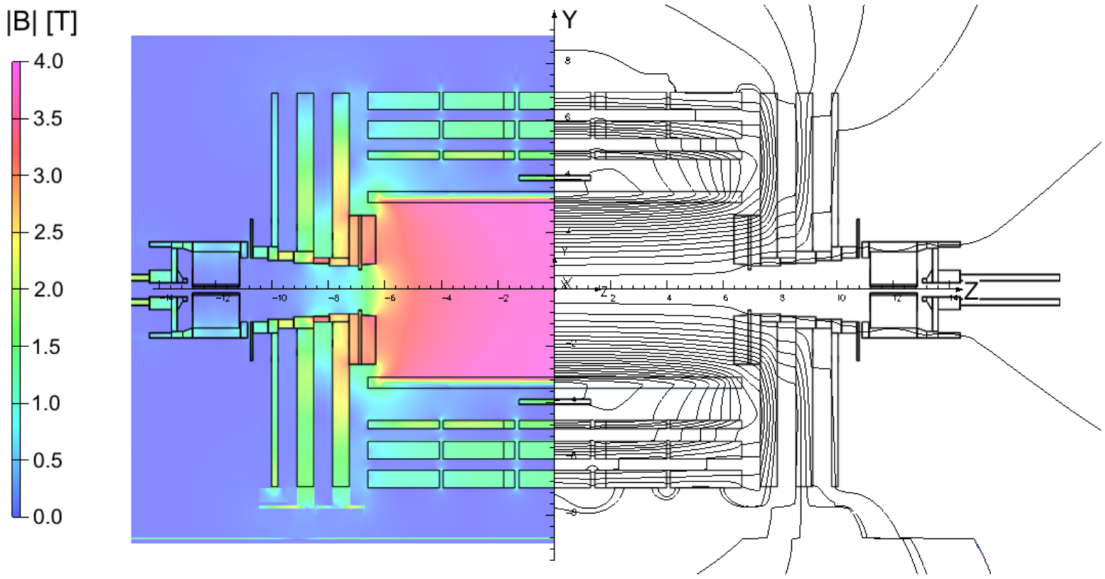

Figure 5.4: Value of the magnitude of the magnetic field $|\vec{B}|$ (left half) and field lines (right half) on a longitudinal section of the CMS detector. Figures extrated from Ref. (180).

the magnetic field, the more narrower the arc of circumference becomes. For this reason, one of the main components of the CMS detector is its superconducting solenoid, which generates a magnetic field of 3.8 teslas. Such a magnetic field is about 100 thousand times stronger than the magnetic field generated by the Earth. The superconducting coil, the vacuum tank, and the magnet yoke are the three main components of the CMS magnet system.

The solenoid consists of four layers of niobium-titanium superconducting strands, which were extruded with pure aluminium and mechanically reinforced with an aluminium alloy. The superconducting coil is in vacuum and is thermally insulated. It operates in superconducting mode by letting electric currents flow without resistance. The yoke is a twelve-sided iron structure that surrounds the magnet coils and is responsible for the return of the magnetic flux, which is why sometimes it is referred to as a "return yoke." At the same time, the yoke provides structural support of the CMS detector.

A map of the magnitude of the magnetic field is shown in Fig. 5.4 for one half of the detector. The colors represent the strength of the magnetic field. The direction of the field lines are represented in black and white on the other half of the detector in Fig. 5.4.

The CMS magnet is such that it bends the paths of electrically charged particles that emerge from the high-energy collisions. This helps identify the charge of the particle, since way the particles trajectories are bent depend on whether the particles are positively or negatively charged. It is also essential for the measurement of particle momenta; the more momentum a charged particle has, the less its path is curved by the magnetic field. The magnetic field in CMS is such that the particle trajectories are bent on the x–y transverse plane, whereas the component of the trajectory on the z direction remains (mostly) unaffected.

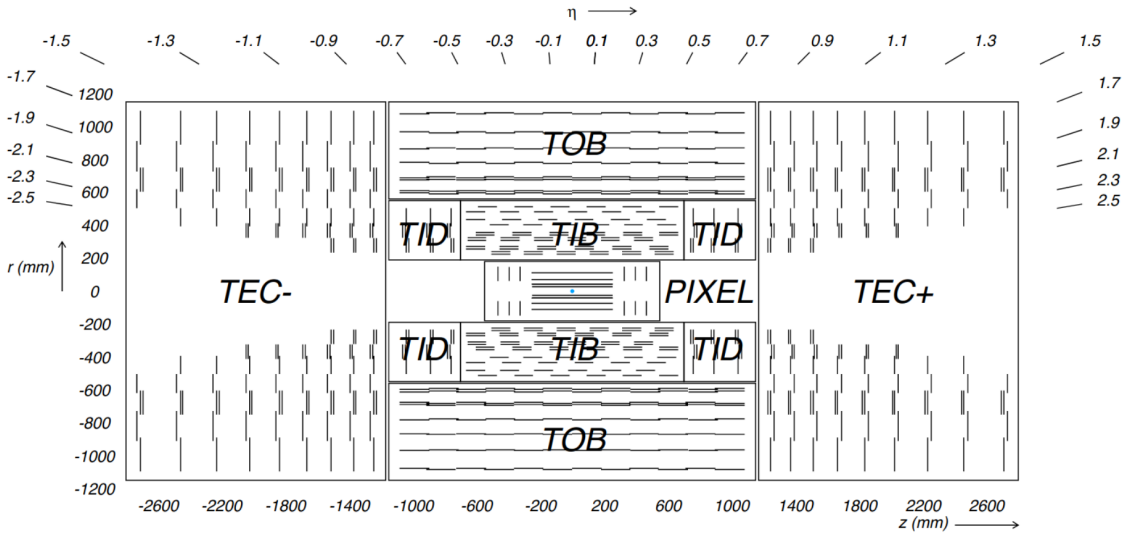

Figure 5.5: Schematic diagram of the CMS tracker. Each line represents a detector module. Double lines indicate back-to-back modules that deliver stereo hits. Figure extracted from Ref. (181).

5.3.2 Tracker

CMS utilizes a series of subdetectors to identify the paths taken by the electrically charged particles whose trajectories are bent by the aforementioned superconducting solenoid. The tracking detectors of the CMS experiment are the closest detectors to the collision point. Overall, they cover a pseudorapidity range of $|\eta| < 2.5$. The tracking system was designed to have high granularity to record and reconstruct particle trajectories with high precision. The material is such that particles do not lose much energy as they traverse the material. When an electrically charged particle passes through the tracker, it interacts with the silicon atoms of the tracker creating electron-hole pairs in the process. The free electrons are then drifted with an external electric field, creating an electric signal that is amplified and detected registering a hit. The trajectory of the particle is reconstructed by joining the hits produced by the particle in the different layers of the detector.

The silicon tracker of the CMS detector occupies a cylindrical volume of 5.8 m in length and 2.5 m in diameter, with its axis closely aligned to the beam line. The tracker utilizes both silicon pixel and strip technologies to measure the charged particle trajectories with

extreme precision.

The pixel tracker consists of 1440 modules organized into three coaxial barrel layers located at radii of 4.4, 7.3, and 10.2 cm. The aforementioned barrel layers are supplemented with two endcap disks on both sides of the barrel, both of which are located at $|z| = 34.5$ cm and 46.5 cm from the IP. The pixel detector measures the interaction of charged particles with its sensors and records the hits in three-dimensions. Each hit is reconstructed with a granularity of 10 microns and 20–40 microns in the transverse and longitudinal directions, respectively.

The strip tracker surrounds the pixel tracker, which extends out to a radius of 110 cm. The strip tracker consists of 15 148 silicon strip modules organized into 10 coaxial barrel layers supplemented by three small and nine large endcap disks. The strip tracker is comprised of four subsystems: the Tracker Inner Barrel (TIB), the Tracker Outer Barrel (TOB), the Tracker Inner Disks (TID), and the Tracker Endcaps (TEC). The schematic diagram of the silicon tracker of CMS is shown in Fig. 5.5.

5.3.3 Electromagnetic Calorimeter

The Electromagnetic CALorimeter (ECAL) of CMS is desgined to fully absorb and measure the energy of electrons and photons. It is made of lead-tungstate ($PbWO_4$) crystals chosen for the material's small Molière radius. The Molière radius is a characteristic constant of a material that is a proxy of the scale of the transverse dimension of the fully contained electromagnetic shower initiated by an incident high energy electron or photon. In other words, the electromagnetic shower will most likely be contained within a narrow cone, rather than being "dissipated" transverse to the incident direction. The material allows for the construction of a compact, fine granularity calorimeter. The metallic, yet transparent, crystals are aligned in the barrel region and the endcaps, as shown on Fig. 5.6. The barrel contains about 61,200 crystals grouped in 36 supermodules, while each of the endcaps contains 7324 crystals assembled in units of 5x5 crystals. The ECAL

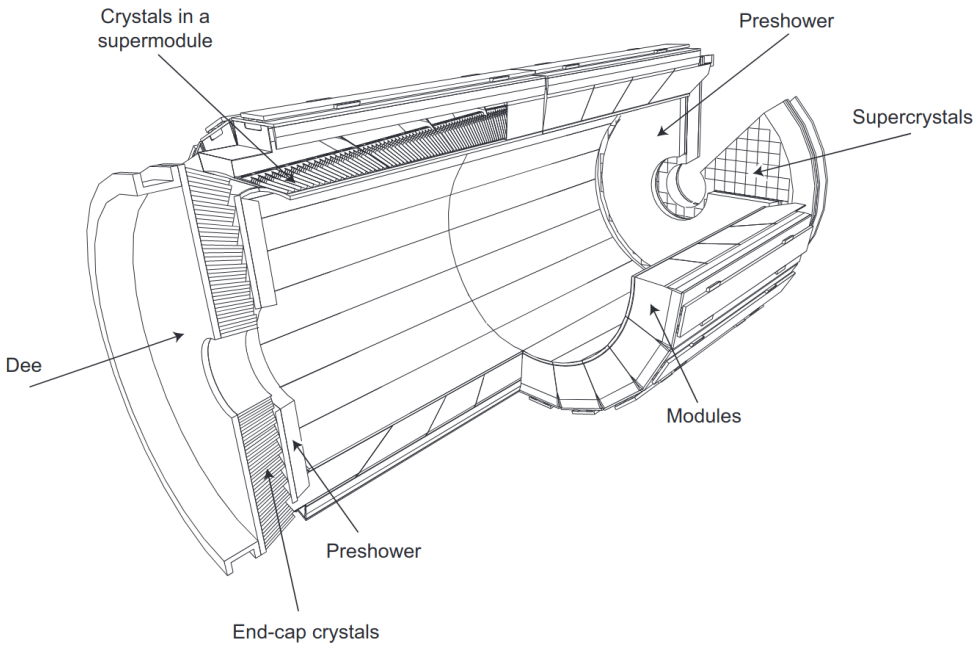

Figure 5.6: The CMS electromagnetic calorimeter (ECAL) is a homogeneous and hermetic calorimeter. The preshower detector, based on lead absorbers that are equipped with silicon strip sensors,is placed in front of the endcap crystals, to enhance photon identification capabilities (181).

covers the pseudorapidity range $|\eta| < 3$.

When a high energy photon or electron passes through ECAL, it deposits energy in the crystals through bremsstrahlung and electron-positron pair production. The photons, electrons, and positrons that result from this cascade will also undergo bremsstrahlung and electron-positron pair production, until all their energy has been absorbed by the detector. This results in scintillation light emitted in the crystals and then measured by photodetectors. The amount of produced light is well approximated by a linear function of the photon or electron initial energy (182). The photodetectors in the barrel are avalanche photodiodes mounted in pairs on the back of each crystal, while the vacuum phototriodes are used in the endcaps, attached to the back of each crystal. Excellent energy resolution is obtained with ECAL (182), of about 0.4% for energies of 100 GeV or above.

The ECAL also contains preshower detectors installed in front of the endcaps con-

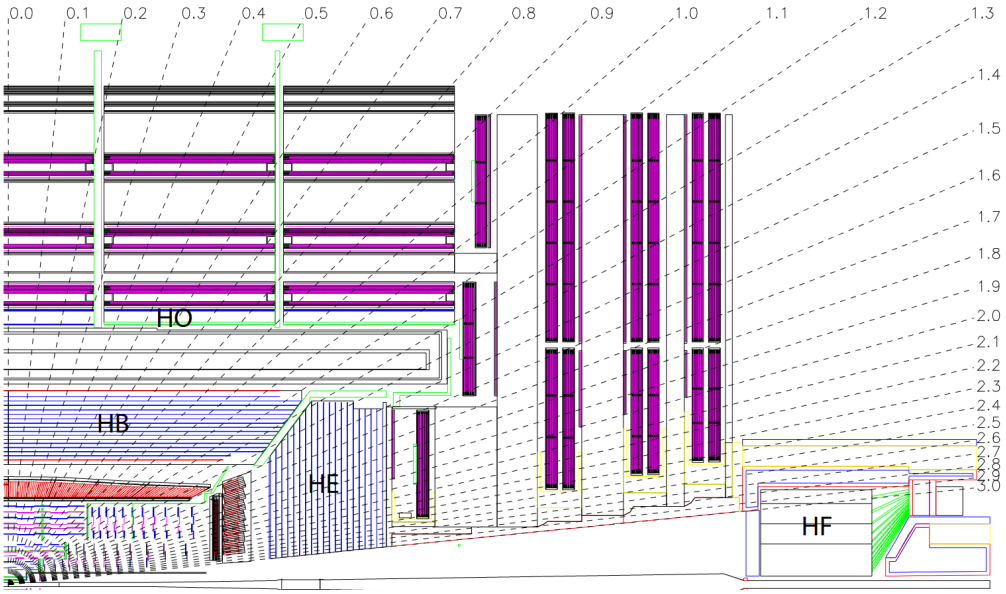

Figure 5.7: Schematic the Hadronic Calorimeter (HCAL) and its subsystems in the r–z plane. The colors represent different longitudinal segmentations. Schematic taken from Ref.

sisting of two layers of lead, each followed by a layer of silicon strip detectors. This preshower setup allows for the identification of neutral pions in the endcaps. It also helps identify electrons against minimum ionizing particles, and improves the position determination of electrons and photons. The crystals are kept at a temperature of 18° C, since the response of the crystals and signal amplification depend on the operating temperature. Since the transparency of the crystals to scintillation light is affected by radiation, a monitoring system is installed to track the radiation-induced transparency variations using laser pulses.

5.3.4 Hadronic Calorimeter

The Hadronic Calorimeter (HCAL) measures the position, energy, and arrival time of hadrons through the use of successive layers of absorber and scintillating materials. The absorber material is typically very dense, such that it forces the interaction of an energetic hadron with a heavy nucleus of the material. The debris from this interaction then induces scintillation in the subsequent layer, and the remaining energetic particles are

forced to interact with the next layer of absorber. In CMS, four subsystems conform the HCAL, which extends the coverage both inside and outside of the magnetic field of the solenoid. Located within the magnetic field are the barrel (HB) and endcap (HE) components, while the outer barrel (HO) and forward (HF) subsystems are located outside the solenoid within the return flux, where the magnetic field is significantly smaller.

A schematic of one side of HCAL and its subsystems is shown in Fig. 5.7. The other side of HCAL is symmetric to the one shown in this schematic. The HB subsystem provides a coverage in η of $|\eta| < 1.4$, and is split into two half barrel sections that span 1777 < r < 2876.5 mm from the beam line. Each half barrel is split into 18 identical wedges of 20° in ϕ, which ensures a nearly-symmetric detector layout in the transverse plane. Within each wedge, there are brass-alloy absorber plates and active plastic scintillator plates of $\Delta\eta \times \Delta\phi = 0.087 \times 0.087$ rad. There are 17 layers of scintillator plates that are alternately stacked with absorber plates to form 16 projective towers in η of size $\Delta\eta \times \Delta\phi = 0.087 \times 0.087$ for each half barrel. The net optical signal for each tower is converted to an electrical signal by pixelated hybrid photodiodes mounted at the ends of the barrel section.

5.3.5 Muon chambers

Muons are very special particles to detect. Owing to their mass, muons do not undergo brehmsstrahlung radiation as easily as electrons. Since they are leptons, they do not interact strongly. Therefore, muons can penetrate several meters of iron without being absorbed. Most of the time, energetic muons will most likely go through the HCAL and ECAL subdetectors, leaving only a trace of their trajectory in the silicon tracker. The detection of muons can be optimized by, in addition, reconstructing the muon track in a special set of detectors known as "muon chambers." Physics analyses that rely on muons greatly benefit from the excellent performance of the identification of muons and the calibration of the four-momenta of the muon.

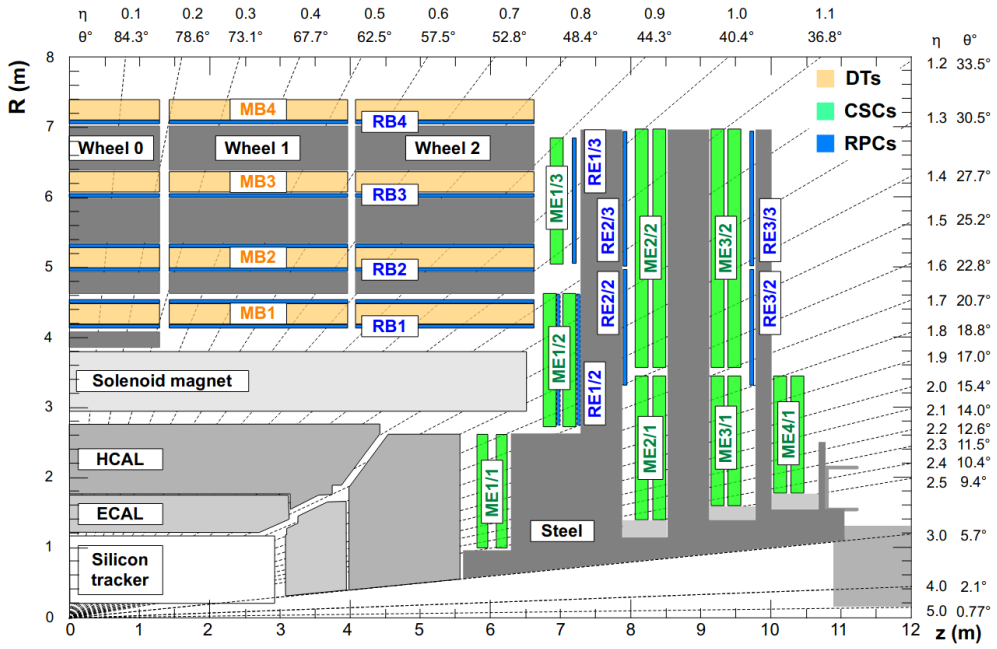

Figure 5.8: Quadrant of the CMS detector showing the locations of the drift tubes (orange), cathode strip chambers (green) and resistive plate chambers (blue). Figure extracted from Ref. (183).

To identify muons and measure their momenta, CMS uses three types of detector: drift tubes (DT), cathode strip chambers (CSC), and resistive plate chambers (RPC). A schematic diagram of the muon detection equipment of CMS is shown in Fig. 5.8.

The DT system measures the position of muons in the barrel region. Each tube contains a stretched wire within a gas volume. When a muon passes through the volume, it knocks electrons off the atoms of the gas. An electric field makes them end up at the positively charged wire. By registering where along the wire electrons hit, as well as by calculating the muon's original distance away from the wire, DTs give two coordinates for the muon's position. Each DT chamber, on average 2×2.5 m^2 in size, consists of 12 aluminum layers, each with up to 60 tubes: the middle group measures the coordinate along the direction parallel to the beam and the two outside groups measure the perpendicular coordinate.

The CSC are used in the endcap disks where the magnetic field is not uniform and particle rates are high. CSCs consist of arrays of positively (anode) charged wires crossed

with negatively charged copper cathode strips within a gas volume. When muons pass through, they knock electrons off the gas atoms, which flow and group to the anode wires creating an avalanche of electrons. Positive ions move away from the wire and towards the copper cathode, also inducing a charge pulse in the strips. Because the strips and the wires are perpendicular, we get two coordinates for each passing muon. Each CSC module contains six layers making it able to accurately identify muons and match their tracks to those in the tracker. The CSCs are fast detectors suitable for triggering as well.

The RPCs are fast gas detectors that provide a muon trigger system parallel to those of the DTs and CSCs. The RPCs consist of two parallel plates, a positively charged anode and a negatively charged cathode, both made of a highly resistive, plastic material and separated by a gas volume. When a muon passes through the chamber, electrons are knocked off the gas atoms. These electrons in turn hit other atoms, causing an avalanche of electrons. The electrodes are transparent to the signal, which are instead picked up by external metallic strips after a short time delay. The pattern of hit strips gives a measure of the muon momentum. The latter can be used for triggering purposes. The RPCs combine an excellent space and time resolution of just about 1 ns.

5.3.6 Very forward detectors of CMS

Several subdetectors are specifically designed to operate in the very forward region, effectively extending the acceptance of CMS. Due to their proximity to the beam, they are not inserted during the standard runs of CMS, as they would be exposed to intense amounts of radiation. Within CMS, we have CASTOR (Centauro And STrange Objects Research) forward detector, which covers the pseudorapidity range of $-6.6 < \eta < -5.1$, and the ZDCs (Zero Degree Calorimeter) installed at a distance of 140 m on both sides of the IP of CMS. CASTOR has been used in special low-luminosity runs in pp collisions, and when the LHC operated in pPb and PbPb collision modes, and is able to measure the energy of very forward hadrons scattered at very small angles with respect to the beam. The ZDC

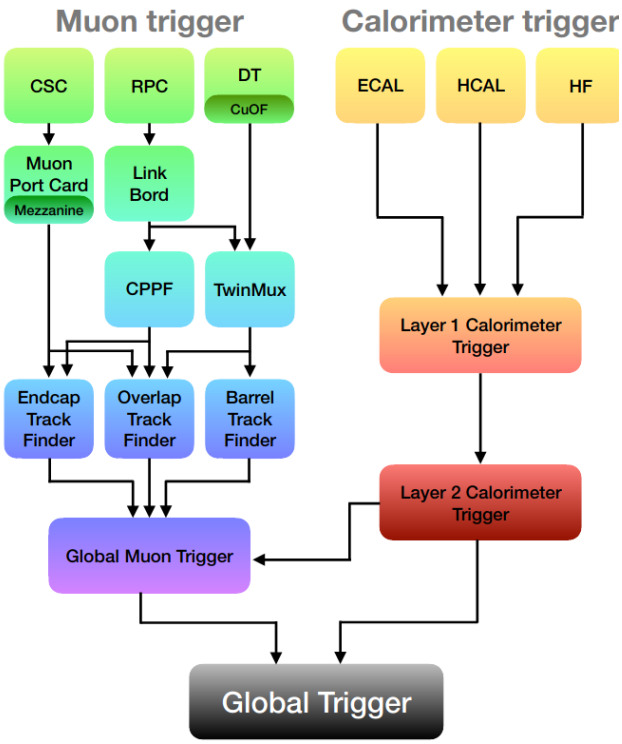

Figure 5.9: Block diagrams of the L1 trigger system, based on the diagrams in Ref. (185).

is used to detect the neutrons emitted from heavy-ions that undergo quasi-real photon exchange in ultraperipheral collisions, where the heavy-ion may scattered in an excited state and emit a neutron in the forward region (184). Neither CASTOR nor the ZDC are used for the analyses described in this thesis, but these detectors can be used for very interesting physics processes that are connected to the topics presented in this thesis, such as ultraperipheral heavy-ion collisions and very forward jet production.

5.3.7 Trigger

Most of the events produced in proton-proton collisions are due to long-distance physics interactions. These interactions are collectively called "minimum-bias." While these interactions are very interesting in their own right for a better understanding of strong interactions, we are mostly interested in studying the production of particles at high transverse momentum and at high-masses, where the hard energy scales are orders of

magnitude larger than the confinement energy scale (typically tens of GeV to the TeV scale). The analogy of finding a needle in a haystack is often cast when discussing this basic problem in data collection.

The amount of data we can record in a given run, as well as the overall read-out bandwidth of the detector, is finite. Therefore, unfortunately we do not have the luxury of saving every single proton-proton collision event for offline analysis. Instead, we need to make a decision based on *which* events are worth keeping, and which ones is best to throw out (while keeping a representative sample of these unwanted events as a control sample used for the calibration of the detector or validation of specific algorithms). This problem is solved by means of strongly biasing our data collection procedure using a "trigger." In CMS, two stages of triggers are required to select events of interest. These two selection stages are called Level 1 trigger (L1) and the High-Level Trigger (HLT), where we select the events given a maximal rate of 100 kHz for L1 and 100 Hz for HLT.

The L1 trigger is mostly comprised of high frequency, adjustable electronics that run over a minimal set of simplified information. The simplified information is, for example, the merging of hits in both ECAL and HCAL into superclusters that represent the combined energy deposit, or information from one of the subdetectors of CMS, for example from the muon system. The L1 trigger returns a collection of Boolean bits with a latency of about 3 microseconds once the decision is taken. These bits are then propagated to the HLT to let it stop or to continue collecting with more detailed information. At the HLT, most of the clustered data is unpacked and processed in a dedicated HLT software component. If the event is observed to pass a predefined set of higher-level constraints, it is directly stored onto the disks for further processing. The HLT trigger reduces the 100 kHz input from the L1 trigger down to about 100 Hz, which is the bandwidth for data transfer by the CERN main computing farm. The events are then stored on tape for future (offline) analyses. A schematic diagram of the triggering process in CMS is shown in Fig. 5.9.

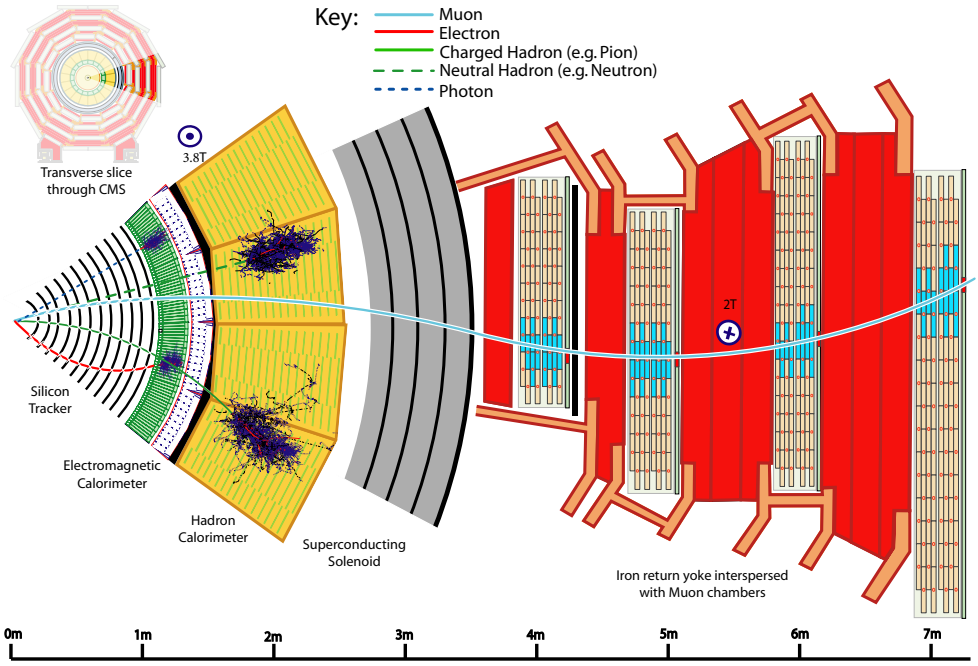

Figure 5.10: Schematic diagram of object reconstruction via the particle-flow (PF) algorithm of CMS. An electron leaves a signature in the tracker and is fully absorbed by ECAL. The neutrino is undetected. An unconverted photon is absorbed in the ECAL without leaving tracks. A charged hadron leaves a signature in the tracker and is fully absorbed by HCAL. A neutral hadron leaves a signature in the HCAL and no track. The muon leaves a signature in the tracker and on the muon chambers, with no absorption in ECAL nor HCAL.

5.3.8 CMS object reconstruction

After collecting the "raw" data, one can process this with sophisticated algorithms for the "object" reconstruction. The objects are proxies for physical particles that passed through the detectors. Indeed, the CMS apparatus features properties well suited to particle-flow (PF) reconstruction: a highly-segmented tracker, a fine-grained electromagnetic calorimeter, a hermetic hadron calorimeter, a strong magnetic field, and an excellent muon spectrometer. A fully-fledged PF reconstruction algorithm tailored for the CMS detector capabilities was therefore developed and has been consistently used in physics analyses. For each collision, the comprehensive list of final-state particles identified and reconstructed by the algorithm provides a global event description that leads to unprecedented CMS

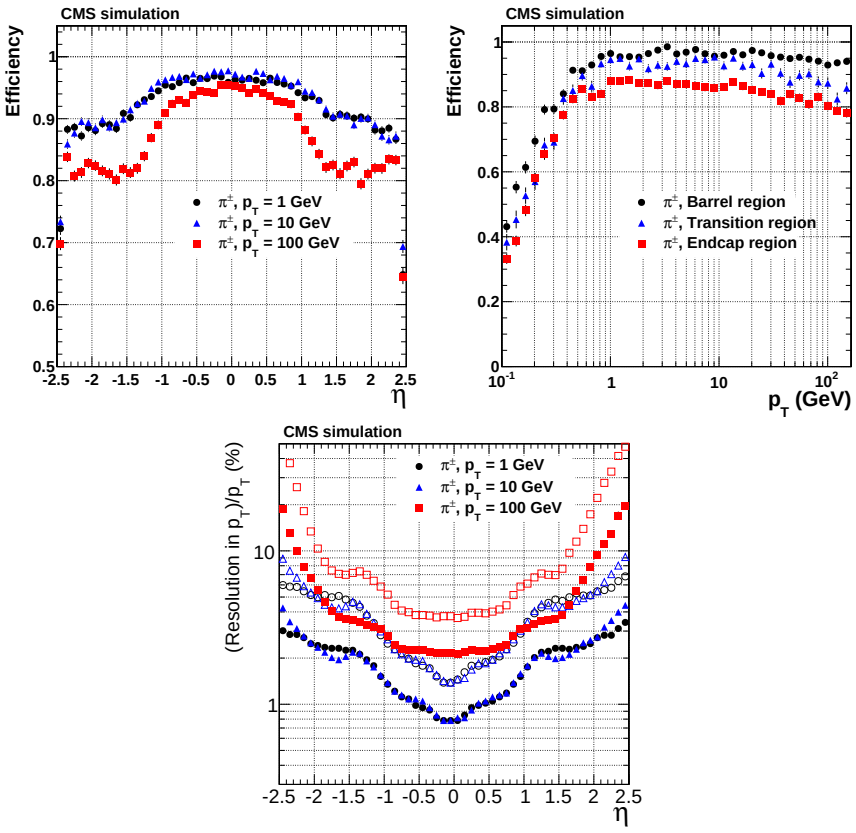

Figure 5.11: Upper panels: charged-particle track reconstruction efficiency for high-purity pion tracks as a function of η (left) and p_T (right). Lower panel: resolution in p_T for high-purity pion tracks as a function of η. The figures are extracted from Ref. (186).

performance for jet and hadronic tau decay reconstruction, missing transverse momentum determination, and electron and muon identification.

The PF algorithm (187) aims to reconstruct and identify each individual particle (physics-object) in an event, with an optimized combination of information from the various elements of the CMS detector. A schematic diagram with a slice of the CMS detector is shown in Fig. 5.10. The energy of unconverted photons is obtained from the ECAL measurement. The energy of electrons is determined from a combination of the electron momentum at the primary interaction vertex as determined by the tracker, the energy of the corresponding ECAL cluster matched to a track, and the energy sum of all bremsstrahlung photons spatially compatible with originating from the electron track. The energy of muons is obtained from the curvature of the corresponding track in the tracker and in the muon chambers. The energy of charged hadrons is determined from a combination of their momentum measured in the tracker and the matching ECAL and HCAL energy deposits, corrected for the response function of the calorimeters to hadronic showers. Finally, the energy of neutral hadrons is obtained from the corresponding corrected ECAL and HCAL energies. The missing transverse energy is calculated as the negative vector sum of the transverse momentum of the measured particles within the CMS acceptance, and may be used as a proxy for the undetected neutrino transverse momentum for certain data analyses. Dedicated identification and isolation criteria may be used for analyses that target the production of energetic photons, electrons, and muons, which is outside of the scope of this thesis.

Tracks are reconstructed with the standard iterative algorithm of CMS (186). To reduce the misidentification rate, tracks are required to pass standard CMS quality criteria. In the analyses presented in this thesis in Chapters 6 and 7, the charged-particle tracks used are part of the so-called *high-purity* track collection. High-purity tracks satisfy requirements on the number of hits and the χ^2 of the track-fit. The requirements are functions of the charged particle track p_{T} and η, as well as the number of layers with a hit. A more detailed

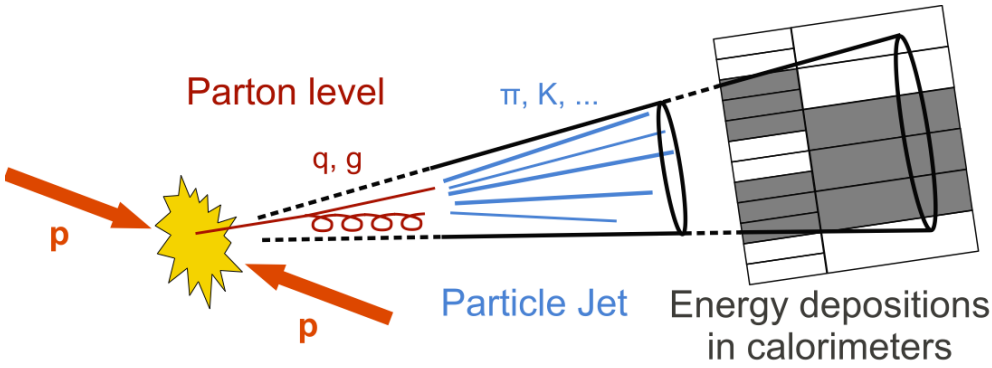

Figure 5.12: Schematic diagram of jet production in a proton-proton collision. The struck quark emits a shower of partons, which then transitions to a collection of collimated hadrons that are detected by the CMS tracker and calorimeters. The goal of the jet calibration is to optimize the jet response at detector-level relative to particle-level.

discussion of the combinatorial track finding algorithm and the definition of high-purity tracks is reported in Ref. (186). The reconstruction efficiency for high-purity tracks is about 75% with $p_{\mathrm{T}} > 200$ MeV. The candidate vertex with the largest value of summed physics-object p_{T}^2 is taken to be the primary pp interaction vertex. In the vertex fit, each track is assigned a weight between 0 and 1, which reflects the likelihood that it genuinely belongs to the vertex. The number of degrees of freedom in the fit is strongly correlated with the number of tracks arising from the interaction region, as described in Ref. (186).

A schematic diagram of jet production and reconstruction in CMS is shown in Fig. 5.12. The jets are clustered using the infrared- and collinear-safe anti-k_T algorithm (79; 188), with a distance parameter of $R = 0.4$, which is the standard distance parameter used for Run-2 analyses with CMS. The anti-k_T clustering is performed with the FastJet package (188). The jet momentum is determined as the vector sum of all particle momenta in the jet. The simulations show that the CMS detector response is within 5–10% of the true hadron-level momentum over a wide range of the jet p_T and η. The jet energy calibration is performed in sequential steps, which are graphically depicted in Fig. 5.13. Jet energy corrections are derived from simulation to bring, on average, the measured jet energies to the known energies at the generator level (189). *In situ* measurements of the momentum balance in dijet, photon + jet, Z + jet, and multijet events are used to correct any residual

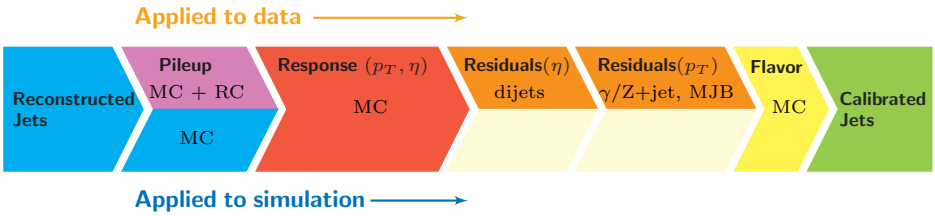

Figure 5.13: Sequential steps of the jet energy correction procedure of CMS, as applied in data and simulation. On the left, one starts with the uncorrected jet collection, and on the right one ends with the fully-calibrated jet collection. Figure extracted from Ref. (189).

differences in the jet energy scale in data and simulation (189).

The jet energy corrections have uncertainties of about 2% for jet $p_T \simeq 40$ GeV at central η, and increases to about 5% at forward η for the same jet p_{T} value. The simulated jet response as a function of the jet η for 2015 CMS data is shown in Fig. 5.14. The associated experimental uncertainties for the calibration of the jets is shown in Fig. 5.15. The jet energy resolution typically amounts to about 15% at 40 GeV, 10% at 100 GeV, and 4% at 1 TeV, and depends weakly on the amount of pileup, as shown in Fig. 5.16.

There are various effects that propagate as an uncertainty in the jet energy calibration (189). Time stability accounts for the time-dependent corrections, which mostly affect forward jets throughout a given run. The absolute scale uncertainty are extracted from the difference of a constant scale and p_T-dependent absolute scale extracted from global fits to Z+jet, γ+jet, and multijet data. The flavor response uncertainty accounts for the fact that jets come from different parton flavors (light-flavor jets, heavy-flavor jets, and gluon jets), which in principle have different responses in the detector. The flavor response differences are quantified by using different Monte Carlo event generators, whose jets are propagated through the data-based calibration chain.

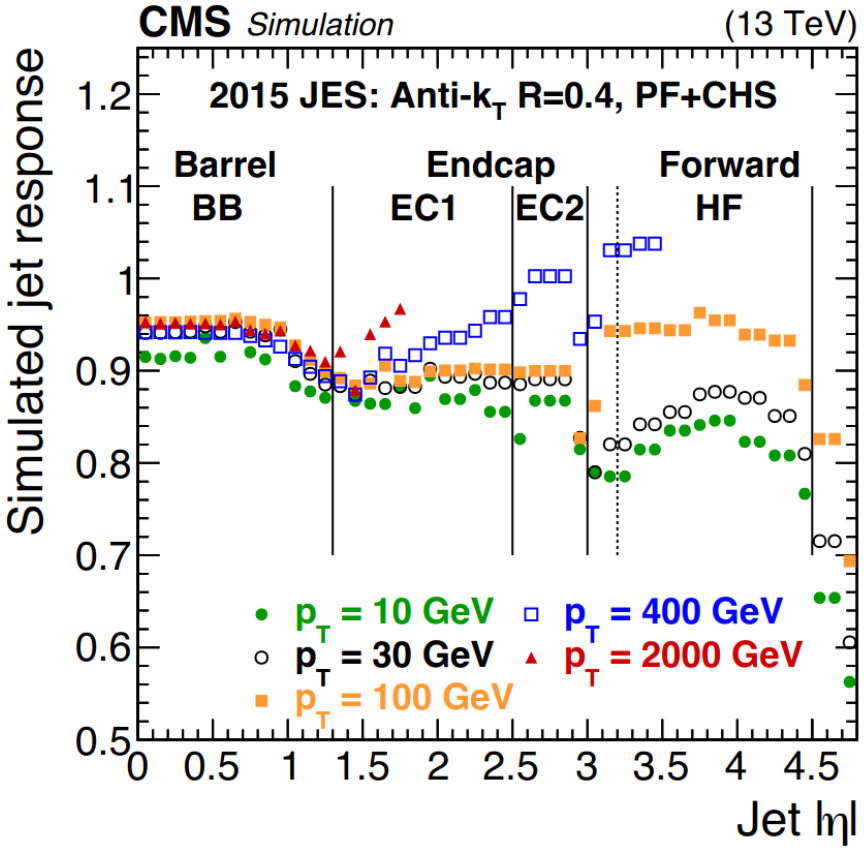

Figure 5.14: Simulated jet response in 2015 after pileup subtraction as a function of the jet pseudorapidity for different jet p_T.

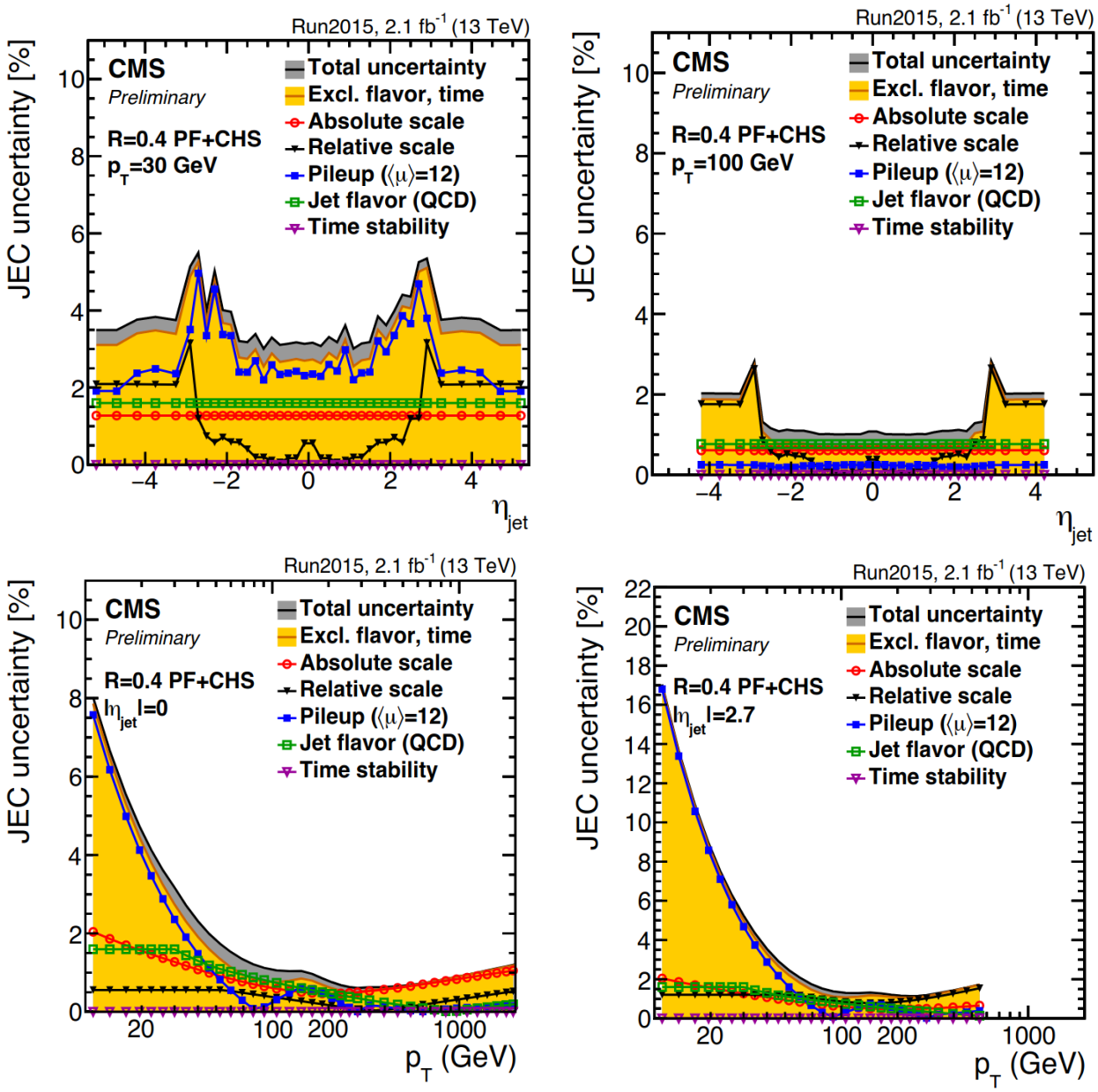

Figure 5.15: 2015 jet energy calibration as a function of the jet η for a pileup of $\mu = 12$.

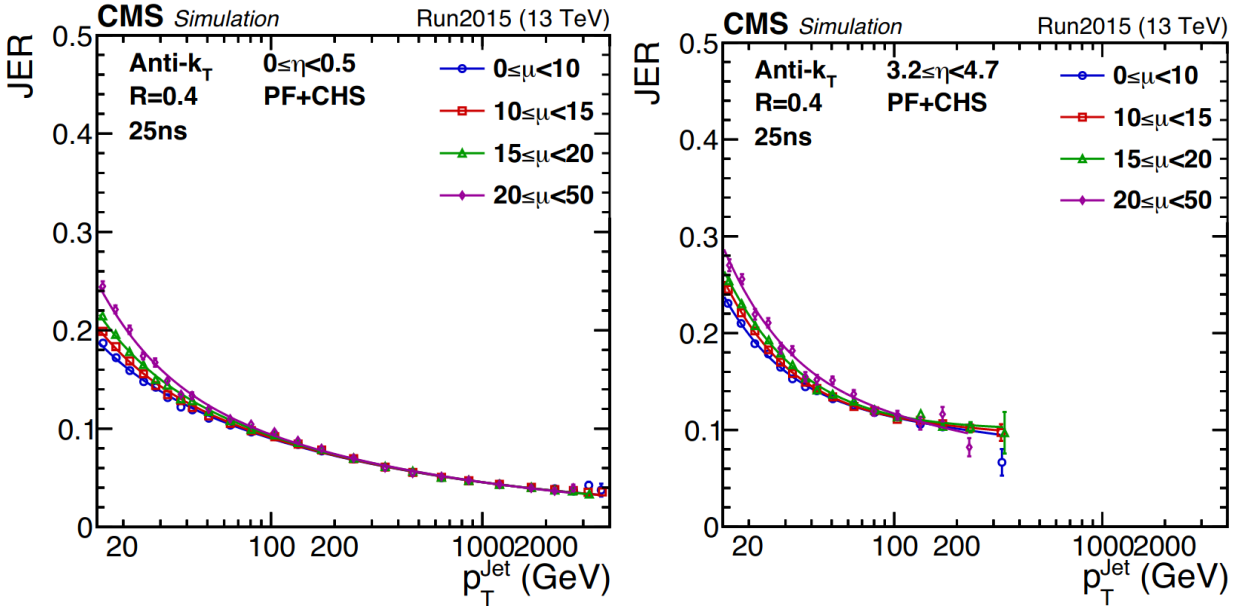

Figure 5.16: Jet energy resolution (JER) as a function of the jet p_{T} for anti-k_T jets with $R = 0.4$ in 2015. The resolution is of about 10% for $p_T > 100$ GeV. The left panel is for central jets $|\eta| < 0.5$, whereas the right panel is for forward jets $3.2|\eta| < 4.7$.

5.4 The TOTEM experiment

The proton spectrometer of the TOTEM experiment consists of two sets of near-beam telescopes, known as Roman pots (RP) stations: one on the left hand side of IP5 and one on the right hand side of IP5, which are known as sector 45 (positive pseudorapidities in the CMS coordinate system) and sector 56 (negative pseudorapidities in the CMS coordinate system) respectively, since they correspond to the regions connecting IP4 to IP5 and IP5 to IP6, respectively.

A RP is a movable beam-pipe insertion capable of approaching the LHC beam to a distance of less than a millimeter in order to detect protons deflected at small scattering angles (measured w.r.t. the beamline) of only a few microrradians. The RPs house silicon strip detectors, and can bring these very close to the beam without affecting the vacuum, beam stability, or other aspects of the accelerator operation. The scattered protons leave a linear track in these tracking detectors in the RPs. The data used in the analyses of Chapters 6, 7, and 8 have been collected with three RP station for each arm: 210-far, 220-near, 220-far in both sector 45 and sector 56. Such a configuration is shown in Fig. 5.17). A schematic layout of the silicon strip detectors on the transverse plane can be seen in Fig. 5.18. With slight abuse of terminology, we hereafter use "RPs" to refer to the silicon strip detectors housed in the RPs, as is often the standard. Before being detected, the protons' trajectories are influenced by the magnetic fields of the accelerator lattice, and the intact proton kinematics are reconstructed after modelling correctly the transport of the protons from the IP to the detector.

On the 2015 run, each RP station was located between $\pm$214.63 m and $\pm$220 m w.r.t. the IP5, and they are composed of two units: "near" ($\pm$214.63 m w.r.t. IP5) and "far" ($\pm$220 m w.r.t. IP5). A unit consists of 3 RPs labelled as "top", "horizontal" and "bottom", due to their positions relative to the beamline on the transverse plane. Each RP houses a stack of 10 silicon strip detectors with 66 μm pitch with a U-V layout, where U and V refer to two mutually perpendicular strip orientations (154), which provides spatial

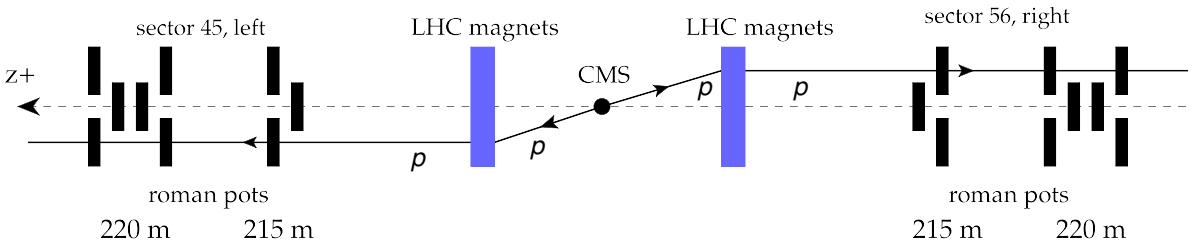

Figure 5.17: Configuration of CMS-TOTEM combined run set up in October 2015. The horizontal dashed line indicates the beamline. The CMS detector is symbolically denoted by the black dot in the center, where the dijet activity is measured, while the intact proton(s) are transported via the accelerator magnetic fields (denoted diagramatically by the blue rectangles), eventually passing through the silicon detectors housed in the RPs (denoted as the black rectangles) of the TOTEM experiment. Sector 45 is located towards the positive pseudorapidities in the CMS coordinate system, while sector 56 is located towards negative pseudorapidities in the CMS coordinate system.

track reconstruction resolution of 11 μm. The sensors were designed with the specific objective of reducing the insensitive area at the edge facing the beam to only a few tens of micrometers. Due to the 5 m long lever arm between the near and far RP units, the local track horizontal and vertical scattering angles can be reconstructed with a precision of about 3 μ rad.

Special high-β^* LHC running conditions, where β^* is the amplitude function at the IP, were designed in order to optimize the kinematic acceptance and reconstruction of the scattered intact protons that arrive at the RPs after traversing the LHC magnetic lattice segment around IP5. β^* is determined by the accelerator magnet configuration (the quadrupole magnet arrangement) and powering of the machine. Nominally, for the Run-2 instantaneous luminosities delivered by the LHC, the amplitude function is set to values of $\beta^* = 0.4$ m on the basis that one wants to achieve the highest instantaneous luminosity as possible (the beams are spatially squeezed). The $\beta^* = 90$ m optics have been found to be the best option for hard diffractive studies (154), which allows for a better reconstruction of the proton kinematics. The TOTEM Collaboration has published results on elastic scattering, total cross section measurement, and hard diffraction using these optics settings, proving that the chain of alignment, accelerator magnetic lattice parametrization

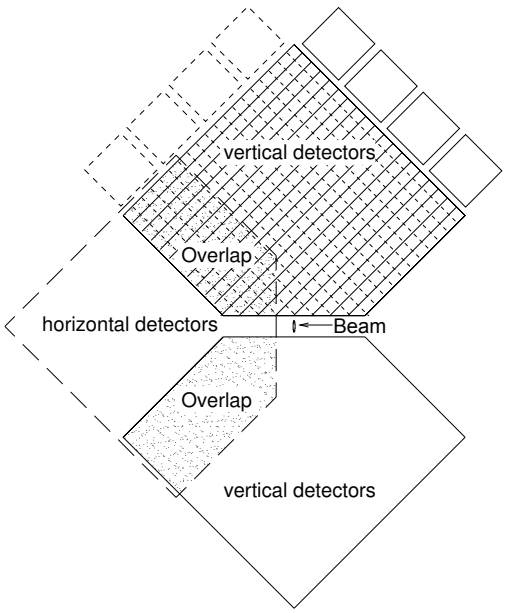

Figure 5.18: Schematic diagram of a plane of silicon detectors housed in the RP detectors of TOTEM. We distinguish top, bottom and horizontal RPs. The layout is on the plane transverse to the beam. The shaded region shows the overlap between the detectors in a single plane.

and physics chain is well-understood (190; 191; 192).

5.4.1 Proton kinematics reconstruction

The RPs are aligned following the standard techniques developed by the TOTEM Collaboration. The trajectory of the protons produced with transverse position x^*, y^* at IP5 (with values of the order of $\sim$ 10mm) relative to the beamline, and horizontal and vertical scattering angles, denoted respectively as θ_x^* and θ_y^* (with values of the order of $\sim 10\mu$ rad), and the longitudinal fractional momentum loss of the intact proton $\xi = \Delta p/p$, where p and Δp are the nominal beam momentum and the proton longitudinal momentum loss, respectively, is described by the linear equation,

$$\vec{d} = T(s) \cdot \vec{d}^* \tag{5.3}$$

where $\vec{d} = (x, \theta_x, y, \theta_y, \xi)$ is a five-entry vector containing the vertical and horizontal

scattering angles (θ_x, θ_y), transverse positions (x,y), and the fractional momentum loss of the proton ξ, all of them measured after the proton is transported to the RP stations at a distance s with respect to the IP. The superscript * is used for the same set of variables at the IP, before any magnetic transport effects have taken place. The proton transport equation has to be inverted in order to reconstruct the proton kinematics at the IP. The matrix $T(s)$ is known as the single-pass proton transport matrix or simply as the transport matrix, and its elements are defined in terms of optical functions (193; 194). The x coordinate is directly related to the measurement of ξ, following a linear relation in first approximation. For $\xi \approx 0$, the transferred four-momentum square is related to the scattering angles at the interaction vertex via $t = -p^2(\theta_x^{*2} + \theta_y^{*2})$, where p denotes the beam momentum. Generally, $t = (p_f - p_i)^2$, where p_f and p_i are the four-momenta of the final- and initial-state protons. With these optics settings, the acceptance is extended to reconstruct intact protons that have lost up to ∼25% of the initial beam energy during the running conditions at $\beta^* = 90$ m. The single proton trigger and track reconstruction efficiency is close to 99%.

5.5 Precision Proton Spectrometer

The TOTEM RP detectors based on silicon strip detectors, as well as the techniques used to reconstruct the proton kinematics, are not optimized for operation at high pileup conditions with the standard $\beta^* = 0.4$ m optics of the LHC (low β^*). For the nominal instantaneous luminosities at the LHC, we need detectors that are radiation hard, and another strategy for the reconstruction of the proton kinematics and alignment of the detectors. This is because, with $\beta^* = 0.4$ m optics, there are no other.

The Precision Proton Spectrometer (PPS) system of the CMS and TOTEM experiments is used to investigate photon-exchange processes in pp collisions ($pp \to pXp$, where X is a system produced by $\gamma^*\gamma^* \to X$ collisions), whose production rate is much smaller than those of hard diffractive interactions (195; 196). Based on the previous experience with

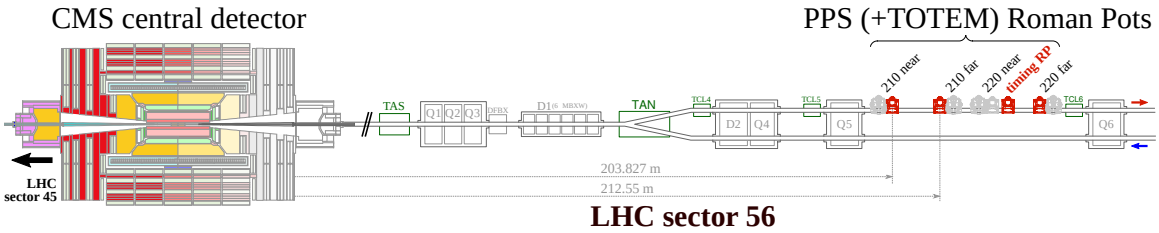

Figure 5.19: Schematic diagram of the Precision Proton Spectrometer (PPS) system in sector 56 (negative pseudorapidities).

the CMS-TOTEM low-luminosity, high β^* special runs, this reinvigorated the efforts for a joint project for measuring the rarer two-photon exchange processes. The detector technology, alignment, trigger, and calibration of such a system is optimized for the higher beam-background environment present in standard high luminosity runs. Another challenge to face is that, for the smaller $\beta^* = 0.4$ m conditions, it is not possible to use the vertical and horizontal RPs simultaneously during the physics runs. This means that the procedure for reconstructing the proton kinematics is distinct from the experience at larger β^*, where the use of vertical and horizontal RPs is possible. The PPS system has been successfully brought online for data taking in 2016, effectively acting as another subdetector of the CMS experiment during the rest of Run-2 (2016, 2017, and 2018 years). A schematic diagram of the PPS system is shown in Fig. 5.19. The ATLAS experiment brought online an analogous experimental setup, known as ATLAS Forward Proton (AFP), in 2017.

The author of the present thesis contributed to the alignment and calibration of pre- and post-TS2 2017 data of the PPS detector. The offline alignment of the PPS detector is absolutely necessary to reconstruct the proton object. (see Fig. 5.21, for an example of the horizontal calibration of the PPS as a function of time for different data streams). The particle physics phenomenology studies quoted in Chapter 9 of this thesis are based on the PPS capabilities. The data analyses of Chapters 6, 7, and 8 presented in this thesis do not rely on the PPS system.

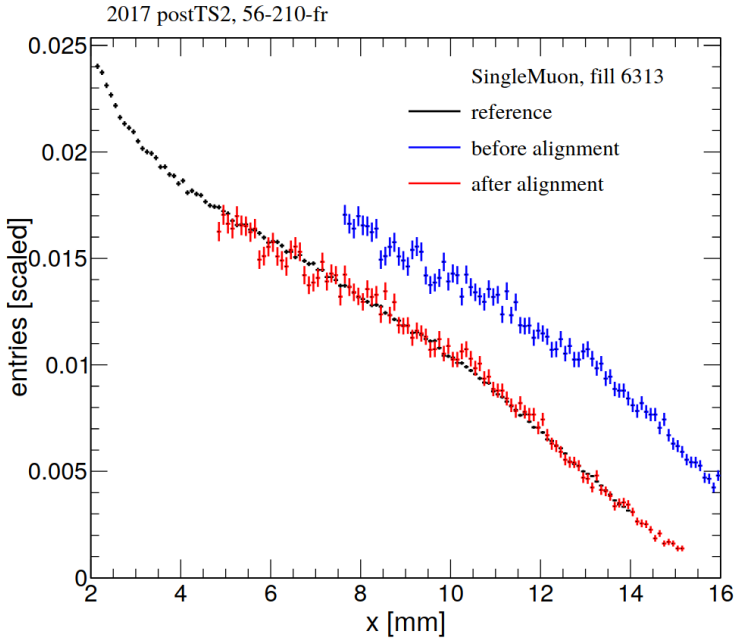

Figure 5.20: Horizontal alignment of the PPS detector. The black data points ("reference") represents the fully calibrated data from the reference run. The blue histogram represents the data from the physics run from the SINGLEMUON data stream. The calibration is such that the blue histogram is shifted to the left to obtain the best match with the reference calibration data.

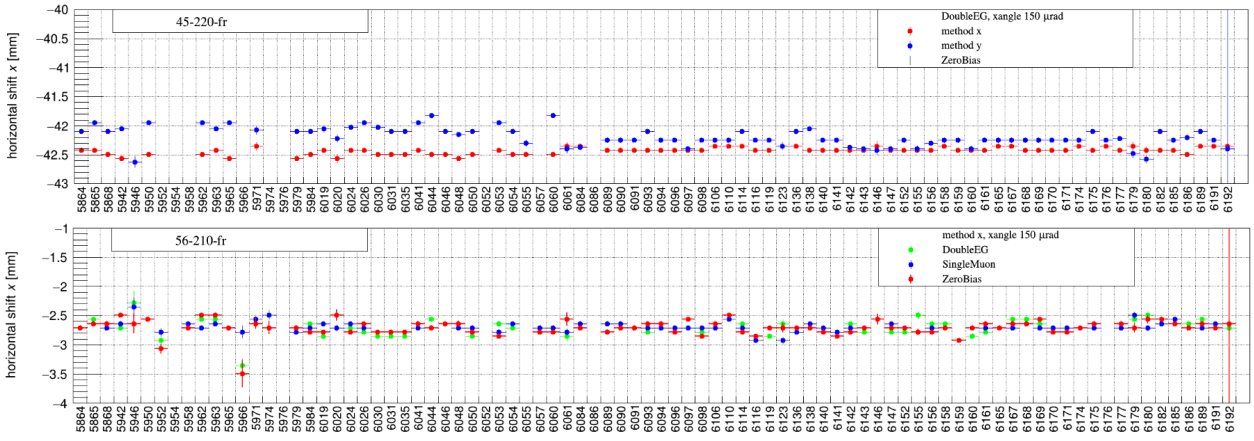

Figure 5.21: Subset of figures for the horizontal alignment of the PPS for 2017 pre-TS2 data. The upper panel Plot created by the author of the thesis.

5.6 Summary of the Chapter

We have given an overview of the CERN LHC, and the CMS and the TOTEM experiments. The CMS detector allows for the reconstruction of energetic jets –collimated sprays of hadrons–, which can be used to further understand strong interactions. The TOTEM experiment can be used to study special reactions with forward intact protons, which are scattered at small angles with respect to the beam, which are detected with Roman pot detectors located in the forward region. Special runs where both experiments collect data simultaneously can be used to study hard diffractive reactions with intact protons and jets. Together with the theoretical context and motivation laid down in Chapter 4 for the study of jets separated by a pseudorapidity gap and the study of jet production with intact protons, we are now ready to discuss the data analyses carried out by the author in Chapters 6, 7, and 8.

Chapter 6

Analysis of hard color-singlet exchange in dijet events in proton-proton collisions at $\sqrt{s} = 13$ TeV

In this Chapter and Chapter 7, we describe the main measurement of this thesis, namely the measurement of hard color-singlet exchange in dijet events in pp collisions at $\sqrt{s} = 13$ TeV with the CMS and TOTEM experiments. The physics motivation is presented in Section 4.2.5 of Chapter 4. In this Chapter, we focus on the analysis of jet-gap-jet in inclusive dijet production (dubbed "CMS-only" analysis). In Chapter 7, we discuss the study of jet-gap-jet events with an intact proton (p-gap-jet-gap-jet diffractive topology) with the CMS-TOTEM combined data sample (the "CMS-TOTEM" component of the analysis). A summary of the whole hard color-singlet exchange analysis is presented at the end of Chapter 7. An Appendix with supplementary analysis information is found at the end of this thesis. The author of this thesis was the analysis contact person and main author of the data analysis (CMS-SMP-19-006 and CMS internal analysis note AN-18-174). The results presented in this Chapter and Chapter 7 are direct contributions from the author. The corresponding CMS-TOTEM paper was published in Phys. Rev. D (1).

6.1 Color-singlet exchange in partonic scattering

As mentioned in Section 4.2.5 of Chapter 4, we can isolate the onset of BFKL dynamics in events where two jets are separated by a large pseudorapidity gap, an η interval between the jets that is void of particle radiation (125). The pseudorapidity gap is created

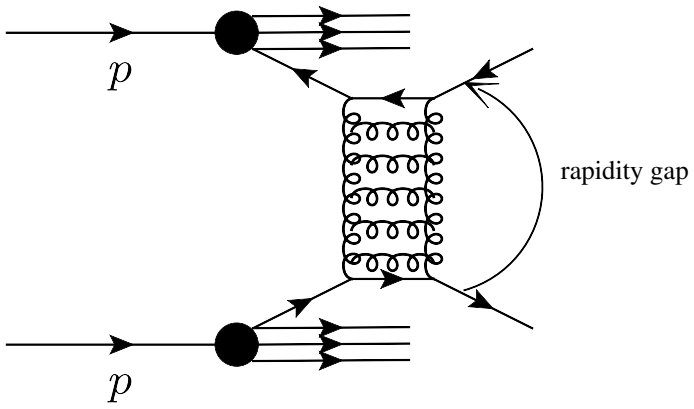

Figure 6.1: Schematic diagram of a gluon ladder exchange in a pp collision, which yields the jet-gap-jet signature. The two-gluon ladder exchange leads to a rapidity gap between the jets. $qq \to qq$ scattering is shown explicitly, but the gluon ladder can be exchanged in $gg \to gg$ and $qg \to qg$ scattering as well.

by strongly interacting color-singlet exchange (124) (see Fig. 6.1). In QCD, the simplest color-singlet exchange consists of the t-channel two-gluon exchange between partons. In the limit where the center-of-mass energy of the colliding partons is much larger than any other energy scale, this simple t-channel two-gluon exchange process is enhanced due to the multiple virtual gluon exchanges that become relevant in this regime of QCD interactions. In the BFKL framework, this corresponds to perturbative pomeron exchange. The larger the pseudorapidity separation between the jets is, the more important the onset of BFKL dynamics becomes since $\Delta\eta_{jj} \approx \ln(\hat{s}/|\hat{t}|)$ (for massless particles). Color-exchange dijet events, which dominate the inclusive dijet cross section and where the inter-dijet radiation is successfully described by the DGLAP evolution, is heavily suppressed when the condition of a pseudorapidity gap between the jets is applied. A detailed discussion of the phenomenology of jet-gap-jet events, as well as the previous measurements of this process, is covered in Section 4.2.5 of Chapter 4.

The main observable of interest for this measurement is the fraction of color-singlet exchange events f_{CSE}, also called gap fraction, which is defined by

$$f_{\mathrm{CSE}} = \frac{\mathrm{d}N}{\mathrm{d}\mathscr{O}}^{\mathrm{singlet}} \Big/ \frac{\mathrm{d}N}{\mathrm{d}\mathscr{O}}^{\mathrm{all}} \tag{6.1}$$

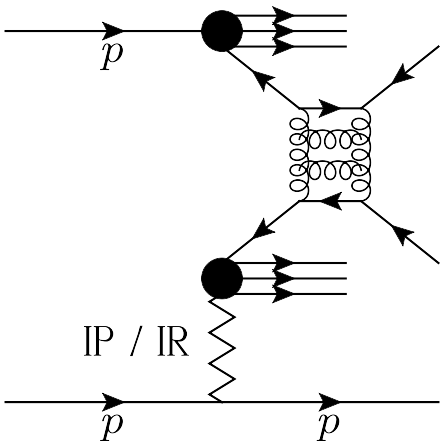

Figure 6.2: Schematic diagram of a hard color-singlet exchange (large four-momentum transfer squared $-t \sim \mathcal{O}(10^3)\ GeV^2$) in a hard single diffractive process (coherent color-singlet exchange emitted off the proton which carries low transferred four-momentum squared $-t \sim \mathcal{O}(1)\ GeV^2$). The jet-gap-jet signature is reconstructed in the CMS detector, while the surviving intact proton is tagged with the forward proton spectrometer of TOTEM. This process is discussed on a second part of this analysis in Chapter 7.

where $\frac{dN}{d\mathcal{O}}^{\text{singlet}}$ is the yield for dijet production where a color-singlet exchange has taken place (leading to a jet-gap-jet topology) and $\frac{dN}{d\mathcal{O}}^{\text{all}}$ is the yield for inclusive dijet production, including dijet production with and without color-singlet exchange, and $\mathcal{O}$ can be any kinematic variable of the dijet system of interest (pseudorapidity separation between the leading momentum jets, transverse momenta of the jets, azimuthal angle separation between the jets, or others). The fraction f_{CSE} quantifies the nature of the strongly interacting color-singlet exchange relative to the net color-exchange dijet events (126; 129; 130; 128; 131).

As mentioned also in Chapter 4, it has been suggested that the jet-gap-jet process can be better analyzed in single-diffractive or double-pomeron exchange dijet events using the proton tagging technique (153). It is expected that the soft rescattering effects that destroy the central rapidity gap would be suppressed in single-diffractive or double-pomeron exchange processes, since there are no remnant partons in the collision from both protons being destroyed that would produce additional radiation in the central gap between the jets. We study for the first time the hard color-singlet exchange carrying a

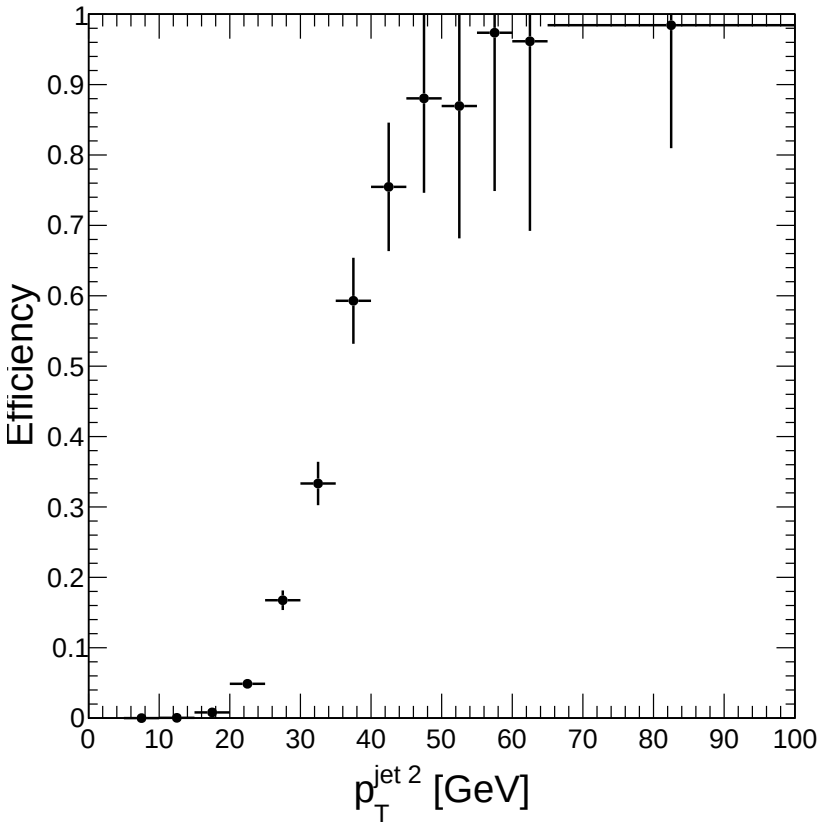

Figure 6.3: Dijet trigger efficiency as a function of the subleading jet transverse momentum $p_{\mathrm{T,\,jet\,2}}$. The trigger efficiency is estimated from data based on a zero-bias triggered sample collected during the same runs.

large amount of momentum transfer in single diffractive dijet events, as in Fig. 6.2. The scattered intact proton in these diffractive processes $pp \to pX$ can be measured with the dedicated forward proton spectrometers of the TOTEM experiment located at about 210 m with respect to the CMS detector nominal interaction point. This aspect of the measurement is discussed separately in Chapter 7.

6.2 Data sample and trigger selection

The data used in this analysis were collected in a combined run by the CMS and TOTEM detectors at the LHC in pp collisions in October 2015, when the LHC operated at $\sqrt{s} = 13$

TeV with low probability of overlapping pp interactions in the same bunch crossing (pileup). The measured amount of pileup ranges from $\mu = 0.05 - 0.10$ secondary interactions per bunch crossing. These low pileup conditions are ideal and necessary for studies of events with a diffractive exchange signature, since the rapidity gaps could be destroyed by the overlapping additional pp interactions. In addition, low pileup conditions allow the measurement of very forward-backward dijet configurations originating from the same pp collision, which are otherwise highly contaminated by jet production in uncorrelated multiple pp collisions in the same bunch crossing. The instantaneous luminosity was of 4×10^{30}–13×10^{30} cm^{-2} s^{-1}. The integrated luminosity for the CMS data set alone is of 0.66 pb^{-1}.

The data were collected online with an unprescaled inclusive dijet trigger which requires the presence of at least two jets with minimum transverse momentum of 32 GeV in $|\eta| < 5$ (`HLT_DoubleJet32`). There are 25 million dijet events recorded on tape for offline analysis. We used the CMS-TOTEM end-of-year reprocessing dijet samples. . About 7 M events from a zero-bias dataset (non-empty bunch crossings) is used for checks when needed throughout the analysis. The trigger efficiency is estimated from data using a sample of dijets in the zero-bias sample, and is found to be nearly 100% efficient at $p_{\mathrm{T,\,jet\,2}} = 50$ GeV, as can be seen in Fig. 6.3.

About 90% of dijet events have a single vertex reconstructed, consistent with the number of pileup interactions during the special run. The pseudorapidity distribution and transverse momentum distribution of each charged particle track for dijet events satisfying our event selection are presented in Fig. 6.4. Charged particles are distributed uniformly in the central region $-1 < \eta < 1$ and carry mostly low transverse momentum. The N_{tracks} in $-1 < \eta < 1$, for charged particles with $p_{\mathrm{T}} > 200$ MeV can be seen in Fig. 6.5. The N_{tracks} where the BFKL jet-gap-jet signal could manifest is seen in Fig. 6.6.

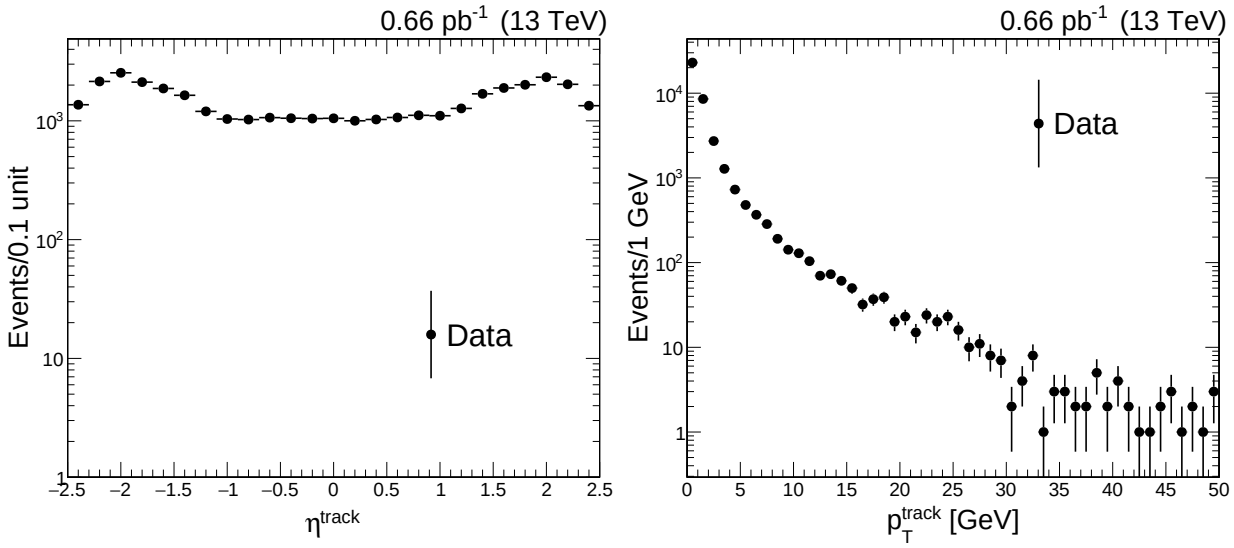

Figure 6.4: Pseudorapidity and transverse momentum distributions of charged particles for jets satisfying $|\eta_{\text{jet1,2}}| > 1.4$, $\eta_{\text{jet1}}\eta_{\text{jet2}} < 0$ and $p_{\text{T,jet1,2}}$.

6.3 Monte Carlo simulated samples

Although the main results of the analysis do not rely on Monte Carlo simulated events, these are used to give further confidence on the data-driven techniques used to estimate the color-exchange background contributions and for additional consistency checks and guidance throughout the analysis.

Two sets of Monte Carlo generated samples are used. The first one is related to inclusive dijet production simulated in `Pythia8` with the underlying event tune CUETP8M1, using leading-order matrix elements for $2 \to 2$ partonic processes, with initial- and final-state radiation effects turned on. No hard color-singlet exchange effects are included in this sample. The second set corresponds to the simulation of color-singlet exchange dijet events embedded in the `Herwig` 6.5 Monte Carlo event generator (subprocess with IPROC 2400 on). This implementation is based in BFKL leading-logarithm calculations of the Mueller-Tang process. Neither `Pythia8`, nor `Herwig++`, nor other standard modern Monte Carlo generators count with such subprocess, which is why we rely on `Herwig` 6.5 for the full detector simulation of color-singlet exchange dijet events. Both sets have no

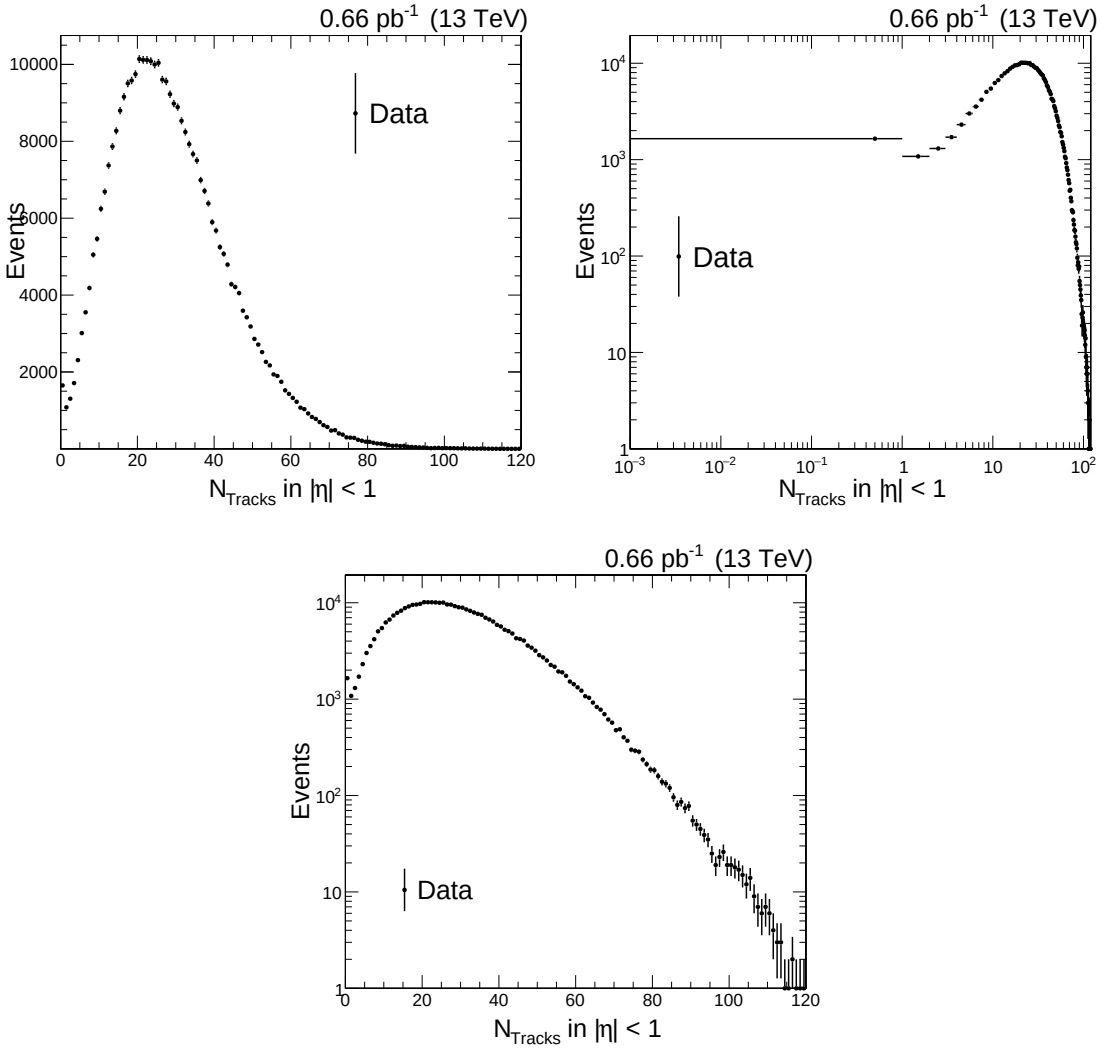

Figure 6.5: N_{tracks} in the fixed pseudorapidity region $|\eta| < 1$ for dijet events satisfying $p_{\text{T,jet2}} \geq 40$ GeV, $1.4 < |\eta_{\text{jet}}| < 4.7$, $\eta_{\text{jet1}}\eta_{\text{jet2}} < 0$. For visualization purposes, we show the same distrbution in different combinations of linear and logarithmic scales in the horizontal and vertical axis. There is an excess at $N_{\text{tracks}} = 0$ in an otherwise smooth distribution.

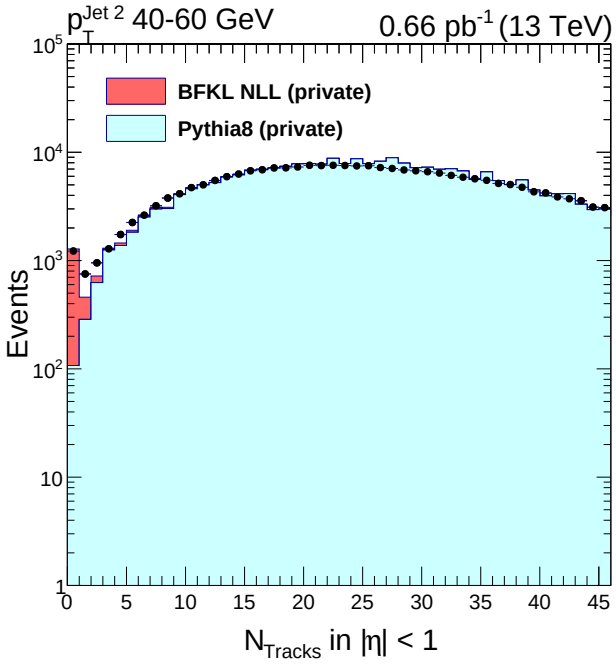

Figure 6.6: N_{tracks} in the fixed pseudorapidity region $|\eta| < 1$ for dijet events satisfying $|\eta_{\text{jet}}| > 1.4$, $p_{\text{T,jet}} = 40$–60 GeV, $\eta_{\text{jet1}}\eta_{\text{jet2}} < 0$. Hadron-level predictions for jet-gap-jet events from BFKL at NLL (red) simulated in HERWIG 6.5 and for inclusive dijet production with LO PYTHIA 8 (blue) are shown here for illustrative purposes (normalized to describe data). The jet-gap-jet signal predicted by BFKL is localized at low N_{tracks}. The Monte Carlo simulated histograms are normalized to reproduce the data.

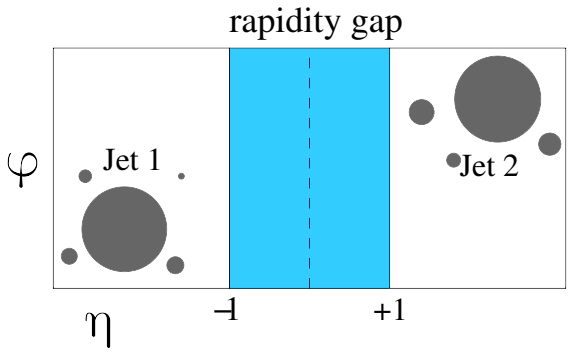

Figure 6.7: Jet-gap-jet event signature in the $\eta - \phi$ plane. The blue area represents the fixed pseudorapidity region $-1 < \eta < 1$ where the N_{tracks} distribution is measured in this analysis.

pileup simulation, since our data sample has pileup of 0.05–0.10 interactions per bunch crossing.

6.4 Event selection

The jet-gap-jet signal events are located at very low charged particle multiplicities in the central pseudorapidity region between the leading two jets (see schematic diagram Fig. 6.7). Thinking of this, the event selection requirements are:

- *Events are required to have at least two jets that pass the CMS jet identification criteria*; there is no requirements for additional jets in the event.

- *The two leading jets must lie in opposite hemispheres of the CMS detector,* $\eta_{jet\ 1}\eta_{jet\ 2} < 0$, *and have pseudorapidity values of* $1.4 < |\eta_{jet\ 1,\ jet\ 2}| < 4.7$. This widens the phase space necessary for the color-singlet exchange process to take place and make the signal easier to isolate from the color-exchange background. The minimum value of pseudorapidity was chosen as $|\eta_{\text{min}}| = 1.4$ since jets have a distance parameter $R = 0.4$, the standard radius used by CMS for 13 TeV analyses, and the fixed pseudorapidity region used to measure the N_{tracks} is located in $|\eta| < 1$. The bound at $|\eta_{\text{max}}| = 4.7$ is due to the acceptance of the CMS detector. With this selection, we can reach pseudorapidity differences between the leading two jets in $2.8 < \Delta\eta_{jj} < 9.4$ units.

- *The two leading jets have a minimum transverse momentum* $p_{\mathrm{T}} \geq 40$ *GeV*. This selection ensures a large amount of dijet events for this analysis. The trigger is not 100% efficient until about 50 GeV of the subleading jet transverse momentum, but since our main results are presented in ratios of yields of dijet events, these effects cancel in the ratio. In addition, it is important to make the comparison within a similar phase space integration volume as the one in the 7 TeV analysis, where the minimum transverse momentum was of the subleading jet was of $p_{\mathrm{T}} > 40$ GeV as well (152).

- *The number of primary vertices in the event is required to be at most one*. This selection is mainly for pileup rejection purposes. A vertex with a minimum of 2 degrees of freedom is considered a primary vertex in our selection. The zero vertex selection retains dijet events with a rapidity gap within the tracker volume, which might yield no reconstructed vertex since there are not enough reconstructed charged particle tracks for the vertex finding algorithm to work properly. In addition, jets in the forward region (mainly HF jets), which are of extreme importance for this analysis, are more likely to yield no reconstructed vertex, so it is important to retain them with the zero vertex selection. We confirmed, based on data, that the dijet distributions of single vertex dijet events and zero vertex dijet events have the same characteristic $\Delta\phi_{\mathrm{jj}}$ and $p_{\mathrm{T,jet2}}/p_{\mathrm{T,jet1}}$ distributions (see Fig. 6.9), including very forward-backward dijet configurations. If the zero vertex events were dominated by pileup, we would observe a rather uniform component on these distributions, as expected from jets arising from uncorrelated secondary interactions in the same bunch crossing, confirming that the zero vertex selection is safe for this measurement and that the very low pileup conditions are ideal for the measurement.

- The primary vertex is required to be within a longitudinal distance $|z| < 24$ cm with respect to the nominal interaction point of CMS.

There are $362,915$ dijet events passing the above selection requirements.

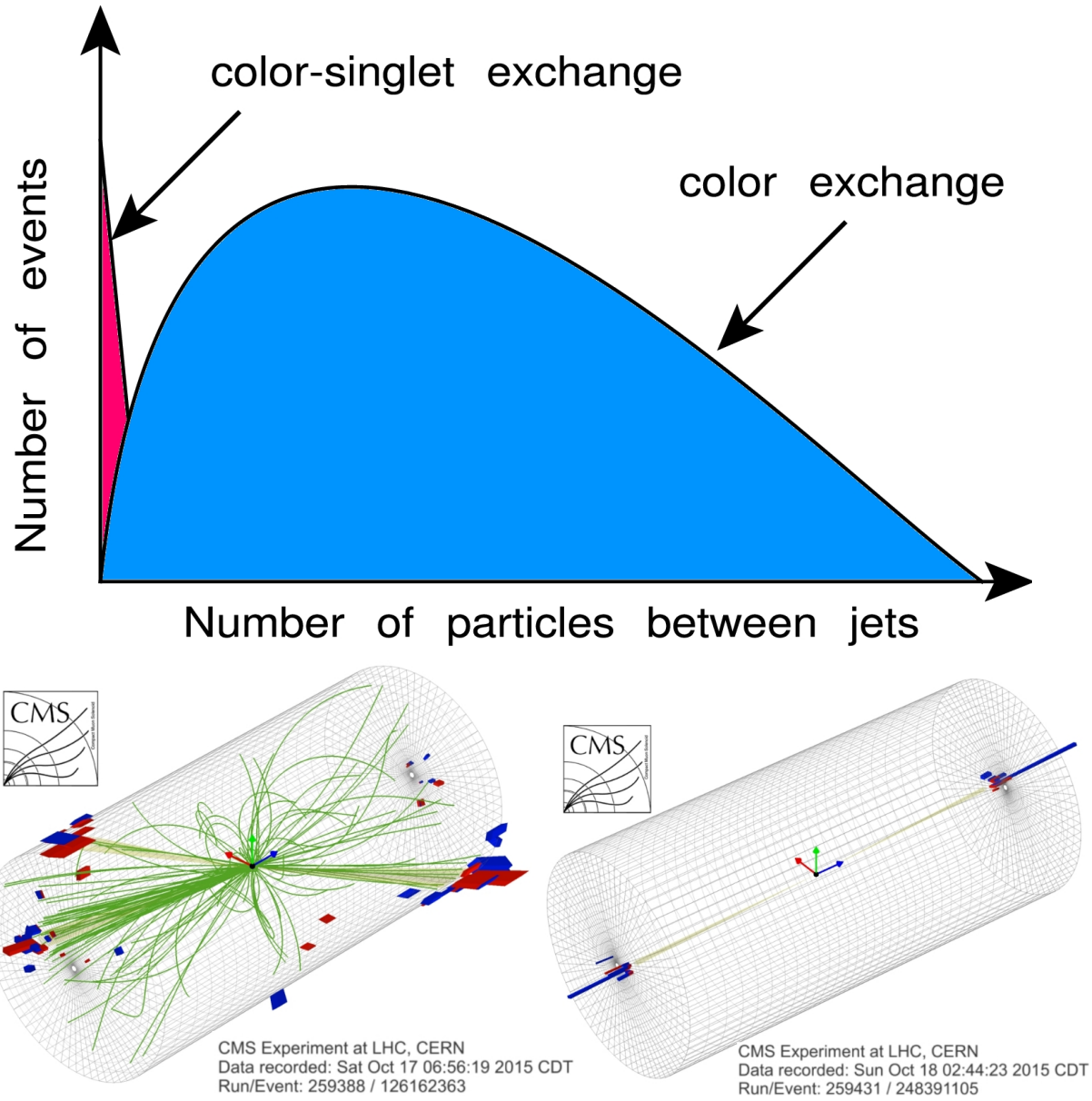

Figure 6.8: Event display for a background-like color-exchange dijet event candidate (left) and for a hard color-singlet exchange dijet event candidate (right). The events pass the selection criterion described in the text. Schematic diagram of the contribution of color-exchange dijet events and color-singlet exchange dijet events by analyzing the particle multiplicity between the two hardest jets. The magenta peak on the left-hand side of the plot represents the expected signature of the color-singlet exchange dijet events over the smooth background coming from color-exchange dijet events.

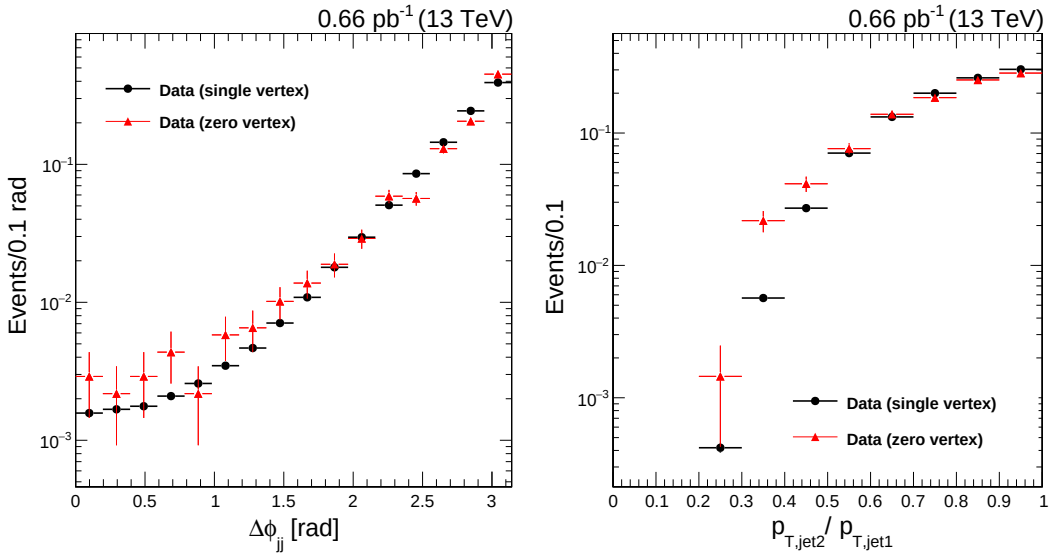

Figure 6.9: Azimuthal angle separation between the leading two jets and the ratio of the transverse momentum of the subleading jet to the transverse momentum of the leading jet within the single vertex and zero vertex subsamples. Both distributions are normalized to unity. Dijet events satisfy the $|\eta_{\text{jet}}| > 1.4$, $\eta_{\text{jet1}}\eta_{\text{jet2}} < 0$ and $p_{\text{T}} \geq 40$ GeV. If the backward and forward jets were originated from uncorrelated interactions (pileup), the distributions for the zero vertex sub-sample would yield a uniform distribution. The single vertex and zero vertex yield compatible results, confirming that the pileup contamination is negligible in this analysis, and it is safe to use the zero vertex sample.

One way to discriminate between the color-singlet exchange (CSE) events from the color-exchange (CE) events is via the charged multiplicity distribution in a fixed pseudorapidity region between the two leading jets, where the CSE signal populates the lowest multiplicity bins. The charged particle multiplicity (N_{tracks}) is defined as the number of reconstructed charged particles, where each charged-particle track has a minimum transverse momentum of $p_{\text{T}} > 200$ MeV in the fixed pseudorapidity interval $-1 < \eta < 1$. This thresholds ensures good track reconstruction efficiency in the barrel region for high-purity pion tracks (186), and is low enough to allow a separation of the color-singlet exchange signal events from the background events. In addition, the measured relative transverse momentum resolution of each charged particle is required to be smaller than 10%; this reduces the contribution from tracks not associated with the primary vertex, badly reconstructed tracks, and low-quality tracks. The last requirement follows the standard of previous CMS analyses on charged particle spectra in minimum-bias events at 13 TeV (197) as well as the measurement of the inelastic pp cross section at 13 TeV (198). Reconstructed charged particle tracks satisfy the *high-purity* criteria of CMS described in Ref. (186). The chosen pseudorapidity range (central region) ensures high reconstruction efficiency of charged particle tracks (especially for charged pion tracks) and, at the same time, is large enough to suppress the contribution from gaps produced via color-exchange fluctuations in the lowest multiplicity bins. There are 1650 dijet events with $N_{\text{tracks}} = 0$, which are mostly jet-gap-jet signal events. The two leading jets are separated by at least 2.8 units of pseudorapidity. The fixed pseudorapidity interval is far from the edges of the jets since each of the leading jets has a pseudorapidity $|\eta_{\text{jet1,2}}| > 1.4$ and distance parameter $R = 0.4$, the standard jet size used for 13 TeV analyses in CMS. This definition of the gap also allows for a more direct comparison with previous measurements at the Tevatron and at the LHC carried out at lower $\sqrt{s}$.

An enlarged fixed pseudorapidity interval does not change the conclusions of the analysis. Enlarging the interval biases the N_{tracks} distribution towards larger multiplic-

ities, including the jet-gap-jet signal region. In addition, jet-gap-jet signal events with pseudorapidity gap intervals larger than the interval used in the analysis $-1 < \eta < 1$ are kept as signal events with this definition, so they are not excluded from the analysis.

A "floating" pseudorapidity gap, which is defined event-by-event depending on the pseudorapidity values of each of the two leading jets, is not restricted to the same interval of Lorentz boosts of the partonic system of the "fixed" pseudorapidity gap method described above. However, it is more difficult to control the various sources of experimental uncertainties with the floating gap method, since different sections of the detector are used event-by-event. For this reason, larger energy thresholds would become necessary for some of the dijet configurations, which is not ideal for a jet-gap-jet analysis. On the other hand, the fixed pseudorapidity gap method is capable of separating jet-gap-jet contributions from color-exchange dijet contributions, and at the same time keeps the various sources of systematic uncertainties under control. An additional advantage of using the fixed pseudorapidity gap method is that it allows for a more direct comparison with previous measurements at lower $\sqrt{s}$, which is highly important to understand the role of the gap survival probability in proton-(anti)proton collisions.

At the beginning of this analysis, we examined the possibility of using the particle-flow objects of CMS to define the pseudorapidity gap. Unfortunately, the thresholds cannot be arbitrarily lowered to the 200 MeV scale as with charged tracks. Instead, the thresholds should be set on the order of 0.5 GeV and 1 GeV for photons and neutral particles respectively (calorimeter noise level), which leads to a larger contamination of non-CSE events in the signal region than it is desired, and is not ideal for the jet-gap-jet analysis. We verified that low charged particle activity is correlated with low neutral hadron and photon multiplicities within the same pseudorapidity region, as it should for a jet-gap-jet process.

Some of the important kinematic features of color-singlet exchange dijet candidate events are shown in Fig. 6.10. Events with $N_{\text{Tracks}} = 0$ are dominated by color-singlet

exchange, while events with $N_{\text{Tracks}} \geq 3$ are dominated by color-exchange dijet events. Jet-gap-jet candidates are strongly correlated in their transverse momenta and the azimuthal angle separation between the jets. The jet multiplicity with jets of $p_{\text{T}}^{\text{extrajet}} \geq 15$ GeV are shown on the bottom of Fig. 6.10. The majority of the jet-gap-jet candidates are pure dijet events. The presence of additional jets for jet-gap-jet candidates can be attributed to hadronization effects (verified in Monte Carlo generated events).

6.5 Observable

We measure the color-singlet exchange fraction f_{CSE}, also known as f_{CSE} fraction, which is defined as

$$f_{\text{CSE}} = \frac{N_{\text{events}}^{\text{F}} - N_{\text{non-CSE}}^{F}}{N_{\text{events}}} \equiv \frac{\text{Number of jet-gap-jet events}}{\text{Number of dijet events}} \tag{6.2}$$

where $N_{\text{events}}^{\text{F}}$ is the number of events in the three first bins of the multiplicity distribution $N_{\text{tracks}} < 3$, $N_{\text{non-CSE}}^{F}$ is the number of events with a central rapidity gap ($N_{\text{tracks}} < 3$) coming from dijet events with no color-singlet exchange (requires modelling), and N_{events} is the total number of dijet events with $N_{\text{tracks}} \geq 0$ (includes both non-CSE and CSE contributions). The yields $N_{\text{events}}^{\text{F}}$ and N_{events} are directly extracted via event counting. The extraction of the non-CSE yield $N_{\text{non-CSE}}^{F}$ requires modelling. The main background for this process comes from fluctuations in the charged track multiplicity distribution of dijet events where no color-singlet exchange takes place. The fraction f_{CSE} is computed differentially by dividing the sample of dijets in subsamples binned in kinematic variables of interest. In this analysis, we measured the fraction f_{CSE} as a function of:

- The pseudorapidity separation $|\Delta\eta_{jj}|$ between the leading two jets;
- The subleading jet transverse momentum $p_{\text{T, jet 2}}$;
- The azimuthal angle separation between the leading two jets $\Delta\phi_{jj}$;

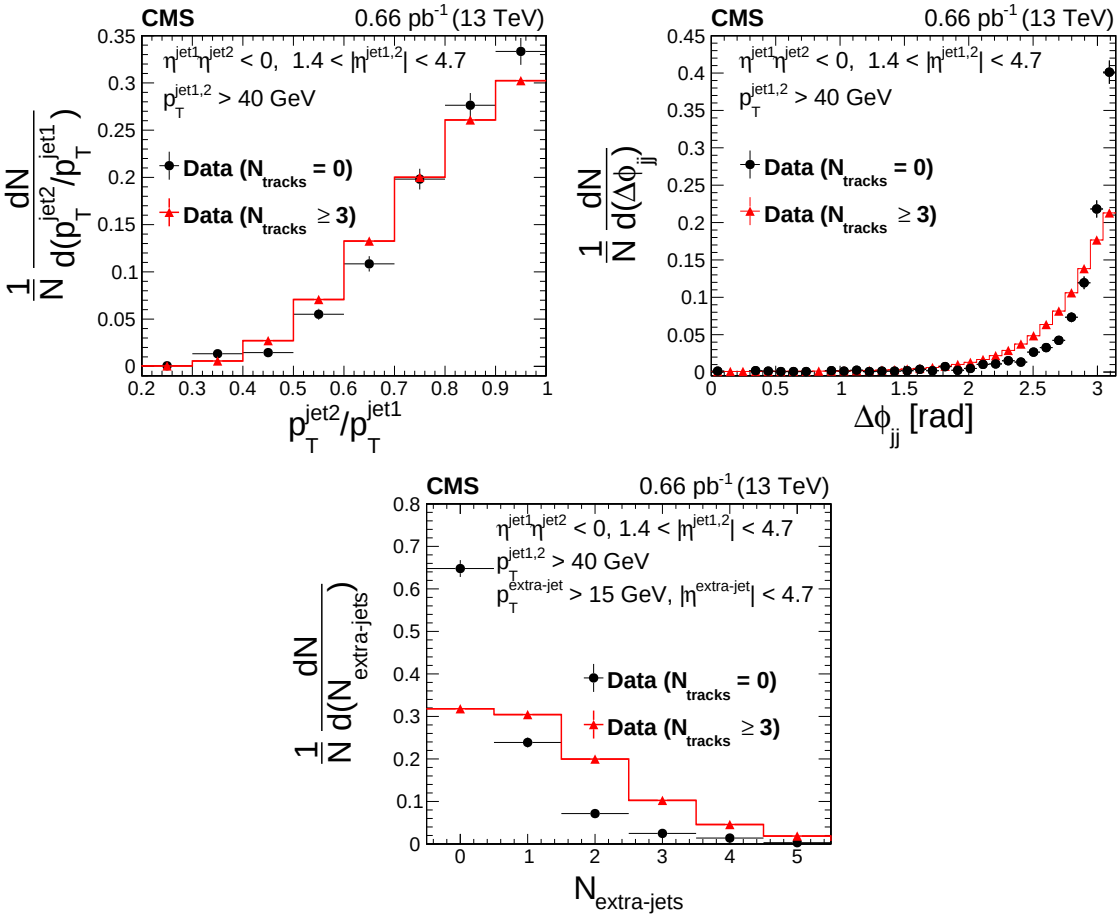

Figure 6.10: Distributions of the ratio of the subleading jet to leading jet transverse momenta $p_{\mathrm{T}}^{\mathrm{jet2}}/p_{\mathrm{T}}^{\mathrm{jet1}}$ (left panel), the azimuthal angular separation between the two leading jets $\Delta\phi_{\mathrm{jj}}$ (right panel), and the number of additional jets $N_{\text{extra-jets}}$ with $p_{\mathrm{T}}^{\text{extra-jet}} > 15$ GeV (lower panel), for jet-gap-jet candidates with $N_{\text{tracks}} = 0$ in $|\eta| < 1$ (black circle) and color-exchange dijet candidates $N_{\text{tracks}} \geq 3$ in $|\eta| < 1$ (red triangle). The vertical bars represent the statistical uncertainties, which are smaller than the marker for some data points. The horizontal bars represent the bin width. The distributions are normalized to unity. The plots are the same as those extracted in Ref. (1).

The measurement as a function of $\Delta\eta_{jj}$ is the most important one in order to test predictions by pQCD within the BFKL framework. The reason is that, the resummation of large logarithms of energy in BFKL is directly related to the regime of large pseudorapidity differences between the final state jets.

We chose to perform the analysis as a function of $p_{\mathrm{T,jet2}}$ guided by phenomenology studies which predict a weak dependence on the f_{CSE} fraction as a function of $p_{\mathrm{T,jet2}}$ based on BFKL calculations and in order to make a direct comparison with the previous measurement by CMS at 7 TeV; we verified the results on the f_{CSE} fraction are the same (within statistical uncertainties) when studying the f_{CSE} fraction as a function of $p_{\mathrm{T,jet1}}$ and $\langle p_{\mathrm{T}} \rangle = \frac{p_{\mathrm{T,jet1}} + p_{\mathrm{T,jet2}}}{2}$. With this measurement, we are comparing any possible modifications to the gluon propagator (which is responsible for the p_T dependence of the cross section) that may be present in color-singlet exchange and not in color-exchange dijet events. Another good reason to use the second-leading jet p_T is that one can suppress the selection bias related to multijet event topologies. For color-singlet exchange, the two highest p_{T} jets balance each other in momentum most of the time. For color-exchange dijet events, it is more likely that multiple jets balance the transverse momentum between each other. Thus, a comparison of the average p_{T} among these may result in a spurious selection bias effect.

Finally, we wanted to measure the f_{CSE} fraction as a function of some measure of the momentum balance of the dijet system, and decided to report it as a function of the azimuthal angle separation between the leading two jets $\Delta\phi_{jj}$. The CDF Collaboration reported the measurement of the gap fraction as a function of the third jet $p_{\mathrm{T,jet3}}$ (150). These observables are sensitive to effects of the jet energy scale determination, and thus we decided to report the measurement on the azimuthal angle separation between the leading two jets instead. The interest of having the gap fraction as a function of the acoplanarity of the leading two jets is to test effects from higher order corrections for the jet-gap-jet process in the BFKL approach. NLO corrections to the coupling of the perturbative pomeron

to quarks and gluons of the colliding protons can induce azimuthal angle decorrelations between the two leading jets [1]. It is important to have this piece of information to have a global picture of the nature of the color-singlet exchange mechanism, as well as for future comparisons with theoretical calculations. In the Appendix of this thesis, we show the gap fraction as a function of $p_{\mathrm{T,jet3}}$ and $|\vec{p}_{\mathrm{T,jet1}} + \vec{p}_{\mathrm{T,jet2}}|$, with similar qualitative conclusions as the result found in $\Delta\phi_{\mathrm{jj}}$. We had also explored the possibility of measuring the gap fraction as a function of the average longitudinal partonic momentum fraction $\langle x \rangle$, but due to sensitivity of this observable to jet energy scale determination (x would have to be determined via the transverse momentum and pseudorapidities of the jets), and since $\langle x \rangle$ is correlated to a measurement of pseudorapidity differences between the two highest p_T jets, we decided not to use this variable as the analysis matured.

Throughout this analysis, we show the N_{tracks} distributions for values up to $N_{\mathrm{tracks}} < 45$, which covers the region of interest to perform the jet-gap-jet analysis. However, the N_{tracks} distributions can extend up to values of $N_{\mathrm{tracks}} \sim 120$. The high N_{tracks} events are populated by underlying event activity effects. Throughout this analysis, we represent the integrated yield for multiplicities $N_{\mathrm{tracks}} > 45$ on the 45th bin.

6.6 Background estimation

As motivated in the previous section, we require some modelling for the N_{tracks} distribution in color-exchange events, so that we can understand what is their contribution in the low multiplicity bins in our data sample. Two data-driven techniques are used to describe the non-CSE contribution in the lowest multiplicity bins. One of them relies on a dijet sample orthogonal to the one we use to study jet-gap-jet events, while the second one relies on a well-understood parametrization of N_{tracks} distributions in hadronic collisions. These methods are cross-checked with predictions from `Pythia8` simulations at

[1] Private communication with colleagues Federico Deganutti, who has worked on the jet-gap-jet phenomenology with NLO impact factors (141)

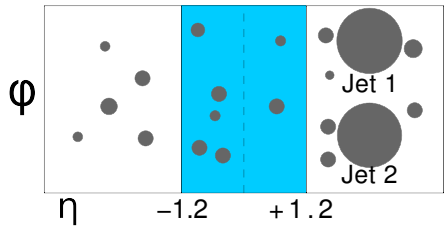

Figure 6.11: Schematic diagram of a same-side (SS) dijet event in the $\eta - \phi$ plane (grey circles indicate radiation). The N_{tracks} distribution on the fixed pseudorapidity region $|\eta| < 1.2$ is used for a data-driven estimation of the background contamination of color-connected dijet events at low charged particle multiplicities. Minimum forward calorimeter activity is required to suppress the contribution of single-diffractive dijet with a large rapidity gap.

low multiplicities, as discussed in later.

Same-side dijet sample method (SS method): A second N_{tracks} distribution is obtained from a sample of events where the two highest p_{T} jets are reconstructed on the same side of the CMS detector ($\eta_1\eta_2 > 0$) with jets satisfying the selection $1.4 < |\eta_{1,2}| < 4.7$ and $p_{\text{T}} > 40$ GeV (see Fig. 6.11). There are 1 M of these events in the inclusive dijet data sample. This orthogonal sample of dijet events is referred hereafter as "SS dijet sample". The presence of jet-gap-jet events is heavily suppressed in this sample, since the pseudorapidity separations between the highest p_{T} jets can only be of a maximum of ~ 3 units. Thus, the N_{tracks} distributions on a fixed pseudorapidity region stemming from this sample is dominated by non-CSE dijet events, and can be used to estimate the non-CSE contamination at low multiplicities. This method was first introduced by the CDF Collaboration (151; 150). In addition to the aforementioned selections, we require minimum calorimeter activity on the forward region opposite to the SS dijet system in order to suppress single-diffractive dijet contributions (gap-jet-jet topology), which might bias the N_{tracks} distribution at low multiplicities. Specifically, we require at least one calorimeter tower within pseudorapidities $3 < |\eta| < 5$ in HF with a minimum energy deposition of 5 GeV. Similar selections that yield single diffractive enhancement (depletion) have been used in previous analyses in CMS, for example the measurement of charged particle spectra in minimum-bias events at 13 TeV (197), the measurement of the inelastic pp cross section at 13 TeV (198) or the

measurement of very forward inclusive jet cross section in pPb collisions at $\sqrt{s_{NN}} = 5.02$ TeV (199). Results are stable when varying the threshold between 4.5 GeV and 5.5 GeV. This additional requirement improves the χ^2/ndf between the SS distribution and the opposite-side dijet distribution ($\eta_1\eta_2 < 0$), hereafter referred to as the "OS dijet sample", and the SS dijet sample in the region $N_{\text{tracks}} \geq 3$.

The N_{tracks} distribution with fixed $|\eta| < 1$ is biased differently in the SS sample relative to the OS dijet sample, where we expect the jet-gap-jet signal events to be in. To compensate for this bias and obtain a better superposition of the SS dijet sample and the OS dijet sample multiplicity distribution for $N_{\text{tracks}} \geq 3$ (where the multiplicity distribution is dominated by color- events), the fixed pseudorapidity region for the SS dijet sample needs to be adjusted. The optimal gap region for the orthogonal sample is found to be $|\eta| < 1.2$, in consistence with findings by CDF and CMS (200; 151; 150; 152). The adjusted multiplicity distribution in the SS sample is normalized to the one for the OS dijet sample (where the CSE signal events are present) in the control region [3,40] which is dominated by non-CSE background events and contains the maximum value of the multiplicity distribution, and the number of events in the first multiplicity bins [0,2] is taken as the estimate of the non-CSE contamination. This method is directly applicable in subsamples binned in the subleading jet transverse momentum $p_{\text{T, jet2}}$. This method is dubbed "SS method" hereafter. The SS dijet sample and SS method are used for systematic checks in this analysis.

Negative binomial distribution fit method (NBD method, <u>nominal method</u>): The second method for the background estimation relies on a fit to the N_{tracks} distribution with a negative binomial distribution (NBD) function, which is typically used to describe color-exchange multiplicity distributions. The NBD function is fit in an interval of the N_{tracks} dominated by color-exchange dijet events. The color-exchange contamination in the low multiplicity region is estimated by an extrapolation of the fit. Mathematically, the NBD gives the probability of having $n-1$ successes with a probability p of success with k fail-

ures in $k+n+1$ trials, with success on the $(k+n)$th trial. The probability density function is defined by

$$\mathrm{NBD}(k;n,p) = \frac{(k+n-1)!}{k!(n-1)!}p^n(1-p)^k \tag{6.3}$$

the method relies on the successful description of N_{tracks} distributions for color-exchange processes by the NBD function (201; 202). This was first observed by UA5 (203; 204), who studied particle multiplicities in proton-antiproton collisions at the energies of $\sqrt{s} = 540$ and 900 GeV at the SPS. This has been further confirmed in pp collisions by the ALICE experiment at the collision energies of 0.9, 2.36, 2.76, 7 and 8 TeV (205). One of the main advantages of the NBD fit is that, aside from the normalization constant, only two parameters are necessary to describe the color-exchange N_{tracks} distribution.

It was noted that the NBD function stops giving a good description of N_{tracks} distributions for energies larger than $\sqrt{s} = 900$ GeV across the whole multiplicity spectrum (204; 205). Indeed, a shoulder-like structure appears at high multiplicities due to additional mechanisms participating in the collision that enhance charged particle production. A double-NBD function gives a better description if the intention is to describe the full N_{tracks} spectra, including high multiplicities (204; 205). For our studies, a single NBD function fit is sufficient, since we are interested only on the low charged particle multiplicities region for a jet-gap-jet analysis.

We fit the NBD on for multiplicities $N_{\mathrm{Tracks}} = 3$–35, where we expect non-CSE events to dominate the N_{tracks} distribution, and extrapolate the fit results to $N_{\mathrm{Tracks}} = 0-2$, where the CSE events are present. The maximum of the multiplicity distribution $N_{\mathrm{Tracks,\,max}} \sim 25$ is well-contained within the fit region. Furthermore, we focus on the low multiplicity region, since this is the region where we are less sensitive to possible remaining effects on multiple pp interactions per bunch crossing. Values of χ^2/ndf of the fit to data ranges from 1–2 in the control region for the different subsamples used in this analysis. The NBD method for estimating the non-CSE background contributions in jet-gap-jet events

has been used by D0 and CMS (206; 207; 147; 152).

In this analysis, we choose the NBD method as the nominal method for the background estimation, since it allows us to compute the fraction f_{CSE} differentially in different kinematic observables, as opposed to the former SS method which is only applicable to the $p_{\mathrm{T},2}$ bins. The NBD method is mainly limited by the number of events available in the control region (large multiplicities) necessary for the fit. The estimated background is stable with respect to the ending and starting points of the fit region relative to the mean of the distribution.

The SS method is used to estimate the systematic uncertainties related to the background subtraction procedure and the SS-sample for cross-checks of the stability of the NBD fit and to see if there are possible detector effects that may induce a change of slope of the N_{tracks} distribution in the signal region. Color-singlet exchange events yield between 80–90% of the dijet events in the $N_{\mathrm{tracks}} = 0^{\mathrm{th}}$ bin, about 40–60% in the $N_{\mathrm{tracks}} = 1^{\mathrm{st}}$ bin, and between 10–20% in the $N_{\mathrm{tracks}} = 2^{\mathrm{nd}}$ bin across the subsamples. We show a comparison between the two methods in subsamples of the subleading jet p_{T} can be seen in Fig. 6.12, 6.13, 6.14. The bin-by-bin difference results can be seen in Fig. 6.15.

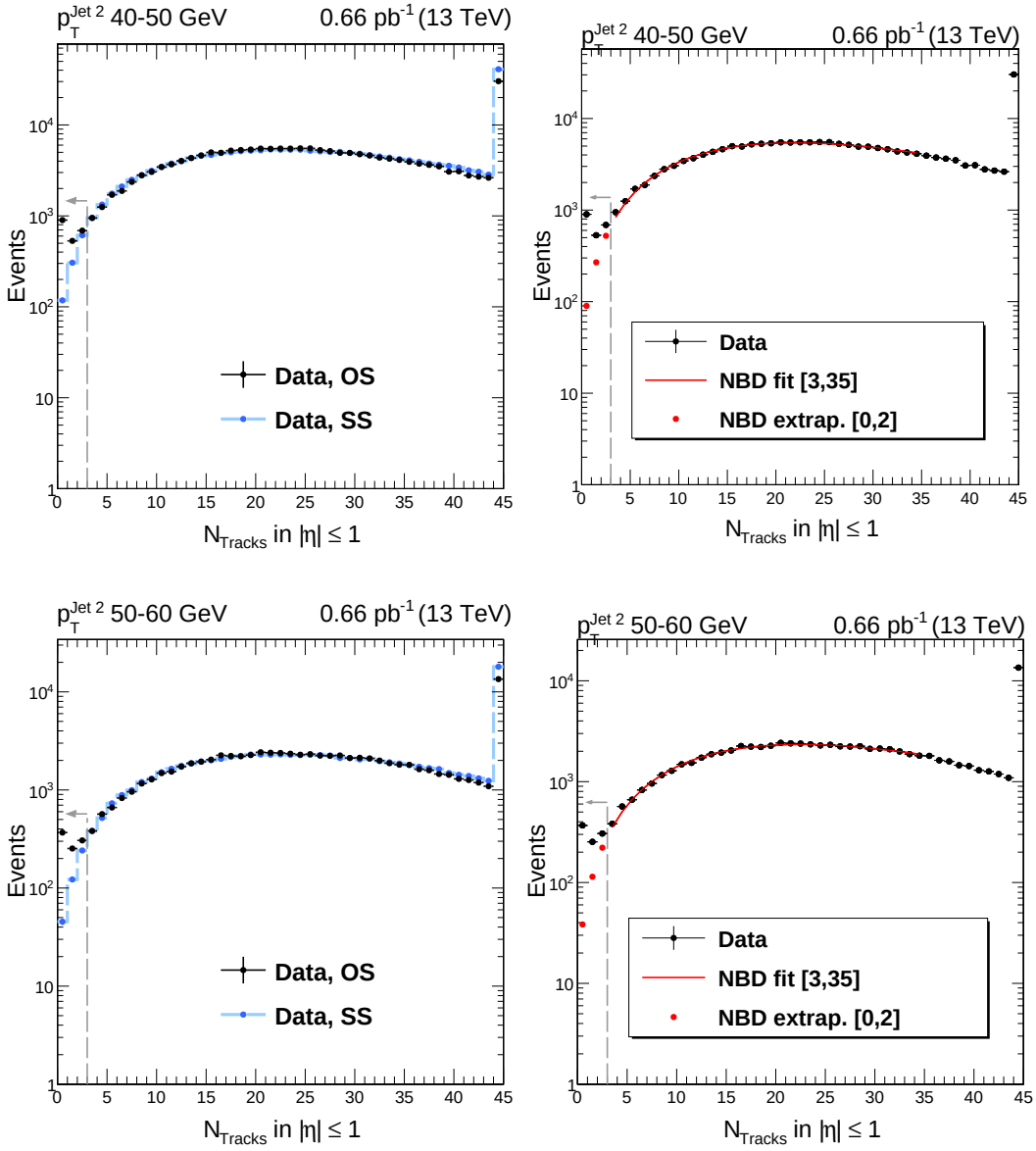

Figure 6.12: N_{tracks} distribution in the fixed pseudorapidity region $|\eta| < 1$ for tracks with $p_{\text{T}}^{\text{track}} > 0.2$ GeV in different bins of $p_{\text{T}}^{\text{jet2}}$. The distributions are for highest p_{T} jets which satisfy $p_{\text{T}} > 40$ GeV and $1.4 < |\eta_{1,2}| < 4.7$ and $\eta_1 \eta_2 < 0$. Error bars indicate the statistical uncertainties only. On the left, we show the results for background estimation using the SS method described in text, and on the right the background estimated from an extrapolation of the NBD fit to the lower multiplicity bins. An excess at very low multiplicities is observed (left-hand side w.r.t. the vertical grey dashed line), which we attribute to the presence of events with a strongly interacting hard color-singlet exchange. The excess of events at low charged particle multiplicities correspond to the jet-gap-jet events.

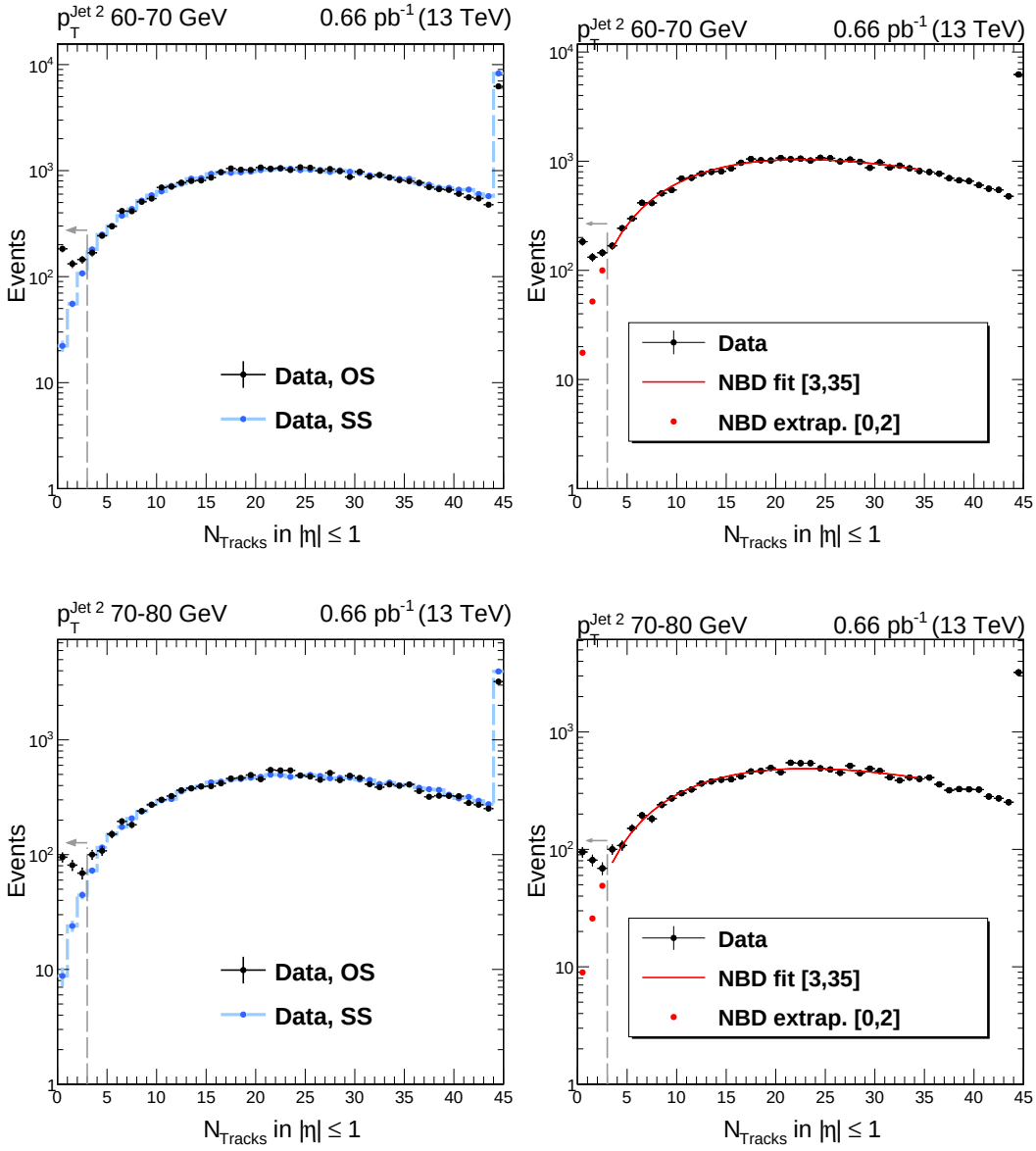

Figure 6.13: N_{tracks} distribution in the fixed pseudorapidity region $|\eta| < 1$ for tracks with $p_{\text{T}}^{\text{track}} > 0.2$ GeV in different bins of $p_{\text{T}}^{\text{jet2}}$. The distributions are for highest p_{T} jets which satisfy $p_{\text{T}} > 40$ GeV and $1.4 < |\eta_{1,2}| < 4.7$ and $\eta_1 \eta_2 < 0$. Error bars indicate the statistical uncertainties only. On the left, we show the results for background estimation using the SS method described in text, and on the right the background estimated from an extrapolation of the NBD fit to the lower multiplicity bins. An excess at very low multiplicities is observed (left-hand side w.r.t. the vertical grey dashed line), which we attribute to the presence of events with a strongly interacting hard color-singlet exchange. The excess of events at low charged particle multiplicities correspond to the jet-gap-jet events.

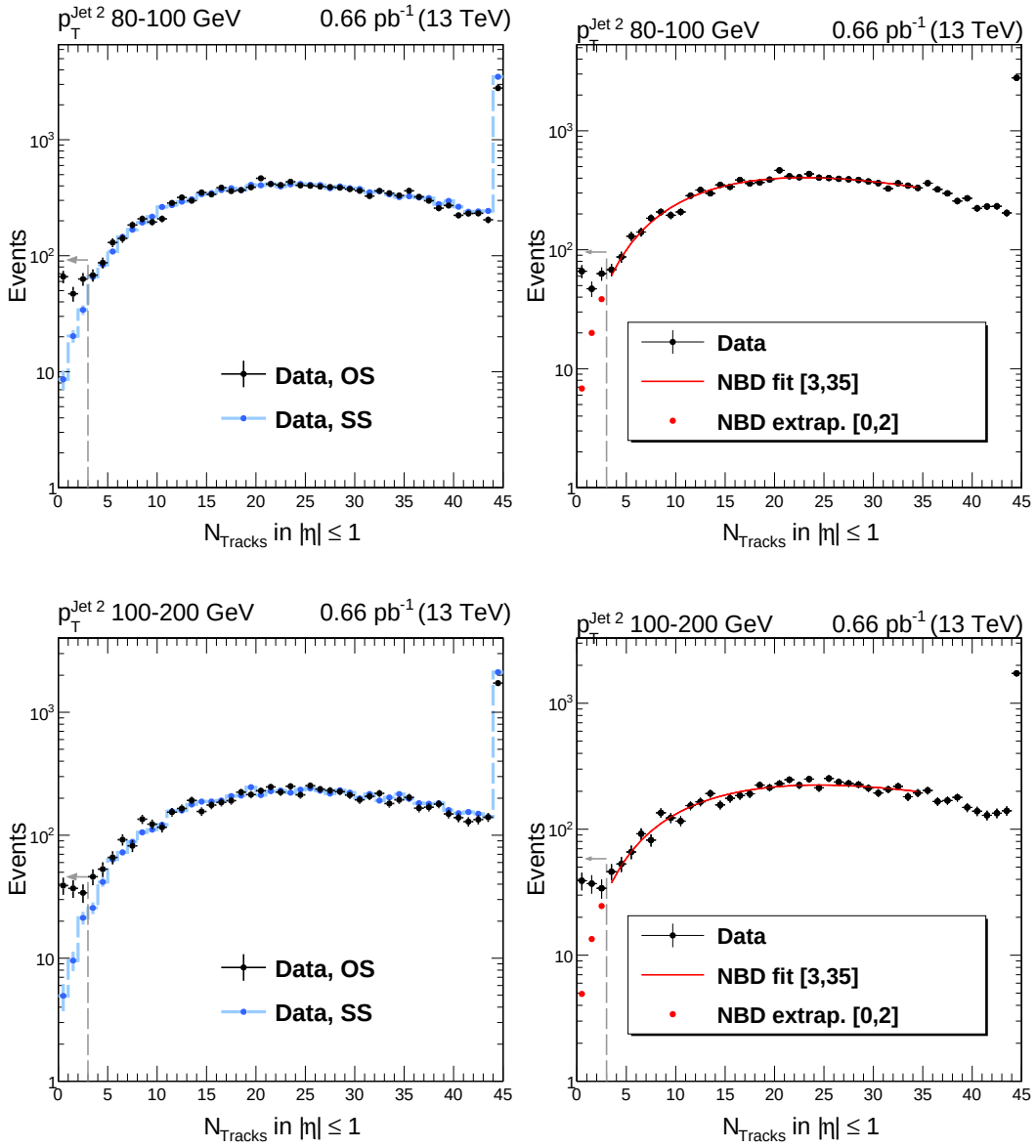

Figure 6.14: N_{tracks} distribution in the fixed pseudorapidity region $|\eta| < 1$ for tracks with $p_{\text{T}}^{\text{track}} > 0.2$ GeV in different bins of $p_{\text{T}}^{\text{jet2}}$. The distributions are for two highest p_{T} jets which satisfy $p_{\text{T}} > 40$ GeV and $1.4 < |\eta_{\text{jet 1,jet 2}}| < 4.7$ and $\eta_{\text{jet 1}}\eta_{\text{jet 2}} < 0$. Vertical error bars represent the statistical uncertainties only. On the left, we show the results for background estimation using the SS method described in text, and on the right the background estimated from an extrapolation of the NBD fit to the lower multiplicity bins. An excess at very low multiplicities is observed (left-hand side w.r.t. the vertical grey-dashed line), which we attribute to the presence of events with a strongly interacting hard color-singlet exchange. We show the multiplicities $N_{\text{Tracks}} < 45$ since these are relevant to the jet-gap-jet analysis, although the multiplicities extend in principle up to $N_{\text{Tracks}} \sim 120$.

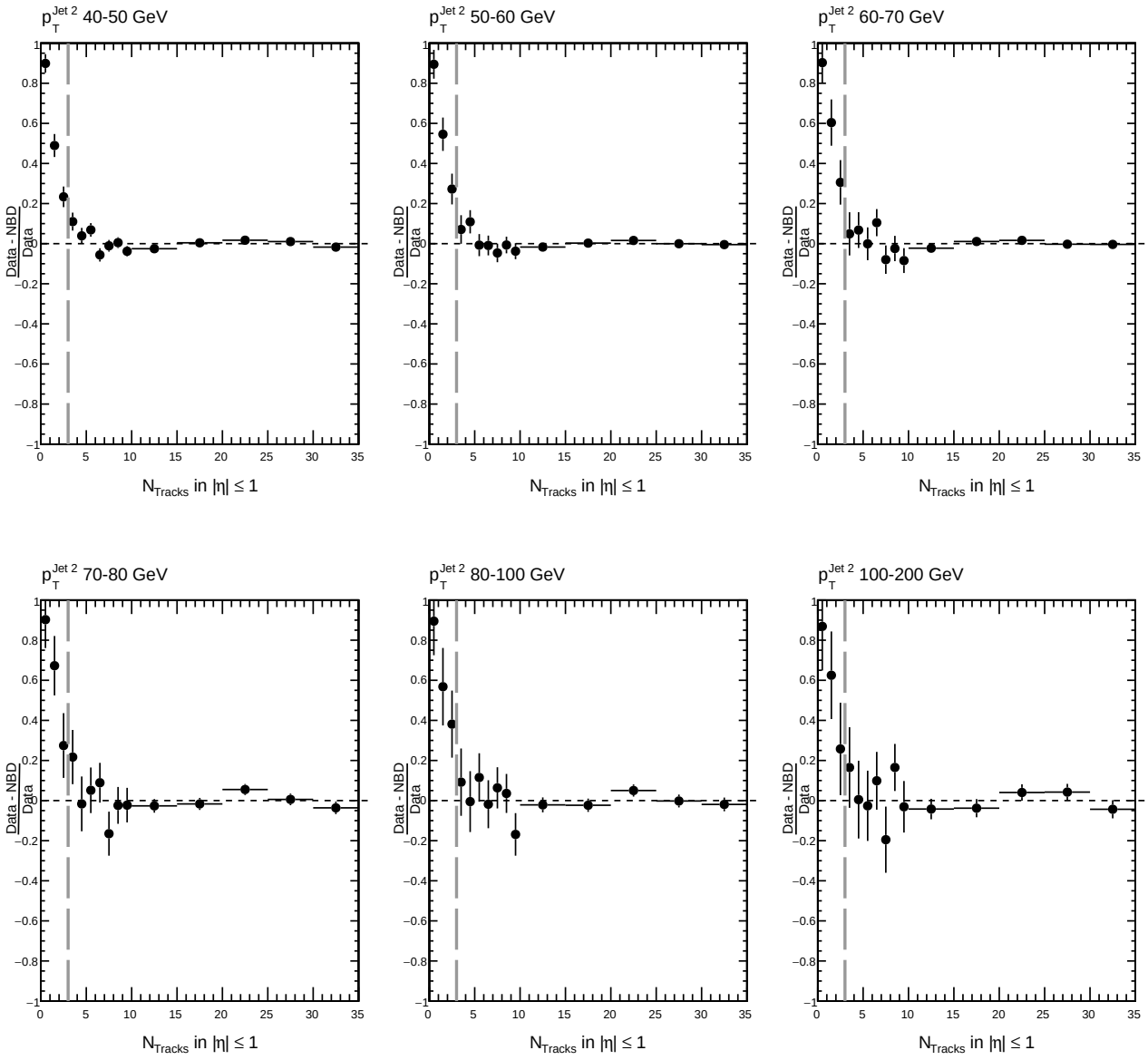

Figure 6.15: Bin-by-bin difference between data and the NBD fit results as a function of $p_{T,jet\,2}$, normalized to the number of events in the data. The NBD extrapolation lies on the left-hand side w.r.t. the vertical dashed line, where an excess on the low multiplicity bins is observed. Vertical error bars represent statistical uncertainties only. The deviation from 0 at low multiplicities corresponds to the presence of jet-gap-jet events.

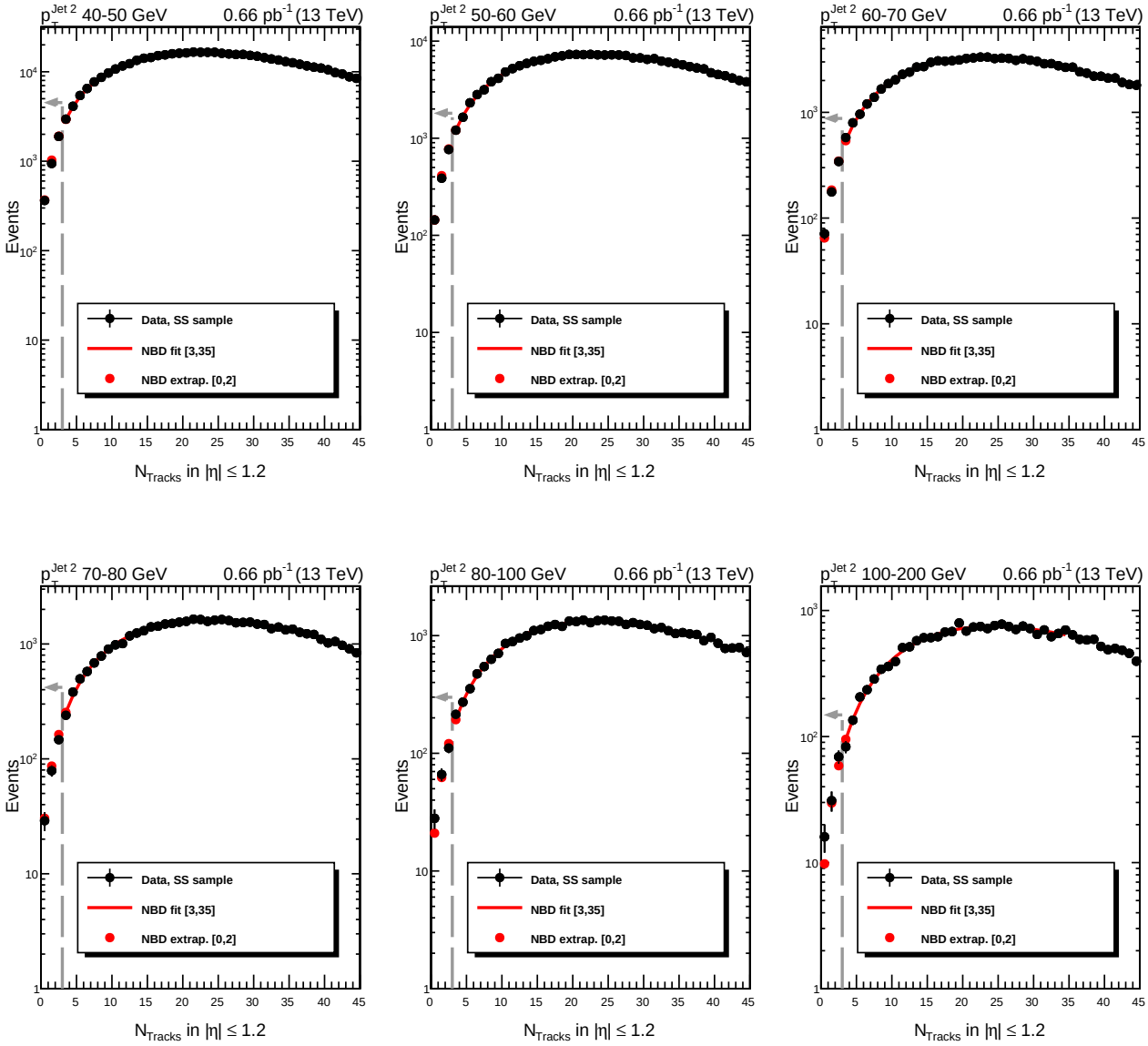

Figure 6.16: N_{tracks} in the fixed pseudorapidity region $|\eta| < 1.2$ for tracks with $p_{\text{T}}^{\text{track}} > 0.2$ GeV in different bins of $p_{\text{T}}^{\text{jet2}}$. The distributions are for the two highest p_{T} jets jets that satisfy $p_{\text{T}} > 40$ GeV and $1.4 < |\eta_{1,2}| < 4.7$ and $\eta_1\eta_2 > 0$. Error bars indicate statistical uncertainties only. The NBD distribution is fitted in [3,35] and extrapolated to the first multiplicity bins [0,2]. The NBD extrapolation correctly describes the SS multiplicity.

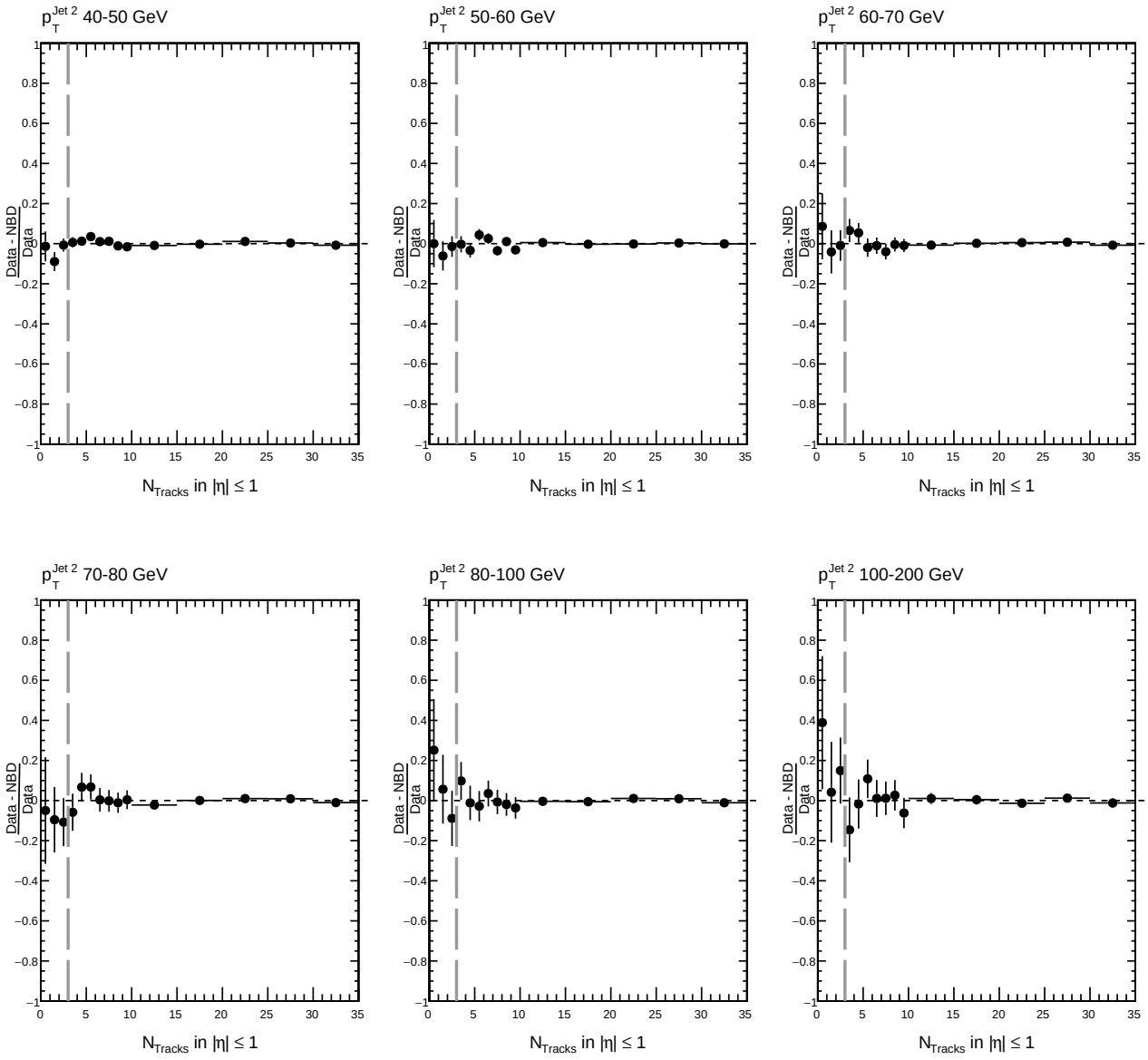

Figure 6.17: Bin-by-bin difference between data and the NBD fit results as a function of $p_{T,jet\,2}$, normalized to the number of events in data for the SS dijet sample of events which is dominated by non-CSE events. The NBD extrapolation lies on the left-hand side w.r.t. the vertical dashed line, and seems to describe the SS dijet sample multiplicity distribution within uncertainties, including the extrapolation to the low multiplicity bins. Vertical error bars represent statistical uncertainties only.

For the gap fraction measurement, we bin the various kinematic distributions ($\Delta\eta_{jj}$, $p_{\mathrm{T,jet2}}$, $\Delta\phi_{jj}$) such that they yield a smooth enough N_{tracks} in the control region $N_{\mathrm{tracks}} = [3,45]$, so the NBD fit is robust and well constrained in order to have stable extrapolations of the fit to the first multiplicity bins, as well as to have a large enough number of jet-gap-jet signal events to be extracted at low charged particle multiplicities.

6.6.1 Performance of NBD method to describe non-CSE distributions

To test the performance of the NBD method and the existence of any possible bias in the background subtraction method in this analysis, we apply the NBD method to two samples of dijet events enriched in color-exchange events extracted from the data. The first is the SS sample of dijet events that was introduced in the previous section, whereas the second one is a tri-jet sample of dijet events.

We cross-check the reliability of the NBD method by fitting the NBD in the control region [3,35] in the SS sample and extrapolating the NBD to the first multiplicity bins [0,2]. Since the SS sample is highly enriched in non-CSE events, the NBD extrapolation should describe the N_{tracks} distribution correctly. The results can be seen in Figs. 6.16, and the relative residuals of the NBD fit and the extrapolation to low multiplicities can be seen in Fig. 6.17. The NBD correctly describes the N_{tracks} distribution for the SS dijet sample.

To further test the NBD method performance, we study a tri-jet sample where the two leading jets satisfy $p_{\mathrm{T,\,jet\,1,\,jet\,2}} > 40$ GeV, $1.4 < |\eta_{\mathrm{jet\,1,jet\,2}}| < 4.7$ and $\eta_{\mathrm{jet\,1}}\eta_{\mathrm{jet\,2}} < 0$; and the third jet satisfies $p_{\mathrm{T,\,jet\,3}} > 15$ GeV and $|\eta_{\mathrm{jet\,3}}| < 1$. The tri-jet sample is depleted in jet-gap-jet events. The presence of a third jet in this sample is caused mainly by interjet radiation between the outermost jets, rather than the hadronization process of one of the two leading jets, which would yield a third jet almost collinear to one of the original jets in the forward (backward) region. The N_{tracks} in the fixed pseudorapidity region $|\eta| < 1$ in the tri-jet sample is used to test the performance of the NBD method, as seen in

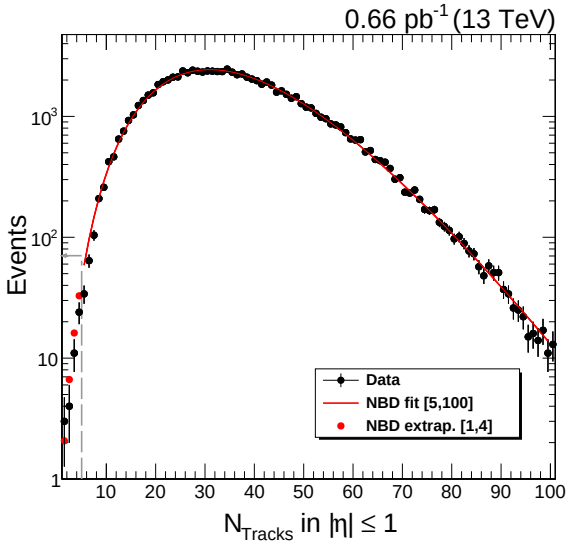

Figure 6.18: N_{tracks} of tri-jet sample in the fixed pseudorapidity region $|\eta| < 1$. The leading two jets are required to be on $1.4 < |\eta_{\text{jet 1,2}}| < 4.7$ and on opposite hemispheres of the detector $\eta_{\text{jet 1}}\eta_{\text{jet 2}} < 0$, whereas the third jet is required to be in $|\eta_{\text{jet 3}}| < 1$ with a minimum $p_{\text{T, jet 3}} > 15$ GeV. The sample is enriched in color-exchange events. An NBD is fitted in the control region [5,100] (smooth red line) and its extrapolation to lower multiplicity bins (red dots in [1,4]) gives a good description of the N_{tracks}.

Fig. 6.18. We fit the NBD in the region [5,100], and extrapolate the NBD fit results to the first multiplicity bins [1,4]. There is good agreement between the data at low multiplicities and the expectation from the NBD fit extrapolation. It is worth noting that there is no excess at low multiplicities due to detector effects in either the SS dijet sample or the tri-jet sample.

6.6.2 SS method in bins of $|\Delta\eta_{jj}|$

The SS method is only directly applicable in bins of $p_{\text{T, jet 2}}$. The method cannot be directly applied in bins of pseudorapidity separations between the leading jets $|\Delta\eta_{jj}|$, since the dijets in the SS-sample are restricted to be on the same hemisphere of the CMS detector, which leads to a minimum pseudorapidity separation between the two leading jets of 0 units and a maximum pseudorapidity difference between the two of ~ 3 units. In order

to have a good control on the background subtraction method and understanding of the non-CSE background, ideally we have to have at least one other independent method applicable on other kinematic observables.

We devised a method which relies on the subleading jet transverse momentum spectrum per bin of $|\Delta\eta_{\mathrm{jj}}|$ in the OS dijet data sample and the non-CSE dominated SS dijet samples. We start from the assumption that, to a first approximation, the non-CSE background present per bin of $|\Delta\eta_{jj}|$ should correspond to a superposition of the non-CSE distributions. This is supported by the fact that the sum of NBD functions yield another NBD shaped distribution, provided that the distributions have the same p parameter, which is approximately the case for the various sub-samples in bins of $\Delta\eta_{\mathrm{jj}}$. Furthermore, bins of $|\Delta\eta_{\mathrm{jj}}|$ restrict the analysis on a given region of pseudorapidity for each jet, which in turn restricts the analysis on a given portion of the subleading jet transverse momentum spectrum.

The method consists in the following:

- Obtain the relative weight of every bin of $p_{\mathrm{T,\,jet\,2,i}}$ in a given bin of $|\Delta\eta_{jj}|$ from data;
- Build an effective distribution $N^{\mathrm{eff}}_{\mathrm{Tracks}}(|\Delta\eta_{jj}|)$ for the bin $|\Delta\eta_{jj}|$ by summing up the N_{tracks} distributions from the SS dijet sample $N^{\mathrm{SS\text{-}sample}}_{p_{\mathrm{T,\,jet\,2,i}}}$

$$N^{\mathrm{eff}}_{\mathrm{Tracks}}(|\Delta\eta_{jj}|) = \sum_i N^{\mathrm{SS\text{-}sample}}_{\mathrm{Tracks}}(p_{\mathrm{T,\,jet\,2,i}})w_i \tag{6.4}$$

  where i corresponds to the i-th bin of $p_{\mathrm{T,\,jet\,2}}$ and w_i is the corresponding relative weight in the bin of $|\Delta\eta_{jj}|$.

- The effective non-CSE charged particle distribution $N^{\mathrm{eff}}_{\mathrm{Tracks}}(|\Delta\eta_{jj}|)$ is normalized to the opposite hemisphere data sample of interest in the control region [3,40], and the values in the lowest multiplicities [0,2] are interpreted as the non-CSE contribution in the sample.

This procedure yields results compatible with the results obtained with the NBD method, as can be seen in the N_{tracks} distributions in Figs. 6.19, 6.20, 6.21, 6.22, 6.23 and the bin-by-bin difference in Fig. 6.24.

The N_{tracks} distributions for the azimuthal angle separation between the leading two jets, as well as the NBD function fit results, can be seen in Fig. 6.25 and the respective residuals in Fig. 6.26. The N_{tracks} distribution is biased differently depending on the azimuthal angle separation between the leading two jets. For smaller $\Delta\phi_{jj}$ separations, the N_{tracks} is biased towards larger values due to the larger amount of interjet radiation which is causing the large angular decorrelations.

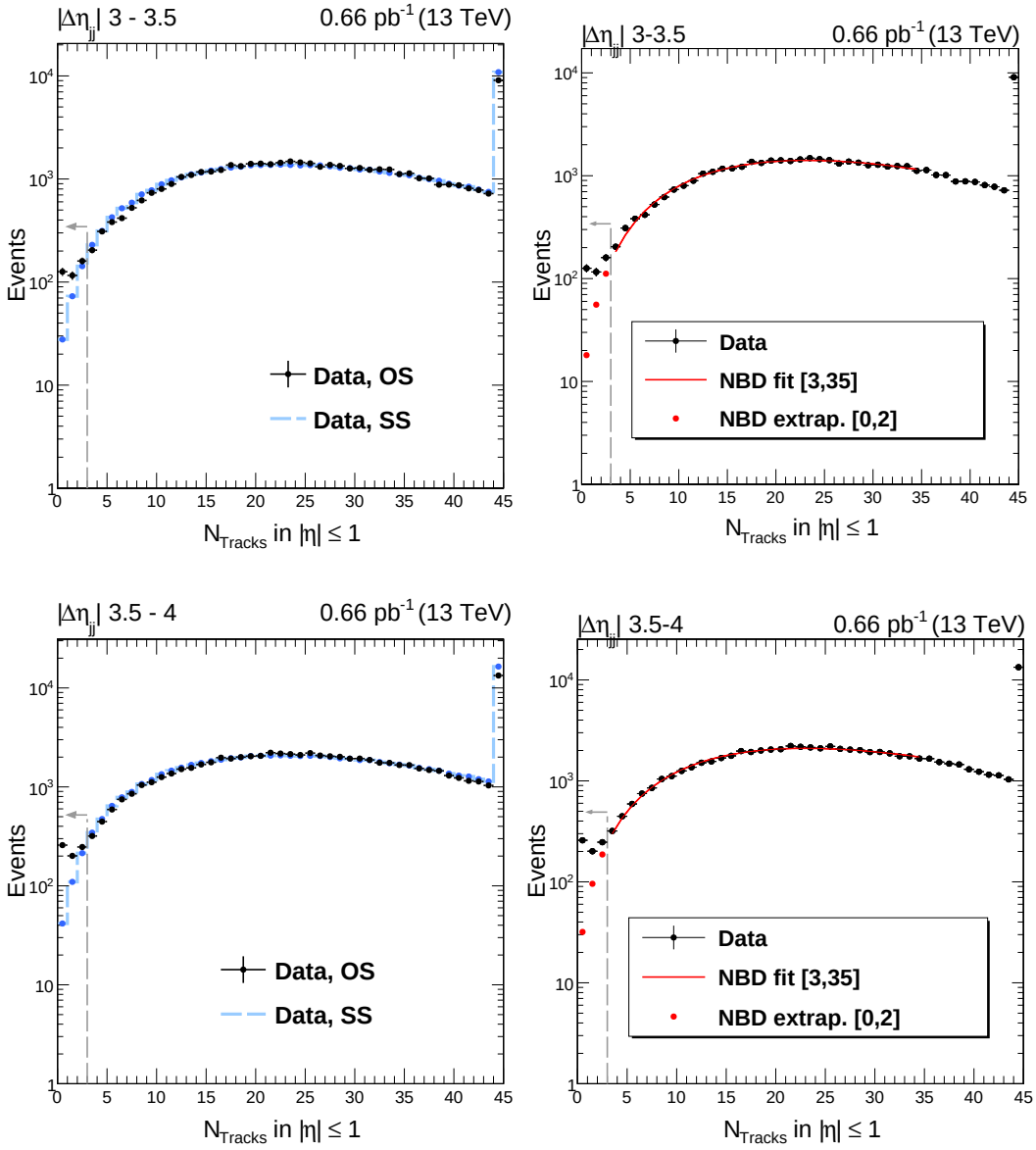

Figure 6.19: N_{tracks} in the fixed pseudorapidity region $|\eta| < 1$ for tracks with $p_{\text{T}}^{\text{track}} > 0.2$ GeV in different bins of $p_{\text{T}}^{\text{jet2}}$. The distributions are for leading jets which satisfy $p_{\text{T}} > 40$ GeV and $1.4 < |\eta_{1,2}| < 4.7$ and $\eta_{\text{jet 1}}\eta_{\text{jet 2}} < 0$. Error bars indicate statistical uncertainties only. On the left, we have the background estimated with the orthogonal dijet sample described in text, and on the right the background estimated from an extrapolation of the NBD fit to the lower multiplicity bins. An excess at very low multiplicities is observed, which we attribute to the presence of events with a strongly interacting hard color-singlet exchange. The number of events with multiplicities larger than $N_{\text{Tracks}} \geq 45$ are represented by the 46th bin, and are not shown explicitly here since they correspond to the non-CSE activity.

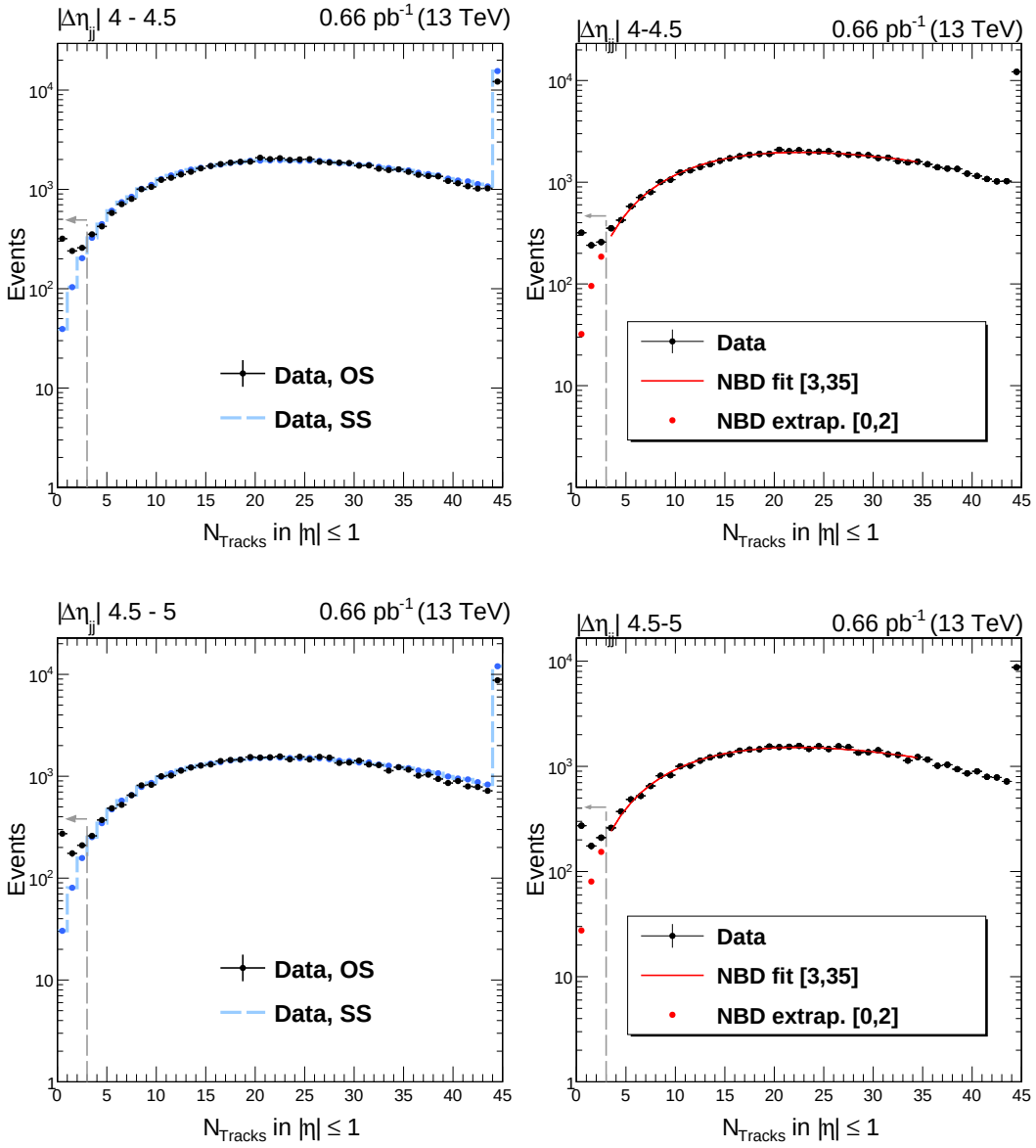

Figure 6.20: N_{tracks} in the fixed pseudorapidity region $|\eta| < 1$ for tracks with $p_{\text{T}}^{\text{track}} > 0.2$ GeV in different bins of $p_{\text{T}}^{\text{jet2}}$. The distributions are for leading jets which satisfy $p_{\text{T}} > 40$ GeV and $1.4 < |\eta_{1,2}| < 4.7$ and $\eta_{\text{jet 1}}\eta_{\text{jet 2}} < 0$. Error bars indicate statistical uncertainties only. On the left, we have the background estimated with the orthogonal dijet sample described in text, and on the right the background estimated from an extrapolation of the NBD fit to the lower multiplicity bins. An excess at very low multiplicities is observed, which we attribute to the presence of events with a strongly interacting hard color-singlet exchange. The number of events with multiplicities larger than $N_{\text{Tracks}} \geq 45$ are represented by the 46th bin, and are not shown explicitly here since they correspond to the non-CSE activity.

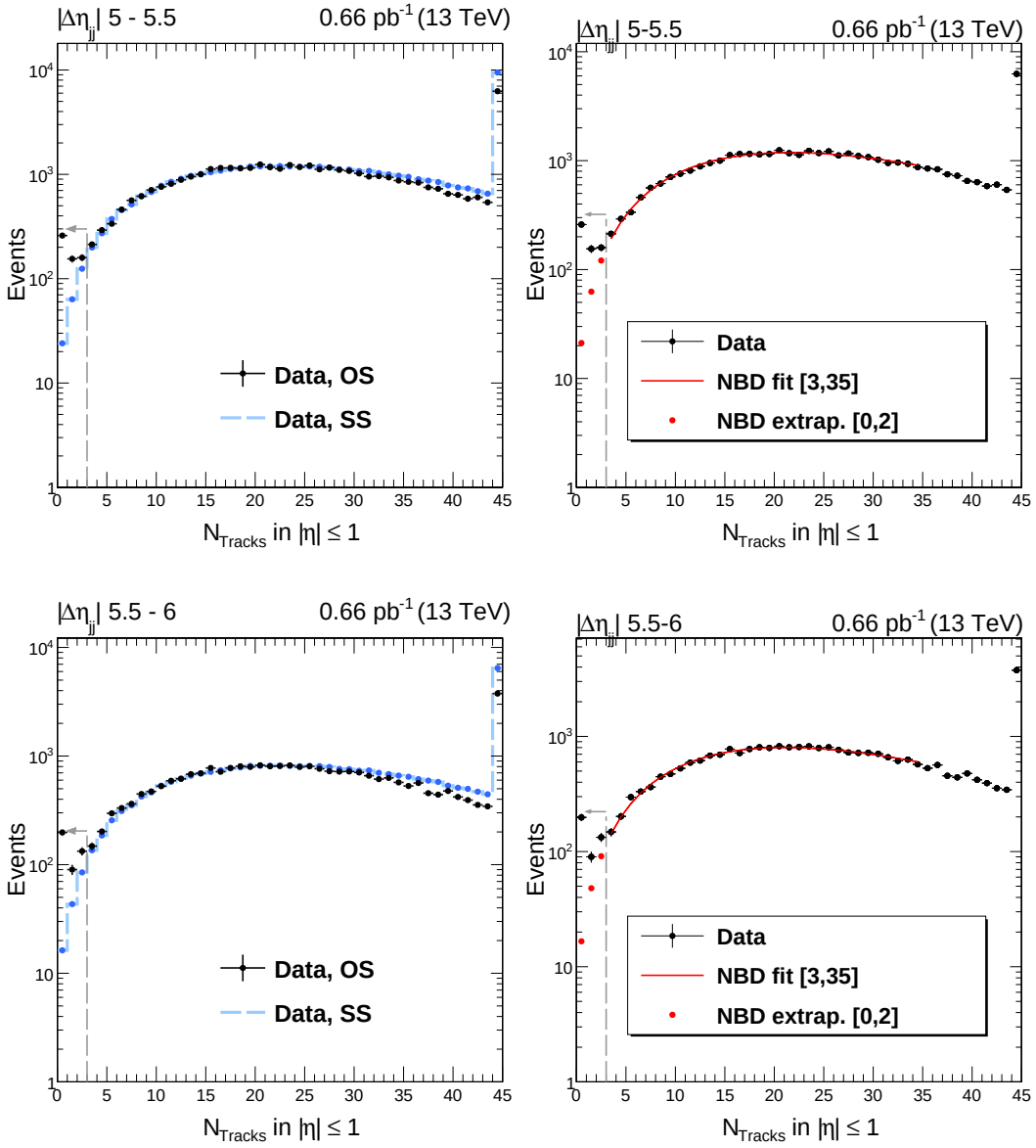

Figure 6.21: N_{tracks} in the fixed pseudorapidity region $|\eta| < 1$ for tracks with $p_{\text{T}}^{\text{track}} > 0.2$ GeV in different bins of $p_{\text{T}}^{\text{jet2}}$. The distributions are for leading jets which satisfy $p_{\text{T}} > 40$ GeV and $1.5 < |\eta_{1,2}| < 4.7$ and $\eta_1 \eta_2 < 0$. Error bars indicate statistical uncertainties only. On the left, we have the background estimated with the orthogonal dijet sample described in text, and on the right the background estimated from an extrapolation of the NBD fit to the lower multiplicity bins. An excess at very low multiplicities is observed, which we attribute to the presence of events with a strongly interacting hard color-singlet exchange.

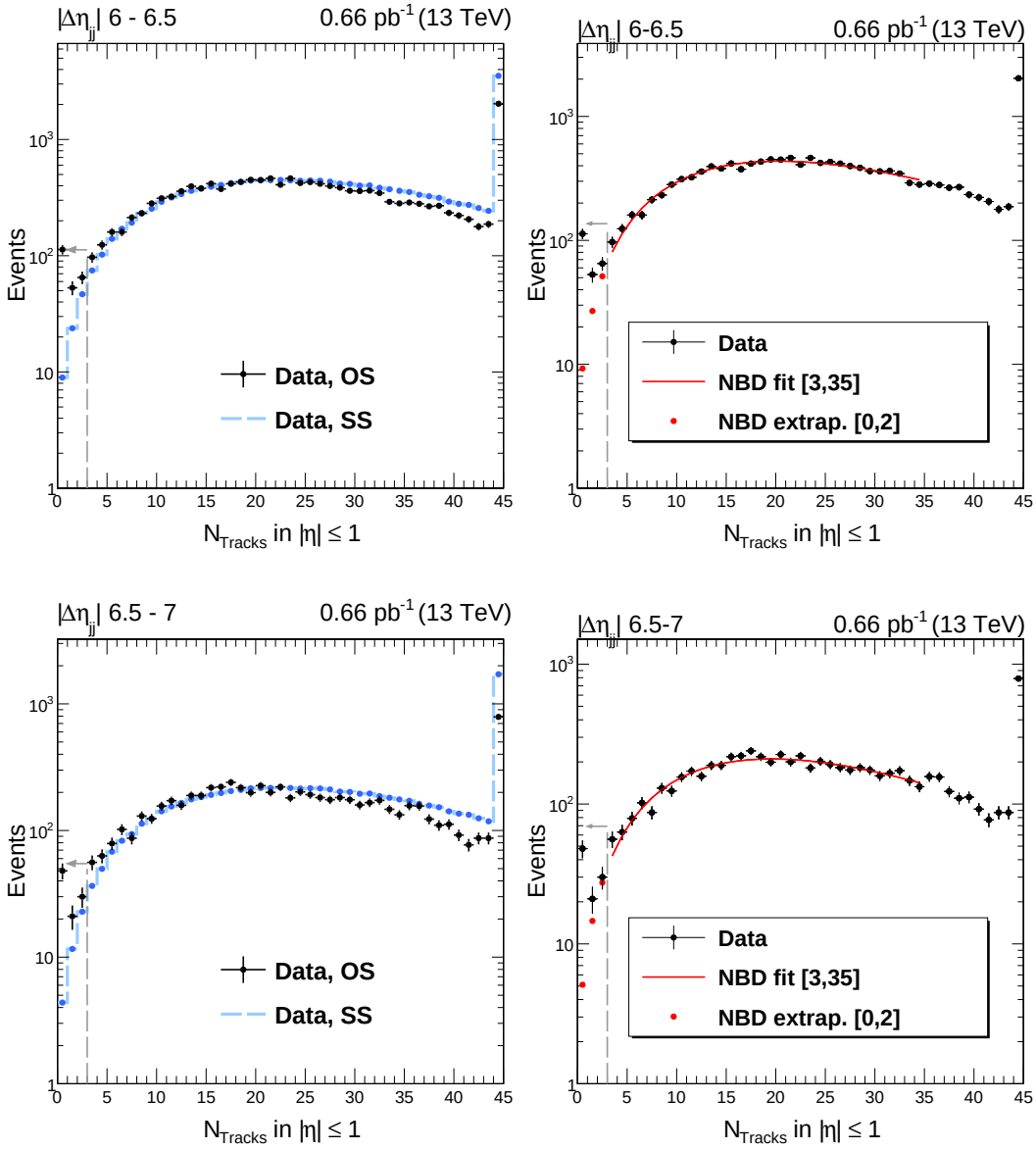

Figure 6.22: N_{tracks} in the fixed pseudorapidity region $|\eta| < 1$ for tracks with $p_{\text{T}}^{\text{track}} > 0.2$ GeV in different bins of $p_{\text{T}}^{\text{jet2}}$. The distributions are for leading jets which satisfy $p_{\text{T}} > 40$ GeV and $1.5 < |\eta_{1,2}| < 4.7$ and $\eta_1 \eta_2 < 0$. Error bars indicate statistical uncertainties only. On the left, we have the background estimated with the orthogonal dijet sample described in text, and on the right the background estimated from an extrapolation of the NBD fit to the lower multiplicity bins. An excess at very low multiplicities is observed, which we attribute to the presence of events with a strongly interacting hard color-singlet exchange.

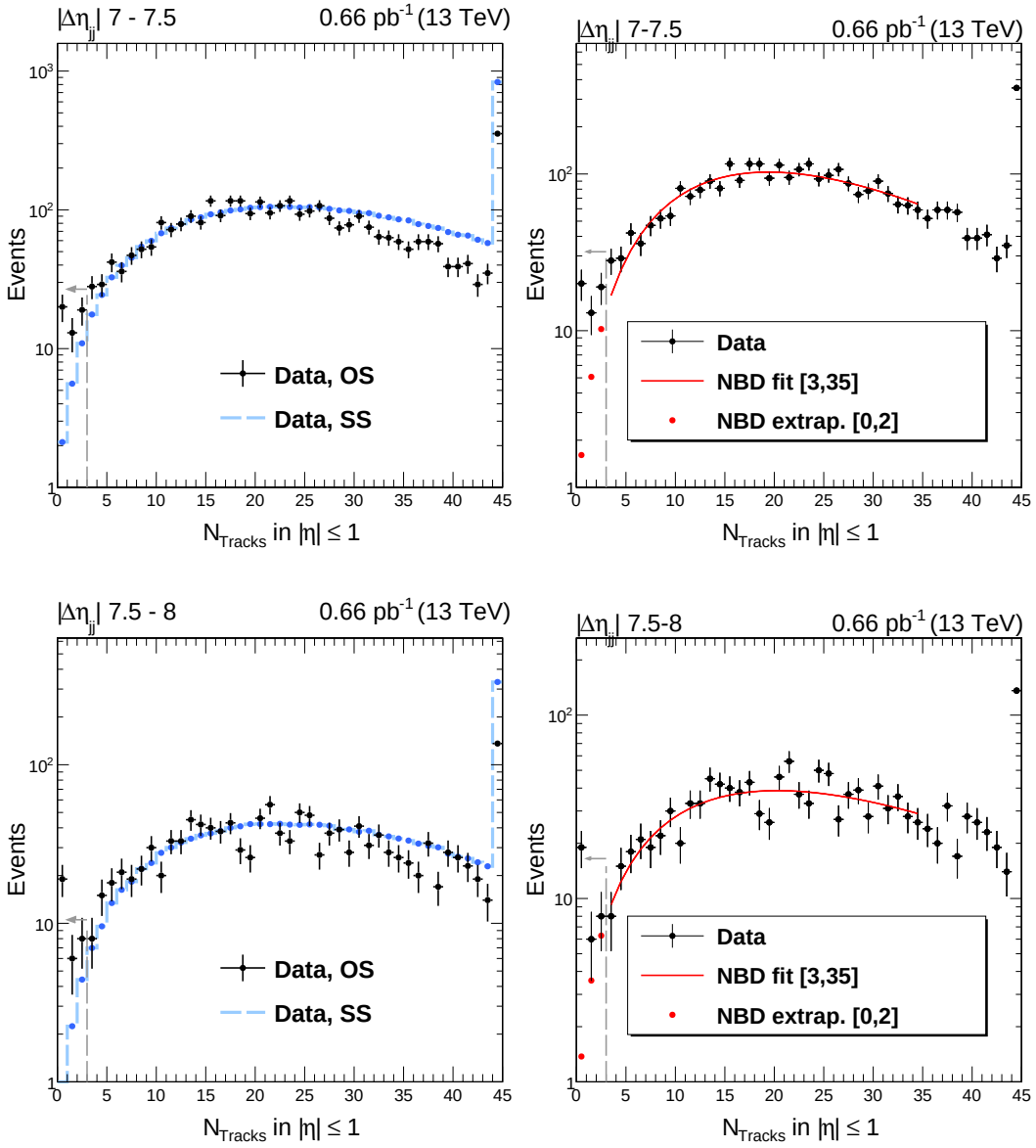

Figure 6.23: N_{tracks} in the fixed pseudorapidity region $|\eta| < 1$ for tracks with $p_{\text{T}}^{\text{track}} > 0.2$ GeV in different bins of $p_{\text{T}}^{\text{jet2}}$. The distributions are for leading jets which satisfy $p_{\text{T}} > 40$ GeV and $1.5 < |\eta_{1,2}| < 4.7$ and $\eta_1 \eta_2 < 0$. Error bars indicate statistical uncertainties only. On the left, we have the background estimated with the orthogonal dijet sample described in text, and on the right the background estimated from an extrapolation of the NBD fit to the lower multiplicity bins. An excess at very low multiplicities is observed, which we attribute to the presence of events with a strongly interacting hard color-singlet exchange.

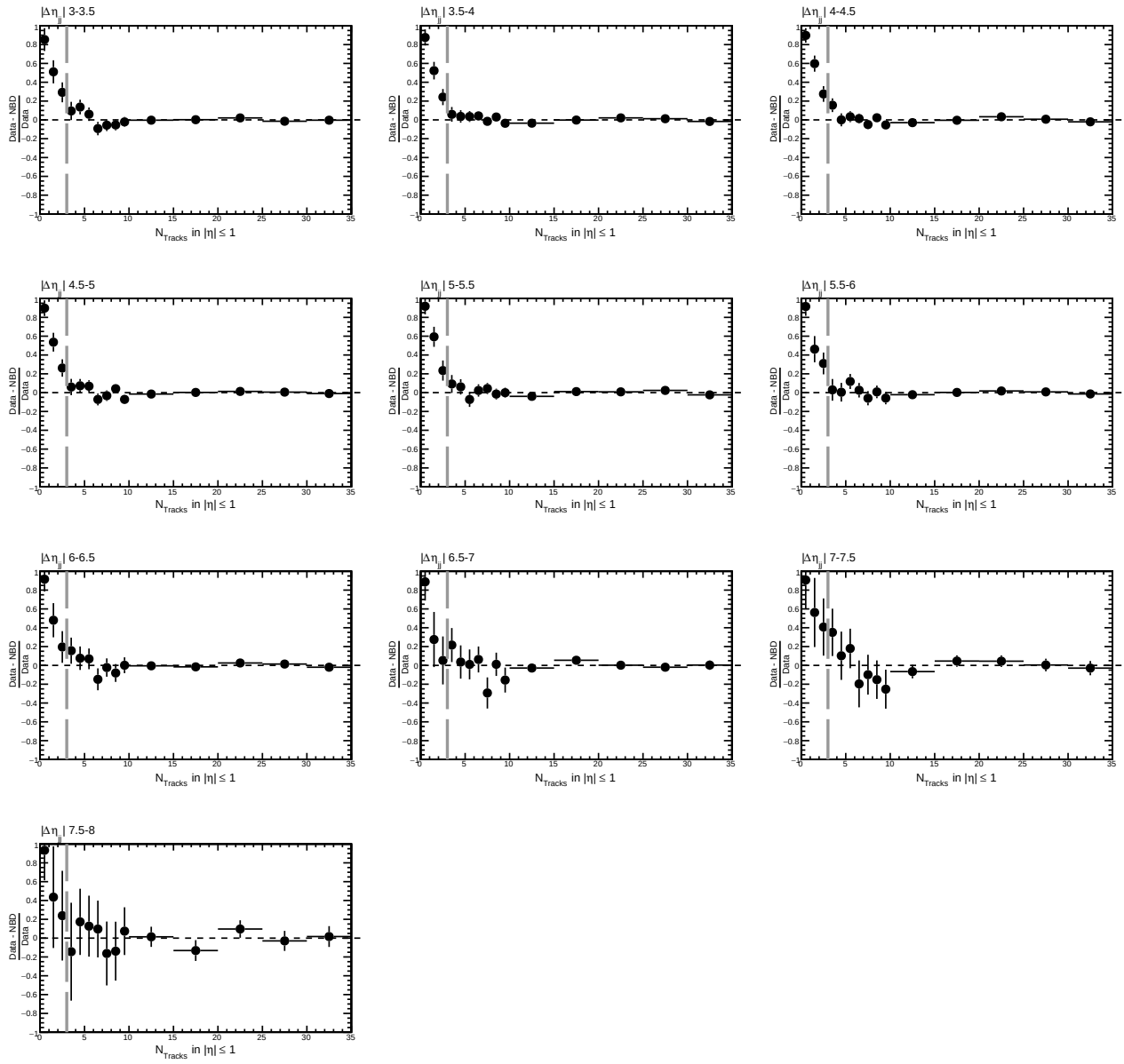

Figure 6.24: Bin-by-bin difference between data and the NBD fit results as a function of $\Delta\eta_{jj}$, normalized to the number of events in the data. The NBD extrapolation lies on the left-hand side w.r.t. the vertical dashed line, where an excess on the low multiplicity bins is observed. Vertical error bars represent statistical uncertainties only.

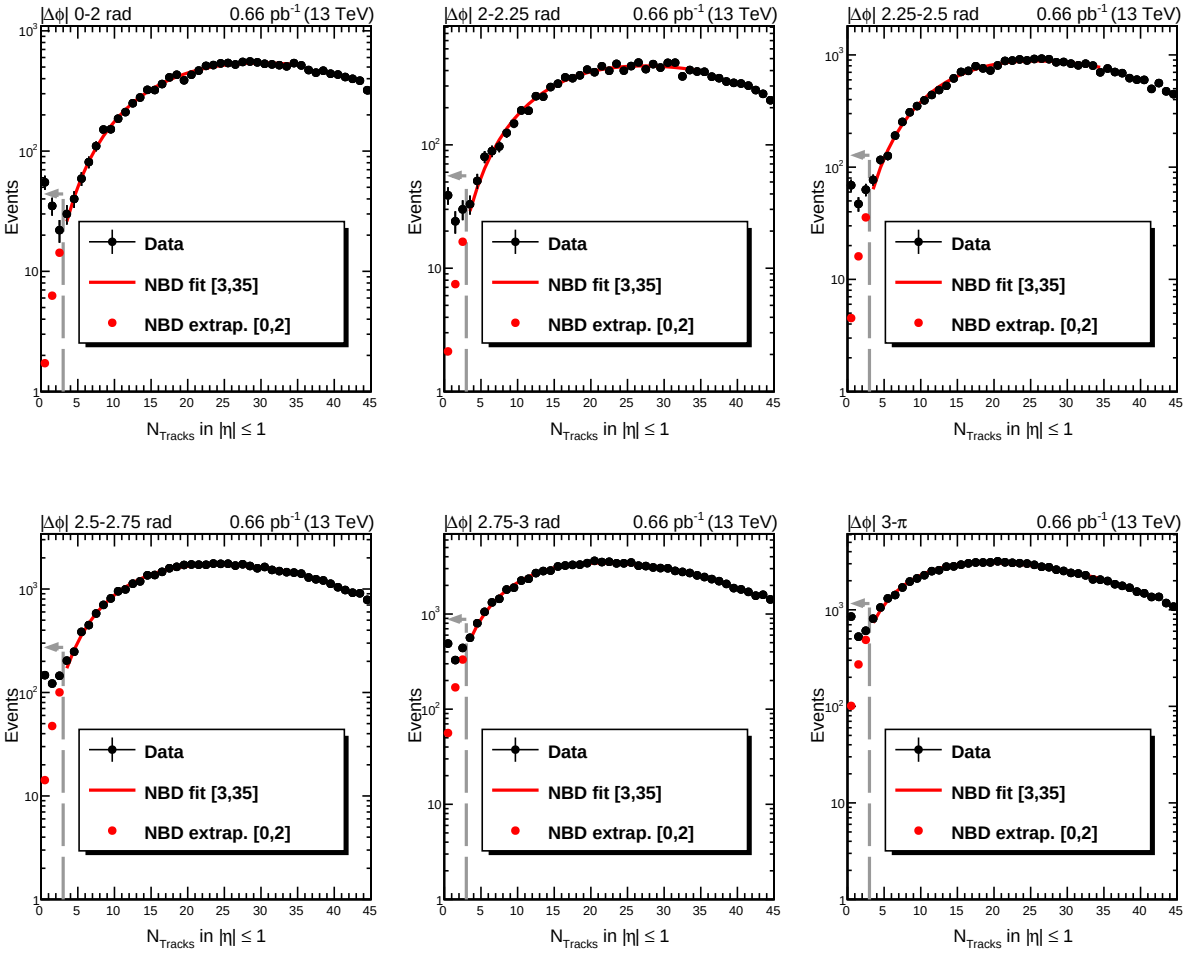

Figure 6.25: N_{tracks} distributions in fixed pseudorapidity distribution $|\eta| < 1$ in bins of the angular separation between the leading two jets $\Delta\phi_{jj}$ for dijet events satisfying the dijet selection described in text. The NBD is fit in the control region [3,35] and extrapolated down to the first three multiplicity bins [0,2] to estimate the non-CSE background. For larger $\Delta\phi_{jj}$ separations, the N_{tracks} is biased towards larger values due to the larger amount of inter-jet radiation which is causing the large angular decorrelations.

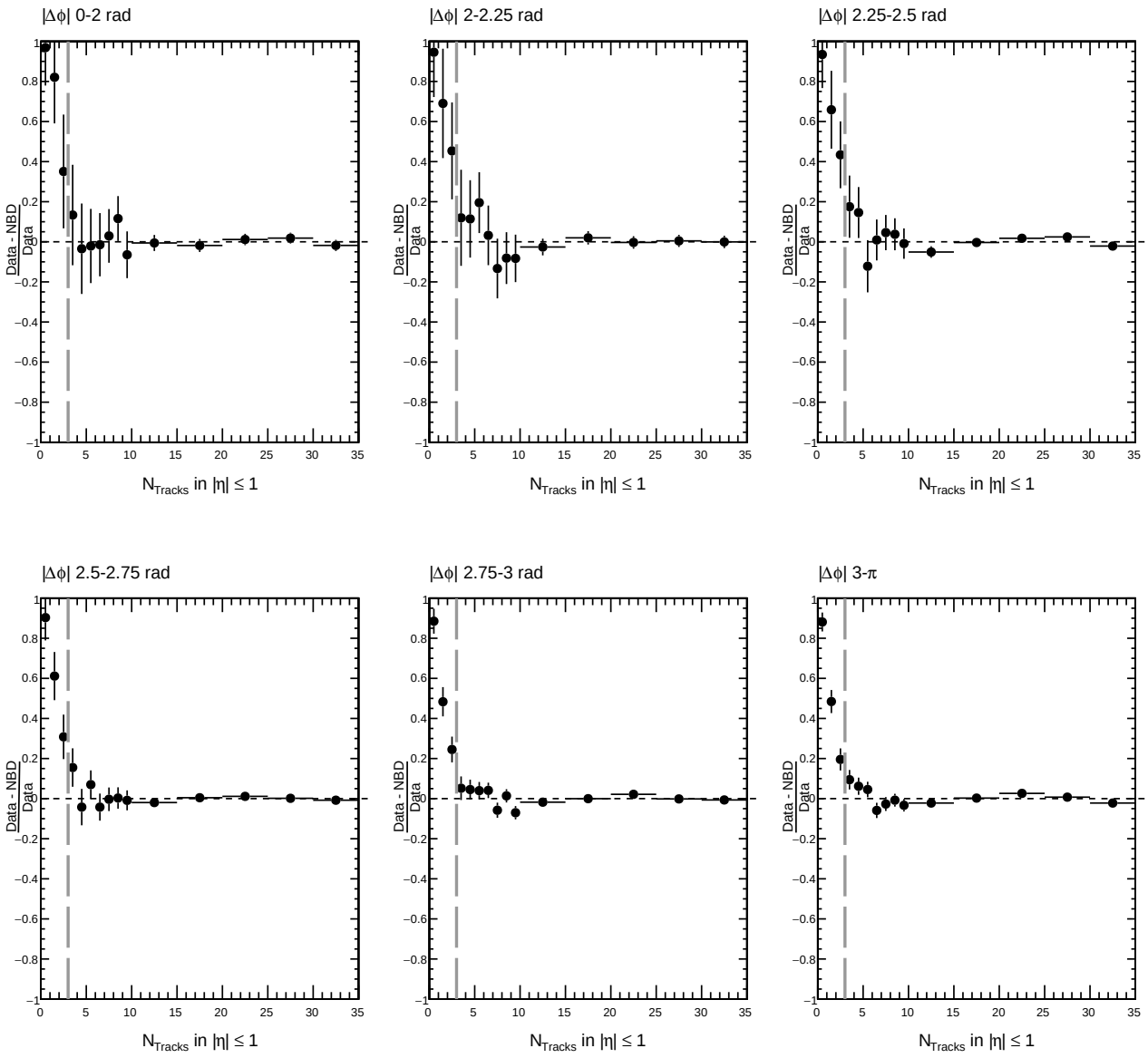

Figure 6.26: Bin-by-bin difference between data and the NBD fit results as a function of $\Delta\phi_{jj}$, normalized to the number of events in the data. The NBD extrapolation lies on the left-hand side w.r.t. the vertical dashed line, where an excess on the low multiplicity bins is observed. Vertical error bars represent statistical uncertainties only.

The NBD fit parameters in bins of the kinematic variables of interest are shown in Fig. 6.27. There are two fit parameters that control the shape of the NBD function: n and p (see Eqn. 6.3). The parameters n and p have a smooth dependence on the kinematic variables of interest, for the most part consistent with each other within the statistical uncertainties. This reflects the fact that the multiplicity of charged particles between the jets is, for the most part, largely independent of the jet kinematics. The deviations typically occur in bins where the amount of data is more limited than in other bins. As a function of $\Delta\phi_{\mathrm{jj}}$, there is a stronger dependence of the fit parameters. This stronger dependence is expected, since there is more particle activity between the jets for configurations where the jets are nearly collinear ($\Delta\phi \to 0$). This is because these strong angular decorrelations are due to the production of mini-jets or other unclustered hadrons that recoil against the high-p_T jets. As a function of p_T, we see a mild evolution of n and p at larger p_T. This is because, for this configuration, it is more likely that the high-p_T jets get closer to the rapidity gap region, which in turn modifies the measured N_{tracks} distribution. As a function of $\Delta\eta_{\mathrm{jj}}$, the fit parameters n and p are consistent with each other within the statistical uncertainties. The last bin is more statistically limited.

The extracted gap fractions with the MC method, SS method and the NBD method can be seen in Fig. 6.28, Fig. 6.29, and Fig. 6.30. In the case of the gap, fraction as a function of $\Delta\eta_{\mathrm{jj}}$, the results are compatible within statistical uncertainties except at the smallest pseudorapidity separations, whereas in the gap fraction as a function of the subleading jet transverse momentum $p_{\mathrm{T,jet\,2}}$ the SS method underestimates the gap fraction relative to the NBD method results at low transverse momentum. The stability of the signal for different fit regions on the gap fraction can be seen in Fig. 6.31.

6.7 Signal region definition and optimization

We integrate the first three bins of the multiplicity distribution $N_{\mathrm{Tracks}} \leq 2$ in order to extract the number of CSE events, and subtract the non-CSE contamination estimated from

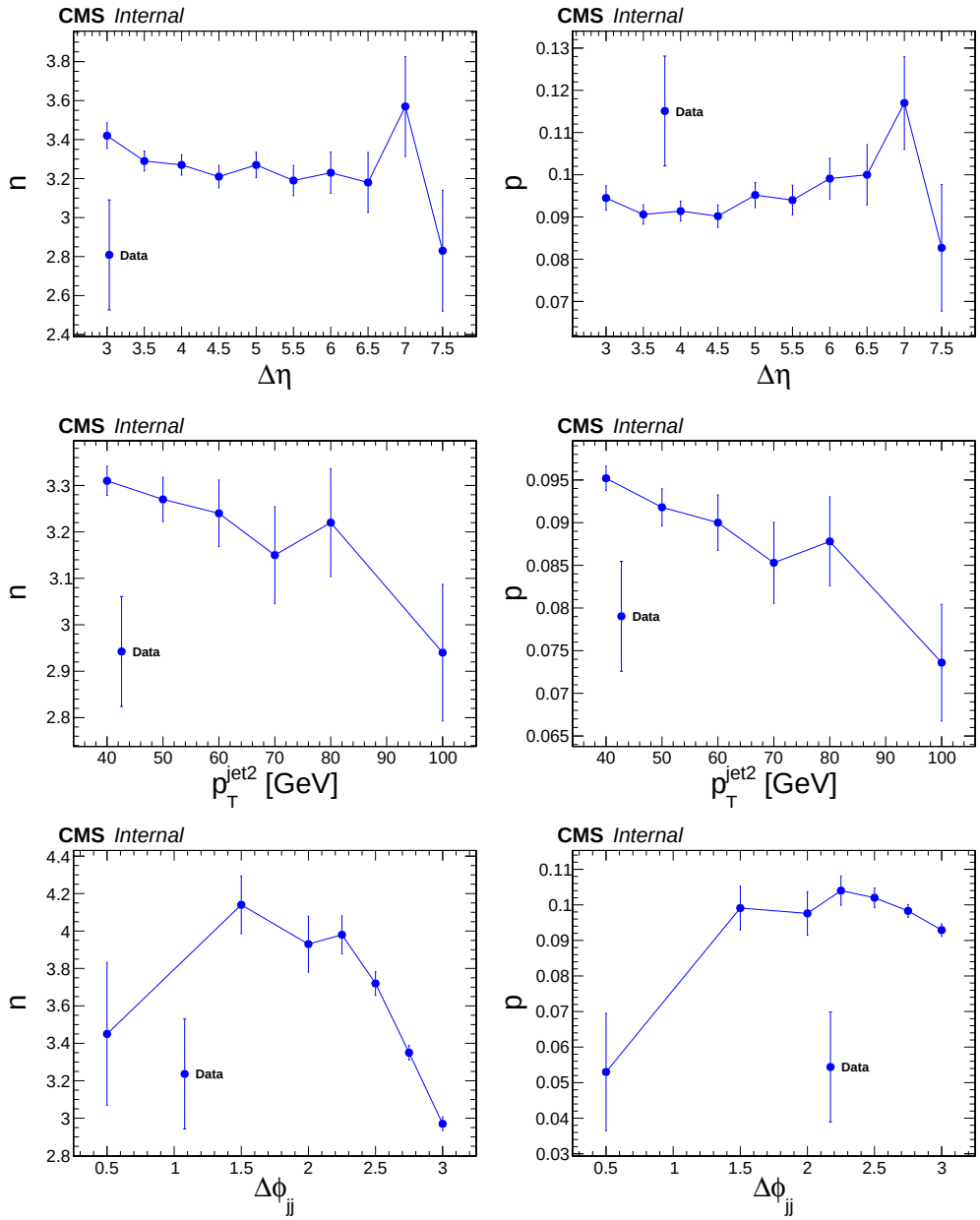

Figure 6.27: Negative binomial distribution parameters n and p obtained with the fits to N_{tracks} data, according to Eqn. 6.3. The n and p fit parameters are presented as a function of $\Delta\eta_{\text{jj}}$, $p_{\text{T}}^{\text{jet2}}$ and $\Delta\phi_{\text{jj}}$.

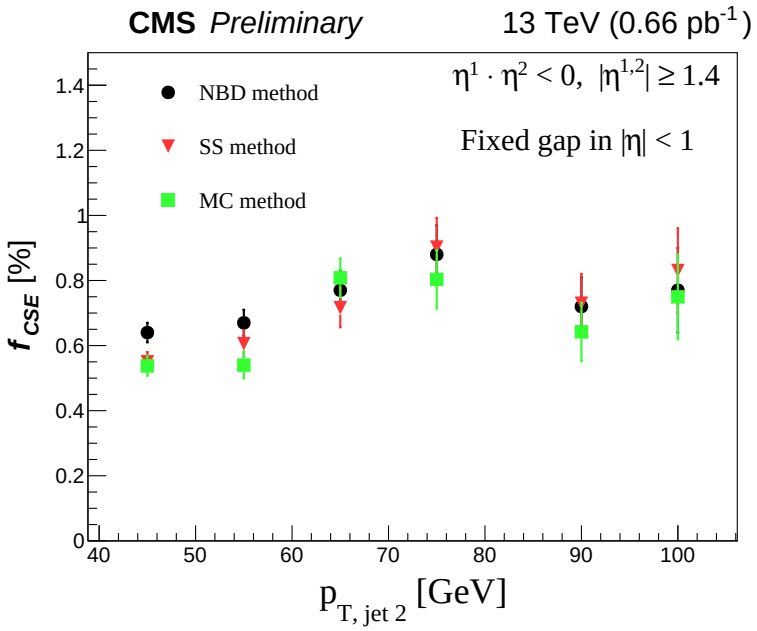

Figure 6.28: Comparison between the MC method, SS method, and NBD method results for the extraction of the fraction of color-singlet events as a function of the subleading jet transverse momentum. The vertical error bars represent the statistical uncertainties only

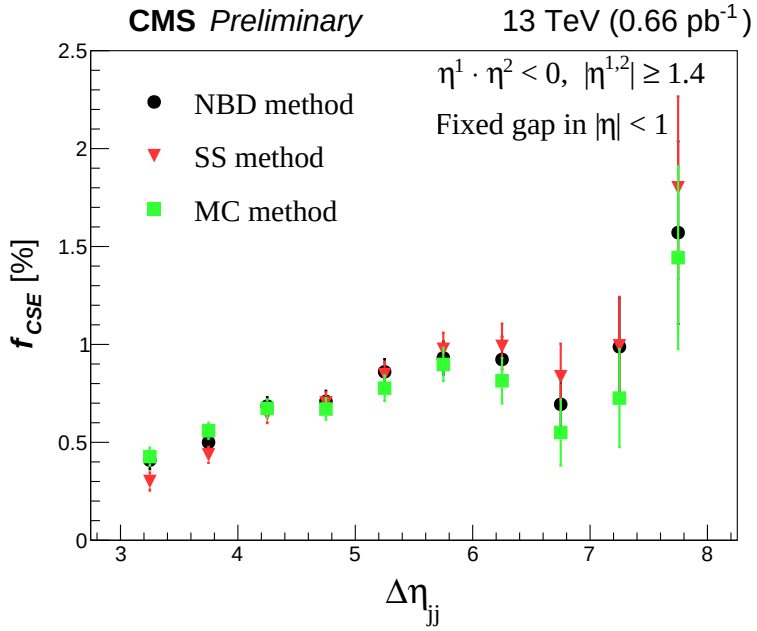

Figure 6.29: Comparison between the MC method, SS method and NBD method results for the extraction of the fraction of color-singlet events as a function of the pseudorapidity separation between the two leading jets. The vertical error bars represent the statistical uncertainties only.

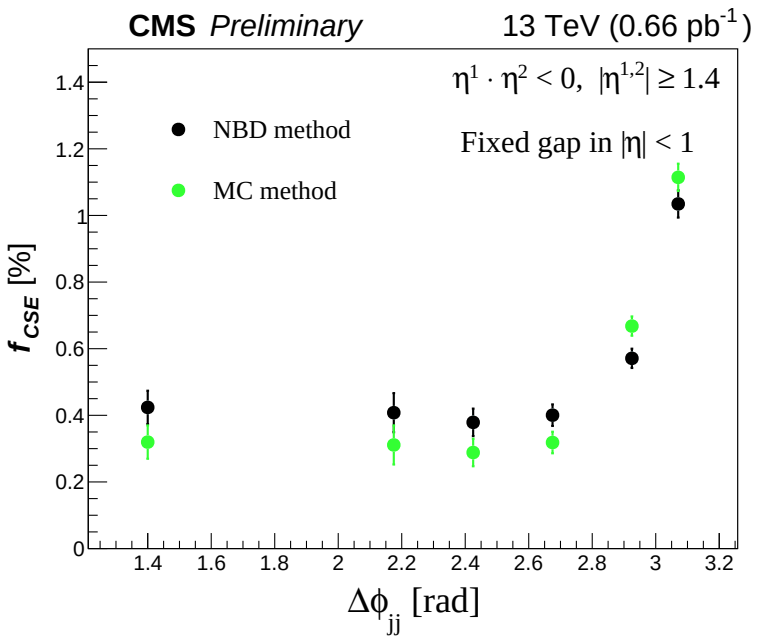

Figure 6.30: Comparison between the MC method, and NBD method results for the extraction of the fraction of color-singlet events as a function of the azimuthal angle separation between the leading two jets. The vertical error bars represent the statistical uncertainties only.

data as described in this section. The region is selected by observing that both the SS method and NBD method yield an excess over the estimated non-CSE distribution in that region. Monte Carlo generator-level simulations for jet-gap-jet with BFKL calculations at NLL confirm this criteria as well. The results assuming different integration regions for the jet-gap-jet signal is shown in Fig. 6.32. We can see there is a significant difference between including only the $N_{\text{Tracks}} = 0$ and $N_{\text{Tracks}} \leq 1$ region, but the fraction stabilizes after considering the first three multiplicity bins $N_{\text{Tracks}} \leq 2$. The spill of signal events (which should otherwise populate the $N_{\text{tracks}} = 0$ bin) to non-zero multiplicity bins is due hadronization effects, which may lead to charged particles populating the fixed pseudorapidity interval outside of the jets cones. Indeed, for events at low nonzero N_{tracks}, strong correlations in η–ϕ between the charged particles and the jets are observed. This suggests that the "spillings" observed correspond to charged particle constituents of the jet falling into the $|\eta| < 1$ region. In Fig. 6.33, we see the angular correlation between the tracks in

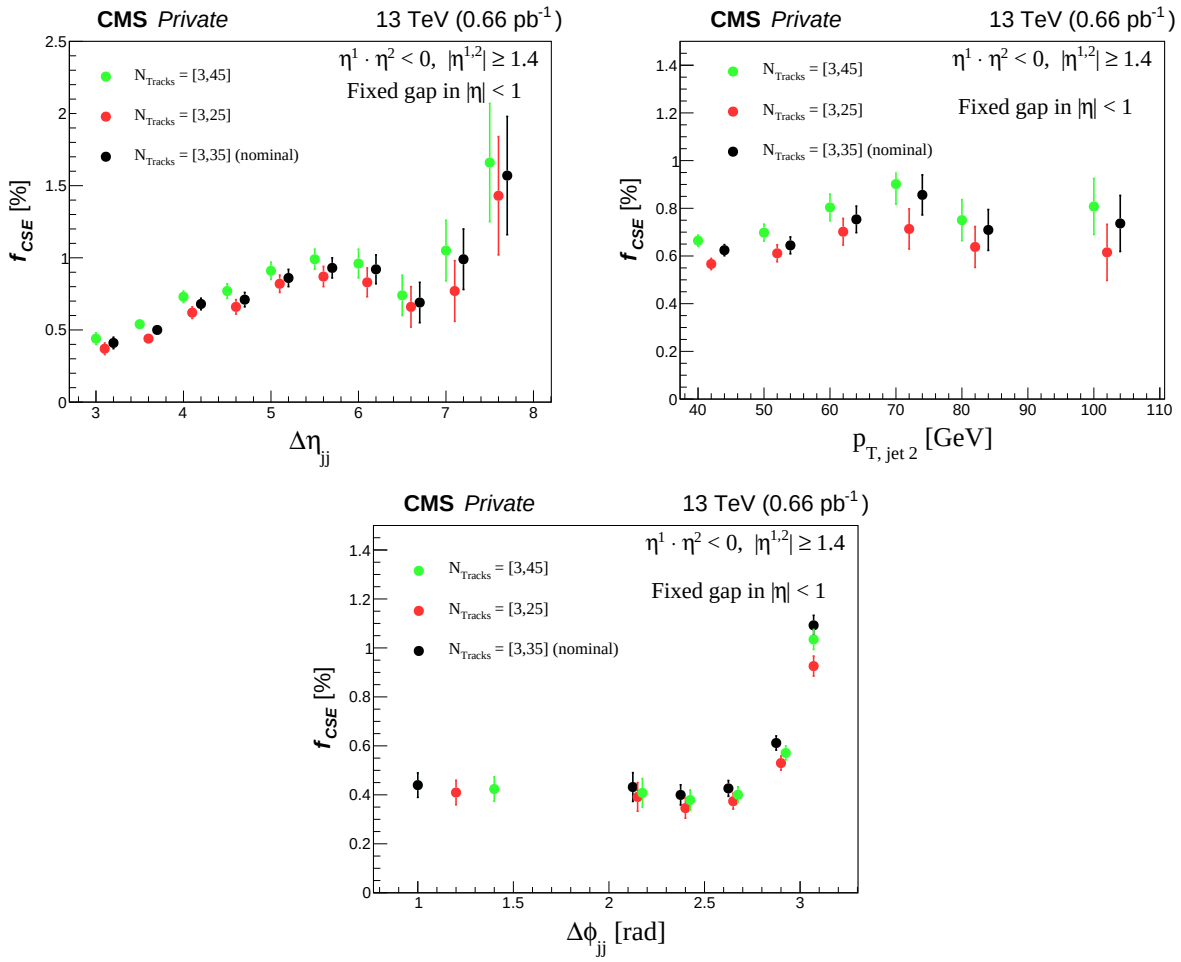

Figure 6.31: Stability on the gap fraction as a function of the fit range region. Error bars represent statistical uncertainties only. For visualization purposes, the bin of $p_{\mathrm{T,\,jet\,2}} = 100$–$200$ GeV is plotted around 100 GeV. Black symbols correspond to the nominal selection.

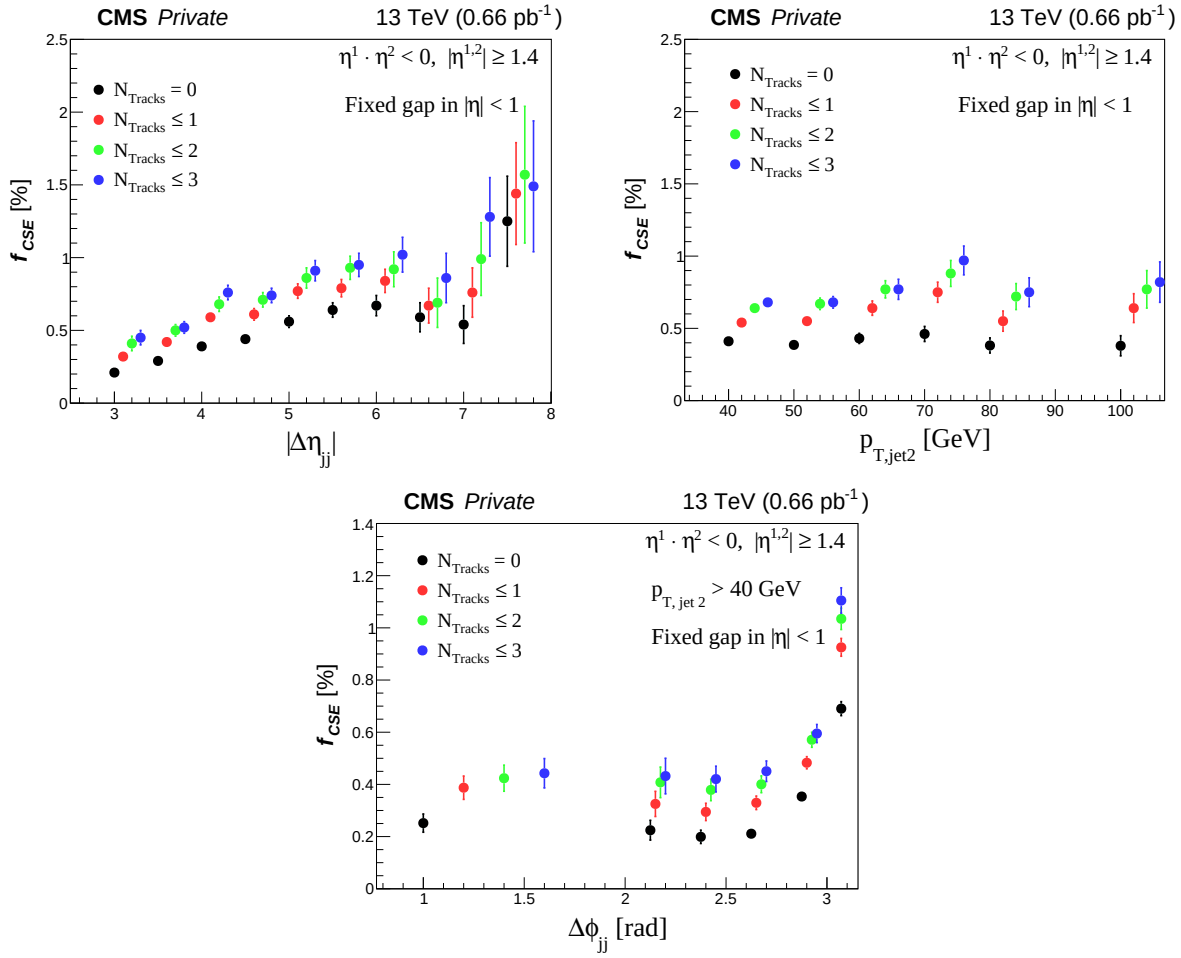

Figure 6.32: Stability of the extracted gap fraction for various signal integration region cuts. The green dots correspond to the nominal selection. Error bars represent statistical uncertainties only. For visualization purposes, the bin of $p_{\mathrm{T,\,jet\,2}} = 100$–$200$ GeV is plotted around 100 GeV.

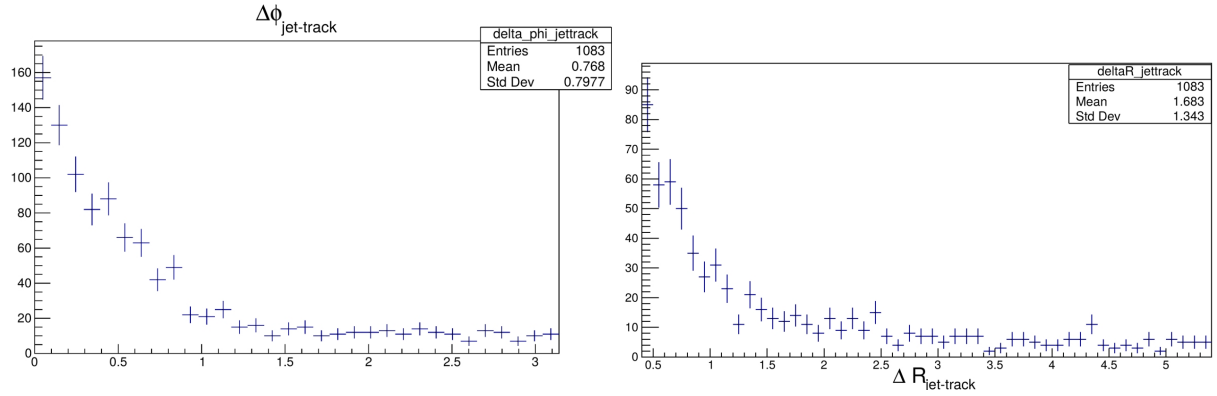

Figure 6.33: Angular correlations between the charged particle track and the high p_T jet in the same hemisphere of the detector.

the central gap and the jet located in the same hemisphere of the detector for $N_{\text{tracks}} = 1$. We inspect the angular correlation in $\Delta\phi_{\text{track-jet}}$ and $\Delta R = \sqrt{\Delta\eta^2_{\text{track-jet}} + \Delta\phi^2_{\text{track-jet}}}$. The data shows that the charged-particle track is strongly correlated in ϕ with the jet in the same hemisphere of the detector. The plot in ΔR supports these strong correlations near to the jet core, but also suggests that these emissions in principle can be at wide angles relative to the jet axis.

6.8 Closure test

In this analysis, we extract the gap fractions f_{CSE} using detector-level charged-particle multiplicities. Here, we explore the use of generator-level variables on the gap fraction. We extract the gap fractions using the NBD method using the collection of generator-level charged-particles (absence of track reconstruction inefficiencies), and using generator-level anti-k_t jet collection (jet true transverse momenta and pseudorapidity). For this, we use `Pythia8` color-exchange simulated dijet events and `Herwig6.5` color-singlet exchange simulated dijet events, which together form charged-particle multiplicity distributions like the ones we find in data. The hadron-level particles correspond to stable particles with lifetime $c\tau > 10$ mm. We apply the same selection requirements at generator-level and at detector-level that we use in the analysis for the jet collection and charged-particle

collection. We show the results when considering the signal region in $N_{\text{Tracks}} = 0$, and when integrating over the first three multiplicity bins as in our analysis $N_{\text{Tracks}} < 3$, depicted explicitly for $p_{\text{t, jet 2}}$, $\Delta\eta_{\text{jj}}$, and $\Delta\phi_{\text{jj}}$ in Figs. 6.34, 6.35, 6.36.

There is a small difference between the gen-level and detector-level results when considering only the first multiplicity bin for the gap fraction calculation. This is because at generator-level, the color-singlet exchange dijet events are more localized at $N_{\text{Tracks}} = 0$ than the detector-level distributions. After integrating over the first multiplicity bins, $N_{\text{Tracks}} < 3$, the gen-level and detector-level gap fractions f_{CSE} agree within statistical fluctuations. Track reconstruction inefficiencies influence the charged-particle counts of color-exchange dijet events, whereas the jet-gap-jet signal events are not affected, since these correspond to the absence of charged-particle tracks. Since we are subtracting the background, the results on the gap fraction f_{CSE} remain the same at generator-level and detector-level, provided one integrates the signal region correctly. The number of Monte Carlo generated color-singlet exchange events with $\Delta\eta_{\text{jj}} > 7$ or with $\Delta\phi_{\text{jj}} < 2.25$ rad is not large enough to perform the study in these bins. A good agreement between the results extracted on detector-level and hadron-level provides a closure test for the method applied.

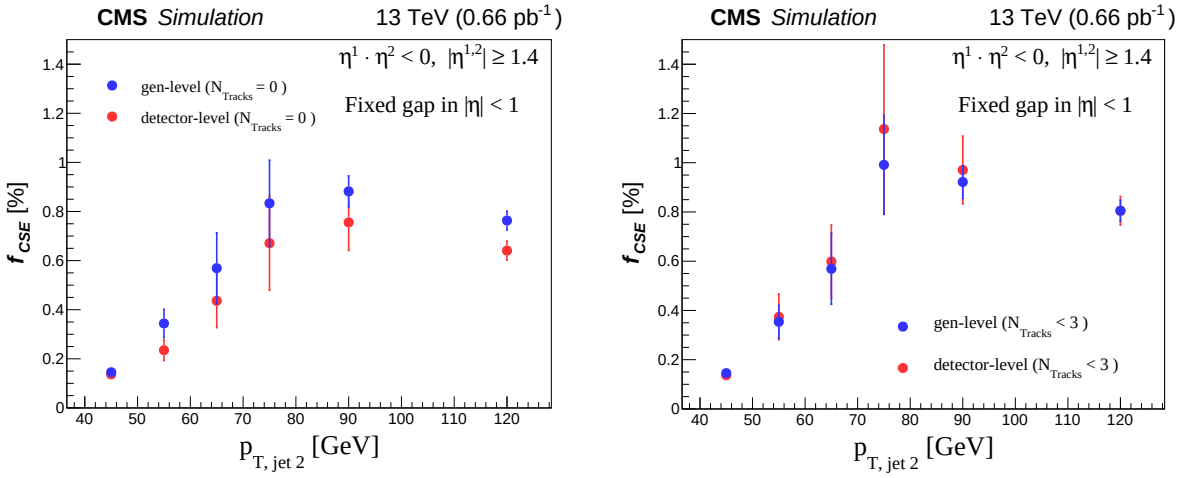

Figure 6.34: Color-singlet exchange fractions, f_{CSE}, in bins of $p_{\text{T, jet 2}}$ calculated for two definitions of the signal region, $N_{\text{Tracks}} = 0$ (left), and $N_{\text{Tracks}} < 3$(right), based on detector-level distributions (red) or the generator-level distributions (blue).

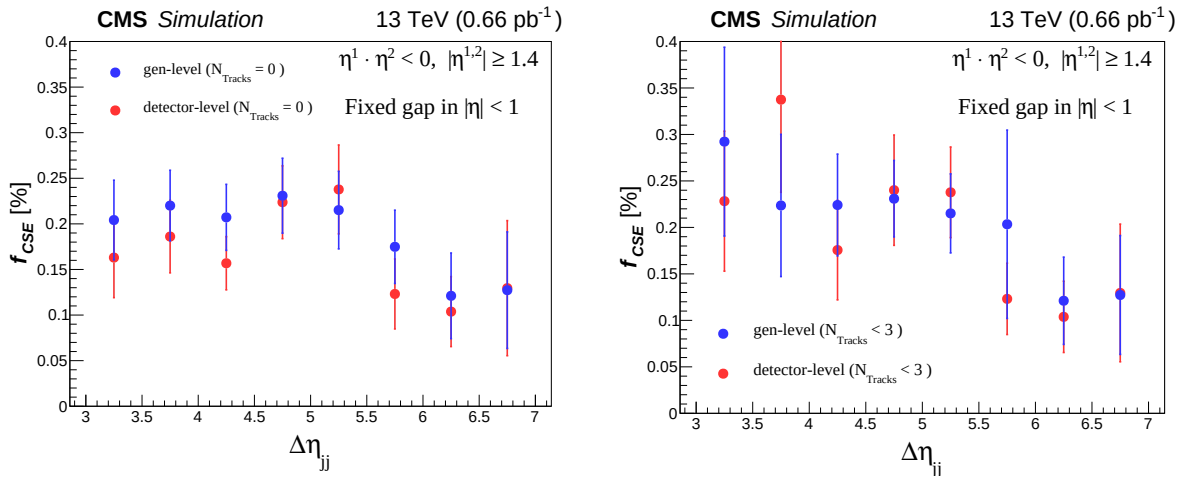

Figure 6.35: Color-singlet exchange fractions, f_{CSE}, in bins of $\Delta\eta_{\mathrm{jj}}$ calculated for two definitions of the signal region, $N_{\mathrm{Tracks}} = 0$ (left), and $N_{\mathrm{Tracks}} < 3$(right), based on detector-level distributions (red) or the generator-level distributions (blue).

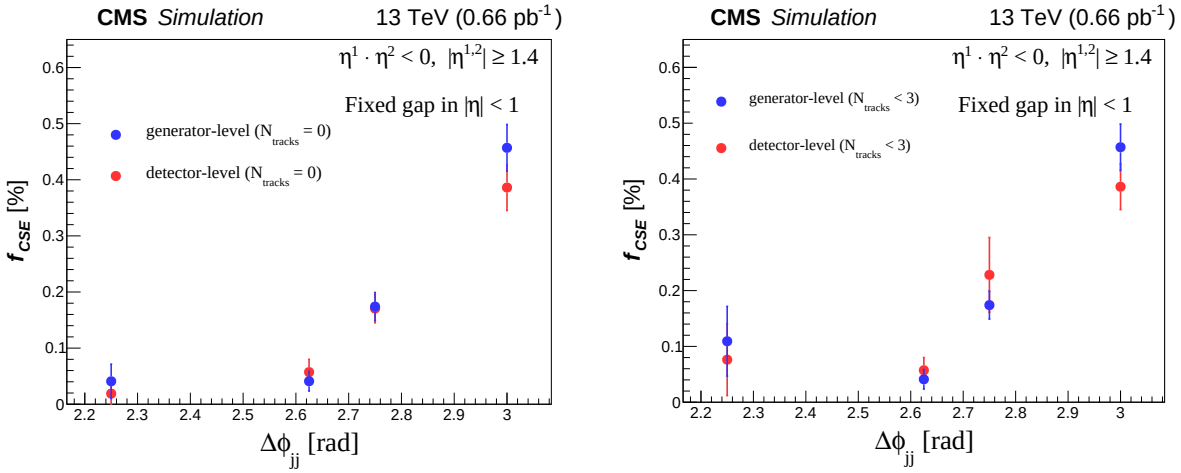

Figure 6.36: Color-singlet exchange fractions, f_{CSE}, in bins of $\Delta\phi_{\mathrm{jj}}$ calculated for two definitions of the signal region, $N_{\mathrm{Tracks}} = 0$ (left), and $N_{\mathrm{Tracks}} < 3$(right), based on detector-level distributions (red) or the generator-level distributions (blue).

6.9 Systematic uncertainties

The sources of systematic uncertainties for the f_{CSE} fraction measurement are:

Jet energy scale: The p_{T} of each jet is varied with $p_{\mathrm{T}} \to p_{\mathrm{T}} \pm \delta p_{\mathrm{T}}(p_{\mathrm{T}}, \eta)$, where $\delta p_{\mathrm{T}}(p_{\mathrm{T}}, \eta)$ is the jet energy scale uncertainty as a function of the jet p_{T} and η. The new jet collection

is reordered in p_T, and the analysis is repeated. The difference in the extracted fraction f_{CSE} relative to the results found with the nominal jet energy corrections is a measure of the associated systematic uncertainty. The resulting relative uncertainty is 0.5–6.0%.

Track quality: The selection criteria used to define high-purity tracks are loosened and the difference in f_{CSE} with respect to the nominal selection is taken as the associated systematic uncertainty. The loose quality criteria correspond to the minimum requirements yielding well-reconstructed tracks in the CMS detector, as described in Ref. (186). The corresponding uncertainty in f_{CSE} is 1.5–8.0%.

Charged particle p_T threshold: Charged particles with $p_T < 200$ MeV are not considered in identifying a central gap. To study the sensitivity of the results to this threshold, the analysis is repeated with p_T thresholds of 150 and 250 MeV for particles with $|\eta| < 1$. The corresponding relative differences in the measured f_{CSE} fractions are 1.1–5.8% and are assigned as systematic uncertainties.

Background subtraction method: The background determined using the SS method is compared with the adopted NBD background approach, and the difference is the associated systematic uncertainty. This reflects the imperfect knowledge of the N_{tracks} distributions for color-exchange dijet events. At lower p_T^{jet2} values, with $40 < p_T^{jet2} < 50$ GeV, the relative systematic uncertainty is 14.6%, whereas for larger values, $p_T^{jet2} > 80$ GeV, it is 2–5%.

NBD fit parameters: The NBD function has three free parameters, including an overall normalization. The color-exchange dijet yields in the signal region are recalculated by varying the NBD fit parameters within their uncertainties. Correlations between the fit parameters are included in this procedure. The maximal differences relative to the nominal results are a measure of the associated systematic uncertainty. These calculations result in a relative uncertainty of less than 2.6% in the extracted f_{CSE}.

Functional form of the fit: To quantify the systematic uncertainty associated with the functional form chosen to fit the N_{tracks} distribution at large multiplicities, the N_{tracks} dis-

tribution is fit instead with a double NBD function (a sum of two NBD functions) to extract f_{CSE}. The double NBD function has been found to be an alternative empirical parametrization of charged particle multiplicities in hadronic collisions at various $\sqrt{s}$, particularly for very wide N_{tracks} intervals (202; 204; 205). The symmetrized difference of the f_{CSE} extracted with the double NBD fit with respect to the nominal f_{CSE} fraction is taken as the respective systematic uncertainty. The relative uncertainty in the extracted f_{CSE} is 2–7%.

The results of the systematic uncertainties considered in this study can be seen in Tabs. 6.1. The leading systematic uncertainty is related to the background subtraction procedure. The subleading source of systematic uncertainty is the choice of track quality used to build the N_{tracks} distribution.

Source	$\Delta\eta_{\mathrm{jj}}$	p_T^{jet2}	$\Delta\phi_{\mathrm{jj}}$
Jet energy scale	1.0–5.0	1.5–6.0	0.5–3.0
Track quality	6.0–8.0	5.4–8.0	1.5–8.0
Charged particle p_{T} threshold	2.0–5.8	1.6–4.0	1.1–5.8
Background subtraction method	4.7–15	2–15	12
NBD fit parameters	0.8–2.6	0.6–1.7	0.1–0.6
Functional form of the fit	2–7.3	1.4–8.0	0.6–7.8
Total	7–23	9–15	12–18.5

Table 6.1: Relative systematic uncertainties in percentage for the measurements of f_{CSE} in jet-gap-jet events. The jet-gap-jet results summarize the systematic uncertainties in bins of the kinematic variables of interest p_T^{jet2}, $\Delta\eta_{\mathrm{jj}}$, and $\Delta\phi_{\mathrm{jj}}$. When an uncertainty range is given, the range of values is representative of the variation found in f_{CSE} in bins of the kinematic variables of interest.

As mentioned before in this Chapter, no neutral particles are used in the definition of the pseudorapidity gap because of the relatively large p_{T} thresholds above the calorimeter noise for neutral hadrons and photons. Most dijet events with low N_{tracks} in the region $|\eta| < 1$ have little, if any, neutral particle activity in that region. Simulation studies that include the detector response suggest that the neutral hadron and photon activity observed in data originate from the emission of jet constituents into the $|\eta| < 1$ region, together

with residual contributions of the calorimeter noise. The f_{CSE} fractions remain mostly unaffected if the contribution of neutral particles at central η is included in the analysis. In particular, if the vector p_T sum of the neutral hadrons and photons for $|\eta| < 1$ is required to be less than 15 GeV, the results for f_{CSE} are the same, within the statistical uncertainties of f_{CSE}. This is consistent since the color-exchange dijet background is already subtracted in the determination of f_{CSE}.

6.10 Results

The measured fractions f_{CSE} are presented in Fig. 6.37 and Tables 6.2–6.4. As a function of $\Delta\eta_{jj}$, the f_{CSE} fraction shows a uniform increase from 0.4 to 1.0% for $\Delta\eta_{jj}$ between 3 and 6 units. Within the experimental uncertainties, f_{CSE} is about 0.7%, and shows little, if any, dependence on $p_{T,\,jet\,2}$. As a function of $\Delta\phi_{jj}$ between the two leading jets, the f_{CSE} fraction exhibits a peak near $\Delta\phi_{jj} = \pi$ with a value of 1%, which suggests that jet-gap-jet events are more strongly correlated in the transverse plane than inclusive dijet events. A constant value of about 0.4% is found for $\Delta\phi_{jj} < 2.8$; this implies that color-singlet exchange dijet events decorrelate at a similar rate as color-exchange dijet events in this interval.

The present results are compared with BFKL-based theoretical calculations of Royon, Marquet, Kepka (RMK) (129; 130) and Ekstedt, Enberg, Ingelman, Motyka (EEIM) (128; 131), the results of which are shown in Fig. 6.37. The RMK and EEIM model predictions include dominant NLL corrections to the BFKL evolution of the parton-level cross section using LO impact factors. The RMK predictions are supplemented with a gap survival probability of $|\mathscr{S}|^2 = 10\%$, whose value is used to match the f_{CSE} values observed in data. The RMK predictions use an updated parametrization of the BFKL NLL amplitudes that include the larger phase space available at LHC energies (136), which are then implemented in the HERWIG6 generator (130). The theoretical uncertainties in the RMK prediction are due to renormalization and factorization scales uncertainties in the BFKL calculation (130). The EEIM predictions include soft rescattering effects based on

MPI or MPI supplemented with SCI. In the EEIM approach, the spectator parton activity originating from perturbative gluons is modeled in terms of initial- and final-state parton showers, MPI, and hadronization processes, as implemented in PYTHIA6 (128; 131). The SCI accounts for possible gap destruction effects caused by color exchange with negligible momentum transfer that rearrange the color field created in the pp collision (128). The free parameters of the SCI model are fit to describe the previous 7 TeV measurement by CMS (131). The remaining nonperturbative corrections are either modeled with a survival probability of $|\mathscr{S}^2 = 1.2\%$ to match the f_{CSE} value found in data (purple dashed line in Fig. 6.37) or with SCI (orange dotted line in Fig. 6.37). The theoretical uncertainties in the EEIM model predictions are dominated by the cutoff p_{T} scale used for MPI in the simulation.

According to both the RMK and EEIM model calculations, f_{CSE} should have a weak dependence on $p_{\mathrm{T,\,jet\,2}}$. Within the uncertainties, this feature is consistent with the observed f_{CSE} values. The predictions by RMK and EEIM (with MPI only) yield a decreasing f_{CSE} with increasing $\Delta\eta_{\mathrm{jj}}$. This is in disagreement with the data, which show a f_{CSE} that generally grows with larger $\Delta\eta_{\mathrm{jj}}$. The EEIM model predictions, when supplemented with SCI, correctly describe f_{CSE} as a function of $\Delta\eta_{\mathrm{jj}}$ within the uncertainties. The predictions of the RMK model for f_{CSE} as a function of $\Delta\phi_{\mathrm{jj}}$ are consistent with the data within the uncertainties for medium angular separations $1 < \Delta\phi_{\mathrm{jj}} < 3$, but underestimate the experimental result by about 10% near $\Delta\phi_{\mathrm{jj}} = \pi$. The model significantly underestimates the observed f_{CSE} for small angular separations with $\Delta\phi_{\mathrm{jj}} < 1$. The EEIM model uses LO 2→2 hard processes resulting in back-to-back hard jets, such that $\Delta\phi_{\mathrm{jj}} \approx \pi$, with only small deviations due to the leading logarithmic parton showers, but no hard NLO $2 \to 3$ processes causing larger deviations.

The decrease of the f_{CSE} predictions is linked with the fact that large $\Delta\eta_{\mathrm{jj}}$ between the jets corresponds to high Bjorken-x from both protons. Since the two-gluon color-singlet exchange is coupled more strongly to gluons than to quarks, the hadron-level

$\Delta\eta_{jj}$	$\langle\Delta\eta_{jj}\rangle$	f_{CSE} [%]
3.0–3.5	3.24	$0.41 \pm 0.02^{+0.11}_{-0.04}$
3.5–4.0	3.75	$0.50 \pm 0.02^{+0.07}_{-0.07}$
4.0–4.5	4.25	$0.68 \pm 0.02^{+0.07}_{-0.06}$
4.5–5.0	4.74	$0.71 \pm 0.03^{+0.06}_{-0.06}$
5.0–5.5	5.24	$0.86 \pm 0.04^{+0.06}_{-0.08}$
5.5–6.0	5.73	$0.93 \pm 0.04^{+0.06}_{-0.09}$
6.0–6.5	6.22	$0.92 \pm 0.06^{+0.11}_{-0.09}$
6.5–7.0	6.71	$0.69 \pm 0.07^{+0.15}_{-0.05}$
7.0–7.5	7.22	$0.99 \pm 0.14^{+0.07}_{-0.15}$
7.5–8.0	7.73	$1.57 \pm 0.27^{+0.35}_{-0.56}$

Table 6.2: Measured values of the fraction of color-singlet exchange events f_{CSE} in bins of the pseudorapidity difference between the two leading jets $\Delta\eta_{jj}$. The first column indicates the $\Delta\eta_{jj}$ intervals and the last column represents the measured fraction. The first and second uncertainties correspond to the statistical and systematic components, respectively. The results are integrated over the allowed p_T^{jet2} and $\Delta\phi_{jj}$ values. The mean values of $\Delta\eta_{jj}$ in the bin are given in the middle column.

cross section drops significantly due to the drop of the gluon PDFs. This can be overcome with parton-flavor dependent survival probability, or with kinematic-dependent survival probability effects. It is worth mentioning that calculations include partial corrections at NLO in α_s within the BFKL framework, namely the resummation of large logarithms of energy at NLL accuracy using LO impact factors. Higher-order corrections to impact factors are known to have significant effects in the description of similar processes, such as Mueller–Navelet jets (137). Recently, major progress has been made in the calculation of NLO impact factors for the jet-gap-jet process (208; 209). These corrections have yet to be included in the BFKL theoretical calculations to complete the NLO analysis of the jet-gap-jet process.

6.11 Comparison with previous results

In Fig. 6.38, the current results are compared with previous measurements of f_{CSE} with a central gap in $|\eta| < 1$ by the D0 and CDF Collaborations at the Tevatron in $p\bar{p}$ collisions at

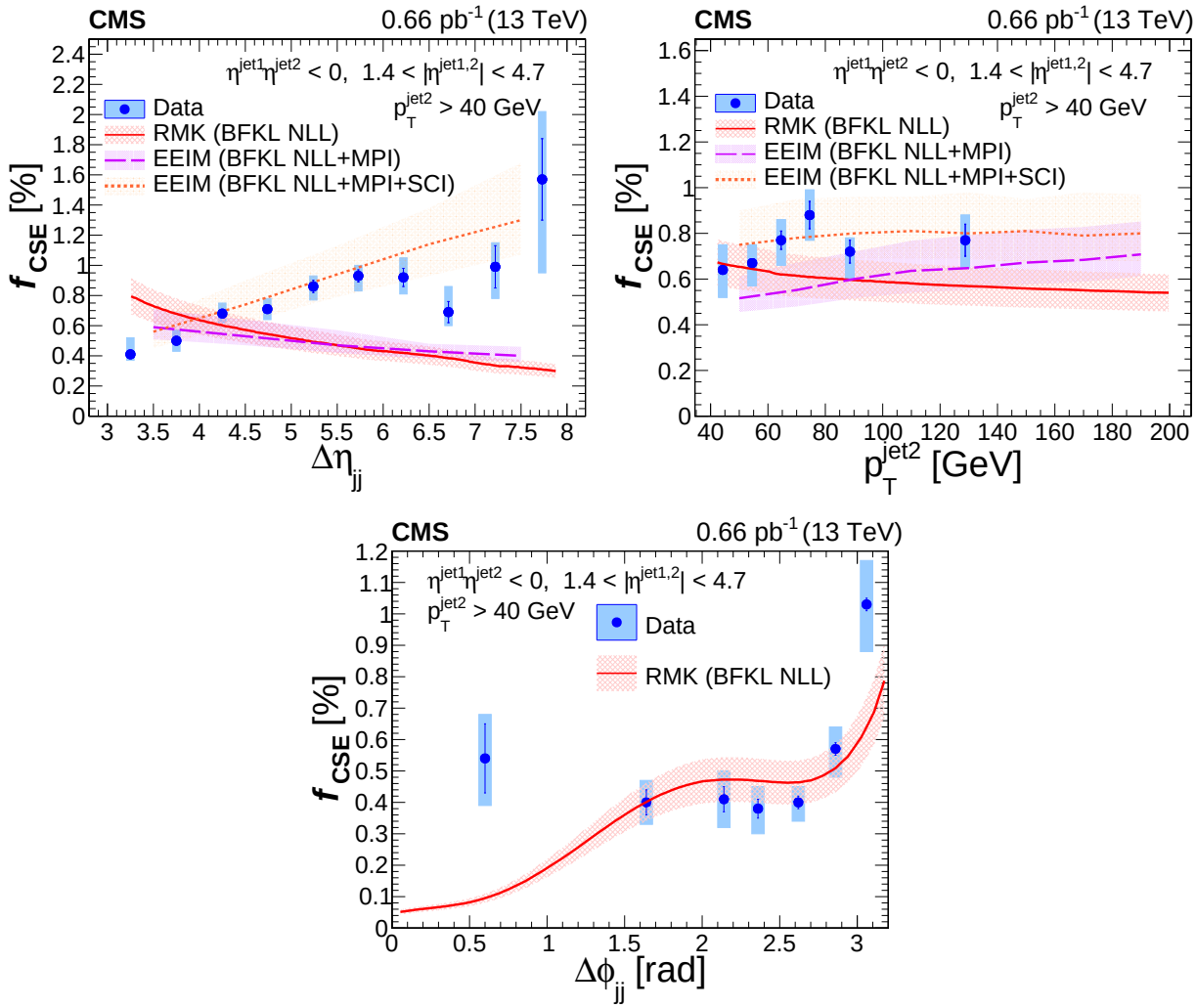

Figure 6.37: Fraction of color-singlet exchange dijet events, f_{CSE}, measured as a function of $\Delta\eta_{\mathrm{jj}}$, $p_{\mathrm{T}}^{\mathrm{jet2}}$, and $\Delta\phi_{\mathrm{jj}}$ in pp collisions at $\sqrt{s} = 13$ TeV. The vertical bars represent statistical uncertainties, while boxes represent the combination of statistical and systematic uncertainties in quadrature. The results are plotted at the mean values of $\Delta\eta_{\mathrm{jj}}$, $p_{\mathrm{T,\,jet2}}$, and $\Delta\phi_{\mathrm{jj}}$ in the bin. For a given plot of f_{CSE} versus a kinematic variable of interest ($p_{\mathrm{T,\,jet2}}$, $\Delta\eta_{\mathrm{jj}}$, or $\Delta\phi_{\mathrm{jj}}$), the other kinematic variables are integrated over their allowed range. The red solid curve corresponds to theoretical predictions based on the RMK model (129; 130) with gap survival probability of $|\mathscr{S}|^2 = 10\%$. The EEIM model (128; 131) predictions with MPI-only contributions and $|\mathscr{S}|^2 = 1.2\%$ or MPI+SCI are represented by the purple dashed and orange dotted curves, respectively. The bands around the curves represent the associated theoretical uncertainties. The EEIM model has only small contributions far from back-to-back jets since no hard NLO $2 \to 3$ processes are included, and thus predictions are not shown for the lower panel of f_{CSE} versus $\Delta\phi_{\mathrm{jj}}$. The figure is the same as the paper version one in Ref. (1).

p_T^{jet2} [GeV]	$\langle p_T^{jet2} \rangle$ [GeV]	f_{CSE} [%]
40–50	44.3	$0.64 \pm 0.01^{+0.11}_{-0.12}$
50–60	54.5	$0.67 \pm 0.02^{+0.08}_{-0.10}$
60–70	64.6	$0.77 \pm 0.04^{+0.08}_{-0.10}$
70–80	74.5	$0.88 \pm 0.06^{+0.09}_{-0.09}$
80–100	88.6	$0.72 \pm 0.05^{+0.04}_{-0.11}$
100–200	128.8	$0.77 \pm 0.07^{+0.09}_{-0.10}$

Table 6.3: Measured values of the fraction of color-singlet exchange events f_{CSE} in bins of the subleading jet transverse momentum p_T^{jet2}. The first column indicates the p_T^{jet2} bin intervals and the last column represents the measured fraction. The first and second uncertainties correspond to the statistical and systematic components, respectively. The results are integrated over the allowed $\Delta\eta_{jj}$ and $\Delta\phi_{jj}$ values. The mean values of p_T^{jet2} in the bin are given in the middle column.

$\Delta\phi_{jj}$	$\langle \Delta\phi_{jj} \rangle$	f_{CSE} [%]
0.00–1.00	0.60	$0.54 \pm 0.11^{+0.09}_{-0.10}$
1.00–2.00	1.64	$0.40 \pm 0.04^{+0.06}_{-0.06}$
2.00–2.25	2.14	$0.41 \pm 0.04^{+0.08}_{-0.08}$
2.25–2.50	2.36	$0.38 \pm 0.03^{+0.06}_{-0.07}$
2.50–2.75	2.62	$0.40 \pm 0.02^{+0.05}_{-0.06}$
2.75–3.00	2.86	$0.57 \pm 0.02^{+0.07}_{-0.09}$
3.00–π	3.06	$1.03 \pm 0.02^{+0.14}_{-0.15}$

Table 6.4: Measured values of the fraction of color-singlet exchange events f_{CSE} in bins of the azimuthal angular difference between the two leading jets $\Delta\phi_{jj}$. The first column indicates the $\Delta\phi_{jj}$ bin intervals and the last column represents the measured fraction. The first and second uncertainties correspond to the statistical and systematic components, respectively. The results are integrated over the allowed p_T^{jet2} and $\Delta\eta_{jj}$ values. The mean values of $\Delta\phi_{jj}$ in the bin are given in the middle column.

$\sqrt{s} = 0.63$ and 1.8 TeV (207; 147; 151; 150), and by the CMS Collaboration in pp collisions at 7 TeV (152). There are differences in the phase space volumes populated by the two leading jets, jet clustering algorithms, and distance parameters, which are described in the next paragraphs. Simulation studies that rely on hadron-level particle distributions indicate that the choice of the jet reconstruction algorithm (cone or anti-k_T algorithms) has a negligible effect on the shape of the charged particle multiplicity distribution between the jets. The value of the distance parameter R influences the charged particle multiplicity distribution shape of jet-gap-jet signal events. For large values of R, it is less likely for charged particle constituents of the jet to populate the central $|\eta| < 1$ region since the jet axes are further away from the edges of the gap region. This yields a sharper jet-gap-jet signal excess at $N_{\text{tracks}} = 0$ for large jet distance parameter. At small distance parameter R, there is more spillage of charged particles into the gap region, since the jet axes can approach the edge of the $|\eta| < 1$ interval more closely. The shape of the multiplicity distribution of color-exchange dijet events remains mostly unaffected by the size of R. In these simulation studies, these effects are negligible provided that f_{CSE} is extracted over the first multiplicity bins $N_{\text{tracks}} < 3$, as is done in this measurement.

The study by the D0 Collaboration (147) uses the calorimeter tower multiplicity distribution in $|\eta| < 1$, where each calorimeter tower has transverse energy $E_{\text{T}} > 200$ MeV. The 0.63 and 1.8 TeV studies consider jets with $E_{\text{T}}^{\text{jet}} > 12$ GeV and $1.9 < |\eta^{\text{jet}}| < 4.1$. The CDF Collaboration measured jet-gap-jet events at 0.63 and 1.8 TeV (151; 150). The N_{tracks} value in the region $|\eta| < 1$ with $E_{\text{T}} > 300$ MeV is used in the CDF analyses. Each of the two leading jets has $1.8 < |\eta^{\text{jet}}| < 3.5$, with $E_{\text{T}}^{\text{jet}} > 8$ GeV and > 20GeV for the 0.63 and 1.8 TeV studies, respectively. The jets are clustered using the cone algorithm with $R = 0.7$ for both CDF and D0 studies. The measurement by CMS at 7 TeV is done in three bins of $p_{\text{T}}^{\text{jet2}} = 40$–60, 60–100, and 100–200 GeV (152). The jets are clustered with the anti-k_T algorithm with $R = 0.5$ in the previous CMS study. Each of the two leading jets has $1.5 < |\eta^{\text{jet}}| < 4.7$, and the signal extraction is based on the N_{tracks} distribution with $p_{\text{T}} > 200$ MeV in $|\eta| < 1$.

In Fig. 6.38, the D0 and CDF Collaborations find that f_{CSE} decreases by a factor of 2.5 ± 0.9 (147) and 3.4 ± 1.2 (150), respectively, when $\sqrt{s}$ increases from 0.63 to 1.8 TeV. Similarly, the results by the CMS experiment at 7 TeV show a f_{CSE} that decreases by a factor of around 2 with respect to the 1.8 TeV results at the Tevatron (152). The observed energy dependence of the previous measurements is generally attributed to a larger number of soft parton interactions with increasing $\sqrt{s}$, which enhances the probability of the gap being destroyed. The 13 TeV results show there is no further decrease of the f_{CSE} values relative to the 7 TeV results, within the uncertainties. This could be an indication that the rapidity gap survival probability stops decreasing at the center-of-mass energies probed at the LHC for the jet-gap-jet process.

The present measurement of f_{CSE} expands the reach in $\Delta\eta_{\mathrm{jj}}$ covered in the earlier 7 TeV CMS measurement (152), as seen in Fig. 6.39. The measurement of f_{CSE} as a function of $\Delta\eta_{\mathrm{jj}}$ at 7 TeV is carried out in three bins of $\Delta\eta_{\mathrm{jj}} = 3$–4, 4–5, and 5–7 units for each bin of $p_{\mathrm{T}}^{\mathrm{jet2}}$. The dependence of f_{CSE} as a function of $\Delta\eta_{\mathrm{jj}}$ at 13 TeV confirms the trend observed by CMS at 7 TeV and extends the range previously explored towards large values of $6.5 < \Delta\eta_{\mathrm{jj}} < 8$.

6.12 Summary of jet-gap-jet analysis in inclusive dijet production

We have studied events with two jets separated by a large pseudorapidity gap, consistent with the presence of a strongly interacting color-singlet exchange in pp collisions at the center-of-mass energy of 13 TeV. We measured the fraction of dijet events separated by a large pseudorapidity gap as a function of the pseudorapidity separation between the leading two jets, the transverse momentum of the subleading jet and the azimuthal angle separation between the leading jets. This is the only measurement of jet-gap-jet events at 13 TeV. Together with the previous measurement by CMS at 7 TeV, these are the only results on jet-gap-jet events at the LHC.

For the first time, we have measured the color-singlet exchange fraction for pseudora-

pidity separations $\Delta\eta_{jj}$ larger than ≈ 6.5 units in pseudorapidity. This is of great importance for the QCD community to understand the mechanism responsible for the color-singlet exchange process, particularly when we cast predictions of perturbative QCD described by the BFKL evolution equations. This can only be done thanks to the large center-of-mass energy of the colliding protons, the successful low instantaneous luminosity run campaign, and the excellent jet reconstruction performance of the CMS detector at large pseudorapidities. We compare our results with previous measurements from the D0 and CDF experiments at the Tevatron at 0.63 TeV and 1.8 TeV and the previous measurement at 7 TeV by CMS at the LHC. We observe there is no further suppression of the gap fraction between the 7 TeV and the 13 TeV measurements, in contrast to the observed decreasing gap fraction at increasing energies found in previous studies at smaller collision energies.

In Chapter 7, we discuss how one can suppress the effect of soft-parton activity (which can destroy the rapidity gap signature) in events with an intact proton. A summary of the whole hard color-singlet exchange analysis is presented at the end of Chapter 7.

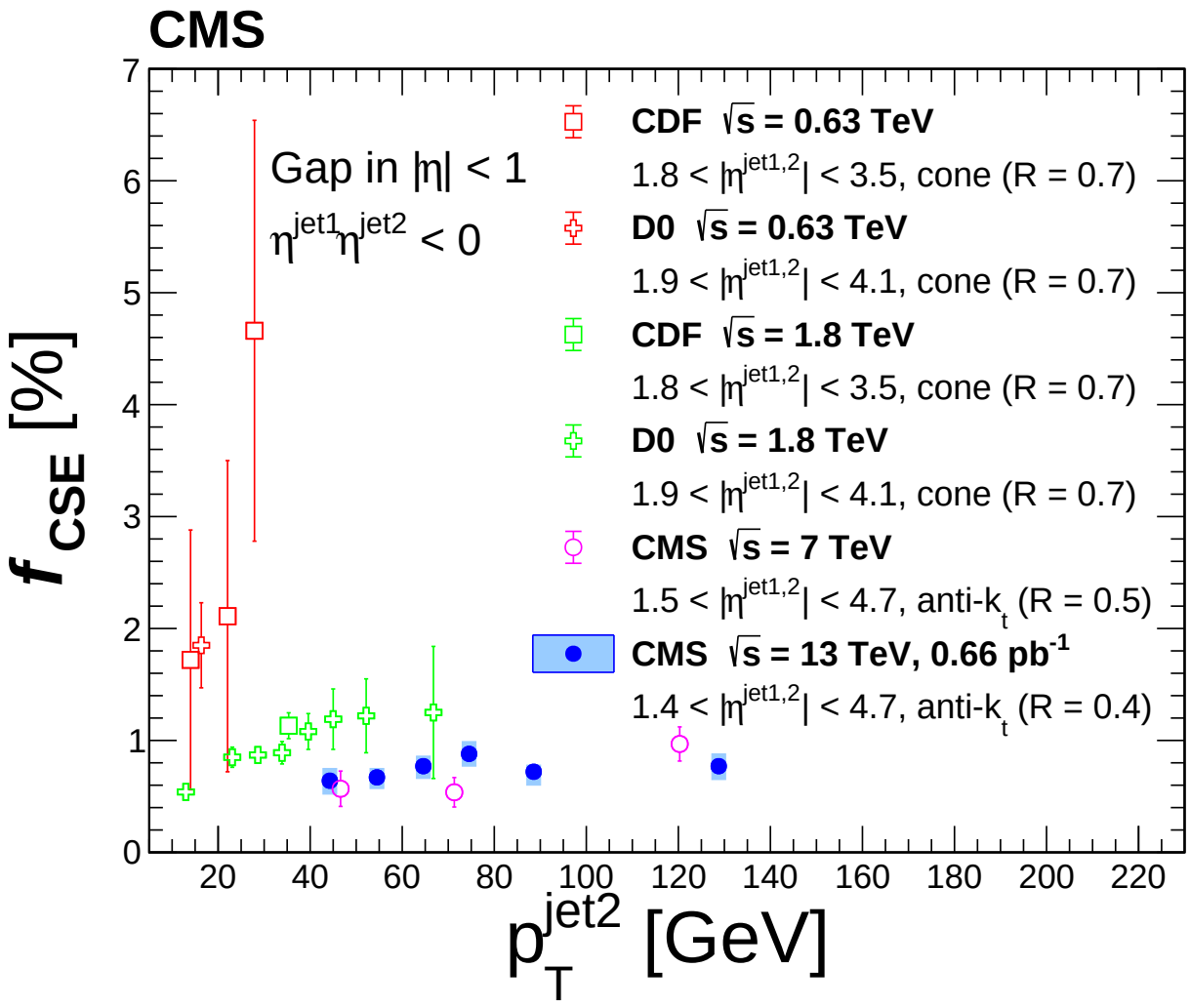

Figure 6.38: Fraction of color-singlet exchange dijet events, f_{CSE}, measured as a function of $p_{\mathrm{T}}^{\mathrm{jet2}}$ by the D0 and CDF Collaborations (147; 151; 150) at $\sqrt{s} = 0.63$ (red open symbols) and 1.8 TeV (green open symbols), by the CMS Collaboration (152) at 7 TeV (magenta open symbols), and the present results at 13 TeV (filled circles). The vertical bars of the open symbols represent the total experimental uncertainties. The vertical bars of the 13 TeV measurement represent the statistical uncertainties, and boxes represent the combination of statistical and systematic uncertainties in quadrature. The central gap is defined by means of the particle activity in the $|\eta| < 1$ interval in these measurements, as described in the text. The jet p_{T} and η requirements of the previous measurements are specified in the legend of the plot. No phase space extrapolations are made in plotting this figure. The figure is the same as the paper version one in Ref. (1).

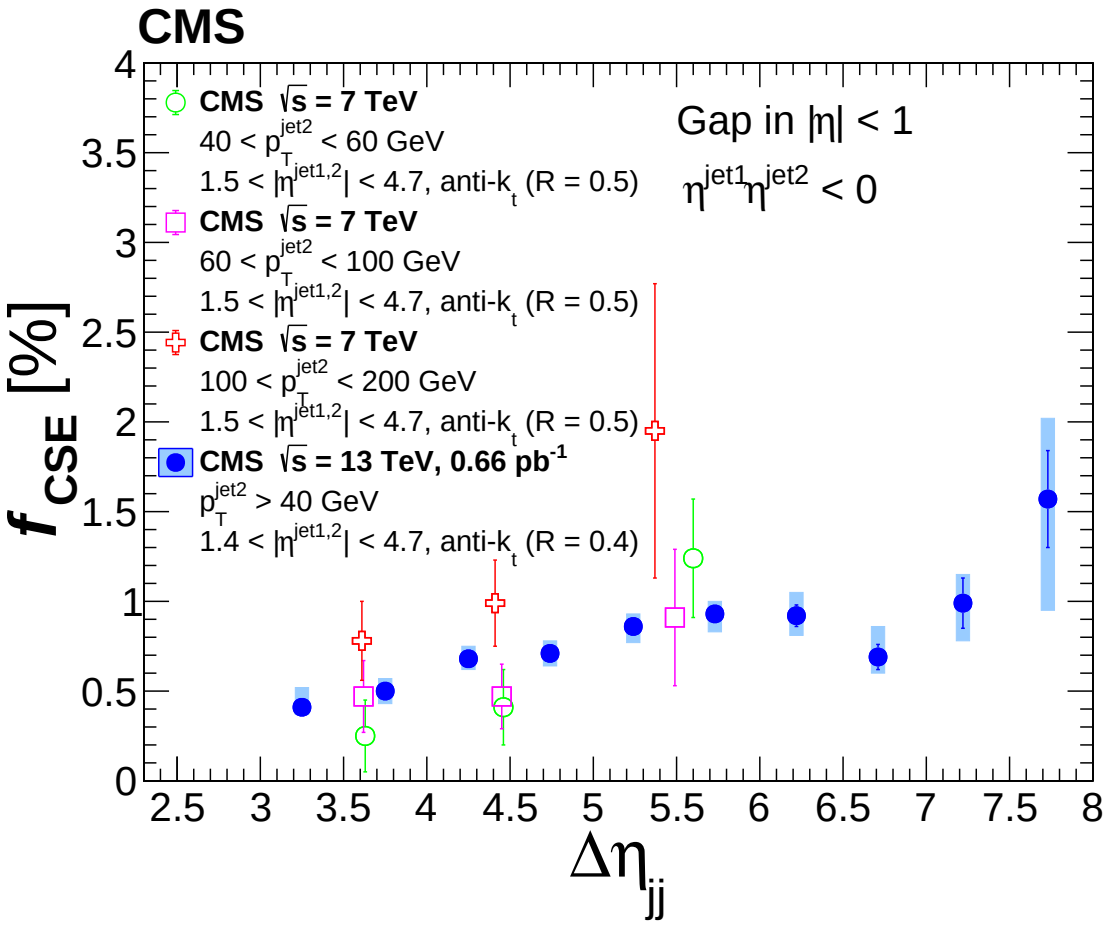

Figure 6.39: Fraction of color-singlet exchange dijet events, f_{CSE}, measured as a function of $\Delta\eta_{\mathrm{jj}}$ by CMS at 7 TeV (152) and the present measurement at 13 TeV. The 7 TeV measurement was performed in three bins of $p_{\mathrm{T}}^{\mathrm{jet2}} = 40$–$60$, 60–100, and 100–200 GeV, which are represented by the open circle, open square, and open cross symbols, respectively. The present 13 TeV results are represented by the filled circles. The vertical bars of the 7 TeV measurement represent the total experimental uncertainties. The vertical bars of the 13 TeV measurement represent the statistical uncertainties, and boxes represent the combination of statistical and systematic uncertainties in quadrature. The figure is the same as the paper version one in Ref. (1).

Chapter 7

Jet-gap-jet events with an intact proton with CMS-TOTEM data

In this Chapter, we describe the second aspect of the measurement of hard color-singlet exchange dijet events. This analysis uses the combined CMS-TOTEM data sample of the special run of 2015, which is a subset of the data used for the analysis of jet-gap-jet events described in Chapter 6. The CMS aspects of the analysis are the same as those covered in Chapter 7. In addition to the jet and central pseudorapidity gap definitions, we carefully consider the set of challenges that come with the intact protons tagged with the Roman pot (RP) detectors of the TOTEM experiment. The goal here is to extract the fraction of single-diffractive dijet events with a central gap between the jets. This ratio can then be compared to that extracted in the standard jet-gap-jet analysis. A conclusion of the CMS-TOTEM part of this analysis is presented at the end of this Chapter. A Summary of the analysis is presented at the end of this Chapter.

7.1 Jet-gap-jet with an intact proton

Jet-gap-jet events with an intact proton (p-gap-jet-gap-jet topology) can be studied using the combined sample of CMS and TOTEM collected during the same runs as in the inclusive jet-gap-jet analysis. The surviving intact proton is tagged with the TOTEM forward proton detectors installed in the forward region on both sides of IP5 along the beamline, while the jet-gap-jet signature is studied with the CMS experiment following the same

technique discussed on the first part of this paper. The components of the TOTEM experiment relevant to this analysis are covered in Chapter 5 of this thesis.

The presence of a hard scale and two rapidity gaps originating from strongly interacting color-singlet exchanges has not been reported before by any collider experiment. For the sake of clarity, we do not ask for an additional rapidity gap on the forward region; this is one of the great advantages of forward proton detection. From the physics point of view, it would be interesting to measure the value of the fraction of p-gap-jet-gap-jet events within the p-gap-jet-jet events, since the presence of an intact proton may reduce soft rescattering effects that would otherwise destroy the central pseudorapidity gap (which originates from spectator partons activity), leading to a larger fraction of jet-gap-jet events within the single diffractive dijet sample, in contrast to the situation in inclusive dijet production where both protons are destroyed. This would give an important input for phenomenological modelling of the soft interactions that lead to the destruction of rapidity gap signatures. Another interesting measurement would be that of jet-gap-jet in double diffractive exchange processes (proton-p-gap-jet-gap-jet-gap-proton, where there is a large amount of transferred four-momentum across the central pseudorapidity gap, and small momentum transfers across the outer-most pseudorapidity gaps) (153). The number of two-proton tagged dijet events in the present analysis is not large enough to perform an analysis on jet-gap-jet in double pomeron exchange events (p-gap-jet-gap-jet-gap).

In the past decades, there have been several measurements of dijet production in hard diffractive reactions $pp \to pJJX$ and $pp \to pJJXp$, where p in the right hand side are leading intact proton(s) carrying a substantially large amount of the original momentum of the incoming proton, and X any other products of the collision (210; 164; 211; 212; 213; 214; 215). Conceptually, we could think of single diffractive dijet production as a two-step process, where a color-singlet (pomeron or reggeon exchange) is emitted by one of the protons, which in turn interacts with the other proton to produce jets (156), as seen in

Fig. 7.1. The color-singlet exchange off the proton may leave a rapdity gap signature in the direction of the outgoing proton, as seen in Fig. 7.2. In this picture, one can parametrize the diffractive exchange by means of a diffractive structure function of the proton which is a function of the amount of momentum transfer squared in the hard scattering process Q^2 and of the Bjorken scaling variable x_{Bj} of the interacting parton from the proton, which in turn is related to the color-singlet exchange via $x = \xi\beta$, where ξ is the fraction of the proton initial momentum carried by the color-singlet exchange and β is the fraction of momentum carried by the parton relative to the color-singlet exchange. For purposes of this analysis, all we have to consider is that there are special reactions characterized by a rapidity gap between the outgoing intact proton and the dijet system. If in addition, there is a color-singlet exchange between the partons initiating the hard scattering process (as in Fig. 7.1), a central pseudorapidity gap would be present (as in Fig. 7.2). Since our main results are in terms of ratios of yields of single diffractive events, we do not have to take into consideration any parametrization of the diffractive structure function.

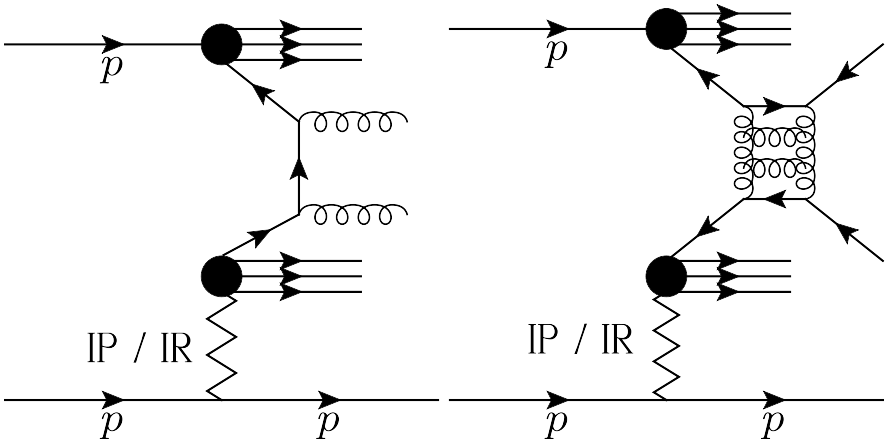

Figure 7.1: (Left) Schematic diagram of dijet production in single diffractive reactions. The intact proton is tagged with TOTEM's forward proton spectrometer. The symbols $\mathbb{P}$ and $\mathbb{R}$ indicate pomeron or reggeon exchange respectively. (Right) Schematic diagram of a jet-gap-jet event with an outgoing intact proton. This process leads to a p-gap-jet-gap-jet signature, which is the target process of this part of the analysis.

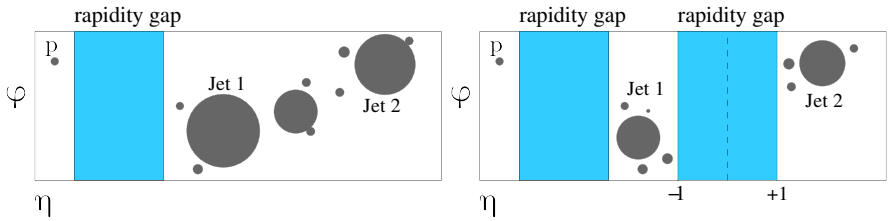

Figure 7.2: (Left) Schematic diagram of a single diffractive dijet event topology (p-gap-jet-jet) in η–ϕ plane. These events dominate the single diffractive dijet sample, and fluctuations in the N_{tracks} may lead to a p-gap-jet-gap-jet signature. (Right) Schematic diagram of event topology in η–ϕ plane for a jet-gap-jet event in single diffractive dissociation (p-gap-jet-gap-jet). Two rapidity gaps are present: one is due to the color-singlet exchange between the partonic system initiating the hard scattering process with a large amount of momentum transfer across the rapidity gap, while the second rapidity gap comes from the low momentum transfer color-singlet exchange by one of the protons.

7.2 Combined CMS-TOTEM data sample at $\sqrt{s} = 13$ TeV

The common CMS-TOTEM data sample used in this analysis was recorded in 2015 in pp collisions at $\sqrt{s} = 13$ TeV using a dedicated $\beta^* = 90$ m beam optics. The RPs were inserted at a distance of $10\sigma_{\text{beam}}$ w.r.t. the beam axis. An integrated luminosity of 0.4 pb^{-1} of CMS-TOTEM data is used for this analysis, corresponding to data taking of about 30 h. The pileup was of $\mu = 0.065 - 0.1$, so there were mostly single proton-proton collisions per bunch crossing. The data were recorded, reconstructed, and calibrated independently by CMS and TOTEM. The dijet and intact proton samples were merged offline based on beam-orbit and bunch crossing numbers matching between the two samples, leading to a common CMS-TOTEM sample of about 13 M dijet events (before making any further offline event selection).

If CMS-only information is used, the fractional momentum loss of the proton can be estimated from the energies and longitudinal momenta of the particles reconstructed using the particle-flow (PF) algorithm of CMS as,

$$\xi^{\pm}_{\text{CMS}} = \frac{\sum_i E^i \pm p^i_z}{\sqrt{s}} \tag{7.1}$$

where E^i and p^i_z are the energy and longitudinal momentum component of the i-th

PF object	η region	Energy Thres. [GeV]
Photon	Barrel	1.2
	Endcap	3.0
	Transition	3.0
Neutral hadron	Barrel	1.7
	Endcap	3.25
	Transition	4.5
Charged hadron	Barrel	0.2
	Endcap	0.2
	Transition	4.0
Muon, electrons	Barrel	0.2
	Endcap	0.2
	Transition	3
EM HF tower	Transition	4.5
	Forward	4.5
Hadron HF tower	Transition	4.5
	Forward	4.5

Table 7.1: Energy thresholds applied on the CMS particle-flow objects for the measurement of $\xi^{\pm}_{\mathrm{CMS}}$ in a given dijet event. The energy threshold for charged particles within the silicon tracker acceptance is taken as 200 MeV.

particle in the event. The positive (negative) sign corresponds to the scattered proton moving towards the positive (negative) z direction, or sector 45 and sector 56 respectively. The reconstruction of ξ_{CMS} is estimated from the reconstructed PF candidates in the event. Each PF candidate has an η-dependent energy threshold applied to it, which is listed in Table 7.1. The thresholds were optimized with a zero-bias samples by comparing the enengy deposits in empty bunch crossings with those with non-empty bunch crossings with a primary vertex. Such optimization is described in the Appendix of this thesis.

For single diffractive events, one would expect $\xi_{\mathrm{CMS}} = \xi_{\mathrm{TOTEM}}$ within the uncertainties, but since the CMS detector cannot detect every remnant of the collision due to its limited response, the fact that we cannot apply arbitrarily low energy thresholds for calorimeter towers, and limitation on the geometrical acceptance in pseudorapidity $|\eta| < 5.2$, hard diffractive events satisfy instead the inequality $\xi_{\mathrm{CMS}} - \xi_{\mathrm{TOTEM}} \leq 0$, which defines the sig-

nal region for single diffractive events. The positive region $\xi_{\mathrm{CMS}} - \xi_{\mathrm{TOTEM}} > 0$ is dominated by (mostly non-diffractive) dijet events overlapped with intact protons which arise from beam-halo events or pileup interactions; this region is kinematically forbidden by signal diffractive events. This constitutes the control region of this measurement, and provides a handle to estimate the background with a purely data-driven approach.

The two-dimensional distribution of forward track impact points in the transverse plane as measured in the RPs can be seen for dijet events with a proton tag can be seen in Fig. 7.3, where no additional requirement on $\xi_{\mathrm{CMS}} - \xi_{\mathrm{TOTEM}}$ is applied. The concentration of events at $x \sim 0$ is dominated by contamination from elastic scattering events ($\xi = 0$). The results where the $\xi_{\mathrm{CMS}} - \xi_{\mathrm{TOTEM}} \leq 0$ selection is applied can be seen in Fig. 7.4. In this case, it is clear that diffractive dijet events populate the higher-x region, whereas events with x coordinates close to 0 mm are suppressed with this selection. This can be more clearly seen on Fig. 7.5; events in the control region $\xi_{\mathrm{CMS}} - \xi_{\mathrm{TOTEM}} > 0$ are concentrated at $x \sim 0$.

In order to check for any bias on either arm of the forward proton spectrometers, as well as testing whether the diffractive selection is indeed selecting diffractive dijet events, we test elementary distributions as a function of the average pseudorapidity of the dijet system $\eta^* = \frac{1}{2}(\eta_{\mathrm{jet1}} + \eta_{\mathrm{jet2}})$, the azimuthal angle separation between the leading two jets, jet multiplicity, and transverse momentum distribution of the subleading jet. We compare single diffractive dijet distributions with inclusive dijet distributions sample (which are largely dominated by non-diffractive dijet events), as seen in Fig. 7.6. In addition, it is instructive to see whether we are rejecting non-diffractive dijet events with the event selection. We look at the same distributions for events satisfying the selection $\xi_{\mathrm{CMS}} - \xi_{\mathrm{TOTEM}} > 0$, where we expect these distributions to follow the general features of the non-diffractive dijet sample. Results for the diffractive event selection as well as the events that were rejected can be seen in Fig. 7.7.

We find there is agreement between the two arms datasets in the distributions tested.

The average pseudorapidity of the dijet system in the single diffractive dijet event sample are shifted on the positive or negative region for sector 45 and sector 56 respectively by about 0.85 units in pseudorapidity relative to 0, as is expected for single diffractive events. In addition, single diffractive dijet events are more strongly correlated in their azimuthal angle separation than non-diffractive dijet events, since the energy available for dijet production is smaller than in non-diffractive events, and thus additional radiation activity between the final state partons is smaller than for non-diffractive dijet events. Following this idea, we find that the single diffractive dijet event sample consists of mainly dijet events, and only a small fraction of the events contains additional jet activity. The transverse momentum distribution is found to be the same between the non-diffractive and single diffractive samples, as expected, since the slope of this distribution is generated mainly by the $1/p_{\mathrm{T}}^4$ dependence of the cross section in QCD. The features of these distributions are consistent with single diffractive events. If we draw the same comparison for the rejected events ($\xi_{\mathrm{CMS}} - \xi_{\mathrm{TOTEM}} > 0$) and the inclusive dijet sample, we find that they are consistent within the uncertainties, as expected. This supports the use of the present diffractive selection used in the analysis, which effectively rejects a large amount of non-diffractive events contamination in our sample.

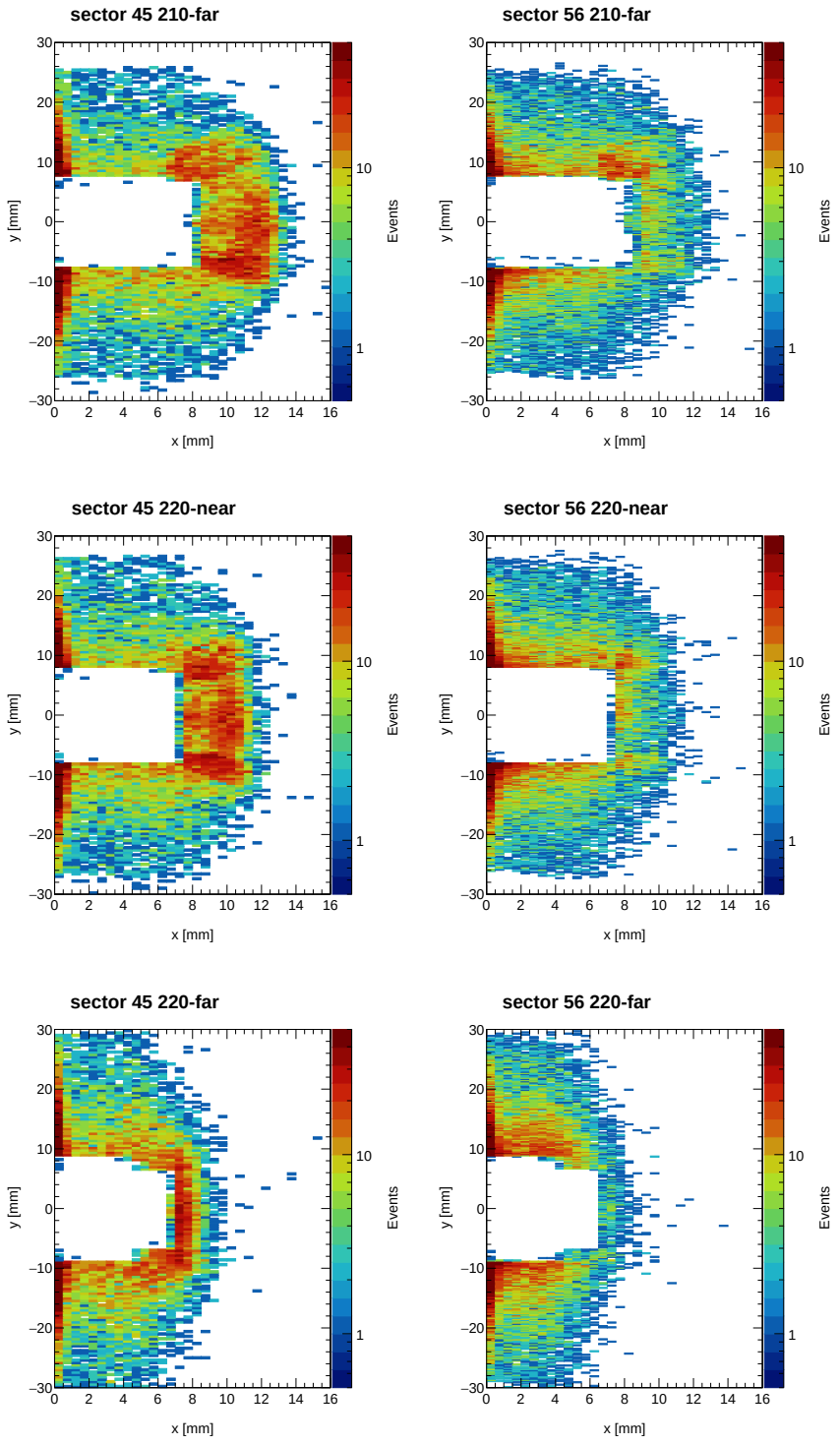

Figure 7.3: Two-dimensional distribution of reconstructed forward tracks impact points in the silicon strip detectors for dijet events satisfying $p_{\mathrm{T,\,jet\,2}} \geq 40$ GeV and $|\eta_{\mathrm{jet\,1,\,jet\,2}}| < 4.7$. On the left-hand side, we have the distributions in sector 45 for the three different planes of silicon detectors, and on the right-hand side, we have the distributions in sector 56 for the three different planes of silicon detectors.

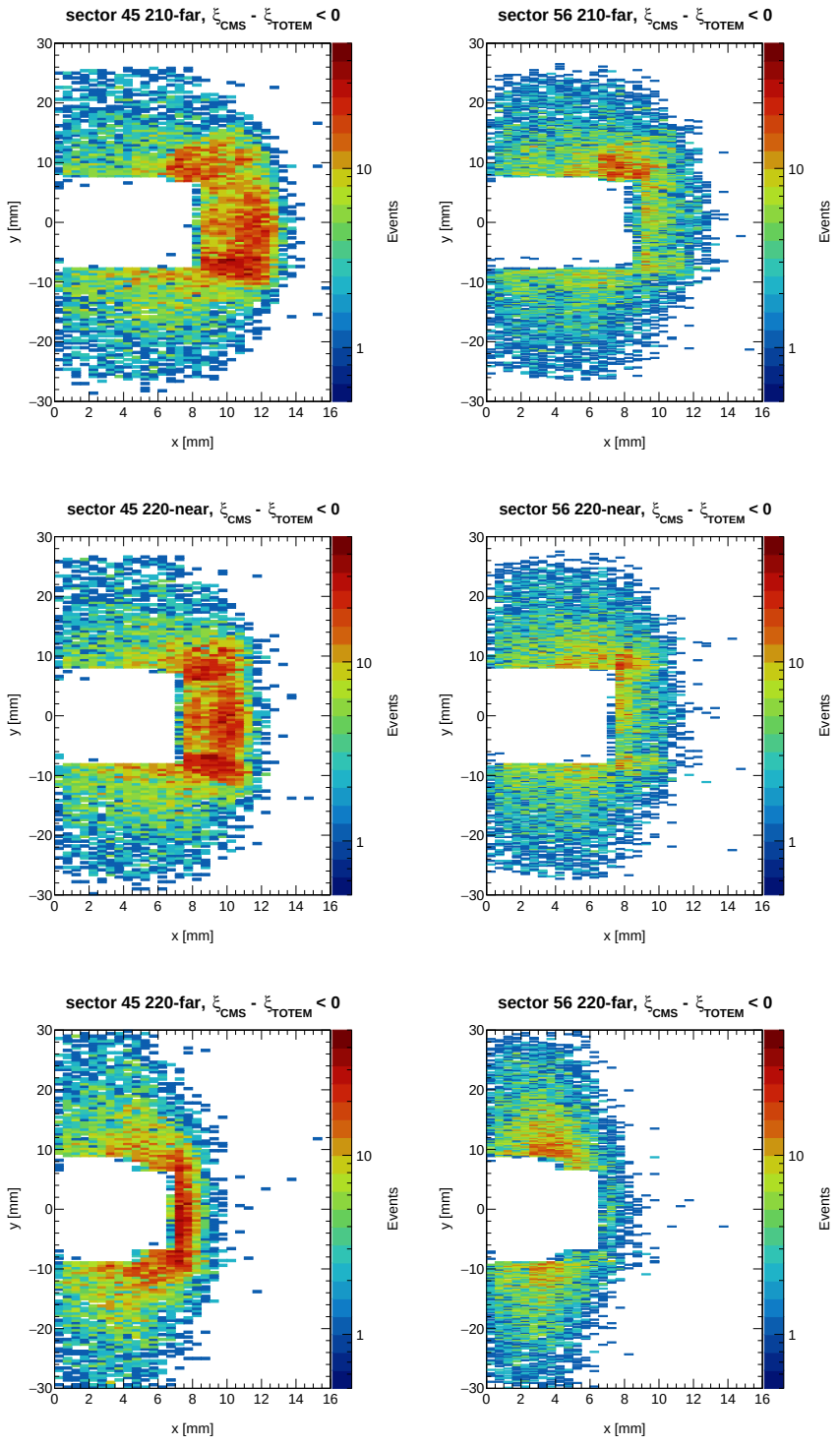

Figure 7.4: Two-dimensional distribution of reconstructed forward tracks impact points in the silicon strip detectors for dijet events satisfying $p_{\mathrm{T,\,jet\,2}} \geq 40$ GeV and $|\eta_{\mathrm{jet\,1,\,jet\,2}}| < 4.7$. On the left-hand side, we have the distributions in sector 45 for the three different planes of silicon detectors, and on the right-hand side, we have the distributions in sector 56 for the three different planes of silicon detectors. A selection for the single diffractive events $\xi_{\mathrm{CMS}} - \xi^{\mathrm{RP}}_{\mathrm{TOTEM}} < 0$ is applied. Notice that mostly the events with low x values (corresponding to single diffractive and elastic scattering protons, since low x corresponds to low ξ_{TOTEM}) are rejected with this selection requirement, which constitute the dominating background.

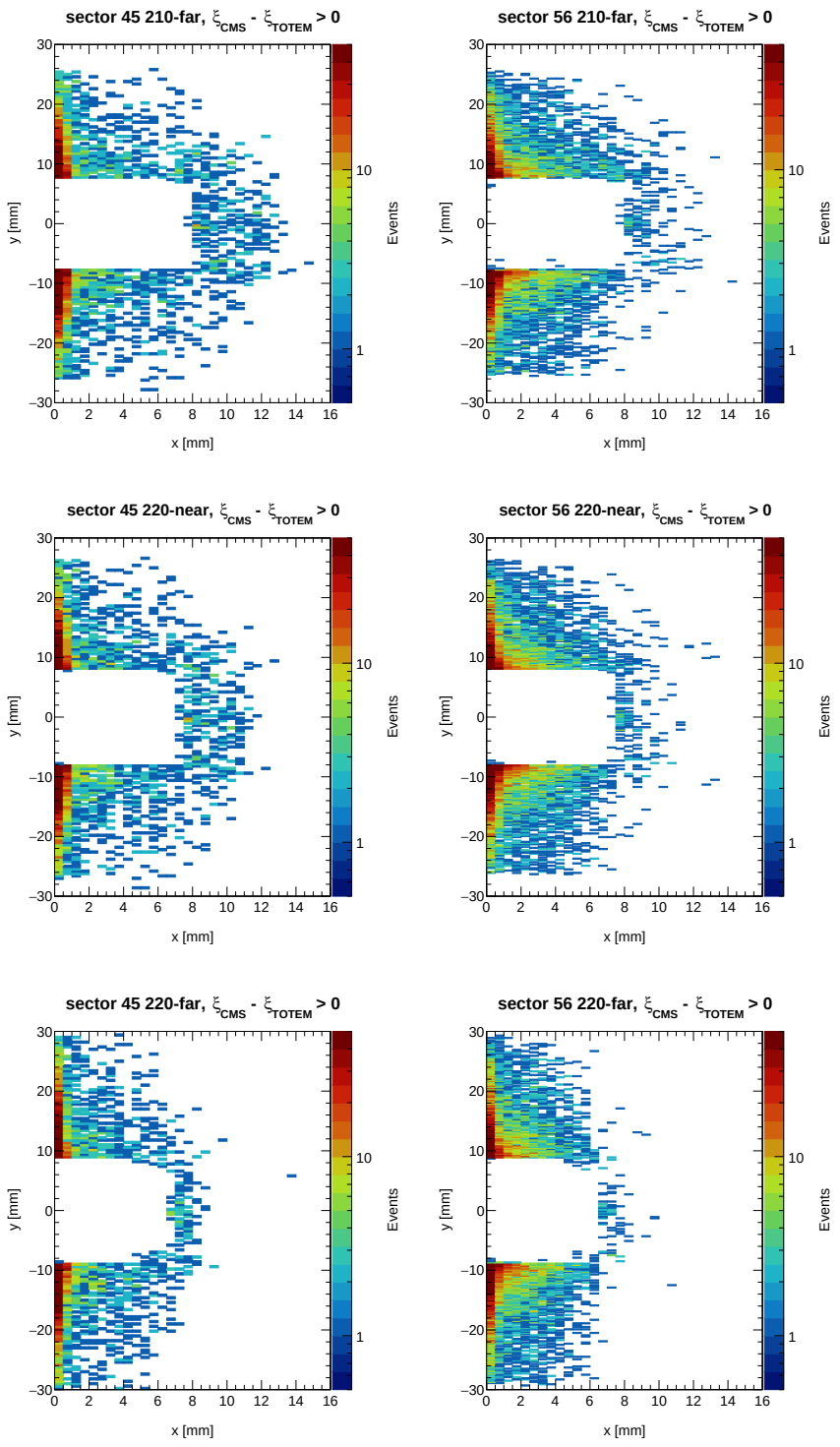

Figure 7.5: Two-dimensional distribution of reconstructed forward tracks impact points in the silicon strip detectors for dijet events satisfying $p_{\mathrm{T,\,jet\,2}} \geq 40$ GeV. On the left-hand side, we have the distributions in sector 45 for the three different planes, and on the right-hand side, we have the distributions in sector 45 for the three different planes. A selection for the single diffractive events $\xi_{CMS} - \xi^{\mathrm{RP}}_{\mathrm{TOTEM}} > 0$ is applied.

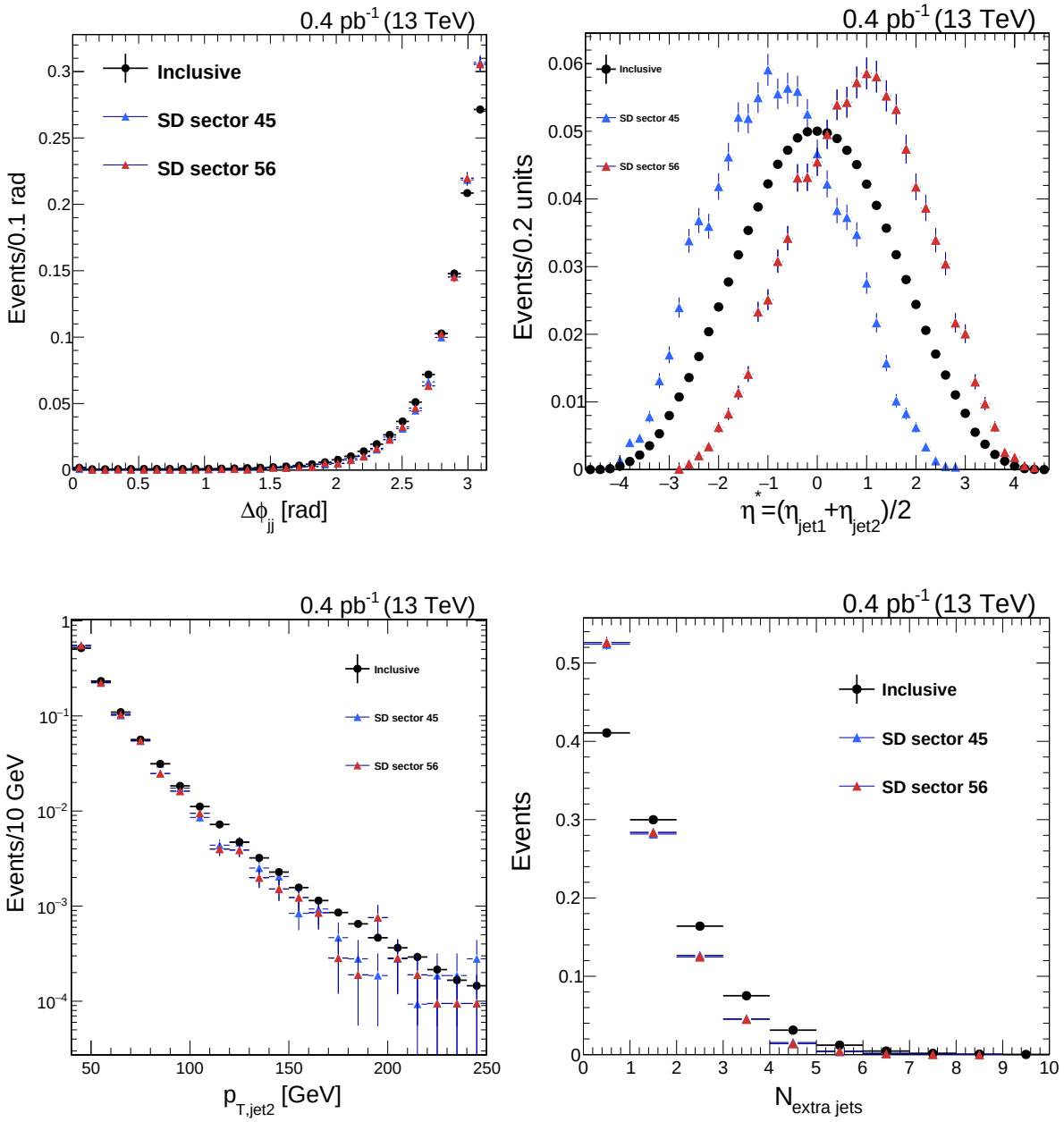

Figure 7.6: Azimuthal angle separation between the two leading jets, average pseudorapidity of dijet system $\eta^* = (\eta_{\text{jet}\,1} + \eta_{\text{jet}\,2})/2$, jet multiplicity, and transverse momentum distribution for the inclusive dijet sample (data points in black) and for the dijet sample enriched in single diffractive events ($\xi_{\text{CMS}} - \xi_{\text{TOTEM}} \leq 0$). Blue and red data points correspond to sector 45 and sector 56, respectively. SD events have less available energy and access to phase space due to the effective center-of-mass energy of the collision $\sqrt{s}$.

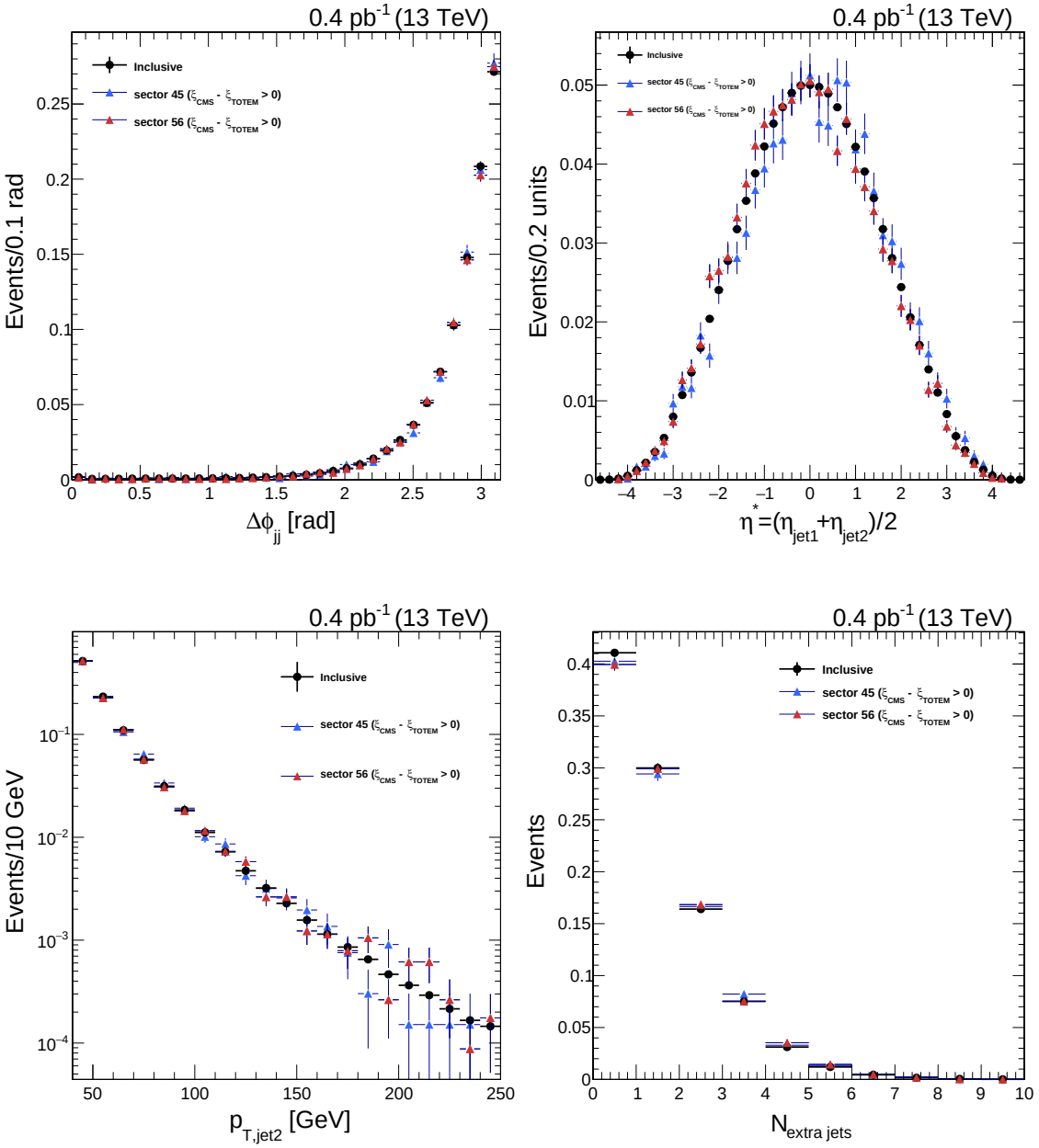

Figure 7.7: Azimuthal angle separation between the two leading jets, average pseudorapidity of dijet system $\eta^* = (\eta_{\text{jet}\,1} + \eta_{\text{jet}\,2})/2$, jet multiplicity, and transverse momentum distribution for the inclusive dijet sample (data points in black) and for the dijet sample with an intact proton depleted in single diffractive events ($\xi_{\text{CMS}} - \xi_{\text{TOTEM}} > 0$). Blue and red data points correspond to sector 45 and sector 56, respectively. General features of dijet events with an intact proton with incompatible kinematics ($\xi_{\text{CMS}} - \xi_{\text{TOTEM}} > 0$) are consistent with the ones in inclusive dijet events.

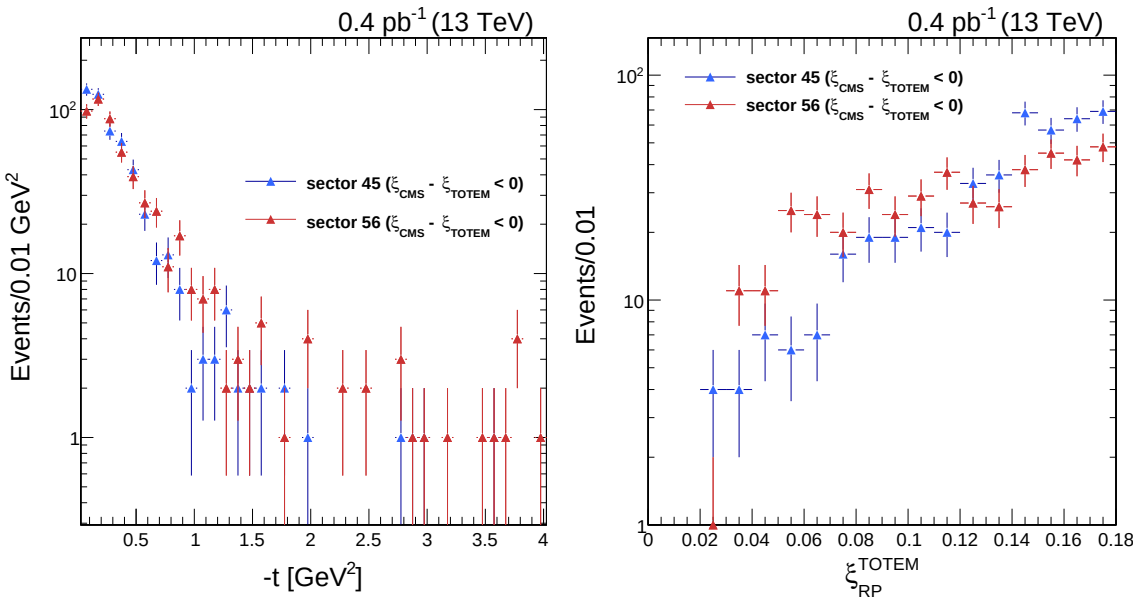

Figure 7.8: Square of four-momentum transfer off the proton $-t$ and fractional momentum loss ξ_{TOTEM} distributions for dijet events satisfying the jet-gap-jet pre-selection requirements described in text for sectors 45 and sectors 56. There is no beam background subtraction in these figures.

7.3 Event selection

We follow the same strategy as in the jet-gap-jet measurement within the inclusive dijet sample, and extract the gap fraction by means of the N_{tracks} on the fixed pseudorapidity region $|\eta| < 1$, where the charged particle tracks satisfy the *high-purity* criteria, have transverse momentum above $p_{\mathrm{T}} > 200$ MeV, and satisfy $\sigma_{p_{\mathrm{T}}}/p_{\mathrm{T}} < 10$ %. The sample of diffractive dijet events contains about 20,000 diffractive dijet events for jets satisfying $p_{\mathrm{T,jet\,2}} \geq 40$ GeV and with an intact proton with compatible kinematics with the dijet central system. Our event selection requirements take into consideration that the main observable is the ratio of yields of the p-gap-jet-gap-jet events relative to the p-gap-jet-jet events integrated over the pseudorapidity and transverse momentum of the leading two jets and the fractional momentum loss and transferred four-momentum squared of the proton.

The same event selection requirements on the dijet and on the track collection are

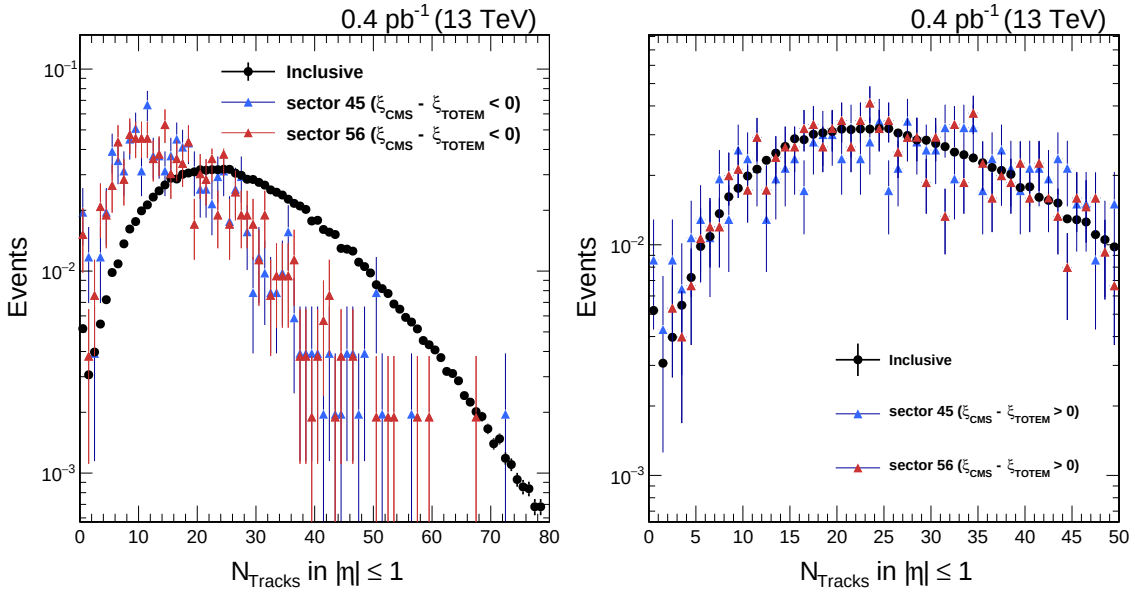

Figure 7.9: N_{tracks} distribution in fixed pseudorapidity region $|\eta| < 1$. Dijet events satisfy the jet-gap-jet preselection requirements. Black data points represent the results from the inclusive dijet sample (mostly non-diffractive). In blue and red, we have the results for dijet events with an intact proton in sector 45 and 56, respectively. For the positive region $\xi_{\text{CMS}} - \xi_{\text{TOTEM}} > 0$, the shape of the N_{tracks} distribution is the same as in the inclusive dijet sample, which confirms that the control region is populated by non-diffractive events.

applied. For the intact proton selection, we require:

- At least one valid proton tag on either arm (sector 45 or sector 56).
- The proton track has to transverse at least two overlapping RP units (e.g., top-top, horizontal-horizontal).
- The fractional momentum loss of the proton ξ_{TOTEM} has a maximum value of 0.20, within the acceptance of the RPs.
- The amount of four-momentum transfer squared $-t$ is greater than 0.025 GeV^2 and smaller than 4 GeV^2; this selection requirement was chosen to increase the event yield.
- The track impact points satisfy the fiducial selection requirements: $8 < |y| < 30$ mm

and $0 < x < 20$ mm for vertical pots, and $|y| < 25$ mm and $7 < x < 25$ mm for horizontal RPs. This ensures good efficiency and acceptance within the silicon detector volume.

Finally, if a dijet event satisfies the above selection requirements, we apply the following requirement in order to isolate the hard diffractive events:

- $\xi_{\mathrm{CMS}} - \xi_{\mathrm{TOTEM}} \leq 0$, where $\xi_{\mathrm{CMS}} = \frac{\sum_i E^i \pm p_z^i}{\sqrt{s}}$ is calculated based on the PF objects of CMS.

There are 341 and 336 diffractive dijet events in sector 45 and sector 56, respectively, satisfying the selection requirements. Combining sector 45 and sector 56 results, 11 events with a central pseudorapidity gap $N_{\mathrm{tracks}} = 0$ are found in the diffractive dijet sample. Since the sample of single diffractive dijets is much smaller than the inclusive dijet sample, the study cannot be performed differentially as a function of the variables $|\Delta\eta_{jj}|$, $\Delta\phi_{jj}$, $p_{\mathrm{T,\,jet\,2}}$ or ξ, $-t$. Instead, our focus is on the fraction of p-gap-jet-gap-jet within the p-gap-jet-jet sample of events integrated over the phase space volume of the dijet and intact proton systems described above. The four-momentum transfer squared of the protons $-t$ and the fractional momentum loss ξ_{TOTEM} for events satisfying the above selection can be seen in Fig. 7.8.

We compare the N_{tracks} distribution between the sector 45 and 56 for the dijet events satisfying the diffractive selection and the jet-gap-jet pre-selection with the one found in inclusive dijet production (see Fig. 7.9). The mean N_{tracks} is about 15 in the single diffractive dijet sample, whereas the one in the inclusive dijet sample is of about 27. The reason is that the energy available for particle production in single diffractive events is smaller than the energy available for particle production in non-diffractive events, followed by a suppression of the color-flow of single-diffractive interactions. Color-singlet exchange off the proton provides a cleaner final state. It is worth to point out that there is a fair agreement in the shape of the distributions between sectors 45 and 56. Since there is a

low number of events in our final selection, and the control distributions between sector 45 and sector 56 are in good agreement between each other, we report our main results using the sum of yields of sector 45 and sector 56.

The average pseudorapidity distributions of the dijet system in single diffraction suggests that a natural choice for the N_{tracks} distributions would be to build them on shifted fixed pseudorapidity intervals, for example $-2 < \eta < 0$ and $0 < \eta < 2$ for sector 45 and sector 56, respectively. We explored this possibility with the data, but found there was no significant difference with respect to the nominal choice of the fixed pseudorapidity interval $-1 < \eta < 1$. Thus, we measured the N_{tracks} in the fixed pseudorapidity region $-1 < \eta < 1$. This allows for a more straight-forward comparison with the results from the standard jet-gap-jet analysis. In addition, generator-level checks with the Forward Physics Monte Carlo (FPMC) event generator, which simulates the diffractive exchange and the BFKL at NLL amplitude, confirm that the signal can be extracted with a similar acceptance with a central symmetric fixed pseudorapidity gap or with the shifted pseudorapidity gap interval.

7.4 Observable

We measure the fraction of jet-gap-jet events within the diffractive dijet sample,

$$f_{\text{CSE}} = \frac{N^{\text{F}}_{\text{events}} - N^{\text{F}}_{\text{non-CSE, SD}} - N^{\text{F}}_{\text{beam bkg}}}{N_{\text{events}} - N_{\text{events, beam bkg}}} \equiv \frac{\text{Number of p-gap-jet-gap-jet events}}{\text{Number of p-gap-jet-jet events}}$$

where $N^{\text{F}}_{\text{events}}$ is the number of diffractive dijet events with $N_{\text{tracks}} < 2$ in $|\eta| < 1$, N_{events} is the number of diffractive dijet events with $N_{\text{tracks}} \geq 0$ in $|\eta| < 1$, $N^{\text{F}}_{\text{non-CSE, SD}}$ is the number of diffractive dijet events where no hard color-singlet exchange in the hard scattering process took place, $N_{\text{events, beam bkg}}$ is the number of dijet events with $N_{\text{tracks}} \geq 0$ in $|\eta| < 1$ with an intact proton from beam-halo interactions or protons from residual pileup inter-

actions. This definition of f_{CSE} allows for a more direct comparison with the measurement of the "inclusive" jet-gap-jet events.

Generally, the N_{tracks} is lower in events with an intact proton than in inclusive dijet production events. For events passing the dijet and forward proton selection requirements, the mean multiplicity in the $|\eta| < 1$ region is $\langle N_{\mathrm{tracks}} \rangle \approx 17$, compared to the larger $\langle N_{\mathrm{tracks}} \rangle \approx 28$ in inclusive dijet production. This is consistent with the overall suppression of spectator parton interactions and lower energy available for production of particles in single-diffractive events. Since the N_{tracks} distributions in sectors 45 and 56 are similar in shape, the N_{tracks} values from the two sectors are summed for the analysis.

7.5 Background estimation

The leading background stems from single-diffractive dijet events (p-gap-jet-jet events), whose charged particle multiplicities may fluctuate to low charged particle multiplicities. We use the NBD and SS methods to estimate the number of p-gap-jet-jet events at the lowest N_{tracks}, as described in Chapter 6. The subleading background originates from (mostly non-diffractive) dijet events paired with uncorrelated intact protons that originate from secondary interactions in the same bunch crossing or beam-halo particles. This background is heavily reduced by exploiting the correlation between the dijet system and the intact proton in diffractive events.

7.5.1 Beam-background

It is not possible to discriminate a single diffractive dijet event from a non-diffractive dijet event overlapped with an uncorrelated intact proton on an event-by-event basis. However, we can estimate the beam background contamination based on a data-driven method that profits from the correlation between the forward proton and the dijet system. We count with a sample of zero-bias events (non-empty bunch crossings) collected during

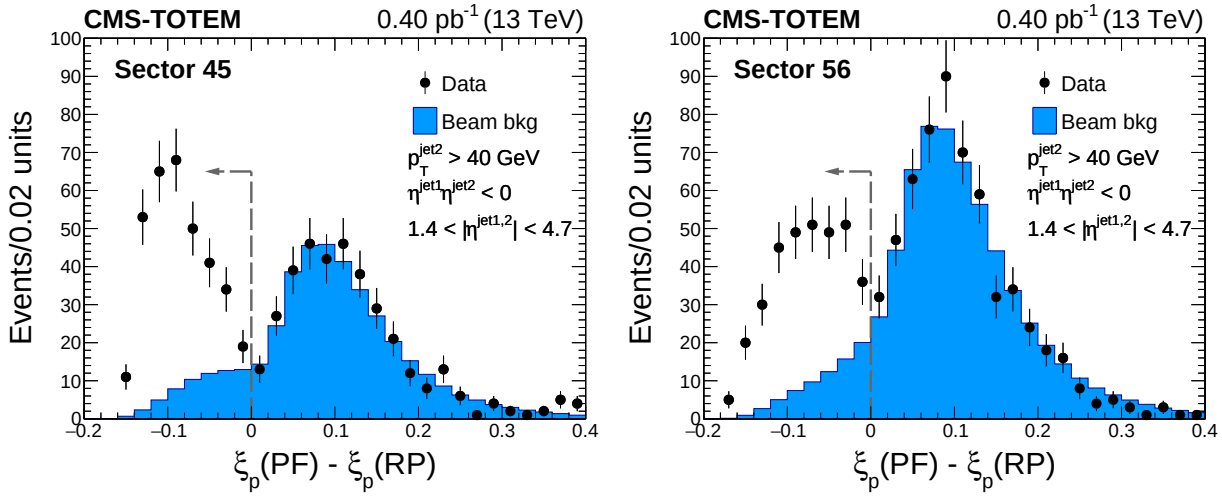

Figure 7.10: Distribution of $\xi_{\text{CMS}} - \xi_{\text{TOTEM}}$ in sector 45 (left) and sector 56 (right). The data are indicated by the solid circles. The estimated background contamination (non-diffractive dijet overlapped with protons from pileup or beam-halo) is in blue, and is estimated from the data. No central rapidity gap is asked at this point. Vertical bars indicate statistical uncertainties only. The labels of the plots are those presented in the paper ($\xi_{\text{CMS}} = \xi_p(\text{PF})$ and $\xi_{\text{TOTEM}} = \xi_p(\text{RP})$. The figure is the same as the paper version one in Ref. (1).

the same runs, which, from the point of view of the RPs, constitute a sample of protons like the ones contaminating the single diffractive dijet events in our data. Similar methods have been employed in previous measurements with proton tagging (210; 164; 211; 212; 213; 214; 215). We have the large inclusive dijet sample used for the standard jet-gap-jet analysis, which is largely dominated by non-diffractive dijet events (the single-diffractive component is less than 0.1% of the inclusive dijet sample). Hence, we can use only data to estimate this background.

To estimate this background, we pair the dijet events from the inclusive dijet sample with protons from events recorded using a zero-bias trigger. The dijet and intact proton events satisfy the same event selection as in the nominal diffractive dijet sample. The dijet events are largely dominated by non-diffractive events. The number of events from the event mixing procedure is normalized to data in the positive region $\xi_{\text{CMS}} - \xi_{\text{TOTEM}} > 0$ (normalization fixes the pileup and presence of beam-halo rates), and the extrapolation to the negative region $\xi_{\text{CMS}} - \xi_{\text{TOTEM}} < 0$ (signal region) is taken as the background esti-

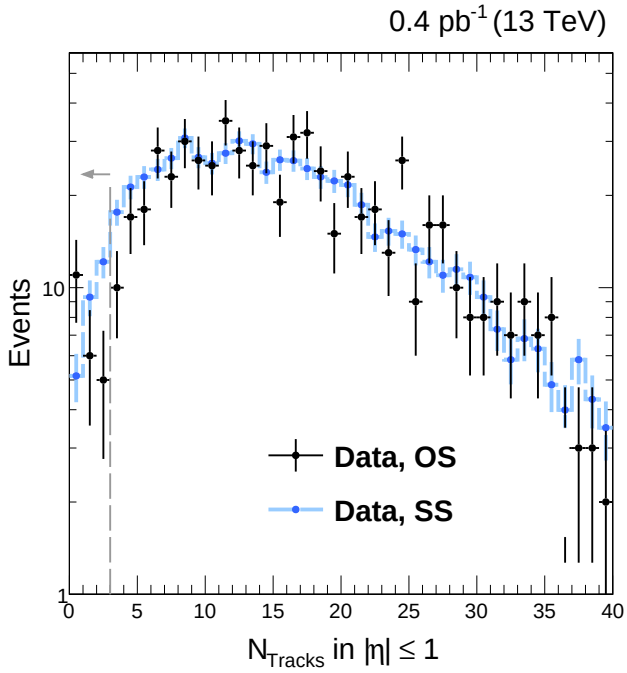

Figure 7.11: N_{tracks} distribution for opposite-side diffractive dijet events (black) and same-side diffractive dijet events (blue). The SS dijet events are normalized to the OS dijet events for $N_{\text{tracks}} \geq 3$. The SS diffractive dijet sample cannot be used to estimate the fraction of p-gap-jet-gap-jet events to p-gap-jet-jet events (see text). It can be employed as a control dijet sample to show that there is no excess at $N_{\text{tracks}} \geq 0$ in an orthogonal dijet sample depleted in hard color-singlet exchange events.

mation. The results of this procedure can be seen in Fig. 7.10. Beam background contamination constitutes 18.6 and 21.5% of the sample in sectors 45 and 56, respectively.

The advantage of using the event mixing method to estimate the beam background is that it does not rely on any Monte Carlo event simulation assumptions on the ξ_{CMS} spectra, and furthermore, we can extract directly the N_{tracks} distribution of beam background events contaminating the nominal diffractive dijet sample. The use of Monte Carlo event generators to understand the N_{tracks} depends heavily on the modelling of the underlying event, which is tune-dependent.

7.5.2 Single-diffractive dijet contamination at low multiplicities

Standard single-diffractive dijet events can yield a central gap between the jets by fluctuations in N_{tracks}, analogous to the fluctuations of color-exchange dijet events in inclusive dijet production. The methods introduced in Chapter 6 are used to estimate these contributions with modifications that account for differences in the sample with intact protons.

We employ the NBD method to extract the number of jet-gap-jet with an intact proton. We build the N_{tracks} distribution in the fixed pseudorapidity interval $1 < \eta < 1$ for dijet events satisfying the diffractive selection. We use a different fit range for the NBD function fit for the single diffractive dijet analysis than in the inclusive dijet analysis, since the shape of the distribution found in data is different (smaller average of N_{tracks}). We fit the NBD distribution from multiplicities from 2 – 25, where the value of 25 was chosen in order to minimize the bias induced by the non-diffractive contamination at high multiplicities $N_{\text{tracks}} \geq 35$, and to take into account the smaller average of the N_{tracks}. The fit range covers the maximum of the distribution, as well as the concavity of it. We fit the NBD function on the data before the background subtraction, to avoid any bias in the background estimation procedure for non-diffractive events. We consider this as a systematic uncertainty in the measurement by extracting the results for the beam background-subtracted distribution, and then applying.

We fit the NBD distribution to the data before background subtraction, to avoid biasing the multiplicity distribution found in data with the background estimation method used to extract the charged particle track multiplicity. The contamination of p-gap-jet-jet events in the 0th multiplicity bin is of about 10%, consistent with the contamination found within the inclusive jet-gap-jet sample.

The SS method introduced in the inclusive dijet analysis section cannot be directly used for dijet events with intact protons. The mean η of the jets is not centered at zero in single-diffractive events. This is because single-diffractive dijet events are intrinsically boosted along the beam direction, in a direction opposite to the scattered proton. Thus, in

considering single-diffractive dijet events located in the same hemisphere of the CMS detector, the N_{tracks} in the $|\eta| < 1.2$ region is directly influenced by the intrinsic boost effects. To account for this, the N_{tracks} distribution of the SS dijet sample is instead measured in intervals of $-2.0 < \eta < 0.4$ or $-0.4 < \eta < 2.0$ for protons detected in sector 45 or 56, respectively. These intervals are determined based on the mean jet η in the data for events with an intact proton in sectors 45 and 56, which corresponds to boosts of about 0.8 units in negative and positive η, respectively. The two leading jets are located on the same side relative to these η intervals, *i.e.*, $\eta^{\text{jet}} < -2.2$ or $\eta^{\text{jet}} > 0.6$ for intact protons in sector 45 and $\eta^{\text{jet}} < -0.6$ or $\eta^{\text{jet}} > 2.2$ for protons in sector 56. The location of the jet axes is 0.2 units away from the η interval, as in the construction of the SS dijet sample of the standard jet-gap-jet analysis. The resulting N_{tracks} distribution of the SS dijet sample matches that of the OS sample at moderate multiplicities after these adjustments. The N_{tracks} distribution of the SS dijet sample is normalized to that of the nominal sample in the range $2 \leq N_{\text{tracks}} \leq 40$. The number of events of the SS dijet sample in the lowest multiplicity bins is then used to estimate the standard single-diffractive dijet production at low multiplicities $N_{\text{tracks}} \leq 1$, as shown in Fig. 7.12. An excess of events over the expected background counts is observed, which is attributed to the presence of p-gap-jet-gap-jet events.

7.6 Signal region definition and optimization

For this, we use the NBD fit in the track multiplicity region from 2 to 25, extrapolated to the first two bins of the multiplicity distribution (see Fig. 7.12). We combine the N_{tracks} distributions found in sector 45 and sector 56, in order to build a combined N_{tracks} with both arms with a large enough number of events to constrain the NBD distribution and isolate the p-gap-jet-gap-jet events with stronger confidence. The number of events on the individual sectors is not large enough to perform the analysis individually per arm.

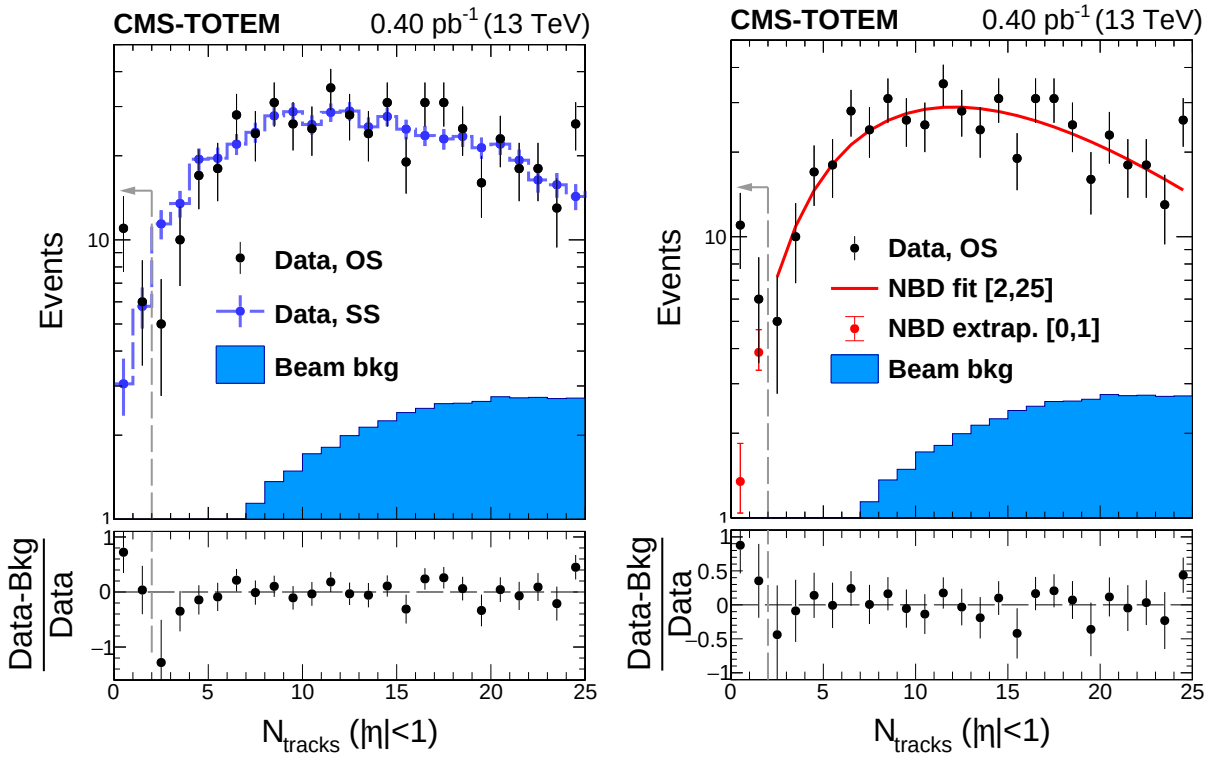

Figure 7.12: N_{tracks} distribution in the $|\eta| < 1$ region after the dijet and proton selection. Opposite side (OS) dijet events satisfy $\eta^{\text{jet1}}\eta^{\text{jet2}} < 0$. The vertical bars represent the statistical uncertainties. The filled histogram represents the residual beam background contamination. The contribution of standard diffractive dijet events that feature a central gap is modeled with the same side (SS) dijet events (left) and with the negative binomial distribution (NBD) function fit (right), as described in the text. The NBD function is fit in the interval $2 \leq N_{\text{tracks}} \leq 25$, and extrapolated to $N_{\text{tracks}} = 0$. The dashed-line arrow represents the region $N_{\text{tracks}} < 2$ used for signal extraction in the analysis. The vertical bars of the NBD extrapolation points represent the uncertainty in the extrapolation based on the fit parameter uncertainties extracted in the $2 \leq N_{\text{tracks}} \leq 25$ interval.The figure is the same as the paper version one in Ref. (1).

7.7 Systematic uncertainties

The components of the systematic uncertainties can be divided into two parts: one of them has to do with the dijet and central gap definition, whereas the second has to do with the intact proton. For the former, we use the same set of sources of systematic uncertainties as in the inclusive jet-gap-jet measurement of Chapter 6. In addition to the sources of systematic uncertainties that are also present in the jet-gap-jet measurement, we consider the following:

- *Calorimeter energy scale variation:* The single diffractive dijet sample is selected with the inequality $\xi_{\mathrm{CMS}} - \xi_{\mathrm{TOTEM}} \leq 0$. ξ_{CMS} is reconstructed from the PF objects of CMS, and is thus sensitive to energy scale calibration uncertainties.

- *Horizontal dispersion determination:* The reconstruction of ξ_{TOTEM} value depends on the LHC optics parametrization via the optical functions elements that enter in the transport matrix connecting the kinematics of the proton at the IP5 with the ones at the RPs. The determination of the horizontal dispersion D_x term in the transport matrix directly affects the measurement of ξ_{TOTEM}. The associated systematic uncertainty is taken into account by scaling the value of ξ_{TOTEM} by $\pm 10\%$.

- *Fiducial selection requirements for $x-y$ coordinates:* We modify the vertical and horizontal fiducial selection requirements by 200 μm and 1 mm respectively;

- *NBD fit range:* Since the number of events in our final selection is small, the NBD function fit is loosely constrained in the control region, and becomes dependent on the chosen fit region. We vary the NBD fit region for fit ranges of [2,15] and [2,35]. The difference of the extracted gap fraction for these fit regions relative to the nominal selection obtained with the fit region [2,25] is taken as a systematic uncertainty.

Source of systematic uncertainty	Relative uncertainty [%]
Jet energy scale determination up	$^{+0.7}_{-0}$
Track quality loose	$^{+7.9}_{-0}$
Calorimeter energy scale	$^{+3.7}_{-5.1}$
Horizontal dispersion	$^{+6.0}_{-4.3}$
Charged-particle track p_{T} threshold	$^{+10.9}_{-0}$
Fiducial RP selection requirements	$^{+0}_{-2.6}$
Background subtraction	$^{+28.3}_{-28.3}$
NBD fit parameter unc.	$^{+4.2}_{-7.0}$
NBD fit range region	$^{+12.0}_{-4.6}$
Functional form of the fit	± 11.5
Total	$^{+36.4}_{-32.6}$

Table 7.2: Percentage contributions of the various sources of systematic uncertainties affecting the determination of the fraction f_{CSE} within the CMS-TOTEM combined sample.

The total systematic uncertainty is calculated as the quadratic sum of the individual contributions. The contribution of each source of systematic uncertainties can be seen in Tab. 7.2.

7.8 Results

The fraction of the number of p-gap-jet-gap-jet events to the number of p-gap-jet-jet events where each of the leading two jets has a minimum transverse momentum of $p_{\mathrm{T,jet}} > 40$ GeV, have pseudorapidity values of $1.4 < |\eta_{\mathrm{jet}}| < 4.7$, and are on opposite hemispheres of the CMS detector $\eta_{\mathrm{jet1}}\eta_{\mathrm{jet2}} < 0$ and an intact proton satisfying $\xi < 0.2$ and $0.025 < -t < 4$ GeV^2, is found to be

$$f_{\mathrm{CSE}}^{\mathrm{SD}} = 1.92 \pm 0.46(\mathrm{stat})^{+0.69}_{-0.62}(\mathrm{syst})\ \% \tag{7.2}$$

this fraction is $2.91 \pm 0.70^{+1.08}_{-1.01}$ times larger than the gap fraction value found in jet-gap-jet events within the inclusive dijet sample at 13 TeV in previous sections of this analysis. This is shown graphically in Fig. 7.13, where the gap fraction f_{CSE} is presented as

a function of $\Delta\eta_{jj}$ and $p_{T,\,jet\,2}$ with CMS-only data and CMS-TOTEM combined data shown together. The difference on the value of f_{CSE} between the two classes of processes, jet-gap-jet and p-gap-jet-gap-jet, can be interpreted as a consequence of the reduced spectator-parton activity in single-diffractive reactions with an intact proton detected relative to non-diffractive reactions, where soft-parton exchanges may take place between proton remnants and the struck partons and spoil the central gap signature. A similar effect has been observed in other diffractive topologies in dijet events with two rapidity gaps by the CDF Collaboration in $p\bar{p}$ collisions at $\sqrt{s} = 1.8$ TeV, where they compared the ratio of yields of single-diffractive dijet events to non-diffractive dijet events, $R_{SD/ND}$, and the ratio of double-pomeron exchange dijet events to single-diffractive dijet events, $R_{DPE/SD}$, and found that the double-ratio had a value of $R_{ND}^{SD}/R_{SD}^{DPE} = 0.19 \pm 0.07$ (216).

The double-ratio uncertainties are found to be mostly driven by the systematic uncertainties inherited from the uncertainties on f_{CSE} from the CMS-TOTEM measurement. The final result for the double-ratio, accounting for the aforementioned discussion on the propagation of uncertainties, is found to be $R = f_{CSE}(\text{CMS} - \text{TOTEM})/f_{CSE}(\text{CMS}) = 2.91 \pm 0.70(\text{stat})^{+1.08}_{-1.01}(\text{syst})$.

7.9 Summary of analysis of jet-gap-jet events with intact protons

We have observed jet-gap-jet in single diffraction events, where there is a large amount of momentum transferred across the central rapidity gap and a small amount of momentum transfer by the color-singlet exchange off the proton. There are 11 single-diffractive dijet events separated by a central pseudorapidity gap ($N_{tracks} = 0$) in the CMS-TOTEM sample used in this analysis. The fraction of p-gap-jet-gap-jet events to p-gap-jet-jet events was found to be $f_{CSE}^{SD} = 1.92 \pm 0.46(\text{stat})^{+0.69}_{-0.62}(\text{syst})$ %, about $2.91 \pm 0.70(\text{stat})^{+1.08}_{-1.01}(\text{syst})$ times larger than the fraction found in inclusive jet-gap-jet events in Chapter 7 for similar phase space volume of the dijet system, consistent with previous dijet topologies with two rapidity gaps.

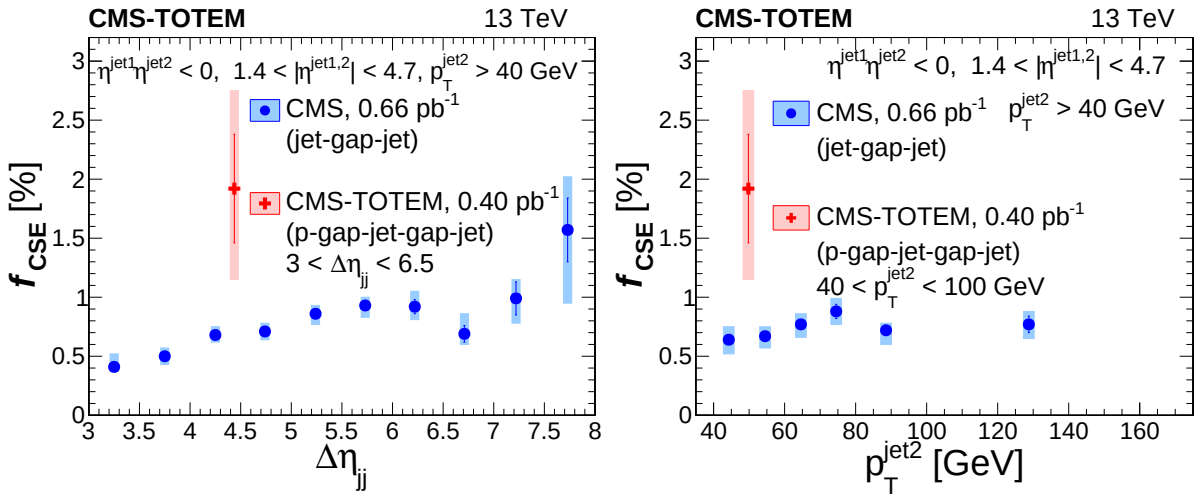

Figure 7.13: Fraction of hard color-singlet exchange dijet events f_{CSE}, measured as a function of $\Delta\eta_{jj}$ (left) and p_T^{jet2} (right) extracted in inclusive dijet event production (labeled CMS, represented by the blue circle markers) and in dijet events with an intact proton at 13 TeV (labeled CMS-TOTEM, represented by the red cross marker). The vertical bars represent the statistical uncertainties, and boxes represent the combination of statistical and systematic uncertainties in quadrature. The CMS results are plotted at the mean values of $\Delta\eta_{jj}$ and p_T^{jet2} in the bin. Similarly, the CMS-TOTEM result is plotted at the mean value of $\Delta\eta_{jj}$ and p_T^{jet2} in the CMS-TOTEM combined sample. The $40 < p_T^{jet2} < 100$ GeV and $3.0 < \Delta\eta_{jj} < 6.5$ ranges below the CMS-TOTEM legend represent the dijet phase space covered by events with an intact proton with the present sample size, rather than a selection requirement, as described in the text. The figure is the same as the paper version one in Ref. (1).

7.10 Summary of hard color-singlet exchange analysis

Events with two leading jets separated by a large pseudorapidity (η) gap have been studied in pp collisions at $\sqrt{s} = 13$ TeV with the CMS and TOTEM experiments at the CERN LHC in 2015. The pseudorapidity gap is defined by the absence of charged particles with transverse momentum $p_T > 200$ MeV in the $|\eta| < 1$ region. Each of the two leading p_T jets has $1.4 < |\eta^{jet}| < 4.7$ and $p_T^{jet} > 40$ GeV, with $\eta^{jet1}\eta^{jet2} < 0$, where jet1 and jet2 are the leading and subleading jets in p_T. The pseudorapidity gap signature is assumed to be caused by hard color-singlet exchange, which is described in terms of two-gluon exchange in perturbative quantum chromodynamics. Color-singlet exchange events appear as an excess of events over the expected N_{tracks} contribution from color-exchange dijet events at the lowest N_{tracks}. The ratio of color-singlet exchange events to all dijet events, f_{CSE}, has been measured as a function of p_T^{jet2}, the η difference between the two leading jets, $\Delta\eta_{jj} \equiv |\eta^{jet1} - \eta^{jet2}|$, and the azimuthal angular separation between the two leading jets, $\Delta\phi_{jj} \equiv |\phi^{jet1} - \phi^{jet2}|$.

The measured f_{CSE} values are in the range of 0.6–1.0%. The ratio f_{CSE} increases with $\Delta\eta_{jj}$, has a weak dependence on p_T^{jet2}, and increases as $\Delta\phi_{jj}$ approaches π. No significant difference in f_{CSE} is observed between the 13 TeV results and those presented by the CMS Collaboration at 7 TeV. This is in contrast to the trend found at lower energies of 0.63 and 1.8 TeV by the D0 and CDF Collaborations, where a significant decrease of f_{CSE} with increasing $\sqrt{s}$ was observed, as illustrated in Fig. 6.38. The results are compared with calculations based on the BFKL framework of pQCD (82; 81; 217) with resummation of large logarithms of energy at next-to-leading logarithmic accuracy using leading order impact factors, and various treatments of gap survival probability effects. The implementation by Royon, Marquet, and Kepka (129; 130) describes some features of the data, but is not able to simultaneously describe all aspects of the measurements. The implementation by Ekstedt, Enberg, Ingelman, and Motyka (128; 131) gives a fair description of the data in $\Delta\eta_{jj}$ and p_T^{jet2} within the uncertainties only when considering survival probability effects

based on multiple-parton interactions and their soft color interaction model.

The jet-gap-jet analysis could be improved by considering further characterization of the hard color-singlet exchange in dijet events. This could be achieved by considering an analysis with a varying rapidity gap width, or by considering an extension of the study to other center-of-mass energies. It would be interesting to see also how these events behave at much larger p_{T}. So far, it seems that the production rate of color-singlet exchange dijet events scales similarly with p_{T} as the standard color-exchange dijet events.

In addition, a sample of dijet events with intact protons collected by the CMS and TOTEM experiments is used to study jet-gap-jet events with intact protons, which correspond to p-gap-jet-gap-jet topologies. This is the first analysis of this diffractive event topology. The f_{CSE} value extracted in this sample is $2.91 \pm 0.70(\mathrm{stat})^{+1.08}_{-1.01}(\mathrm{syst})$ times larger than that found in inclusive dijet production, possibly suggesting a larger abundance of jets with central gaps in events with detected intact protons. This can be interpreted in terms of a lower spectator parton activity in events with intact protons, which decreases the likelihood of the central gap signature being spoiled. The study could be extended by using a larger sample of diffractive dijet events which would allow for a more "differential" measurement of the f_{CSE}. An integrated luminosity of about 20 pb^{-1} would allow for such a differential measurement for dijet events with at least one intact proton.

Chapter 8

Study of diffractive dijet production at $\sqrt{s} = 13$ TeV

In this Chapter, we briefly describe the progress on the analysis of diffractive dijet production using the same CMS-TOTEM data as for the SMP-19-006 analysis at $\sqrt{s} = 13$ TeV of Chapter 7. For this study, we focus on the hard diffractive production of jets. The idea is that this measurement can be used to extend the efforts started by the $\sqrt{s} = 8$ TeV CMS-TOTEM diffractive dijet analysis(218), and previous measurements at the Tevatron at lower $\sqrt{s}$. Preliminary beam-background studies are presented, as well as the physics prospects with the 13 TeV data set for low-p_{T} jets. Prospects for the continuation of the analysis are drawn at the end of the Chapter.

The general physics motivation for this study is outlined more in detail in Section4.3 of Chapter 4 for hard diffraction. In a nutshell, what we would like to do is to characterize the hard diffractive exchange off the proton in a completely unexplored kinematic regime. The increase in center-of-mass energy and larger data sample in comparison with the $\sqrt{s} = 8$ TeV CMS-TOTEM analysis (169), and the use of higher-ξ data, gives us ideal conditions for an experimental analysis of diffractive dijet events. Measurements of hard diffraction with proton tagging have not been performed at $\sqrt{s} = 13$ TeV. Previous measurements of diffractive dijet production probed ξ values of at most 10% ($\xi < 0.1$). Hence, we have a unique opportunity of studying the hard diffractive exchange in a completely unexplored domain of ξ and t variables. We describe the preliminary work on single-diffractive dijet events and double-pomeron exchange dijet events in Sections 8.1 and 8.4, respectively. Prospects for future work are laid down at the end of this Chapter. The goal is to present the physics possibilities that we have with this data set.

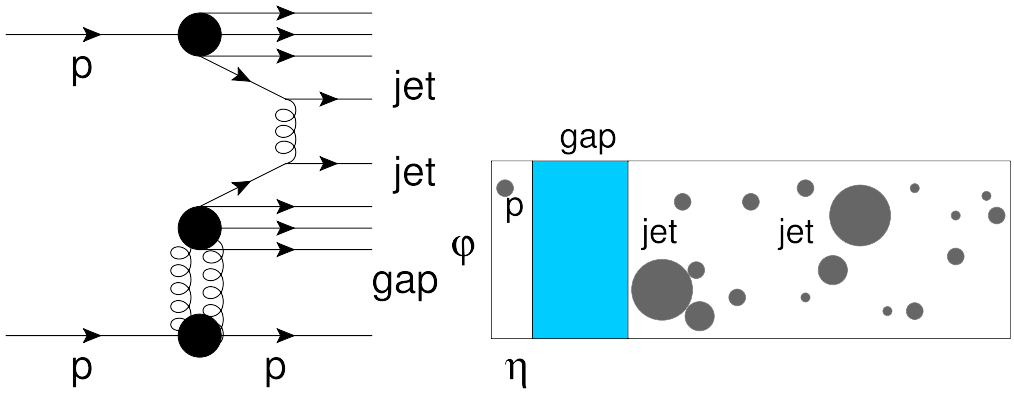

Figure 8.1: Schematic diagram of single-diffractive dijet production with intact protons. (Right) Signature in η–ϕ plane.

8.1 Single-diffractive dijet events at $\sqrt{s} = 13$ TeV

In this Section, we describe the study of single-diffractive dijet production with CMS-TOTEM 13 TeV data (pp$\rightarrow$ p JJ X). A schematic diagram of the process is shown in Fig. 8.1. The description of the CMS and TOTEM detector components relevant to this analysis are presented in Chapter 5. Details and control plots related to the proton-tracks at the Roman pots and dijet kinematic variable distributions for single-diffractive dijet candidates were presented in Chapter 7. A description of the CMS-TOTEM data sample was also presented in Chapter 7. In this Chapter , we just highlight some of the work done to develop the analysis of $pp \rightarrow pJJX$ (single-diffractive dijets) and $pp \rightarrow pJJXp$ (double-pomeron exchange dijet) for 13 TeV data.

The jet collection is the same as the one of Chapter 7. For the analysis of diffractive dijet production, the events we consider are all those where the two highest-p_T jets have $p_T >$ 40 GeV each and have $|\eta| < 4.7$. There are no other selection requirements for additional jets in the event. We use only events with at most one primary vertex, to suppress residual pileup contributions.

In contrast to the $\sqrt{s} = 8$ TeV analysis, we allow the jets to go to larger values of η. The $\sqrt{s} = 8$ TeV used jets with $p_T > 40$ GeV as well, but with a more restricted window in $|\eta| < 4.4$, since there was interest in comparing the results with the rapidity gap based

analysis at 7 TeV. In our case, we are interested in studying the hard diffractive dijet process, where the jets are allowed to populate as much of the phase-space as it is possible. Since we are detecting the intact protons, *there is no need to require any forward rapidity gap.*

The intact protons satisfy the following requirements:

- At least one proton must be detected in either sector 45 or 56 RP stations.
- The proton track must cross at least two overlapping RP units (*e.g.*, top-top, bottom-bottom), to ensure quality proton reconstruction.
- The ξ reconstructed with the RP ($\xi_p(\mathrm{RP})$) must have values of $\xi_p(\mathrm{RP}) < 0.18$ and t must have values of $-4 < t < -0.025$ GeV^2. These bounds are based on acceptance studies of the RPs.
- The proton track impact location at the RP must satisfy the fiducial selection requirements $8 < |y(\mathrm{RP})| < 30$ mm and $0 < x(\mathrm{RP}) < 20$ mm for vertical RPs, and $|y(\mathrm{RP})| < 25$ mm and $7 < x(\mathrm{RP}) < 25$ mm for horizontal RPs, where $x(\mathrm{RP})$ and $y(\mathrm{RP})$ denote the horizontal and vertical coordinates of the tracks in the plane transverse to the beam-line at the RP. The beam position is at $x(\mathrm{RP}) = y(\mathrm{RP}) = 0$. This selection requirement ensures good proton reconstruction efficiency and acceptance within the RPs, and is based on acceptance studies of the RPs.

There is no "veto" on the intact proton activity on the other side. If there is another intact proton on the other side, we check that the two protons are not correlated in θ_y^*. The latter is only expected from elastic scattering events. A rejection of events with two intact protons strongly correlated like this filters out all other events. This leaves us with 10.5k events in sector 45 and 11k events in sector 56. There is also no rapidity gap requirement in the analysis; the rapidity gap is "inferred" from the detected intact proton. This is in fact what gives us edge for this analysis.

It is expected that the size of the rapidity gap depends logarithmically on the ξ value of the intact proton $\Delta\eta^{\mathrm{gap}} \propto -\ln(1/\xi)$. The smaller ξ is, the larger the rapidity gap on the

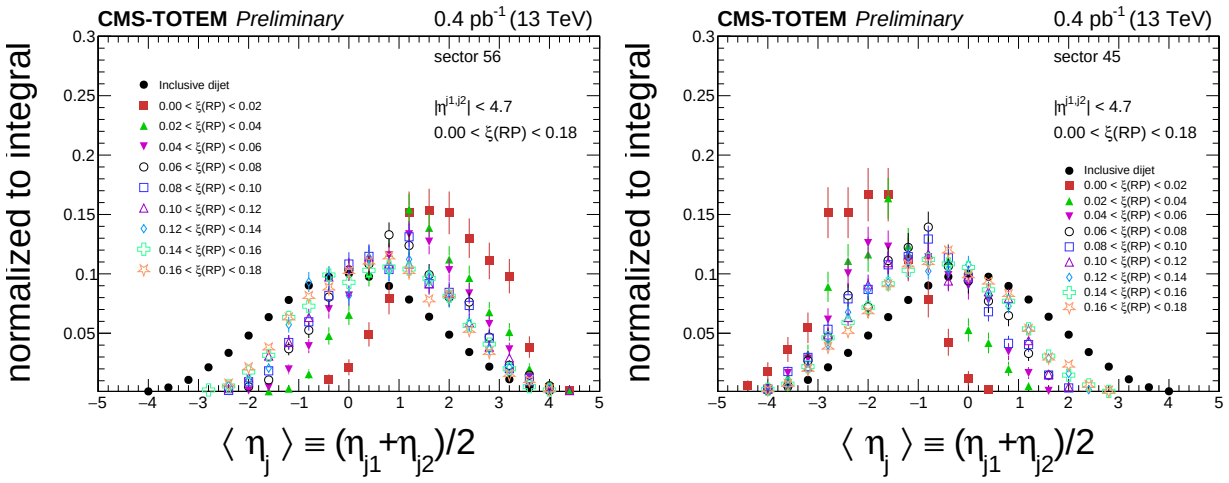

Figure 8.2: Average pseudorapidity of the highest p_T jets in bins of the intact proton ξ. The left and right panels are associated to the protons scattering towards positive and negative pseudorapidities, respectively. There is no background subtraction for these plots.

outgoing proton direction becomes. The larger ξ is, the more the pseudorapidity distribution of the jets resembles the distribution of the standard QCD jets. Indeed, the boost of the jets seems to follow such a behavior, as shown for the single-diffractive candidates for protons scattering in sectors 45 and 56 in Fig. 8.2. In addition, we examined the multiplicity of PF candidates with energy $E > 5$ GeV in the forward region in the direction of the outgoing proton in Fig. 8.3. We see that the smaller ξ is, the more narrow the PF multiplicity distribution at N_{PF} become, leading to very clean rapidity gaps just by selecting the intact proton. The jets are allowed to populate all of phase space in principle, and yet the detection of the proton acts as an effective filter, as expected.

8.2 Beam background estimation

The dominant background in this analysis is the beam-background, i.e., the detection of (mostly) non-diffractive dijet events with uncorrelated protons from residual pileup interactions or from beam-halo activity. Such a background was found to be subleading in the proton-gap-jet-gap-jet analysis of Chapter 7. The beam-background is illustrated

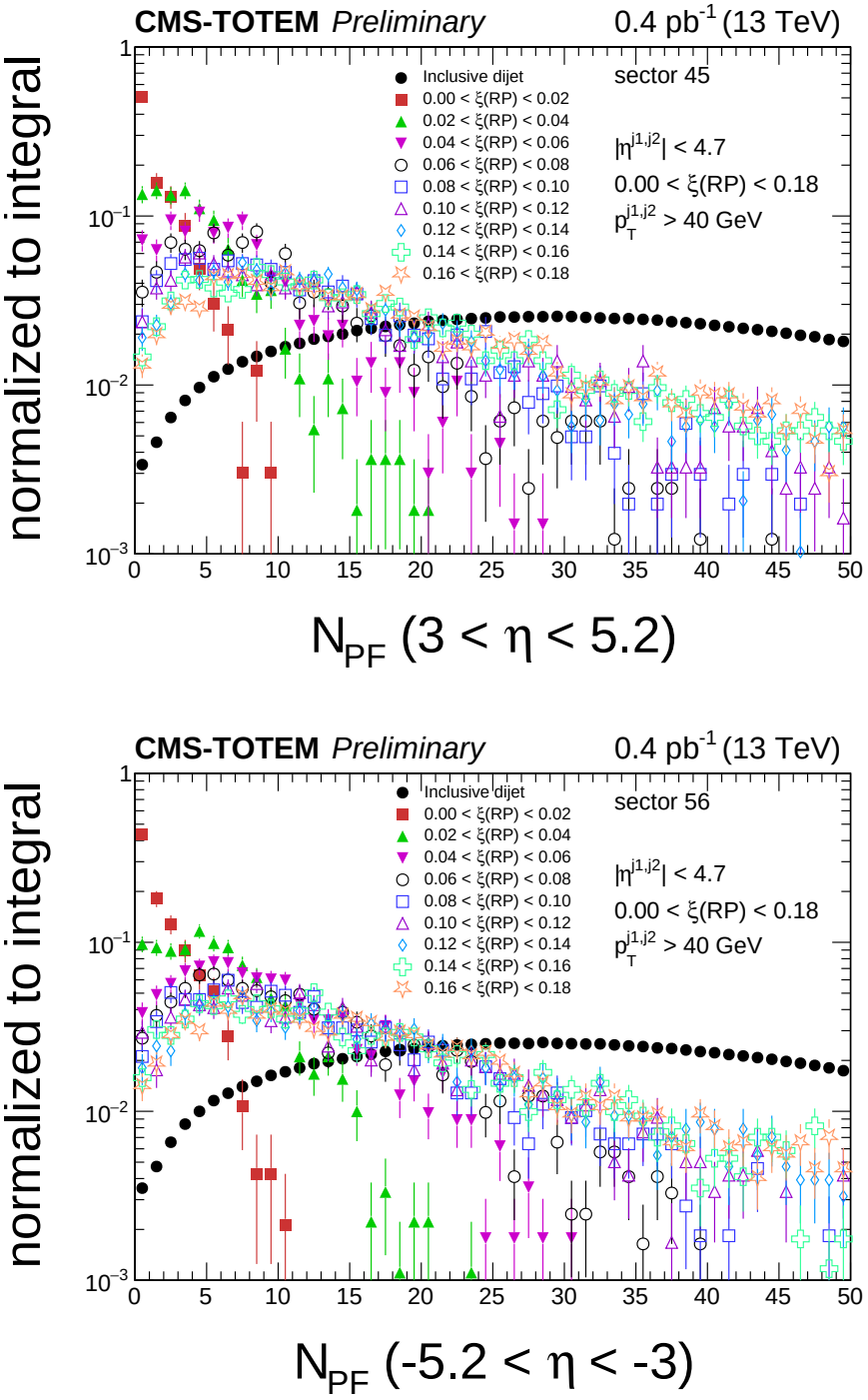

Figure 8.3: Multiplicity of PF candidates in $\pm 3 < \eta < \pm 5.2$ (for an outgoing intact proton with $\pm\eta_p$) in bins of ξ(PF). The PF candidates have $E > 5$ GeV. The upper panel is for protons scattering towards positive pseudorapidity (sector 45), whereas the lower panels are for protons scattering towards negative pseudorapidities (sector 56).

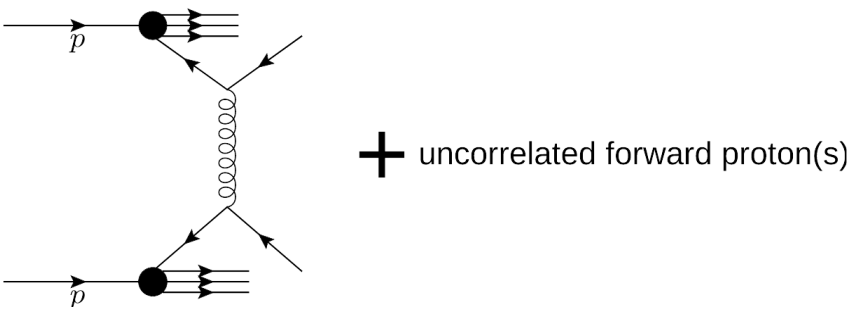

Figure 8.4: Dominant background of diffractive dijet production.

schematically in Fig. 8.4.

To suppress the beam-related background, we analyze the kinematic correlations between the central dijet system and the forward protons. This can be done by analyzing the fraction of momentum loss calculated with the CMS detector PF candidates $\xi(\mathrm{PF})$, and with the one reconstructed by the TOTEM experiment. We can analyze their difference, $\xi(\mathrm{PF}) - \xi(\mathrm{RP}$. Most of the signal events are expected to be located in $\xi(\mathrm{PF}) - \xi(\mathrm{RP} < 0$, as seen in Chapter 7. The variable $\xi(\mathrm{PF})$ is reconstructed via,

$$\xi(\mathrm{PF}) \equiv \frac{1}{\sqrt{s}} \sum_{i \in PF} (E \pm p_z) \tag{8.1}$$

where the sum is over the PF candidates, and the $\pm$ sign is for protons scattering towards positive or negative rapidities. The PF candidates pass the same η-dependent thresholds described in Chapter 7, which were optimized with zero-bias data as described therein.

In order to reduce the systematic uncertainty related to the subtraction of the beam-background, it is best to have two independent methods to do such an estimation. The first method is based on the event mixing procedure described in Chapter 7. The difference here is that, since we have more events, we have to be more careful in the definition of the control region and the signal region. Indeed, by inspecting the $\xi(\mathrm{PF}) - \xi(\mathrm{RP})$ distributions in sectors 45 and sectors 56, together with the background-template created from the event mixing procedure, it seems that there is an excess of events at $0 <$

$\xi(\mathrm{PF}) - \xi(\mathrm{RP}) < 0.02$. This appears in sector 45 and 56 in Fig.8.5. In Chapter 7, we were asserting that the signal events are exclusively located at $\xi(\mathrm{PF}) - \xi(\mathrm{RP}) < 0.0$. There is a caveat to such an assertion: that implicitly assumes that the events that we are dealing with have mostly $\xi(\mathrm{RP}) \gg 0$. In this case, since we are not asking for a topology where the two leading jets are back-to-back like in the analysis of Chapter 7, and we have way more events, we actually have a non-negligible amount of events at very low $0 \approx \xi(\mathrm{RP}) < 0.02$. In this region, the formula used to estimate the fraction of momentum loss using the PF candidates of the CMS detector actually gives a very close approximation to the actual value of ξ. Mathematically, this means that,

$$\lim_{\xi(\mathrm{RP})\to 0} \xi(\mathrm{PF}) \equiv \frac{1}{\sqrt{s}} \sum_{i \in PF} (E \pm p_z) = \xi(\mathrm{RP}) \tag{8.2}$$

this means that the $\xi(\mathrm{PF}) - \xi(\mathrm{RP})$ distribution at low $\xi(\mathrm{RP})$ should be symmetrical about 0. The smearing around 0 is due to the smearing of $\xi(\mathrm{PF})$ and $\xi(\mathrm{RP})$. For this reason, for the single-diffractive dijet analysis, we divide the event mixing procedure into two regions: the low-ξ ($\xi(\mathrm{RP}) < 0.04$) and high-ξ ($0.04 < \xi(\mathrm{RP}) < 0.18$) region. We see that by dividing the event mixing procedure like this, we can effectively isolate the single-diffractive dijet signal events in sectors 45 and 56, as shown in Fig. 8.6 and 8.7.

The second method is based on the measured $\xi(\mathrm{PF})$ spectra. We can extract different sets of $\xi(\mathrm{PF})$ curves for a given bin in $\xi(\mathrm{RP})$. This method has the advantage that it does not need of any event mixing procedure or MC-based methodology to estimate the background. The idea is the following: if there are single-diffractive dijet event candidates in the sample, then we should be able to use the tail of the $\xi(\mathrm{PF})$ distribution, which should be dominated by non-diffractive dijet events paired with uncorrelated forward particles detected in the RP detectors. This way, we can use this region to normalize the distribution from non-diffractive dijet events from the inclusive dijet sample (which consists of $\approx 99\%$ non-diffractive events), and then we can see the predicted background at low $\xi(\mathrm{PF})$ values, where the signal single-diffractive dijet events are expected to be located.

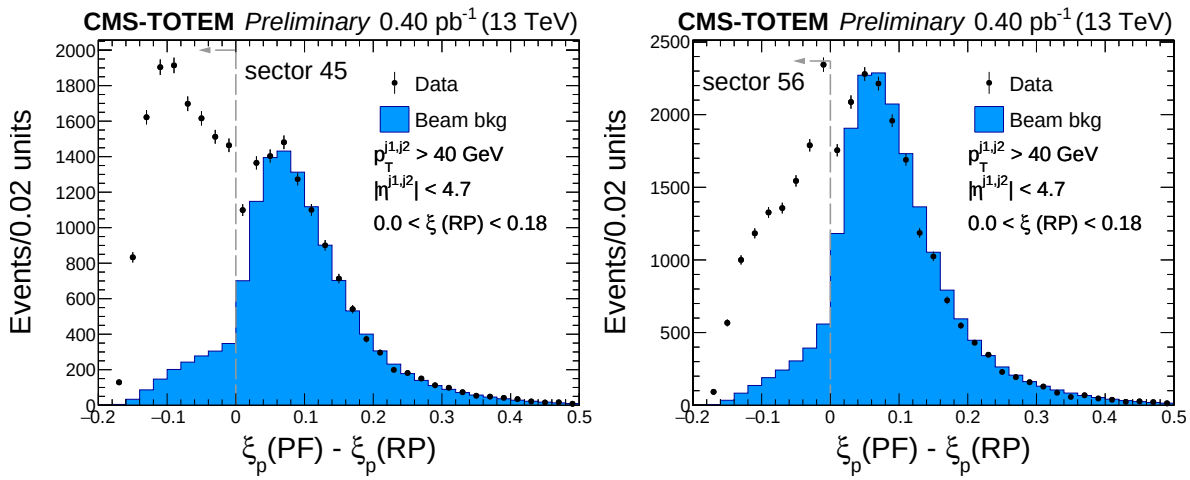

Figure 8.5: $\xi_p(\mathrm{PF}) - \xi_p(\mathrm{RP})$ difference, with the estimated background represented by the blue, solid histogram. The left panel is for protons detected in sector 45, whereas the right panel is for protons scattering in sector 56. There is an excess of events at $\xi_p(\mathrm{PF}) - \xi_p(\mathrm{RP}) \approx 0^+$. As discussed in the text, this is in fact not due to mismodelling, but rather the contribution of very large rapidity gap events in the data.

Indeed, by doing this exercise, we find that there is an excess of events at low $\xi(\mathrm{PF})$ in the nominal sample compared to the normalized non-diffractive dijet $\xi(\mathrm{PF})$ spectra. The location of the excess of events depends on $\xi(\mathrm{RP})$. It is very interesting that the excess of events manifests in the data just by selecting a given bin in $\xi(\mathrm{RP})$. This is also a good cross check of the calibration of TOTEM and of CMS, since it yields the excess of events precisely how we expect it. The results of the procedure are shown in Figs. 8.9 and 8.8.

The background-subtracted ξ distribution is shown in Fig. 8.10. The two methods agree with each other within 1%. The second method, dubbed "$\xi(\mathrm{PF})$ spectra", is used as a cross check of the event mixing method. The event mixing procedure has the advantage that it yields a collection of background-like events that can be used for the proton and dijet information.

A result of the t, ξ, and β distributions for sectors 45 and 56 with the expected background is shown in Figs. 8.12, 8.13, and 8.11.

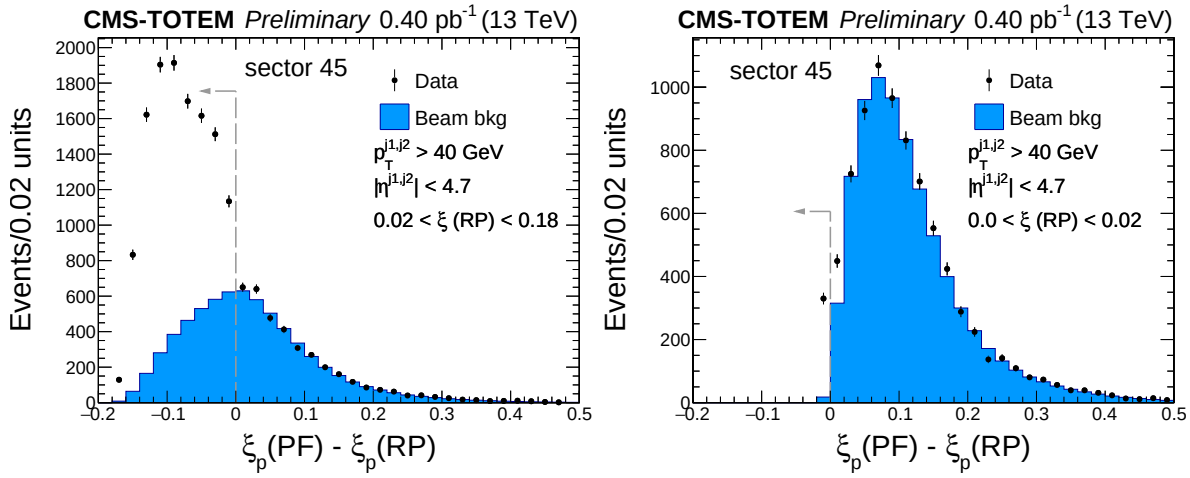

Figure 8.6: $\xi_p(\mathrm{PF}) - \xi_p(\mathrm{RP})$ difference in sector 45 split in two regions: low-ξ (left panel) and high-ξ (right panel), with the estimated background.

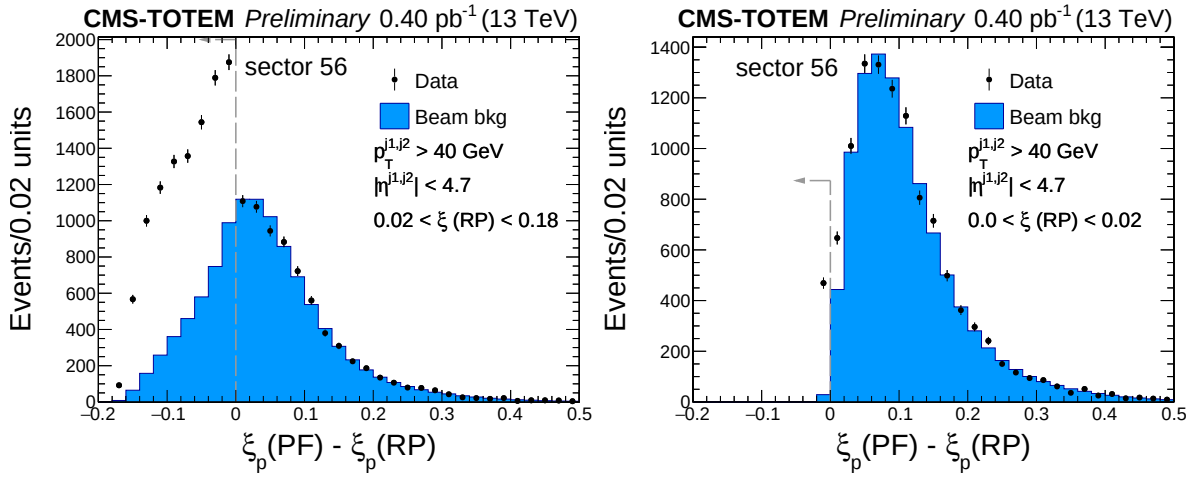

Figure 8.7: $\xi_p(\mathrm{PF}) - \xi_p(\mathrm{RP})$ difference in sector 56 split in two regions: low-ξ (left panel) and high-ξ (right panel), with the estimated background.

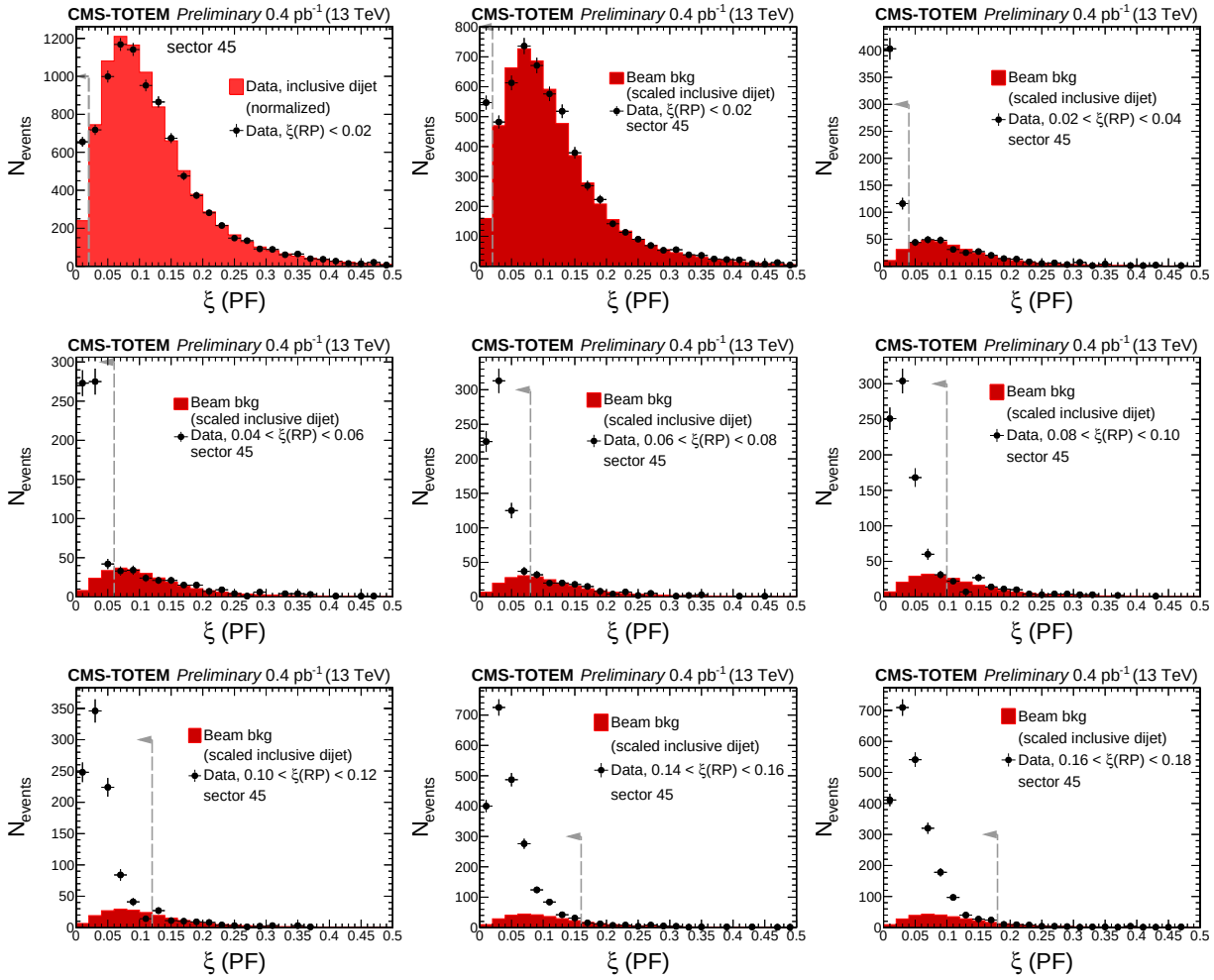

Figure 8.8: ξ(PF) spectra for events with an intact proton scttering towards sector 45. Each panel represents a different bin in ξ(RP). The red, solid histogram represents a control sample built from the inclusive dijet data sample (dominated by non-diffractive interactions), which is normalized to the data at the tail of the distributions. The dashed arrow represents the region where the single-diffractive dijet events are expected to populate.

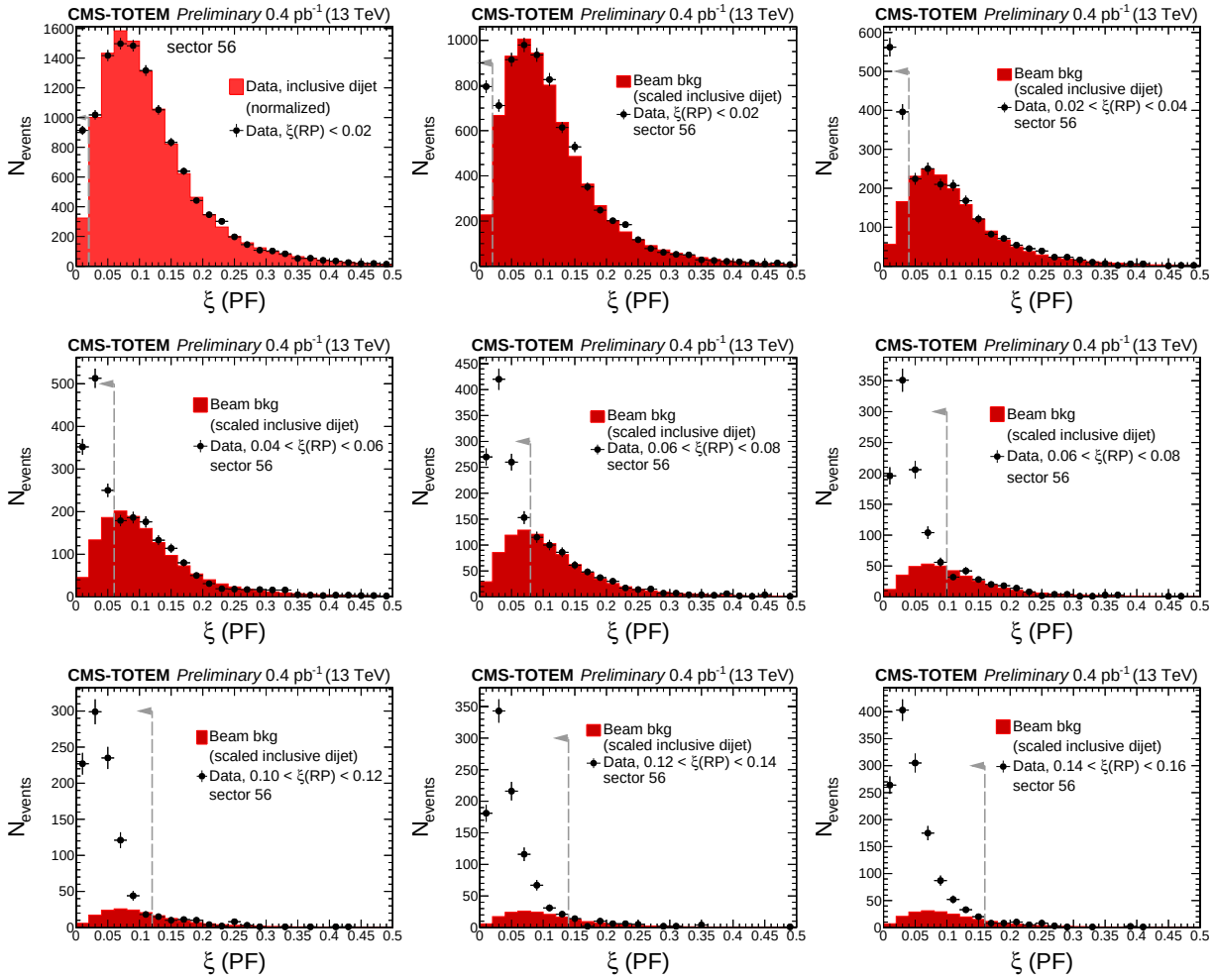

Figure 8.9: ξ(PF) spectra for events with an intact proton scttering towards sector 56. Each panel represents a different bin in ξ(RP). The red, solid histogram represents a control sample built from the inclusive dijet data sample (dominated by non-diffractive interactions), which is normalized to the data at the tail of the distributions. The dashed arrow represents the region where the single-diffractive dijet events are expected to populate.

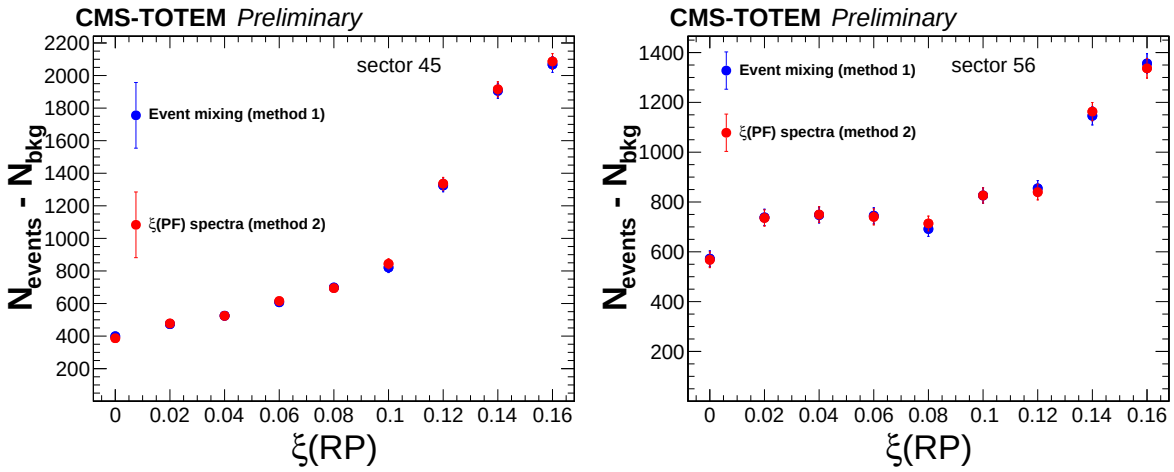

Figure 8.10: Spectrum of ξ(RP for sector 45 (left) and sector 56 (right) after background subtraction with two different methods. The blue markers represent the result using the event mixing procedure, whereas the red markers indicate the result based on the ξ(PF) spectra method. The background-subtracted yields are the same within a few percent for one method or the other.

8.3 Preliminary physics prospects

See that, in addition, we compute the ratio of single-diffractive dijet event candidates relative to the number of inclusive dijet events for protons scattering towards sector 56 and those scattering towards sector 45. This is similar to the ratio distribution extracted at 1.96 TeV by CDF (213) and at 8 TeV and CMS-TOTEM (169), respectively. The ratio is defined as

$$R(x, p_{\mathrm{T}}^{\mathrm{jet1,2}}) = \frac{N^{\mathrm{SD}}}{N^{\mathrm{all\ jets}}} \tag{8.3}$$

where N^{SD} is the number of single-diffractive dijet events with at least one intact proton, and $N^{\mathrm{all\ jets}}$ is the number of events with at least two jets. The ratio may be extracted as a function of the momentum fraction carried by the parton initiating the hard scattering process x,

$$x^{\pm} = \frac{\sum_{\mathrm{jets}} \left(E^{\mathrm{jet}} \pm p_z^{\mathrm{jet}}\right)}{\sqrt{s}}, \tag{8.4}$$

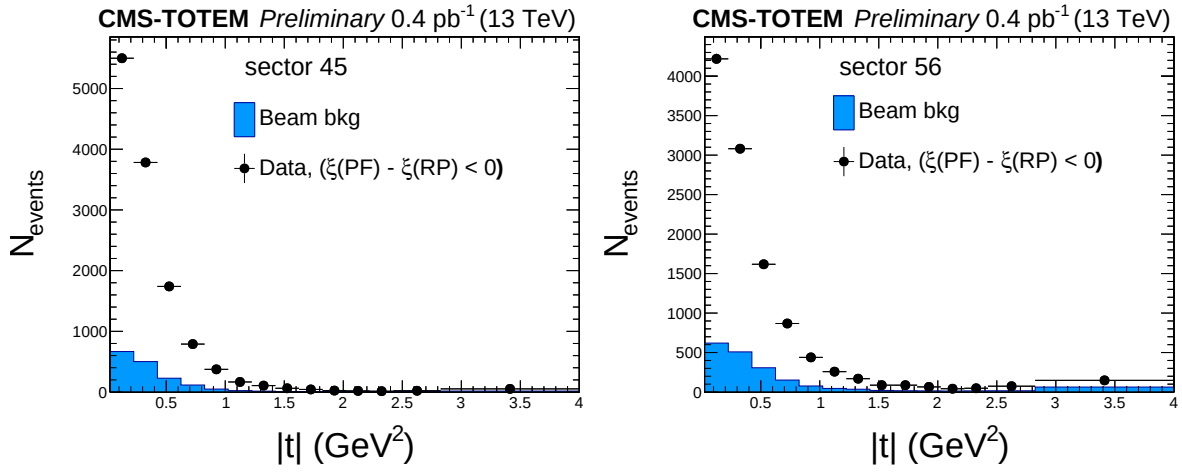

Figure 8.11: Number of events as a function of the four-momentum transfer square at the proton vertex $|t|$. The blue, solid histogram represents the expected background yield calculated with the event mixing procedure described in text. The left (right) panel is for protons detected in sector 45 (56).

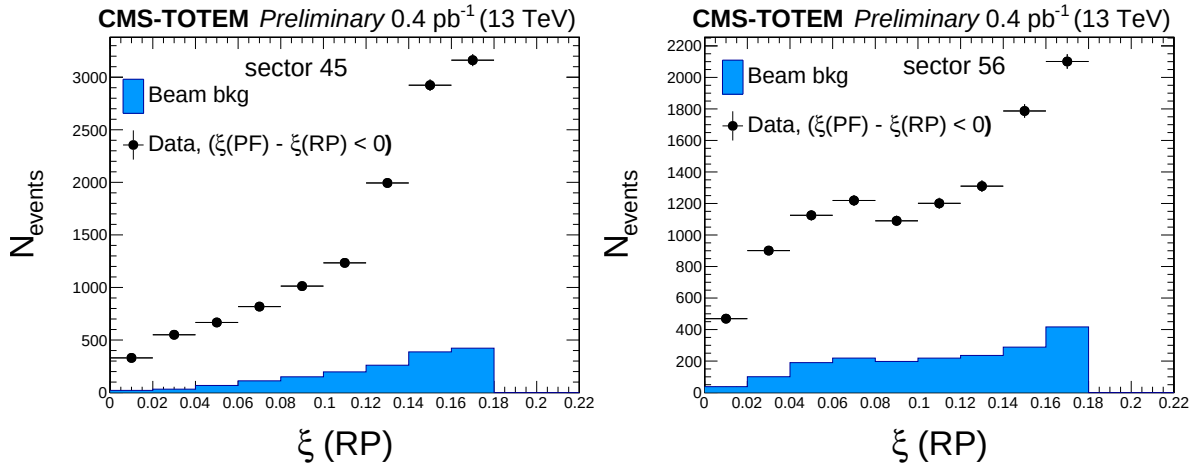

Figure 8.12: Number of events as a function of $\xi(\mathrm{RP})$. The blue, solid histogram represents the expected background yield calculated with the event mixing procedure described in text.

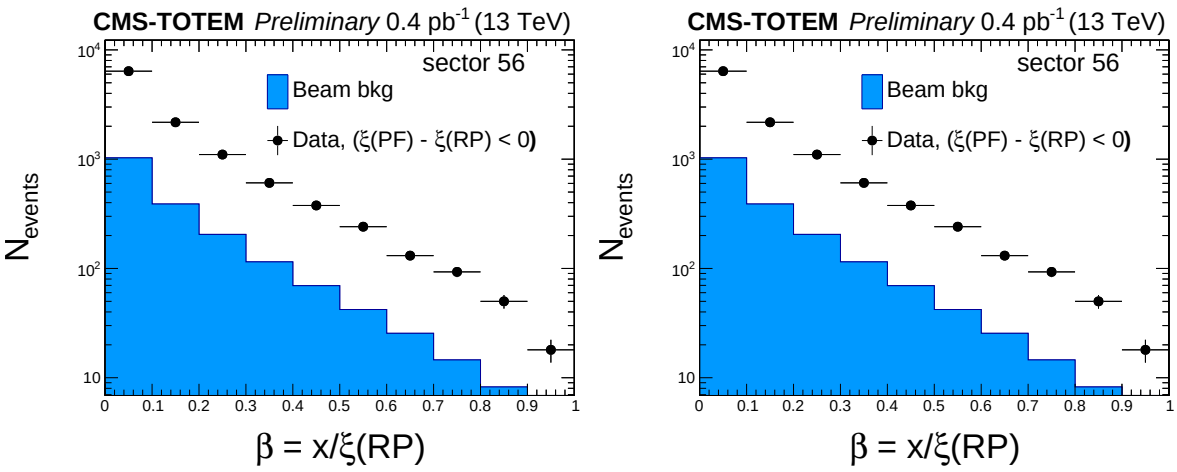

Figure 8.13: Number of events as a function of $\beta = x/\xi(\mathrm{RP})$, the parton momentum fraction relative to the pomeron exchange. The blue, solid histogram represents the expected background yield calculated with the event mixing procedure described in text.

where the sum is carried out with the two highest transverse momentum jets in the event and an additional third jet, if present. The latter is selected with $p_{\mathrm{T}}^{\mathrm{jet3}} > 15$ GeV. The positive (negative) sign refers to the incoming proton towards the positive (negative) z direction.

We present said ratios R as a function of the jet p_{T} in Fig.8.14 for protons scattering towards sectors 45 and 56. The ratio increases towards smaller values of x as a consequence of the intrinsic boosts of single-diffractive dijet events in the direction opposite to the detected proton. This is a similar shape as that previously reported by the CDF and CMS-TOTEM analyses at lower $\sqrt{s}$ (164; 165; 169). The advantage of having the sector 45 and 56 data sets is that they can be used as independent data samples, which can help identify numerous aspects of the physics targeted in the analysis with more confidence.

In Fig. 8.14, we observe that the ratio R as a function of Bjorken-x in bins of p_{T} is consistent with the behavior of a universal curve within the statistical uncertainties. This means that, to the level of the analysis, the data favors a diffractive structure function that obeys DGLAP evolution, just as the standard proton structure function. This confirms the conclusion by the CDF experiment at $\sqrt{s} = 1.96$ TeV (213). The CMS-TOTEM analysis at

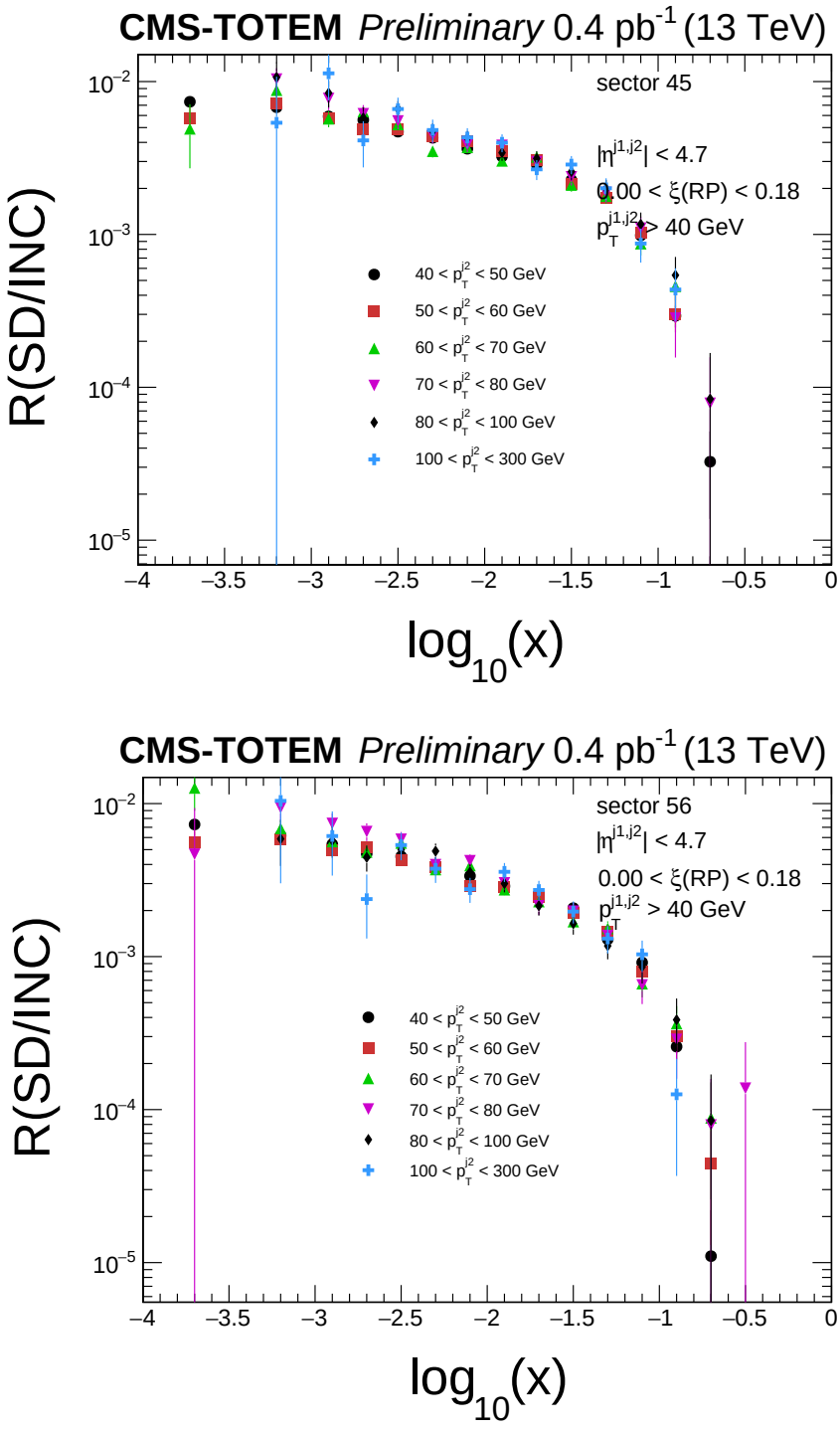

Figure 8.14: Ratio of single-diffrative dijet event candidates to inclusive dijet events as a function of the reconstructed Bjorken-x in bins of p_{T} of the second-leading jet. The upper (lower) panel represents the results for protons detected in sector 45 (56). The jet and proton requirements are indicated in the figure.

$\sqrt{s} = 8$ TeV was limited in the sample size, which hindered the possibility of doing an analysis of the R in bins of p_{T} of the jets.

In addition to the analysis in bins of p_{T}, we can also extract the ratio R in bins of ξ to test the properties of factorization of the diffractive process. According to Regge factorization, the dependence on ξ should decouple from the dependence on $\beta = x/\xi$, where β is the parton momentum fraction relative to the pomeron exchange. In the picture of Regge factorization, calculating the ratios R in bins of ξ is equivalent to probing different intervals of β. If Regge factorization holds, we should be able to compare the ratios R for the same intervals of x and obtain the same answer as a function of x regardless of the binning in ξ, modulo the effects that come from kinematics. If the ξ-dependence is completely decoupled from the β dependence of the PDFs, this should be reflect on the slopes of the R versus Bjorken-x. That is, for the same Bjorken-x intervals, there should be a different trend for different ξ values.

The preliminary ratios in bins of ξ are shown in Fig. 8.16 and 8.15 for sectors 45 and 56. The amount of data permits the use of bins of 0.02 units in $\xi(\mathrm{RP})$ for each of the curves. We note that the ratios R are cut-off at smaller values of x for smaller $\xi(\mathrm{RP})$ values. The drop of the ratios R as a function of x in bins of ξ is due to the kinematic bound $x < \xi(\mathrm{RP})$, i.e., the active parton initiating the hard scattering process cannot take more energy than the energy carried by the diffractive exchange. We see that, at this level of analysis there does not seem to be too strong of a dependence on ξ at smaller values of Bjorken-x across the sample; the slopes of $R(x)$ seem to be independent of ξ. The advantage of the current CMS-TOTEM sample that we are using for the 13 TeV data is that we can access the unexplored interval of $0.10 < \xi < 0.18$, which the HERA, Tevatron, and LHC experiments have not been able to explore before in the study of hard diffraction.

To continue this analysis, one would have to convert the x dependence into a β dependence via $\beta = x/\xi(\mathrm{RP})$, and perform power-law fits on the resulting distributions. If the slopes are found to be consistent with each other within the experimental uncertainties,

this would be consistent with the hypothesis of Regge factorization.

The dependence of the $|t|$ distribution on the second-leading jet p_{T} is presented in Fig. 8.17 for protons detected in sector 45 and 56. We do not observe a dependence within the statistical uncertainties of $|t|$ as a function of $p_{\mathrm{T}}^{\mathrm{jet2}}$, confirming the previous observation by the CDF Collaboration at 1.96 TeV (165). We do not see a diffractive dip in the region of $|t|$ accessible in this measurement.

We will now move forward to discuss the analysis of double-pomeron exchange dijet events in 2015 pp data in the next Section.

8.4 Double-pomeron exchange dijet events

In addition to the single-diffractive dijet event analysis, we also investigated the double-pomeron exchange dijet event candidates in the sample. The schematic diagram is shown in Fig. 8.18. In this case, we strengthen the requirement of *at least* one intact proton detected one of the arms of the TOTEM experiment to *exactly two* protons detected in the RPs in both arms. This requirement, not being done carefully, may open ourselves up to another background: elastic scattering $pp \to pp$ events with $\xi(\mathrm{RP}) \approx 0$ overlapped with non-diffractive dijet events. To take care of this, we apply an additional selection requirement to remove these events quite efficiently. We require that the intact protons are *not* correlated in their scattering angle at the IP. The scattering angle θ_y^* is more appropriate for this selection requirement, since it is possible to look at the back-to-back scattering events like this. As a proof of concept, we can see that by applying this selection requirement on the θ_y^* correlations for protons detected in sector 45 and sector 56, we are able to suppress this contamination from elastic scattering events. In Fig. 8.19, for example, we see the $\theta_y^*(45) + \theta_y^*(56)$ distribution for events that satisfy the $\xi(\mathrm{PF}) - \xi(\mathrm{RP}) > 0$ selection requirements for both protons, and for those that satisfy $\xi(\mathrm{PF}) - \xi(\mathrm{RP}) < 0$ for both protons, where the double-pomeron exchange dijet candidate events are expected to be observed. The distribution is flat for double-pomeron exchange candidate events.

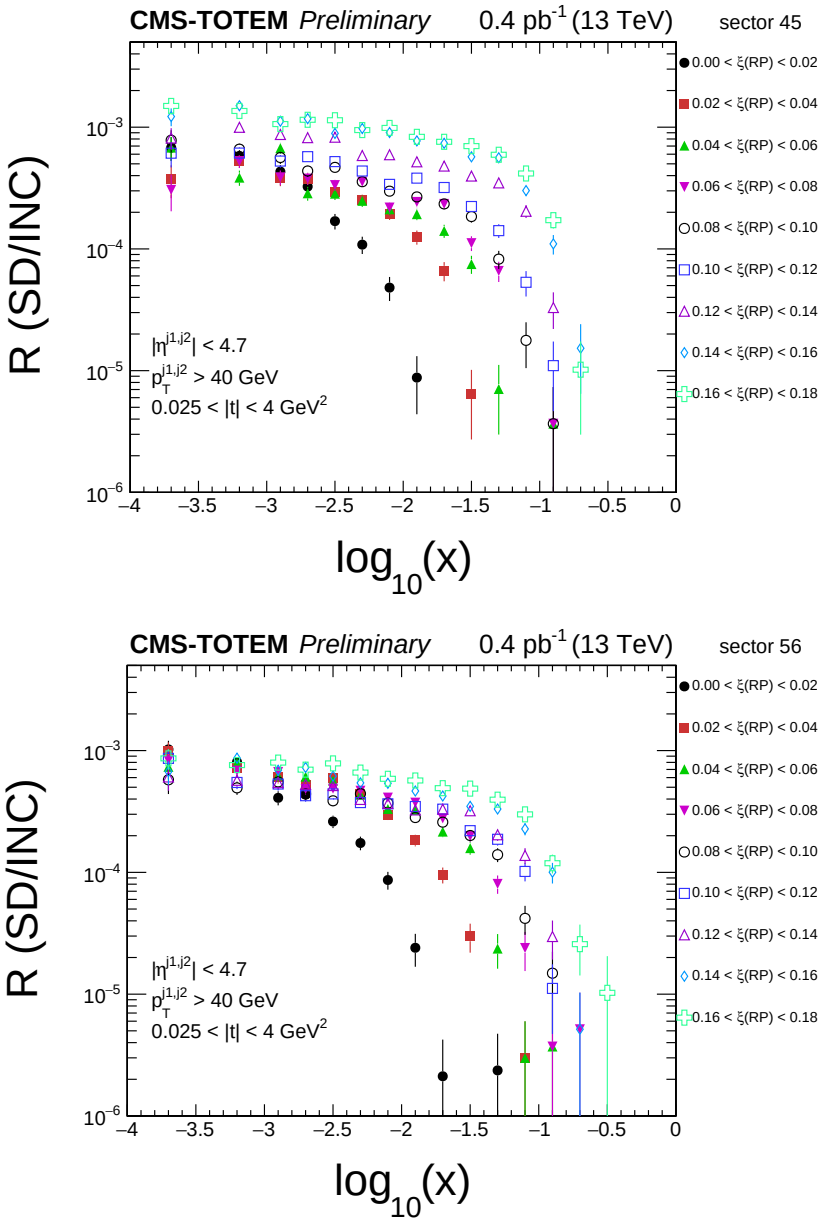

Figure 8.15: Ratio of single-diffrative dijet event candidates to inclusive dijet events as a function of the reconstructed Bjorken-x in bins of $\xi(RP)$. The lower-most data points are for $\xi(\mathrm{RP}) < 0.02$, whereas the upper-most data points are for $0.16 < \xi(\mathrm{RP}) < 0.18$. The upper (lower) panel represents the results for protons detected in sector 45 (56). The jet requirements are indicated in the figure.

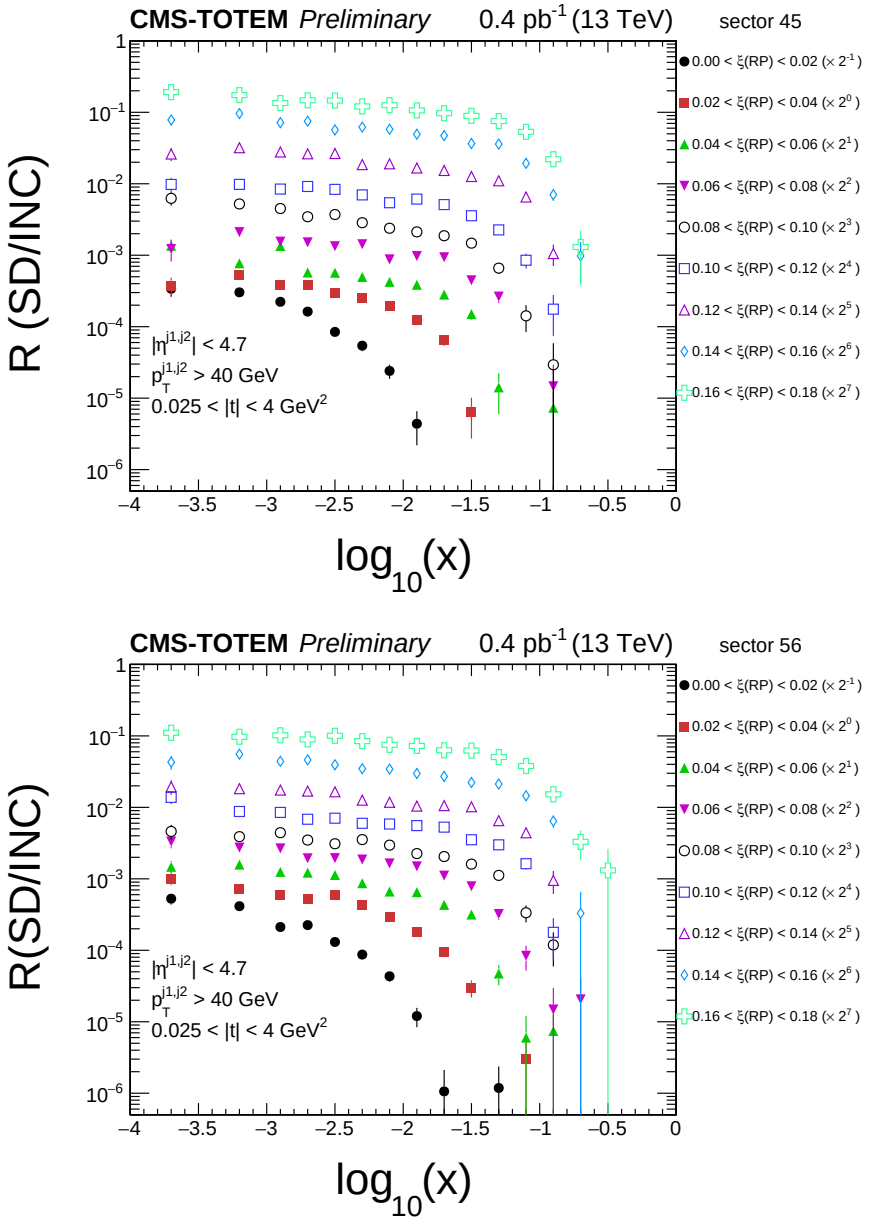

Figure 8.16: Ratio of single-diffrative dijet event candidates to inclusive dijet events as a function of the reconstructed Bjorken-x in bins of $\xi(RP)$. The lower-most data points are for $\xi(\mathrm{RP}) < 0.02$, whereas the upper-most data points are for $0.16 < \xi(\mathrm{RP}) < 0.18$. The upper (lower) panel represents the results for protons detected in sector 45 (56). The data points are artificially displaced by powers of 2^n for visibility purposes. The jet requirements are indicated in the figure.

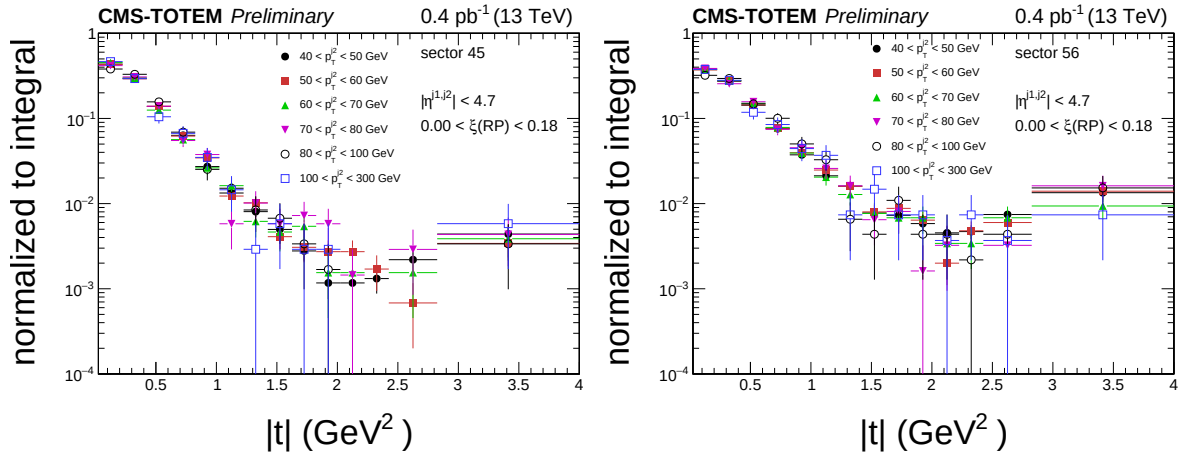

Figure 8.17: $|t|$-distributions for hard diffractive dijet production as a function of the p_T of the second-leading jet. The distributions are all normalized to unity. No significant dependence on the jet p_T is observed at this level of analysis.

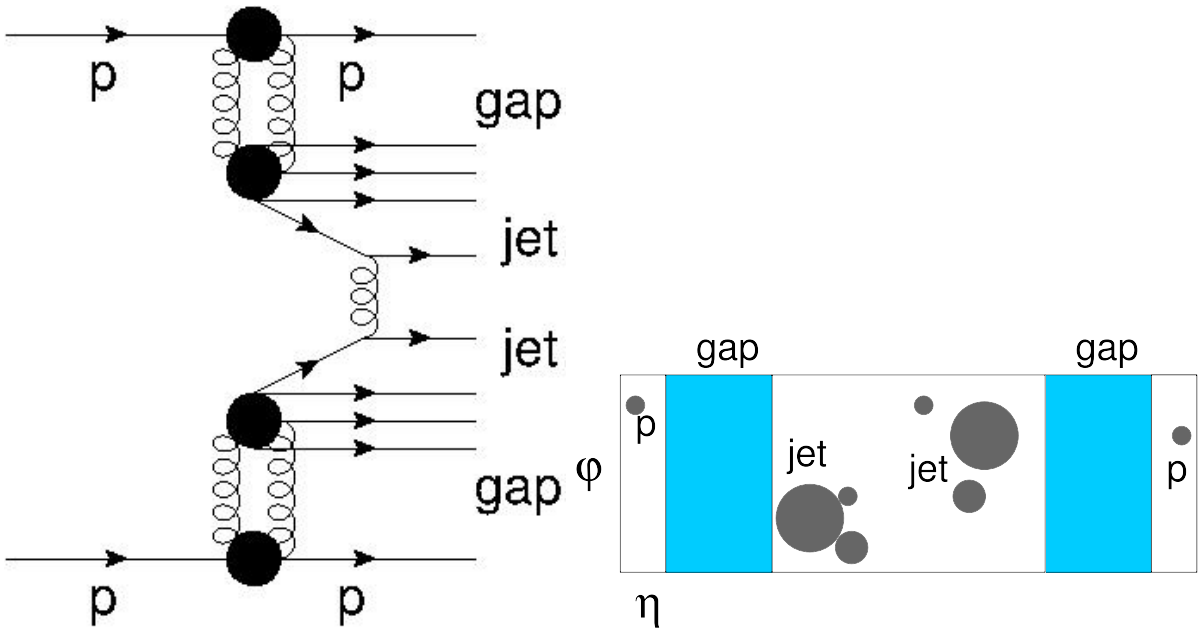

Figure 8.18: Schematic diagram of double-pomeron exchange dijet production with two intact protons.

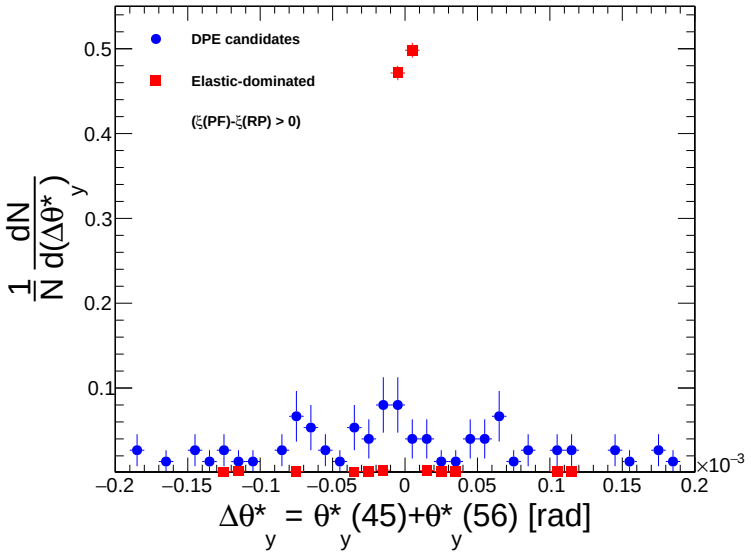

Figure 8.19: Difference of the vertical scattering angle at the proton vertex θ_y^* for a proton scattering towards sector 45 and a proton scattering scattering towards sector 56. In red, we have the scenario where both intact protons are in the background-dominated region, and hence come mostly from elastic $pp \to pp$ scattering, and the blue points come from the signal-enhanced region.

The kinematic properties of the double-pomeron exchange dijet event candidates is shown in Fig. 8.20. We see that the dijet events are more centered in η. The jet multiplicity for jets with $p_{\mathrm{T}} > 15$ GeV in $|\eta| < 4.7$, is also more suppressed. The kinematic properties of the intact protons are similar to the ones observed in the single-diffractive dijet events, consistent with the expectation that each of the pomerons exchanged from each proton are decoupled from one another (not shown graphically here). The mass fraction variable, which is defined as the ratio of the dijet mass divided by the diffractive mass $m_jj/m_X^{\mathrm{diff}} = m_{jj}/\sqrt{\xi(56)\xi(45)s} = \sqrt{\beta(56)\beta(45)}$, shows that about 10–15% of the energy of the two pomerons being exchanged is used to create the hard dijet system (see Fig. 8.21). The rest of the energy is used to produce other hadrons that are not clustered into hard jets. At the Tevatron, they found that about half of the energy of the two pomerons was used to create the hard jets (), although the jets in this analysis were softer than the ones we use for the CMS-TOTEM analysis. If there were central exclusive production dijet

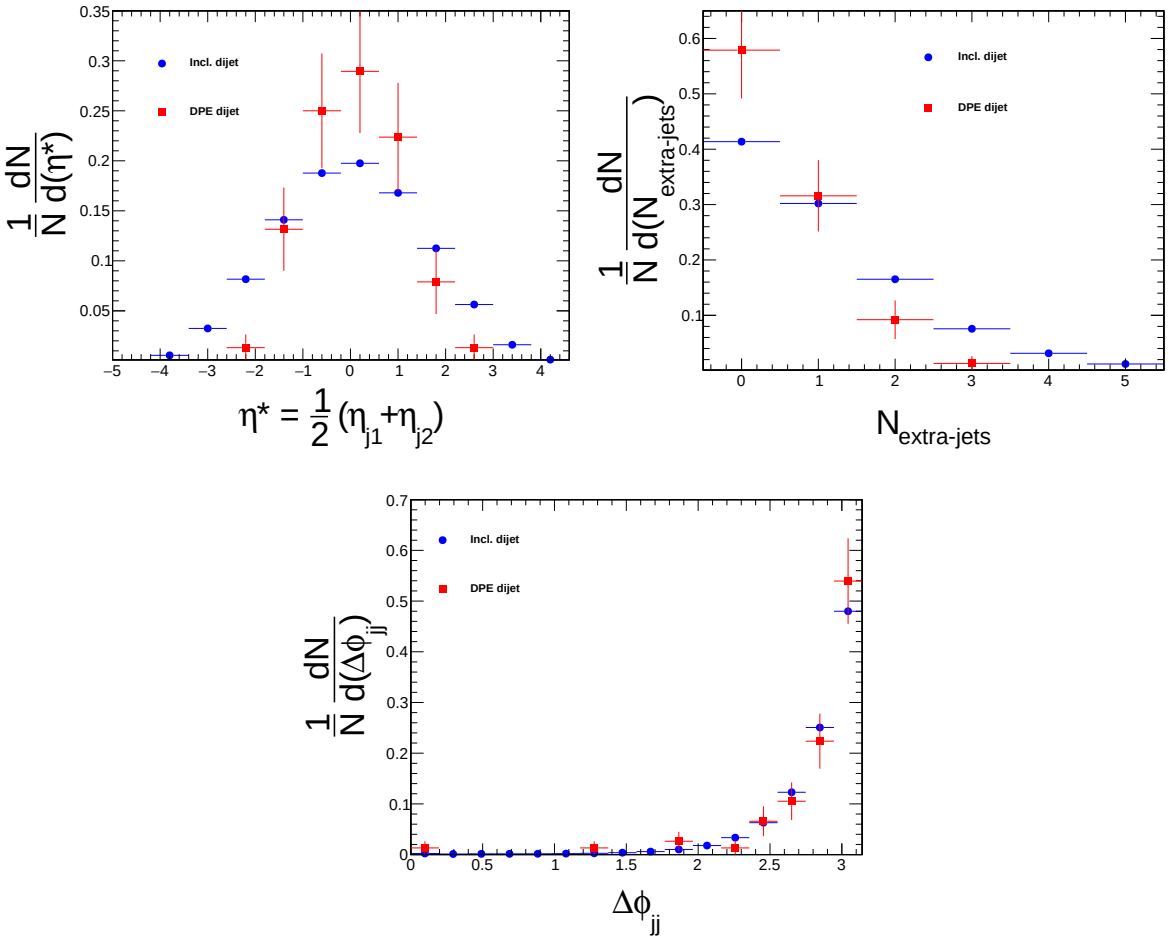

Figure 8.20: Kinematic properties of double-pomeron exchange dijet event candidates. On the upper left panel, the average pseudorapidity of the leading two jets is shown. On the upper right panel, the number of jets with $p_T > 15$ GeV. On the lower panel, the azimuthal angle difference between the leading two jets $\Delta\phi_{jj}$.

events, we would see events with $m_j j / m_X^{\rm diff} = 1$ (without accounting for smearing effects). We do not observe such events in the sample.

A particularly interesting observable that we can extract for the double-pomeron exchange dijet events is the double ratio of the double-pomeron exchange dijet events to the single-diffractive dijet events $R_{\rm SD}^{\rm DPE}$ divided by the ratio of single-diffractive dijet events to inclusive dijet events $R_{\rm INC}^{\rm SD}$. Indeed, the CDF Collaboration used such a comparison between these two ratios in order to test if factorization can be *restored*. If factorization was not broken in hard diffractive reactions in hadron-hadron physics, we would see that

$$R_{\rm INC}^{\rm SD} / R_{\rm SD}^{\rm DPE} = 1 \tag{8.5}$$

the CDF Collaboration found that this ratio is very different from unity (216),

$$R_{\rm INC}^{\rm SD} / R_{\rm SD}^{\rm DPE} = 0.19 \pm 0.07 \tag{8.6}$$

this means that the likelihood for having a rapidity gap increases in the presence of other gaps. In other words, factorization is effectively *restored*, since the spectator parton activity is suppressed (216).

As mentioned in Chapter 4 of this thesis, the CDF experiment did not rely on the detection of the antiproton and the proton with RPs. They were using a RP detector to tag the antiproton, and the rapidity gap method for the outgoing proton region. For the measured antiproton, it was possible to reconstruct $0.035 < \xi_{\bar{p}} < 0.095$. On the other hand, ξ_p from the (undetected) intact proton is estimated from the calorimeter towers and tracks in the central CDF detector. Hence, the sensitivity is mostly in $0.01 < \xi_p < 0.03$. Thus, in order to calculate the double-ratio quantity of Eqn. (8.6), they had to make an extrapolation of the measured $\xi_{\bar{p}}$ distribution of the intact antiproton into the low ξ region. In the measurement that we are describing now in this thesis, we do not have to make such an extrapolation. We are now able to detect both outgoing protons with

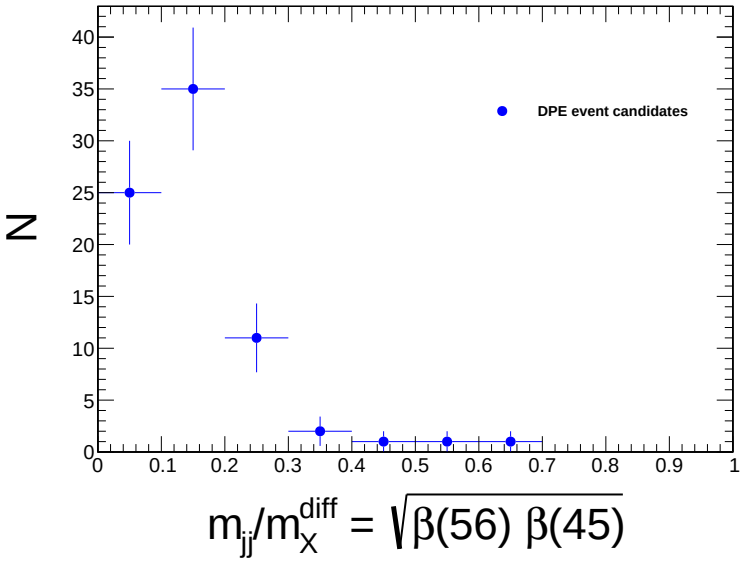

Figure 8.21: Ratio of the dijet mass to the mass of the diffractive system deduced from the ξ measurements for both intact protons. The ratio suggests that about 10% of the energy of the two pomerons being exchanged goes into the production of the dijet system. The rest of the energy is not clustered into the hardest jets, and is present as additional energy propagated elsewhere.

RP detectors, without requesting any rapidity gap. In this sense, the measurement of the double-ratio quantity is cleaner.

We can see in Fig.8.22 that, with the current level of the experimental analysis, we confirm the previous measurement by the CDF Collaboration at $\sqrt{s} = 13$ TeV, shown on the same Figure. The double-ratio at $\sqrt{s} = 13$ TeV case yields approximately $R_{\rm INC}^{\rm SD}/R_{\rm SD}^{\rm DPE} \approx 0.25$ (without quoting experimental uncertainties), consistent with the value of CDF. It is also consistent with what we found for the proton-gap-jet-gap-jet analysis at the end of Chapter 7.

8.5 Prospects for further development of the analysis

The next step for the analysis is to correct the background-subtracted yields for detector acceptance and efficiency effects for the extraction of the fiducial differential cross sections and cross section ratios. While the observables based on ratios are not expected to be

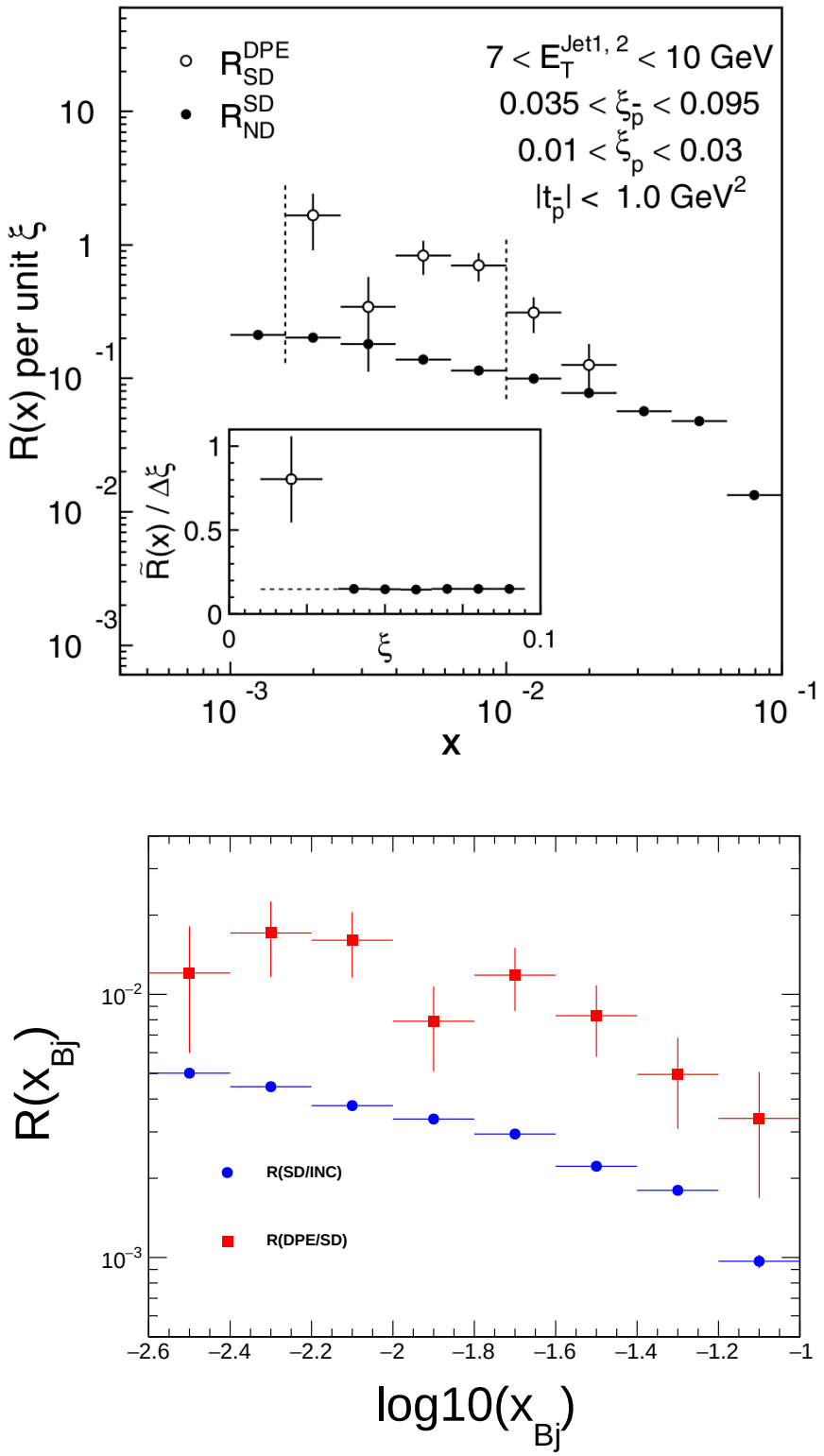

Figure 8.22: Upper panel: CDF result of the ratio of double-pomeron exchange to single-diffractive R_{SD}^{DPE} (open symbols) and single-diffractive to non-diffractive R_{ND}^{SD} (216). Lower panel: Preliminary ratios R_{SD}^{DPE} (red, larger error bars) and R_{ND}^{SD} (blue, small error bars) extracted with CMS-TOTEM 13 TeV data. Our result confirms the result of restoration of factorization in diffractive interactions noted by CDF(216).

very affected by the latter detector effects, the absolute cross sections, such as $\frac{d\sigma}{d\xi}$, $\frac{d\sigma}{d\beta}$, and $\frac{d\sigma}{d|t|}$, can receive more important corrections. Properly accounting for these is crucical for drawing significant physics conclusions. A simulation recipe has been developed for this by members of the CMS-TOTEM group. The analysis developed so far considers the detailed study of the beam-background study, as well as the physics potential with the data. The present detector-level results show numerous characteristics of the diffractive exchange that are expected to persist upon these detector effects corrections.

We see that with the 13 TeV CMS-TOTEM data sample we are able to study hard diffraction in a kinematic regime that has not been explored yet. We analyzed diffractive dijet events with at least one intact proton detected in the Roman pot detectors of TOTEM with $\xi < 0.18$ and $-4 < t < -0.025$ GeV^2, and at least two jets of $p_{\mathrm{T}}^{\mathrm{jet1,2}} > 40$ GeV in CMS. Of particular importance is the reach in ξ, the fraction of energy carried away by the diffractive exchange. The reach in previous experimental analyses was of $\xi < 0.10$ using the proton tagging technique. The rapidity gap method is only sensitive to very small $\xi \lesssim 0.02$. Hence, we have in our hands a very interesting opportunity for studying hard diffraction in an unexplored kinematic domain. The lower (higher) values of ξ imply that we can probe higher (lower) values of β. Higher values of β mean that most of the energy of the diffractive exchange is used to initiate the hard scattering process.

We presented preliminary results of the ratios of single-diffractive to inclusive dijet events $R \equiv N^{\mathrm{SD}}/N^{\mathrm{INC}}$ as a function of the reconstructed parton momentum fraction x relative to the proton that exchanges a pomeron. The variable x is reconstructed from the hard jets in the event. The ratio $R_{\mathrm{INC}}^{\mathrm{SD}}$ has values of about 0.3–0.6%, interestingly close to the fraction of jet-gap-jet events at 13 TeV of Chapter 6. The fact that the ratios are of similar magnitude for the jet-gap-jet process and the single-diffractive dijet process is consistent with previous findings at the Tevatron. The ratio $R = R(x)$ is extracted in bins of the transverse momentum of the second-leading jet, $p_{\mathrm{T}}^{\mathrm{jet2}}$. The shape of the ratio $R(x)$ versus x seems to be independent of the p_{T} of the jets. This suggests that, to this degree of

the experimental analysis, the diffractive structure function of the proton seems to obey DGLAP evolution, just as the standard structure function of the proton. The result is the same for protons scattering towards sector 45 or 56, which are mostly statistically independent subsets of the data (a small fraction of the events have protons in both sector 45 and 56). In addition, we examined the possibility for studying the ratio $R(x)$ in bins of ξ of the intact protons. Assuming that Regge factorization holds, the shape of $R(x)$ should be independent of ξ, modulo the effects from the kinematic bound $x < \xi$ which is responsible for the sharp drop-off of the ratio R at large x. The slope of the ratio $R(x)$ at smaller $x \lesssim 10^{-2}$ does not seem to have a significant dependence on ξ. A more detailed analysis of the slopes, fitted with a power-law function, with the corrected distributions would help establish this observation more conclusively. If an evolution of the slope is found as a function of ξ, this could suggest that Regge factorization does not hold for the kinematics probed in this measurement.

In addition, we have examined the possible dependence of the square of the four-momentum transfer at the proton vertex, t, on the second-leading jet transverse momentum $p_{\mathrm{T}}^{\mathrm{jet2}}$. We do not observe a significant dependence, within the statistical uncertainties, of t as a function of $p_{\mathrm{T}}^{\mathrm{jet2}}$, confirming the previous results by the CDF Collaboration at 1.96 TeV (165). The same finding was obtained for protons detected in sector 45 and 56.

Finally, we have analyzed the prospects for an analysis of double-pomeron exchange dijet events using the CMS-TOTEM data set. We find 114 candidate events with two intact protons and at least two jets. The events satisfy the proton and dijet event requirements, as well as the kinematic requirement of $\xi(\mathrm{PF}) - \xi(\mathrm{RP}) < 0$ for both protons. The candidate events have properties consistent with the expected characteristics of double-pomeron exchange dijet events. We analyzed the ratio of double-pomeron exchange dijet events to single-diffractive dijet events, $R_{\mathrm{SD}}^{\mathrm{DPE}}$, in comparison to the ratio of single-diffractive dijet events to inclusive dijet events (which are mostly non-diffractive), $R_{\mathrm{DPE}}^{\mathrm{SD}}$, which is shown in Fig. 8.22. We find that the likelihood of having a second gap formed is greater in

presence of another gap, confirming the results from the CDF experiment (216). We find a similar double-ratio $R_{\mathrm{DPE}}^{\mathrm{SD}}/R_{\mathrm{SD}}^{\mathrm{DPE}} \approx 0.20$ as CDF (216). This is the first time double-pomeron exchange dijet events are analyzed with two intact protons. Previous techniques used one RP detector in one side, and a rapidity gap on the other side, with assumptions on the expected kinematic behavior of the measured distributions.

Chapter 9

Pure gauge interactions in photon-photon physics

In addition to the contribution to experimental measurements with the CMS and TOTEM experiments, the author of this thesis contributed to a series of phenomenology studies on the prospects of discovering new physics in photon-photon physics at the LHC. As mentioned in Section2.7 in Chapter2, there are good reasons to expect physics beyond the SM (BSM). Several efforts have been conducted in direct searches at the CERN LHC for various new physics scenarios. In our case, we are interested in extending this effort to more indirect, model-independent search strategies.

The phenomenology studies that the author contributed to were published in few-authored papers in peer-reviewed journals (2; 3; 4; 5). The contributions of the author were on the preparation of the papers, the phenomenology analysis and projections on BSM free parameters, and implementation of new processes in the Forward Physics Monte Carlo (FPMC) event generator(219). In this Chapter, we cover the main results of these contributions.

The Chapter summarizes the results of three different studies: the first one is related to the projections on anomalous $\gamma\gamma \to \gamma Z$ production, which is loop-suppressed in the SM, described in Section 9.6. The second one is related to the search for axion-like particles coupled to the electromagnetic field in $\gamma\gamma \to \gamma\gamma$ high-energy scattering, described in Section 9.7. The third one is related to improvements on the projections for $\gamma\gamma \to WW$ scattering, which is induced at tree-level in the SM, and ways of looking for possible deviations from the SM from anomalous coupling contributions at high energies, described in Section 9.8.

9.1 Central exclusive production by photon exchange

Photon-exchange processes can be studied in proton-proton, proton-nucleus or nucleus-nucleus high-energy collisions at the LHC. In these high-energy collisions, the electromagnetic field generated by the proton or nucleus moving at nearly the speed of light can be treated as an effective source of quasi-real photons. Such collisions are *very* peripheral, i.e., there is almost no overlap between the colliding protons or nuclei. In that case, hadronic interactions, which act at shorter distances, are highly suppressed, and one is sensitive mostly to electromagnetic forces. In elastic photon exchange processes, the quasi-real photon is emitted from the proton or nucleus as if it is a single electrically charged object. Theoretical calculations of cross sections are quite accurate, since they rely on the elastic electromagnetic form factors of the proton. The latter have been measured at great experimental precision in electron-proton elastic scattering measurements, covering a wide range of vritualities of the photon emitted from the electron (220; 221; 222; 223). These reactions allow for the possibility of studying SM reactions in high-energy photon-photon collisions.

The program of photon exchange processes in ultraperipheral heavy-ion collisions is very rich, and lots of results have been presented over the last years by BNL and LHC experiments. The effective photon luminosity receives a large enhancement from the large electric charge of the lead ions by a factor of $Z^4 = 82^4 \approx 4.5 \times 10^7$, which allows for the study of photon-photon interactions at low masses with large statistics easily accessible. The discussion in this Chapter will be mostly focused in photon exchange processes in proton-proton collisions, where the photon-photon collisions occur at center-of-mass energies at the TeV scale. For a review of photon-exchange processses in ultraperipheral heavy-ion collisions, we refer to Refs. (224; 225; 226; 227). Generally, these interactions are difficult to access in quark an gluon-initiated processes in pp collisions. These reactions can be probed in pp collisions by detecting the scattered intact proton with a set of RP detectors, similar to those used in the analysis of Chapters 6 and 7 but for high-luminosity

operation, or by using the rapidity gap method to isolate ultraperipheral collisions of heavy-ions.

9.2 Equivalent photon approximation

In high energy pp collisions, the electromagnetic fields generated by the relativistic protons can be treated as a source of quasi-real photons (228; 229). Thus, in addition to the standard quark or gluon exchanges in pp collisions, one can study reactions with quasi-real photon exchange off the proton at the LHC, and use this to study photon-photon collisions at high energies. In some of these interactions with quasi-real photon exchange, the proton may survive the interaction, and will be scattered afterwards at very small angles with respect to the beam. The scattered protons can be tagged with near-beam tracking detectors, known as Roman Pots (RPs), located at about 200 m with respect to the interaction point. The ATLAS and CMS-TOTEM Collaborations have added RP detectors during Run-2 at the LHC, known as ATLAS Forward Proton (AFP) and CMS-TOTEM Precision Proton Spectrometer (PPS) (230; 195). The PPS detector system was described in Chapter 5 of this thesis.

We use the equivalent photon approximation (EPA) (232), (229) to describe the $pp \to pXp$ process via quasi-real photon exchange off each proton. In this approximation, the almost real photons (with low virtuality $Q^2 = -q^2$) are emitted by the incoming protons producing a state X, $pp \to pXp$, through photon fusion $\gamma\gamma \to X$. The photon spectrum of virtuality Q^2 and energy E_γ is proportional to the fine-structure constant α_{em} and reads:

$$dN = \frac{\alpha_{\text{em}}}{\pi} \frac{\mathrm{d}E_\gamma}{E_\gamma} \frac{\mathrm{d}Q^2}{Q^2} \left[\left(1 - \frac{E_\gamma}{E}\right) \left(1 - \frac{Q^2_{\text{min}}}{Q^2}\right) F_E + \frac{E_\gamma^2}{2E^2} F_M \right] \tag{9.1}$$

where E is the energy of the incoming proton of mass m_p, $Q^2_{\text{min}} = m_p^2 E_\gamma^2 / [E(E - E_\gamma)]$ the photon minimum virtuality allowed by kinematics and F_E and F_M are functions of the electric and magnetic form factors G_E and G_M. In the dipole approximation, the latter

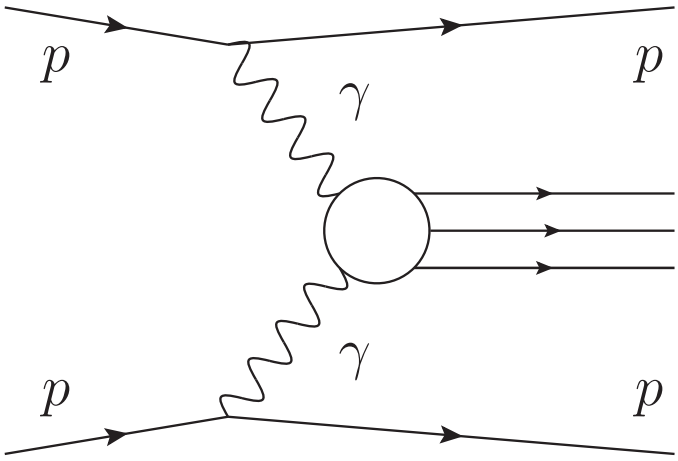

Figure 9.1: Photon-photon interaction in high energy proton proton collisions. The three-lines in the center is a symbolic representation of a massive state produced with the photon-photon interaction. The protons remain intact as a result of the colorless quasi-real photon exchange. The figure is extracted from Ref. (231).

reads

$$F_M = G_M^2 \qquad F_E = (4m_p^2 G_E^2 + Q^2 G_M^2)/(4m_p^2 + Q^2) \qquad G_E^2 = G_M^2/\mu_p^2 = (1 + Q^2/Q_0^2)^{-4}\,. \quad (9.2)$$

the magnetic moment of the proton is $\mu_p^2 = 7.78$ and the fitted scale $Q_0^2 = 0.71$ GeV^2. Since the electromagnetic form factors fall steeply as a function of Q^2, the cross section can be factorized into the matrix element of the photon fusion process and the two photon fluxes. In order to obtain the production cross section, the photon fluxes are first integrated over Q^2

$$f(E_\gamma) = \int_{Q^2_{\rm min}}^{\infty} \frac{dN}{dE_\gamma dQ^2} dQ^2\,. \quad (9.3)$$

the result is given in Ref. (233). An effective two-photon luminosity can be defined based on the individual photon fluxes $dL^{\gamma\gamma}/dW$ obtained by integrating $f(E_{\gamma 1})\, f(E_{\gamma 2})\, dE_{\gamma 1}\, dE_{\gamma 2}\, \delta(W - 2\sqrt{E_{\gamma 1} E_{\gamma 2}})$ where W is invariant mass of the diphoton system. Using the effective photon luminosity, the total cross section for the $pp \to pXp$ process reads

$$\sigma = \int \sigma_{\gamma\gamma\to X} \frac{{\rm d}L^{\gamma\gamma}}{{\rm d}W} dW \quad (9.4)$$

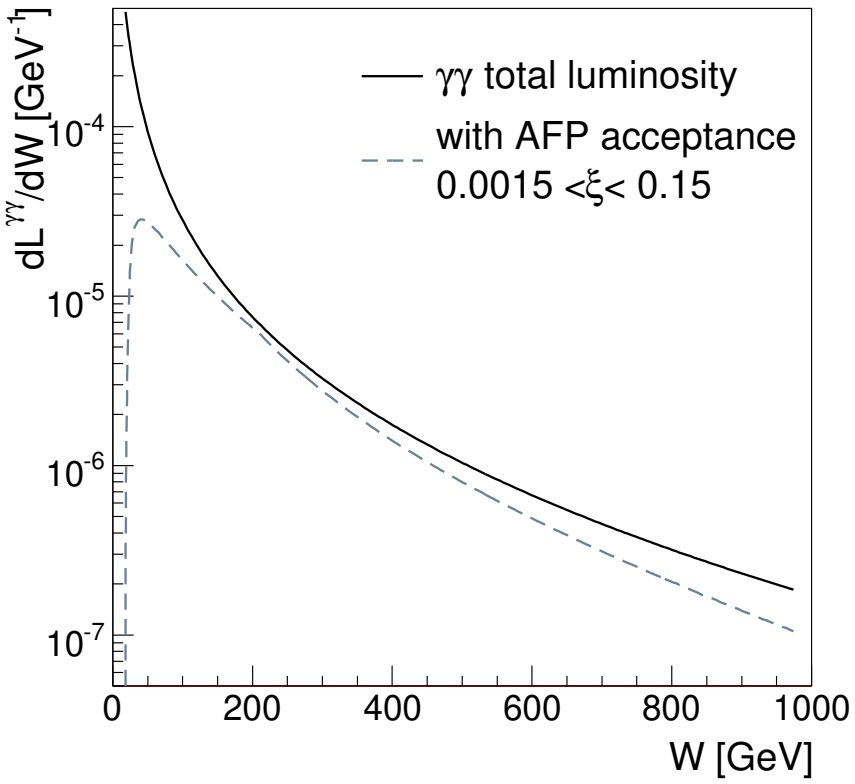

Figure 9.2: Relative effective $\gamma\gamma$ luminosity in pp collisions at $\sqrt{s} = 14$ TeV as a function of the two-photon invariant mass, $W_{\gamma\gamma}$. The maximal virtualities of the emitted photons are set to $Q^2_{\text{max}} = 2$ GeV^2 in this plot. The dashed curve shows the photon spectrum within the ATLAS or CMS forward detector nominal acceptance. The figure is extracted from Ref. (231).

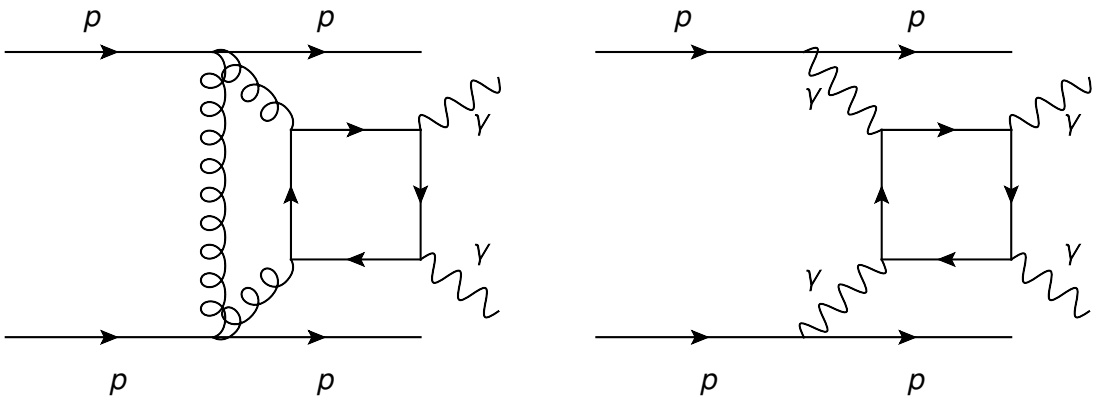

Figure 9.3: Left: central exclusive diphoton production by two-gluon exchange in a color-singlet configuration (Khoze–Martin–Ryskin process). Right: central exclusive production by two-photon exchange (light-by-light scattering). In both left and right panels, the protons remain intact after the interaction.

where $\sigma_{\gamma\gamma\to X}$ denotes the cross section of the sub-process $\gamma\gamma \to X$, dependent on the invariant mass of the two-photon system. In addition to the photon exchange, there might be additional soft gluon exchanges that might destroy the protons. To take into account this effect, we can introduce the so-called survival probability that the protons remain intact in photon-induced processes (234), (235). In this series of studies, we assumed a survival probability of 90%.

9.3 Khoze-Martin-Ryskin two-gluon exchange versus photon-exchange

The central exclusive production mechanism in pp collisions is dominated by two-gluon exchange at low-mass, where one of the gluons screens the color charge enchanged by the other gluon. This type of processes is sometimes called Khoze-Martin-Ryskin (KMR) two-gluon exchange.

At high-masses, however, the cross section for central exclusive production processes is dominated by photon-exchange processes. The reason is that the two-gluon exchange process is suppressed due to the requirement of no further radiation emission. The latter necessitates the introduction of a Sudakov form factor in the theoretical calculation, which quantifies the probability of no particle emission above a given perturbative threshold in

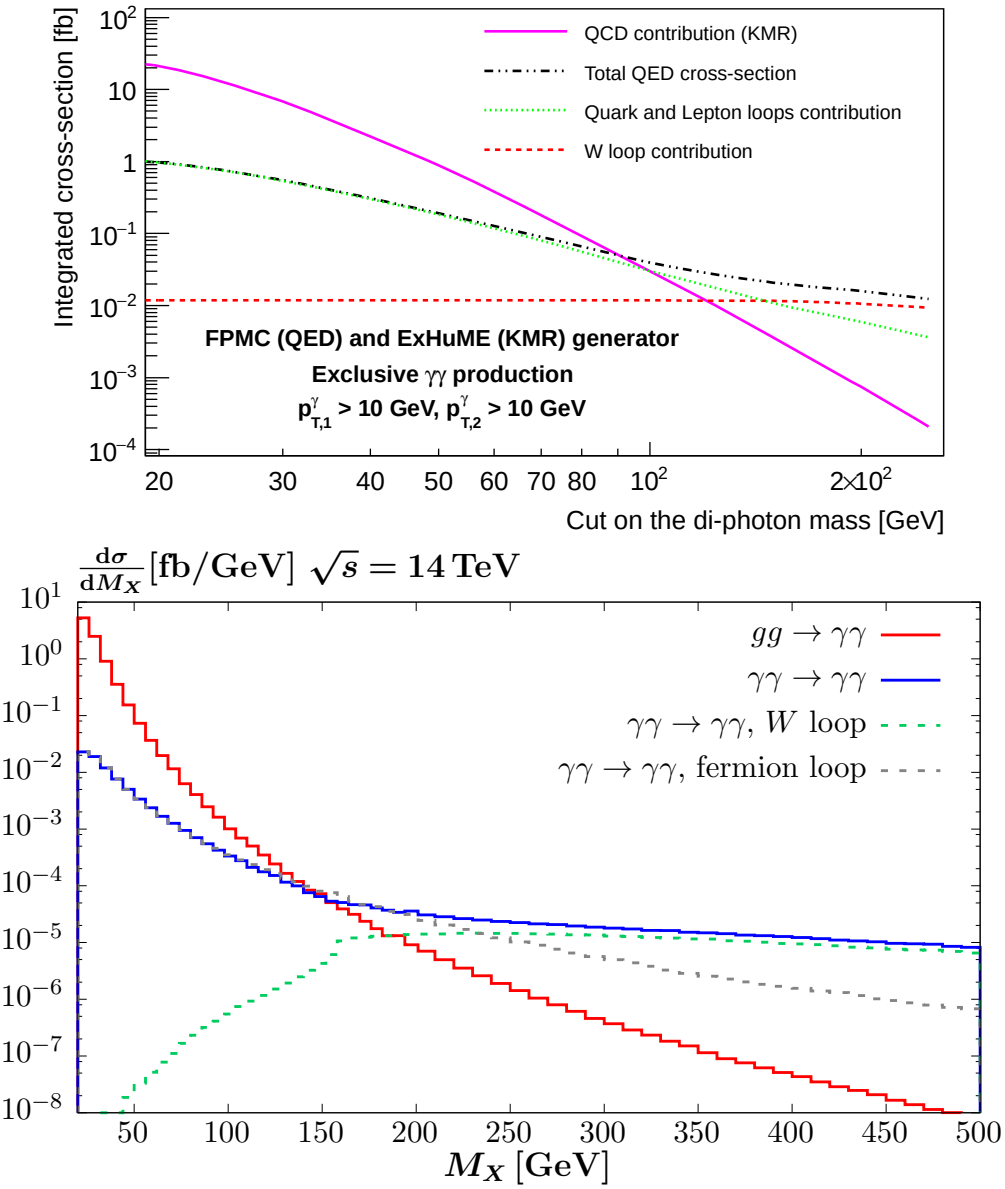

Figure 9.4: Cross section as a function of the invariant mass of the $\gamma\gamma$ pair in central exclusive production with intact protons. The two-gluon process a la KMR is largely suppressed at large masses, since the probability that there are no additional gluon emissions is largely reduced at large $\gamma\gamma$ masses. The $\gamma\gamma \to \gamma\gamma$ contribution dominates at diphoton invariant masses larger than about 200 GeV. The upper panel is based on predictions presented in Ref. (236), whereas the lower panel is based on predictions presented in Ref. (237).

QCD. This suppression is stronger at larger masses, since the exchanged gluons have more phase-space available for emitting additional gluons. Thus, for invariant masses at half a TeV and beyond, the QCD two-gluon exchange mechanism is largely suppressed for central exclusive production. In the case of quasi-real photon exchange off the protons, the corresponding Sudakov form factor in QED is significantly larger, and can be assumed to be close to unity when expressed in terms of probability. This is owing to the smallness of the electromagnetic coupling strength and the lack of self-interactions of the photon being exchanged. Hence, there is no such suppression for large invariant masses as in the case of QCD.

A graphical depiction of such an interplay between the two-gluon exchange and the photon-exchange for the central exclusive production of photon pairs, $pp \to p\gamma\gamma p$, is shown in Fig. 9.4 for the `SuperChic3` generator and the `FPMC` and `ExHuMe` generators, respectively. For masses above 200 GeV for the initial-state diphoton system, the photon exchange mechanism dominates over the QCD mechanism for central exclusive production. Since the acceptance of the forward proton detectors starts at about ≈ 300 GeV for the ATLAS and CMS experimental setups, we are in a phase-space region where we are mostly looking at photon-induced processes when analyzing central exclusive production processes. We keep this in mind for the remainder of this thesis Chapter.

9.4 Forward proton detectors

The LHC magnets around the interaction points of CMS and ATLAS act as a precise momentum spectrometer on the protons that have lost a fraction of their original momentum due to the photon exchange. As mentioned in Chapter 5, the CMS and ATLAS experiments are equipped with a set of forward proton detectors to tag the intact protons scattered at small angles with respect to the beam during normal instantaneous luminosity operators. The detectors capable of studying central exclusive production in Run-2 of the LHC are the ATLAS Forward Physics (AFP) (230) and the CMS-TOTEM Precision Pro-

ton Spectrometer (PPS) (238), which were brought online in 2017 and 2016 respectively. The forward proton detectors are equipped with charged particle trackers to tag the intact protons, the Roman pot detectors. The proton fractional momentum loss $\xi = \Delta p/p$ is reconstructed offline. Compared to other exclusive production searches, which usually rely on vetoes on the detector activity (for example, absence of calorimeter activity in the forward and backward rapidities above a given energy threshold), the proton tagging method directly measures the proton surviving the elastic photon emission. For the experimental analyses presented in this thesis described in Chapters 7 and 8, we relied on such a technology with the TOTEM experiment, albeit the data used for such analyses was at lower instantaneous luminosity and at a different β^*.

The forward detectors, together with the central detector, enable the complete reconstruction of the collision event. This sets a kinematical constraint on the final state that allows an efficient offline selection for central exclusive processes with large background rejection factors. Other phenomenology studies based on proton tagging at the LHC for new physics searches can be found in (233; 239; 240; 241; 242; 243; 244; 245; 246; 247; 248; 249; 250; 251; 236; 252; 253; 254; 255; 256; 2; 257).

PPS reported the first physics result at the LHC using the proton tagging method by observing the $pp \to p(\gamma\gamma \to \ell^+\ell^-)p$ reaction (196), which serves as a proof of principle

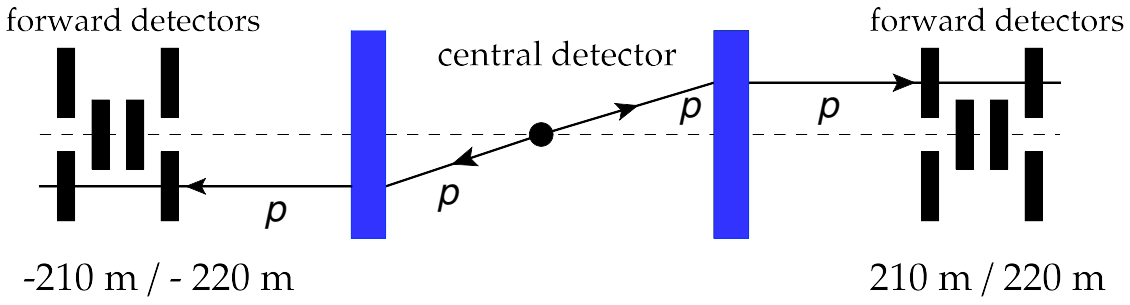

Figure 9.5: Schematic diagram of the proton tagging method at the LHC in central exclusive processes. The central detector (circle) collects the photon pair. The LHC magnets (blue) act as a precise momentum spectrometer on the outgoing intact protons. The protons pass through the forward detectors (black boxes) and their kinematic information is reconstructed offline. The dashed line represents the beamline.

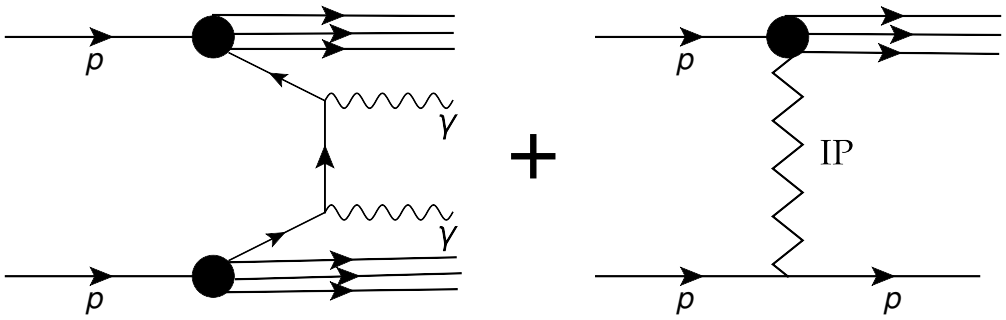

Figure 9.6: The dominant background for central exclusive diphoton production comes from non-exclusive photon pair production (left) overlapped with uncorrelated protons coming from soft diffractive processes in the additional interactions per bunch crossing (right).

of the proton tagging method to study $\gamma\gamma$ collisions above the electroweak scale. About 100 fb^{-1} of data has been recorded independently by AFP and PPS. The nominal acceptance of such detectors is considered to be $0.015 < \xi < 0.15$, where ξ is the fractional momentum lost by the proton relative to the beam energy. Experimentally, the ATLAS and CMS-TOTEM Collaborations have observed $\gamma\gamma \to \ell^+\ell^-$ using the proton tagging technique (258; 259). The CMS and TOTEM Collaborations reported a first search of central exclusive $\gamma\gamma$ production using the proton tagging technique (260).

9.5 Pileup background

The number of pileup interactions μ sets a huge background environment on the search for exclusive events. Intact forward protons arising from the pileup together with an uncorrelated non-exclusive process in the central detector can mimic the central exclusive production signal events. For example, we refer to Figure 9.6, where a QCD-initiated photon pair is detected in association with intact protons from soft diffractive pileup interactions. The unaware analyzer would identify this event as a $pp \to p\gamma\gamma p$ event. For Run-2 conditions, there are 30 to 50 interactions per bunch crossing at the current LHC luminosity. The pileup is expected to go up to $\mu = 200$ interactions at the High Luminosity LHC, which will pose a challenge on the search for new physics.

The detection of the two outgoing protons and reconstruction of ξ provides the complete kinematic information on the event, which in turn allows us to select central exclusive production processes by looking at kinematic relations between the central system and the forward protons. For a central exclusive production process $pp \to pXp$, we expect the following two mathematical relations to hold,

$$m_X = \sqrt{\xi_1 \xi_2 s} \equiv m_{pp}, \qquad\qquad y_X = \frac{1}{2} \ln\left(\frac{\xi_1}{\xi_2}\right) \equiv y_{pp} \tag{9.5}$$

where the mass and rapidity of the central system X is denoted by m_X and y_X. The quantities m_X and y_X can be reconstructed with the central detector information, or with the information from the forward proton detectors (namely ξ_1 and ξ_2), which we denote by m_{pp} and y_{pp}. With abuse of language, the quantities m_{pp} and y_{pp} are called the missing diproton mass and rapidity, respectively. The expressions in Eqn. 9.5 are derived from four-momentum conservation, and in the limit where $\mathcal{O}(m_p/m_X) \approx 0$. An experimental proof of concept for such kinematic correlations is shown in Fig. 9.7 for exclusive dilepton production by CMS and TOTEM using the PPS. The kinematic correlation is examined by reconstructing $\xi^{\pm}(\ell^+\ell^-) = \frac{1}{\sqrt{s}}\left(p_{\mathrm{T}}^{\ell^+} \exp(\pm y^+) + p_{\mathrm{T}}^{\ell^-} \exp(\pm y^-)\right)$, where the $\pm$ sign corresponds to the sign(η) of the forward proton. The expression is mathematically equivalent to the mass and rapidity matching mentioned a few paragraphs above. As shown in the plot by PPS, only events that satisfy $\xi(\ell^+\ell^-) = \xi(\mathrm{RP})$ (within the uncertainties) can be considered as candidate events. The remaining QCD dilepton events have low values of $\xi(\ell^+\ell^-)$.

These methods provide a strong pileup background rejection factors, which is the key feature of the forward proton detectors in isolating central exclusive production processes. Indeed, QCD-initiated hard processes paired with uncorrelated protons from pileup interactions would only satisfy the relations in Eqn. (9.5) by chance. Further background rejection can be achieved with the use of fast timing detectors. Timing detectors have been installed in additional RPs in PPS and ATLAS. The measurement of the time-

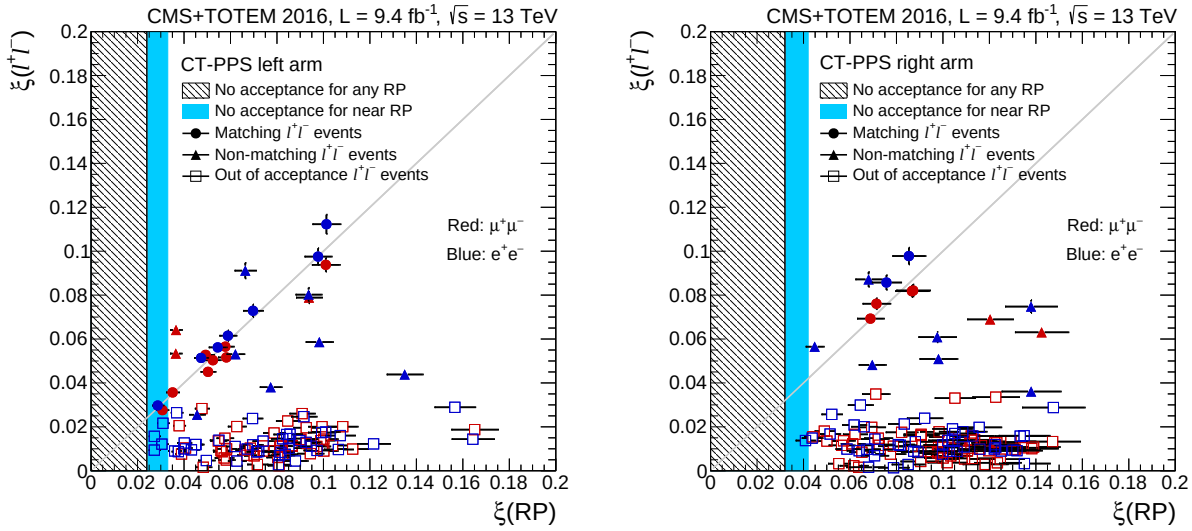

Figure 9.7: Correlation between the fractional values of the proton momentum loss measured in the central dilepton system, $\xi(\ell^+\ell^-)$, and in the RPs, ξ(RP). The hatched region corresponds to the kinematical region outside the acceptance of both the near and far RPs, while the shaded (pale blue) region corresponds to the region outside the acceptance of the near RP. For the events in which a track is detected in both, the ξ value measured at the near RP is plotted. The horizontal error bars indicate the uncertainty of ξ(RP), and the vertical bars the uncertainty of $\xi(\ell^+\ell^-)$. The events labeled "out of acceptance" are those in which $\xi(\ell^+\ell^-)$ corresponds to a signal proton outside the RP acceptance; in these events a background proton is detected with nonmatching kinematics. Figure extracted from Ref. (196).

of-flight difference between the two protons gives an independent determination of the primary interaction vertex, in addition to the determination obtained with conventional tracking by CMS and ATLAS. For a timing precision of $\approx$ 15 ps, which would allow to determine the interaction vertex of the protons with a 2.2 mm precision, thus allowing a large background rejection by a factor of $\sim$ 40 (261) by requiring that the track- and timing-based vertices are compatible with each other. The use of time-of-flight difference measurement is not necessary for all exclusive production channels, but it is useful for those which are dominated by high production cross section QCD processes.

We now move on to describe the phenomenology studies of $\gamma\gamma\gamma Z$ in Section 9.6, of axion-like particles coupled to the electromagnetic field in Section 9.7, and $\gamma\gamma WW$ in Section 9.8.

9.6 The $\gamma\gamma\gamma Z$ interactions in the SM and beyond

As shown in Chapter 2, while there are various triple and quartic coupling between the electroweak gauge bosons, there is no tree-level $\gamma\gamma\gamma Z$ coupling in the SM. The $\gamma\gamma\gamma Z$ interaction is induced at one-loop level in the SM via loops of fermions and W bosons. The amplitudes for the SM $\gamma\gamma \to \gamma Z$ process have been first computed in Ref. (262), and, just like the SM light-by-light scattering process, it is greatly reduced for central exclusive production due to the acceptance of the forward detectors. The rare SM decay $Z \to \gamma\gamma\gamma$ is another process sensitive to the anomalous $\gamma\gamma\gamma Z$ interaction, which is the standard probe of such an anomalous coupling between the Z boson and the photons. It has a branching ratio predicted to be $\mathscr{B}^{\rm SM}(Z \to \gamma\gamma\gamma) = 5.4 \times 10^{-10}$. The fermion loops have been computed in Refs. (263; 264) and the W loop contribution in (265), the latter is found to be subdominant. The $pp \to p(\gamma\gamma \to \gamma Z)p$ proccess can be probed via the detection of two intact protons in the forward proton detectors of CMS and ATLAS, and the detection of the Z boson decay and the photon in the respective central detector.

In the presence of new physics with a mass scale Λ heavier than the experimentally accessible energy E, all new physics manifestations can be described using an effective Lagrangian valid for $\Lambda \gg E$. In this low-energy effective field theory (EFT), the $\gamma\gamma\gamma Z$ interactions are described by two dimension-eight $\gamma\gamma\gamma Z$ operators

$$\mathscr{L}_{\gamma\gamma\gamma Z} = \zeta \mathscr{O}^{\gamma Z} + \tilde{\zeta}\tilde{\mathscr{O}}^{\gamma Z} = \zeta F^{\mu\nu}F_{\mu\nu}F^{\rho\sigma}Z_{\rho\sigma} + \tilde{\zeta}F^{\mu\nu}\tilde{F}_{\mu\nu}F^{\rho\sigma}\tilde{Z}_{\rho\sigma}\,, \tag{9.6}$$

with $\tilde{F}^{\mu\nu} = \frac{1}{2}\varepsilon^{\mu\nu\rho\sigma}F_{\rho\sigma}$.

Where ζ and $\tilde{\zeta}$ are the (dimensionful) coupling strength coefficients. These operators can be seen as arising from a SU(2)$_L\times$ U(1)$_Y$ effective Lagrangian with operators such as $B^{\mu\nu}B_{\mu\nu}B^{\rho\sigma}B_{\rho\sigma}$, where B denotes the hypercharge gauge field. The $SU(2)_L \times U(1)_Y$ effective Lagrangian contains ten such operators, see *e.g.* (266; 267; 242; 245). The $SU(2)_L \times U(1)_Y$ effective Lagrangian also generates $\gamma\gamma\gamma\gamma$, $\gamma\gamma ZZ$ interactions, as described in (245).

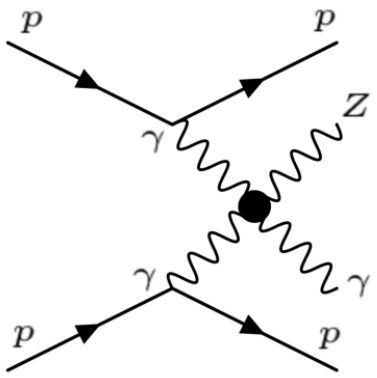

Figure 9.8: Anomalous $\gamma\gamma \to \gamma Z$ production via photon fusion with intact protons in the final state.

Because of the large number of effective operators in the $SU(2)_L \times U(1)_Y$ Lagrangian, anomalous interactions in the broken phase can be considered as independent for a phenomenology analysis.

The operators of Eqn. (9.6) induce an anomalous $Z \to \gamma\gamma\gamma$ decay (268), with a partial width that in our notation reads

$$\Gamma^{\rm NP}(Z \to \gamma\gamma\gamma) = \frac{m_Z^9(2\zeta^2 + 2\tilde{\zeta}^2 - \zeta\tilde{\zeta})}{8640\pi^3}. \tag{9.7}$$

An anomalous $\gamma\gamma \to \gamma Z$ reaction is also induced, which is the focus of this work. We find the unpolarized differential cross section to be

$$\frac{d\sigma^{\rm NP}_{\gamma\gamma\to\gamma Z}}{d\Omega} = \frac{\beta}{16\pi^2 s}\Big[(3\zeta^2 + 3\tilde{\zeta}^2 - 2\zeta\tilde{\zeta})(st + tu + us)^2 - 4(\zeta^2 + \tilde{\zeta}^2 - \zeta\tilde{\zeta})m_Z^2 stu\Big], \tag{9.8}$$

where s, t, and u are the Mandelstam variables and $\beta = 1 - m_Z^2/s$ for the γZ final state.

A breakdown of unitarity is expected at high energies for this set of EFT operators. Using partial wave analysis (269), we can estimate for what values of ζ, $\tilde{\zeta}$, and s the theory remains unitary. By imposing unitarity on the S-wave of the EFT amplitudes and

neglecting the Z boson mass one finds the conditions:

$$|\zeta + \tilde{\zeta}|s^2 < 4\pi\,, \quad |\zeta - \tilde{\zeta}|s^2 < \frac{12\pi}{5}\,. \tag{9.9}$$

As most of the recorded γZ events have $\sqrt{s}$ below 2 TeV, we expect the EFT to remain unitary for couplings up to

$$\zeta, \tilde{\zeta} < (10^{-12} - 10^{-11})\ \text{GeV}^{-4}\,. \tag{9.10}$$

The sensitivities we derive in Sec. 9.6.6 are much lower than these unitarity bounds. We stress that, unless the underlying new physics model is very strongly coupled, the EFT typically breaks down before unitarity is violated.

9.6.1 New physics scenarios that could be probed in $\gamma\gamma \to \gamma Z$ scattering

Physics with masses Loops of heavy particles charged under $SU(2)_L \times U(1)_Y$ contribute to the $\gamma\gamma\gamma Z$ couplings. These loop contributions only depend on the mass and quantum numbers of the particle in the loop and can thus be given in full generality. Denoting hypercharge by Y, sine and cosine of the Weinberg angle by s_w and c_w and labeling the $SU(2)_L$ representation by its dimension d, we can write (245)

$$\left(\zeta, \tilde{\zeta}\right) = \left(c_s, \tilde{c}_s\right) \frac{\alpha_{\text{em}}^2}{s_w c_w m^4}\, d \left(c_w^2 \frac{3d^4 - 10d^2 + 7}{240} + (c_w^2 - s_w^2)\frac{(d^2-1)Y^2}{4} - s_w^2 Y^4 \right), \tag{9.11}$$

with

$$c_s = \begin{cases} \frac{7}{360} & s = 0 \\ \frac{2}{45} & s = \frac{1}{2} \\ \frac{29}{40} & s = 1 \end{cases}, \quad \tilde{c}_s = \begin{cases} \frac{1}{360} & s = 0 \\ \frac{7}{90} & s = \frac{1}{2} \\ \frac{27}{40} & s = 1 \end{cases} \tag{9.12}$$

where s denotes the spin of the heavy particle running in the loop. [1]

Beyond perturbative contributions to ζ, $\tilde{\zeta}$ from charged particles, non-renormalizable interactions of neutral particles are also present in common extensions of the SM. Such theories can contain scalar, pseudo-scalar and spin-2 resonances, respectively denoted φ, $\tilde{\varphi}$, $h^{\mu\nu}$, that couple to the photon as

$$\begin{aligned}\mathscr{L}_{\gamma\gamma} =& \varphi \left[\frac{1}{f_{0^+}^{\gamma\gamma}} (F_{\mu\nu})^2 + \frac{1}{f_{0^+}^{\gamma Z}} F_{\mu\nu} Z_{\mu\nu} \right] + \tilde{\varphi} \left[\frac{1}{f_{0^-}^{\gamma\gamma}} F_{\mu\nu} \tilde{F}_{\mu\nu} + \frac{1}{f_{0^-}^{\gamma Z}} F_{\mu\nu} \tilde{Z}_{\mu\nu} \right] \\ &+ h^{\mu\nu} \left[\frac{1}{f_2^{\gamma\gamma}} (-F_{\mu\rho} F_{\nu}^{\rho} + \eta_{\mu\nu} (F_{\rho\lambda})^2/4) + \frac{1}{f_2^{\gamma Z}} (-F_{\mu\rho} Z_{\nu}^{\rho} + \eta_{\mu\nu} F_{\rho\lambda} Z_{\rho\lambda}/4) \right],\end{aligned} \tag{9.13}$$

and generate the $\gamma\gamma\gamma Z$ couplings by tree-level exchange as

$$(\zeta, \tilde{\zeta}) = \frac{1}{f_s^{\gamma\gamma} f_s^{\gamma Z} m^2} (d_s, \tilde{d}_s) \tag{9.14}$$

where

$$d_s = \begin{cases} 1 & s = 0^+ \\ 0 & s = 0^- \\ \frac{1}{4} & s = 2 \end{cases}, \quad \tilde{d}_s = \begin{cases} 0 & s = 0^+ \\ 1 & s = 0^- \\ \frac{1}{4} & s = 2 \end{cases}. \tag{9.15}$$

The $f^{\gamma Z}$ couplings vanish if the neutral particle couples universally to the W^i and B kinetic terms of the SU(2)$_L\times$ U(1)$_Y$ Lagrangian density. This happens in particular if the neutral particle couples to gauge bosons via the stress-energy tensor. It is the case of the Kaluza Klein (KK) graviton that is present in models of warped extra dimensions with gauge fields on the IR brane, as well as the radion and the KK graviton in bulk gauge field scenarios with small IR brane kinetic terms (245; 246). This feature of the $\gamma\gamma\gamma Z$ coupling becomes very interesting when put together with the measurement of the $\gamma\gamma\gamma\gamma$ interaction; if a $\gamma\gamma \to \gamma\gamma$ signal is observed, the γZ channel could provide a clear test whether or not the underlying physical mechanism is universally coupled to the gauge

[1] The coefficients c_s, $\tilde{c}_s$ have been determined Ref. (268) in a specific case.

kinetic terms of the SM.

9.6.2 Reconstruction of centrally produced $Z\gamma$ system

In ATLAS and CMS, high-energy photons can be reconstructed in the central detectors instrumented with electromagnetic calorimeters which cover the pseudorapidity range $|\eta| < 2.5$ and provide excellent resolution in terms of energy (less than a percent at $p_T >$ 100 GeV) and position (0.001 units of η and 1 mrad on the azimuthal angle ϕ) for photons and electrons with p_T ranging from a few GeV up to the TeV scale. Photon identification efficiency is expected to be around 75% for $p_T > 100$ GeV. In addition, about 1% of the electrons and jets are misidentified as photons (270).

In this study we consider both leptonic (electrons and muons) for both Z bosons and the hadronic decay of at least one Z boson. For ATLAS, the fiducial acceptance corresponds to leptons with tranverse momenta $p_T^{\ell} > 25$ GeV and absolute rapidity $\eta_{\ell} <$ 2.5. For Z boson production, the dilepton invariant mass $m_{\ell\bar{\ell}}$ is required to be between $66 < m_{\ell\bar{\ell}} < 116$ GeV. Similar requirements are made in CMS. For the Z boson decay into hadrons, the jet is reconstructed by clustering particles deposited in the electromagnetic and hadronic calorimeters. The energy of photons is obtained directly from the electromagnetic calorimeter measurement. The energy of a charged hadron is determined from a combination of the track momentum and the corresponding electromagnetic and hadronic calorimeter energies. The energy of a neutral hadron is obtained from the calibrated energies in electromagnetic and hadronic calorimeters. The typical jet energy resolution is between 5–10% for jets with $p_T > 200$ GeV. Commonly, the anti-k_T jet clustering-algorithm with a radius parameter of $R = 0.5$ is used in CMS and ATLAS (271; 272).

9.6.3 Event generation and simulation setup

The anomalous $\gamma\gamma \to \gamma Z$ process with intact protons in the final state has been implemented in the Forward Physics Monte Carlo (FPMC) generator (219). The contributions and simulations of the various backgrounds are discussed in the subsections below. In order to model experimental uncertainties on the respective final states, we have applied Gaussian smearings on the photon, lepton and hadron energies of 1%. In addition, we apply Gaussian smearings of 15 % in the individual reconstructed jet energy, as well as 0.1% for the pseudorapidity and 1 mrad for the azimuthal angle.

9.6.4 Pileup backgrounds

The largest background to the $pp \to p\gamma Zp$ process originates from γZ detection in the central detectors simultaneously with the detection of two uncorrelated intact protons from pileup. We characterize the backgrounds depending on the decay channel of the Z boson into jets or leptons.

The background contamination in the $jj\gamma$ channel is dominated by $W^{\pm}\gamma$ and γZ in association with pileup protons if we restrict ourselves to two-jet final states. Around 1% of the electrons are misidentified as photons, thus the background $q\bar{q}e$ in association with pileup is also considered in our study. The non-exclusive background processes were simulated in PYTHIA8 (273) at leading order. Jets are reconstructed with the anti-k_T clustering-algorithm with FastJet (188) using $R = 0.5$ at the hadron level, which is close to the standard CMS and ATLAS parameter choice for jet reconstruction. We assign a 15% resolution smearing to the reconstructed jets energy. Gaussian smearings on the ϕ_j and η_j are applied to the individual particles that form the jet.

In the $\ell\bar{\ell}\gamma$ channel, the dominant background is the leptonic decay of the non-exclusive γZ production in association with pileup protons, as can be seen in Figure 9.9. We also consider misidentification of jets and electrons as photons as part of the background.

The pileup events were simulated as follows. For each non-exclusive background event generated on PYTHIA8, the number of pileup interactions in the event is drawn from a Poisson distribution with mean $\mu = 50, 200$ respectively for the low and high luminosity scenarios. We draw the tag probability for the protons arising from the pileup interactions from a uniform distribution and compare it with the single, double or no tag probabilities, which were computed by propagating single and double diffractive protons generated on PYTHIA8 along the beamline up to the proton detectors within their acceptance (see (274; 261) for more details). We assign the fractional momentum loss $\xi = \Delta p/p$ of these pileup protons, which would be reconstructed by the forward detectors in AFP or TOTEM, by randomly sampling the distribution $f(\xi) = 1/\xi$ (which is a first approximation to the ξ distribution of soft diffractive interactions) defined in $0.015 < \xi < 0.15$ via its inverse transform. When the forward detectors have at least one proton tagged in each arm, we compare the diproton mass $\sqrt{\xi_1 \xi_2 s}$ and rapidity $\frac{1}{2}\log(\xi_1/\xi_2)$ with the central mass and rapidity of the γZ final state, and select the best match for both observables. Only events with two proton tags pass through the rest of the selection requirements quoted in Tables 9.1 and 9.2.

For the exclusive backgrounds, the SM predicts $pp \to pZ\gamma p$ scattering at one-loop with two intact protons via two mechanisms: KMR two-gluon exchange process (275)), and two-photon fusion. The elastic two-gluon fusion contribution can be neglected at large $m_{Z\gamma}$ (within the proton taggers acceptance), since the soft gluon emission in the gluon ladder has to be suppressed in order to get an exclusive diffractive event with intact protons. In practice, a Sudakov form factor is introduced to suppress this emission, which, as in the light-by-light scattering case, it decreases significantly with increasing center-of-mass energies of the central system (275). For high-mass production, the SM cross section for $\gamma\gamma \to Z\gamma$ is a fraction of a fb, similar to the SM $\gamma\gamma$ cross section. Thus, in this study we consider that the QCD and QED exclusive $Z\gamma$ contributions are negligible, and then focus on the non-exclusive pileup background contribution, which constitutes the dominant

background in this search.

9.6.5 Event selection

The $(jj),\gamma$ $(\ell\bar{\ell}),\gamma$ final states from the new physics signal are typically back-to-back and have similar transverse momenta. In the dijet (dilepton) case, this translates to selection requirements on $|\Delta\phi_{jj\gamma} - \pi| < 0.02$ ($|\Delta\phi_{\ell\bar{\ell}\gamma} - \pi| < 0.02$) and $p_{T\gamma}/p_{Tjj} > 0.90$ ($p_{T\gamma}/p_{T\ell\bar{\ell}}) > 0.95$). As can be seen in Figures 9.9 and 9.11, the signal events appear in the high mass region, allowing for further background rejection by asking $m_{jj\gamma} > 700$ GeV ($m_{\ell\bar{\ell}\gamma} > 600$ GeV).

The probability to detect at least one proton in each of the forward detectors is estimated to be 32%, 66% and 93% for 50, 100 and 200 additional interactions respectively. The pileup background is further suppressed by requiring the proton missing invariant mass m_{pp} to match the $Z\gamma$ invariant mass within 10% (5%) resolution, $m_{\gamma jj} = \sqrt{\xi_1\xi_2 s} \pm 10\%$ ($m_{\gamma\ell\bar{\ell}} = \sqrt{\xi_1\xi_2 s} \pm 5\%$) and the γZ system rapidity and the rapidity of the two protons $y_{pp} = \frac{1}{2}\ln(\xi_1/\xi_2)$ to be the same within $|y_{\gamma jj} - y_{pp}| < 0.10$ ($|y_{\gamma\ell\bar{\ell}} - y_{pp}| < 0.03$) units in rapidity for the hadronic (leptonic) channel. This is the key background rejection tool provided by the forward detector information.The number of expected signal and background events passing their respective selections can be seen in Table 9.1, (Table 9.2) for the $jj\gamma$ channel ($\ell\bar{\ell}\gamma$ channel) for an integrated luminosity of 300 fb^{-1} (≈ 3 years of data-taking at the LHC) and moderate pileup interactions $\mu = 50$ at $\sqrt{s} = 13$ TeV.

Cut/Process	Signal ζ ($\tilde{\zeta}=0$)	Signal $\zeta=\tilde{\zeta}$	γZ +pileup	$W^{\pm}\gamma$ +pileup	$jje^{\pm}$ +pileup
$0.015<\xi_{1,2}<0.15$, $p_{T\gamma}>150$ GeV $p_{Tjj}>100$ GeV]	38.6	51.4	1951.8	1631	8.47
$m_{\gamma Z}>700$ GeV	37	49.5	349.8	358.9	1.3
$p_{Tjj}/p_{T\gamma}>0.90$, $\lvert\Delta\phi-\pi\rvert<0.02$	33.8	45.1	144.7	145.4	0.54
$\sqrt{\xi_1\xi_2 s}=m_{\gamma Z}\pm 10\%$	28.2	35.7	19.7	19.3	0.1
$\lvert y_{pp}-y_{\gamma Z}\rvert<0.05$	25.5	32.7	1.5	1.6	0

Table 9.1: Number of signal and background events in the $jj\gamma$ channel after the selection requirements for an integrated luminosity of $300\,\text{fb}^{-1}$ and $\mu=50$ at $\sqrt{s}=13\,\text{TeV}$, and for $\zeta=4\times10^{-13}\,\text{GeV}^{-4}$. Non-exclusive events were simulated on PYTHIA8 at leading-order and signal events in the FPMC. Jets are reconstructed with the anti-k_t clustering-algorithm using $R=0.5$ and $p_{T\,\text{min}}=10$ GeV.

Cut/Process	Signal ζ ($\tilde{\zeta}=0$)	Signal $\zeta=\tilde{\zeta}$	γZ +pileup	$\ell\bar{\ell}j$ +pileup	$\ell\bar{\ell}e^{\pm}$ +pileup
$[0.015<\xi_{1,2}<0.15$, $p_{T\gamma}>100$ GeV $p_{T\ell\bar{\ell}}>100$ GeV]	13.2	17.4	2239.2	64.5	1.2
$m_{\gamma Z}>600$ GeV	12.9	17.1	227	3.8	0.2
$p_{T\gamma}/p_{T\ell\bar{\ell}}>0.95$, $\lvert\Delta\phi-\pi\rvert<0.02$	12.6	16.7	175	0	0
$\sqrt{\xi_1\xi_2 s}=m_{\gamma Z}\pm 5\%$	12.2	16.4	12.7	0	0
$\lvert y_{pp}-y_{\gamma Z}\rvert<0.03$	10	13.7	0.6	0	0

Table 9.2: Same as Tab. 9.1 for the $\ell\bar{\ell}\gamma$ channel. The selection yields a signal efficiency of about 75% with an essentially background-free measurement in this channel.

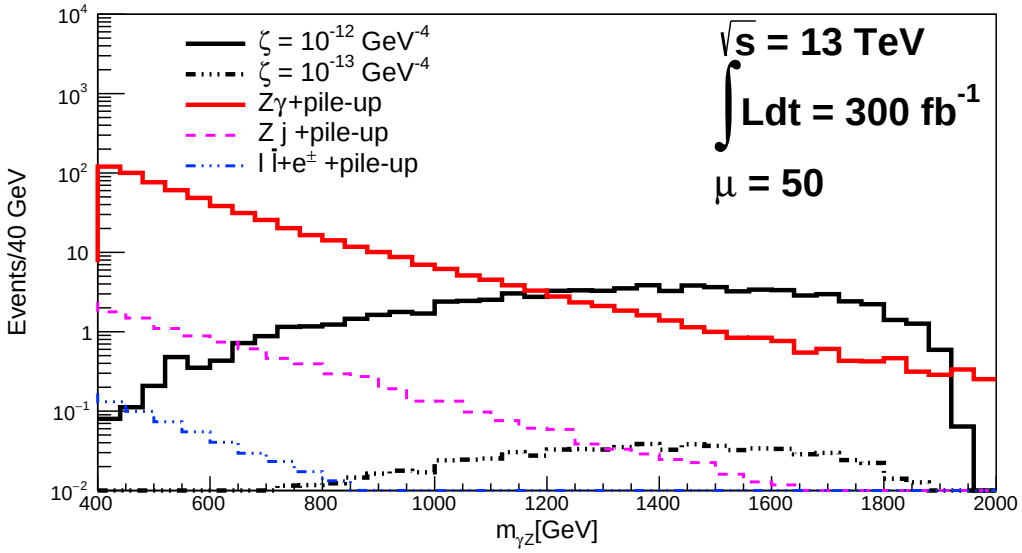

Figure 9.9: Invariant mass of the reconstructed γZ for the signal (black histograms) in the $\ell\bar{\ell}\gamma$ channel for two different coupling values ($\zeta = 10^{-12}$ and 10^{-13} GeV^{-4}). The plot is for events within the $0.015 < \xi < 0.15$ proton detectors acceptance and the requirement on transverse momenta $p_{T\gamma}, p_{T\ell\bar{\ell}} > 100$ GeV. The main contribution to the background is the SM $Z\gamma$ production in association with protons arising from the pileup. The plot assumes an integrated luminosity of $300\,\text{fb}^{-1}$ and an average pileup of $\mu = 50$. The plot corresponds to the one published in Ref. (2).

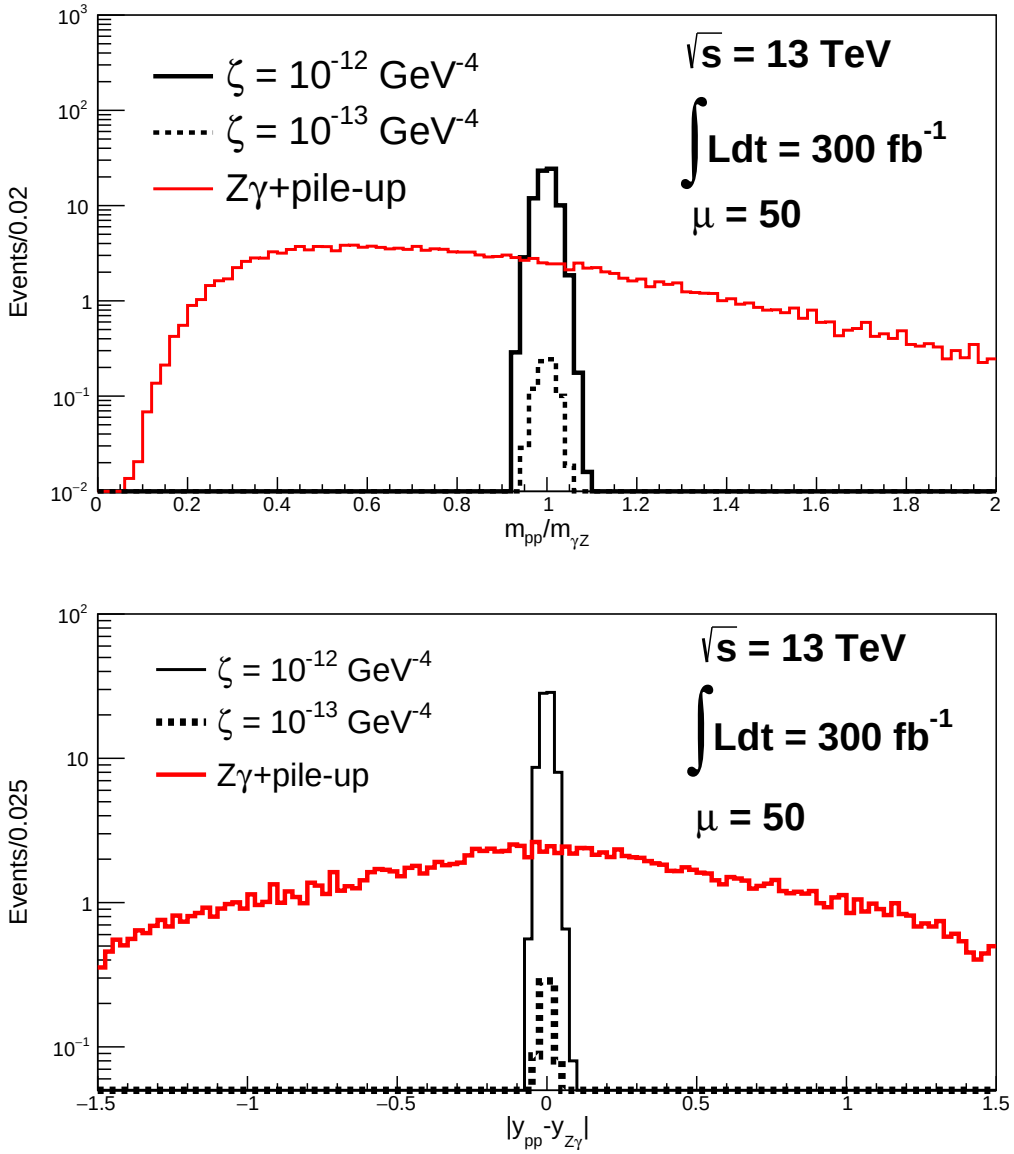

Figure 9.10: Missing diproton mass $m_{pp} = \sqrt{\xi_1 \xi_2 s}$ to central mass ratio distribution (upper) and rapidity difference distribution (lower) in the $\ell\bar{\ell}\gamma$ channel for signal and background within the acceptance $0.015 < \xi_{1,2} < 0.15$ considering two different coupling values after applying the requirements on the acceptance, p_T, invariant mass $m_{\gamma Z}$, p_T ratios and angle separation according to Table 9.2. The width of the signal is due mainly to the $\xi_{1,2}$ resolution. The integrated luminosity is 300 fb^{-1} and the average pileup is $\mu = 50$. The plot corresponds to the one published in Ref. (2).

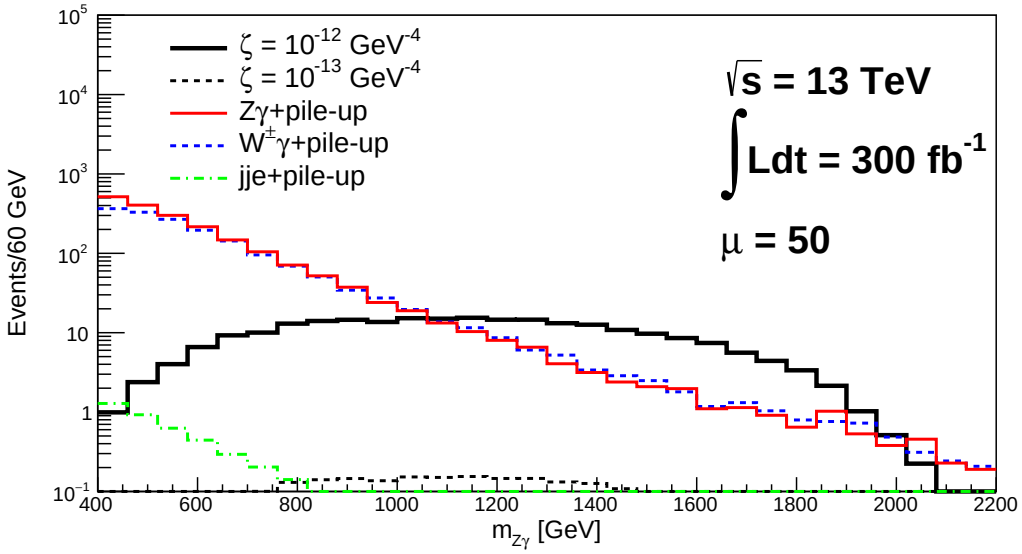

Figure 9.11: γZ mass distribution for the signal in the $jj\gamma$ channel for two coupling values ($\zeta = 10^{-12}, 10^{-13}$ GeV^{-4}, $\tilde{\zeta} = 0$) for events within the $0.015 < \xi_{1,2} < 0.15$ proton detectors acceptance and after the transverse momenta requirement as in Table 9.1. The plot assumes an integrated luminosity of 300 fb^{-1} and an average pileup of $\mu = 50$. The plot corresponds to the one published in Ref. (2).

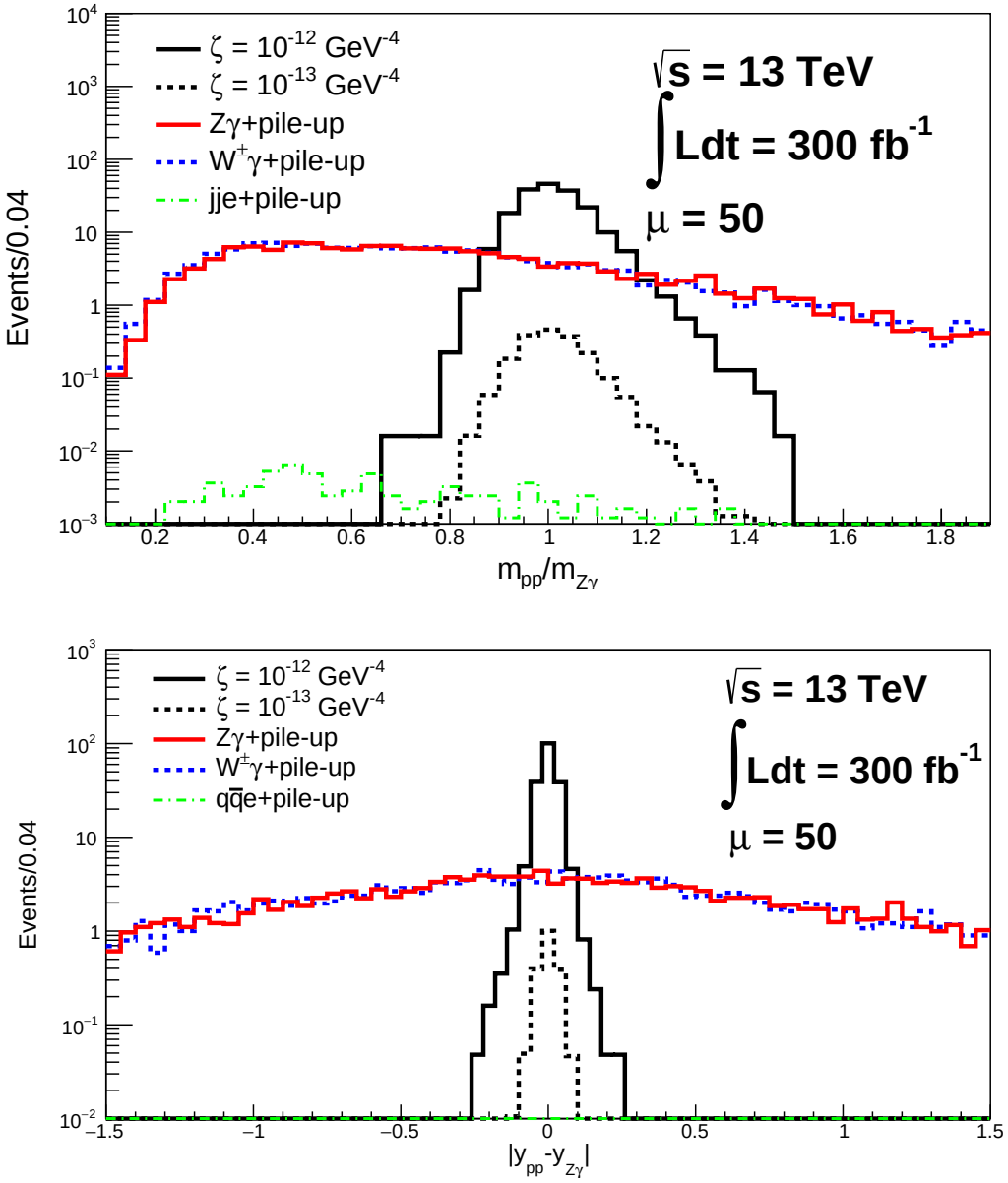

Figure 9.12: Missing diproton mass $m_{pp} = \sqrt{\xi_1 \xi_2 s}$ to central mass ratio distribution (top) and rapidity difference distribution (bottom) in the $jj\gamma$ channel for the signal and background within the acceptance $0.015 < \xi_{1,2} < 0.15$ considering two different coupling values after applying the requirement on p_T, invariant mass $m_{Z\gamma}$, p_T ratios and angle separation according to Table 9.1. The integrated luminosity is 300 fb^{-1} and the average pileup is $\mu = 50$. The signal width is due to a combined effect of the reconstructed jet energy low resolution ($\approx 15\%$) and the $\xi_{1,2}$ resolution from the proton detectors. The asymmetry on the $m_{pp}/m_{Z\gamma}$ distribution is due to the resolution on the jet energy. The plot corresponds to the one published in Ref. (2).

Exploiting the full event kinematics with the forward proton detectors allows us to suppress the non-exclusive background in both channels with a high signal selection efficiency of $\sim 70\%$. (for $\mu = 50$ average pileup interactions), as can be seen in Tables 9.1 and 9.2 and Figures 9.12 and 9.10. For a coupling value of $\zeta = 4 \times 10^{-13}$ GeV $^{-4}$, the signal cross section within the proton taggers acceptance is ~ 1.1 fb. We expect about 25 events in $jj\gamma$ and 10 events in $\ell\bar{\ell}\gamma$ channels for an integrated luminosity of 300 fb^{-1} for this coupling value after selection requirements.

In addition, we include a similar study at a higher number of pileup interactions per bunch crossing $\mu = 200$ and an integrated luminosity of 3000 fb^{-1}. We consider the $\ell\bar{\ell}\gamma$ final states in this scenario, since we do not obtain much improvement in the hadronic channel in comparison to the 300 fb^{-1}. We optimized the selection requirements for this case to increase the background rejection even further. In particular, we increased the mass requirement to $m_{\gamma Z} > 1100$ GeV and required harder Z and γ p_T of 200 GeV. We end up with a projected number of 2 γZ QCD events with two intact protons with the updated selection. The detailed Table is shown in our paper (2).

A significant fraction of the Z boson hadronic final states are reconstructed as a single jet, since the dijet system is boosted in the high mass regime where the signal is enhanced. The QCD background from $q\gamma$ and $g\gamma$ final states is very large, and contributes to $\mathcal{O}(10^3)$ background events after selection requirements. For this reason, we restricted ourselves to the dijet final states in this study. A more detailed jet substructure analysis can in principle efficiently discriminate between large-radius (large-R) jets from the decay of a boosted Z boson and from QCD (276) but this goes beyond our study.

9.6.6 Expected sensitivities

Expected sensitivities to the ζ, $\tilde{\zeta}$ coefficients are shown in Tabs. 9.3, 9.4 and in Fig. 9.13. The sensitivities are roughly of $\sim 2 \times 10^{-13}$ GeV^{-4} for both 300 fb^{-1} at low luminosity and 3000 fb^{-1} at high luminosity. The reach at high luminosity is limited by the large pileup.

Coupling (GeV^{-4})	ζ ($\tilde{\zeta}=0$)		$\zeta=\tilde{\zeta}$	
Luminosity	300 fb^{-1}		300 fb^{-1}	
pileup (μ)	50		50	
Channels	5 σ	95% CL	5 σ	95% CL
$\ell\bar{\ell}\gamma$	2.8×10^{-13}	1.8×10^{-13}	2.5×10^{-13}	1.5×10^{-13}
$jj\gamma$	2.3×10^{-13}	1.5×10^{-13}	2×10^{-13}	1.3×10^{-13}
$jj\gamma\bigoplus\ell\bar{\ell}\gamma$	1.93×10^{-13}	1.2×10^{-13}	1.7×10^{-13}	1×10^{-13}

Table 9.3: 5σ discovery and 95% CL exclusion limits on the quartic couplings ζ, $\tilde{\zeta}$ in units of GeV^{-4}. Sensitivities are given for $300\,\text{fb}^{-1}$ for $\mu=50$ pileup interactions. The last row corresponds to the search of $Z\gamma$ production in both channels with their respective selection requirements.

Coupling	ζ ($\tilde{\zeta}=0$)		$\zeta=\tilde{\zeta}$	
Luminosity	$3000\,\text{fb}^{-1}$		$3000\,\text{fb}^{-1}$	
pileup	200		200	
Channel	5σ	95 % C.L.	5σ	95% C.L.
$\ell\bar{\ell}\gamma$	1.8×10^{-13}	1.1×10^{-13}	1.25×10^{-13}	7.8×10^{-14}

Table 9.4: 5σ discovery and 95% CL exclusion limits on the quartic gauge couplings ζ, $\tilde{\zeta}$ in units of GeV^{-4}. Sensitivities are given for $3000\,\text{fb}^{-1}$ and $\mu=200$ average pileup interactions, which corresponds to the High Luminosity LHC. Sensitivities for the $jj\gamma$ channel are not quoted in this scenario, due to the high number of background events which compromises significantly the signal efficiency.

The leptonic final state turns out to be the cleanest channel for this search with nearly background-free events without the use of timing detectors. Decent sensitivity is obtained in the hadronic channel at moderate Run-2 pileup conditions, with an expected number of three background events after all the event selection requirements. The remaining background events that may pass the selection requirements can be further rejected by a factor of ≈ 40 with the use of time-of-flight detectors in AFP and PPS.

The $\mathscr{B}(Z\to\gamma\gamma\gamma)$ branching ratio has been constrained at LEP (277; 278; 279). Since then, a stronger bound has been reported by ATLAS using 8 TeV collision data (280). This bound is set at $\mathscr{B}(Z\to\gamma\gamma\gamma)<2.2\times10^{-6}$. This bound translates as a limit

$$\sqrt{\zeta^2+\tilde{\zeta}^2-\frac{\zeta\tilde{\zeta}}{2}}<1.3\times10^{-9}\,\text{GeV}^{-4}\ \ (95\%\text{CL})\,. \tag{9.16}$$

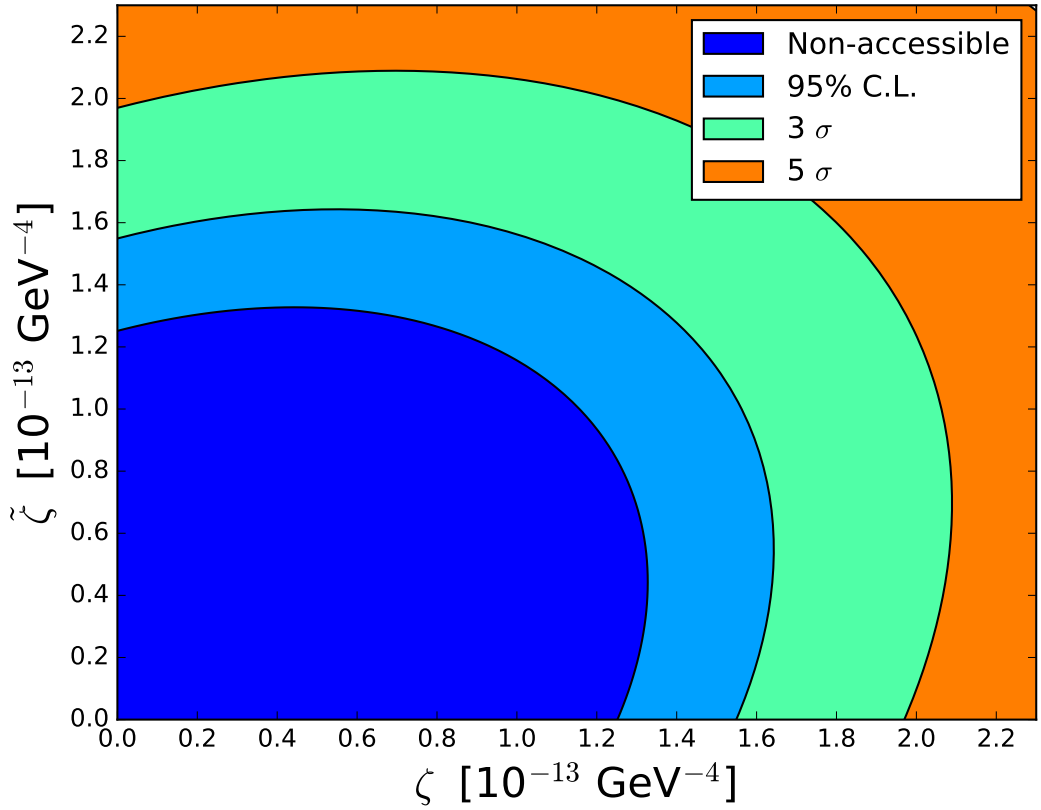

Figure 9.13: Sensitivity in the $\zeta - \tilde{\zeta}$ plane for 300 fb^{-1} and $\mu = 50$. Orange, green and light blue can be probed at 5 σ, 3σ, and 95% C.L. using the proton tagging technique at the LHC, as described in this Section. The dark blue region corresponds to ≈ 0 signal events after selection requirements within the proton detectors acceptance, thus unaccessible in PPS/AFP. The plot corresponds to the one published in Ref. (2).

At the time of writing this thesis, no updated $Z \to \gamma\gamma\gamma$ analysis based on Run-2 data has been presented yet. Imagining the same search is done at 13 TeV data with 300 fb^{-1} in the same conditions, we expect an improvement by about an order of magnitude with respect to the existing bound of ATLAS from Eqn. 9.16. In addition, the current number of pileup interactions at 13 TeV sets a challenge to the measurement of 3γ final states. This remains far away from the expected sensitivities obtained in the exclusive channel at the same luminosity by roughly three orders of magnitudes.

$$m < 2.3\,\text{TeV} \times \left(\frac{1\,\text{TeV}}{\sqrt{f^{\gamma\gamma} f^{\gamma Z}}} \right) \quad \text{in the } \gamma Z \text{ channel} , \tag{9.17}$$

$$m < 4.5\,\text{TeV} \times \left(\frac{1\,\text{TeV}}{f^{\gamma\gamma}} \right) \quad \text{in the } \gamma\gamma \text{ channel} . \tag{9.18}$$

Depending on the relative strength of the $f^{\gamma\gamma}$ and $f^{\gamma Z}$ couplings, a similar reach can be obtained in the two channels. The reach on the $\gamma\gamma$ channel is stronger, since in this case we do not have to account for a branching fraction as in the γZ case.

We would like to stress that in order for these bounds to be the most sensitive probe of a new particle, one has to assume that the couplings to gluons are somewhat suppressed, as otherwise gluon fusion processes can provide stronger bounds. For instance, in the case of the KK graviton coupling universally to all SM fields, our 5σ sensitivity in Eqn. (9.18) translates to $m_{\text{KK}} < 1.4\,\text{TeV}\sqrt{\kappa/0.1}$, where κ is the universal KK graviton coupling strength. This bound is slightly weaker than those of standard searches. However, our method becomes more sensitive at large coupling, both because the resonance becomes too broad for standard searches to resolve them in a "bump search", and also because we are very sensitive to mass regions outside the kinematic reach of the LHC. Finally, even if our method did not provide the primary discovery channel, Eqns. (9.17) and (9.18) show that the γZ channel could efficiently determine whether the underlying particle couples universally to $(B^{\mu\nu})^2$, $(W^{i,\mu\nu})^2$ (see discussion in Sec. 9.6.1).

The sensitivity to charged particles is fairly weak, unless large d, Y or a large multiplicity of these new particles are taken into account. For a vector particle in the $\text{SU}(2)_L$ adjoint representation, for example, one has $d = 3, Y = 0$ and the reach in mass is found to be $m \approx 120$ GeV. For N vectors, the bound would increase as $N^{1/4}$. Only for a large multiplicity the sensitivity is decent. On the other hand, this bound on charged particles is very model-independent, as it depends only on the quantum numbers of the underlying particle (see Eqn. (9.11)). The measurement is complementary to direct searches for charged

particles, which can be very model-dependent. The method we propose based on $\gamma\gamma$ fusion has the advantage that, since it is model-independent, we can be recast numerous new physics scenarios that would induce the $\gamma\gamma\gamma Z$ coupling.

9.7 Axion-like particles in light-by-light scattering

The presence of light (pseudo)scalars coupled to SM particles would have numerous consequences from the subatomic to the cosmological scale. Axion-like particles (ALPs) appear in many extensions of the SM. For example, CP-odd scalars typically appear in the string theory landscape (281; 282; 283; 284; 285; 286), or theories with spontaneously broken approximate symmetries (287). A CP-even scalar can be the radion mode from an extra dimension (288), the dilaton arising from spontaneous breaking of conformal symmetry (289), or the radial mode of the symmetry-breaking vacuum in composite Higgs models (290). Any new neutral spin-0 particle added to the SM typically couples to fermions only via dimension-five operators proportional to the fermion mass, while its dominant coupling to gauge bosons is via dimension-five operators containing derivatives. Therefore, at energies above the top quark mass, these particles are mostly accessible via their couplings to gauge bosons or the Higgs boson. Here, we are primarily interested in their coupling to photons.

These particles have been strongly constrained by numerous observations, some of them by dedicated experiments. A number of these constraints are model-independent, in the sense that they can be shown in the plane of mass versus (pseudo)scalar–photon coupling. This landscape of constraints tends to vanish at high masses, where searches are collider-based. Indeed, searching for a particle relying only on its coupling to photons is not an easy task at a lepton or hadron collider.

A particularly interesting proposal to study the ALP–photon coupling is via elastic scattering of light-by-light in ultraperipheral heavy-ion collisions, as pointed out in Ref. (291). In these collisions, the photon-photon luminosity is proportional to Z^4 ($Z = 82$

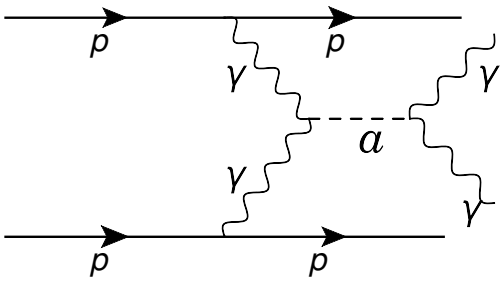

Figure 9.14: Schematic diagram of an axion-like particle production in two-photon exchange in pp collisions. The scattered intact protons are tagged with the forward proton detectors and the photon pair is detected in the central detector.

for lead), which enhances significantly the cross section for exclusive diphoton production. Evidence for light-by-light scattering in ultraperipheral heavy-ion collisions has been reported by ATLAS and CMS (292; 293; 294), from which bounds on the ALP–photon coupling were correspondingly extracted were derived shortly afterwards. These bounds are quite robust for masses from 1 to 100 GeV, with its reach in mass limited from above mainly by the minimum impact parameter required in ultraperipheral heavy-ion collisions. For larger masses however, usually accessible in pp collisions at the LHC, the ALP search remains very challenging.

We present an extension of the search for a (pseudo) scalar in light-by-light scattering at the LHC. We propose to search for ALPs in central exclusive diphoton production in pp collisions (see Fig. 9.14),

$$pp \to p(\gamma\gamma \to a \to \gamma\gamma)p \tag{9.19}$$

where the photon pair is measured in the central detector, like CMS or ATLAS, and the scattered intact protons are tagged with the RP detectors of the CMS or ATLAS experiments. Using proton tagging, we can reach diphoton invariant masses between 350 GeV and 2 TeV for $\sqrt{s} = 13$ TeV, where the acceptance of the forward detectors is nearly 100% efficient.

Qualitatively, the interest of our proposed search method compared to the ones mentioned at the beginning is that the mass reach is limited only by the center-of-mass en-

ergy of the pp system and the acceptance of the forward detectors. The photon-photon luminosity for the $\gamma\gamma \to \gamma\gamma$ subprocess is much smaller than the one in an ultraperipheral heavy-ion collision, but on the other hand the reach in the center-of-mass energy of the photon pair is higher, which enhances the sensitivity for the ALP search since the (pseudo) scalar–photon coupling vertex comes from an effective dimension-5 operator and thus grows rapidly with the diphoton collision energy. Another advantage of the exclusive channel in pp collisions is that it does not need to rely on a dedicated bump search in the diphoton spectrum. Therefore, the results we can obtain are valid for a very broad resonance, which could be missed by an analysis relying on the diphoton mass spectrum lineshape.

9.7.1 The $pp \to p(\gamma\gamma \to \gamma\gamma)p$ process

The hadron-level cross section can be calculated as a convolution of the effective photon fluxes and the $\gamma\gamma \to \gamma\gamma$ subprocess matrix elements within the equivalent photon approximation (229).

In order to describe the interaction of the (pseudo) scalar a with photons we use the effective interaction models

$$\mathscr{L}^{+} = \frac{1}{f} a F_{\mu\nu} F^{\mu\nu} \quad \text{(CP-even)}, \quad \mathscr{L}^{-} = \frac{1}{f} a F_{\mu\nu} \tilde{F}^{\mu\nu} \quad \text{(CP-odd)}, \tag{9.20}$$

where f^{-1} is the ALP–photon coupling and $\tilde{F}^{\mu\nu} = \frac{1}{2}\varepsilon^{\mu\nu\rho\sigma} F_{\rho\sigma}$. The contributions to the $\gamma\gamma \to \gamma\gamma$ helicity amplitudes in both cases read

$$\mathscr{M}_{++++} = -\frac{4}{f^2} \frac{s^2}{s - m_a^2}, \tag{9.21}$$

$$\mathscr{M}_{++--} = -(CP) \frac{4}{f^2} \left(\frac{s^2}{s - m_a^2} + \frac{t^2}{t - m_a^2} + \frac{u^2}{u - m_a^2} \right), \tag{9.22}$$

$$\mathscr{M}_{+++-} = 0, \tag{9.23}$$

and $\mathscr{M}_{+-+-}(s,t,u) = \mathscr{M}_{++++}(u,t,s)$, $\mathscr{M}_{+--+}(s,t,u) = \mathscr{M}_{++++}(t,s,u)$, where s, t and u are the Mandelstam variables of the diphoton system and m_a is the mass of the ALP. This is an effective theory valid roughly up to energy $\sqrt{s} \sim 4\pi f$. The amplitude grows with s and unitarity would be violated above this scale. The projections we derive in Sec. 9.7.4 yield coupling values well below these unitarity bounds. The unpolarized differential cross-section is given by

$$\frac{d\sigma}{d\Omega} = \frac{1}{128\pi^2 s}\left(|\mathscr{M}_{++++}|^2 + |\mathscr{M}_{+-+-}|^2 + |\mathscr{M}_{+--+}|^2 + |\mathscr{M}_{++--}|^2\right). \tag{9.24}$$

Each term in Eqn. (9.24) contains the SM light-by-light process. The CP odd and even cases yield the same differential unpolarized cross section. The scalar, being coupled to photons, has a minimal decay width of

$$\Gamma(a \to \gamma\gamma) = \frac{m_a^3}{4\pi f^2}. \tag{9.25}$$

In our projections, the decay width of a is a free parameter that satisfies the $\Gamma \geq \Gamma(a \to \gamma\gamma)$ condition. The decay width is parametrized via the branching ratio into photons $\mathscr{B}(a \to \gamma\gamma) = \Gamma(a \to \gamma\gamma)/\Gamma$.

It is instructive to examine the amplitudes when taking into account our knowledge of the forward detectors. The forward detectors have access to the process in a given interval of center-of-mass energy of the diphoton system $\sqrt{s_{\gamma\gamma}} \in [\sqrt{s}_0, \sqrt{s}_1]$, where $\sqrt{s}_0$ is sizeable. For the forward detectors installed at ATLAS and CMS, we have roughly $\sqrt{s}_0 \sim 350$ GeV, $\sqrt{s}_1 \sim 2$ TeV, where the acceptance is efficient. It follows that one can distinguish three regimes for the diphoton production rate relative to the ALP properties.

If $m_a < \sqrt{s}_0$, the mass of the particle is negligible with respect to the $\gamma\gamma$ energy. Then, based on the amplitudes for the ALP, the sensitivity on the coupling f^{-1} will be independent of m and of the width of the particle. The cross section still grows as s increases in this regime, hence the search for a light particle coupled to photons can benefit a lot from

an increase in collision energy. If $\sqrt{s}_0 < m_a < \sqrt{s}_1$, the scalar is produced resonantly. In that regime a bump search can be performed, unless the resonance is very broad. When the resonance is narrow, the cross section behaves as

$$\sigma_{\gamma\gamma\to a\to\gamma\gamma} \propto f^{-2}\mathscr{B}_{a\to\gamma\gamma}. \tag{9.26}$$

Finally if $m_a > \sqrt{s}_1$, the scalar is too heavy to be produced resonantly within the acceptance of the detector. Taking the $m_a \gg \sqrt{s}$ limit, the amplitude can then be described by the low-energy EFT

$$\mathscr{L}^{+}_{\text{eff}} = \frac{1}{2f^2 m_a^2}(F_{\mu\nu}F^{\mu\nu})^2, \qquad \mathscr{L}^{-}_{\text{eff}} = \frac{1}{2f^2 m_a^2}(F_{\mu\nu}\tilde{F}^{\mu\nu})^2, \tag{9.27}$$

Hence the cross section will scale with $(fm_a)^4$ in this limit. These three regimes will clearly appear on the sensitivity plots.

9.7.2 Analysis framework

Our event selection treatment follows the method used in Ref. (233; 239; 236; 252; 254; 2; 257) and resembles analyses reported by ATLAS and CMS on search for exclusive diphoton production in pp and Pb-Pb collisions (292; 295). We consider pp collisions at a $\sqrt{s} = 13$ TeV and an integrated luminosity of 300 fb^{-1}. We look for photons reconstructed in the barrel region $|\eta| < 2.5$, where the reconstruction efficiency is on average 80% for energetic photons (270; 296). The photon energy resolution $\Delta E^{\gamma}/E^{\gamma}$ is taken as 1% since we are dealing with multi-GeV photons. We ask for the leading (subleading) photon to have a minimum p_{T} of 200 (100) GeV. To better isolate elastically produced photon pairs, we apply a cut on the azimuthal angle separation between the two photons $|\Delta\phi^{\gamma\gamma} - \pi| < 0.01$ and their p_{T} ratio $p^{\gamma}_{\text{T},2}/p^{\gamma}_{\text{T},1} > 0.95$. We verified the stability of the elastic selection on the signal by varying the azimuthal angle separation between the two

photons as $|\Delta\phi^{\gamma\gamma} - \pi| < 0.04$ and $p^{\gamma}_{\mathrm{T},2}/p^{\gamma}_{\mathrm{T},1} > 0.90$. This diphoton selection yields an acceptance of about 80% on the signal. Finally, we apply a cut on the invariant mass of the photon pair of 600 GeV for background suppression purposes. We assume that the trigger efficiency is close to 100% at the end of our offline selection.

Since the forward detectors cannot get arbitrarily close to the proton beam, and the position of the LHC beam collimators limits the acceptance of the forward detectors from above, the resulting design acceptance on the protons fractional momentum loss is $0.015 \leq \xi \leq 0.15$. We assume that ξ is known to 5% precision.

The backgrounds for exclusive photon pair production in pp collisions can be classified in reducible and irreducible backgrounds. The irreducible background comes from the SM light-by-light scattering process, which is induced at one-loop at leading order. This background is greatly reduced within the mass acceptance of the forward proton detectors. Two-gluon exchange between the two colliding protons can lead to a photon pair with intact protons in the final state. However, this background is suppressed more rapidly compared to the SM light-by-light scattering at larger invariant diphoton masses are (275; 236), on grounds of preserving the exclusivity of the final state by way of a Sudakov form factor. Exclusive $pp \to p(\gamma\gamma \to e^+e^-)p$ is also considered, where the dielectron is misidentified as a photon pair.

The dominant background is QCD-initiated photon pairs detected simultaneously with protons coming from uncorrelated, soft diffractive interactions. Central exclusive production events satisfy $m_{\gamma\gamma} = \sqrt{\xi_1\xi_2 s}$ and $y_{\gamma\gamma} = \frac{1}{2}\log(\frac{\xi_1}{\xi_2})$. This can be used to filter out the beam background contamination. Thus, we apply a cut $|\sqrt{\xi_1\xi_2 s}/m_{\gamma\gamma} - 1| < 0.03$ and $|y_{\gamma\gamma} - \frac{1}{2}\log(\frac{\xi_1}{\xi_2})| < 0.03$.

Other processes contributing to the reducible background are misidentified photon pairs overlapped with soft diffractive protons. We consider non-exclusive e^+e^- pair production (Drell-Yan), since electrons and positrons can fake the diphoton pair, and non-exclusive dijet production, since hard partons can hadronize into a large number of π^0

mesons which subsequently decay into photon pairs, which can fake the photon detection.

Finally, there is a semi-exclusive contribution from diphoton production in double-pomeron exchange. This color-singlet exchange can lead to surviving protons and two energetic photons in the final state. However, the production yield falls rapidly as a function of the diphoton invariant mass, and the intact protons and the diphoton are not strongly correlated kinematically since part of the energy is carried by the hadronization of the pomeron. This contribution is negligible in our final selection.

After applying the offline event selection described in this section, we end up with an almost background-free probe for light-by-light scattering in pp collisions at high diphoton invariant masses, sensitive to cross sections as small as a fraction of a fb, as found before in Refs. (236; 2).

9.7.3 Simulation results

The signal $\gamma\gamma \to a \to \gamma\gamma$ subprocess was implemented and generated with the FPMC generator (219). FPMC is an event generator for diffractive and photon-induced processes in hadronic collisions. The SM light-by-light scattering process is also simulated in FPMC, which includes contributions from charged leptons and the W boson in the one-loop diagram. We also simulated exclusive dielectron production with this generator.

We also employed FPMC for the double-pomeron exchange background. FPMC uses the fits based on H1 inclusive diffractive results (297) of the pomeron in the Ingelman–Schlein (298) pomeron PDF parametrization. The diffractive parton distribution functions are convoluted with the hard scattering processes library in HERWIG 6.5 (72). FPMC includes a survival probability of 0.03 (234; 235) for pomeron exchange processes. It is not known what the pomeron flux would be at 13 TeV, as it has to be constrained experimentally. One may consider this as a theoretical uncertainty. We recomputed the background yield by rescaling it by a factor of 10 and 100. In neither of these cases we see a significant

Sequential selection	ALP	Excl. SM	DPE $\gamma\gamma$	e^+e^- / dijet +pileup	$\gamma\gamma$ + pile up
$[0.015 < \xi_{1,2} < 0.15,$ $p_{\mathrm{T1,(2)}} > 200, (100)$ GeV]	23.1	0.1	0.1	1.2	1246
$m_{\gamma\gamma} > 600$ GeV	23.1	0.06	0	0.1	440
$[p_{\mathrm{T2}}/p_{\mathrm{T1}} > 0.95,$ $\lvert\Delta\phi^{\gamma\gamma} - \pi\rvert < 0.01]$	23.1	0.06	0	0	35
$\lvert m_{pp}/m_{\gamma\gamma} - 1\rvert < 0.03$	21.8	0.06	0	0	1.2
$\lvert y_{\gamma\gamma} - y_{pp}\rvert < 0.03$	21	0.06	0	0	0.2

Table 9.5: Signal and background yields after applying the event sequential selections. For illustrative purposes, we choose an ALP with mass $m_a = 1200$ GeV and a coupling value of $f^{-1} = 0.1$ TeV^{-1}. We assume an integrated luminosity of 300 fb^{-1} an average of 50 additional interactions per bunch crossing at $\sqrt{s} = 13$ TeV. Excl. stands for the exclusive backgrounds and DPE for double-pomeron exchange background. Non-exclusive diphoton overlapped with soft diffractive protons (rightmost column) constitute the dominating background. The first two rows correspond to the diphoton offline preselection. The third row corresponds to the elastic selection. The last two rows correspond to the exclusive selection, with $m_{pp} = \sqrt{\xi_1 \xi_2 s}$ and $y_{pp} = \frac{1}{2}\log(\frac{\xi_1}{\xi_2})$.

contamination after the final selection.

Non-exclusive backgrounds, which include diphoton production, dijet production and e^+e^- in Drell-Yan, are simulated in PYTHIA8 (299) using the parton distribution function set NNPDF2.3 QCD+QED LO parametrization. We verified that our results do not depend on the particular choice of the PDF set. For the misidentified jets, we use the anti-k_{T} algorithm with the FASTJET package (188) with a cone radius $R = 0.4$. The probability of tagging at least one proton per diffractive interaction is estimated from the minimum bias library of PYTHIA8 (261), as was done for the $\gamma\gamma\gamma Z$ phenomenology analysis described in the previous Section.

The signal and background yields after the sequential selection cuts described in Sec. 9.7.2 can be seen in Tab. 9.5. After all the selection cuts, we end up with a near background-free probe of light-by-light scattering in pp collisions. The differential yield for the exclusive diphoton candidates can be seen in Fig. 9.15. The high signal selection efficiency of the exclusive selection is illustrated in Fig. 9.16.

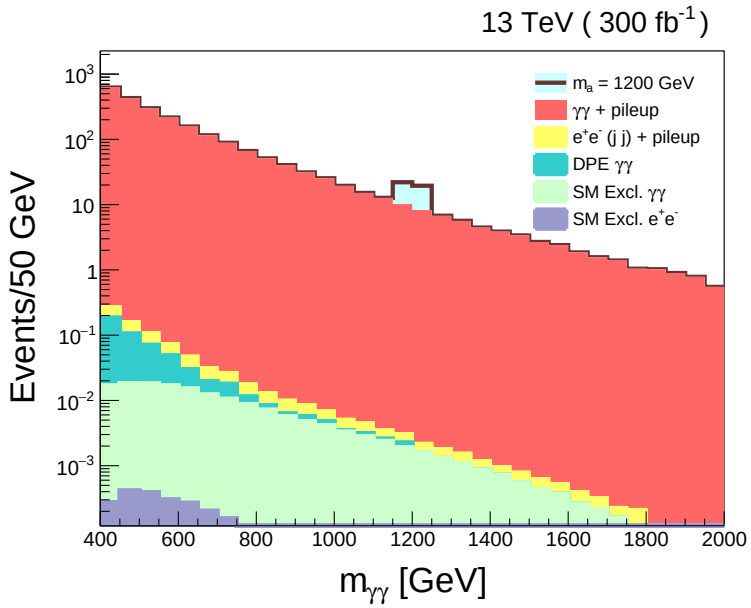

Figure 9.15: Differential yield as a function of the photon pair invariant mass for exclusive diphoton candidates with two tagged protons within the acceptance $0.015 < \xi_{1,2} < 0.15$. No elastic or exclusive offline selection is applied for the diphoton candidates in this plot. We assume there are in average 50 secondary interactions per bunch crossing. For illustrative purposes, we show an instance of a resonant ALP production with $m_a = 1200$ GeV and a coupling value $f^{-1} = 0.1$ TeV^{-1}. The figure is the same as that shown in Ref. (3).

9.7.4 Results and discussion

The expected sensitivity from the exclusive diphoton search can be represented in the $m_a - f$ plane. No other assumption is needed except in the region of resonant production where the branching ratio into photons has to be fixed. The expected bound is displayed in Fig. 9.17 in the ALP–photon coupling and mass plane for a centrally produced ALP with branching ratio $\mathscr{B}(a \to \gamma\gamma) = 1$. The lowest coupling values range between 0.02 TeV^{-1} and 0.06 TeV^{-1} for masses between 600 GeV to 1.5 TeV. The bound increases rapidly from 1.5 TeV to 2 TeV and follows a power-law-like behavior for masses larger than 2 TeV independently of the particle width. For masses below 600 GeV, the coupling is independent of the particle width and has a value of about 0.4 TeV^{-1}. Bounds with different fixed branching ratios can be seen in Fig. 9.18.

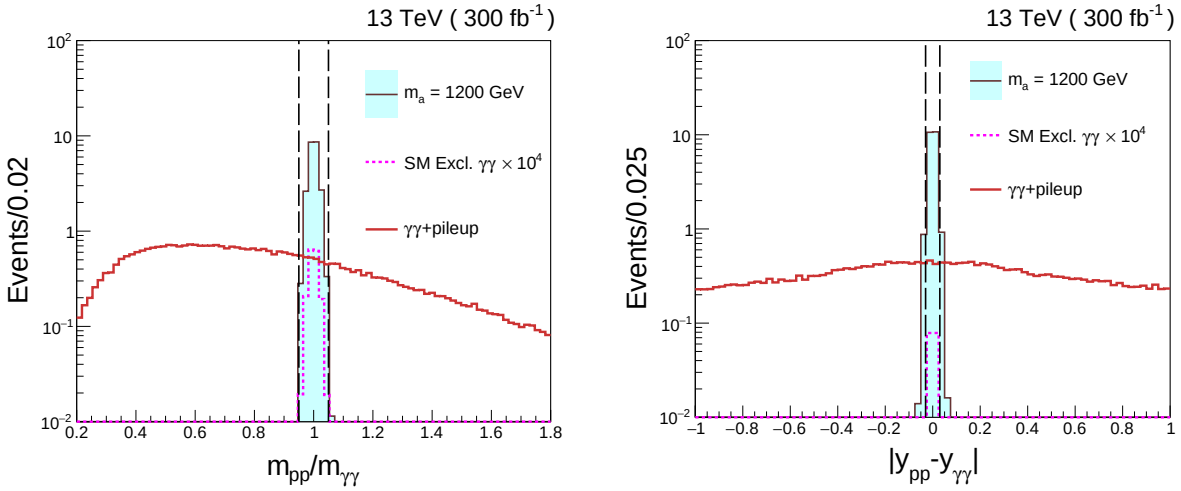

Figure 9.16: Distributions of the ratio of the diphoton mass reconstructed with the forward detectors $m_{pp} = \sqrt{\xi_1 \xi_2 s}$ to the reconstructed diphoton mass $m_{\gamma\gamma}$ (left) and the difference of the diphoton rapidity $y_{\gamma\gamma}$ and the rapidity reconstructed with the forward detectors $y_{pp} = \frac{1}{2}\log(\frac{\xi_1}{\xi_2})$ distribution (right). Diphoton candidates in these plots have passed the elastic selection and the mass lowerbound of 600 GeV. A strong correlation between the forward-backward and central information can be seen for the signal (light blue), while for the background (red line) we see these variables are uncorrelated. We select diphoton candidates lying inside the dashed vertical lines. The width of the signal in these plots is caused mainly by the $\xi_{1,2}$ resolution. The integrated luminosity is 300 fb^{-1} and the average number of pileup interactions is $\mu = 50$. The intact protons lie within the acceptance $0.015 < \xi_{1,2} < 0.15$. The plots are the same as that shown in Ref. (3)

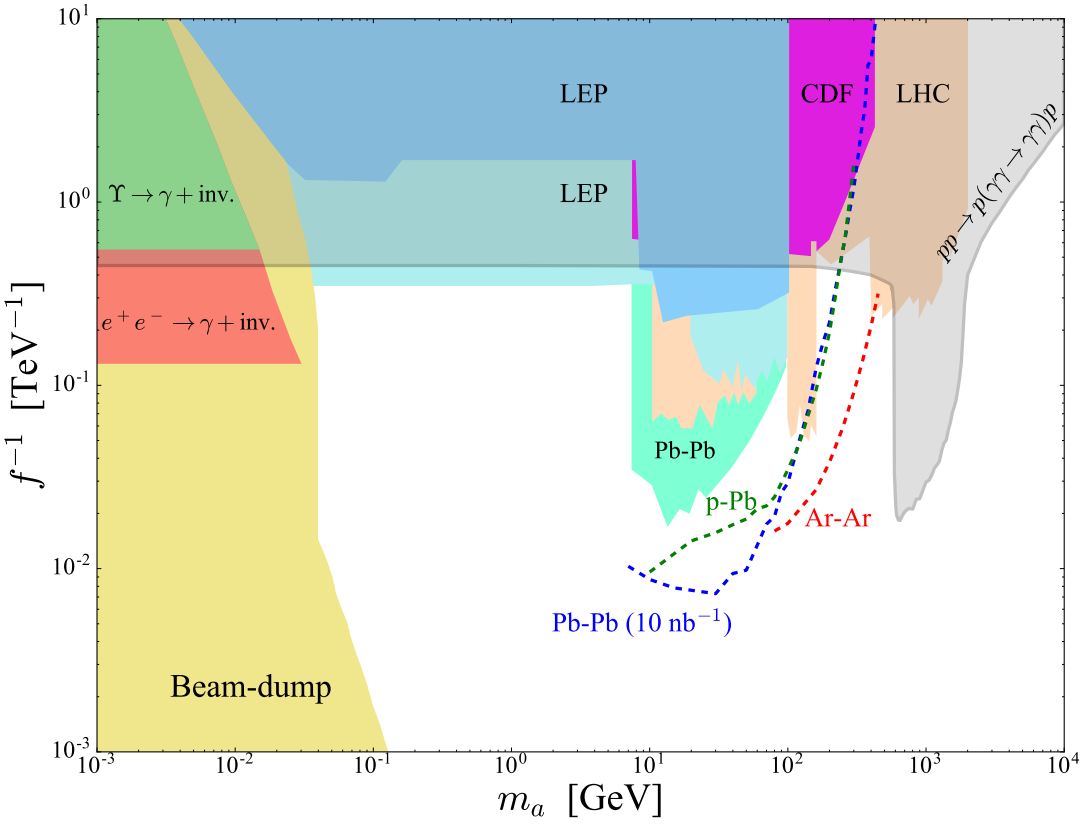

Figure 9.17: Exclusion regions on the ALP–photon coupling f^{-1} and mass of the ALP m_a plane. On light-shaded grey, we have the expected 95%CL exclusion limit in $pp \to p(\gamma\gamma \to \gamma\gamma)p$ events assuming $\mathscr{B}(a \to \gamma\gamma) = 1$ for 300 fb^{-1} in Run-2 of the LHC. The blue dashed line labelled "PbPb" is the projection from light-by-light scattering in PbPb collisions scaled to a luminosity of 10 nb^{-1}. The projections for pPb and ArAr collisions are respectively shown in green and red dotted lines, respectively, and match those of Ref. (4). Existing bounds are in solid color, and were extracted from Ref. (300). The projection for $pp \to p(\gamma\gamma \to \gamma\gamma)p$ matches the one presented in Ref. (3).

We extracted the existing exclusion limits [2] from the compilation in Ref. (300). We show a subset of these bounds for masses between 10^{-3} GeV and 2 TeV and coupling values as low as 10^{-3} TeV^{-1}, although this landscape of bounds exists down to values of 10^{-15} GeV in mass and 10^{-10} TeV^{-1} in the coupling. Beam dump searches probe resonant production of neutral pseudoscalar mesons in photon interactions with nuclei (Primakoff effect). Different beam dump runs at SLAC collectively yield the area in yellow (301; 302; 303). Upsilon meson decays searched at the CLEO and BaBar experiments (304; 305) exclude the region shaded in green. Bounds from collider-based searches for ALPs include measurements of mono-photons with missing transverse energy ($e^+e^- \to \gamma$+invisible) at the LEP (orange), tri-photon searches on and off the Z pole ($e^+e^- \to 3\gamma$) at the LEP (light blue and dark blue), and searches for the same final states in p-$\bar{\text{p}}$ collisions at CDF (magenta) and in pp collisions at the LHC (peach). The derivation of these collider-based bounds are discussed in detail in Ref. (306; 307; 308; 291). The region labelled as "Pb-Pb" (light green) was derived in Ref. (309) based on the measurement of light-by-light scattering in ultraperipheral heavy-ion collisions by ATLAS (292). Such a constraint has been updated recently in light of the CMS and ATLAS analyses of light-by-light scattering, which improved the bound by a factor of about ≈ 1.5 on the ALP–photon coupling compared to what is shown in our plot. These collider-based bounds assume $\mathscr{B}(a \to \gamma\gamma) = 1$.

The LHC region at high mass comes from CMS and ATLAS bump searches in the $\gamma\gamma$ spectrum recasted for ALPs in Ref. (306). A basic extrapolation at 300 fb^{-1} and $\sqrt{s} =$ 13 TeV luminosity tells that this LHC exclusion region would be improved by a factor $\sim 4-5$. In the $0.6-2$ TeV mass region, this is still below the expected sensitivity of our exclusive diphoton search by a factor $\sim 3-4$, showing that our method is competitive with respect to standard bump searches.

For $\mathscr{B}(a \to \gamma\gamma) < 1$, the sensitivity of our exclusive diphoton search in the $0.6-2$ TeV

[2] The ALP–photon coupling in (300) is related to our coupling convention via $f^{-1} = \frac{C_{\gamma\gamma}^{\text{eff}}}{\Lambda} e^2$.

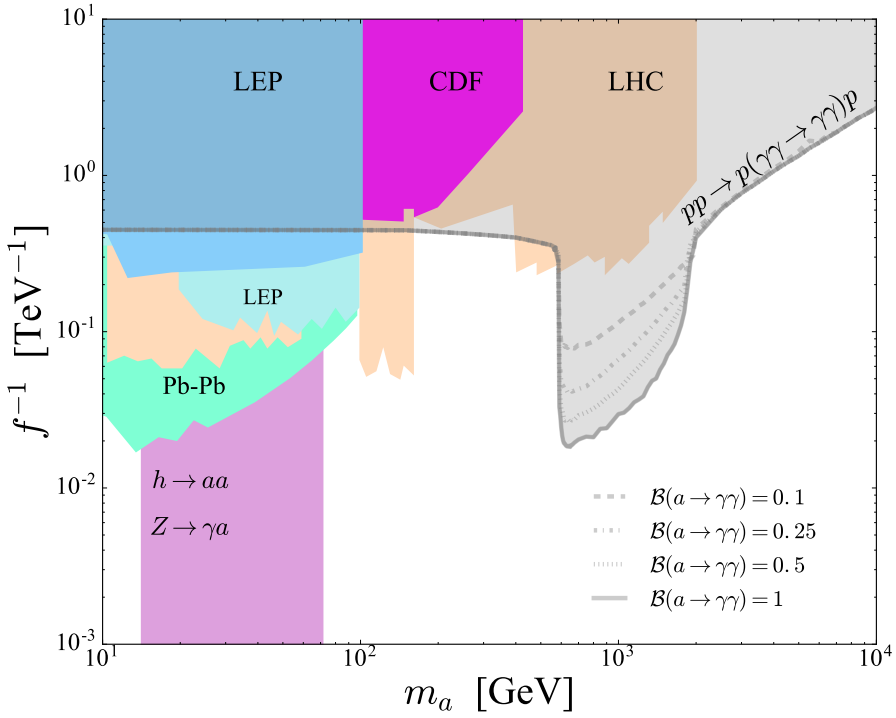

Figure 9.18: Exclusion regions on the ALP–photon coupling f^{-1} and mass m_a plane. On light-shaded grey, we have the expected 95%CL exclusion limit for 300 fb^{-1} in central exclusive diphoton production events for different branching ratios of the ALP into two photons. Current excluded regions for $\mathcal{B}(a \to \gamma\gamma) = 1$ are in solid color, as they were presented in Ref. (300). The Higgs and Z boson related exclusion regions have additional assumptions on the couplings of the ALPs. The figure is the same as that shown in Ref. (3).

mass range decreases as shown in Fig. 9.18. This decrease comes simply from the lower signal rate. The total decay width increases for decreasing $\mathcal{B}(a \to \gamma\gamma)$, (as $\Gamma(a \to \gamma\gamma)$ is fixed by Eqn. (9.25)), but the efficiency of our search is width-independent as it consists of a mere counting of the total event number. The region from LHC bump searches shrinks similarly when lowering $\mathcal{B}(a \to \gamma\gamma)$. However, these searches are valid only for a narrow enough resonance, typically $\Gamma < 0.05\, m_a$ (306). For sufficiently small $\mathcal{B}(a \to \gamma\gamma)$, the resonance width exceeds this threshold value in the LHC exclusion region at large m_a, causing the bump search to lose its power. As a consequence, our exclusive diphoton search gains extra competitiveness in case of a broad resonance.

The phenomenology analysis of $pp \to p(\gamma\gamma \to a \to \gamma\gamma)p$ considered rather harsh selec-

tion requirements on the individual photon transverse momenta and acoplanarity. This was mostly for the purpose of suppressing the pileup background, which readily gives excellent sensitivity in a nearly background-free parameter region of the axion-like particle mass and coupling to the photon field. These selection requirements can in fact be relaxed, and a strategy based on a bump-search analysis thus be deployed. The ALP signal would manifest itself as a bump over a smooth background, where the smooth background comes from the QCD diphoton production with pileup protons. This could improve the sensitivity, but complicates the analysis. This is, however, a possible direction for improvement, particularly for the experimental analysis refinements.

Considering light-by-light scattering in ultraperipheral PbPb collisions and pp collisions, one can cover in principle ALP masses between 1 to 100 GeV and from about 600 to about 2000 GeV for PbPb and pp collisions for resonant production of ALP particles, respectively. The different reach in mass for PbPb and pp collisions is due to the different impact parameter of the ultraperipheral collision. This affects the energy spectrum of the quasi-real photons emitted off the colliding particles. In order to cover the gap between the reach in resonant production of ALPs in PbPb and pp collisions, we can consider collisions of lighter heavy-ion nuclei, such as Argon-Argon (ArAr) at $\sqrt{s}_{\mathrm{NN}} = 7$ TeV and pPb at $\sqrt{s}_{\mathrm{NN}} = 8.16$ TeV collisions. We conducted such an investigation in a follow-up study, to see what would be the needs in luminosity for such a study. We found that, with the conservative luminosity projections for possible special ArAr runs of 3 pb^{-1} at the LHC (310), we would be able to cover the gap between masses of about 100 to about 400 GeV, complementary to the PbPb and pp cases. We considered the same exclusive diphoton selection that was used by ATLAS and CMS in their light-by-light scattering studies in PbPb collisions for this projection. These plots are included in Fig. 9.17.

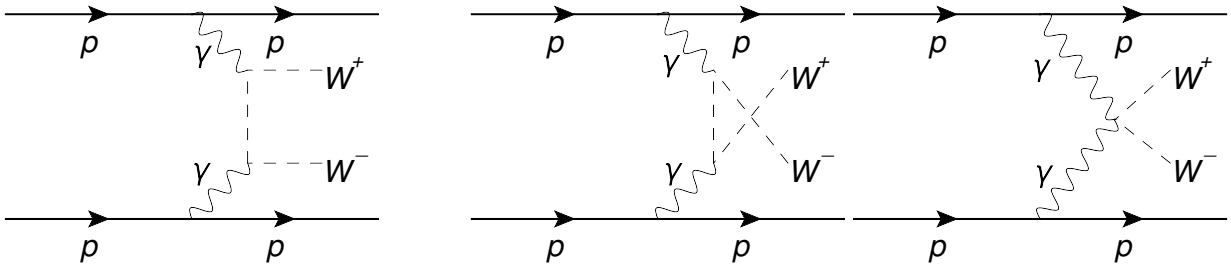

Figure 9.19: Leading order SM diagrams contributing to $pp \to pW^+W^-p$. The upper two diagrams represent the t- and u-channels contribution induced by the SM γW^+W^- coupling, whereas the lower diagram corresponds to the SM $\gamma\gamma W^+W^-$ coupling in the SM.

9.8 Extension of central exclusive $\gamma\gamma \to W^+W^-$

As discussed in Chapter 2, by virtue of the non-abelian nature of electroweak sector of the SM, direct interaction couplings between the vector gauge bosons are possible. The LHC experiments have gathered evidence for some of these non-abelian couplings, while others are very difficult to probe. Recent reviews on these topics can be found in Refs. (311; 312). Here, we are mostly interested in the interactions between photons and W bosons, which interact via triple (γW^+W) and quartic ($\gamma\gamma W^+W^-$) couplings in the SM. These interactions can be directly probed via two-photon fusion $\gamma\gamma \to W^+W^-$ in pp collisions, as shown in Fig. 9.19. This process is the main topic of discussion in the study described in this Section. The corresponding publication is in Ref. (5).

Thus, the $\gamma\gamma \to W^+W^-$ process can be studied in central exclusive production of W boson pairs $pp \to pW^+W^-p$ (231; 313). Previous phenomenology studies based on the use of the proton tagging technique to study two-photon fusion interactions can be found in Refs. (314; 315; 254; 251; 316; 256; 242; 317; 247; 246; 248; 318; 319; 313; 320; 3; 321; 322). Other interesting studies that aim also to describe photon fluxes in processes with proton dissociation, treated in the k_T factorization framework, are presented in Refs. (323; 324; 325). Since our studies rely on events with proton tagging, no such treatment is necessary.

Early searches sensitive to $\gamma\gamma W^+W^-$ couplings were done at the CERN LEP electron-

positron collider by the OPAL and DELPHI Collaborations in $W^+W^- \to \gamma\gamma$ scattering (326; 327; 328; 329), followed by the D0 experiment at the Fermilab Tevatron in proton-antiproton collisions at $\sqrt{s} = 1.96$ TeV(330) and by the CMS and ATLAS experiments at the CERN LHC (331; 332; 333) at 7 and 8 TeV in central exclusive production of W^+W^- pairs in pp collisions ($pp \to p^{(*)}(\gamma\gamma \to W^+W^-)p^{(*)}$), the protons may dissociate into a low mass excited state or remain intact. In a recent conference note (30), ATLAS reported the observation of $\gamma\gamma \to W^+W^-$ scattering at 8.4σ in the $e^{\pm}\mu^{\mp}$ channel without proton tagging, consistent with the SM expectations. In order to obtain a robust understanding of this scattering process, one needs to consider an expansion in the search strategy, especially for a better understanding of in the high invariant mass regime. As an additional advantage, one can use these as standard candle processes for the proton spectrometer calibration, acceptance and efficiency determination, of crucial importance for physics searches based on proton tagging.

In previous studies, only leptonic decays of each W boson have been considered in central exclusive production. Indeed, purely leptonic final-states leave a very clean signature in the detectors: two leptons (e^+e^-, $\mu^+\mu^-$, $e^{\pm}\mu^{\mp}$) with an amount of missing transverse momentum p_T^{miss} associated to the p_{T} carried away by the undetected neutrinos. Such a signature has allowed us to study central exclusive W^+W^- with a moderate number of pileup. However, the visible cross section is largely reduced due to the small branching fraction of the W boson decay into leptons (less than 5% of W boson pairs decay into muon or electron flavored leptons). Thus, in the interest of better understanding this electroweak gauge boson scattering process within the SM in a wider kinematic range, and also to enhance our chances of discovering physics beyond the SM, one can consider the decay of the W boson into $q\bar{q}$ pairs, which has a much larger branching fraction. The study with at least one $W \to q\bar{q}'$ decay has a larger background contribution from standard mechanisms of jet production in QCD, which need to be quantified. New strategies need to be developed in order to use these channels.

If the W boson is highly boosted, the hadronic decay of a single W boson can result in a single large-R jet whose mass is compatible with that of the W boson. In this study, we consider fully-hadronic (JJ), semi-leptonic (J+$\ell\nu$), and fully-leptonic ($\ell\nu\bar{\ell}\bar{\nu}$) decays of the W^+W^- system in central exclusive production, where J is a large-R jet, ℓ is either a muon or an electron, and ν the corresponding neutrino. The branching ratio of W^+W^- pair decay in hadronic, semi-leptonic, and leptonic channels is, in principle, about 46%, 29%, and 4.7%, respectively (considering electrons or muons for leptonic decays where the remaining 20% of the branching fraction corresponds to decays in tau leptons). In the present paper, as an extension of the study in Refs. (231; 313), we explicitly include the contribution of pileup backgrounds since our goal is to perform this measurement in standard pileup luminosity at the LHC at an integrated luminosity of 300 fb^{-1}. In this thesis, we describe the semi-leptonic and fully-hadronic channels, since the purely leptonic channel has been described elsewhere. The leptonic results can be found in Ref. (5).

In addition to the SM study of exclusive W^+W^- production, we consider scenarios where the presence of new particles at much larger energies may induce anomalous contributions to the $\gamma\gamma \to W^+W^-$ scattering. In our study, we parametrize these new physics contributions by means of an EFT approach. Our focus in this part of the phenomenology study is on the improvement of the sensitivity to the anomalous interaction couplings by studying high-mass exclusive W^+W^- production in hadronic and semi-leptonic final states, compared to standard benchmark sensitivities in the purely leptonic final state. The $pp \to pW^+W^-p$ process can be probed with the detection of two intact protons in the forward proton detectors in the AFP or PPS (230; 195) and the reconstruction of the W^+W^- boson decay products. The latter is discussed in Section 9.8.1.

9.8.1 Reconstruction of W^+W^- decay products

As mentioned in the introduction, we consider three decay channels of the W^+W^- system: hadronic (two large-R jets), semi-leptonic (one large-R jet in association with an isolated

lepton and p_T^{miss}), and purely leptonic ($\ell_1^+\ell_2^-$ and missing transverse momentum). Here, we consider that jets can be reconstructed within pseudorapidities of $|\eta| < 5$, and consider electrons and muons to be reconstructed within pseudorapidities of $|\eta| < 2.5$. For W bosons decaying hadronically, the corresponding large-R jet is clustered with the infrared and collinear safe anti-k_t algorithm (79) using particles at the stable particle level with the FASTJET package (188), using a distance parameter of $R = 0.8$. The value of $R = 0.8$ is based on standard choices by ATLAS and CMS for large-R jet analyses. The leptonic channel, which had been previously studied, is not discussed in detail in the thesis, but we refer to our paper for details on this channel (5).

The phenomenology analysis is performed using stable particles at gen-level. In order to mimic detector effects, we apply smearing effects on the transverse momenta and pseudorapidity and azimuthal angular of particles and jets reconstructed at generator-level. For jets, a conservative smearing of 2% on jet p_{T} is used based on Refs. (334; 335). The latter is a combination of jet energy scale and resolution effects for large-R jets. In addition, angular smearings of 1 mrad for azimuthal and polar angles are applied to each jet. The jet mass is computed at gen-level and smeared by about 10%, based on reports by ATLAS and CMS on jet mass resolution studies (336; 337; 338). The jet energy is also smeared by 10%, and the longitudinal component of the jet momentum is determined following the energy-momentum relation. For charged leptons in $|\eta| < 2.5$, a smearing of 2% is applied on the reconstructed transverse momenta (339; 340) and additional angular smearings of 1 mrad for azimuthal and polar angles are applied to each lepton. The missing transverse momentum is defined at generator-level as the negative vector sum of the transverse momentum of each final-state particle within acceptance $|\eta| < 5$. A smearing of 20% is applied on the reconstructed missing transverse momentum, based conservatively on the observed performance of the ATLAS and CMS detectors in the reconstruction of this variable (341; 334).

In the last years, special attention has been given to the better understanding of large-R

jets and jet substructure techniques (342). It has become increasingly important to distinguish large-R jet objects that originate from the merging of the decay products of high-transverse momenta W bosons (W jet) from those initiated by light-flavor quarks or gluons in standard QCD interactions (QCD jets). The CMS and ATLAS Collaborations have presented results related to the decay of W or Z bosons using groomed and ungroomed large-R jets in recent years (336; 338). The most important kinematic discriminant is the invariant mass of the jet. The W boson jet mass arises from the kinematics of the two jet cores associated to the decay and fragmentation of the two quarks, with some broadening induced by the soft-gluon emissions during the parton shower evolution and jet clustering effects. In contrast, the QCD jet mass arises mostly from soft-gluon radiation, resulting in a quickly falling distribution in the invariant mass of the jet. Thus, a selection requirement on the invariant mass of the large-R jet around the mass of the W boson already provides a robust selection requirement to suppress the contribution of QCD jets and to isolate W boson large-R jet candidates. Further discriminant variables based on jet substructure have been explored by the ATLAS and CMS experiments (342). In this first study, we use a simple approach and choose not to apply these jet substructure techniques by default, and thus use the jet mass as the main jet substructure variable to identify the W boson large-R jet. This is because in central exclusive production, the events are very clean, not “contaminated" by soft QCD radiation. Additional soft parton exchanges between proton remnants are absent (since the protons remain intact), as well as underlying event activity, and QCD initial-state radiation. These contributions need to be properly removed in standard W boson large-R jet analyses. The use of the discriminant variables introduced by ATLAS and CMS can only improve our performance studies, and need to be accounted for on top of the jet invariant mass for the experimental analysis.

9.8.2 Signal and background treatment

Central exclusive production of W^+W^- pairs is simulated with the FPMC generator (219). The process $pp \to pW^+W^-p$ accounts for scattering amplitudes induced by the SM γW^+W^- and $\gamma\gamma W^+W^-$. These amplitudes were calculated with the CalcHEP package (343), and coded into FPMC (344; 313). The SM cross section is 95.6 fb for central exclusive W^+W^- production, and 5.9 fb for a W^+W^- invariant mass above 1 TeV for $\sqrt{s} = 14$ TeV (344; 313).

The dominant backgrounds to exclusive W^+W^- production originate from non-diffractive events that mimic the W^+W^- decay signature in the central detector detected in coincidence with intact protons that originate from soft diffractive pileup events. Backgrounds related to single- and double-pomeron exchange W^+W^- production lead to a negligible contribution in high-mass W^+W^- pair production, as found in previous phenomenology analyses (231; 313), as well as in previous studies by ATLAS and CMS (331; 332; 333; 30). These backgrounds can be suppressed by exploiting the kinematic correlations between the forward two proton system and the central system. We assume a conservative number of 50 pile up events per bunch crossing for our projections at $\sqrt{s} = 14$ TeV.

The dominant background corresponds to non-diffractive diboson production processes ($VV = W^+W^-, W^\pm Z, ZZ$), W+jets, Z+jets $t\bar{t}$, single-top, and QCD jets (jet production with quark and gluon strong interactions) detected in association with protons from uncorrelated pileup interactions in the same bunch crossing. In this study, we refer to these backgrounds as W^+W^-+pileup, ZZ+pileup, WZ+pileup, W+jets+pileup, Z+jets+pileup, $t\bar{t}$+pileup, single-top+pileup, and QCD jets + pileup, respectively. The combination of all these backgrounds is referred to as "pileup background" throughout this study. Standard QCD jets are the most important source of background in the fully-hadronic final state, as demonstrated later.

The SM diboson backgrounds are generated with the leading order HERWIG6.5 event generator(345), and the top quark and QCD jet backgrounds are simulated with the PYTHIA8 generator (71).

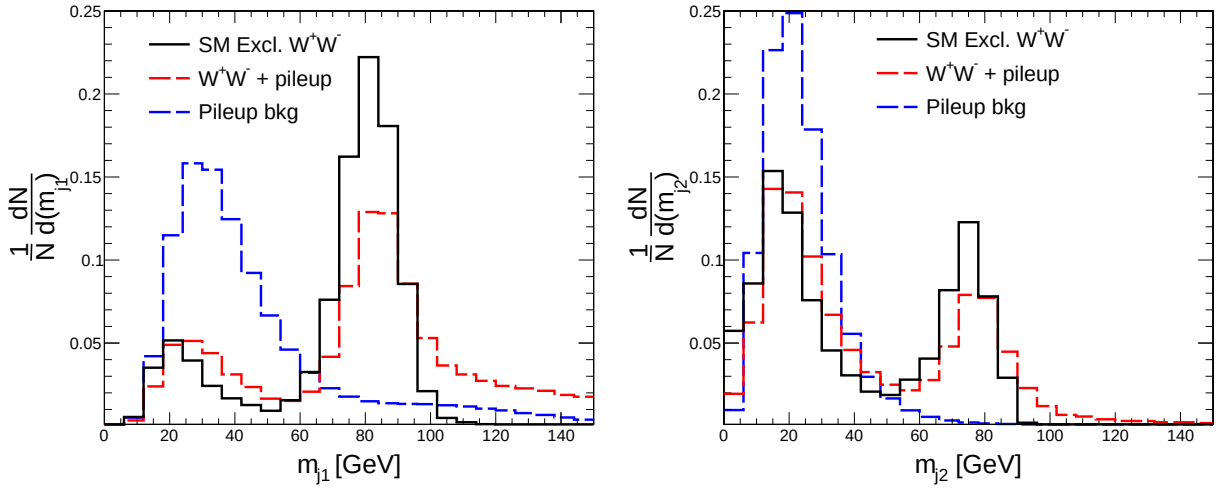

Figure 9.20: large-R jet invariant mass distribution for the leading (left) and subleading (right) in mass in the hadronic channel. The distributions are normalized to unity. The SM exclusive W^+W^- pair production is displayed in black full line, the pileup background in blue dashed line (after preselection requirements), and the pileup background subcomponent of W^+W^-+pileup is shown in red. The peak at around 80 GeV corresponds to the W boson rest mass. The peak at lower masses corresponds to cases where only one of the quarks of the W boson decay is tagged as a jet in the final state, or more generally for light-flavor quark jets or gluon jets.

9.8.3 Study of SM $\gamma\gamma \to W^+W^-$ events

Our focus in this section is to describe the event selection of high-mass W^+W^- exclusive production within the SM. As mentioned in the previous section, we are mostly interested in suppressing the pileup background since this will be the leading one. It is clear that requiring two intact protons to be detected in PPS or AFP is not enough, since protons originating from pileup might overlap with a non-exclusive event.

For pileup protons, we use a distribution $1/\xi$ (as expected for soft diffractive reactions), and consider the nominal acceptance of the proton detectors to be $0.015 < \xi < 0.15$. The probability of detecting protons within the RP acceptance is calculated with PYTHIA8 simulated events (71). This is the same approach adopted in Refs. (320; 315; 314; 3).

In the next subsections, we discuss the specific event selection requirements optimized for the hadronic (two large-R jet, zero isolated leptons), semi-leptonic (one large-R jet, one

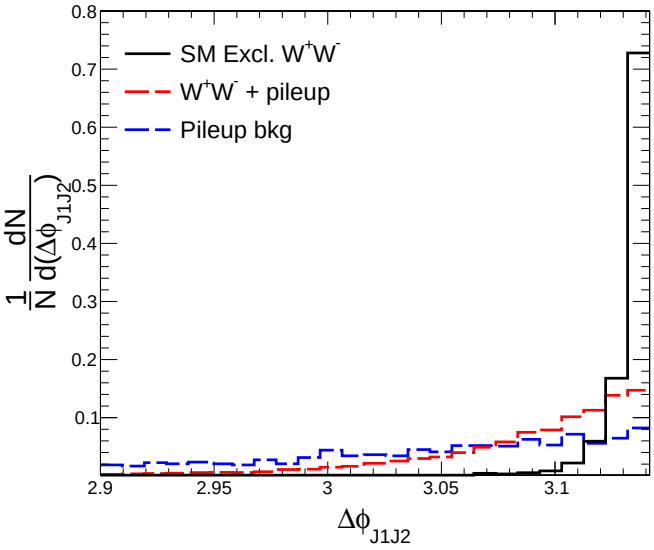

Figure 9.21: Azimuthal angular difference between the two large-R jets corresponding to the decay of the W bosons, $\Delta\phi_{\mathrm{j1j2}} = |\phi_{\mathrm{j1}} - \phi_{\mathrm{j2}}|$ after preselection and m_{j1} and m_{j2} requirements. SM central exclusive W^+W^- events are represented by the black histogram, and non-diffractive W^+W^-+pileup background events are represented in red. The pileup background distribution (blue dashed histogram) is flatter due to the effect of initial-state radiation and underlying event activity in non-exclusive interactions. The distributions are normalized to unity.

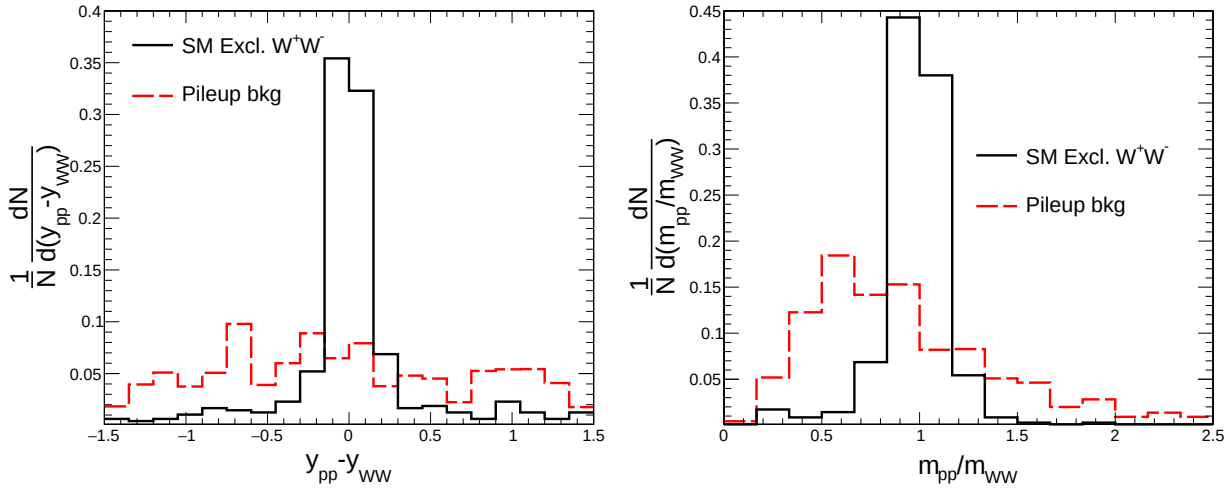

Figure 9.22: Distributions of difference in rapidity $y_{WW} - y_{pp}$ (left) and mass ratio m_{pp}/m_{WW} (right) between the W^+W^- and pp system for central exclusive W^+W^- (black solid line) and pileup background (red dashed line) to illustrate the effectiveness of the mass and rapidity matching in order to reject pileup background. The figures are plotted after the m_{j1}, m_{j2}, m_{WW}, $p_T^{\mathrm{j2}}/p_T^{\mathrm{j1}}$ and $|\phi_{\mathrm{j1}} - \phi_{\mathrm{j2}}|$ selection requirements described in text. The distributions are normalized to unity. The figures match those presented in Ref. (5).

isolated lepton) and leptonic (two isolated leptons, no jets) channels, where a lepton is considered to be isolated if the distance between it and all other particles originating from the same vertex $\Delta R_{lp} = \sqrt{(\Delta y_{lp})^2 + (\Delta\phi_{lp})^2}$ is larger than 0.4. The selection requirements used in this phenomenology study yield mutually exclusive event categories.

9.8.4 Hadronic decays of both W bosons

We consider the hadronic decays of both W bosons, leading to the production of at least two large-R jets with $p_T^{\text{jet}} > 100$ GeV, and no isolated leptons with $p_T^{\ell} > 25$ GeV. The latter condition ensures the exclusivity of the W^+W^- signal event category.

Not all of the W boson jets result in single large-R jets. Most of the time, these are partially merged, so they cannot all be tagged in a single large-R jet. In order to account for these partially merged jet topologies, we combine nearby large-R jets with $p_T > 25$ GeV if they are separated by $\Delta R_{jj} = \sqrt{\Delta\phi_{jj}^2 + \Delta y_{jj}^2} < 2$ with respect to the hardest p_T^{jet} candidates, and calculate the vector sum of the four-momenta of these two nearby jets. If they yield a better invariant mass on the reconstructed W boson jet candidate, the event is retained, and the jets are merged. If the softer large-R jets do not yield a better W boson invariant mass (i.e., yields a m_j closer to $m_W = 80.379$ GeV), or if they are farther than $\Delta R_{jj} > 2$, the event is rejected. In this study, we refer to this procedure as "jet merging". For SM $\gamma\gamma \to W^+W^-$, the latter constitutes about 45% of events in the fully-hadronic final state (it occurs about 25% of the semi-leptonic cases). Events with exactly two large-R jets or two partially-merged jets are kept after this requirement. This set of requirements is referred to as "preselection" in the rest of the paper.

Each of the reconstructed large-R jets must have an invariant mass of $70 < m_{\text{j1}} < 90$ GeV and $60 < m_{\text{j2}} < 85$ GeV for the leading and second leading jet in mass, respectively (see Fig. 9.20). In order to favor exclusive W^+W^- events and suppress pileup background, we require the two large-R jets to be back-to-back in the transverse plane since the W bosons recoil against each other since there is no additional radiation in the process. In

practice, we consider only large-R jets strictly back-to-back $|\Delta\phi - \pi| < 0.01$ rad. As shown in Fig. 9.21, this selection requirement largely suppresses the pileup background, while the central exclusive production is retained. This is a particularly important selection requirement, as it exploits the $2 \to 2$ topology of the signal process. Event candidates are required to have $m_{WW} > 500$ GeV. This is to further suppress non-diffractive backgrounds, which dominate at lower invariant masses m_{WW}. Since exclusive W boson are balanced in the transverse plane, we further require them to satisfy $p_{\mathrm{T}}^{\mathrm{j2}}/p_{\mathrm{T}}^{\mathrm{j1}} > 0.90$. Similar requirements were found to optimize the signal-to-background ratio in exclusive $\gamma\gamma$ production and exclusive $Z\gamma$ production phenomenology studies (315; 314).

In order to suppress the remaining pileup background, we exploit the kinematic correlation between the intact protons and the reconstructed W^+W^- system for exclusive W^+W^- production. The mass and rapidity computed using the W^+W^- bosons are, within uncertainties, similar to the ones computed using ξ_1 and ξ_2 of the protons, The distributions of $y_{pp} - y_{WW}$ and m_{pp}/m_{WW} are shown in Figs. 9.22. In Figs. 9.22, signal events are observed to peak at $y_{pp} - y_{WW} = 0$ and $m_{pp}/m_{WW} = 1$ due to the aforementioned kinematic correlation between protons and the W^+W^- system. The distributions of pileup background events in these variables are respectively found to be rather flat for $y_{pp} - y_{WW}$ or decreasing for m_{pp}/m_{WW} in the hadronic channel, since the protons are uncorrelated to the central W^+W^- boson pair. We select events that satisfy $|y_{pp} - y_{WW}| < 0.2$ and $0.7 < m_{pp}/m_{WW} < 1.6$ simultaneously. This selection requirement strongly suppresses the remaining pileup backgrounds, which in turn allows us to extract the exclusive W^+W^- contributions. A summary of the number of events assuming a luminosity of 300 fb^{-1} at $\sqrt{s} = 14$ TeV is given in Table 9.6. We assume, in addition, a precision of the fast timing detectors of either 50 or 20 ps in order to measure the proton time-of-flight. We predict a W^+W^- exclusive signal of 92 events for a background of about 1640 events for 300 fb^{-1}. The QCD jet component dominates by far the pileup background in the fully-hadronic channel.

For this phenomenology study, we used the invariant mass of the jets to separate quark and gluon jets from QCD interactions from the W boson jets created in central exclusive production, as this is one of the most robust jet substructure variables (342). The bottom two rows in Table 9.6 represent an estimation of possible further suppression of the remaining QCD jet background in association with pileup protons based on the use of N-subjettiness ratio τ_2/τ_1 cuts, which quantifies the likelihood that the large-R jet has a two-prong substructure, as first suggested in Ref. (346), further confirmed by the CMS and ATLAS experiments (338; 336; 337). Based on these performance reports, it was shown that the N-subjettiness ratio cut $\tau_2/\tau_1 < 0.5$ can improve the QCD jet background rejection by an additional factor of ≈ 6 in addition to the jet mass selection requirement. The jet mass requirement used in our analysis, together with a τ_2/τ_1 requirement, yield a combined inefficiency of about 20% for W boson jets decay relative to the yields extracted with the jet mass cut alone, while the background rejection factor from the jet mass requirement together with the ratio τ_2/τ_1 cut increases by a factor of about 6 when tagging both W boson jets, relative to the jet mass cut alone (338). This estimation assumes that the jet mass requirement and the τ_2/τ_1 cut is mostly independent from the jet kinematics, which seems to be true for most of the p_T values of interest as reported by the CMS in Ref (338). Thus, the 1600 events at 20 ps time-of-flight precision could be further reduced to about 270 with the additional use of N-subjettiness ratio, with a decrease in the signal efficiency of about 80% relative to the jet mass requirement alone used in our study. A combination of very precise time-of-flight measurement, together with a judicious choice of jet substructure variables, could help cope with the large QCD jets background, leading to a signal-to-background ratio of about 25%.

Recently, ATLAS presented a new set of tools based on the so-called Unified Flow Object (UFO) algorithm (347), which showed a significant improvement on the background rejection rate of QCD jets while retaining a good signal efficiency rate for retaining W boson jets. Thus, the hadronic channel can become quite competitive in the study of high

Selection requirements	Excl. W^+W^-	W^+W^- +pileup	WZ pileup	ZZ +pileup	Wj +pileup	Zj +pileup	$t\bar{t}$ +pileup	single-top +pileup	QCD jets +pileup	Total bkg.
Preselection	990	1.4×10^5	7.8×10^4	2.7×10^4	1.9×10^7	7.7×10^6	1.1×10^6	5.2×10^5	1.4×10^{10}	1.4×10^{10}
$70 < m_{j1} < 90$ GeV	591	4.1×10^4	1.4×10^4	6×10^3	3.8×10^6	1.1×10^6	2.04×10^5	9.30×10^4	8.3×10^8	8.34×10^8
$65 < m_{j2} < 85$ GeV	274	1.5×10^4	4×10^3	2.1×10^3	2.5×10^5	6.8×10^4	6.35×10^4	4.72×10^3	4.62×10^7	4.7×10^7
$\mid \Delta\phi_{j1\,j2} - \pi \mid < 0.01$	203	2.2×10^3	521	265	2.4×10^4	5.1×10^3	2.4×10^3	237	3.62×10^6	3.65×10^6
$m_{WW} > 500$ GeV	143	1.09×10^3	264	151	1.9×10^4	4.2×10^3	1.2×10^3	139	2.43×10^6	2.45×10^6
$p_T^{j2}/p_T^{j1} > 0.90$	142	1.04×10^3	221	135	1.0×10^4	2.48×10^3	708	65	1.43×10^6	1.45×10^6
$\lvert y_{pp} - y_{WW} \rvert < 0.2$	100	182	31	27	1112	201	28	11	1.51×10^5	1.52×10^5
$0.7 < m_{pp}/m_{WW} < 1.6$	95	92	15	13	589	87	0	7	6.45×10^4	6.53×10^4
$\delta t = 50$ ps	92	12	0	1	34	0	0	0	3.8×10^3	3.9×10^3
$\delta t = 20$ ps	92	6	0	0	15	2	0	0	1.62×10^3	1.64×10^3
$\delta t = 50$ ps + τ_2/τ_1 estimation	69	9	0	0	29	0	0	0	633	670
$\delta t = 20$ ps + τ_2/τ_1 estimation	69	0	0	0	3	0	0	0	270	273

Table 9.6: Number of events for 300 fb^{-1} at 14 TeV after each selection criterion for W^+W^- exclusive signal (when both Ws decays hadronically into large-R jets), and non-diffractive W^+W^-+ pileup, $W^\pm Z$+ pileup, ZZ+ pileup, W+jet backgrounds. The preselection requires the presence of two large-R jets of $p_T > 100$ GeV each, no isolated lepton and at least one proton on each side with $0.015 < \xi < 0.15$. The four first lines describe the selection on the W bosons sides using the central CMS or ATLAS detector, the two next lines the exclusivity requirements using the proton detectors. Yields estimated for time-of-flight difference with precision values of 50 ps or 20 ps are shown as well. The bottom rows correspond to an estimation based on the N-subjettiness ratio τ_2/τ_1 cut based on ATLAS and CMS performance results (338; 336; 337).

mass central exclusive W^+W^- production, if it is supplemented by these jet substructure techniques developed by ATLAS and CMS. This calls for a judicious selection of jet substructure variables or use of advanced techniques by the experimental collaborations. For a thorough review on the performance of these methods, which are outside of the scope of this study, we refer to Ref. (342).

9.8.5 Semi-leptonic decays of the W bosons

Turning to the semi-leptonic decay scenario, we start by requiring the presence of at least one large-R jet with $p_T^{\text{jet}} > 25$ GeV and exactly one charged isolated lepton of $p_T^\ell > 25$ GeV. As in the previous section, if there is more than one large-R jet, we merge jets within $\Delta R_{jj} < 2$ with the criteria described in Sec. 9.8.4, then exactly one large-R jet or merged

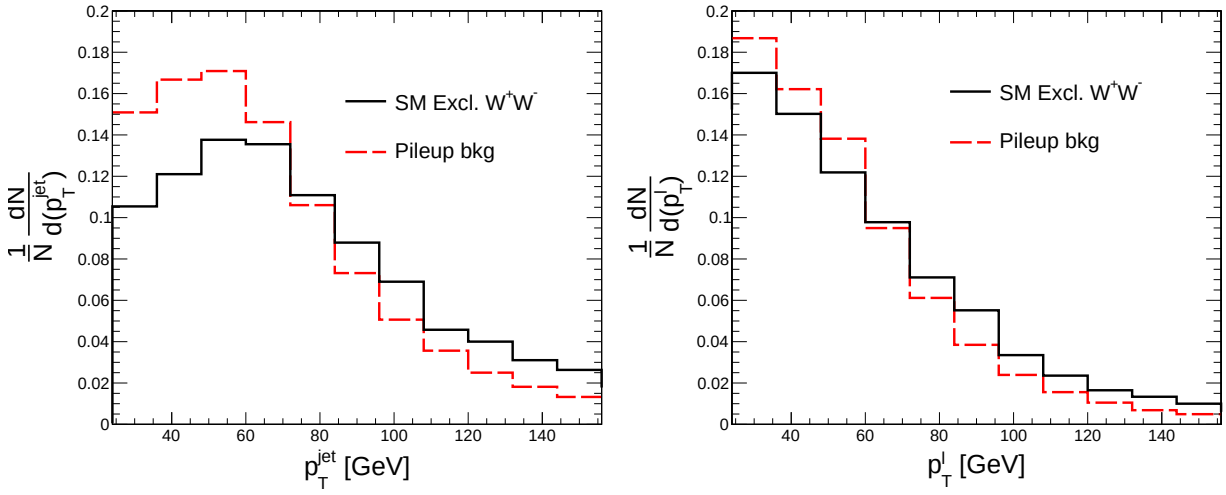

Figure 9.23: Jet p_T (left) and charged lepton p_T (right) distributions normalized to unity for semi-leptonic SM exclusive W^+W^- production (black full line) and pileup background (red dashed line) after preselection requirements. The figures match those presented in Ref. (5).

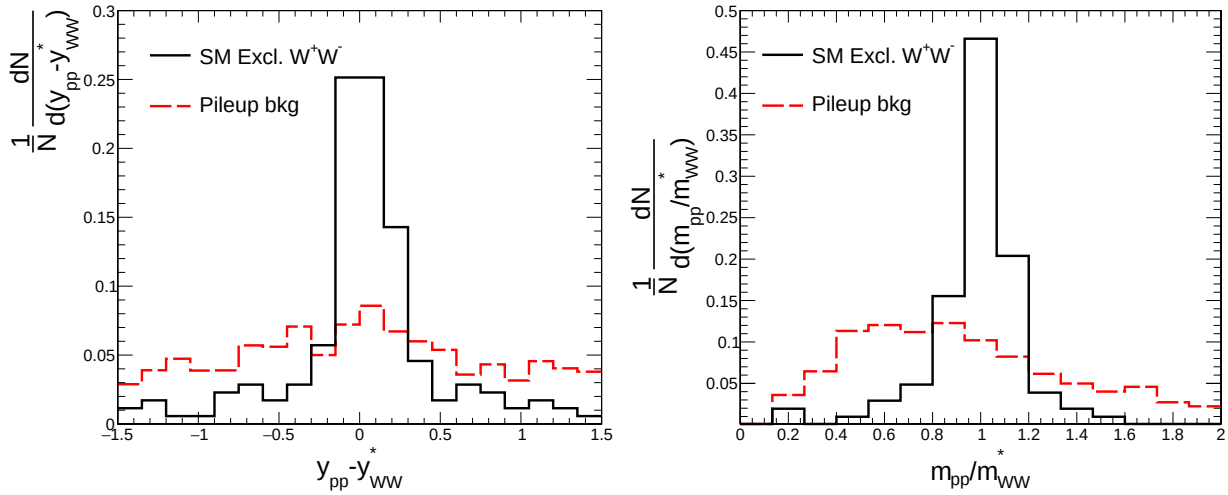

Figure 9.24: Rapidity difference $y_{pp} - y^*_{WW}$ (left) and mass ratio m_{pp}/m^*_{WW} (right) distributions for semi-leptonic decays of SM exclusive W^+W^- events (black full line) and pileup background (red dashed line) normalized to unity, after preselection requirements, and lepton jet kinematic requirements summarized in Table 9.7. The figures match those presented in Ref. (5).

Selection requirements	Excl. W^+W^-	W^+W^- +pileup	$W^\pm Z$ +pileup	ZZ +pileup	Wj +pileup	Zj +pileup	$t\bar{t}$ +pileup	single-top +pileup	Total bkg.
Preselection	3.9×10^3	6×10^5	7.3×10^4	5.9×10^4	6.8×10^6	5.3×10^5	1.3×10^5	3.2×10^4	8.3×10^6
$p_{\mathrm{T}}^{\mathrm{j1}} > 120$ GeV	7.6×10^2	5.8×10^4	8.4×10^3	7.1×10^3	3.6×10^6	2.6×10^5	4.4×10^4	1.9×10^4	4×10^6
$p_{\mathrm{T}}^{\ell} > 100$ GeV	334	2.3×10^4	3014	2.52×10^3	1.56×10^6	1.92×10^5	1.5×10^4	5979	1.8×10^6
$m^*_{WW} > 500$ GeV	144	7698	1040	1077	70595	7970	699	987	9×10^4
$70 < m_{\mathrm{j1}} < 90$ GeV	74	2035	171	216	4211	459	224	14	7331
$p_{\mathrm{T}}^{\mathrm{miss}} > 30$ GeV	52	1628	141	172	3540	242	196	0	5919
$\lvert y_{pp} - y^*_{WW}\rvert < 0.2$	29	265	31	31	587	28	84	0	1026
$0.7 < m_{pp}/m^*_{WW} < 1.3$	27	101	13	16	168	16	28	0	342
$\delta t = 50$ ps	22	6	2	0.5	10	1	2	0	21.5
$\delta t = 20$ ps	22	5	1	0	4	0	1	0	11

Table 9.7: Number of events for 300 fb^{-1} after each selection criterion for W^+W^- exclusive signal (when one W boson decays leptonically and the other one into hadrons), non-diffractive W^+W^-+ pileup, $W^\pm Z$+ pileup, ZZ+ pileup, $W^\pm$+jet +pileup, $t\bar{t}$+pileup, single-top+pileup backgrounds. The bottom two rows correspond to the options of time-of-flight difference measurement of the scattered protons with precision of 50 ps or 20 ps.

dijet with $p_T^{\mathrm{j}} > 120$ GeV. The slightly larger p_T^{jet} is optimized to yield a better signal-to-background ratio. This is the respective "preselection" step for this channel.

Unlike the hadronic decay channel, a complete reconstruction of the final state is not possible in the semi-leptonic decay channel because of the undetected neutrino. The energy and momentum of the neutrino along the beam direction, E^ν and p_z^ν, are unknown. In order to estimate the invariant mass and rapidity of the W^+W^- system (which is later used to calculate the correlations between the central system and the forward protons), we consider $E^\nu = p_T^{\mathrm{miss}}$ and $p_z^\nu = 0$ strictly for the m_{WW} and y_{WW} evaluation, and assign the missing transverse momentum of the neutrino with p_T^{miss}, as is usually done. The choice of fixing $p_z^\nu = 0$ is based on the p_z^ν distribution observed in simulated events, which peaks around 0 with a standard deviation of about 100 GeV for central exclusive W^+W^- events. This spread of 100 GeV results in an additional smearing on the estimated invariant mass and rapidity of the reconstructed W^+W^- kinematics. Since we are not reconstructing all the decay products of the W^+W^- system due to the undetected neutrino, we refer to the mass and rapidity of the diboson event candidate as m^*_{WW} and y^*_{WW}, respectively, to emphasize that this is an estimation of the actual variables m_{WW} and y_{WW} that we aim to ideally reconstruct. The m^*_{WW} and y^*_{WW} variables were comparable with the y_{WW} and m_{WW}

variables at generator-level. We found that, on average, y^*_{WW} is closer to 0 than the true y_{WW}, while m^*_{WW} is lower than m_{WW} on average, due to the missing E^ν and p^ν_Z information. By comparing this estimation with truth-level information available from the MC generated event (i.e., assuming we could indeed reconstruct the neutrino E^ν and p^ν_z), we found that the exclusive W^+W^- signal yield would improve by a factor of about 1.6 relative to that obtained with our conservative approach. The E^ν and p^ν_z of the neutrino could be estimated, up to a two-fold ambiguity, by assuming that the undetected neutrino, together with the detected charged lepton, has to yield the rest mass of the W boson. Such a method was employed by CDF in Ref. (348). Such an approach could be considered for the experimental analysis for Run-3 at the CERN LHC.

In order to suppress the non-diffractive backgrounds, and to favor boosted topologies for large-R jet reconstruction, we further require that $p_T^{\rm jet} > 120$ GeV and $p_T^\ell > 100$ GeV. These requirements are determined based on the distributions observed in the pileup background and SM exclusive W^+W^- signal, as shown in Fig. 9.23. Furthermore, the invariant mass of the reconstructed central system is required to be m^*_{WW} >600 GeV. The aforementioned requirement further suppresses the non-diffractive background, and favors the reconstruction of boosted topologies of the W boson decay products in large-R jets. We use the reconstructed $p_T^{\rm miss} > 30$ GeV to estimate the $p_{\rm T}$ carried away by the undetected neutrino.

The rapidity difference between the central system and the forward two protons is taken as $|y^*_{WW} - y_{pp}| < 0.2$ and the mass ratio $0.7 < m_{pp}/m^*_{WW} < 1.3$ for the semi-leptonic channel, as shown in Fig. 9.24. The latter set of criteria are optimized in order to reject as much pileup background as possible, while retaining most of the SM exclusive W^+W^- events. Note that the selection window on these variables is narrower in this final-state, even if we do not have the E^ν and p^ν_z of the missing neutrino. The reason is that we do not have the same smearing effects as in the fully-hadronic final state. It is also worth to note that we can still exploit these kinematic correlations between the forward protons

and central W boson pair in semi-leptonic final states. The number of events for signal and background after each selection criterion is given in Table 9.7 assuming in addition a resolution of the fast timing detectors of either 50 or 20 ps in order to measure the proton time-of-flight. With this set of selection criterion, we expect 22 SM $\gamma\gamma \to W^+W^-$ events in the semi-leptonic channel, versus a expected background of 11 events, which is largely dominated by $W^{\pm}$+jets with pileup protons. We found that the acoplanarity between the charged lepton and the large-R jet does not provide much discrimination between pileup backgrounds and central exclusive W^+W^- events. For this reason, no acoplanarity cut is applied in the semi-leptonic channel.

9.8.6 Discussion of SM analysis

We note that only in the semi-leptonic and hadronic channels one can access high mass W^+W^- production with large W boson transverse momenta p_T^W for future differential cross section studies, which are absolutely necessary to test predictions based on the SM non-abelian coupling between photons and W bosons. The purely leptonic channel offers the possibility of studying the SM processes, albeit at lower masses and softer p_T of the W boson. For leptons with $p_T^{\ell 1,\ell 2} > 100$ GeV, the expected number of exclusive W^+W^- events is 0. In other words, for harder $\gamma\gamma \to W^+W^-$ production can only be studied in the semi-leptonic and hadronic channels.

We emphasize that exclusive production of W^+W^- boson pairs can be used as a standard candle process for a better understanding of the RP detector calibration and proton reconstruction, as well as for a better understanding of trigger efficiency studies. In fact, since every decay channel is independent from one another, they can be used separately to cross check the proton spectrometer overall calibration. This is complementary to the $pp \to p\ell^+\ell^- p$ process, where $\ell = e, \mu$, used by the CMS-TOTEM and ATLAS Collaborations to calibrate their proton spectrometers (258; 259). More concretely, calibration at higher ξ can be achieved with the hadronic and semi-leptonic channels, while the cali-

bration at low ξ could be done with the purely leptonic channel.

9.8.7 Anomalous $\gamma\gamma \to W^+W^-$ scattering

Deviations from the SM from possible new physics contributions at energies much larger than those accessible at the LHC can be described in an EFT formalism. Indeed, by integrating out potential heavy degrees of freedom present at the new physics energy scale or beyond, residual interaction terms are obtained at energy scales presently probed at LHC energies (349; 350). This corresponds to gauge invariant non-renormalizable effective operators, which allows us to constrain several families of extensions of the SM in a single framework. In this study, we consider dimension-six operators directly related to $\gamma\gamma W^+W^-$ quartic couplings. By imposing $\mathrm{U(1)_{em}}$ and global custodial $\mathrm{SU(2)_C}$ symmetries, two such operators are allowed with their respective coupling strength parameters denoted by a_0^W and a_C^W. The EFT framework used in the present paper follows of Ref. (231; 313),

$$\mathscr{L}_6^{\mathrm{eff}} = -\frac{e^2}{8} a_0^W F_{\mu\nu} F^{\mu\nu} W^{+\alpha} W^-_{\alpha} - \frac{e^2}{16} a_C^W F_{\mu\alpha} F^{\mu\beta} \left(W^{+\alpha} W^-_{\beta} + W^{-\alpha} W^+_{\beta} \right) \tag{9.28}$$

where F and W represent the field strength tensors of electromagnetic and weak interactions after EWSB, respectively. The interaction $\gamma\gamma \to W^+W^-$ induced by this effective operator may violate unitarity at high energies for sufficiently large couplings. In order to suppress this nonphysical feature of the anomalous $\gamma\gamma \to W^+W^-$ process, we consider a dipole form factor with a cutoff scale $\Lambda_{\mathrm{cutoff}}$ which modifies the coupling as:

$$a_{0,C}^W(W_{\gamma\gamma}^2) \to \frac{a_{0,C}^W}{\left(1 + W_{\gamma\gamma}^2/\Lambda_{\mathrm{cutoff}}^2\right)^2} \tag{9.29}$$

here, $W_{\gamma\gamma}$ is the center of mass energy of the initial-state diphoton system and $\Lambda_{\mathrm{cutoff}}$ represents the energy scale where new physics may manifest. For our projections, we consider a scenario where $\Lambda_{\mathrm{cutoff}} = 2$ TeV, and the case where $\Lambda_{\mathrm{cutoff}} \to \infty$, which corresponds

to the case where unitarity might be violated, i.e., no form factor. In our case, most of the events produced at high W^+W^- invariant mass are rejected in our analysis due to the RP acceptance cut, $\xi < 0.15$. Because of this, it has been found in previous studies with intact protons that the difference in the results with and without form factors is not very large (see for example Refs. (314; 315; 231)). A direct relation between dimension-eight and dimension-six couplings $\gamma\gamma W^+W^-$ operator is found when assuming that an anomalous $WWZ\gamma$ vertex vanishes, as discussed in Refs. (351; 352). Therefore, our projections can be mapped to the dimension-eight couplings under this assumption.

In contrast to the SM $\gamma\gamma \to W^+W^-$ process, the production rate of central exclusive W^+W^- boson pairs induced by anomalous couplings increases with the invariant mass of the diboson system and with the p_{T} of each W boson, p_T^W. This means that boosted topologies will be largely favored in anomalous interactions, distinct from SM expectations. Since potential events induced by anomalous coupling interactions are expected to appear mostly at large m_{WW} and p_T^W, the search strategy originally tailored to isolate SM central exclusive W^+W^- production needs to be modified accordingly. For illustration, we show the leading and second leading large-R jet p_T and the reconstructed W^+W^- mass for SM and anomalous W^+W^- production in the hadronic channel in Figs. 9.25 and 9.26, respectively. The anomalous contribution is shown in black for different values of anomalous couplings, whereas the SM $\gamma\gamma \to W^+W^-$ contribution is shown in red dashed line. We note that events induced by anomalous interactions contribution mostly at larger jet p_T and mass.

In the hadronic case, we require the p_{T} of both large-R jets to be $p_T^{\mathrm{jet}} > 400$ GeV (as seen in Fig. 9.25). Similarly, we require that the invariant mass of the reconstructed W^+W^- candidate to be $m_{WW} > 1$ TeV (see Fig. 9.26). The latter cut reduces most of the residual SM exclusive W^+W^- contributions, while retaining a large fraction of anomalous W^+W^- event candidates. After these updated selection requirements, we end up with 87 pileup background events, and about 5 SM $\gamma\gamma \to WW$ background events. This is used to extract the

respective projections. In a similar way, the higher p_T and mass requirements eliminate most of the SM $\gamma\gamma \to W^+W^-$ in case of the semi-leptonic decays. In this case, we tighten the jet and lepton kinematics as $p_T^{\ell} > 250$ GeV and $p_T^{\text{jet}} > 350$ GeV, with $m_{WW}^{*} > 1200$ GeV. We end up with a pileup-background free environment after these updated cuts, with an expected number of 1 SM $\gamma\gamma \to WW$ events in the semi-leptonic channel. The detailed results are given in our paper (5).

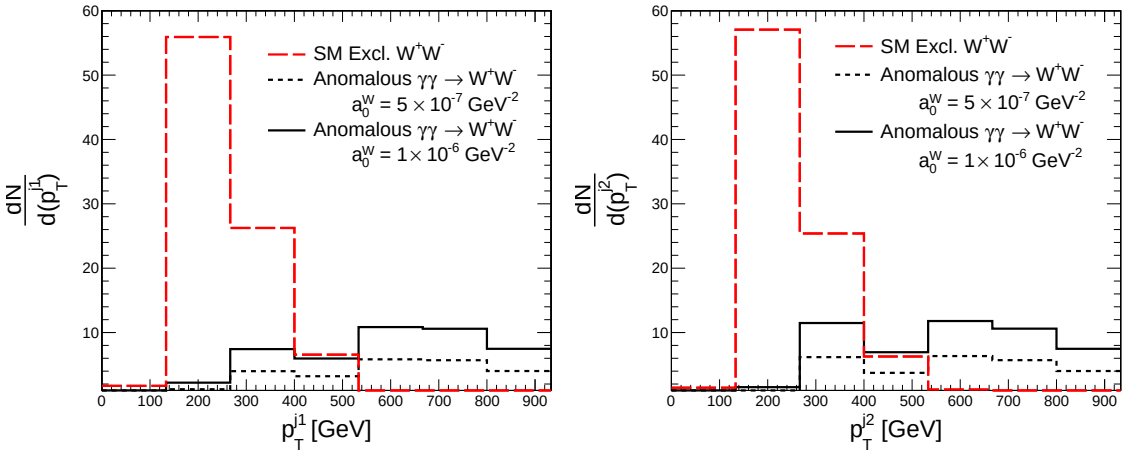

Figure 9.25: Leading (left) and second leading (right) large-R jet p_T for the $\gamma\gamma \to W^+W^-$ process, where each W boson decays hadronically. The anomalous contribution is shown in black solid and dashed lines, which represent two different values of anomalous coupling $a_0^W = 5 \times 10^{-7}$ and $a_0^W = 10^{-6}$ GeV^{-2} with fixed $a_C^W = 0$. The SM $\gamma\gamma \to W^+W^-$ contribution is shown in the red dashed line (after time-of-flight requirement, normalized to 300 fb^{-1} of luminosity). No matching cut in rapidity or mass is applied for these plots. The figures match those presented in Ref. (5).

For the leptonic final state, we use the same strategies as in previously published work (195; 230; 231). The one-dimensional sensitivity on anomalous couplings is of the order of 4.3×10^{-6} GeV^{-2} and 1×10^{-5} GeV^{-2} for a_0^W and a_C^W at 95% CL for the leptonic final state alone, respectively. We note here that, in contrast to the findings of the SM analysis, the boosted large-R jet topologies are significantly favored for events with a contribution from anomalous coupling vertices. The leptonic channel is not as sensitive to deviations from the SM as the hadronic or semi-leptonic channel. This is mostly because of the much smaller branching fraction which does not allow to populate the phase space at large m_{WW}

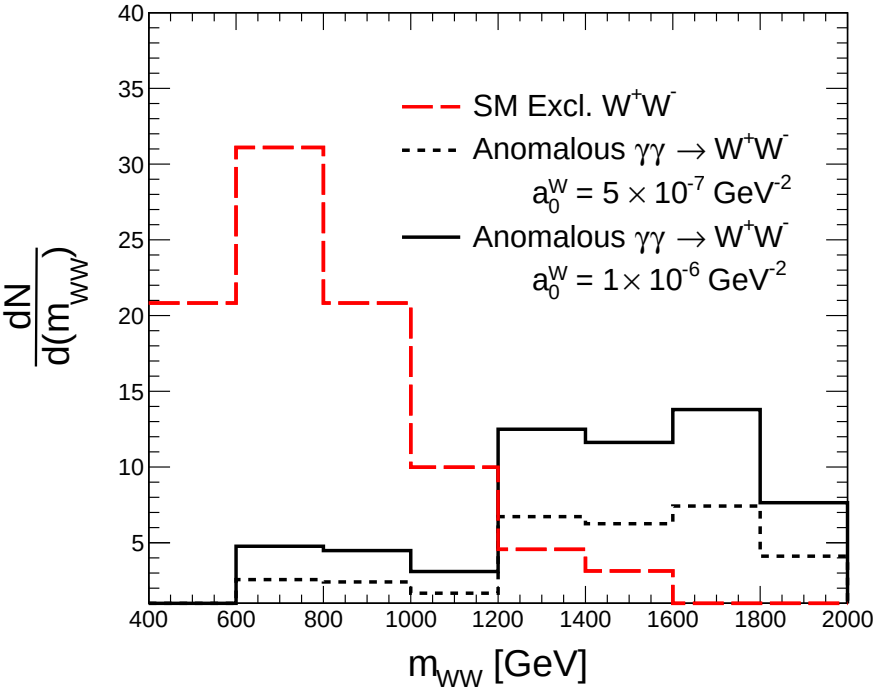

Figure 9.26: W^+W^- invariant mass reconstructed using the fully-hadronic final state. The SM $\gamma\gamma \to W^+W^-$ contribution is in red dashed line, whereas the anomalous contribution is in black solid and dashed lines, corresponding to different coupling values. The distributions are normalized to an integrated luminosity of 300 fb^{-1}. Contributions induced by anomalous couplings are present mostly at higher mass (no form factor applied). The figures match those presented in Ref. (5).

and p_T^W, where anomalous coupling contributions are most significant.

9.8.8 Results of anomalous coupling studies

The expected 95% CL limit and 5σ sensitivity for a_C^W and a_0^W anomalous couplings for 300 fb^{-1} of luminosity with and without form factor are shown in Figs. 9.27 and 9.28, respectively, and the one-dimensional projections on the anomalous couplings are presented in Table 9.8. The statistical significance is calculated with $Z = \sqrt{2(S+B)\ln(1+S/B) - 2S}$, with S and B representing the signal and background event counts, respectively (353). By combining all the decay channels, we obtain a sensitivity of 3.7×10^{-7} GeV^{-2} for a_0^W and 3×10^{-6} GeV^{-2} for a_C^W at 95%CL, when fixing one of the couplings to 0 and varying the other, without the use of form factor. The hadronic channel has the best sensitivity

for deviations treated in the dimension-six EFT formalism, as shown explicitly in the expected limit calculation in Table 9.8. In order to draw a comparison with the hadronic, semi-leptonic, and leptonic final state results, we show the expected limits of the leptonic decay using similar selection criteria as in Ref. (231) in Table 9.8. The sensitivity in the leptonic channel alone is similar for anomalous couplings with and without form factor, since form factor acts at larger invariant masses and p_T, which the leptonic channel does not populate completely. For these projections, we do not assume possible improvements with jet substructure variable cuts. We estimate that the one-dimensional bounds could be potentially be further improved down to values of $|a_0^W| < 3 \times 10^{-7}$ GeV^{-2} and $|a_C^W| < 7.4 \times 10^{-7}$ GeV^{-2} at 95% CL by applying a similar cut on the N-subjettiness ratio $\tau_2/\tau_1 < 0.5$, as discussed in Section 9.8.4, i.e., an improvement of factor of ≈ 1.3 over our projections without the use of these advanced techniques. This means that, in searching for these anomalous contributions, jet substructure techniques are not as crucial as in the SM analysis.

The ATLAS and CMS experiments set one-dimensional bounds on the interaction couplings without form factors of $|a_0^W| < 1.1 \times 10^{-6}$ GeV^{-2} and $|a_C^W| < 4.1 \times 10^{-5}$ GeV^{-2} at 95% CL based on the 7 and 8 TeV analysis results (331; 332; 333). However, a direct comparison of our projections to existing limits published by the ATLAS and CMS experiments is not very straightforward. The reason is that, in these studies, the anomalous production of W^+W^- pairs is allowed to contribute at arbitrarily large invariant masses of the diboson system. As mentioned in Sec. 9.8.7, the production cross section of the $\gamma\gamma \to W^+W^-$ interaction induced by the dimension-six effective operator increases with m_{WW}, eventually leading to a violation of unitarity. Thus, the sensitivity is artificially enhanced in studies where no upper cut in the invariant mass of the W boson pair is imposed. In our case, such an upperbound in mass is imposed due to the acceptance in ξ of the protons reconstructed at the RPs. This has been noted in other studies with anomalous coupling interactions using the proton tagging technique, such as in Refs. (314; 315). To avoid quoting limits on

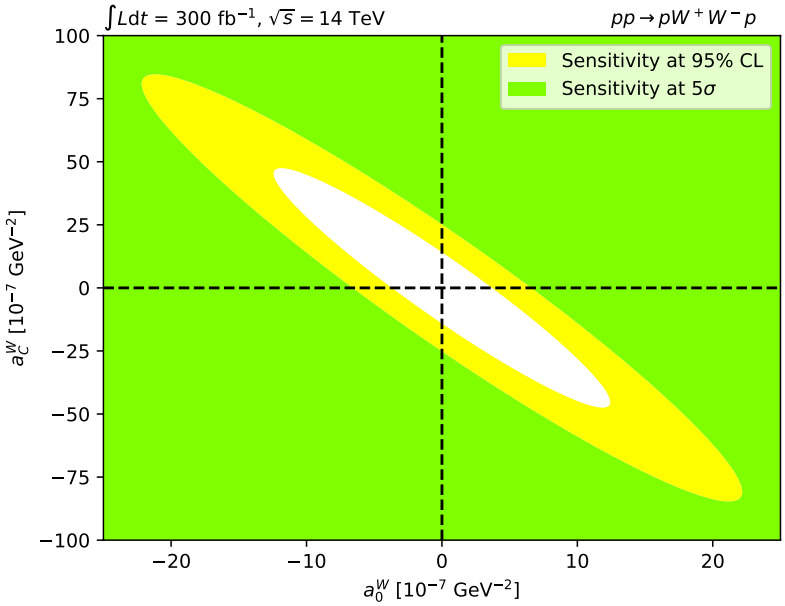

Figure 9.27: Projected sensitivities on the anomalous coupling parameters a_0^W and a_C^W without form factors. The projections are shown for $pp \to pW^+W^-p$ at 14 TeV assuming an integrated luminosity of 300 fb^{-1}. The yellow and green areas represent respectively the projected sensitivities at 95% CL and 5σ combining the hadronic, semi-leptonic, and leptonic decay channels of the W^+W^- system. The blank area in the center represents the region where we do not expect sensitivity to the anomalous coupling parameter. Time-of-flight measurements with 20 ps precision is assumed. The figures match those presented in Ref. (5).

the kinematic region where unitarity violation takes place, ATLAS and CMS presented exclusion limits on the anomalous couplings using a dipole form factor with an energy cutoff at $\Lambda_{\text{cutoff}} = 500$ GeV (331; 332; 333). The one-dimensional limits at 95% CL with said form factor are $|a_0^W| < 0.9 \times 10^{-4}$ GeV^{-2} and $|a_C^W| < 3.6 \times 10^{-4}$ GeV^{-2} (331; 332; 333). However, the energy cutoff $\Lambda_{\text{cutoff}} = 500$ GeV used in the CMS and ATLAS analyses is too low for the study presented in this study, given that the minimum invariant mass of the W boson pair in our study starts at 1 TeV, i.e., the cross section vanishes for the phase-space we can probe. For these reasons, a direct comparison with existing limits is not possible. No limits on anomalous couplings from the 13 TeV analysis of $\gamma^*\gamma^* \to W^+W^-$ by ATLAS were reported.

We draw a comparison with projections presented in the CMS-TOTEM PPS technical

design report (195). In these studies, only leptonic decays are considered, for $0.015 < \xi < 0.15$. PPS expects $4 \times 10^{-6} (1 \times 10^{-5})$ GeV^{-2} for $|a_0^W|$ ($|a_C^W|$) in the leptonic channel alone for an integrated luminosity of 100 fb^{-1} at 13 TeV (195), within the same order of magnitude as those obtained here for the leptonic channel as expected. Thus, when considering the hadronic and semi-leptonic final states, we can improve this bound by an order of magnitude over those original projections. In a recent study (354), it was proposed to use central exclusive $W^+W^-\gamma$ production to probe non-abelian couplings between photons and W bosons of the SM. The latter can be used to constrain anomalous gauge quartic couplings, and it was found that for the dimension-six operators couplings they have a sensitivity of $|a_0^W| < 10^{-6}$ GeV^{-2} at 95% CL, i.e., similar to the sensitivity we have in leptonic decays of exclusive W^+W^- events. It would be interesting to see how much the

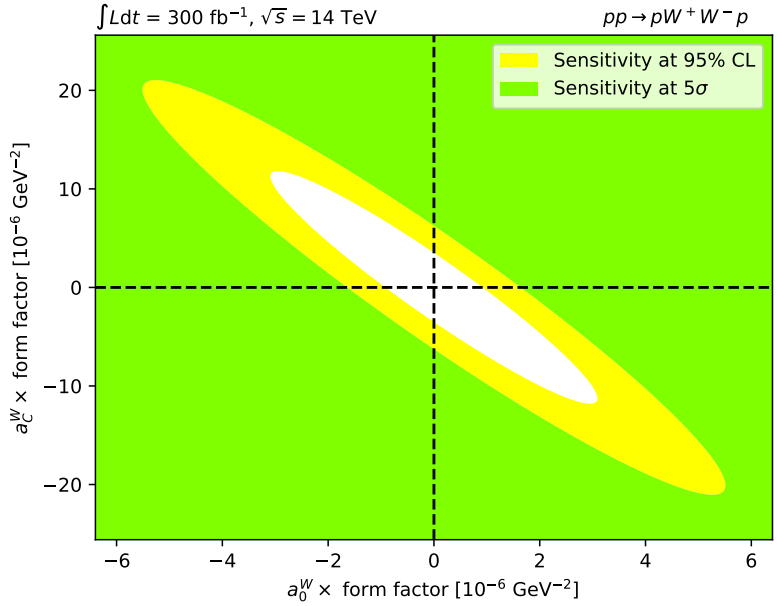

Figure 9.28: Projected sensitivities on the anomalous coupling parameters a_0^W and a_C^W with a dipole form factor with cutoff energy of $\Lambda_{\text{cutoff}} = 2$ TeV. The projections are shown for $pp \to pW^+W^-p$ at 14 TeV assuming an integrated luminosity of 300 fb^{-1}. The yellow and green areas represent the projected sensitivities at 95% CL and 5σ, respectively. The results correspond to a combination of hadronic, semi-leptonic, and leptonic decay channels of the W^+W^- system. The blank area in the center represents the region where we do not expect sensitivity to the anomalous coupling parameter. Time-of-flight measurements with 20 ps precision is assumed. The figures match those presented in Ref. (5).

W^+W^- decay channel	Hadronic		Semi-leptonic		Leptonic		Combined	
Coupling [10^{-7} GeV^{-2}]	5σ	95% CL	5σ	95% CL	5σ	95% CL	5σ	95% CL
$\lvert a_0^W\rvert$, $a_C^W = 0$ (no form factor)	6.9	3.8	10	4.9	43	24	6.6	3.7
$\lvert a_0^W\rvert$, $a_C^W = 0$ (form factor)	17	9.4	27	13	43	24	16	9.2
$\lvert a_C^W\rvert$, $a_0^W = 0$ (no form factor)	17	9.5	25	12	107	59	16	9
$\lvert a_C^W\rvert$, $a_0^W = 0$ (form factor)	42.0	23	67	33	107	59	41	23

Table 9.8: Sensitivities to the anomalous couplings a_0^W and a_C^W assuming an integrated luminosity of 300 fb^{-1} and a center of mass energy of $\sqrt{s} = 14$ TeV. The sensitivities for each decay channel of the W^+W^- is displayed in the columns. The combined sensitivities are presented in the last column. Sensitivities assuming no form factor and a form factor with cutoff scale $\Lambda_{\text{cutoff}} = 2$ TeV are displayed in the rows. These sensitivities establish the coupling values probed at 5σ or those which could be excluded at 95% CL.

projections presented in Ref. (354) could be improved if semi-leptonic or hadronic decays of W bosons are considered. In Ref. (319), the sensitivity to the same anomalous quartic vertex is estimated for the Future Circular Collider in electron-proton mode (FCC-he) at $\sqrt{s} = 5.29$ TeV at an integrated luminosity of 1 ab^{-1} of luminosity, with a focus on the process $e^- p \to e^- W^+ \gamma q X$. The sensitivity to interaction couplings $|f_{M,0}/\Lambda^4|$ associated to dimension-eight $\gamma\gamma W^+W^-$ operators is expected to be of the order of 9 TeV^{-4} at 95% CL under the aforementioned assumptions (319). This translates to a projection on $|a_0^W| < 2.3 \times 10^{-7}$ GeV^{-2} at 95% CL, with the relations between dimension-six and dimension-eight operators described in Refs. (351; 352). Our projections are thus competitive with these potential future collider scenarios, while ours are readily accessible at current LHC collider energies and running conditions.

9.9 Summary of the Chapter

In this Chapter, we covered some photon-photon physics phenomenology studies that target the prospects for new physics discovery in central exclusive production processes with intact protons, $pp \to pXp$, where the two outgoing protons are scattered at small angles with respect to the beam direction, and retain most of the original beam energy,

and X is a central system produced by two-photon fusion.

The studies where the author of the thesis directly contributed to are three: one of them is the study of $\gamma\gamma\gamma Z$ couplings via the $\gamma\gamma \to \gamma Z$ scattering process, the second is related to the search for axion-like particles (ALPs) in light-by-light scattering ($\gamma\gamma \to \gamma\gamma$) in pp collisions, which was then extended to include proton-lead (pPb) and argon-argon (ArAr) collisions, and the third one is related to an improvement in the strategies used to study the $\gamma\gamma \to WW$ process at the LHC. The tagging of the protons drastically reduces the background in all cases, which allows to study very rare high-energy photon-photon interactions. The main takeaways from these studies is summarized below.

The contributions to the $\gamma\gamma\gamma Z$ couplings from tree-level exchange of neutral particles and from loops of particles with arbitrary electroweak charge were calculated. The resulting amplitudes were implemented in the Forward Physics Monte Carlo (FPMC) generator. For 300 fb^{-1} of integrated luminosity, the projected sensitivity on the anomalous coupling coefficient of the $\gamma\gamma\gamma Z$ operator, ζ, is down to $\zeta = 2 \cdot 10^{-13}$ GeV^{-4} with a 5σ statistical significance. This sensitivity goes beyond the one expected from the $Z \to \gamma\gamma\gamma$ decay searches at the LHC by roughly three orders of magnitude (based on a repeated measurement at $\sqrt{s} = 13$ TeV during Run-2 with similar event selection requirements).

We also analyzed the search prospects for ALPs coupled to the electromagnetic field in light-by-light scattering in pp collisions for $\sqrt{s} = 13$ TeV for an integrated luminosity of 300 fb^{-1}. We have found that the bounds on the ALP–photon coupling for masses above 600 GeV can be improved significantly in the central exclusive photon pair production channel. These regions are constrained by standard LHC bump searches. We conclude that ALP search via light-by-light scattering in central exclusive production in pp collisions complements other LHC searches, especially in the $0.6 - 2$ TeV mass range. We also examined the possible extension of this search in light-by-light scattering in pPb and ArAr collisions. An interplay between the cross section and the different in reach in mass for resonant production of ALPs is examined as part of this study, which was published

in a separate follow-up paper.

Finally, we derived projections for central exclusive production of high-mass W^+W^- boson pairs in pp collisions assuming an integrated luminosity of 300 fb^{-1} at $\sqrt{s} = 14$ TeV. In previous phenomenology and experimental studies, only the leptonic final state of the diboson system has been considered due to its clean experimental signature, and its feasibility to be carried out without the use of the proton tagging technique. However, in order to probe larger WW invariant masses with moderate pileup conditions, we have to consider additional decay channels other than the standard leptonic decay. Using the forward proton detectors, one can consider every combination of final-state decays of the W bosons. What we find is that the hadronic channel is only accessible if a judicious choice of jet substructure variables is used in addition to the selection related to central exclusive production processes. The semi-leptonic channel gives a more balanced and accessible channel to study high-mass WW production in the SM.

In addition to the aforementioned study, we considered scenarios where deviations from the SM expectations are present. We parametrize these deviations by means of an anomalous $\gamma\gamma WW$ vertex in a dimension-six EFT framework. Such deviations from the SM manifest as modifications of the tails of the p_T^W and m_{WW} spectra from the SM expectations. The selection requirements can be tailored to account for this localized manifestation of new physics. Here, the hadronic final state gives much better sensitivity to beyond SM deviations at high-mass and high-p_T of each W boson. The hadronic channel yields the best sensitivity, followed by the semi-leptonic and leptonic channels. The interaction couplings a_0^W and a_C^W of the EFT operators can be probed down to values of 3.7×10^{-7} GeV^{-2} and 9.2×10^{-7} GeV^{-2} at 95% CL by combining all decay channels (one-dimensional projections, while keeping one of the coupling parameters fixed to zero, without form factors). This is contrast to the sensitivity reached with the leptonic channel alone of 4.3×10^{-6} GeV^{-2} and 10^{-5} GeV^{-2} at 95% CL.

Chapter 10

Summary and Prospects

In this thesis, we considered two main fronts of research of short-distance elementary particle interactions. The first one was the experimental investigation of emergent properties of the strong force that are expected from the interactions of quark and gluons in quantum chromodynamics (QCD). These experimental measurements were done with the Compact Muon Solenoid (CMS) and TOTal Elastic and diffractive cross section Measurement (TOTEM) experiments at the CERN Large Hadron Collider (LHC) in proton-proton collisions at $\sqrt{s} = 13$ TeV. The second aspect of this thesis was related to phenomenology efforts to extend our current theory of elementary interactions in photon-photon interactions in high-energy proton-proton collisions. We analyzed the possible ways that new physics may manifest in future measurements.

For the data analysis, we analyzed Mueller–Tang jets in proton-proton (pp) collisions at $\sqrt{s} = 13$ TeV with the CMS and TOTEM experiments at the CERN LHC in 2015. These consist of events with two leading jets separated by a large pseudorapidity (η), and hence are known as "jet-gap-jet" events. The gap in η is defined by the absence of charged particles with transverse momentum $p_{\mathrm{T}} > 200$ MeV in the $|\eta| < 1$ region. Each of the two leading p_{T} jets has $1.4 < |\eta^{\mathrm{jet}}| < 4.7$ and $p_{\mathrm{T}}^{\mathrm{jet}} > 40$ GeV, with $\eta^{\mathrm{jet1}}\eta^{\mathrm{jet2}} < 0$, where jet1 and jet2 are the leading and subleading jets in p_{T}. The pseudorapidity gap signature is assumed to be caused by hard color-singlet exchange, which is described in terms of t-channel two-gluon exchange in a color-singlet configuration in perturbative quantum chromodynamics (pQCD). Such two-gluon exchange may receive radiative corrections in the limit where the two jets are largely separated in (pseudo)rapidity, known as the high-

energy limit of QCD. In this case, the color-singlet exchange corresponds to perturbative pomeron exchange. Hard color-singlet exchange events appear as an excess of events over the expected contribution from color-exchange dijet events at the lowest multiplicity of particles between the jets. Color-exchange dijet events dominate the inclusive dijet cross section. The fraction of dijet events produced via color-singlet exchange, f_{CSE}, has been measured as a function of $p_{\mathrm{T}}^{\mathrm{jet2}}$, the η difference between the two leading jets, and the azimuthal angular separation between the two leading jets. The analysis has been published in Phys. Rev. D (1).

The measured f_{CSE} values are in the range of 0.4–1.0%. As seen in Fig.6.37 in Chapter7, the ratio f_{CSE} increases with $\Delta\eta_{\mathrm{jj}}$, has a weak dependence on $p_{\mathrm{T}}^{\mathrm{jet2}}$, and increases as $\Delta\phi_{\mathrm{jj}}$ approaches π. No significant difference in f_{CSE} is observed between the 13 TeV results and those presented by the CMS Collaboration at 7 TeV, as shown in Fig. 6.38. This is in contrast to the trend found at lower energies of 0.63 and 1.8 TeV by the D0 and CDF Collaborations, where a significant decrease of f_{CSE} with increasing $\sqrt{s}$ was observed, as illustrated in Fig. 6.38. The present measurement of f_{CSE} expands the reach in $\Delta\eta_{\mathrm{jj}}$ covered in the earlier 7 TeV CMS measurement (152), as seen in Fig. 6.39. The results in Fig.6.37 are compared with calculations based on the Balitsky–Fadin–Kuraev–Lipatov (BFKL) framework (82; 81; 217) with resummation of large logarithms of energy at next-to-leading logarithmic accuracy using leading order impact factors, and various treatments of gap survival probability effects. The implementation by Royon, Marquet, and Kepka (129; 130) describes some features of the data, but is not able to simultaneously describe all aspects of the measurements. The implementation by Ekstedt, Enberg, Ingelman, and Motyka (EEIM) (128; 131) gives a fair description of the data in $\Delta\eta_{\mathrm{jj}}$ and $p_{\mathrm{T}}^{\mathrm{jet2}}$ within the uncertainties only when considering survival probability effects based on multiple-parton interactions and their soft color interaction model. The BFKL-based calculation with next-to-leading order impact factors has yet to be done, and it is possible that the comparison of the purely perturbative calculation with the data changes with this

update.

The phenomenon of hard color-singlet exchange remains to be fully understood from the SM point of view. The presence of a hard scale in the process suggests that, in principle, we should be able to understand this process using perturbation theory techniques. However, we have seen here that it is extremely challenging to have a coherent description of the process. We know that t-channel electroweak gauge boson exchanges between quarks, while they can lead to the same rapidity gap signature between the jets, they are not able to account for the observed production rates of the jet-gap-jet process. The simple two-gluon color-singlet exchange of QCD, while it has a larger production cross section than the single-electroweak boson exchange between quarks, is not able to explain the observed rates either. The BFKL pomeron exchange gives the right order of magnitude for the production rate, but is not able to easily describe all features of the data without the introduction of kinematic-dependent rapidity gap survival probability (at least for the partial NLO calculations available at the time of writing this thesis). It is likely that the jet-gap-jet process we observe in the data is a special combination of short-distance physics mechanism, perhaps the perturbative pomeron exchange, together with long-distance physics mechanism(s), for example soft parton exchanges that may rearrange the color fields of the partons created in the collision such that they create or destroy gaps between the jets. Perhaps with other processes with rapidity gaps, or by repeating the jet-gap-jet measurement with another set of judicious of observables, it would be possible to get a better understanding of the nature of the color-singlet exchange. For the time being, this remains, in the opinion of the author of this thesis, a very interesting and puzzling problem to solve from the point of view of QCD.

The studies of jet-gap-jet events can be further expanded by considering different ways of defining the pseudorapidity gap between the jets. There have been proposals for setting an upper bound on the invariant mass of the system outside of the rapidity gap to ensure well-behaved predictions from pQCD, particularly when including higher-

order corrections to the impact factors, as suggested in Refs.(138; 139; 140). It would be interesting also to see the measurement repeated at various $\sqrt{s}$ at the CERN LHC, for instance at $\sqrt{s} = 2.76$, 5.02, and at 8 TeV. Data that has been collected for the pp reference runs for the heavy-ion community could be used for this purpose, since they are also at low pileup and with a decent amount of luminosity and appropriate jet triggers available. Measurements like this could help solidify our interpretation of the survival probability dependence on $\sqrt{s}$ by providing data points at collision energies between the Tevatron and Run-1 and Run-2 energies at the LHC. Another way of expanding the jet-gap-jet study is by considering a measurement of the f_{CSE} for different η gap intervals. This could help disentangle the possible contributions from soft-color interactions versus those of perturbative QCD. It would be interesting to see also results reported by other experiments. Other than the CMS experiment, ATLAS would be the natural LHC experiment to carry out such measurements, since it has similar acceptance and jet reconstruction capabilities as the CMS detector. Such an independent measurement would help solidify the experimental characterization of the hard color-singlet exchange process.

We also explored the possibility of studying the jet-gap-jet process in proton-proton collision events where at least one of the protons remains intact as the result of exchanging a t-channel multiparton color-singlet exchange, known as pomeron exchange. The first measurement of jet-gap-jet with an intact proton presented in this thesis, a joint CMS-TOTEM effort, demonstrated the feasibility of doing these investigations with proton tagging, as well as the cleaner hadronic environment that one can obtain in this configuration. The intact protons in the analysis have a fractional momentum loss (ξ) of up to 20%, with values of the square of the four-momentum transfer at the proton vertex (t) in the range between -4 and -0.025 GeV^2, whereas the jets satisfy the same selection requirements as those in the "standard" jet-gap-jet analysis. The f_{CSE} value extracted in this sample is 2.91 ± 0.70 (stat) $^{+1.08}_{-1.01}$ (syst) times larger than that found in inclusive dijet production, possibly suggesting a larger abundance of jets with central gaps in events

with detected intact protons. The respective plots where this enhancement is observed are shown in Fig. 7.13. This can be interpreted in terms of a lower spectator parton activity in events with intact protons, which decreases the likelihood of the central gap signature being spoiled. The analysis is reported jointly with the CMS-only jet-gap-jet analysis (1). Future dedicated runs with an integrated luminosity of more than about 20 pb^{-1} at high β^* would be necessary to carry out the differential version of this measurement with a similar experimental precision as the analysis we presented for the "standard" jet-gap-jet analysis.

Ideally, the measurement of jet-gap-jet events with two intact protons would be the ultimate probe of Mueller–Tang jets, absent in spectator parton activity that could "skew" the data away from the pure pQCD calculation. These events with a jet-gap-jet signature in the central detector and two intact protons would yield an effective three rapidity gap signature (p-gap-jet-gap-jet-gap-p). In this case, since both protons remain intact, factorization is expected to be fully restored, according to the findings by the CDF Collaboration of double-pomeron exchange dijet events. The caveat in this case is that one would need much more data to carry out a detailed analysis. Assuming factorization is fully restored, and assuming similar kinematic requirements on the jets as those used in this thesis, one would expect that with about 500 pb^{-1} of low pileup data we should be able to perform a "differential" analysis of jet-gap-jet events with two intact protons. Future special runs with ATLAS or with CMS-TOTEM may target such an amount of luminosity to carry out this study. This would help us better understand the role of spectator parton activity in the destruction of the central gap, as well as whether the BFKL framework is the correct mathematical approach towards the description of the hard color-singlet exchange process.

We also demonstrated the feasibility of carrying out a differential study of hard diffractive dijet production with $\sqrt{s} = 13$ TeV CMS-TOTEM data. By diffractive dijet production, we mean pp$\rightarrow$ p JJX, where J represents a jet and X represents a hadronic system

X. At least one of the protons remains intact due to pomeron exchange and is tagged with the RP detectors, and the two jets have $p_{\mathrm{T}}^{\mathrm{jet1,2}} > 40$ GeV with $|\eta^{\mathrm{jet}}| < 4.7$. For this, we showed preliminary background analyses and distributions over observables of interest. This can be used to test several ideas we have about the hard diffractive exchange process. For example, whether the pomeron parton densities actually obey Dokshitzer–Gribov–Lipatov–Altarelli–Parisi (DGLAP) evolution, just as the proton PDFs, or whether Regge factorization –the mathematical decomposition of the hard diffractive process into a pomeron flux and a pomeron parton density– breaks down at some point. The dependence of the t-slope with the p_{T} of the jets could also help us identify the distribution of gluons in impact parameter space. To this extent, we see that the shape of the t distribution for single-diffractive dijet event candidates does not have a strong dependence with p_T of the jets, within the uncertainties 8.17. A more detailed analysis would entail analyzing the background-subtracted, unfolded t distribution. We also observed that, within the uncertainties, there is no strong jet p_{T} dependence of the ratio of single-diffractive dijet event yields to the inclusive dijet event yields, $R_{\mathrm{INC}}^{\mathrm{SD}}$, as a function of the reconstructed Bjorken-x variable, as shown in Fig. 8.14. This could suggest that the diffractive structure function continues to evolve with DGLAP evolution for the phase-space region of the protons and jets probed in the measurement, just as the standard structure function of the proton. We observe that it is feasible to analyze the diffractive production of dijets in narrow bins of ξ, as demonstrated in Fig. 8.16. Following the steps of the CDF Collaboration, we should be able to analyze the slopes of the ratios $R_{\mathrm{INC}}^{\mathrm{SD}}$ as a function of Bjorken-x in bins of ξ to test the hypothesis of Regge factorization. If Regge factorization holds, the slope of the ratio $R_{\mathrm{INC}}^{\mathrm{SD}}$ versus Bjorken-x should be independent of ξ. If so, it might be possible to test the composition of pomeron- and reggeon-like exchanges for the hard diffractive process using a similar methodology as the CDF experiment with a dedicated analysis of the effective diffractive structure function. The ratio $R_{\mathrm{INC}}^{\mathrm{SD}}$ has values of 0.2–0.6%, a similar order of magnitude as the hard color-singlet exchange fraction f_{CSE} of the jet-gap-jet

analysis.

In addition, we studied double-pomeron exchange dijet events, pp $\rightarrow$ p JJX p, using the same CMS-TOTEM data set. Such an event topology has not been previously studied with two intact protons. The previous study by CDF tagged the outgoing antiprotons with RP detectors, and used the rapidity gap method for the outgoing undetected proton, as well as an extrapolation based on assumptions of the diffractive exchange at low ξ in order to calculate the double-ratio of the single-diffractive exchange dijet event rate,$R^{\mathrm{SD}}_{\mathrm{INC}}$, to the ratio of single-diffractive dijet event to inclusive dijet event yields double-pomeron exchange dijet event yields, $R^{\mathrm{DPE}}_{\mathrm{SD}}$. We observe 114 double-pomeron exchange dijet candidate events in the CMS-TOTEM dijet data sample after all event selection requirements. The preliminary double ratio $R^{\mathrm{SD}}_{\mathrm{INC}}/R^{\mathrm{DPE}}_{\mathrm{SD}} \approx 0.25$ calculated for this diffractive dijet topology is consistent with the one reported by the CDF experiment $R^{\mathrm{SD}}_{\mathrm{INC}}/R^{\mathrm{DPE}}_{\mathrm{SD}} = 0.19 \pm 0.07$ (216), without the need for making extrapolations under assumptions of the hard diffractive exchange. If there was no breakdown of factorization in hadron-hadron hard diffractive interactions, then $R^{\mathrm{SD}}_{\mathrm{INC}}/R^{\mathrm{DPE}}_{\mathrm{SD}} = 1$. We thus confirm the breakdown of factorization previously observed by CDF by comparing the relative rates of double-pomeron exchange to single-diffractive dijet events to those of single-diffractive to inclusive dijet event rates. As demonstrated in Fig. 8.22, factorization seems to be broken at a similar degree as CDF reported, according to the preliminary results shown in this thesis. Interestingly, the double-ratio $R^{\mathrm{SD}}_{\mathrm{INC}}/R^{\mathrm{DPE}}_{\mathrm{SD}}$ with the 13 TeV CMS-TOTEM data is consistent with the double-ratio of color-singlet exchange fractions f_{CSE} of jet-gap-jet events with an intact proton and without an intact proton calculated in Chapter 7, perhaps indicating a universal behavior of two rapidity gap signatures.

For future hard diffraction studies at the CERN LHC, it would be interesting to see the use of other hard probes, such as top quark (produced singly or in pairs) with an intact proton, or to extend the program started at the Tevatron of diffractive electroweak gauge boson production at the LHC. Special runs with moderately large amounts of luminosity

(hundreds of pb^{-1}) and with a small amount of pileup could be used for this purpose using the Precision Proton Spectrometer (PPS) or the ATLAS Forward Proton (AFP) apparatus. Such larger amounts of luminosity would be useful for the analysis of diffractive dijet production for jet p_{T} at the TeV scale, something that has not been probed before. One could then extend the search from deviations of DGLAP evolution of the diffractive structure function, complementing the lower p_{T} analysis shown in this thesis, and the previous published work by the HERA, Tevatron, and LHC experiments.

For the particle physics phenomenology studies, we see that there is great potential for new physics discovery or opportunities for setting stronger constraints on new physics scenarios by considering photon-photon collisions with masses at the TeV scale in interactions of the type $pp \to pXp$, where X is a particle system created by two-photon fusion. The forward intact protons are tagged with RP detectors as well, but operating during a more challenging background environment due to the different magnetic lattice used to bend the beams and the larger amount of pileup interactions present in standard luminosity LHC runs. The advantage of these channels is the strong suppression that we have for the QCD-initiated backgrounds, leaving us with a relatively clean channel to test high-energy photon-photon interactions. In Chapter 9 of this thesis, we demonstrated the discovery potential of anomalous vector gauge boson scattering processes, namely for $\gamma\gamma \to \gamma Z$ scattering, for axion-like particle production by light-by-light scattering $\gamma\gamma \to a \to \gamma\gamma$, and how we can better understand the SM $\gamma\gamma \to WW$ process or look for deviations from new physics at energies beyond those reached at the LHC. These are analyses and techniques that can be carried out with readily available data collected by the ATLAS and CMS experiments. In the case of the $\gamma\gamma \to WW$ process, this could in principle be used to calibrate the spectrometers of the ATLAS and CMS experiments, in complementarity to the exclusive dilepton channels $\gamma\gamma \to \ell^+\ell^-$.

For the $\gamma\gamma \to \gamma Z$ process, we extracted projections for the coupling strength of CP-even and CP-odd effective dimension-eight $\gamma\gamma\gamma Z$ operators, shown in Fig. 9.13. For the study

of ALPs in light-by-light scattering, we derived projections in a parameter region of the ALP–photon coupling versus ALP mass plane that is difficult to access, specifically for ALP masses at the TeV scale. We made such projections for $pp \to p\gamma\gamma p$ scattering, where the $\gamma\gamma$ system is produced by $\gamma\gamma \to \gamma\gamma$ scattering. The analysis was extended to ALP masses of the order of 100 – 200 GeV by considering light-by-light scattering in ultra-peripheral proton-lead and argon-argon collisions. The latter complements the expected sensitivity from exclusive diphoton production in ultraperipheral lead-lead collisions for a luminosity of 20 nb^{-1} at $\sqrt{s_{\text{NN}}} = 5.02$ TeV. The projections for light-by-light scattering in pp, proton-lead, argon-argon, and the expected sensitivity for future LbL analyses in lead-lead collisions, is shown in Fig. 9.17. For the $\gamma\gamma \to WW$ scattering analysis, we extended the projections by considering the hadronic and semi-leptonic final states in the high-mass, high-p_{T} regime. The resulting sensitivity on the coupling strength for two dimension-six $\gamma\gamma WW$ operators projected for 300 fb^{-1} at 14 TeV is shown in Fig. 9.27. In the case of $\gamma\gamma \to WW$, one can use this process as a standard candle to calibrate the proton spectrometer system, in addition to the $\gamma\gamma \to \ell^+\ell^-$ process.

A natural extension of the phenomenology program laid down in this thesis is to analyze the SM amplitudes of other electroweak gauge boson processes, for example the scattering $\gamma\gamma \to ZZ$ scattering. Due to the absence of tree-level couplings between the Z and photon fields, this process can only occur via virtual particle fluctuations, just as the light-by-light scattering process. This process is induced only when considering box diagram virtual corrections at leading order in the SM, which renders a cross section $\sigma \propto \sigma^2_{\text{em}}\sigma^2_{\text{weak}}$. In this case however, since the Z boson can be reconstructed at significantly lower p_T than single photons at the ATLAS or CMS experiments (for example, if we consider decays of the $Z \to \mu^+\mu^-$), it is possible that a larger cross section is achieved by considering special phase-space regions inaccessible in $\gamma\gamma \to \gamma\gamma$. Other processes of interest would be the anomalous production of $\gamma\gamma \to t\bar{t}$ using the proton tagging technique, for example. Such a process has not been experimentally measured at the time of writing this thesis.

Modifications to the electric or magnetic dipole moments of the top quark would yield a modification of the cross section for this photon-photon process. A comprehensive program of direct searches of BSM particles with direct couplings to the electromagnetic field could be carried out as well (for example, electrically charged supersymmetric particles), in regions of phase-space where the standard searches are more complicated. It will be very interesting to see the set of measurements by the ATLAS and CMS Collaborations on central exclusive production based on the Run-2 data collected with the RP detectors.

Finally, it would be interesting to draw further projections for a future scenario where we have RP detectors installed at 420m with respect to the interaction point. This additional set of RPs located even more forward would give access to lower invariant masses of the central system produced in exclusive production. Indeed, one could access masses as low as 100 GeV, extending the standard reach of about 350–400 GeV with the 220m RPs. This could open the possibility for studying the central exclusive production of Higgs boson, axion-like particles at lower masses, or searches for supersymmetric particles that are otherwise hard to constrain.

References

[1] A. M. Sirunyan *et al.*, "Hard color-singlet exchange in dijet events in proton-proton collisions at $\sqrt{s} = 13$ TeV," *Phys. Rev. D*, vol. 104, p. 032009, Aug 2021.

[2] C. Baldenegro, S. Fichet, G. von Gersdorff, and C. Royon, "Probing the anomalous $\gamma\gamma\gamma Z$ coupling at the LHC with proton tagging," *JHEP*, vol. 06, p. 142, 2017.

[3] C. Baldenegro, S. Fichet, G. von Gersdorff, and C. Royon, "Searching for axion-like particles with proton tagging at the LHC," *JHEP*, vol. 06, p. 131, 2018.

[4] C. Baldenegro, S. Hassani, C. Royon, and L. Schoeffel, "Extending the constraint for axion-like particles as resonances at the LHC and laser beam experiments," *Phys. Lett. B*, vol. 795, pp. 339–345, 2019.

[5] C. Baldenegro, G. Biagi, G. Legras, and C. Royon, "Central exclusive production of W boson pairs in pp collisions at the LHC in hadronic and semi-leptonic final states," *JHEP*, vol. 12, p. 165, 2020.

[6] C. MissMJ, "The Standard Model of Particle Physics, Wikimedia Commons https://commons.wikimedia.org/wiki/File:Standard_Model_of_Elementary_Particles.svg,"

[7] C. N. Yang and R. L. Mills, "Conservation of isotopic spin and isotopic gauge invariance," *Phys. Rev.*, vol. 96, pp. 191–195, Oct 1954.

[8] G. 'tHooft, "Renormalization of massless Yang–Mills fields," *Nuclear Physics B*, vol. 33, no. 1, pp. 173–199, 1971.

[9] G. Hooft, "Renormalizable Lagrangians for massive Yang–Mills fields," *Nuclear Physics B*, vol. 35, no. 1, pp. 167–188, 1971.

[10] R. P. Feynman, "Space-time approach to quantum electrodynamics," *Phys. Rev.*, vol. 76, pp. 769–789, Sep 1949.

[11] J. Schwinger, "On quantum-electrodynamics and the magnetic moment of the electron," *Phys. Rev.*, vol. 73, pp. 416–417, Feb 1948.

[12] J. Schwinger, "Quantum electrodynamics. i. a covariant formulation," *Phys. Rev.*, vol. 74, pp. 1439–1461, Nov 1948.

[13] S. Tomonaga, "On a Relativistically Invariant Formulation of the Quantum Theory of Wave Fields*," *Progress of Theoretical Physics*, vol. 1, pp. 27–42, 08 1946.

[14] E. Fermi, "An attempt of a theory of beta radiation. 1.," *Z. Phys.*, vol. 88, pp. 161–177, 1934.

[15] C. S. Wu, E. Ambler, R. W. Hayward, D. D. Hoppes, and R. P. Hudson, "Experimental test of parity conservation in beta decay," *Phys. Rev.*, vol. 105, pp. 1413–1415, Feb 1957.

[16] S. L. Glashow, "The renormalizability of vector meson interactions," *Nuclear Physics*, vol. 10, pp. 107–117, 1959.

[17] A. Salam and J. C. Ward, "Weak and electromagnetic interactions," *Il Nuovo Cimento*, vol. 11, pp. 568–577, 1959.

[18] S. Weinberg, "A model of leptons," *Phys. Rev. Lett.*, vol. 19, pp. 1264–1266, Nov 1967.

[19] G. Arnison and et al., "Experimental observation of isolated large transverse energy electrons with associated missing energy at $\sqrt{s}$=540 GeV," *Physics Letters B*, vol. 122, no. 1, pp. 103–116, 1983.

[20] M. Banner *et al.*, "Observation of single isolated electrons of high transverse momentum in events with missing transverse energy at the CERN $\bar{p}p$ collider," *Phys. Lett. B*, vol. 122, pp. 476–485, 1983.

[21] G. Arnison *et al.*, "Experimental observation of lepton pairs of invariant mass around 95 GeV at the CERN SPS Collider," *Phys. Lett. B*, vol. 126, pp. 398–410, 1983.

[22] P. Bagnaia *et al.*, "Evidence for $Z^0 \to e^+e^-$ at the CERN $\bar{p}p$ Collider," *Phys. Lett. B*, vol. 129, pp. 130–140, 1983.

[23] F. Englert and R. Brout, "Broken symmetry and the mass of gauge vector mesons," *Phys. Rev. Lett.*, vol. 13, pp. 321–323, Aug 1964.

[24] P. W. Higgs, "Broken symmetries and the masses of gauge bosons," *Phys. Rev. Lett.*, vol. 13, pp. 508–509, Oct 1964.

[25] G. S. Guralnik, C. R. Hagen, and T. W. B. Kibble, "Global conservation laws and massless particles," *Phys. Rev. Lett.*, vol. 13, pp. 585–587, Nov 1964.

[26] J. Goldstone, "Field Theories with Superconductor Solutions," *Nuovo Cim.*, vol. 19, pp. 154–164, 1961.

[27] G. Aad, T. Abajyan, B. Abbott, J. Abdallah, S. Abdel Khalek, A. Abdelalim, O. Abdinov, R. Aben, B. Abi, M. Abolins, and et al., "Observation of a new particle in the search for the standard model higgs boson with the atlas detector at the lhc," *Physics Letters B*, vol. 716, p. 1–29, Sep 2012.

[28] S. Chatrchyan *et al.*, "Observation of a New Boson at a Mass of 125 GeV with the CMS Experiment at the LHC," *Phys. Lett. B*, vol. 716, pp. 30–61, 2012.

[29] P. Zyla *et al.*, "Review of Particle Physics," *PTEP*, vol. 2020, no. 8, p. 083C01, 2020.

[30] G. Aad *et al.*, "Observation of photon-induced W^+W^- production in pp collisions at $\sqrt{s} = 13$ TeV using the ATLAS detector," *Phys. Lett. B*, vol. 816, p. 136190, 2021.

[31] G. Zweig, *An SU(3) model for strong interaction symmetry and its breaking*. 2 1964.

[32] M. Gell-Mann, "A schematic model of baryons and mesons," *Physics Letters*, vol. 8, no. 3, pp. 214–215, 1964.

[33] H. D. Politzer, "Reliable perturbative results for strong interactions?," *Phys. Rev. Lett.*, vol. 30, pp. 1346–1349, Jun 1973.

[34] D. J. Gross and F. Wilczek, "Ultraviolet behavior of non-abelian gauge theories," *Phys. Rev. Lett.*, vol. 30, pp. 1343–1346, Jun 1973.

[35] H. Fritzsch, M. Gell-Mann, and H. Leutwyler, "Advantages of the Color Octet Gluon Picture," *Phys. Lett. B*, vol. 47, pp. 365–368, 1973.

[36] C. Abel, S. Afach, N. Ayres, C. Baker, G. Ban, G. Bison, K. Bodek, V. Bondar, M. Burghoff, E. Chanel, and et al., "Measurement of the permanent electric dipole moment of the neutron," *Physical Review Letters*, vol. 124, Feb 2020.

[37] K. G. Wilson, "Confinement of quarks," *Phys. Rev. D*, vol. 10, pp. 2445–2459, Oct 1974.

[38] Y. Nambu and G. Jona-Lasinio, "Dynamical model of elementary particles based on an analogy with superconductivity. i," *Phys. Rev.*, vol. 122, pp. 345–358, Apr 1961.

[39] S. J. Brodsky, G. P. Lepage, and P. B. Mackenzie, "On the Elimination of Scale Ambiguities in Perturbative Quantum Chromodynamics," *Phys. Rev. D*, vol. 28, p. 228, 1983.

[40] F. Herzog, B. Ruijl, T. Ueda, J. A. M. Vermaseren, and A. Vogt, "The five-loop beta function of Yang-Mills theory with fermions," *JHEP*, vol. 02, p. 090, 2017.

[41] J. M. Maldacena, "The Large N limit of superconformal field theories and supergravity," *Adv. Theor. Math. Phys.*, vol. 2, pp. 231–252, 1998.

[42] J. D. Bjorken and E. A. Paschos, "Inelastic electron-proton and γ-proton scattering and the structure of the nucleon," *Phys. Rev.*, vol. 185, pp. 1975–1982, Sep 1969.

[43] R. P. Feynman, *The Behavior of Hadron Collisions at Extreme Energies*, pp. 289–304. Dordrecht: Springer Netherlands, 1988.

[44] J. I. Friedman and H. W. Kendall, "Deep inelastic electron scattering," *Annual Review of Nuclear Science*, vol. 22, no. 1, pp. 203–254, 1972.

[45] E. D. Bloom, D. H. Coward, H. DeStaebler, J. Drees, G. Miller, L. W. Mo, R. E. Taylor, M. Breidenbach, J. I. Friedman, G. C. Hartmann, and H. W. Kendall, "High-energy inelastic $e-p$ scattering at 6° and 10°," *Phys. Rev. Lett.*, vol. 23, pp. 930–934, Oct 1969.

[46] C. G. Callan, Jr and D. J. Gross, "High-energy electroproduction and the constitution of the electric current," *Phys. Rev. Lett., 22: 156-9 (Jan. 27, 1969).*, 1 1969.

[47] C. H. Llewellyn Smith, "Inelastic lepton scattering in gluon models," *Phys. Rev. D*, vol. 4, pp. 2392–2397, Oct 1971.

[48] V. N. Gribov and L. N. Lipatov, "Deep inelastic ep scattering in perturbation theory," *Sov. J. Nucl. Phys.*, vol. 15, p. 438, 1972.

[49] G. Altarelli and G. Parisi, "Asymptotic freedom in parton language," *Nucl. Phys. B*, vol. 126, p. 298, 1977.

[50] Y. L. Dokshitzer, "Calculation of the structure functions for deep inelastic scattering and e+ e- annihilation by perturbation theory in quantum chromodynamics," *Sov. Phys. JETP*, vol. 46, p. 641, 1977.

[51] R. D. Ball *et al.*, "Parton distributions from high-precision collider data," *Eur. Phys. J. C*, vol. 77, no. 10, p. 663, 2017.

[52] T.-J. Hou *et al.*, "New CTEQ global analysis of quantum chromodynamics with high-precision data from the LHC," *Phys. Rev. D*, vol. 103, no. 1, p. 014013, 2021.

[53] R. Brandelik *et al.*, "Evidence for Planar Events in e+ e- Annihilation at High-Energies," *Phys. Lett. B*, vol. 86, pp. 243–249, 1979.

[54] G. Hanson, Abrams, and et al., "Evidence for jet structure in hadron production by e^+e^- annihilation," *Phys. Rev. Lett.*, vol. 35, pp. 1609–1612, Dec 1975.

[55] D. P. Barber and et al., "Discovery of three-jet events and a test of quantum chromodynamics at petra," *Phys. Rev. Lett.*, vol. 43, pp. 830–833, Sep 1979.

[56] C. Berger *et al.*, "Evidence for Gluon Bremsstrahlung in e+ e- Annihilations at High-Energies," *Phys. Lett. B*, vol. 86, pp. 418–425, 1979.

[57] W. Bartel *et al.*, "Observation of Planar Three Jet Events in e+ e- Annihilation and Evidence for Gluon Bremsstrahlung," *Phys. Lett. B*, vol. 91, pp. 142–147, 1980.

[58] B. A. et al., "A test of qcd based on 4-jet events from z0 decays," *Physics Letters B*, vol. 248, no. 1, pp. 227–234, 1990.

[59] S. Kluth, "Jet physics in e^+e^- annihilation from 14 to 209 gev," *Nuclear Physics B - Proceedings Supplements*, vol. 133, p. 36–46, Jul 2004.

[60] V. M. Abazov *et al.*, "Comparison of pp and $p\bar{p}$ differential elastic cross sections and observation of the exchange of a colorless C-odd gluonic compound," 12 2020.

[61] R. D. Peccei and H. R. Quinn, "CP Conservation in the Presence of Instantons," *Phys. Rev. Lett.*, vol. 38, pp. 1440–1443, 1977.

[62] N. Arkani-Hamed, S. Dimopoulos, and G. R. Dvali, "The Hierarchy problem and new dimensions at a millimeter," *Phys. Lett. B*, vol. 429, pp. 263–272, 1998.

[63] N. Arkani-Hamed, S. Dimopoulos, and G. R. Dvali, "Phenomenology, astrophysics and cosmology of theories with submillimeter dimensions and TeV scale quantum gravity," *Phys. Rev. D*, vol. 59, p. 086004, 1999.

[64] L. Randall and R. Sundrum, "Large mass hierarchy from a small extra dimension," *Phys. Rev. Lett.*, vol. 83, pp. 3370–3373, Oct 1999.

[65] S. Dimopoulos and G. L. Landsberg, "Black holes at the LHC," *Phys. Rev. Lett.*, vol. 87, p. 161602, 2001.

[66] S. Dimopoulos, S. Raby, and F. Wilczek, "Supersymmetry and the scale of unification," *Phys. Rev. D*, vol. 24, pp. 1681–1683, Sep 1981.

[67] S. Dimopoulos and H. Georgi, "Softly Broken Supersymmetry and SU(5)," *Nucl. Phys. B*, vol. 193, pp. 150–162, 1981.

[68] S. Rappoccio, "The experimental status of direct searches for exotic physics beyond the standard model at the Large Hadron Collider," *Reviews in Physics*, vol. 4, p. 100027, 2019.

[69] ATLAS, "Summary plots from the ATLAS Exotic physics group , https://atlas.web.cern.ch/Atlas/GROUPS/PHYSICS/CombinedSummaryPlots/EXOTICS/,"

[70] SM, "Summary plots from the CMS SMP group , https://twiki.cern.ch/twiki/bin/view/CMSPublic/PhysicsResultsCombined,"

[71] T. Sjostrand, S. Mrenna, and P. Z. Skands, "A Brief Introduction to PYTHIA 8.1," *Comput. Phys. Commun.*, vol. 178, p. 852, 2008.

[72] G. Corcella, I. G. Knowles, G. Marchesini, S. Moretti, K. Odagiri, P. Richardson, M. H. Seymour, and B. R. Webber, "HERWIG 6: an event generator for hadron emission reactions with interfering gluons (including supersymmetric processes)," *JHEP*, vol. 01, p. 010, 2001.

[73] E. Bothmann *et al.*, "Event Generation with Sherpa 2.2," *SciPost Phys.*, vol. 7, no. 3, p. 034, 2019.

[74] J. C. Collins, D. E. Soper, and G. Sterman, "Factorization for short distance hadron-hadron scattering," *Nuclear Physics B*, vol. 261, pp. 104–142, 1985.

[75] J. C. Collins, D. E. Soper, and G. Sterman, "Soft gluons and factorization," *Nuclear Physics B*, vol. 308, no. 4, pp. 833–856, 1988.

[76] S. Osman and DESY, *Multiple Parton Interactions in Deep Inelastic ep-scattering at HERA*. Dr., Univ. of Lund, Lund, 2008. Univ. of Lund, Lund, Diss., 2008.

[77] B. Andersson, G. Gustafson, G. Ingelman, and T. Sjöstrand, "Parton fragmentation and string dynamics," *Physics Reports*, vol. 97, no. 2, pp. 31–145, 1983.

[78] B. R. Webber, "A QCD Model for Jet Fragmentation Including Soft Gluon Interference," *Nucl. Phys. B*, vol. 238, pp. 492–528, 1984.

[79] M. Cacciari, G. P. Salam, and G. Soyez, "The anti-k_t jet clustering algorithm," *JHEP*, vol. 04, p. 063, 2008.

[80] V. Khachatryan *et al.*, "Measurement of the double-differential inclusive jet cross section in proton–proton collisions at $\sqrt{s} = 13\,\text{TeV}$," *Eur. Phys. J. C*, vol. 76, no. 8, p. 451, 2016.

[81] I. I. Balitsky and L. N. Lipatov, "The Pomeranchuk Singularity in Quantum Chromodynamics," *Sov. J. Nucl. Phys.*, vol. 28, pp. 822–829, 1978. [Yad. Fiz.28,1597(1978)].

[82] E. A. Kuraev, L. N. Lipatov, and V. S. Fadin, "The Pomeranchuk Singularity in Nonabelian Gauge Theories," *Sov. Phys. JETP*, vol. 45, pp. 199–204, 1977. [Zh. Eksp. Teor. Fiz.72,377(1977)].

[83] V. S. Fadin and L. N. Lipatov, "BFKL pomeron in the next-to-leading approximation," *Phys. Lett.*, vol. B429, pp. 127–134, 1998.

[84] M. Ciafaloni and G. Camici, "Energy scale(s) and next-to-leading BFKL equation," *Phys. Lett.*, vol. B430, pp. 349–354, 1998.

[85] V. S. Fadin, "Particularities of the NNLLA BFKL," *AIP Conference Proceedings*, vol. 1819, no. 1, p. 060003, 2017.

[86] A. Accardi and et al., "Electron ion collider: The next qcd frontier - understanding the glue that binds us all," 2014.

[87] J. Jalilian-Marian, A. Kovner, A. Leonidov, and H. Weigert, "The Wilson renormalization group for low x physics: Towards the high density regime," *Phys. Rev. D*, vol. 59, p. 014014, 1998.

[88] J. Jalilian-Marian, A. Kovner, A. Leonidov, and H. Weigert, "The BFKL equation from the Wilson renormalization group," *Nucl. Phys. B*, vol. 504, pp. 415–431, 1997.

[89] H. Weigert, "Unitarity at small Bjorken x," *Nucl. Phys. A*, vol. 703, pp. 823–860, 2002.

[90] E. Iancu, A. Leonidov, and L. D. McLerran, "Nonlinear gluon evolution in the color glass condensate. 1.," *Nucl. Phys. A*, vol. 692, pp. 583–645, 2001.

[91] I. Balitsky, "Operator expansion for high-energy scattering," *Nucl. Phys. B*, vol. 463, pp. 99–160, 1996.

[92] Y. V. Kovchegov, "Unitarization of the BFKL pomeron on a nucleus," *Phys. Rev. D*, vol. 61, p. 074018, Mar 2000.

[93] J. Gayler, "Proton structure function measurements from hera," *Multiparticle Dynamics*, Jul 2003.

[94] R. D. Ball, V. Bertone, M. Bonvini, S. Marzani, J. Rojo, and L. Rottoli, "Parton distributions with small-x resummation: evidence for bfkl dynamics in hera data," *The European Physical Journal C*, vol. 78, Apr 2018.

[95] M. Hentschinski and E. Padrón Molina, "Exclusive J/Ψ and $\Psi(2s)$ photoproduction as a probe of QCD low x evolution equations," *Phys. Rev. D*, vol. 103, no. 7, p. 074008, 2021.

[96] S. Aid *et al.*, "Elastic photoproduction of rho0 mesons at HERA," *Nucl. Phys. B*, vol. 463, pp. 3–32, 1996.

[97] J. Breitweg *et al.*, "Elastic and proton dissociative ρ^0 photoproduction at HERA," *Eur. Phys. J. C*, vol. 2, pp. 247–267, 1998.

[98] J. Breitweg *et al.*, "Measurement of elastic Υ photoproduction at HERA," *Phys. Lett. B*, vol. 437, pp. 432–444, 1998.

[99] C. Adloff *et al.*, "Elastic photoproduction of J/ψ and Υ mesons at HERA," *Phys. Lett. B*, vol. 483, pp. 23–35, 2000.

[100] C. Adloff *et al.*, "Diffractive photoproduction of psi(2S) mesons at HERA," *Phys. Lett. B*, vol. 541, pp. 251–264, 2002.

[101] S. Chekanov *et al.*, "Exclusive photoproduction of J/ψ mesons at HERA," *Eur. Phys. J. C*, vol. 24, pp. 345–360, 2002.

[102] S. Chekanov *et al.*, "Exclusive electroproduction of J/ψ mesons at HERA," *Nucl. Phys. B*, vol. 695, pp. 3–37, 2004.

[103] S. Chekanov *et al.*, "Exclusive photoproduction of Υ mesons at HERA," *Phys. Lett. B*, vol. 680, pp. 4–12, 2009.

[104] C. Alexa *et al.*, "Elastic and Proton-Dissociative Photoproduction of J/ψ Mesons at HERA," *Eur. Phys. J. C*, vol. 73, no. 6, p. 2466, 2013.

[105] R. Aaij *et al.*, "Updated measurements of exclusive J/ψ and ψ(2S) production cross sections in pp collisions at $\sqrt{s} = 7$ TeV," *J. Phys. G*, vol. 41, p. 055002, 2014.

[106] R. Aaij *et al.*, "Measurement of the exclusive Υ production cross section in pp collisions at $\sqrt{s} = 7$ TeV and 8 TeV," *JHEP*, vol. 09, p. 084, 2015.

[107] B. Abelev *et al.*, "Coherent J/ψ photoproduction in ultraperipheral Pb-Pb collisions at $\sqrt{s_{\rm NN}} = 2.76$ TeV," *Phys. Lett. B*, vol. 718, p. 1273, 2013.

[108] B. B. Abelev *et al.*, "Exclusive J/ψ photoproduction off protons in ultraperipheral p-Pb collisions at $\sqrt{s_{\rm NN}} = 5.02$ TeV," *Phys. Rev. Lett.*, vol. 113, p. 232504, 2014.

[109] J. Adam *et al.*, "Coherent ρ^0 photoproduction in ultraperipheral Pb-Pb collisions at $\sqrt{s_{\rm NN}} = 2.76$ TeV," *JHEP*, vol. 09, p. 095, 2015.

[110] A. M. Sirunyan *et al.*, "Measurement of exclusive Υ photoproduction from protons in pPb collisions at $\sqrt{s_{\rm NN}} = 5.02$ TeV," *Eur. Phys. J. C*, vol. 79, p. 277, 2019.

[111] A. M. Sirunyan *et al.*, "Measurement of exclusive $\rho(770)^0$ photoproduction in ultraperipheral pPb collisions at $\sqrt{s_{\rm NN}} = 5.02$ TeV," *Eur. Phys. J. C*, vol. 79, p. 702, 2019.

[112] I. Bautista, A. Fernández Téllez, and M. Hentschinski, "BFKL evolution and the growth with energy of exclusive J/ψ and Υ photoproduction cross sections," *Phys. Rev. D*, vol. 94, p. 054002, 2016.

[113] A. Arroyo García, M. Hentschinski, and K. Kutak, "QCD evolution based evidence for the onset of gluon saturation in exclusive photo-production of vector mesons," *Phys. Lett. B*, vol. 795, p. 569, 2019.

[114] O. Kepka, C. Royon, C. Marquet, and R. B. Peschanski, "Next-to-leading BFKL phenomenology of forward-jet cross sections at HERA," *Eur. Phys. J. C*, vol. 55, pp. 259–272, 2008.

[115] A. Aktas *et al.*, "Forward jet production in deep inelastic scattering at HERA," *Eur. Phys. J. C*, vol. 46, pp. 27–42, 2006.

[116] A. Mueller and H. Navelet, "An inclusive minijet cross section and the bare pomeron in qcd," *Nuclear Physics B*, vol. 282, pp. 727–744, 1987.

[117] V. Khachatryan *et al.*, "Azimuthal decorrelation of jets widely separated in rapidity in pp collisions at $\sqrt{s} = 7$ TeV," *JHEP*, vol. 08, p. 139, 2016.

[118] G. Aad *et al.*, "Measurements of jet vetoes and azimuthal decorrelations in dijet events produced in pp collisions at $\sqrt{s} = 7$TeV using the ATLAS detector," *Eur. Phys. J. C*, vol. 74, no. 11, p. 3117, 2014.

[119] N. B. de León, G. Chachamis, and A. Sabio Vera, "Average minijet rapidity ratios in Mueller-Navelet jets," 6 2021.

[120] G. Chachamis and A. Sabio Vera, "The high-energy radiation pattern from BFKLex with double-log collinear contributions," *JHEP*, vol. 02, p. 064, 2016.

[121] F. G. Celiberto, D. Gordo Gómez, and A. Sabio Vera, "Forward Drell–Yan production at the LHC in the BFKL formalism with collinear corrections," *Phys. Lett. B*, vol. 786, pp. 201–206, 2018.

[122] A. D. Bolognino, F. G. Celiberto, D. Y. Ivanov, M. M. A. Mohammed, and A. Papa, "Inclusive hadron-jet production at the LHC," *Acta Phys. Polon. Supp.*, vol. 12, no. 4, p. 773, 2019.

[123] F. G. Celiberto, D. Y. Ivanov, M. M. A. Mohammed, and A. Papa, "High-energy resummed distributions for the inclusive Higgs-plus-jet production at the LHC," *Eur. Phys. J. C*, vol. 81, no. 4, p. 293, 2021.

[124] J. D. Bjorken, "Rapidity gaps and jets as a new-physics signature in very-high-energy hadron-hadron collisions," *Phys. Rev. D*, vol. 47, pp. 101–113, Jan 1993.

[125] A. Mueller and W.-K. Tang, "High energy parton-parton elastic scattering in qcd," *Physics Letters B*, vol. 284, no. 1, pp. 123 – 126, 1992.

[126] B. Cox, J. R. Forshaw, and L. Lonnblad, "Hard color singlet exchange at the Tevatron," *JHEP*, vol. 10, p. 023, 1999.

[127] L. Motyka, A. D. Martin, and M. G. Ryskin, "The Nonforward BFKL amplitude and rapidity gap physics," *Phys. Lett. B*, vol. 524, pp. 107–114, 2002.

[128] R. Enberg, G. Ingelman, and L. Motyka, "Hard color singlet exchange and gaps between jets at the Tevatron," *Phys. Lett. B*, vol. 524, p. 273, 2002.

[129] F. Chevallier, O. Kepka, C. Marquet, and C. Royon, "Gaps between jets at hadron colliders in the next-to-leading BFKL framework," *Phys. Rev.*, vol. D79, p. 094019, 2009.

[130] O. Kepka, C. Marquet, and C. Royon, "Gaps between jets in hadronic collisions," *Phys. Rev.*, vol. D83, p. 034036, 2011.

[131] A. Ekstedt, R. Enberg, and G. Ingelman, "Hard color singlet BFKL exchange and gaps between jets at the LHC," 2017.

[132] I. Babiarz, R. Staszewski, and A. Szczurek, "Multi-parton interactions and rapidity gap survival probability in jet–gap–jet processes," *Phys. Lett.*, vol. B771, pp. 532–538, 2017.

[133] V. Barone and E. Predazzi, *High-energy particle diffraction*. Texts and monographs in physics, Berlin: Springer, 2002.

[134] S. Donnachie, G. Dosch, P. Landshoff, and O. Nachtmann, *Pomeron Physics and QCD*. Cambridge Monographs on Particle Physics, Nuclear Physics and Cosmology, Cambridge University Press, 2002.

[135] J. R. Forshaw and D. A. Ross, *Quantum Chromodynamics and the Pomeron*. Cambridge Lecture Notes in Physics, Cambridge University Press, 1997.

[136] P. Świerska and M. Trzebiński, "BFKL Amplitude Parametrisation for the Jet-Gap-Jet Events at the LHC Energies," *Acta Phys. Polon.*, vol. B46, no. 12, pp. 2477–2484, 2015.

[137] D. Colferai, F. Schwennsen, L. Szymanowski, and S. Wallon, "Mueller–Navelet jets at LHC - complete NLL BFKL calculation," *JHEP*, vol. 12, p. 026, 2010.

[138] M. Hentschinski, J. D. Madrigal Martínez, B. Murdaca, and A. Sabio Vera, "NLO Vertex for a Forward Jet plus a Rapidity Gap at High Energies," *AIP Conf. Proc.*, vol. 1654, p. 070013, 2015.

[139] M. Hentschinski, J. D. M. Martínez, B. Murdaca, and A. Sabio Vera, "The gluon-induced Mueller–Tang jet impact factor at next-to-leading order," *Nucl. Phys.*, vol. B889, pp. 549–579, 2014.

[140] M. Hentschinski, "The perturbative Pomeron with NLO accuracy: Jet-Gap-Jet Observables," *PoS*, vol. DIS2015, p. 075, 2015.

[141] F. Deganutti, D. Gordo Gomez, T. Raben, and C. Royon, "Pomeron Physics at the LHC," *EPJ Web Conf.*, vol. 172, p. 06006, 2018.

[142] J. D. Bjorken, "A full-acceptance detector for SSC physics at low and intermediate mass scales: an expression of interest to the SSC," *Int. J. Mod. Phys. A*, vol. 07, p. 4189, 1992.

[143] E. Gotsman, E. Levin, and U. Maor, "Energy dependence of the survival probability of large rapidity gaps," *Phys. Lett. B*, vol. 438, p. 229, 1998.

[144] V. A. Khoze, A. D. Martin, and M. G. Ryskin, "Diffraction at the LHC," *Eur. Phys. J. C*, vol. 73, p. 2503, 2013.

[145] E. Gotsman, E. Levin, and U. Maor, "CGC/saturation approach for soft interactions at high energy: survival probability of central exclusive production," *Eur. Phys. J. C*, vol. 76, p. 177, 2016.

[146] V. A. Khoze, A. D. Martin, and M. G. Ryskin, "Multiple interactions and rapidity gap survival," *J. Phys.*, vol. G45, no. 5, p. 053002, 2018.

[147] B. Abbott *et al.*, "Probing hard color-singlet exchange in $p\bar{p}$ collisions at $\sqrt{s} = 630$ GeV and 1800 GeV," *Phys. Lett. B*, vol. 440, p. 189, 1998.

[148] C. Adloff *et al.*, "Energy flow and rapidity gaps between jets in photoproduction at HERA," *Eur. Phys. J. C*, vol. 24, p. 517, 2002.

[149] M. Derrick *et al.*, "Rapidity gaps between jets in photoproduction at HERA," *Phys. Lett. B*, vol. 369, p. 55, 1996.

[150] F. Abe *et al.*, "Events with a rapidity gap between jets in $\bar{p}p$ collisions at $\sqrt{s} = 630$ GeV," *Phys. Rev. Lett.*, vol. 81, p. 5278, 1998.

[151] F. Abe *et al.*, "Dijet production by color-singlet exchange at the Fermilab Tevatron," *Phys. Rev. Lett.*, vol. 80, p. 1156, 1998.

[152] A. M. Sirunyan *et al.*, "Study of dijet events with a large rapidity gap between the two leading jets in pp collisions at $\sqrt{s} = 7$ TeV," *Eur. Phys. J.*, vol. C78, no. 3, p. 242, 2018.

[153] C. Marquet, C. Royon, M. Trzebiński, and R. Žlebčík, "Gaps between jets in double-pomeron-exchange processes at the lhc," *Phys. Rev. D*, vol. 87, p. 034010, Feb 2013.

[154] T. T. Collaboration *Journal of Instrumentation*, vol. 3, no. 08, p. S08007, 2008.

[155] A. Aktas *et al.*, "Measurement and QCD analysis of the diffractive deep-inelastic scattering cross-section at HERA," *Eur. Phys. J. C*, vol. 48, pp. 715–748, 2006.

[156] G. Ingelman and P. E. Schlein, "Jet Structure in High Mass Diffractive Scattering," *Phys. Lett.*, vol. 152B, pp. 256–260, 1985.

[157] R. Bonino, A. Brandt, J. Cheze, S. Erhan, G. Ingelman, M. Medinnis, P. Schlein, J. Zsembery, J. Zweizig, A. Clark, and J. Hansen, "Evidence for transverse jets in high-mass diffraction: Ua8 experiment," *Physics Letters B*, vol. 211, no. 1, pp. 239–246, 1988.

[158] J. C. Collins, "Proof of factorization for diffractive hard scattering," *Phys. Rev. D*, vol. 57, pp. 3051–3056, 1998. [Erratum: Phys.Rev.D 61, 019902 (2000)].

[159] F. D. Aaron *et al.*, "Diffractive Dijet Photoproduction in ep Collisions at HERA," *Eur. Phys. J. C*, vol. 70, pp. 15–37, 2010.

[160] V. Andreev *et al.*, "Diffractive Dijet Production with a Leading Proton in ep Collisions at HERA," *JHEP*, vol. 05, p. 056, 2015.

[161] S. Chekanov *et al.*, "Diffractive photoproduction of dijets in ep collisions at HERA," *Eur. Phys. J. C*, vol. 55, pp. 177–191, 2008.

[162] S. Chekanov *et al.*, "A QCD analysis of ZEUS diffractive data," *Nucl. Phys. B*, vol. 831, pp. 1–25, 2010.

[163] J. C. Collins, "Factorization in hard diffraction," *J. Phys. G*, vol. 28, pp. 1069–1078, 2002.

[164] T. Affolder *et al.*, "Diffractive dijets with a leading antiproton in $\bar{p}p$ collisions at $\sqrt{s} = 1800$ GeV," *Phys. Rev. Lett.*, vol. 84, pp. 5043–5048, 2000.

[165] T. Aaltonen *et al.*, "Diffractive Dijet Production in $\bar{p}p$ Collisions at $\sqrt{s} = 1.96$ TeV," *Phys. Rev. D*, vol. 86, p. 032009, 2012.

[166] B. Kopeliovich, R. Pasechnik, and I. Potashnikova, "Diffractive dijet production: Breakdown of factorization," *Physical Review D*, vol. 98, Dec 2018.

[167] S. Chatrchyan *et al.*, "Observation of a Diffractive Contribution to Dijet Production in Proton-Proton Collisions at $\sqrt{s} = 7$ TeV," *Phys. Rev. D*, vol. 87, no. 1, p. 012006, 2013.

[168] G. Aad *et al.*, "Dijet production in $\sqrt{s} = 7$ TeV pp collisions with large rapidity gaps at the ATLAS experiment," *Phys. Lett. B*, vol. 754, pp. 214–234, 2016.

[169] CMS and TOTEM Collaborations, "Measurement of single-diffractive dijet production in proton-proton collisions at $\sqrt{s} = 8$ TeV with the CMS and TOTEM experiments," *Eur. Phys. J. C*, vol. 80, p. 1164, 2020.

[170] "Angular correlations in exclusive dijet photoproduction in ultra-peripheral PbPb collisions at $\sqrt{s_{NN}} = 5.02$ TeV," 2020.

[171] O. S. Bröning, P. Collier, P. Lebrun, S. Myers, R. Ostojic, J. Poole, and P. Proudlock, *LHC design report*. CERN-2004-003-v-1, 2004.

[172] E. Mobs, "The CERN accelerator complex - 2019. Complexe des accélérateurs du CERN - 2019," Jul 2019. General Photo.

[173] "The ATLAS Experiment at the CERN Large Hadron Collider," *JINST*, vol. 3, p. S08003. 437 p, 2008. Also published by CERN Geneva in 2010.

[174] S. Chatrchyan *et al.*, "The CMS Experiment at the CERN LHC," *JINST*, vol. 3, p. S08004, 2008.

[175] A. A. Alves, Jr. *et al.*, "The LHCb Detector at the LHC," *JINST*, vol. 3, p. S08005, 2008.

[176] O. Adriani *et al.*, "The LHCf detector at the CERN Large Hadron Collider," *JINST*, vol. 3, p. S08006, 2008.

[177] J. Pinfold, R. Soluk, Y. Yao, S. Cecchini, G. Giacomelli, M. Giorgini, L. Patrizii, G. Sirri, D. H. Lacarrère, K. Kinoshita, J. Jakubek, M. Platkevic, S. Pospísil, Z. Vykydal, T. Hott, A. Houdayer, C. Leroy, J. Swain, D. Felea, D. Hasegan, G. E. Pavalas, and V. Popa, "Technical Design Report of the MoEDAL Experiment," tech. rep., Jun 2009.

[178] G. Antchev *et al.*, "Performance of the Totem Detectors at the LHC," *Int. J. Mod. Phys.*

A, vol. 28, p. 1330046. 41 p, Sep 2013. Comments: 40 pages, 31 figures, submitted to Int. J. Mod. Phys. A.

[179] T. Sakuma, "Cutaway diagrams of CMS detector," May 2019.

[180] S. Chatrchyan *et al.*, "Precise Mapping of the Magnetic Field in the CMS Barrel Yoke using Cosmic Rays," *JINST*, vol. 5, p. T03021, 2010.

[181] CMS and TOTEM collaboration, CERN-LHCC-2014-021, "CMS-TOTEM Precision Proton Spectrometer,"

[182] Q. Ingram, "Energy resolution of the barrel of the CMS electromagnetic calorimeter," *Journal of Instrumentation*, vol. 2, pp. P04004–P04004, apr 2007.

[183] S. Chatrchyan *et al.*, "The Performance of the CMS Muon Detector in Proton-Proton Collisions at $\sqrt{s}$ = 7 TeV at the LHC," *JINST*, vol. 8, p. P11002, 2013.

[184] O. Surányi *et al.*, "Performance of the CMS Zero Degree Calorimeters in pPb collisions at the LHC," *JINST*, vol. 16, no. 05, p. P05008, 2021.

[185] V. Khachatryan *et al.*, "The CMS trigger system," *JINST*, vol. 12, p. P01020, 2017.

[186] CMS Collaboration, "Description and performance of track and primary-vertex reconstruction with the CMS tracker," *JINST*, vol. 9, p. P10009, 2014.

[187] CMS Collaboration, "Particle-flow reconstruction and global event description with the CMS detector." Submitted to JINST; in proof, 2017.

[188] M. Cacciari, G. P. Salam, and G. Soyez, "FastJet user manual," *Eur. Phys. J. C*, vol. 72, p. 1896, 2012.

[189] V. Khachatryan *et al.*, "Jet energy scale and resolution in the CMS experiment in pp collisions at 8 TeV," *JINST*, vol. 12, p. P02014, 2017.

[190] G. Antchev *et al.*, "First measurement of elastic, inelastic and total cross-section at $\sqrt{s}$= 13 TeV by TOTEM and overview of cross-section data at LHC energies. First measurement of elastic, inelastic and total cross-section at $\sqrt{s} = 13$ TeV by TOTEM and overview of cross-section data at LHC energies," *Eur. Phys. J. C*, vol. 79, p. 103. 16 p, Dec 2017. 16 pages, 7 figures, 5 tables. Three figures, the references and the author list was updated, presentation is improved. Submitted for a publication to Phys. Rev. D.

[191] G. Antchev *et al.*, "First determination of the ρ parameter at $\sqrt{s}$ = 13 TeV – probing the existence of a colourless three-gluon bound state," *Phys. Rev. D*, p. 28 p, Dec 2017. Submitted to Phys.Rev.

[192] G. Antchev *et al.*, "Elastic differential cross-section measurement at $\sqrt{s}$ = 13 TeV by TOTEM," Tech. Rep. arXiv:1812.08283, CERN, Geneva, Dec 2018. * Temporary entry *.

[193] G. Antchev *et al.*, "LHC Optics Measurement with Proton Tracks Detected by the Roman Pots of the TOTEM Experiment," *New J. Phys.*, vol. 16, p. 103041, 2014.

[194] F. Nemes, "LHC optics and elastic scattering measured by the TOTEM experiment," in *Proceedings, 17th Lomonosov Conference on Elementary Particle Physics: Moscow, Russia, August 20-26, 2015*, pp. 247–251, 2017.

[195] CMS and TOTEM collaboration, CERN-LHCC-2014-021, "CMS-TOTEM Precision Proton Spectrometer,"

[196] A. M. Sirunyan *et al.*, "Observation of proton-tagged, central (semi)exclusive production of high-mass lepton pairs in pp collisions at 13 TeV with the CMS-TOTEM precision proton spectrometer," *JHEP*, vol. 07, p. 153, 2018.

[197] A. M. Sirunyan *et al.*, "Measurement of charged particle spectra in minimum-bias

events from proton–proton collisions at $\sqrt{s} = 13\,\text{TeV}$," *Eur. Phys. J.*, vol. C78, no. 9, p. 697, 2018.

[198] A. M. Sirunyan *et al.*, "Measurement of the inelastic proton-proton cross section at $\sqrt{s} = 13$ TeV," *JHEP*, vol. 07, p. 161, 2018.

[199] C. Collaboration, "Very forward inclusive jet cross sections in p+Pb collisions at $\sqrt{s_{\text{NN}}} = 5.02$ TeV," 2017.

[200] F. Abe *et al.*, "Observation of rapidity gaps in $\bar{\text{p}}\text{p}$ collisions at 1.8 TeV," *Phys. Rev. Lett.*, vol. 74, p. 855, 1995.

[201] A. Giovannini and L. Van Hove, "Negative binomial multiplicity distributions in high energy hadron collisions," *Zeitschrift für Physik C Particles and Fields*, vol. 30, pp. 391–400, Sep 1986.

[202] P. Ghosh, "Negative binomial multiplicity distribution in proton-proton collisions in limited pseudorapidity intervals at LHC up to $\sqrt{s} = 7$ TeV and the clan model," *Phys. Rev.*, vol. D85, p. 054017, 2012.

[203] G. J. Alner *et al.*, "Multiplicity distributions in different pseudorapidity intervals s at a CMS energy of 540 GeV," *Phys. Lett. B*, vol. 160, p. 193, 1985.

[204] R. E. Ansorge *et al.*, "Charged particle multiplicity distributions at 200 GeV and 900 GeV c.m. energy," *Z. Phys. C*, vol. 43, p. 357, 1989.

[205] J. Adam *et al.*, "Charged-particle multiplicities in proton–proton collisions at $\sqrt{s} =$ 0.9 to 8 TeV," *Eur. Phys. J.*, vol. C77, no. 1, p. 33, 2017.

[206] S. Abachi *et al.*, "Rapidity gaps between jets in $\text{p}\bar{\text{p}}$ collisions at $\sqrt{s} = 1.8$ TeV," *Phys. Rev. Lett.*, vol. 72, p. 2332, 1994.

[207] S. Abachi *et al.*, "Jet production via strongly-interacting color-singlet exchange in $\text{p}\bar{\text{p}}$ collisions," *Phys. Rev. Lett.*, vol. 76, p. 734, 1996.

[208] M. Hentschinski, J. D. Madrigal Martínez, B. Murdaca, and A. Sabio Vera, "The next-to-leading order vertex for a forward jet plus a rapidity gap at high energies," *Phys. Lett. B*, vol. 735, p. 168, 2014.

[209] M. Hentschinski, J. D. Madrigal Martínez, B. Murdaca, and A. Sabio Vera, "The gluon-induced Mueller-Tang jet impact factor at next-to-leading order," *Nucl. Phys. B*, vol. 889, p. 549, 2014.

[210] B. Abbott *et al.*, "Hard single diffraction in $\bar{p}p$ collisions at $\sqrt{s} = 630$ GeV and 1800 GeV," *Phys. Lett.*, vol. B531, pp. 52–60, 2002.

[211] D. Acosta *et al.*, "Diffractive dijet production at $\sqrt{s} = 630$ GeV and 1800 GeV at the Fermilab Tevatron," *Phys. Rev. Lett.*, vol. 88, p. 151802, 2002.

[212] T. Aaltonen *et al.*, "Observation of exclusive dijet production at the fermilab tevatron $\overline{p}p$ collider," *Phys. Rev. D*, vol. 77, p. 052004, Mar 2008.

[213] T. Aaltonen *et al.*, "Diffractive Dijet Production in $\bar{p}p$ Collisions at $\sqrt{s} = 1.96$ TeV," *Phys. Rev.*, vol. D86, p. 032009, 2012.

[214] V. Andreev *et al.*, "Diffractive Dijet Production with a Leading Proton in ep Collisions at HERA," *JHEP*, vol. 05, p. 056, 2015.

[215] "Measurement of dijet production with a leading proton in proton-proton collisions at $\sqrt{s} = 8\,\text{TeV}$," Tech. Rep. CMS-PAS-FSQ-12-033, CERN, Geneva, 2018.

[216] T. Affolder *et al.*, "Dijet production by double pomeron exchange at the Fermilab Tevatron," *Phys. Rev. Lett.*, vol. 85, pp. 4215–4220, Nov 2000.

[217] L. N. Lipatov, "The Bare Pomeron in Quantum Chromodynamics," *Sov. Phys. JETP*, vol. 63, pp. 904–912, 1986. [Zh. Eksp. Teor. Fiz.90,1536(1986)].

[218] A. M. Sirunyan *et al.*, "Measurement of single-diffractive dijet production in proton-proton collisions at $\sqrt{s} = 8$ TeV with the CMS and TOTEM experiments," *Eur. Phys. J. C*, vol. 80, no. 12, p. 1164, 2020. [Erratum: Eur.Phys.J.C 81, 383 (2021)].

[219] M. Boonekamp, A. Dechambre, V. Juranek, O. Kepka, M. Rangel, *et al.*, "FPMC: A Generator for forward physics," 2011.

[220] E. B. Hughes, T. A. Griffy, M. R. Yearian, and R. Hofstadter, "Neutron form factors from inelastic electron-deuteron scattering," *Phys. Rev.*, vol. 139, pp. B458–B471, Jul 1965.

[221] T. Janssens, R. Hofstadter, E. B. Hughes, and M. R. Yearian, "Proton form factors from elastic electron-proton scattering," *Phys. Rev.*, vol. 142, pp. 922–931, Feb 1966.

[222] R. C. Walker, B. W. Filippone, J. Jourdan, R. Milner, R. McKeown, D. Potterveld, L. Andivahis, R. Arnold, D. Benton, P. Bosted, G. deChambrier, A. Lung, S. E. Rock, Z. M. Szalata, A. Para, F. Dietrich, K. Van Bibber, J. Button-Shafer, B. Debebe, R. S. Hicks, S. Dasu, P. de Barbaro, A. Bodek, H. Harada, M. W. Krasny, K. Lang, E. M. Riordan, R. Gearhart, L. W. Whitlow, and J. Alster, "Measurements of the proton elastic form factors for $1 \leq Q^2 \leq 3$ $(\mathrm{GeV}/c)^2$ at slac," *Phys. Rev. D*, vol. 49, pp. 5671–5689, Jun 1994.

[223] L. W. Whitlow, E. M. Riordan, S. Dasu, S. Rock, and A. Bodek, "Precise measurements of the proton and deuteron structure functions from a global analysis of the SLAC deep inelastic electron scattering cross-sections," *Phys. Lett. B*, vol. 282, pp. 475–482, 1992.

[224] S. R. Klein and P. Steinberg, "Photonuclear and two-photon interactions at high-energy nuclear colliders," *Annual Review of Nuclear and Particle Science*, vol. 70, no. 1, pp. 323–354, 2020.

[225] J. G. Contreras and J. D. Tapia Takaki, "Ultra-peripheral heavy-ion collisions at the lhc," *International Journal of Modern Physics A*, vol. 30, no. 08, p. 1542012, 2015.

[226] W. Schäfer, "Photon induced processes: from ultraperipheral to semicentral heavy ion collisions," *Eur. Phys. J. A*, vol. 56, no. 9, p. 231, 2020.

[227] L. Schoeffel, C. Baldenegro, H. Hamdaoui, S. Hassani, C. Royon, and M. Saimpert, "Photon–photon physics at the lhc and laser beam experiments, present and future," *Progress in Particle and Nuclear Physics*, vol. 120, p. 103889, 2021.

[228] C. Carimalo, P. Kessler, and J. Parisi, "Validity of the equivalent-photon approximation for virtual photon-photon collisions," *Phys. Rev. D*, vol. 20, pp. 1057–1068, 1979.

[229] V. Budnev, I. Ginzburg, G. Meledin, and V. Serbo, "The Two photon particle production mechanism. Physical problems. Applications. Equivalent photon approximation," *Phys.Rept.*, vol. 15, pp. 181–281, 1975.

[230] L. Adamczyk, E. Banaś, A. Brandt, M. Bruschi, S. Grinstein, J. Lange, M. Rijssenbeek, P. Sicho, R. Staszewski, T. Sykora, M. Trzebiński, J. Chwastowski, and K. Korcyl, "Technical Design Report for the ATLAS Forward Proton Detector," Tech. Rep. CERN-LHCC-2015-009. ATLAS-TDR-024, May 2015.

[231] E. Chapon, C. Royon, and O. Kepka, "Anomalous quartic $WW\gamma\gamma$, $ZZ\gamma\gamma$, and trilinear $WW\gamma$ couplings in two-photon processes at high luminosity at the LHC," *Phys. Rev. D*, vol. 81, p. 074003, 2010.

[232] H. Terazawa, "Two photon processes for particle production at high-energies," *Rev.Mod.Phys.*, vol. 45, pp. 615–662, 1973.

[233] E. Chapon, C. Royon, and O. Kepka, "Anomalous quartic W W gamma gamma, Z

Z gamma gamma, and trilinear WW gamma couplings in two-photon processes at high luminosity at the LHC," *Phys.Rev.*, vol. D81, p. 074003, 2010.

[234] V. Khoze, A. Martin, and M. Ryskin, "Prospects for new physics observations in diffractive processes at the LHC and Tevatron," *Eur.Phys.J.*, vol. C23, pp. 311–327, 2002.

[235] E. Gotsman, E. Levin, U. Maor, E. Naftali, and A. Prygarin, "Survival probability of large rapidity gaps," 2005.

[236] S. Fichet, G. von Gersdorff, B. Lenzi, C. Royon, and M. Saimpert, "Light-by-light scattering with intact protons at the LHC: from Standard Model to New Physics," *JHEP*, vol. 02, p. 165, 2015.

[237] L. A. Harland-Lang, V. A. Khoze, and M. G. Ryskin, "Exclusive lhc physics with heavy ions: Superchic 3," *The European Physical Journal C*, vol. 79, Jan 2019.

[238] M. Albrow, M. Arneodo, V. Avati, J. Baechler, N. Cartiglia, M. Deile, M. Gallinaro, J. Hollar, M. Lo Vetere, K. Oesterberg, N. Turini, J. Varela, D. Wright, and C. CMS-TOTEM, "CMS-TOTEM Precision Proton Spectrometer," Tech. Rep. CERN-LHCC-2014-021. TOTEM-TDR-003. CMS-TDR-13, Sep 2014.

[239] O. Kepka and C. Royon, "Anomalous $WW\gamma$ coupling in photon-induced processes using forward detectors at the LHC," *Phys.Rev.*, vol. D78, p. 073005, 2008.

[240] I. Sahin and S. C. Inan, "Probe of unparticles at the LHC in exclusive two lepton and two photon production via photon-photon fusion," *JHEP*, vol. 09, p. 069, 2009.

[241] S. Atag, S. C. Inan, and I. Sahin, "Extra dimensions in $\gamma\gamma \to \gamma\gamma$ process at the CERN-LHC," *JHEP*, vol. 09, p. 042, 2010.

[242] R. S. Gupta, "Probing Quartic Neutral Gauge Boson Couplings using diffractive photon fusion at the LHC," *Phys.Rev.*, vol. D85, p. 014006, 2012.

[243] L. N. Epele, H. Fanchiotti, C. A. G. Canal, V. A. Mitsou, and V. Vento, "Looking for magnetic monopoles at LHC with diphoton events," *Eur. Phys. J. Plus*, vol. 127, p. 60, 2012.

[244] P. Lebiedowicz, R. Pasechnik, and A. Szczurek, "Search for technipions in exclusive production of diphotons with large invariant masses at the LHC," *Nucl. Phys.*, vol. B881, pp. 288–308, 2014.

[245] S. Fichet and G. von Gersdorff, "Anomalous gauge couplings from composite Higgs and warped extra dimensions," *JHEP03(2014)102*, 2013.

[246] S. Fichet, G. von Gersdorff, O. Kepka, B. Lenzi, C. Royon, and M. Saimpert, "Probing new physics in diphoton production with proton tagging at the Large Hadron Collider," *Phys. Rev.*, vol. D89, p. 114004, 2014.

[247] H. Sun, "Probe anomalous $tq\gamma$ couplings through single top photoproduction at the LHC," *Nucl.Phys.*, vol. B886, pp. 691–711, 2014.

[248] H. Sun, "Large Extra Dimension effects through Light-by-Light Scattering at the CERN LHC," *Eur.Phys.J.*, vol. C74, p. 2977, 2014.

[249] H. Sun, "Dark Matter Searches in Jet plus Missing Energy in γp collision at CERN LHC," *Phys.Rev.*, vol. D90, p. 035018, 2014.

[250] I. Sahin, M. Koksal, S. C. Inan, A. A. Billur, B. Sahin, P. Tektas, E. Alici, and R. Yildirim, "Graviton production through photon-quark scattering at the LHC," *Phys. Rev.*, vol. D91, p. 035017, 2015.

[251] S. C. Inan, "Dimension-six anomalous $tq\gamma$ couplings in $\gamma\gamma$ collision at the LHC," *Nucl. Phys.*, vol. B897, pp. 289–301, 2015.

[252] S. Fichet, "Prospects for new physics searches at the LHC in the forward proton mode," *Acta Phys. Polon. Supp.*, vol. 8, p. 811, 2015.

[253] G.-C. Cho, T. Kono, K. Mawatari, and K. Yamashita, "Search for Kaluza-Klein gravitons in extra dimension models via forward detectors at the LHC," *Phys. Rev.*, vol. D91, no. 11, p. 115015, 2015.

[254] S. Fichet, "Shining Light on Polarizable Dark Particles," *JHEP*, vol. 04, p. 088, 2017.

[255] S. Fichet, G. von Gersdorff, and C. Royon, "Scattering light by light at 750 GeV at the LHC," *Phys. Rev.*, vol. D93, no. 7, p. 075031, 2016.

[256] S. Fichet, G. von Gersdorff, and C. Royon, "Measuring the Diphoton Coupling of a 750 GeV Resonance," *Phys. Rev. Lett.*, vol. 116, no. 23, p. 231801, 2016.

[257] S. Fichet and C. Baldenegro, "Anomalous gauge interactions in photon collisions at the LHC and the FCC," in *Photon 2017, CERN, Geneva, Switzerland, May 22-26, 2017*, 2017.

[258] A. M. Sirunyan *et al.*, "Observation of proton-tagged, central (semi)exclusive production of high-mass lepton pairs in pp collisions at 13 TeV with the CMS-TOTEM precision proton spectrometer," *JHEP*, vol. 07, p. 153, 2018.

[259] "Observation and measurement of forward proton scattering in association with lepton pairs produced via the photon fusion mechanism at ATLAS," no. ATLAS-CONF-2020-041, 2020.

[260] CMS and TOTEM, "First search for exclusive diphoton production at high mass with intact protons in proton-proton collisions at $\sqrt{s}$ =13 TeV at the LHC," Tech. Rep. CMS-PAS-EXO-18-014, 2020.

[261] C. Royon, M. Saimpert, O. Kepka, and R. Zlebcik, "Timing detectors for proton tagging at the LHC," *Acta Physica Polonica B Proceedings supplement*, vol. 7, p. 735, 2014.

[262] G. Jikia and A. Tkabladze, "gamma Z pair production at the photon linear collider," *Phys. Lett.*, vol. B332, pp. 441–447, 1994.

[263] M. L. Laursen, K. O. Mikaelian, and M. A. Samuel, "Z0 decay into three gluons," *Phys. Rev.*, vol. D23, p. 2795, 1981.

[264] J. J. van der Bij and E. W. N. Glover, "*Z* Boson Production and Decay via Gluons," *Nucl. Phys.*, vol. B313, pp. 237–257, 1989.

[265] M. Baillargeon and F. Boudjema, "Contribution of the bosonic loops to the three photon decay of the Z," *Phys. Lett.*, vol. B272, pp. 158–162, 1991.

[266] G. Belanger, F. Boudjema, Y. Kurihara, D. Perret-Gallix, and A. Semenov, "Bosonic quartic couplings at LEP-2," *Eur. Phys. J.*, vol. C13, pp. 283–293, 2000.

[267] O. J. P. Eboli, M. C. Gonzalez-Garcia, and J. K. Mizukoshi, "p p —> j j e+- mu+- nu nu and j j e+- mu-+ nu nu at O(alpha(em)**6) and O(alpha(em)**4 alpha(s)**2) for the study of the quartic electroweak gauge boson vertex at CERN LHC," *Phys. Rev.*, vol. D74, p. 073005, 2006.

[268] M. Baillargeon, F. Boudjema, E. Chopin, and V. Lafage, "New physics with three photon events at LEP," *Z. Phys.*, vol. C71, pp. 431–442, 1996.

[269] K. Olive *et al.*, "Review of Particle Physics," *Chin.Phys.*, vol. C38, p. 090001, 2014.

[270] V. Khachatryan *et al.*, "Performance of Photon Reconstruction and Identification with the CMS Detector in Proton-Proton Collisions at sqrt(s) = 8 TeV," *JINST*, vol. 10, no. 08, p. P08010, 2015.

[271] M. Schroeder, "Performance of jets at CMS," *J. Phys. Conf. Ser.*, vol. 587, no. 1, p. 012004, 2015.

[272] P. Berta, "ATLAS jet and missing-ET reconstruction, calibration, and performance," *Nucl. Part. Phys. Proc.*, vol. 273-275, pp. 1121–1126, 2016.

[273] T. Sjöstrand, S. Ask, J. R. Christiansen, R. Corke, N. Desai, P. Ilten, S. Mrenna, S. Prestel, C. O. Rasmussen, and P. Z. Skands, "An Introduction to PYTHIA 8.2," *Comput. Phys. Commun.*, vol. 191, pp. 159–177, 2015.

[274] O. Kepka, "Impact of multiple pp interactions on proton tagging, presentation at the LHC Working Group on Forward Physics and Diffraction," *May 15-16 2013*.

[275] V. Khoze, A. Martin, and M. Ryskin, "Prospects for new physics observations in diffractive processes at the LHC and Tevatron," *Eur.Phys.J.*, vol. C23, pp. 311–327, 2002.

[276] J. J. Heinrich, "Reconstruction of boosted $W^{\pm}$ and Z^0 bosons from fat jets," Master's thesis, Bohr Inst., 2014-08-15.

[277] D. Decamp *et al.*, "Searches for new particles in Z decays using the ALEPH detector," *Phys. Rept.*, vol. 216, pp. 253–340, 1992.

[278] M. Z. Akwawy *et al.*, "Measurement of the cross-sections of the reactions $e^+e^- \to \gamma\gamma$ and $e^+e^- \to \gamma\gamma\gamma$ at LEP," *Phys. Lett.*, vol. B257, pp. 531–540, 1991.

[279] P. Abreu *et al.*, "Measurement of the $e^+e^- \to \gamma\gamma(\gamma)$ cross-section at LEP energies," *Phys. Lett.*, vol. B327, pp. 386–396, 1994.

[280] G. Aad *et al.*, "Search for new phenomena in events with at least three photons collected in pp collisions at $\sqrt{s}$ = 8 TeV with the ATLAS detector," *Eur. Phys. J.*, vol. C76, no. 4, p. 210, 2016.

[281] E. Witten, "Some Properties of O(32) Superstrings," *Phys. Lett.*, vol. 149B, pp. 351–356, 1984.

[282] J. P. Conlon, "The QCD axion and moduli stabilisation," *JHEP*, vol. 05, p. 078, 2006.

[283] P. Svrcek and E. Witten, "Axions In String Theory," *JHEP*, vol. 06, p. 051, 2006.

[284] A. Arvanitaki, S. Dimopoulos, S. Dubovsky, N. Kaloper, and J. March-Russell, "String Axiverse," *Phys. Rev.*, vol. D81, p. 123530, 2010.

[285] B. S. Acharya, K. Bobkov, and P. Kumar, "An M Theory Solution to the Strong CP Problem and Constraints on the Axiverse," *JHEP*, vol. 11, p. 105, 2010.

[286] M. Cicoli, M. Goodsell, and A. Ringwald, "The type IIB string axiverse and its low-energy phenomenology," *JHEP*, vol. 10, p. 146, 2012.

[287] E. Masso and R. Toldra, "On a light spinless particle coupled to photons," *Phys. Rev.*, vol. D52, pp. 1755–1763, 1995.

[288] C. Csaki, J. Hubisz, and S. J. Lee, "Radion phenomenology in realistic warped space models," *Phys. Rev.*, vol. D76, p. 125015, 2007.

[289] W. D. Goldberger, B. Grinstein, and W. Skiba, "Distinguishing the Higgs boson from the dilaton at the Large Hadron Collider," *Phys. Rev. Lett.*, vol. 100, p. 111802, 2008.

[290] S. Fichet, G. von Gersdorff, E. Ponton, and R. Rosenfeld, "The Excitation of the Global Symmetry-Breaking Vacuum in Composite Higgs Models," *JHEP*, vol. 09, p. 158, 2016.

[291] S. Knapen, T. Lin, H. K. Lou, and T. Melia, "Searching for Axionlike Particles with Ultraperipheral Heavy-Ion Collisions," *Phys. Rev. Lett.*, vol. 118, no. 17, p. 171801, 2017.

[292] M. Aaboud *et al.*, "Evidence for light-by-light scattering in heavy-ion collisions with the ATLAS detector at the LHC," *Nature Phys.*, vol. 13, no. 9, pp. 852–858, 2017.

[293] G. Aad, B. Abbott, D. Abbott, O. Abdinov, A. Abed Abud, K. Abeling, D. Abhayasinghe, S. Abidi, O. AbouZeid, N. Abraham, and et al., "Observation of light-by-light scattering in ultraperipheral pb+pb collisions with the atlas detector," *Physical Review Letters*, vol. 123, Jul 2019.

[294] A. M. Sirunyan *et al.*, "Evidence for light-by-light scattering and searches for axion-like particles in ultraperipheral PbPb collisions at $\sqrt{s_{\mathrm{NN}}} = 5.02$ TeV," *Phys. Lett. B*, vol. 797, p. 134826, 2019.

[295] S. Chatrchyan *et al.*, "Search for exclusive or semi-exclusive photon pair production and observation of exclusive and semi-exclusive electron pair production in pp collisions at $\sqrt{s} = 7$ TeV," *JHEP*, vol. 11, p. 080, 2012.

[296] J. Mitrevski, "Electron and photon reconstruction with the atlas detector," *Nuclear and Particle Physics Proceedings*, vol. 273-275, pp. 2539 – 2541, 2016. 37th International Conference on High Energy Physics (ICHEP).

[297] C. Royon, L. Schoeffel, S. Sapeta, R. B. Peschanski, and E. Sauvan, "A Global analysis of inclusive diffractive cross sections at HERA," *Nucl. Phys.*, vol. B781, pp. 1–31, 2007.

[298] G. Ingelman and P. Schlein, "Jet structure in high mass diffractive scattering," *Physics Letters B*, vol. 152, no. 3, pp. 256 – 260, 1985.

[299] T. Sjostrand, S. Mrenna, and P. Z. Skands, "A Brief Introduction to PYTHIA 8.1," *Comput. Phys. Commun.*, vol. 178, pp. 852–867, 2008.

[300] M. Bauer, M. Neubert, and A. Thamm, "Collider Probes of Axion-Like Particles," *JHEP*, vol. 12, p. 044, 2017.

[301] E. M. Riordan, M. W. Krasny, K. Lang, P. de Barbaro, A. Bodek, S. Dasu, N. Varelas, X. Wang, R. Arnold, D. Benton, P. Bosted, L. Clogher, A. Lung, S. Rock, Z. Szalata, B. W. Filippone, R. C. Walker, J. D. Bjorken, M. Crisler, A. Para, J. Lambert, J. Button-Shafer, B. Debebe, M. Frodyma, R. S. Hicks, G. A. Peterson, and R. Gearhart, "Search for short-lived axions in an electron-beam-dump experiment," *Phys. Rev. Lett.*, vol. 59, pp. 755–758, Aug 1987.

[302] J. D. Bjorken, S. Ecklund, W. R. Nelson, A. Abashian, C. Church, B. Lu, L. W. Mo, T. A. Nunamaker, and P. Rassmann, "Search for neutral metastable penetrating particles produced in the slac beam dump," *Phys. Rev. D*, vol. 38, pp. 3375–3386, Dec 1988.

[303] B. Döbrich, J. Jaeckel, F. Kahlhoefer, A. Ringwald, and K. Schmidt-Hoberg, "Alptraum: Alp production in proton beam dump experiments," *Journal of High Energy Physics*, vol. 2016, p. 18, Feb 2016.

[304] R. Balest *et al.*, "Υ(1s)$\rightarrow\gamma$+noninteracting particles," *Phys. Rev. D*, vol. 51, pp. 2053–2060, Mar 1995.

[305] P. del Amo Sanchez *et al.*, "Search for Production of Invisible Final States in Single-Photon Decays of $\Upsilon(1S)$," *Phys. Rev. Lett.*, vol. 107, p. 021804, 2011.

[306] J. Jaeckel, M. Jankowiak, and M. Spannowsky, "LHC probes the hidden sector," *Phys. Dark Univ.*, vol. 2, pp. 111–117, 2013.

[307] K. Mimasu and V. Sanz, "ALPs at Colliders," *JHEP*, vol. 06, p. 173, 2015.

[308] J. Jaeckel and M. Spannowsky, "Probing MeV to 90 GeV axion-like particles with LEP and LHC," *Phys. Lett.*, vol. B753, pp. 482–487, 2016.

[309] S. Knapen, T. Lin, H. K. Lou, and T. Melia, "LHC limits on axion-like particles from heavy-ion collisions," in *Photon 2017: International Conference on the Structure and the Interactions of the Photon and 22th International Workshop on Photon-Photon Collisions and the International Workshop on High Energy Photon Colliders CERN, Geneva, Switzerland, May 22-26, 2017*, 2017.

[310] Z. Citron *et al.*, "Report from Working Group 5: Future physics opportunities for high-density QCD at the LHC with heavy-ion and proton beams," *CERN Yellow Rep. Monogr.*, vol. 7, pp. 1159–1410, 2019.

[311] A. B. et al., "Vector boson scattering: Recent experimental and theory developments," *Reviews in Physics*, vol. 3, p. 44, 2018.

[312] M. Gallinaro *et al.*, "Beyond the Standard Model in Vector Boson Scattering Signatures," 2020.

[313] O. Kepka and C. Royon, "Anomalous $WW\gamma$ coupling in photon-induced processes using forward detectors at the CERN LHC," *Phys. Rev. D*, vol. 78, p. 073005, 2008.

[314] C. Baldenegro, S. Fichet, G. von Gersdorff, and C. Royon, "Probing the anomalous $\gamma\gamma\gamma$Z coupling at the LHC with proton tagging," *JHEP*, vol. 06, p. 142, 2017.

[315] S. Fichet, G. von Gersdorff, B. Lenzi, C. Royon, and M. Saimpert, "Light-by-light scattering with intact protons at the LHC: from Standard Model to New Physics," *JHEP*, vol. 02, p. 165, 2015.

[316] A. Senol and M. Köksal, "Analysis of anomalous quartic $WWZ\gamma$ couplings in γp collision at the LHC," *Phys. Lett.*, vol. B742, pp. 143–148, 2015.

[317] A. Senol, "$ZZ\gamma$ and $Z\gamma\gamma$ anomalous couplings in γp collision at the LHC," *Phys. Rev.*, vol. D87, p. 073003, 2013.

[318] S. Taheri-Monfared, S. Fayazbakhsh, and M. Mohammadi-Najafabadi, "Exploring anomalous $HZ\gamma$ couplings in γ-proton collisions at the LHC," *Physics Letters B*, vol. 762, pp. 301 – 308, 2016.

[319] E. Gurkanli, V. Ari, A. Gutiérrez-Rodríguez, M. Hernández-Ruíz, and M. Koksal, "Sensitivity physics expected to the measurement of the quartic $WW\gamma\gamma$ couplings at the LHeC and the FCC-he," 2020.

[320] S. Fichet, G. von Gersdorff, O. Kepka, B. Lenzi, C. Royon, and M. Saimpert, "Probing new physics in diphoton production with proton tagging at the Large Hadron Collider," *Phys. Rev. D*, vol. 89, p. 114004, 2014.

[321] V. P. Gonçalves, D. E. Martins, M. S. Rangel, and M. Tasevsky, "Top quark pair production in the exclusive processes at LHC," 7 2020.

[322] L. Harland-Lang, M. Tasevsky, V. Khoze, and M. Ryskin, "A new approach to modelling elastic and inelastic photon-initiated production at the LHC: SuperChic 4," 7 2020.

[323] A. Szczurek and M. Łuszczak, "Production of W^+W^- and $t\bar{t}$ pairs via photon-photon processes in proton-proton scattering," *PoS*, vol. DIS2019, p. 035, 2019.

[324] M. Łuszczak, W. Schäfer, and A. Szczurek, "Production of W^+W^- pairs via $\gamma^*\gamma^* \to W^+W^-$ subprocess with photon transverse momenta," *JHEP*, vol. 05, p. 064, 2018.

[325] L. Forthomme, M. Łuszczak, W. Schäfer, and A. Szczurek, "Rapidity gap survival factors caused by remnant fragmentation for W^+W^- pair production via $\gamma^*\gamma^* \to W^+W^-$ subprocess with photon transverse momenta," *Phys. Lett. B*, vol. 789, pp. 300–307, 2019.

[326] G. Abbiendi *et al.*, "A study of $W^+W^-\gamma$ events at LEP," *Phys. Lett. B*, vol. 580, p. 17, 2004.

[327] G. Abbiendi *et al.*, "Measurement of the $W^+W^-\gamma$ cross-section and first direct limits on anomalous electroweak quartic gauge couplings," *Phys. Lett. B*, vol. 471, p. 293, 1999.

[328] J. Abdallah *et al.*, "Measurement of the $e^+e^- \to W^+W^-\gamma$ cross-section and limits on anomalous quartic gauge couplings with DELPHI," *Eur. Phys. J. C*, vol. 31, p. 139, 2003.

[329] P. Achard *et al.*, "Study of the $W^+W^-\gamma$ process and limits on anomalous quartic gauge boson couplings at LEP," *Phys. Lett. B*, vol. 527, p. 29, 2002.

[330] V. M. Abazov *et al.*, "Search for anomalous quartic $WW\gamma\gamma$ couplings in dielectron and missing energy final states in $p\bar{p}$ collisions at $\sqrt{s}$ = 1.96 TeV," *Phys. Rev. D*, vol. 88, p. 012005, 2013.

[331] S. Chatrchyan *et al.*, "Study of Exclusive Two-Photon Production of W^+W^- in pp Collisions at $\sqrt{s} = 7$ TeV and Constraints on Anomalous Quartic Gauge Couplings," *JHEP*, vol. 07, p. 116, 2013.

[332] V. Khachatryan *et al.*, "Evidence for exclusive $\gamma\gamma \to W^+W^-$ production and constraints on anomalous quartic gauge couplings in pp collisions at $\sqrt{s} = 7$ and 8 TeV," *JHEP*, vol. 08, p. 119, 2016.

[333] M. Aaboud *et al.*, "Measurement of exclusive $\gamma\gamma \to W^+W^-$ production and search for exclusive Higgs boson production in pp collisions at $\sqrt{s} = 8$ TeV using the ATLAS detector," *Phys. Rev. D*, vol. 94, no. 3, p. 032011, 2016.

[334] A. Sirunyan *et al.*, "Particle-flow reconstruction and global event description with the CMS detector," *JINST*, vol. 12, no. 10, p. P10003, 2017.

[335] M. Aaboud *et al.*, "Jet reconstruction and performance using particle flow with the ATLAS Detector," *Eur. Phys. J. C*, vol. 77, no. 7, p. 466, 2017.

[336] G. Aad *et al.*, "Measurement of the cross-section of high transverse momentum vector bosons reconstructed as single jets and studies of jet substructure in pp collisions at $\sqrt{s} = 7$ TeV with the ATLAS detector," *New J. Phys.*, vol. 16, no. 11, p. 113013, 2014.

[337] "Measurement of large radius jet mass reconstruction performance at $\sqrt{s} = 8$ TeV using the ATLAS detector," Tech. Rep. ATLAS-CONF-2016-008, CERN, Geneva, 2016.

[338] V. Khachatryan *et al.*, "Identification techniques for highly boosted W bosons that decay into hadrons," *JHEP*, vol. 12, p. 017, 2014.

[339] G. Aad *et al.*, "Muon reconstruction performance of the ATLAS detector in proton–proton collision data at $\sqrt{s}$ =13 TeV," *Eur. Phys. J. C*, vol. 76, no. 5, p. 292, 2016.

[340] A. Sirunyan *et al.*, "Performance of the CMS muon detector and muon reconstruction with proton-proton collisions at $\sqrt{s} = 13$ TeV," *JINST*, vol. 13, no. 06, p. P06015, 2018.

[341] M. Aaboud *et al.*, "Performance of missing transverse momentum reconstruction with the ATLAS detector using proton-proton collisions at $\sqrt{s}$ = 13 TeV," *Eur. Phys. J. C*, vol. 78, no. 11, p. 903, 2018.

[342] R. Kogler *et al.*, "Jet Substructure at the Large Hadron Collider: Experimental Review," *Rev. Mod. Phys.*, vol. 91, no. 4, p. 045003, 2019.

[343] A. Belyaev, N. D. Christensen, and A. Pukhov, "CalcHEP 3.4 for collider physics within and beyond the Standard Model," *Comput. Phys. Commun.*, vol. 184, pp. 1729–1769, 2013.

[344] O. Kepka and C. Royon, "Anomalous $WW\gamma$ coupling in photon-induced processes using forward detectors at the LHC," *Phys. Rev. D*, vol. 78, p. 073005, 2008.

[345] G. Corcella, I. Knowles, G. Marchesini, S. Moretti, K. Odagiri, P. Richardson, M. Seymour, and B. Webber, "HERWIG 6: An Event generator for hadron emission reactions with interfering gluons (including supersymmetric processes)," *JHEP*, vol. 01, p. 010, 2001.

[346] J. Thaler and K. Van Tilburg, "Identifying Boosted Objects with N-subjettiness," *JHEP*, vol. 03, p. 015, 2011.

[347] "Optimisation of large-radius jet reconstruction for the ATLAS detector in 13 TeV proton-proton collisions," Tech. Rep. ATLAS-CONF-2020-021, CERN, Geneva, 2020.

[348] T. Aaltonen *et al.*, "Direct Measurement of the W Production Charge Asymmetry in $p\bar{p}$ Collisions at $\sqrt{s} = 1.96$ TeV," *Phys. Rev. Lett.*, vol. 102, p. 181801, 2009.

[349] B. Grzadkowski, M. Iskrzynski, M. Misiak, and J. Rosiek, "Dimension-Six Terms in the Standard Model Lagrangian," *JHEP*, vol. 10, p. 085, 2010.

[350] O. J. Eboli, M. Gonzalez-Garcia, S. Lietti, and S. Novaes, "Anomalous quartic gauge boson couplings at hadron colliders," *Phys. Rev. D*, vol. 63, p. 075008, 2001.

[351] M. Baak *et al.*, "Working Group Report: Precision Study of Electroweak Interactions," in *Community Summer Study 2013: Snowmass on the Mississippi*, 2013.

[352] G. Belanger, F. Boudjema, Y. Kurihara, D. Perret-Gallix, and A. Semenov, "Bosonic quartic couplings at LEP-2," *Eur. Phys. J. C*, vol. 13, pp. 283–293, 2000.

[353] O. Behnke, K. Kröninger, T. Schörner-Sadenius, and G. Schott, eds., *Data analysis in high energy physics: A practical guide to statistical methods*. Weinheim, Germany: Wiley-VCH, 2013.

[354] S. Tizchang and S. M. Etesami, "Pinning down the gauge boson couplings in $WW\gamma$ production using forward proton tagging," 2020.

[355] G. Chachamis, "BFKL phenomenology," in *New Trends in High-Energy Physics and QCD*, (2016), 12 2015.

Appendix A

The high energy limit

In this Appendix, we sketch the discussion on the high-energy limit of QCD interactions, which gives rise to the BFKL equation of perturbative QCD. The appendix is based on the description given in Refs. (133; 134; 355). The focus in this appendix is on the leading-logarithmic approximation for the derivation of the BFKL equation.

We begin by considering the scattering of two quarks at the lowest order in perturbation theory. Since we are interested in the behavior of the interactions in the high-energy limit, where $s \gg -t \gg \Lambda^2_{\rm QCD}$, we focus on the quark-quark interaction via t-channel gluon exchange. We will focus on terms that contribute significantly in the leading-logarithmic approximation, i.e., those that yield a factor of $\ln(s)$ after performing the respective phase space integrals.

The amplitude for the process at hand at LO in α_s is

$$A^{(0)}(s,t) = 8\pi a_s \, \mathscr{C}\mathscr{F}_1 \frac{s}{q^2} = 8\pi a_s \, \mathscr{C}\mathscr{F}_1 \frac{s}{t} \tag{A.1}$$

where $\mathscr{C}\mathscr{F}_1$ denotes a color factor. Herafter, we would be paying mostly attention to the dependence on s and t of the scattering amplitudes. The specific form of the color factors is shown in Refs. (133; 134), and they depend on whether we are considering color-singlet, color-octet, or other color-multiplet exchanges

We see that there are no logarithms of s at Born-level in Eqn. (A.1). Indeed, the logarithms of energy of importance appear upon considering next-to-leading order corrections to the scattering amplitude.

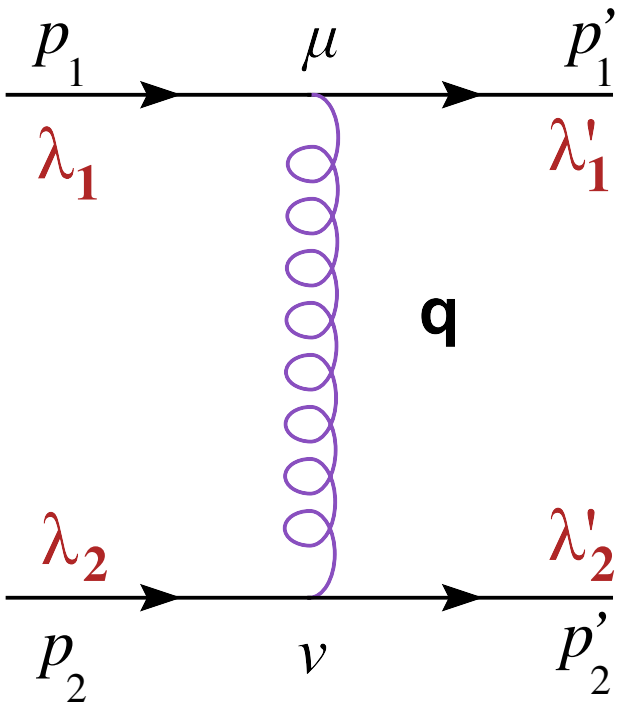

Figure A.1: Leading order diagram for qq scattering in the high-energy limit $s \gg -t \gg \Lambda^2_{\rm QCD}$.

Thus, in moving to the next-to-leading order calculation, we consider additional gluon emissions. The radiative corrections can be virtual or real. For the discussion, we consider the virtual radiative corrections. At any rate, these are the diagrams that are important for the color-singlet exchange contribution of relevance for this thesis.

To calculate the scattering amplitude, one can restrict the analysis to the calculation of its imaginary part. The real part of the amplitude is then determined via dispersion relations connecting real and imaginary parts. The usefulness of the calculation based on the imaginary part of the scattering amplitude is that we can exploit its relation to forward scattering. In particular, we can use Cutkosky's cut rules to more easily calculate amplitudes of probability with virtual corrections by "cutting" the diagram into tree-level diagrams, where the internal propagators are put on-shell. Cutkosky's cutting rules are based on the analyticity and unitarity of scattering amplitudes in S-matrix theory.

One-loop diagrams with self-energy corrections to the propagators and vertex correc-

tions are subleading in the leading-logarithm approximation. Only box diagrams contribute in this case. The dominant ones contribute at the leading-logarithmic approximation are shown in Fig. A.1.

Denoting the NLO amplitude by $A^{(1)}(s,t)$, Cutkosky cutting rules tells us that the imaginary part may be computed as

$$\mathrm{Im}A^{(1)}(s,t) = \frac{1}{2}\int d\mathrm{PS}^{(2)} A^{(0)}(s,k^2) A^{(0)\dagger}(s,(k-q)^2)\,, \tag{A.2}$$

where $A^{(0)}(s,k^2)$ and $A^{(0)\dagger}(s,(k-q)^2)$ are the tree level amplitudes with the quark lines being on shell at the cut points. $A^{(0)\dagger}$ stands for the hermitian conjugate of $A^{(0)}$, and where the two-body phase space $\int d\mathrm{PS}^{(2)}$ is given by

$$\int d\mathrm{PS}^{(2)} = \int \frac{d^4k}{(2\pi)^2}\delta((p_1-k)^2)\delta((p_2+k)^2)\,. \tag{A.3}$$

$$A^{(1)}(s,t) \;=\; -4\frac{\alpha_s^2}{\pi}\mathscr{C}\mathscr{F}_4 \ln(\frac{s}{t})\, s\int \frac{d^2\mathbf{k}}{\mathbf{k}^2(\mathbf{k}-\mathbf{q})^2}\,. \tag{A.4}$$

We define the gluon Regge trajectory,

$$\varepsilon(t) = \frac{N_c\alpha_s}{4\pi^2}\int -\mathbf{q}^2\,\frac{d^2\mathbf{k}}{\mathbf{k}^2(\mathbf{k}-\mathbf{q})^2}\,, \tag{A.5}$$

The importance of $\varepsilon(t)$ will be highlighted later in the calculation. With the definition of $\varepsilon(t)$, Eqn. A.4 can be rewritten as

$$A^{(1)}(s,t) \;=\; -\frac{16\pi\alpha_s}{N_c}\mathscr{C}\mathscr{F}_4\frac{s}{t}\ln(\frac{s}{t})\,\varepsilon(t)\,, \tag{A.6}$$

whereas for the Fig. A.1 diagram in the crossed channel it will be:

$$A^{(1)}_{\mathrm{cross}}(s,t) \;=\; -\frac{16\pi\alpha_s}{N_c}\mathscr{C}\mathscr{F}_5\frac{u}{t}\ln(\frac{u}{t})\,\varepsilon(t)\,. \tag{A.7}$$

After adding the last two equations, and since in the high-energy limit $u \simeq -s$, we obtain the one-loop amplitude. For purposes of illustration, we will focus on the amplitude for color-octet exchange, which yields a simplified result. The color-octet exchange amplitude can be obtained by means of so-called color projection operators. The latter are described in detail in Refs. (133; 134). One notes that the color-octet one-loop amplitude can be expressed in terms of the tree-level one,

$$A_8^{(1)}(s,t) = A^{(0)} \ln(\frac{s}{|t|})\, \varepsilon(t)\,. \tag{A.8}$$

going one higher-order in the perturbative expansion for the virtual radiative corrections, up to $\mathcal{O}(\alpha_s^3)$, one has to consider several Feynman diagrams like the ones shown in Fig. A.5. However, not all of them contribute to the amplitude with leading logarithms of s. Indeed, in the leading logarithmic approximation, the only diagrams that need to be considered are box diagrams, in particular, the two-loop diagrams shown in Fig. A.3.

Using the Cutkosky rules and dispersion relations again, we can calculate the imaginary part of the amplitude of the two-loop diagrams into one-loop and tree-level diagrams. The resulting one-loop and tree-level Feynman diagrams have been calculated already one order lower in α_s in the perturbative expansion. Indeed, in Fig. A.3, after multiplying the amplitudes to the left of the cut line by the hermitian conjugates of the amplitudes to the right of the cut line, and performing the phase space integral, we get the result

$$A_8^{(2)}(s,t) = A^{(0)}(s,t)\, \frac{1}{2} \ln^2(\frac{s}{|t|})\, \varepsilon^2(t) \tag{A.9}$$

where the two-loop amplitude is expressed in terms of the LO one. The expressions for $A_8^{(2)}(s,t)$ and $A_8^{(1)}(s,t)$ tell us that the partial result for the amplitude up to order $\mathcal{O}(\alpha_s^3)$ is

$$A_8^{\text{partial}}(s,t) = A^{(0)}(s,t) \left(1 + \ln(\frac{s}{|t|})\, \varepsilon(t) + \frac{1}{2} \ln^2(\frac{s}{|t|})\, \varepsilon^2(t)\right) \tag{A.10}$$

One can wonder, what happens when we consider α_s^4 diagrams? In this case, the

three-loop contributions that dominate in the leading $\ln(s)$ approximation would be again from box diagrams. We could use again the same strategy of using Cutkosky cutting rules to relate the α_s^4 amplitude with the lower order amplitudes that were already calculated, followed by the use of dispersion relations. And in principle, one could keep doing this for higher-order corrections. When should one stop?

The partial result of Eqn.(A.10) suggests that the all-orders virtual amplitude may have the form

$$A_8(s,t) = A^{(0)}(s,t)\left(1+\ln(\frac{s}{|t|})\,\varepsilon(t)+\frac{1}{2}\ln^2(\frac{s}{|t|})\,\varepsilon^2(t)+\ldots\right) \tag{A.11}$$

namely, a product of the tree level amplitude and something that looks very much like a Taylor series expansion of an exponential function. If we continued the expansion to include all terms of the series, the closed form of the expression would be of the form

$$A_8(s,t) = A^{(0)}(s,t)\left(\frac{s}{|t|}\right)^{\varepsilon(t)}. \tag{A.12}$$

The scattering amplitude of qq scattering for color-octet exchange in the high-energy limit is given by a product of the Born-level scattering amplitude enhanced by a factor of $\left(\frac{s}{|t|}\right)^{\varepsilon(t)}$. This is another way of saying that the cross section scales with a power of s.

In fact, the result of the calculation for virtual radiative corrections to the scattering amplitude in the high-energy limit suggests that one may use an effective gluon propagator that resembles the QCD propagator of the gluon, but with properties that emerge when it is "dressed" by other gluons in the high-energy limit. Such an object is known as a *reggeized gluon*, and it has a propagator given by

$$D_{\mu\nu}(s,q^2) = -i\frac{g_{\mu\nu}}{q^2}\left(\frac{s}{\mathbf{k}^2}\right)^{\varepsilon(q^2)}. \tag{A.13}$$

Eqn. (A.13) states that, in the high energy limit, one can account for an all-orders resummation of large logarithms of s coming from virtual radiative corrections using a

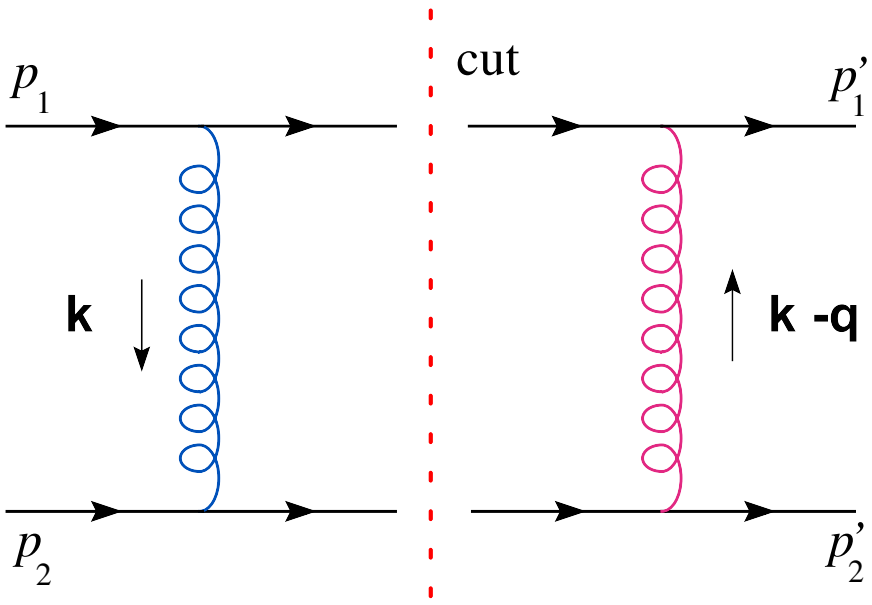

Figure A.2: Two-gluon exchange box diagram cut into two single-gluon exchange diagrams, following Cutkosky cutting rules for the calculation of the imaginary part of the amplitude. Figure from Ref. (355).

modified propagator for the t-channel gluon.

To continue the analysis, now we look into the real radiative corrections for the high-energy qq scattering. The Feynman diagrams for the lowest order radiative corrections are shown in Fig. A.4. All the contributions of $qq \to qqg$ can be collected together in a non-local gauge invariant effective vertex known as "Lipatov effective vertex," symbolically represented in Fig. A.6. The Lipatov vertex is particularly important to understand the behavior of QCD in the high energy limit.

The combination of the various real emission diagrams into a single diagram where we consider one gluon emission in the s-channel that connects to the t-channel gluon by means of a Lipatov effective vertex allows for the iteration of this prescription to cover an arbitrary high n-gluon emissions.

Indeed, to consider the next order calculation, we have to consider diagrams with two real gluon emissions. This would necessitate the inclusion of two Lipatov effective vertices with three reggeized gluon propagators in the t-channel, followed by the respective

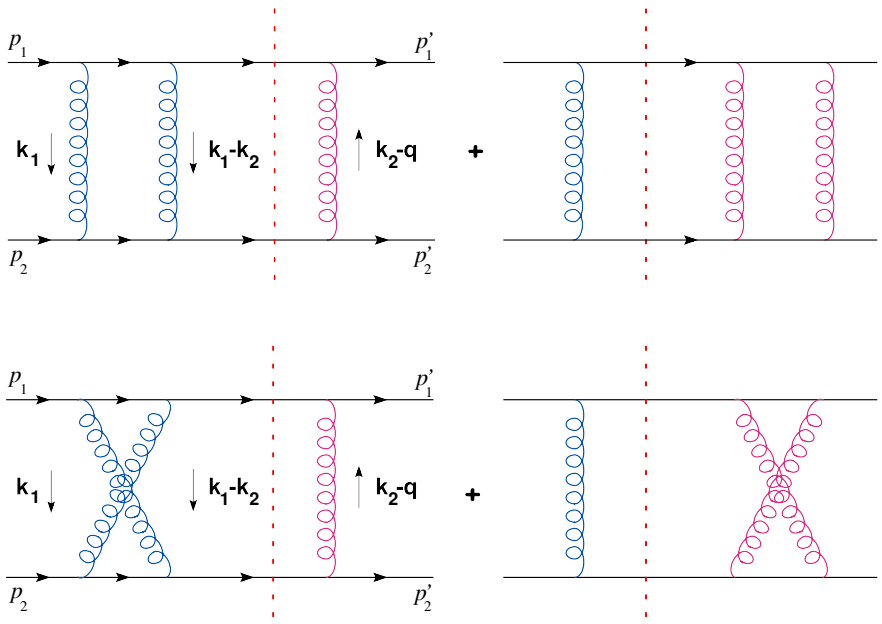

Figure A.3: Dominant $\mathcal{O}(\alpha_s^3)$ virtual-emission diagrams contributing to the amplitude at leading-logarithm in s. The vertical dashed line represents the diagram cuts used when using Cutkosky rules for calculating the imaginary part of the amplitude. Figure from Ref. (355).

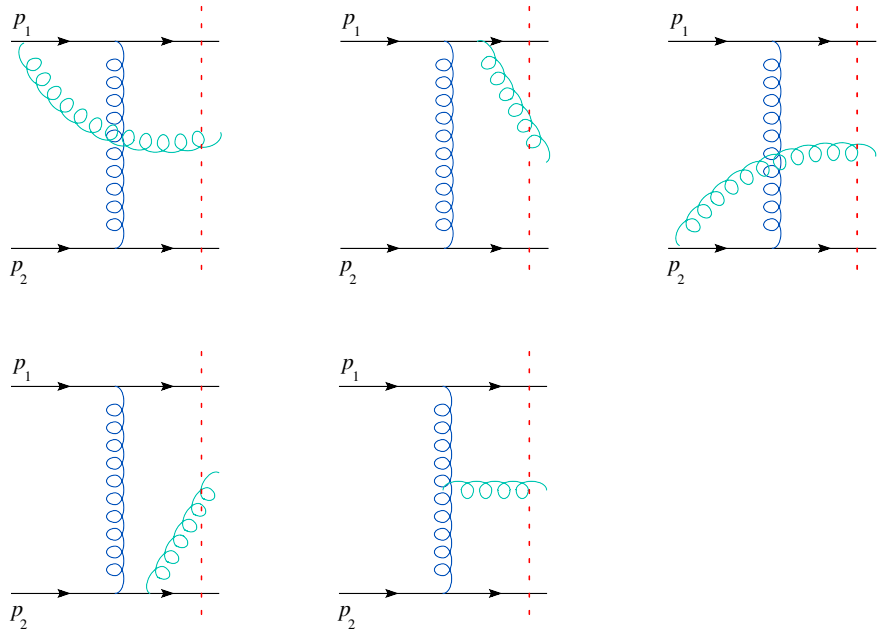

Figure A.4: Dominant one-gluon emission diagrams contributing to the amplitude at leading-logarithm in s. Figure from Ref. (355).

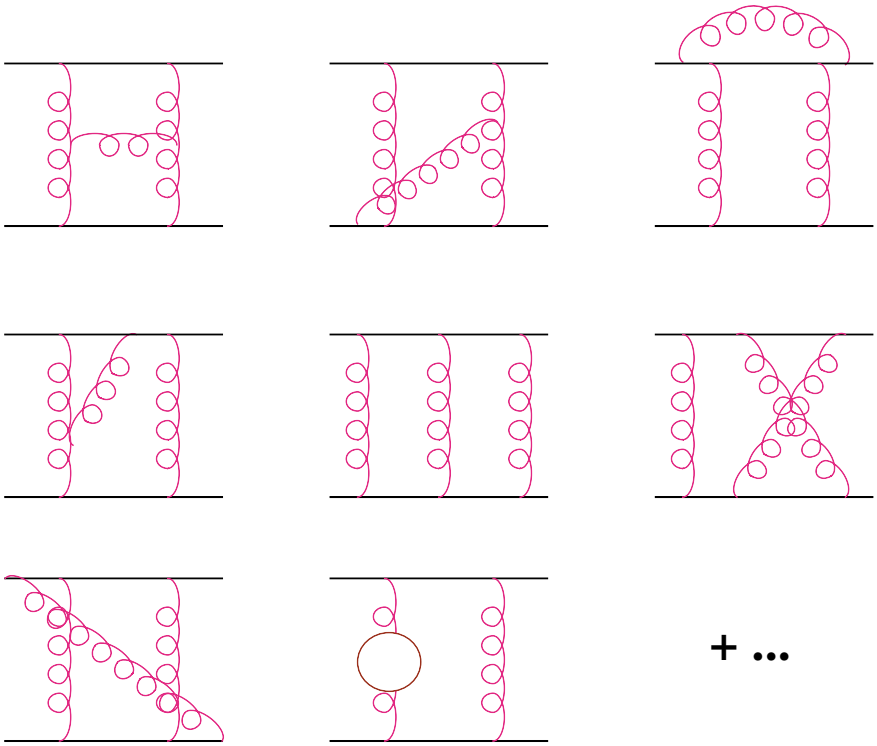

Figure A.5: Two-loop diagrams for qq scattering. In the leading-logarithm approximation in the high-energy limit of QCD, the self-energy and vertex corrections are subleading. Figure from Ref. (355).

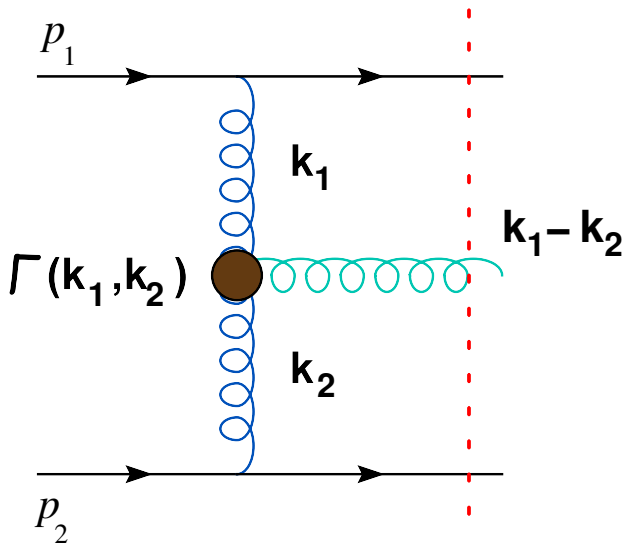

Figure A.6: Diagram of a Lipatov effective vertex. It combines all possible Feynman diagrams with one gluon emission in a single gauge invariant effective vertex with its own tensor structure. Figure from Ref. (355).

phase space integration in order to obtain the logarithm of s. In a similar way, one can then ask: What happens if you consider three real gluon emissions, four real gluon emissions, five real gluon emissions... The result of this iteration leads to a tree-level amplitude that is expressed in terms of products

The aforementioned insertion of Lipatov vertices allows for the construction of *gluon ladder* diagrams. A gluon ladder consists of n gluon rungs connected to the t-channel reggeized gluons via Lipatov effective vertices. For n gluon rungs, the t-channel gluons are partitioned into $n+1$ reggeized propagators. The combination of all the contributions from $n=0$ to $n\to\infty$ leads to the construction of the perturbative pomeron exchange.

In order to construct the gluon ladder diagram, it is useful to note that only diagrams that satisfy a special kinematical configuration need to be considered. This configuration is known as "multi-Regge kinematics." The multi-Regge kinematics are such that

$$\begin{aligned} &\mathbf{k}_1^2 \simeq \mathbf{k}_2^2 \simeq \ldots \simeq \mathbf{k}_n^2 \simeq \mathbf{k}_{n+1}^2 \simeq \mathbf{k}_{n+1}^2 \gg \mathbf{q}^2 \simeq s_0, \\ &\qquad y_1 \gg y_2 \gg y_3 \gg \ldots \gg y_{n-1} \gg y_n \gg y_{n+1} \end{aligned} \tag{A.14}$$

The s-channel gluons carry similar amounts of transverse momenta and have a strong ordering in rapidity. Multi-Regge kinematics ensure that we pick up only the relevant Feynman diagrams that contribute to the scattering amplitude in the leading-logarithm approximation. This kinematic configuration is very useful for us to get a physical picture of the parton emission pattern of relevance in the high-energy limit. We mention here that, in contrast, one can have strong ordering in transverse momenta and a mild ordering in rapidity. The latter kinematic configuration enhances the so-called collinear logarithms (terms of the form $\alpha_s \ln(Q^2/Q_0^2)$, which are resummed in the DGLAP picture.

The nested integration over phase space is rather complicated to carry out in momentum space. Instead, one can use the properties of its Mellin transform to carry out such

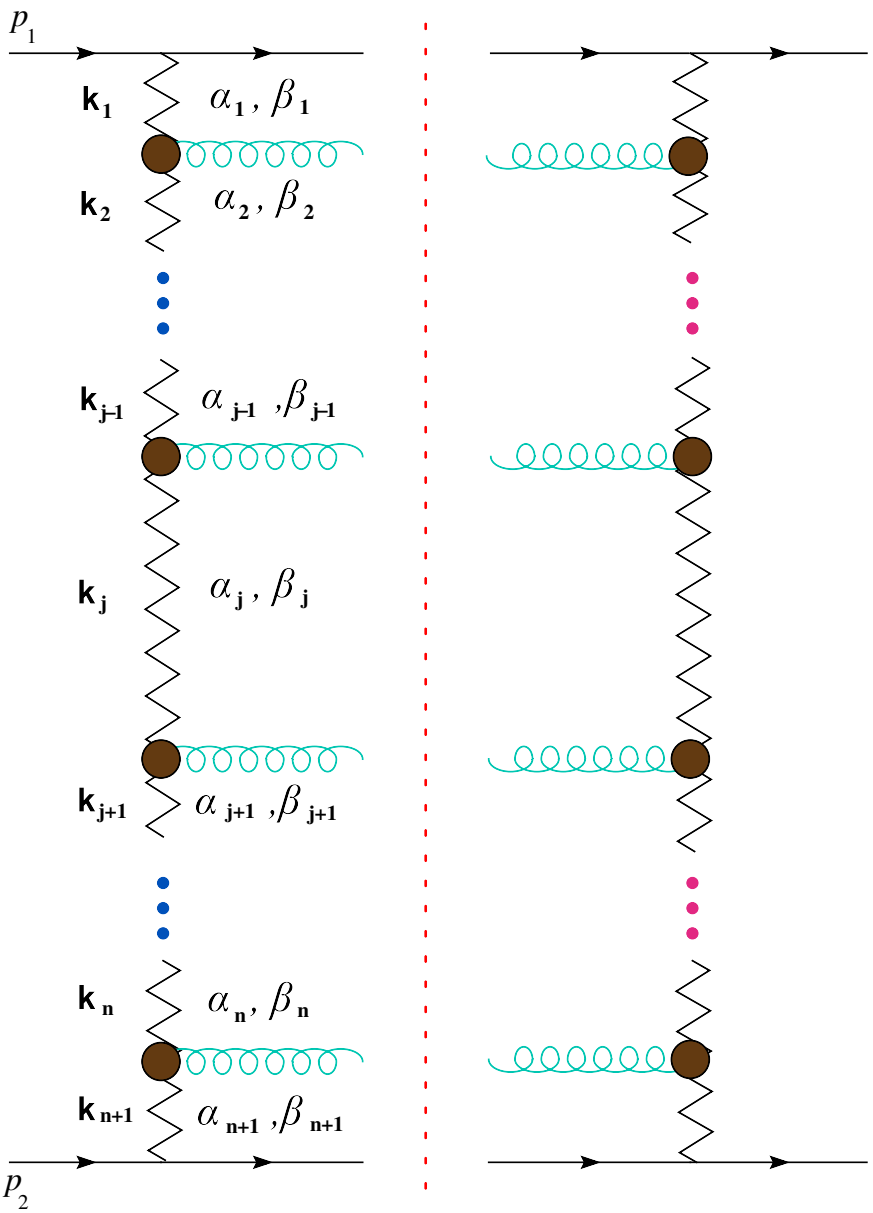

Figure A.7: BFKL gluon-ladder diagram. The disk symbols represent the Lipatov effective vertices.

calculation. One of the properties of the Mellin transform is that, nested integrals such as the ones in hand can be converted into a product of integrals, which is easier to calculate. Once we carry out the calculation in Mellin space, we can apply an inverse transform to go back to the original problem.

The Mellin transform of the imaginary part of the amplitude is defined as

$$f(\omega,t) = \int_1^\infty \mathrm{d}\left(\frac{s}{s_0}\right)\left(\frac{s}{s_0}\right)^{-\omega-1}\frac{\mathrm{Im}\mathscr{A}(s,t)}{s}. \tag{A.15}$$

where the Mellin transform $f(\omega,t)$ is defined in the complex angular momentum space ω, which is the Mellin conjugate variable of s.

One can construct the Mellin transform of the unintegrated scattering amplitude (without performing the integrals over $\mathbf{k}_a$ and $\mathbf{k}_b$, the transverse momenta of the outermost reggeized gluons), which will be defined by the symbol $f_\omega(\mathbf{k}_a,\mathbf{k}_b,t)$. The function $f_\omega(\mathbf{k}_a,\mathbf{k}_b,t)$ is known as the BFKL Green's function. Since $t \simeq -\mathbf{q}^2$, where $\mathbf{q}^2$ is the amount of momentum transfer in the t-channel, we use the notation $f_\omega(\mathbf{k}_a,\mathbf{k}_b,\mathbf{q}^2)$.

One could then take $n=1$ gluon rung in the ladder diagram and calculate the corresponding $f_\omega^{(1)}(\mathbf{k}_a,\mathbf{k}_b,\mathbf{q}^2)$ function. Similarly, for $n=2$ gluon rungs, one would obtain an $f_\omega^{(2)}(\mathbf{k}_a,\mathbf{k}_b,\mathbf{q})$ function. Upon iterating this procedure to $n\to\infty$ and summing up all contributions, one would compute the complete function $f_\omega(\mathbf{k}_a,\mathbf{k}_b,\mathbf{q}^2)$. Doing this manually term-by-term is impossible (humans, like most biological arrangements of atoms, have a finite lifetime!). However, one can exploit the "nesting" properties of the Mellin transform in order to perform such a calculation.

After taking the Mellin transform in Eqn. (A.15) and writing the generic expression for $f_\omega(\mathbf{k}_a,\mathbf{k}_b,\mathbf{q}^2)$ with the phase space integration still to be done, one realizes that there exists an integral equation which governs the behavior of f_ω:

$$\begin{aligned}\omega f_\omega(\mathbf{k}_a,\mathbf{k}_b,\mathbf{q}) &= \delta^2(\mathbf{k}_a-\mathbf{k}_b)\\ &+\frac{\bar{\alpha}_s}{2\pi}\int d^2\mathbf{l}\Bigg\{\frac{-\mathbf{q}^2}{(\mathbf{l}-\mathbf{q})^2\mathbf{k}_a^2}f_\omega(\mathbf{l},\mathbf{k}_b,\mathbf{q})\\ &+\frac{1}{(\mathbf{l}-\mathbf{k}_a)^2}\left(f_\omega(\mathbf{l},\mathbf{k}_b,\mathbf{q}^2)-\frac{\mathbf{k}_a^2 f_\omega(\mathbf{k}_a,\mathbf{k}_b,\mathbf{q})}{\mathbf{l}^2+(\mathbf{k}_a-\mathbf{l})^2}\right)\\ &+\frac{1}{(\mathbf{l}-\mathbf{k}_a)^2}\Bigg(\frac{(\mathbf{k}_a-\mathbf{q})^2\mathbf{l}^2 f_\omega(\mathbf{l},\mathbf{k}_b,\mathbf{q}^2)}{(\mathbf{l}-\mathbf{q})^2\mathbf{k}_a^2}\\ &-\frac{(\mathbf{k}_a-\mathbf{q})^2 f_\omega(\mathbf{k}_a,\mathbf{k}_b,\mathbf{q}^2)}{(\mathbf{l}-\mathbf{q})^2(\mathbf{k}_a-\mathbf{l})^2}\Bigg)\Bigg\}\end{aligned} \tag{A.16}$$

with $\bar{\alpha}_s = N_c\alpha_s/\pi$. This is the color-singlet BFKL equation. It describes the leading logarithmic evolution of the gluon ladder in $\ln(s)$.

The BFKL equation simplifies significantly for no momentum transfer, $\mathbf{q^2}=0$:

$$\begin{aligned}\omega f_\omega(\mathbf{k}_a,\mathbf{k}_b) &= \delta^2(\mathbf{k}_a-\mathbf{k}_b)\\ &+\frac{\bar{\alpha}_s}{2\pi}\int\frac{d^2\mathbf{l}}{(\mathbf{l}-\mathbf{k}_a)^2}\left(f_\omega(\mathbf{l},\mathbf{k}_b)-\frac{\mathbf{k}_a^2 f_\omega(\mathbf{k}_a,\mathbf{k}_b)}{\mathbf{l}^2+(\mathbf{k}_a-\mathbf{l})^2}\right).\end{aligned} \tag{A.17}$$

we can write the BFKL equation in a more compact, symbolic way

$$\omega f_\omega(k_a,k_b) = \delta^2(k_a-k_b)+\int \mathrm{d}^2\ell\,\mathscr{K}(k_a,\ell)f_\omega(\ell,k_b) \tag{A.18}$$

where $\mathscr{K}(k_a,\ell)$ is the so-called BFKL kernel defined as

$$\mathscr{K}(k_a,\ell) = 2\varepsilon(-k^2)\delta^2(k_a-1)+\frac{N_c\alpha_s}{\pi}\frac{1}{(k_a-k_b)^2} \tag{A.19}$$

where the first and second pieces on the right-hand side of the equation corresponds to the virtual and real corrections, respectively. The BFKL expressed in this compact format is telling us something interesting; it is telling us that we can build the gluon Green function iteratively, rung-by-rung. This is shown schematically in Fig. A.8.

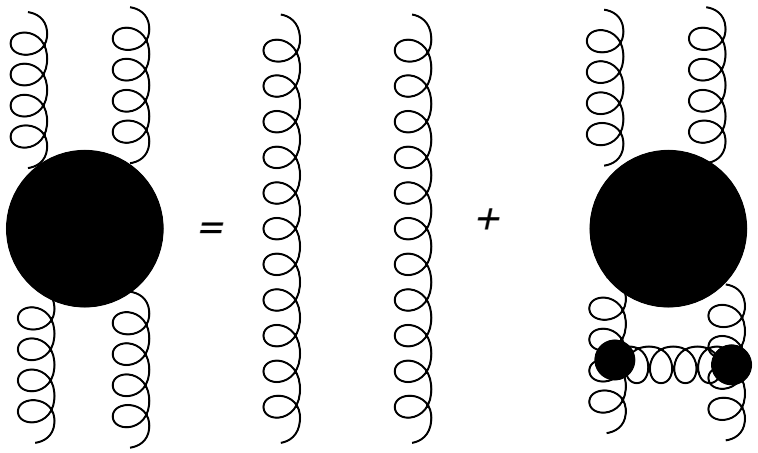

Figure A.8: Symbolic diagram of the BFKL equation. The interpretation is that the BFKL equation recursively adds additional s-channel gluon contributions to the gluon ladder.

Solving the BFKL evolution equation in Mellin space means that we can construct the BFKL gluon Green function in momentum space. From the BFKL gluon Green function, we can construct the imaginary part of the amplitude for $qq \to qq$ scattering in two steps. This is done by applying an inverse Mellin transform to return to standard momentum space (s,t). The inverse Mellin transform is defined as

$$f(s,\mathbf{k}_a,\mathbf{k}_b,\mathbf{q}) = \frac{1}{2\pi i}\int_{c-i\infty}^{c+i\infty} d\omega \left(\frac{s}{s_0}\right)^{\omega} f_\omega(\mathbf{k}_a,\mathbf{k}_b,\mathbf{q}) \tag{A.20}$$

the inverse transform is then convolved with the phase space measures and gluon propagators to obtain the amplitude of interest. We need to integrate over the $\mathbf{k}_a$ and $\mathbf{k}_b$ momenta of the reggeized gluons:

$$\mathscr{A}_{\text{singlet}}(s,t) = i(8\pi\alpha_s)^2 s \frac{N_c^2-1}{4N_c^2}\int \frac{d^2\mathbf{k}_a}{(2\pi)^2}\frac{d^2\mathbf{k}_b}{(2\pi)^2}\frac{f(s,\mathbf{k}_a,\mathbf{k}_b,\mathbf{q})}{\mathbf{k}_b^2(\mathbf{k}_a-\mathbf{q})^2}, \tag{A.21}$$

The amplitude in Eqn. (A.21) is that of a perturbative pomeron exchange between the quarks, which corresponds to the color-singlet exchange of two BFKL gluon ladders. The

respective color factor is written explicitly in Eqn. (A.21).

The BFKL equation can be written symbolically as

$$\omega F = I\!I + \mathscr{K} \otimes F, \tag{A.22}$$

with $\mathscr{K}$ being the BFKL kernel. This expression suggests that one may as well use the complete set of eigenfunctions of $\mathscr{K}$ to solve the BFKL equation, i.e., find an expression for the unknown F. Denoting the eigenfunctions of $\mathscr{K}$ by ϕ_a (sometimes called "BFKL eigenfunctions" with slight abuse of language), we have

$$\mathscr{K} \otimes \phi_a = \omega_a \phi_a \,. \tag{A.23}$$

where ω_a is the eigenvalue associated to ϕ_a. If θ is the azimuthal angle on the transverse plane, then the eigenfunctions can be expressed as,

$$\phi_{n\nu}(|\boldsymbol{k}|,\theta) = \frac{1}{\pi\sqrt{2}}(\boldsymbol{k}^2)^{-\frac{1}{2}+i\nu}\, e^{in\theta}\,. \tag{A.24}$$

with their corresponding eigenvalues

$$\omega_n(\gamma) = \frac{\alpha_s N_c}{\pi}\left(2\psi(1) - \psi(\gamma+\frac{n}{2}) - \psi(1-\gamma+\frac{n}{2})\right),\ \ \psi(\gamma) = \Gamma'(\gamma)/\Gamma(\gamma)$$

and $\gamma = 1/2 + i\nu$. The set of eigenfunctions is complete with ν taking real values between $-\infty$ and ∞. The solution may be expressed using the eigenfunctions as a complete basis,

$$f(\mathbf{k}_a,\mathbf{k}_b,Y) = \frac{1}{\pi\mathbf{k}_a\mathbf{k}_b}\sum_{n=-\infty}^{\infty}\int\frac{d\omega}{2\pi i}e^{\omega\Delta y}\int\frac{d\gamma}{2\pi i}\left(\frac{\mathbf{k}_a^2}{\mathbf{k}_b^2}\right)^{\gamma-\frac{1}{2}}\frac{e^{in\theta}}{\omega-\omega_n(\alpha_s,\gamma)}, \tag{A.25}$$

where $\Delta y = \ln\left(\frac{s}{s_0}\right)$ is the rapidity difference between the outermost gluons carrying

momenta $\mathbf{k}_a$ and $\mathbf{k}_b$. Eqn. (A.25) shows an important prediction from BFKL; the cross section has a power-like growth with energy, which is embedded in the $e^{\omega\Delta y}$ factor. This is one of the most notable features of the BFKL equation. At this point, the BFKL problem could be considered as "solved" at the leading-logarithmic accuracy, so resumming terms of the form $\alpha_s^n \ln^n(s)$ to all orders.

Appendix B

Jet-gap-jet cross checks

A Pseudorapidity interval size

One may object that the size of the fixed pseudorapidity region is not large enough. In this section, we show that larger pseudorapidity intervals do not lead to different conclusions. Larger fixed pseudorapidity regions capture more charged particle tracks. This results in charged particle multiplicities biased towards larger values of the multiplicity (by definition), including possibly existing color-singlet exchange signals. This forces one to redefine the signal integration region to larger multiplicities, and makes the background substraction procedure less reliable (since the signal is spread further, and the fit region for the NBD method is larger). Furthermore, for isolating BFKL dynamics, what we really care about is the pseudorapidity separation between the jets, not the size of the pseudorapidity gap itself. The minimum pseudorapidity interval of 2 units suffices this needs, since it efficiently allows the separation between the two contributions. The charged particle multiplicities for different fixed pseudorapidity intervals can be seen in Fig. B.1 and the extracted color-singlet fraction can be seen in Fig. B.2.

B Energy thresholds determination

PF objects of CMS are used to compute $\xi^{\pm}_{\mathrm{CMS}}$, and this quantity in turn is used to separate diffractive dijet events from non-diffractive dijet events with protons from secondary interactions in the same bunch crossing. Thresholds on the energy of the PF objects are

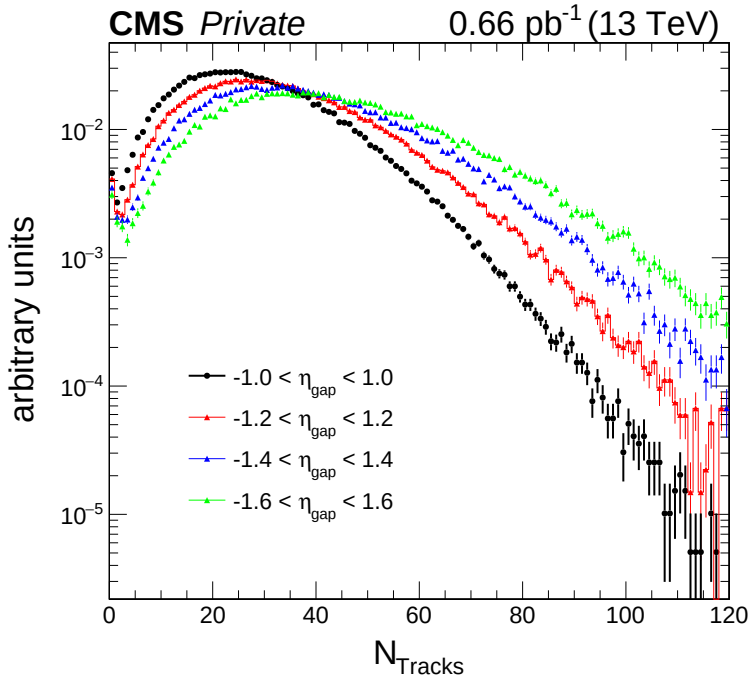

Figure B.1: Charged particle multiplicity as a function of η_{gap} size. The minimum pseudorapidity of the jets is of at least 0.4 units above the edges of the fixed pseudorapidity gaps.

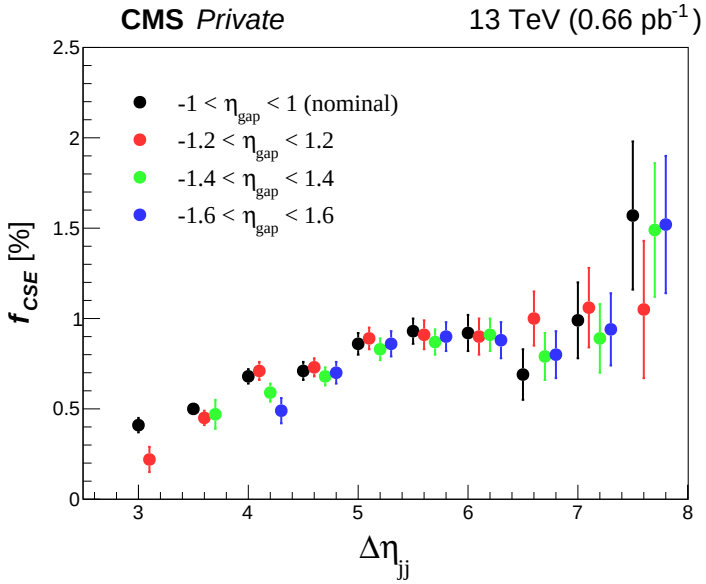

Figure B.2: Color-singlet exchange fraction as a function of $\Delta\eta_{jj}$ for various fixed pseudorapidity region intervals.

necessary.

The energy thresholds for each PF object were determined following a similar procedure as in the analysis of single diffractive dijet at 8 TeV by studying the energy spectrum for different vertices qualities for every PF object for different detector sections based on a zero-bias data sample. The thresholds were chosen to retain at least 90% of the events.

For this study, we considered zero-bias events with a single primary vertex. Four different cuts on the number of degrees of freedom n_{dof} are applied. The "good" vertex selection corresponds to $n_{\text{dof}} \geq 4$. Events with $n_{\text{dof}} = 0$ or $n_{\text{dof}} \leq 2, 3$ are more prone to yield energy spectrums from calorimeter noise at low energies.

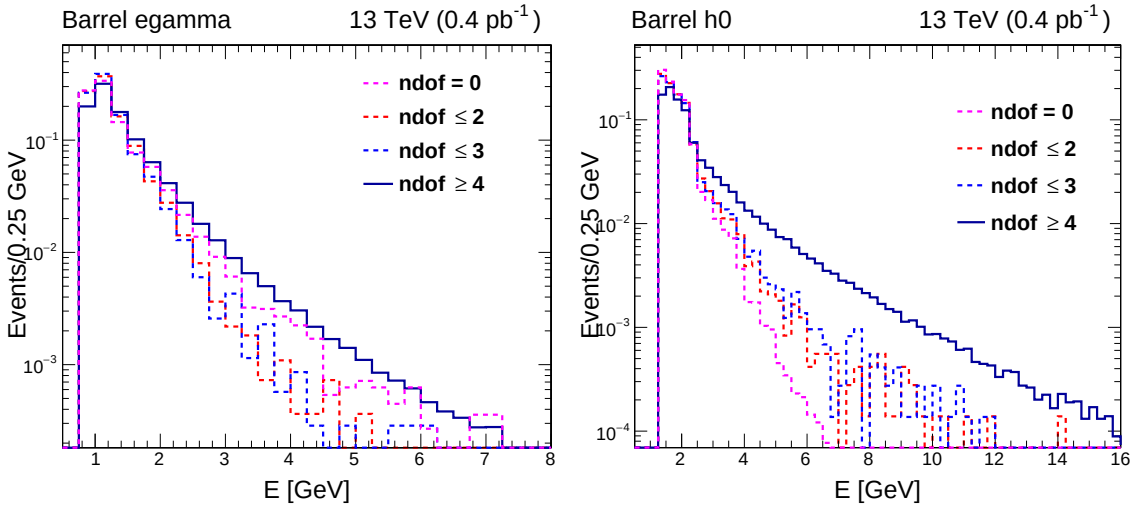

Figure B.3: Energy spectrum for photons and neutral hadrons in the barrel region with a primary vertex satisfying various cuts on the number of degrees of freedom.

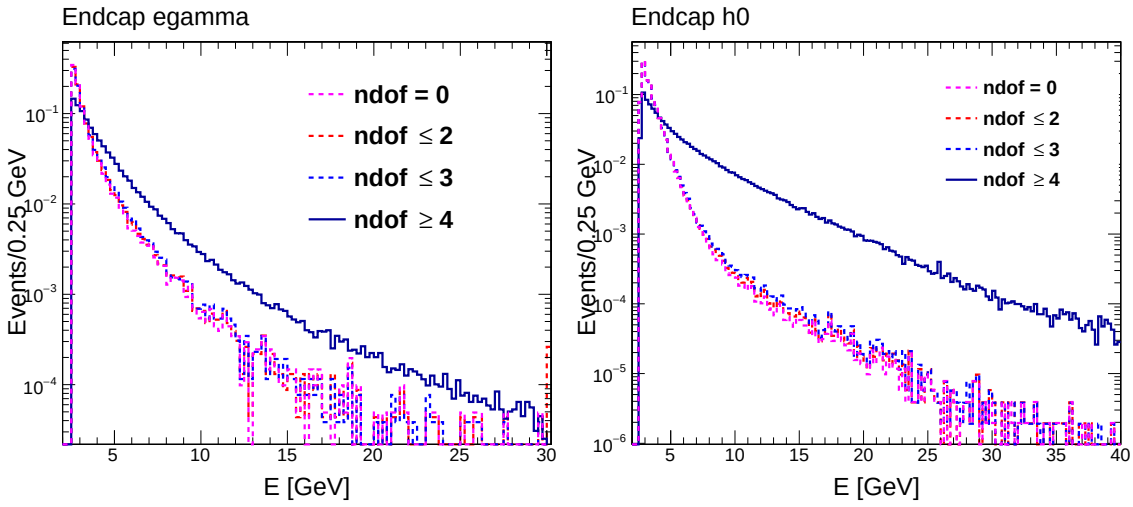

Figure B.4: Energy spectrum of photons and neutral hadrons in the endcap region with a primary vertex satisfying various cuts on the number of degrees of freedom.

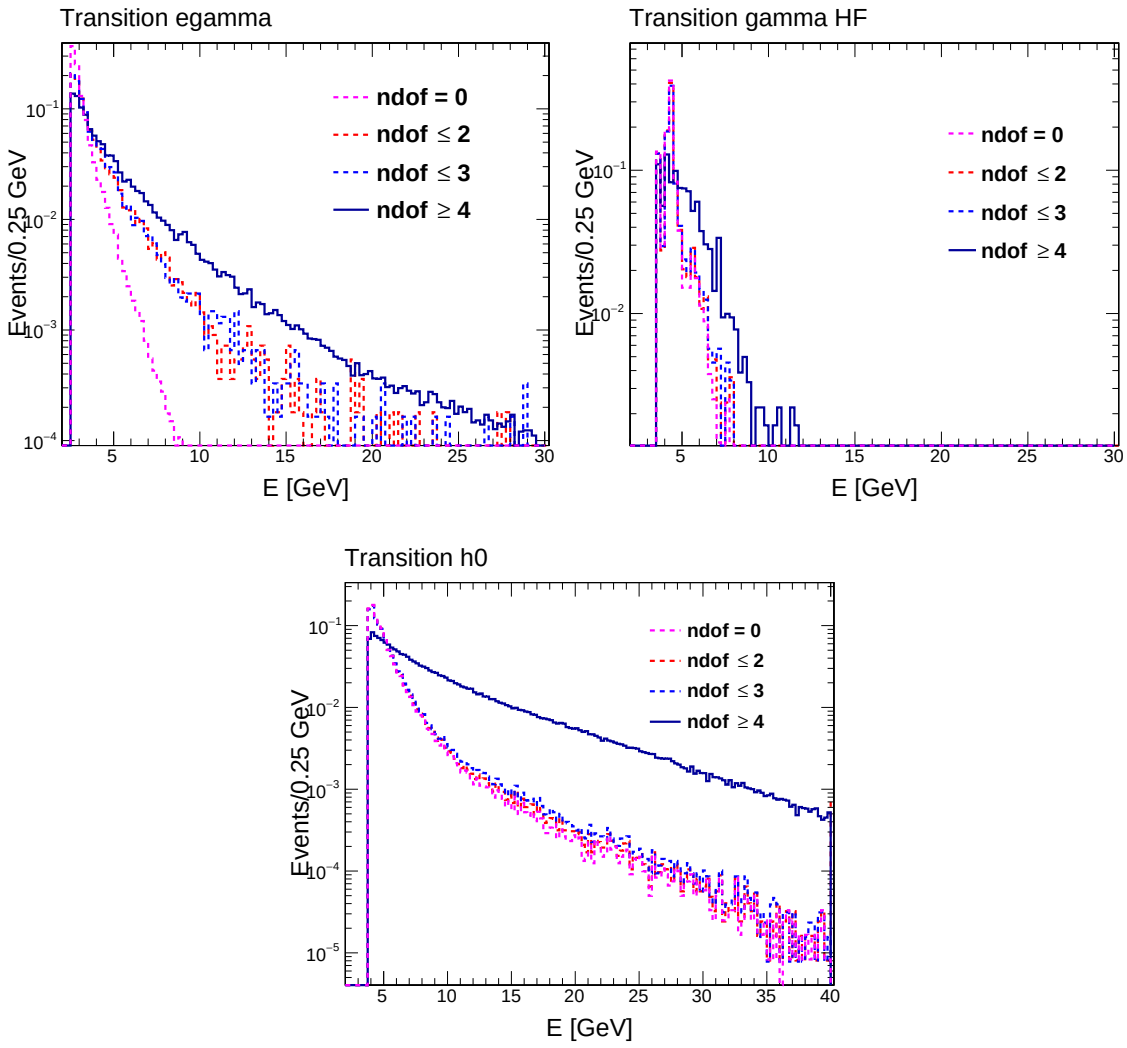

Figure B.5: Energy spectrum of photons and hadrons in the transition region with a primary vertex satisfying various cuts on the number of degrees of freedom.

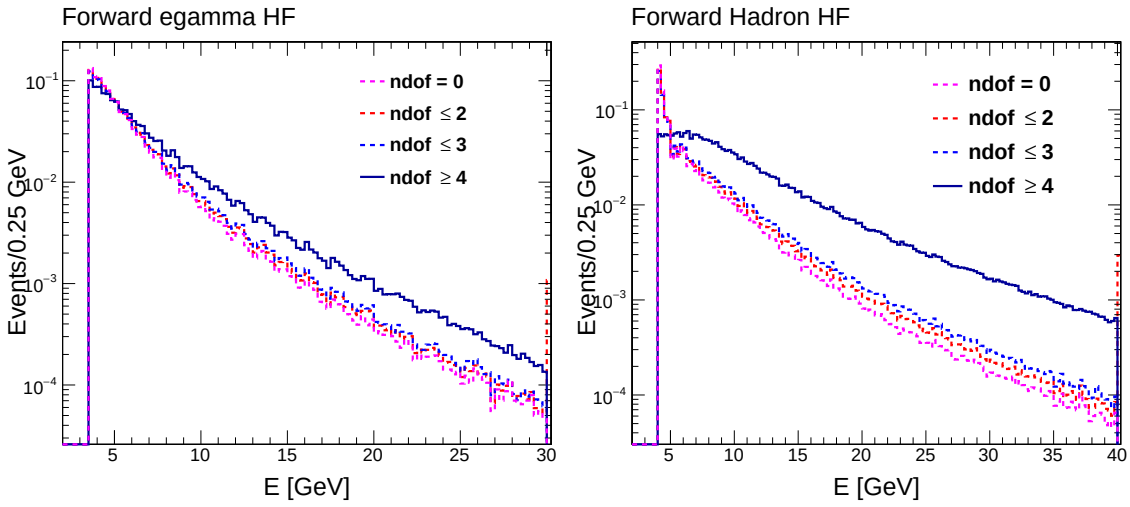

Figure B.6: Energy spectrum of photons and hadrons in the forward region with a primary vertex satisfying various cuts on the number of degrees of freedom.

C Additional color-singlet fractions

As the analysis developed, we tested other kinematic observables that may reveal more information about the color-singlet exchange in addition to the nominal main results shown in this thesis. These other distributions were discarded for the final results since they provide similar information as the distributions shown in our final results.

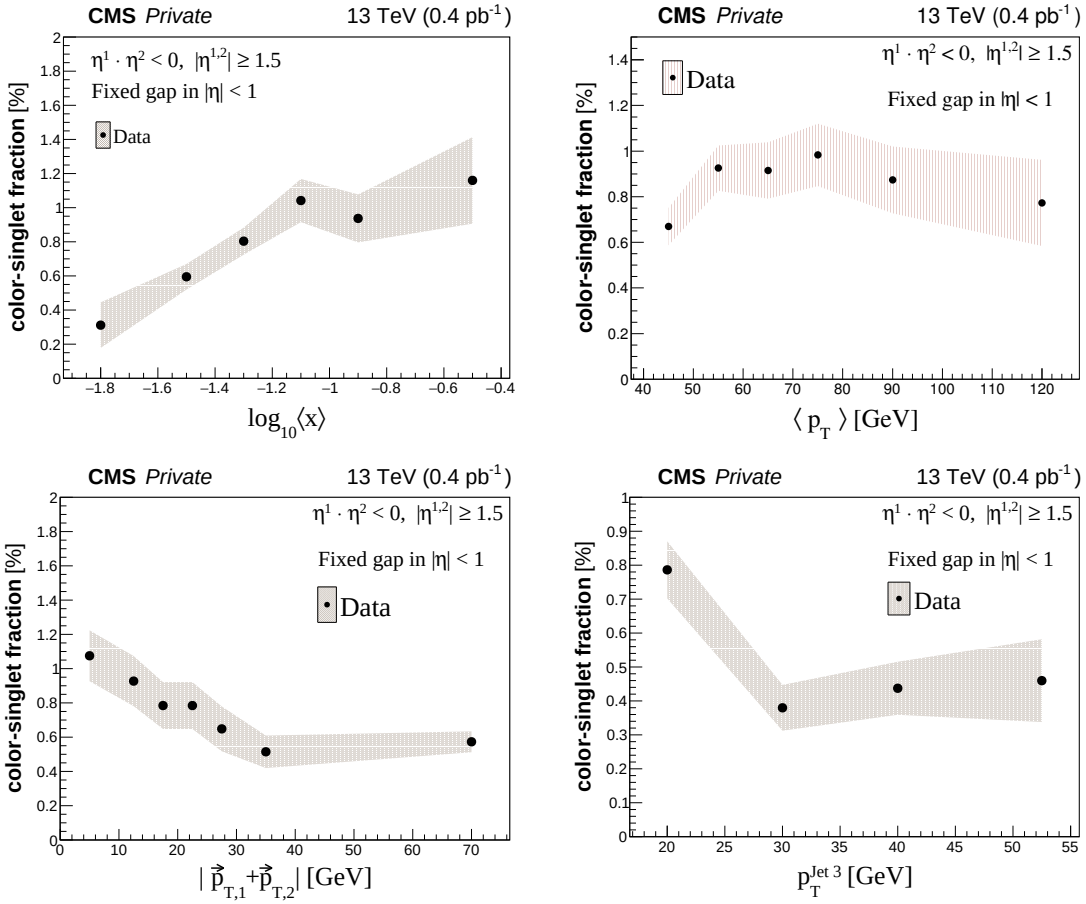

Figure B.7: Fraction of color-singlet exchange in dijet events as a function of the average partonic longitudinal momentum $\langle x \rangle$ (top left), average dijet momentum (top right), the momentum balance (bottom left) and the third jet transverse momentum (bottom right). Error band indicates statistical uncertainties only. Data points are plotted in the middle value of the respective bin.

We show the color-singlet fraction as a function of the average momentum of the leading two-jets, as seen in Fig. B.7.

To study the strong transverse momenta correlation topology favored by the color-

singlet exchange, we measured the color-singlet fraction as a function of the vectorial sum of the transverse momentum $|\vec{p}_{T,1} + \vec{p}_{T,2}|$ (see plot on the bottom left in Fig. B.7). The fraction increases as the momentum balance decreases, consistent with the expected behavior in color-singlet exchanges. Notice that this should not necessarily be the case in general; fluctuations of non-CSE dijet production with a rapidity gap could lead to the same topologies, leading to a flat dependence of the fraction f_{CSE} on the momentum balance.

In about 15% of the jet-gap-jet candidate events, there is at least one hard third jet with $p_T^{jet3} \geq 15$ GeV in dijet events with no tracks in the fixed pseudorapidity region. We verified this extra-jet activity can be attributed to the hadronization process with a generator-level dijet sample (BFKL implementation in HERWIG 6.5 by Royon–Kepka–Marquet). We can extract the fraction of color-singlet exchange events when the third jet is present as a measure of the degree of angular decorrelations between the jet-gap-jet events and the standard QCD dijet event. The extracted fraction as a function of p_T^{jet3} can be seen on the right plot of Fig. B.7. The statistical uncertainty on the fraction f_{CSE} is larger since the number of events with multi-jet activity is much smaller in this subsample, but we can observe that the gap fraction increases (decreases) strongly as the third jet transverse momenta decreases (increases). This observable is inspired by a similar study by the CDF Collaboration in Ref. (151; 150). For the final results of the analysis, we chose to extract f_{CSE} against $\Delta\phi_{jj}$, since the azimuthal angular decorrelation is more resilient to possible miscalibrations of the jet energy. In addition, by measuring the $\Delta\phi_{jj}$ decorrelations, one treats the presence of additional radiation in a more inclusive way, so we are sensitive to the production of hadrons that may not cluster into hard jets.

We also extracted the color-singlet fraction as a function of the average partonic longitudinal momentum fraction $\langle x \rangle = \frac{x^+ + x^-}{2}$ using the leading-order expression $x\pm = \frac{\sum_i E_{T,i} e^{\pm\eta_i}}{\sqrt{s}}$, with the sum performed over the leading jets, where $E_{T,i}$ is the transverse energy (see top plot in Fig. B.7). Since most of the jets have $p_T \approx 40$–50 GeV, the average partonic mo-

mentum fractions reconstructed with the jets are directly related to the pseudorapidity difference between the jets. The larger $\Delta\eta_{jj}$ is, the larger $\langle x \rangle$ is.